JOURNAL OF THE ELECTROCHEMICAL SOCIETY

ELECTROCHEMICAL
SCIENCE AND TECHNOLOGY

SOLID-STATE
SCIENCE AND TECHNOLOGY

REVIEWS AND NEWS

VOL. 122, NO. 10

OCTOBER 1975

JESOAN 122 (10) 1279-1416, 331C-352C

FUTURE MEETINGS
Of The Electrochemical Society

DALLAS, TEXAS—OCTOBER 5, 6, 7, 8, 9 & 10, 1975

Headquarters at the Sheraton Dallas Hotel

Planned symposia for the Dallas Meeting include the following Divisions and subjects:

Battery—Leclanché Cells, Nonaqueous Cells, General Session; **Corrosion**—Repassivation Kinetics, General Session; **Corrosion and Electrodeposition**—Electrodeposition of Organic Coatings; **Corrosion, Electronics, Electrothermics and Metallurgy, and Dielectrics and Insulation**—Techniques for Surface and Thin-Film Analysis and Depth Profiling; **Dielectrics and Insulation**—Dielectric Materials for Hybrid and Thin-Film Circuits, Thermal and Photostimulated Current in Insulators, General Session; **Dielectrics and Insulation and Electronics**—Recent Developments in MOS Technology; **Electrodeposition**—General Session; **Electronics**—Electrochemical Techniques for Electronic Device Fabrication, Semiconductor General Session, Materials and Processes General Session; **Electrothermics and Metallurgy**—High Temperature Processes Induced in Materials by the Absorption of Radiation, General Session; **Electrothermics and Metallurgy and Electronics**—Liquid Phase and Molecular Beam Epitaxy: Electronic and Magnetic Materials; **New Technology Subcommittee and Electrothermics and Metallurgy**—Energy Storage.

WASHINGTON, D.C.—MAY 2, 3, 4, 5, 6 & 7, 1976

Headquarters at the Sheraton Park Hotel

Planned symposia for the Washington Meeting include the following Divisions and subjects:

Battery and Electronics—Materials for Batteries and Fuel Cells; **Corrosion**—Magnetohydrodynamics, General Session; **Dielectrics and Insulation**—Dielectrics for Image and Hologram Storage and Display Devices, Refractory Materials for Display Devices, General Session; **Dielectrics and Insulation and Electronics**—Etching of Dielectrics and Insulators; **Dielectrics and Insulation, Electronics, and Electrothermics and Metallurgy**—Control and Utilization of Defects in Solids; **Electronics**—Semiconductor General Session, Surface Properties of Phosphors and Photoconductors, Luminescence General Session, Materials and Processes General Session; **Electronics and Electrothermics and Metallurgy**—International Symposium on Solar Energy, Seventh International Conference on Electron and Ion Beam Science and Technology; **Electrothermics and Metallurgy and Industrial Electrolytic**—Electrochemical Extraction Processes; **Industrial Electrolytic**—Engineering Analysis and Scale-Up of Electrochemical Systems; **Industrial Electrolytic and Organic and Biological Electrochemistry**—Industrial Electro-Organic Processes; **Physical Electrochemistry**—Spectroscopic Methods in Electrochemical Studies, General Session; **New Technology Subcommittee and Corrosion**—Corrosion in Molten Salts.

LAS VEGAS, NEVADA—OCTOBER 17, 18, 19, 20, 21 & 22, 1976

Headquarters at the Caesar's Palace Hotel

Planned symposia for the Las Vegas Meeting include the following Divisions and subjects:

Battery—Low Maintenance and Maintenance-Free Lead-Acid Batteries, Porous Electrodes, Theory and Practice, General Session; **Corrosion**—Corrosion in Scrubber Systems, Corrosion Problems in Geothermal Energy Systems, General Session; **Corrosion and Electrothermics and Metallurgy**—Properties of High Temperature Alloys; **Dielectrics and Insulation and Electronics**—Dielectrics and Semiconductors on Insulating Electronic Materials and Devices for Storage and Display; **Dielectrics and Insulation, Electronics, and Electrothermics and Metallurgy**—The Chemistry and Crystallography of Chemical Vapor Deposition of Electronic Materials; **Electrodeposition**—General Session; **Electrodeposition and Industrial Electrolytic**—High Current Density Electrode Processes; **Electronics**—LED's Mechanisms and Injection Lasers: Process Technology and Degradation, Semiconductor General Session, Materials and Structures for Integrated Optical Networks, Materials and Processes General Session; **Electrothermics and Metallurgy**—High Temperature Processes of Geological Interest; **New Technology Subcommittee**—Power Conditioning and Power Transport.

© Pellon Corp. 1975

Have you discovered "present shock"?

Immediacy.

Right now...manufacturers are discovering the solid wall of resistance consumers have set up against products of inferior quality. Today consumers demand value...products that perform and endure.

The Pellon Corporation envisioned this a decade ago, directed its research and development activities toward the inevitability of consumer control of the marketplace. Today, Pellon® brand non-wovens are the foundation of quality for products of science and industry.

Only technicians skilled in the Pellon® non-woven technology and capable of contributing to your manufacturing operations are authorized to represent us.

Pellon Corporation,
Industrial Division,
Lowell, Massachusetts 01852
(617) 459-6181

Pellon®

Non-woven textiles, a developing technology for science and industry.
A global organization with affiliated companies in W. Germany, England, Spain, Japan, Argentina, Canada

Corrosion measurements should be made before you start building!

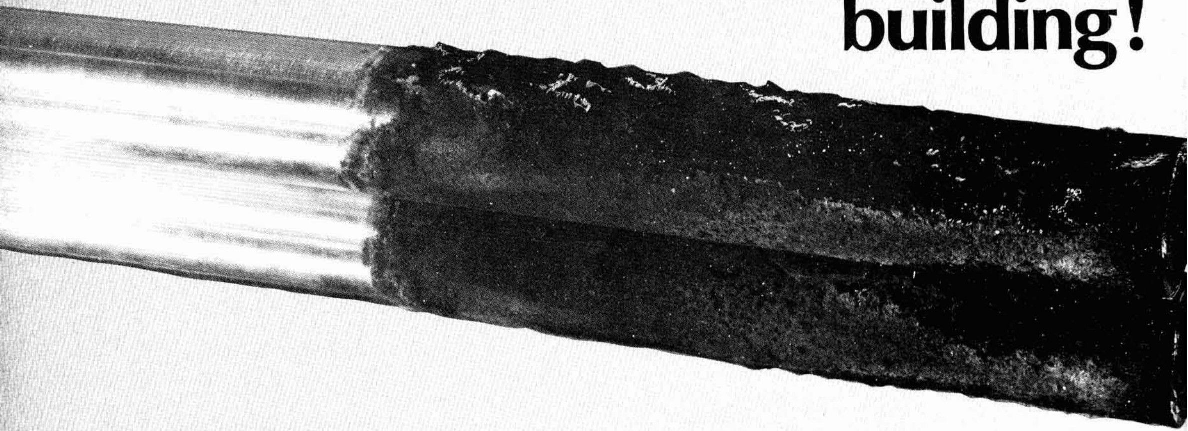

It's a smart engineer who determines the corrosion resistance of his raw materials by testing them in the intended environment. One of the simplest and fastest ways to obtain corrosion resistance information as well as corrosion rate data is by electrochemical testing. Now, for the first time *all* of the hardware and glassware required for electrochemical corrosion testing is available from a single source. Princeton Applied Research Corporation, a recognized leader in electrochemical instrumentation, provides the Model 331-1 Corrosion Measurement System and the Model 9700 Corrosion Cell to help engineers characterize metals for corrosion resistance. All that's lacking is the sample to be tested and the liquid it's to be tested in!

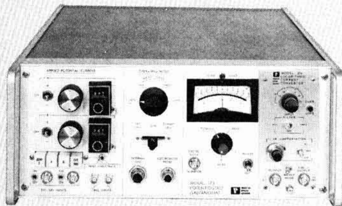

With the 331-1 System and 9700 Cell engineers can do many different types of corrosion testing, including measurements like:

- Potentiodynamic anodic polarization plots per ASTM G-5 specification to examine metals for passivity phenomena.
- Tafel slope plots and linear polarization plots for fast, accurate measurements of corrosion rates.
- Corrosion potential measurements.
- Galvanic corrosion studies.
- Galvanostatic (constant current) polarization experiments.

If you'd prefer an alternative approach to the time-consuming, tedious weight-loss measurements, and if you'd like a rational method of selecting optimum materials-environment combinations, write us. We'll be happy to send descriptive information and an application note to show how easy electrochemical testing can be when all the equipment is available from a single source.

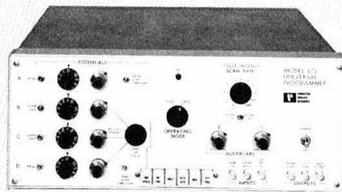

Write or call Princeton Applied Research Corporation, P. O. Box 2565, Princeton, New Jersey 08540, telephone (609) 452-2111. In Europe, contact Princeton Applied Research GmbH, D8034 Unterpfaffenhofen, Waldstrasse 2, West Germany.

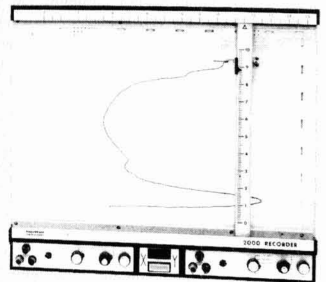

PRINCETON
APPLIED
RESEARCH

Bring back all the answers with the POTENTIODYNE® Analyzer.

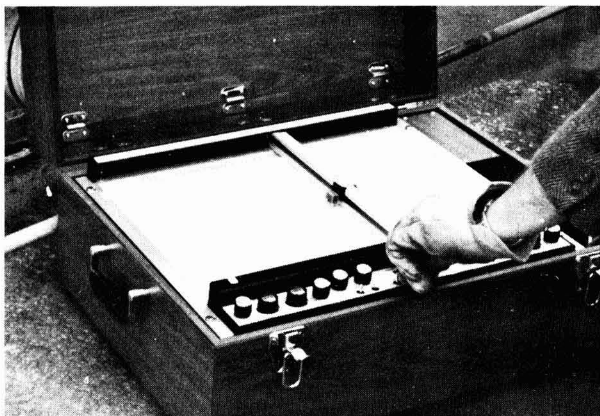

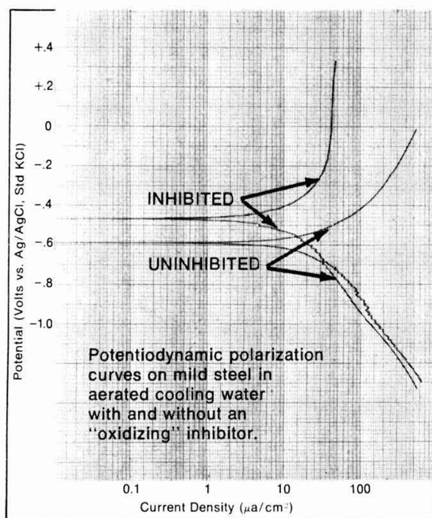

INHIBITOR EVALUATION? Increase efficiency with built-in calibration check, "zero-crossing" bipolar operation, and recording directly in current density.

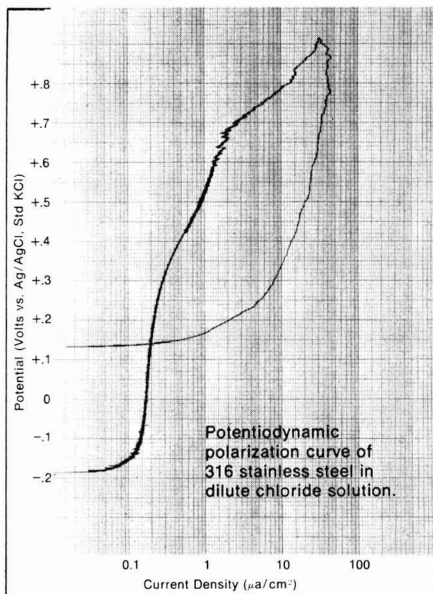

LOCALIZED CORROSION? The POTENTIODYNE system is ideally suited to measurement of the electrochemical parameters used in the study of pitting and crevice corrosion.

It's a precise, portable, automatic potentiostat. And voltage scanner. And log current converter. And X-Y recorder.

Equally suited for plant or lab use, the versatile new PETROLITE® POTENTIODYNE® Analyzer is applicable to studies of electrode reactions, metals and alloy corrosion, inhibitor performance, and other electrochemical processes. This complete measurement system permits corrosion specialists to generate polarization curves **automatically.**

Its capabilities include recording of log current density vs. time at a set potential . . . log current density vs. potential at any voltage sweep rate from 10mV/hour to 100V/hour . . . galvanic current between two samples vs. time . . . and electrode potential vs. time.

Isolated voltage sensing, separate four-wire current and voltage circuits, and solid-state design throughout insure extreme accuracy and dependability. Portable and completely self-contained, the POTENTIODYNE Analyzer requires no external units for potentiodynamic or potentiostatic measurements in either programmed or manual operation. Petreco's complete line of probes and electrodes facilitates adaptability to most operating process streams.

Circuitry, typical polarization curves, and other data are included in a new descriptive brochure. For your free copy and a technical review of "Modern Applications of Potentiodynamic Data in Research and Industry," call or write Petreco.

PA-74-1

PETRECO DIVISION

PETROLITE CORPORATION

5455 Old Spanish Trail (P.O. Box 2546), Houston, Texas 77001

Offices and representatives in Beirut, Calgary, Frankfurt, The Hague, Kuwait, London, Maracaibo, Mexico City, Paris, Port of Spain, Rome, Singapore, Tokyo, Tripoli

JOURNAL OF THE

EDITOR
Norman Hackerman

DIVISIONAL EDITORS

BATTERY
R. J. Brodd
Elton J. Cairns
F. P. Malaspina
G. F. Nordblom
Boone B. Owens
J. L. Weininger

CORROSION
Theodore R. Beck
J. W. Faust, Jr.
Z. A. Foroulis
Jerome Kruger
Ken Nobe
Earl S. Snavely, Jr.
J. Bruce Wagner

DIELECTRICS AND INSULATION
Robert S. Alwitt
Newton Schwartz
Donald M. Smyth
John Szedon
Lawrence Young

ELECTRODEPOSITION
Ugo Bertocci
Nathan Feldstein
Seymour Senderoff

ELECTRONICS
Ephraim Banks
George R. Cronin
Glenn W. Cullen
Murray Gershenzon
James S. Harris
Simon Larach
I. Arnold Lesk
Ernest Paskell
Jerome Prener
Bertram Schwartz
P. Wang
J. M. Woodall

ELECTROTHERMICS AND METALLURGY
Joan B. Berkowitz
Daniel Cubicciotti
W. E. Kuhn
W. W. Smeltzer
Jack H. Westbrook

INDUSTRIAL ELECTROLYTIC
Richard C. Alkire
Scott Lynn

ORGANIC AND BIOLOGICAL ELECTROCHEMISTRY
Manuel M. Baizer
Arthur A. Pilla
Stanley Wawzonek

PHYSICAL ELECTROCHEMISTRY
Allen J. Bard
A. J. de Bethune
Larry R. Faulkner
R. M. Hurd
George J. Janz
Barry Miller
David K. Roe
C. W. Tobias
F. G. Will

EDITORIAL STAFF
Nancy S. Walters, **Assistant to the Editor**
Jack H. Westbrook, **News Editor**
Julius Klerer, **Book Review Editor**

PUBLICATION STAFF
Sarah A. Kilfoyle, **Publication Editor**
Rachel B. Cochran, **Publication Assistant**

PUBLICATION COMMITTEE
Newton Schwartz, **Chairman**
Bruce E. Deal
Robert T. Foley
Norman Hackerman
Jerome Kruger
Paul C. Milner
Jerome S. Prener
Jack H. Westbrook

ADVERTISING OFFICE
P.O. Box 2071
Princeton, N.J. 08540

OCTOBER 1975

ELECTROCHEMICAL SCIENCE AND TECHNOLOGY

TECHNICAL PAPERS

H. R. Kunz, G. A. Gruver . . . 1279 — The Catalytic Activity of Platinum Supported on Carbon for Electrochemical Oxygen Reduction in Phosphoric Acid

H. F. Hunger, J. E. Ellison . . . 1288 — Rate Capability and Electrochemical Stability of Carbon Fluorine Compounds in Organic Electrolytes

A. F. Sammells, J. Z. Gougoutas, B. B. Owens . . . 1291 — High Conductivity Solid Electrolytes Double Salts of Substituted Organic Ammonium Halides and Cuprous Halides

Z. A. Foroulis, M. J. Thubrikar . . . 1296 — On the Kinetics of the Breakdown of Passivity of Preanodized Aluminum by Chloride Ions

V. Bostanov, G. Staikov, D. K. Roe . . . 1301 — Rate of Propagation of Growth Layers on Cubic Crystal Faces in Electrocrystallization of Silver

M. Shabrang, S. Bruckenstein . . . 1305 — Compensation of Ohmic Potential Interactions Occurring at Ring-Disk Electrodes

P. E. Sturrock, B. Vaudreuil, R. H. Gibson . . . 1311 — Studies in Derivative Chronopotentiometry II. Analysis of Multicomponent Systems

K. Tokuda, S. Bruckenstein, B. Miller . . . 1316 — The Frequency Response of Limiting Currents to Sinusoidal Speed Modulation at a Rotating Disk Electrode

TECHNICAL NOTE

K. Abe, T. Chiku . . . 1322 — The Cathodic Reaction of Iron Disulfide Electrode in KCl-LiCl Eutectic Electrolyte

ELECTROCHEMICAL SOCIETY

Vol. 122 • No. 10

SOLID-STATE SCIENCE AND TECHNOLOGY

TECHNICAL PAPERS

M. T. Montojo, F. Jaque, C. Sánchez ... 1325
Role of Anodic Processes in the Electrolytic Coloration of Alkali Halides

G. Romeo, H. S. Spacil, W. J. Pasko ... 1329
The Transport of Chromium in Cr_2O_3 Scales in Sulfidizing Environments

D. E. Carlson ... 1334
The Deposition of Tin Oxide Films from a D-C Glow Discharge

R. M. Anderson, T. M. Reith ... 1337
Microstructural and Electrical Properties of Thin PtSi Films and Their Relationships to Deposition Parameters

R. A. Clarke, R. L. Tapping, M. A. Hopper, L. Young ... 1347
An ESCA Study of the Oxide at the Si-SiO_2 Interface

Y. Watanabe, Y. Arita, T. Yokoyama, Y. Igarashi ... 1351
Formation and Properties of Porous Silicon and Its Application

K. Ikezaki, K. Wada, I. Fujita ... 1356
Temperature Dependence of Characteristics of Plastic Film Thermoelectrets

M. T. Shehata, R. Kelly ... 1359
The Formation and Structure of Anodic Films on Beryllium

F. Chernow, G. F. Ruse, G. W. Eldridge ... 1365
Photoluminescence of Epitaxial ZnSe Layers Grown on Ge

DIVISION OFFICERS

Battery Division
Bernard Agruss, Chairman
Howard R. Karas, Vice-Chairman
John P. Wondowski, Secretary-Treasurer
General Battery Corp.
P.O. Box 1262
Reading, Pa. 19603

Corrosion Division
Roger Staehle, Chairman
Jerome Kruger, Vice-Chairman
Ken Nobe, Secretary-Treasurer
University of California
Dept. of Engineering
Los Angeles, Ca. 90024

Dielectrics and Insulation Division
Benjamin H. Vromen, Chairman
Laurence D. Locker, Vice-Chairman
Kim Ritchie, Treasurer
Rudolf G. Frieser, Secretary
IBM Corp.
Computer Division
Bldg. 330-145, Dept. 365
East Fishkill Facility
Hopewell Junction, N.Y. 12533

Electrodeposition Division
John L. Griffin, Chairman
Vladimir Hospadaruk, Vice-Chairman
Nathan Feldstein, Secretary-Treasurer
Surface Technology, Inc.
P.O. Box 2027
Princeton, N.J. 08540

Electronics Division
Bertram Schwartz, Chairman
Glenn Cullen, Vice-Chairman (Semiconductors)
Melvin Tecotzky, Vice-Chairman (Luminescence)
Mort Panish, Vice-Chairman (General)
Michael Kestigian, Treasurer
Thomas Sedgwick, Secretary
IBM Corp.
Thomas J. Watson Research Center
P.O. Box 218
Yorktown Heights, N.Y. 10598

Electrothermics and Metallurgy Division
Robert Bakish, Chairman
John M. Blocher, Jr., Vice-Chairman
Stephen H. Spacil, Junior Vice-Chairman
J. Bruce Wagner, Jr., Secretary-Treasurer
Northwestern University
Dept. of Materials Science
Evanston, Ill. 60201

Industrial Electrolytic Division
D. N. Goens, Chairman
Thomas C. Jeffery, Vice-Chairman
Richard C. Alkire, Secretary-Treasurer
University of Illinois at Urbana-Champaign
School of Chemical Sciences
Dept. of Chemical Engineering
297 Roger Adams Laboratory
Urbana, Ill. 61801

Organic and Biological Electrochemistry Division
Manuel M. Baizer, Chairman
Arthur A. Pilla, Vice-Chairman
Larry Miller, Secretary-Treasurer
Colorado State University
Dept. of Chemistry
Fort Collins, Colo. 80521

Physical Electrochemistry Division
James D. E. McIntyre, Chairman
Stanley Bruckenstein, Vice-Chairman
Fritz G. Will, Secretary-Treasurer
General Electric Co.
Research and Development Center
Schenectady, N.Y. 12301

20.พ.ย.2518

SOCIETY OFFICERS AND STAFF

Theodore R. Beck, President
Electrochemical Technology Corp.
10035 31st Ave. NE
Seattle, Wash. 98125

Michael J. Pryor, Vice-President
Metals Research Laboratories
Olin Corporation
91 Shelton Ave.
New Haven, Conn. 06504

Douglas N. Bennion, Vice-President
5532 Boelter Hall
University of California
School of Engineering and Applied Science
Los Angeles, Calif. 90024

Dennis R. Turner, Vice-President
Bell Laboratories
Room 7F-506
Murray Hill, N.J. 07974

Paul C. Milner, Secretary
Bell Laboratories
Room 1D-259
Murray Hill, N.J. 07974

Frederick J. Strieter, Treasurer
78-14 Fallmeadow Lane
Dallas, Tex. 75240

V. H. Branneky, Executive Secretary
The Electrochemical Society, Inc.
P.O. Box 2071
Princeton, N.J. 08540

Ernest G. Enck, Executive Secretary Emeritus
The Electrochemical Society, Inc.
P.O. Box 2071
Princeton, N.J. 08540

Marie Falloon, Financial Secretary
The Electrochemical Society, Inc.
P.O. Box 2071
Princeton, N.J. 08540

Manuscripts submitted to the Journal should be sent, in triplicate, to the Editorial Office at P.O. Box 2071, Princeton, N.J. 08540. They should conform to the revised "Instructions to Authors" available from Society Headquarters. Manuscripts so submitted, as well as papers presented before a Society technical meeting, become the property of the Society and may not be published elsewhere in whole or in part without written permission of the Society. Address such requests to the Editor.

The Electrochemical Society does not maintain a supply of reprints of papers appearing in its Journal. A photoprint copy of any particular paper may be obtained from University Microfilms, Inc., 300 N. Zeeb St., Ann Arbor, Mich. 48106.

Inquiries regarding positive microfilm copies of volumes should be addressed to University Microfilms, Inc., 300 N. Zeeb St., Ann Arbor, Mich. 48106.

Walter J. Johnson, Inc., 355 Chestnut St., Norwood, N.J. 07648, have reprint rights to out-of-print volumes of the Journal, and also have available for sale back volumes and single issues, with the exception of the current calendar year. Anyone interested in securing back copies should correspond directly with them.

Published monthly by The Electrochemical Society, Inc., at 215 Canal St., Manchester, N.H.; Executive Offices, Editorial Office and Circulation Dept., and Advertising Office at P.O. Box 2071, Princeton, N.J. 08540, combining the JOURNAL and TRANSACTIONS OF THE ELECTROCHEMICAL SOCIETY. Statements and Opinions given in articles and papers in the JOURNAL OF THE ELECTROCHEMICAL SOCIETY are those of the contributors, and The Electrochemical Society assumes no responsibility for them.

Claims for missing numbers will not be allowed if received more than 60 days from date of mailing plus time normally required for postal delivery of JOURNAL and claim. No claims allowed because of failure to notify the Circulation Dept., The Electrochemical Society, P.O. Box 2071, Princeton, N.J. 08540, of a change of address, or because copy is "missing from files." Subscription to members as part of membership service; subscription to nonmembers $50.00 plus $5.00 for postage outside U.S. and Canada. Single copies $3.25 to members, $5.00 to nonmembers. © Copyright 1975 by The Electrochemical Society, Inc. Second Class Postage Paid at Princeton, New Jersey, and at additional mailing offices. Printed in U.S.A.

SOLID-STATE SCIENCE (Cont.)

M. J. Bowden, E. A. Chandross ... 1370 — Poly(Vinyl Arene Sulfones) as Novel Positive Photoresists

D. E. Davies, J. K. Kennedy, C. E. Ludington ... 1374 — Comparison of Group IV and VI Doping by Implantation in GaAs

R. Bhat, B. J. Baliga, S. K. Ghandhi ... 1378 — Vapor-Phase Etching and Polishing of Gallium Arsenide Using Hydrogen Chloride Gas

V. S. Ban, S. L. Gilbert ... 1382 — Chemical Processes in Vapor Deposition of Silicon I. Deposition from $SiCl_2H_2$ and Etching by HCl

V. S. Ban ... 1389 — Chemical Processes in Vapor Deposition of Silicon II. Deposition from $SiCl_3H$ and $SiCl_4$

R. G. Sommer, E. D. Cater ... 1391 — A Solid-State Galvanic Cell Study of the Ti_2O_3, Ti_3O_5 Equilibrium

T. J. Truex, R. B. Saillant, F. M. Monroe ... 1396 — Mechanisms of Decomposition of Organochromium Compounds in the CVD Process Cycloheptatriene Chromium Tricarbonyl

S. Vojdani, A. E. Dabiri, M. Tavakoli ... 1400 — Theoretical Aspects of the Peltier Effect on the Temperature Distribution in Crystal Grown by the Czochralski Technique

TECHNICAL NOTE

S.-S. Lin ... 1405 — Mass Spectrometric Analyses of Vapor in Chemical Vapor Deposition of Alumina

BRIEF COMMUNICATIONS

R. J. Zeto, C. G. Thornton, E. Hryckowian, C. D. Bosco ... 1409 — Low Temperature Thermal Oxidation of Silicon by Dry Oxygen Pressure above 1 Atm

S. Marshall, R. J. Zeto, C. G. Thornton ... 1411 — Dry Pressure Local Oxidation of Silicon for IC Isolation

S. Okuma ... 1413 — New Method of Manufacturing Sintered-Type Aluminum Solid Electrolytic Capacitor

REVIEWS AND NEWS

W. G. Schneider ... 337C — Science and Technology—The New Challenges

NEWS

... 341C

JOURNAL OF THE ELECTROCHEMICAL SOCIETY

ELECTROCHEMICAL SCIENCE
AND TECHNOLOGY

OCTOBER
1975

EST

The Catalytic Activity of Platinum Supported on Carbon for Electrochemical Oxygen Reduction in Phosphoric Acid

H. R. Kunz and G. A. Gruver

Power Systems, Division of United Technologies Corporation, South Windsor, Connecticut 06074

ABSTRACT

An experimental program was conducted to determine the catalytic activity of high surface area platinum supported on carbon for the electrochemical reduction of oxygen in phosphoric acid. The Tafel slope at 160°C in 96 weight per cent phosphoric acid was found to be approximately 90 mV/decade. The exchange current per unit of real surface area of the supported platinum was found to be approximately the same as that of platinum black or a flat platinum sheet if the effect of electrode prepolarization is considered. Additional tests at other temperatures indicated that the Tafel slope varies as $RT/\mathbf{F}$ and is similar in sulfuric and phosphoric acid at the same temperature. The prediction that a double Tafel slope exists when oxygen diffusional resistance becomes significant in a Teflon-bonded porous electrode was confirmed.

Although a considerable amount of experimental work had been done to determine the Tafel slope and exchange current for the electrochemical reduction of oxygen in acidic electrolytes, uncertainty still existed concerning the true value of these quantities for high surface area platinum when supported on carbon. These uncertainties were present for a number of reasons.

First, the experimental data on Tafel slope were not in good agreement. For example, the data of Vogel and Lundquist (1) at 120°C in 85% phosphoric acid indicated a Tafel slope of 60 mV/decade for platinum black, whereas the data of Appleby (2) indicated a Tafel slope of 80 mV/decade at 116°C in 85% phosphoric acid in what he considered to be an oxide-free platinum sheet. Vogel and Lundquist indicated that this difference could be due to a true difference between the catalytic properties of the two surfaces or due to impurities on the platinum when tested as a smooth surface.

Secondly, the measured temperature effect on Tafel slope was not consistent. Appleby found the Tafel slope in 85% phosphoric acid to be equal to $RT/\mathbf{F}$ on a flat sheet. However, Vogel and Lundquist found the Tafel slope in 85% phosphoric acid at 120°C to be approximately 60 mV/decade and about equal to that in 50% phosphoric acid at 70°C and 20% sulfuric acid at 70°C.

Thirdly, the data of Vogel and Lundquist for platinum black in phosphoric acid was obtained at potentials above 0.9V with respect to a hydrogen reference electrode in the same electrolyte. This was necessary because diffusional resistance to oxygen migration through the electrolyte within the platinum black was found to occur at lower potentials. The Tafel slope was not measured in phosphoric acid at potential levels significantly lower than 0.9V. Since a change in the oxidation state of the platinum surface occurring in the vicinity of 0.9V might cause a change in the mechanism for oxygen reduction (3), extrapolating a linear Tafel line to lower potentials is not justifiable. An extensive study of the surface oxidation state of platinum has been made by Conway *et al.* (4-6).

Fourth, a measurement of the Tafel slope for platinum supported on carbon is difficult at potentials above 0.9V because of the mixed potential caused by oxidation of platinum and carbon.

Finally, if a high surface area platinum supported on carbon is considered, the catalytic properties can be affected by the size of platinum crystallites and the support. Small crystallite sizes of the supported platinum as compared to those of platinum black might affect the Tafel slope and exchange current. Also, a catalytic interaction between the platinum and carbon might be present for small platinum crystallites.

Because of the uncertainties that existed concerning the true activity of high surface area supported platinum for the reduction of oxygen in acidic electrolyte, a theoretical and experimental program was undertaken to clarify this situation.

Theory

A number of theoretical studies have been performed on Teflon-bonded platinum black electrodes. Brown and Horve (7) derived a model based on cylindrical platinum agglomerates and applied this to cathodes operating in potassium hydroxide electrolyte. This model was also used by Giner (8). Kosinski (9) applied this model to phosphoric acid electrolyte and found the model capable of rationalizing the platinum black data of Vogel and Lundquist using a Tafel slope of 65 mV/decade at 120°C in 85% phosphoric acid. This value was essentially the same as that extracted by Vogel and Lundquist.

The use of such a theoretical model is definitely limited because of the number of fitting parameters

Key words: platinum, oxygen reduction, phosphoric acid, cathode theory, Tafel slope.

that are needed to rationalize the experimental data and the assumptions that are made in the model. Tafel slope, exchange current, agglomerate diameter, agglomerate porosity, agglomerate tortuosity, and electrolyte film thickness surrounding the agglomerate are all fitting parameters. Nevertheless, a great deal of information can be obtained about the operating characteristics of electrodes through the use of a theoretical model.

At low levels of current and high potentials, the polarization of an electrode is controlled by a mixed potential between the reduction of oxygen and oxidation of carbon, platinum, and possible impurities (10). As the current is increased, the polarization should follow the Tafel line of the electrochemical reaction if the currents are high enough to make mixed potential effects negligible and other losses are adequately small. These include the losses associated with oxygen, ion, and electron migration to the reaction site. This region of the data can be used to obtain the Tafel slope and exchange current.

Once the centers of the majority of agglomerates start to experience a significantly reduced oxygen activity, the polarization curve starts to follow a slope which is twice the Tafel slope, in the absence of significant ohmic polarization and electrolyte concentration gradients. If a wide distribution of agglomerate sizes is present, a wide transitional region will exist with slopes between the Tafel slope and double Tafel slope. The current at which the polarization curve changes from a single to a double Tafel slope can be used to obtain a measure of an average agglomerate size.

This model was extended to Teflon-bonded electrodes containing supported platinum in order to get a better understanding of their operation. The resulting equations are similar to those derived previously for unsupported catalyst. When all of the electrode polarization is that associated with the finite rate of the electrochemical reaction, the Tafel equation results in the form

$$i = W_{Pt} S_g i_o e^{\alpha N \mathbf{F} \eta / RT} \qquad [1]$$

where i = electrode current density, A/cm^2 frontal area; W_{Pt} = platinum loading, g/cm^2 frontal area; S_g = platinum surface area, cm^2/g; i_o = exchange current, A/cm^2 Pt real area; α = transfer coefficient; N = number of electrons in the rate-determining step, equiv./mole; $\mathbf{F}$ = Faraday constant, coulomb/equiv.; η = polarization, V; R = gas constant, joule/mole°K; T = temperature, °K.

When the ability of oxygen to diffuse through the electrolyte in a porous cylinder of supported catalyst is also controlling, the following equation results for suitably large values of

$$\frac{R_{agg}}{2}\left(\frac{S_g W_{Pt} i_o \tau e^{\alpha N \mathbf{F} \eta/RT}}{N \mathbf{F} L D_{O_2} \alpha_{O_2} \theta}\right)^{1/2}:$$

$$i = \frac{2W_{Pt}}{R_{agg}}\left[\frac{N\mathbf{F} D_{O_2}\alpha_{O_2} S_g i_o}{\rho_s W_{Pt}/W_s}\cdot\frac{\theta}{(1-\theta)\tau}\right]^{1/2} e^{\alpha N \mathbf{F}\eta/2RT} \qquad [2]$$

where R_{agg} = agglomerate radius, cm; L = electrode thickness, cm; W_s = support loading, g/cm^2 frontal area; $D_{O_2}\alpha_{O_2}$ = oxygen diffusivity-solubility product, mole/cm sec; ρ_s = support density, g/cm^3; θ = agglomerate porosity; τ = agglomerate tortuosity.

As demonstrated by Eq. [1], the theory of supported platinum electrodes indicates that in the Tafel region the current at a given potential varies linearly with the catalyst loading if the catalyst specific activity is constant. In the double Tafel region described by Eq. [2], however, if the carbon loading is fixed and the platinum specific activity is fixed, the current at a given potential should vary with the square root of the platinum loading. Therefore, it was concluded that, if experimental data could be obtained over a wide range of platinum loading, the variation of current with loading could be used to determine whether the single or double Tafel slope is occurring. The Tafel slope could therefore be obtained. Since as the catalyst loading is reduced the relative importance of the diffusional resistance to oxygen in the catalyst layer is diminished, it was thought that experimental data on Tafel slope would become available at lower levels of potential, in the range of 0.7V. This potential is significantly below that at which a change in the oxidation state of the platinum occurs.

Such a test series was therefore performed in this study together with investigations of the effect of temperature in phosphoric acid and the effect of changing the electrolyte to sulfuric acid. The latter tests were run to determine whether or not the Tafel slope varies with $RT/\mathbf{F}$ as found by Appleby and to compare results with those of other investigators. Experiments were also performed on cathodes with reduced Teflon content to increase the effective agglomerate size. A well-defined double Tafel slope was hoped to result in these experiments and therefore confirm the findings obtained in the study in which platinum loading was varied. Finally, some experiments were performed on a flat platinum sheet to obtain data at temperatures higher than those investigated by Appleby.

Experiments

The electrodes used in this study contained platinum supported on Vulcan XC-72 (Cabot Corporation). The nitrogen BET surface area of this support was measured and found to be about 220 m^2/g. Platinum was deposited upon this carbon and it was fabricated into Teflon-bonded electrodes.

Electron micrographs of this carbon-containing platinum are shown in Fig. 1 and 2 for untested specimens. Figure 1 is a "bright field" micrograph in which the platinum appears as dark particles overlaid on the semitransparent carbon. In Fig. 2 the white spots are "reflections" arising from (111) platinum (same sample field as in Fig. 1). This micrograph confirms that the dark spots in Fig. 1 are in fact platinum. Platinum

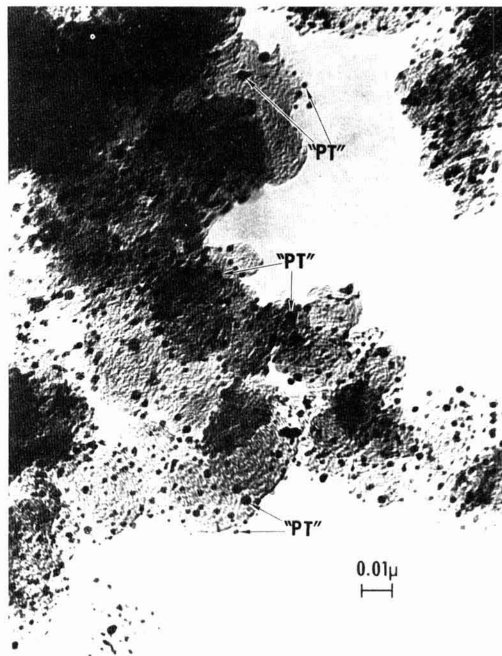

Fig. 1. Electron photomicrograph of platinum supported on Vulcan XC-72 (bright field).

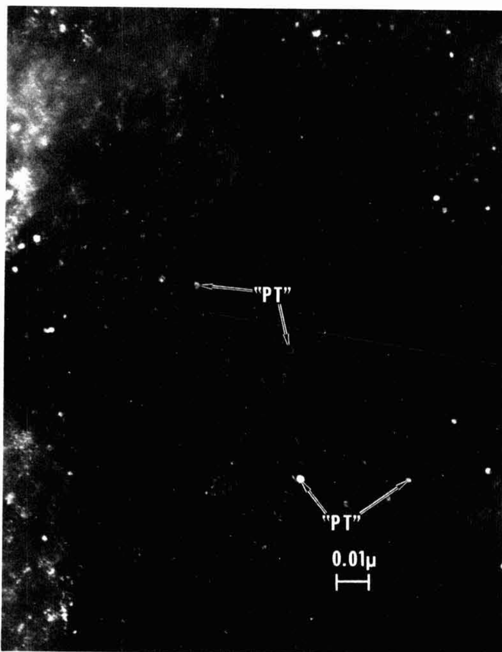

Fig. 2. Electron photomicrograph of platinum supported on Vulcan XC-72 (dark field).

crystallite sizes were measured from these micrographs and found to result in a platinum surface area of approximately 130 m^2/g, assuming the particles to be spherical and all of the platinum surface exposed. The range of surface areas from micrographs of other samples of this catalyst was 109-175 m^2/g.

Platinum surface areas were also measured electrochemically using hydrogen adsorption in sulfuric acid for samples of electrodes containing about 0.25 mg Pt/cm^2. These areas were found to be about 60-70 m^2/g after the electrodes had been tested. These areas are considerably lower than the areas calculated from platinum crystallite sizes measured using the electron microscope micrographs.

The difference in surface areas obtained from the micrographs and from hydrogen adsorption might be due to a number of reasons. For example, some of the platinum crystallite surface is in contact with the carbon and might be blocked with respect to hydrogen adsorption. In addition, part of the platinum area is lost due to recrystallization, part might not be adequately wet by electrolyte to act as effective catalyst, and some might be in poor electronic contact. Since the important platinum area with respect to the determination of catalytic activity is that which is used in an electrode, a typical area of 70 m^2/g was used in the rest of this study.

The supported platinum was fabricated into electrodes using Teflon 30 (E. I. du Pont de Nemours & Company). A photograph of the cross section of an electrode is shown in Fig. 3. Figure 4 shows an electron micrograph of a microtomed section of a catalyst layer. The Teflon and the carbon can be seen to be present in distinct segregated regions.

Electrodes were tested in a glass half-cell apparatus as 1 cm^2 floating electrodes as shown in Fig. 5. The catalyst layer was located facing the electrolyte with the carbon paper facing upward toward the reactant supply. A platinum black hydrogen reference electrode operating in the same electrolyte was used in conjunction with a Luggin capillary. The counterelectrode was a platinum screen enclosed in a separate electrolyte

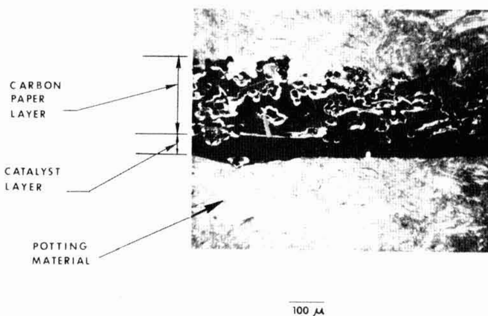

Fig. 3. Optical photomicrograph of an electrode cross section

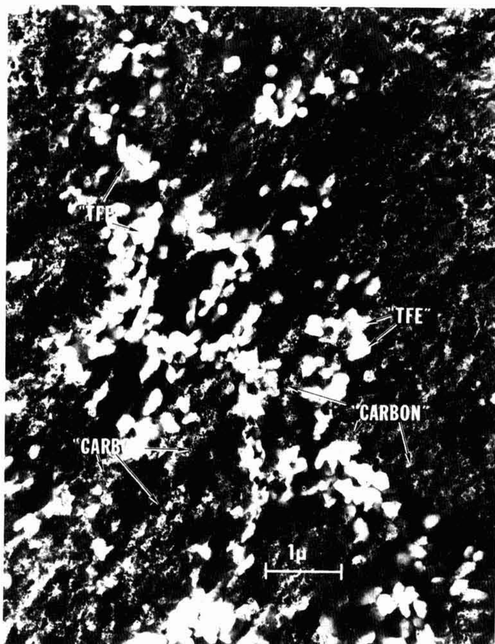

Fig. 4. Electron photomicrograph of an ultramicrotomed section of an electrode catalyst layer.

region. Current was collected from the top of the working electrode using a platinum spring. The volume of electrolyte in the apparatus was approximately 30-40 ml. Both Baker and Adamson reagent grade H_3PO_4 and acid which had been electrochemically cleaned by absorption of impurities on platinum black at hydrogen potential were used. Temperature was controlled using an electrically heated mantle surrounding the electrolyte vessel with the sensing thermocouple in the electrolyte. Electrode potentials, E^*, were measured relative to a hydrogen reference electrode in the same electrolyte and were corrected for external resistance by using a current interrupter. Load currents were supplied by a constant current source and were measured using a precision 1% resistor located in the counterelectrode line. Electrode voltage and current were monitored using either an electronic digital voltmeter accurate to 0.2% of full scale (1.999V) or an electromechanical voltmeter accurate to 0.5%. Reactant gases were saturated to provide a water vapor pressure in equilibrium with the electrolyte.

No prepolarization of electrodes was performed in general since this might introduce errors in the steady-

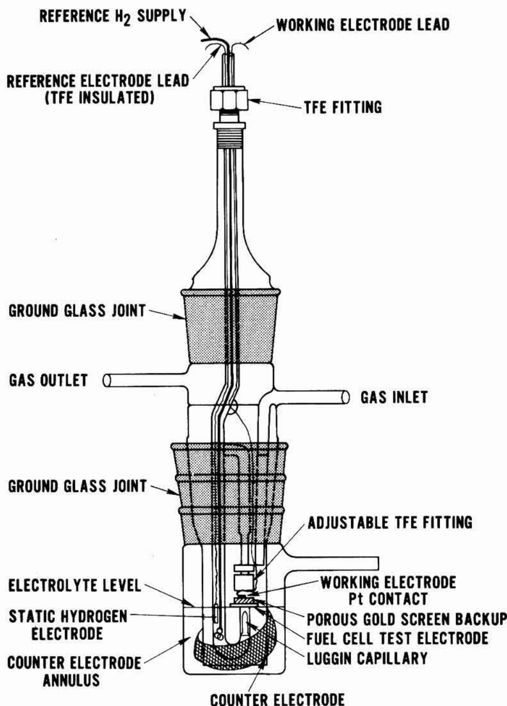

Fig. 5. Half-cell apparatus

state activity due to possible effects of phosphate anion adsorption and the extent of adsorbed oxygen coverage (11). Data were obtained by both increasing current in steps and decreasing current in steps through the potential range of interest, about 0.9-0.7V. Little difference in results was found. Potentials in this range were stable for at least 5 min. Data at higher potentials changed somewhat with time due possibly to anion desorption, platinum oxidation, or mixed potential effects due to oxidation of the carbon, platinum, and possible impurities. Data at high current densities changed with time due to possible electrode heating. Some experiments were performed on a flat platinum sheet to investigate the effect of prepolarization since both Appleby and Vogel and Lundquist incorporated prepolarization treatments.

Results

As discussed in the Theory section, a number of separate experimental studies were conducted to evaluate the activity of platinum. The first of these involved an investigation of the effects of a variation of the platinum loading with a constant carbon loading with phosphoric acid electrolyte. Others involved investigations of the effect of temperature and of operation with sulfuric acid rather than phosphoric acid. In addition, electrodes were evaluated in which definite diffusional losses had been introduced. A final investigation involved tests on flat sheets in order to obtain an extension of the data of Appleby to higher temperatures. The results obtained in these various investigations are presented in the following sections.

Variation of platinum loading.—A series of electrodes were prepared containing 15, 1.5, and 0.15 weight per cent (w/o) platinum applied to Vulcan XC-72. The weight per cent of Teflon in the supported catalyst and Teflon mixture was held constant at 50%. These weight per cents of platinum resulted in platinum loadings of about 0.25, 0.025, and 0.0025 mg/cm^2, respectively. These platinum loadings were verified by chemical analysis.

Each one of these electrodes was tested as a floating electrode in the half-cell apparatus on both oxygen and air at atmospheric pressure at 160°C in unpurified 96% H_3PO_4. Graphs of the experimental data for these various electrodes are presented in Fig. 6 through 8.

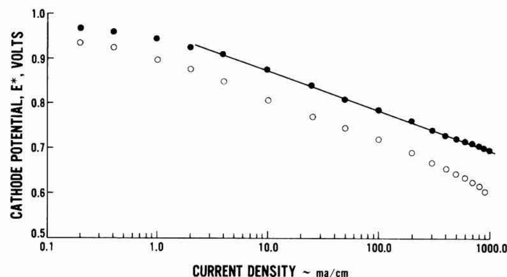

Fig. 6. Cathode performance for 0.25 mg Pt/cm^2 supported on Vulcan XC-72 at 160°C in 96% H_3PO_4. ●, Oxygen; ○, air. A straight line with a slope of 90 mV/decade has been drawn through the oxygen data.

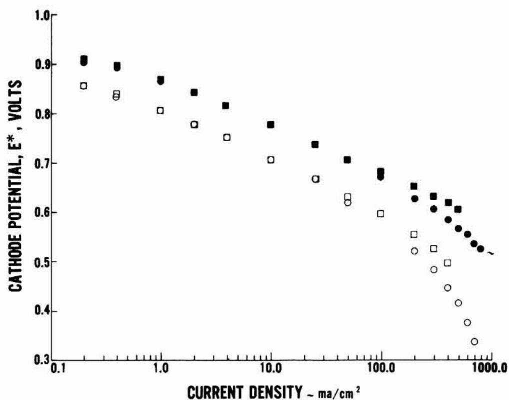

Fig. 7. Cathode performance for 0.025 mg Pt/cm^2 supported on Vulcan XC-72 at 160°C in 96% H_3PO_4. ●, Oxygen; ○, air; with high concentration platinum solution. ■, Oxygen; □, air; with low concentration platinum solution (two sets of data).

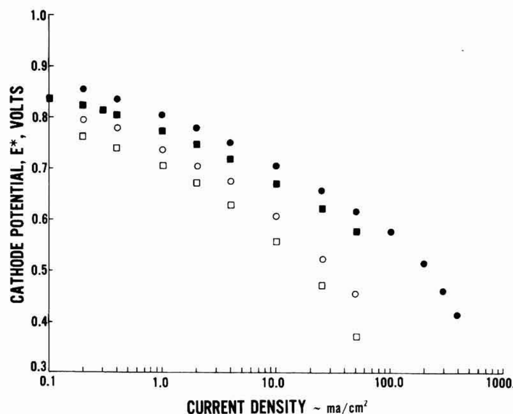

Fig. 8. Cathode performance for 0.0025 mg Pt/cm^2 supported on Vulcan XC-72 at 160°C in 96% H_3PO_4. ●, Oxygen; ○, air; with high concentration platinum solution. ■, Oxygen; □, air; with low concentration platinum solution.

During the fabrication of the electrodes with the loadings of 0.025 and 0.0025 mg Pt/cm^2, two different concentrations of the platinum catalyzation solution were used. This was done in order to investigate whether or not the small quantity of platinum was being uniformly distributed throughout the Vulcan. The data presented in Fig. 7 and 8 show that adequately uniform catalyzation of the Vulcan had been achieved.

By investigating Fig. 6-8 some of these electrodes can be seen to demonstrate a straight line variation of cathode potential with the logarithm of current density over a range of potential below 0.9V. As discussed in the Theory section, if the variation of current at a given potential varies linearly with platinum loading in a straight line region, the straight line region represents a region in which the Tafel slope is occurring. If the variation of current at a given potential varies with the square root of the loading, this straight line region is a double Tafel region rather than a single Tafel region. For this reason a graph was made of current density at 0.7V cathode potential *vs.* loading. This graph is shown in Fig. 9. As can be seen in this figure, all the experimental points fall along an approximate straight line with a slope of 45°, thereby showing a linear dependence between the current at a given potential and the loading. The straight line segments on the performance curves of these various cathodes in the range of 0.7-0.9V therefore represent the true single Tafel slope for the reduction of oxygen. The value of this slope is approximately 90 mV/decade.

The possibility existed in this investigation that a systematic change in the electrode structure might be occurring as the platinum loading is being changed, thereby leading to an erroneous conclusion. To eliminate this possibility, an electrode was fabricated containing no platinum with the same quantity of Vulcan as was used in the study in which the platinum content was varied between 0.25 and 0.0025 mg/cm^2. This electrode was subsequently catalyzed with 0.25 mg Pt/cm^2 and resulted in essentially the same experimental results as the electrode which was precatalyzed with 0.25 mg Pt/cm^2. Therefore, no systematic effect of electrode structure was present in the data.

The theory of fuel cell electrodes indicated that the limiting current should not depend on the platinum loading for a given carbon loading. However, the experimental data obtained here indicated limiting currents on air of approximately 2000 mA/cm^2 for the 0.25 mg/cm^2 loading, 1300 mA/cm^2 for the 0.025 mg/cm^2 loading, and 110 mA/cm^2 for the 0.0025 mg/cm^2 loading. This result at first indicated that perhaps the results for the lowest loading were not being interpreted correctly. However, a theoretical investigation of oxygen diffusion through the electrolyte film surrounding the agglomerate to single platinum crystallites on the surface of the agglomerate indicated that, with this loading, an additional diffusional resistance of oxygen in the electrolyte was present due to the scarcity of the platinum crystallizates on the surface of the agglomerate. This additional diffusional resistance was calculated to be absent at the low currents and high potentials occurring in the range of data that was being used to evaluate the variation of current at a given potential with platinum loading. Therefore, the fact that the limiting current declined with loading is probably of no consequence.

A variation of the platinum specific area with loading would also affect the variation of electrode performance with loading. The platinum specific area might be expected to increase as the loading is reduced. This would tend to make the variation of current at a given potential vary in less than a linear manner with loading in the Tafel region, just as the presence of a diffusional resistance would. Therefore, the variation of platinum specific area with loading is probably not causing this linear dependence. The specific area could not be measured electrochemically for the loadings of 0.025 and 0.0025 mg/cm^2 because of the greater relative capacitive effect of the Vulcan.

Variation of temperature.—A series of tests was performed on the 0.25 mg Pt/cm^2 cathode to determine the variation of the Tafel slope and the current at a given potential with temperature. These tests were run using both unpurified 96% H_3PO_4 and purified and unpurified 85% H_3PO_4 in the half-cell apparatus. The cathode performance data are presented in Fig. 10 and 11. Figures 12 and 13 present a comparison with the experimental data of Appleby. The data on Tafel slope obtained with unpurified 85% H_3PO_4 in this study are in good agree-

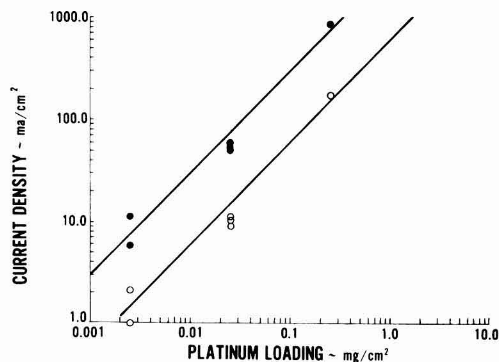

Fig. 9. Variation of current density with Pt loading for Pt supported on Vulcan XC-72 at 160°C in 96% H_3PO_4. ●, Oxygen; ○, air. $E^* = 0.7$ V. Lines represent a linear relationship between variables for oxygen and air.

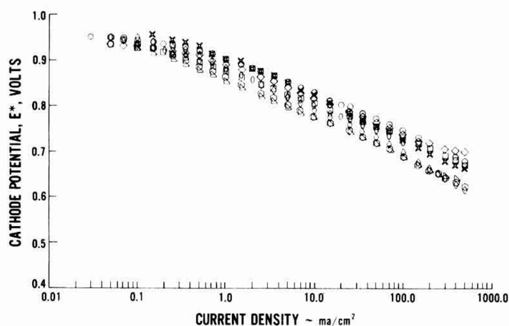

Fig. 10. Cathode performance on oxygen for 0.25 mg Pt/cm^2 supported on Vulcan XC-72 at various temperatures. ○, 121°C; □, 113°C; ◇, 95°C; X, 77°C; ◇, 66°C; ⬡, 54°C; △, 49°C with unpurified 85% H_3PO_4. ○, 46°C with purified 85% H_3PO_4.

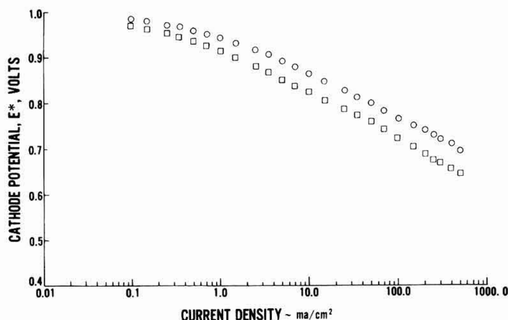

Fig. 11. Cathode performance on oxygen for 0.25 mg Pt/cm^2 supported on Vulcan XC-72 at various temperatures with unpurified 96% H_3PO_4. ○, 129°C; □, 91°C.

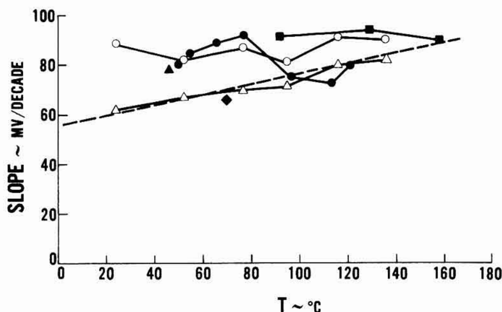

Fig. 12. Variation of oxygen Tafel slope with temperature for various acid compositions. Data of Appleby: △, purified 85% H_3PO_4; ○, analytical grade H_3PO_4. Data of this study: ▲, purified 85% H_3PO_4; ●, unpurified 85% H_3PO_4; ■, unpurified 96% H_3PO_4; ♦, 20% H_2SO_4. The dotted line represents a Tafel slope which is proportional to absolute temperature.

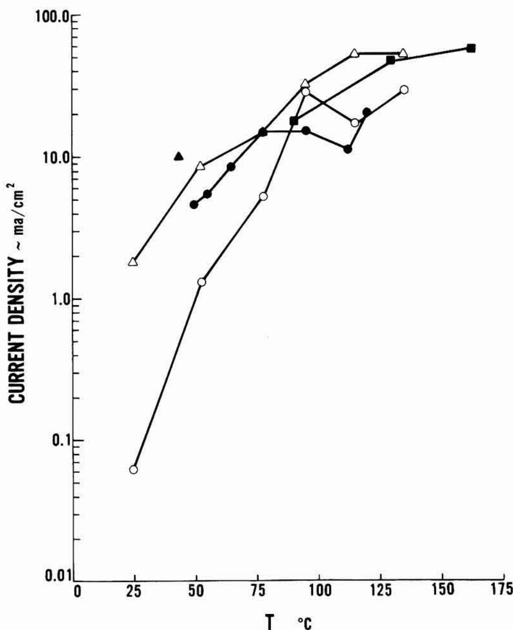

Fig. 13. Variation of oxygen reduction current at 0.8V with temperature for various acid compositions. Data of Appleby: △, purified 85% H_3PO_4; ○, analytical grade H_3PO_4. Data of this study: ▲, purified 85% H_3PO_4; ●, unpurified 85% H_3PO_4; ■, unpurified 96% H_3PO_4.

ment with the data of Appleby for purified acid at temperatures above 95°C. This agreement could be due to the smaller effect of electrolyte impurities on the larger platinum surface area in the fuel cell electrode used here compared to that of the flat sheet used by Appleby. Below 95°C, the Tafel slope obtained with the fuel cell electrode in unpurified and purified 85% H_3PO_4 is in agreement with the data of Appleby for unpurified electrolyte. This increase in Tafel slope at lower temperatures for the fuel cell electrode is probably due to an increase in the relative importance of electrolyte impurities at lower temperature. With unpurified 96% H_3PO_4, the Tafel slope was 90 mV/decade at 160°C, was relatively insensitive to temperature, and showed a trend similar to that of Appleby for unpurified 85% H_3PO_4. This result might be caused by an increase in the effect of impurities in the more highly concentrated electrolyte.

In the comparison of the variation of current at a given potential with temperature with the variation found by Appleby, the area of the platinum on the fuel cell electrode was considered to be 70 m^2/g. Using this value of surface area, the value of current at a given potential can be seen to be in fair agreement with the data obtained by Appleby for 85% H_3PO_4. The data obtained in this study at 96% H_3PO_4 were somewhat higher than that obtained with 85% H_3PO_4.

Tests using sulfuric acid.—Tests were run in 20% H_2SO_4 at 70°C on a sample of a 0.25 mg Pt/cm^2 electrode that demonstrated 90 mV/decade Tafel slope using 96% H_3PO_4 at 160°C. These data are presented in Fig. 14. The data with H_2SO_4 can be seen to indicate a slope of about 65 mV/decade at the currents at which 90 mV/decade occurs with H_3PO_4. The limiting current for air in H_2SO_4 was about 2500 mA/cm^2, a value near that using H_3PO_4. Since the diffusivity-solubility products of oxygen in these two electrolytes are probably of the same order, the same mechanisms are probably controlling performance in the two electrolytes in the 65 and the 90 mV/decade slope ranges. Therefore, the type electrode tested here is probably activation limited with a slope of 65 mV/decade for H_2SO_4 and 90 mV/decade for H_3PO_4. This 65 mV/decade is about what would be expected in H_3PO_4 at 70°C if the Tafel slope varied as $RT/\mathbf{F}$, that is, linearly with temperature as predicted by theory with constant transfer coefficient. This data with H_2SO_4 are shown in Fig. 12 and compares well with Appleby's data with phosphoric acid at the same temperature. It should be noted, however, that the absolute performance level with sulfuric acid was less reproducible than that with H_3PO_4.

Flooded electrode tests.—An electrode was fabricated with 5 w/o Teflon using 15 w/o platinum supported on Vulcan. A small percentage of Teflon was used to cause the electrode to flood with electrolyte and thereby introduce diffusional losses. This electrode was tested in the half-cell apparatus at 160°C in unpurified 96% phosphoric acid and the data are shown in Fig. 15. A slope of 180 mV/decade resulted for almost 2 decades on oxygen. This value is twice the 90 mV/decade slope and indicates that the single Tafel slope is probably 90 mV/decade.

Flat plate tests.—A platinum sheet electrode was submerged in unpurified 96% H_3PO_4 in the half-cell apparatus at 160°C with oxygen over the electrolyte. The data for this electrode are shown in Fig. 16 both with and without oxygen bubbling over the surface of the sheet. Data are also presented both with and without polarization of the electrode to 500 mV prior to the obtaining of each data point. The higher performance obtained with prepolarization is probably due to the desorption of anions or impurities occurring during the prepolarization. Appleby found a similar effect by prepolarizing to 50 mV. This electrode can be seen

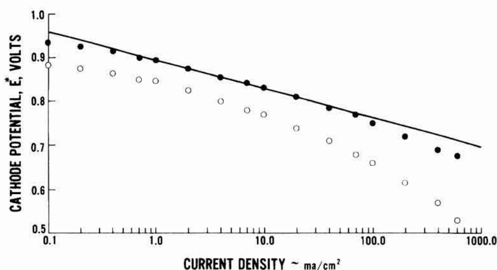

Fig. 14. Cathode performance for 0.25 mg Pt/cm^2 supported on Vulcan XC-72 with 20% H_2SO_4 at 70°C. ●, Oxygen; ○, air. A straight line with a slope of 65 mV/decade has been drawn through the oxygen data.

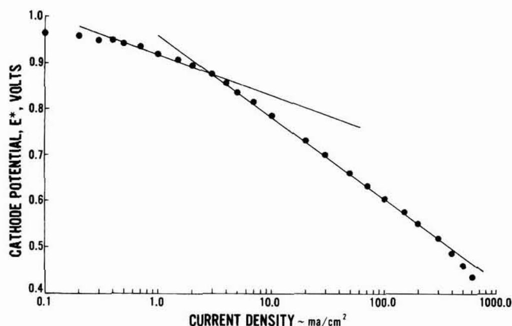

Fig. 15. Cathode performance on oxygen for flooded electrode tested in half-cell apparatus at 160°C in 96% H_3PO_4. Straight lines with slopes of 90 and 180 mV/decade have been drawn through the data.

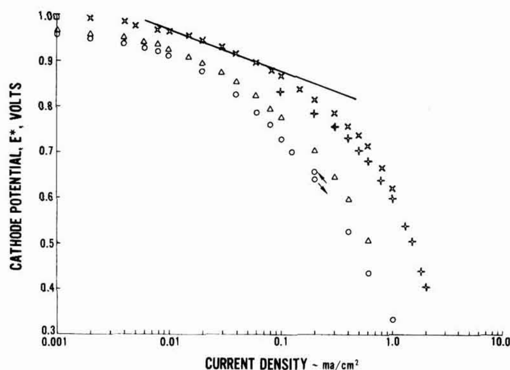

Fig. 16. Cathode performance for oxygen on a flat sheet submerged in unpurified 96% H_3PO_4 in the half-cell apparatus at 160°C. ○, No bubbling, no prepolarization; △, no bubbling, with prepolarization to 500 mV; +, with bubbling, no prepolarization; X, with bubbling, with prepolarization to 500 mV. A line with a slope of 90 mV/decade has been drawn through the highest data.

to have resulted in only a short Tafel slope region. A straight line was drawn through the data obtained using prepolarization to 500 mV and bubbling oxygen and an exchange current calculated. The exchange current, corrected to 1 atm oxygen pressure, is plotted in Fig. 17 where good agreement with an Arrhenius-type extrapolation of Appleby's data can be seen.

Discussion

All the experimental data obtained in this study indicate that the true Tafel slope for the reduction of oxygen in 96% H_3PO_4 at 160°C in the range of potentials below 0.9V is approximately 90 mV/decade.

The series of electrodes that were fabricated with various platinum loadings with a constant carbon loading indicated a linear dependence between current at a given potential and the platinum loading. This result indicated that the performance of these electrodes was controlled only by the activity of platinum. Since these electrodes had a slope on semilogarithmic coordinates of 90 mV/decade this slope is the Tafel slope.

The test sequence that was conducted to investigate the effect of temperature variation with 85% phosphoric acid resulted in data in good agreement with the results obtained by Appleby on a flat platinum sheet above 95°C. The Tafel slope varied as $RT/\mathbf{F}$ and is equal to 90 mV/decade at 160°C.

The tests using H_2SO_4 indicated a Tafel slope of 65 mV/decade with 20% H_2SO_4 at 70°C. This Tafel slope is in agreement with that found by Appleby at the

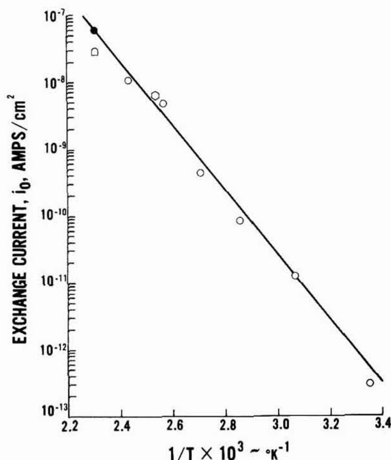

Fig. 17. Exchange current for oxygen reduction as a function of reciprocal temperature. ○, Flat sheet, Appleby, purified 85% H_3PO_4; ●, flat sheet, this study, 96% H_3PO_4; ⬡, platinum black, Vogel and Lundquist, 85% H_3PO_4, 82 mV/decade Tafel slope; △, platinum on Vulcan, this study, 96% H_3PO_4. The straight line represents a fit to the experimental data.

same temperature in 85% H_3PO_4. Therefore, the rate-limiting reactions for the reduction of oxygen in H_2SO_4 and H_3PO_4 are most likely the same. The flooded electrode tests indicated a double Tafel slope of 180 mV/decade, again confirming that the Tafel slope is 90 mV/decade for H_3PO_4 at 160°C.

The experiment conducted on a flat platinum sheet was in good agreement with an extrapolation of Appleby's data. The platinum specific activity obtained from a flat platinum sheet was found to be in fair agreement with the experimental results obtained with platinum supported on carbon as shown in Fig. 17. This means that, down to the range of platinum crystallite sizes obtained with the supported platinum in this study, no large change in the properties of the platinum are occurring with respect to activity. Also, there is apparently no large interaction between the platinum and the carbon with respect to platinum activity.

However, one set of experimental data must still be rationalized, that of Vogel and Lundquist. They found that at 120°C with 85% H_3PO_4 the Tafel slope was apparently 60 mV/decade on platinum black. These experimental data were fit by Kosinski (9) using the cylindrical agglomerate model to obtain a Tafel slope of 65 mV/decade. In order to rationalize the platinum black data of Vogel and Lundquist, additional calculations were performed to determine whether the newly determined Tafel slope in this experimental study could be used to fit their experimental cathode performance curves.

The Tafel slope determined by Appleby for a platinum sheet was used so that the number of fitting parameters was reduced to essentially four: the exchange current, the agglomerate diameter, the agglomerate porosity, and the electrolyte film thickness. Since Vogel and Lundquist's data were obtained at 120°C, a Tafel slope of 82 mV/ decade was used in the fitting of their experimental data. A comparison of their experimental data with the results obtained by fitting the cylindrical agglomerate model is shown in Fig. 18 and 19. Figure 18 shows a comparison between the calculated and experimental results of cathode potential *vs.* current density for one catalyst loading. Figure 19 shows the comparison of current densities *vs.* catalyst loading for various cathode potentials. As can be seen from these figures, an excellent fit was obtained. A comparison between the results of the cylindrical ag-

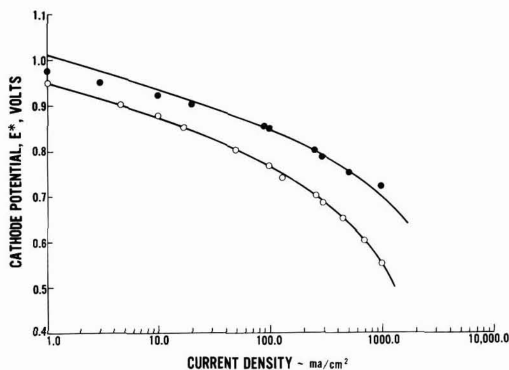

Fig. 18. Comparison between the experimental data of Vogel and Lundquist and calculated results of cathode potential vs. current density for one catalyst loading at 120°C in 85% H_3PO_4 at 1 atm gas pressure. ●, Oxygen; ○, air. Values of parameters used in the calculations: exchange current = 6.5×10^{-9} A/cm²; Tafel slope = 82 mV/decade; Pt loading = 6.0 mg/cm²; Pt surface area = 24 m²/g; agglomerate porosity = 0.80; agglomerate length = 0.0762 mm; agglomerate diameter = 4.0μ; tortuosity = 1.0; electrolyte film thickness = 0.05μ; electrolyte conductivity = 0.42 (ohm-cm)$^{-1}$; oxygen diffusivity-solubility product = 1.0×10^{-11} mole/cm-sec; density of Pt = 21.4 g/cm³.

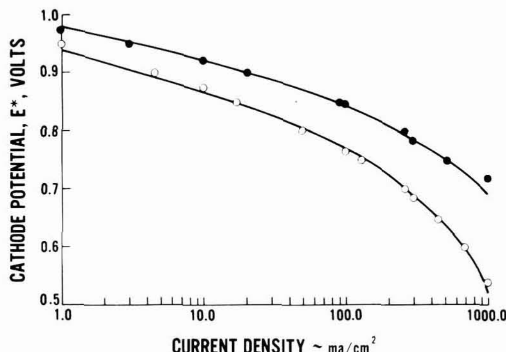

Fig. 20. Comparison between the experimental data of Vogel and Lundquist and calculated results of cathode potential vs. current density for one catalyst loading at 120°C in 85% H_3PO_4 at 1 atm gas pressure. ●, Oxygen; ○, air. Values of parameters used in the calculations: exchange current = 5.3×10^{-10} A/cm²; Tafel slope = 65 mV/decade; Pt loading = 6.0 mg/cm²; Pt surface area = 24 m²/g; agglomerate porosity = 0.60; agglomerate length = 0.0762 mm; agglomerate diameter = 6.0μ; tortuosity = 1.0; electrolyte film thickness = 0.05μ; electrolyte conductivity = 0.42 (ohm-cm)$^{-1}$; oxygen diffusivity-solubility product = 1.0×10^{-11} mole/cm-sec; density of Pt = 21.4 g/cm³.

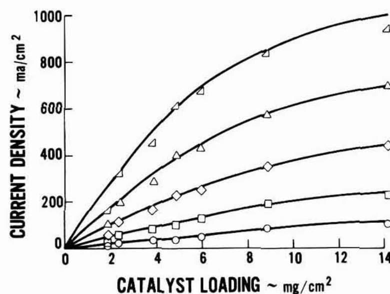

Fig. 19. Comparison between the experimental data of Vogel and Lundquist and calculated results showing the effect of loading upon cathode performance at 120°C in 85% H_3PO_4 with 1 atm air reactant pressure. Cathode potential (mV): ◿ 600; △, 650; ◇, 700; □, 750; ○, 800. Calculated results used same values of parameters as used in Fig. 18.

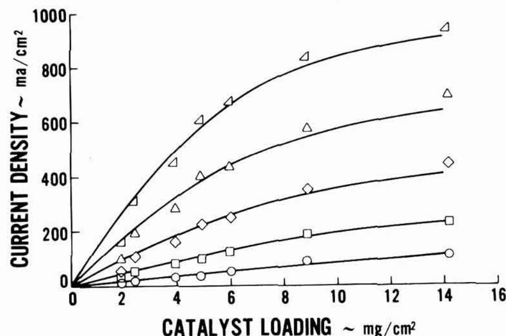

Fig. 21. Comparison between the experimental data of Vogel and Lundquist and the calculated results showing the effect of catalyst loading upon cathode performance at 120°C in 85% H_3PO_4 with 1 atm air reactant pressure. Cathode potential (mV): ◿, 600; △, 650; ◇, 700; □, 750; ○, 800. Calculated results used same values of parameters as used in Fig. 20.

glomerate model and the experimental data using a 65 mV/decade slope obtained previously by Kosinski are shown in Fig. 20 and 21. As can be seen from these figures, an excellent agreement was obtained in this case also.

The comparison between the results of the cylindrical agglomerate model and the experimental data was somewhat better for the 65 mV/decade case at potentials greater than 0.9V. However, since the surface oxidation state of platinum changes above approximately 0.9V, no conclusion can be reached as to which fit of Vogel and Lundquist's data is the better. The value of the exchange current obtained using the 82 mV/decade value of Tafel slope was added to Fig. 17. As can be seen, this value of exchange current for the platinum black electrode is in good agreement with Appleby's results for a flat sheet. A measured surface area of 24 m²/g was used for the platinum black. Both fits of the experimental data lead to reasonable values of agglomerate diameter, agglomerate porosity, and electrolyte film thickness.

Experimental data obtained on an electrode fabricated using platinum supported on Vulcan XC-72 were also fit using the cylindrical agglomerate model to determine if reasonable values of fitting parameters would be obtained. Data were obtained at 160°C so a Tafel slope of 90 mV/decade was used. A comparison of the results of the cylindrical agglomerate model with the data using only the exchange current, the agglomerate diameter, porosity, and electrolyte film thickness as fitting parameters are shown in Fig. 22. Good agreement resulted in this case.

The value of exchange current, corrected to 1 atm oxygen pressure, was added to Fig. 17. This value is lower than the value expected based on the results for 96% H_3PO_4 on a flat sheet. This difference can be partially attributed to the absence of prepolarization in the supported platinum electrode test as shown in Fig. 16. Other reasons for the results of the supported platinum electrode exchange current being low might be that regions of the Teflon-bonded catalyst were excessively flooded by electrolyte, that some regions of the Teflon-bonded electrode were in poor ionic or electronic contact, that slight surface roughness existed on the flat sheet (assumed to be 1.0), and that a slight effect of platinum crystallite size is present. A lower value of current in the supported platinum electrode in 85% H_3PO_4 can also be seen in Fig. 13.

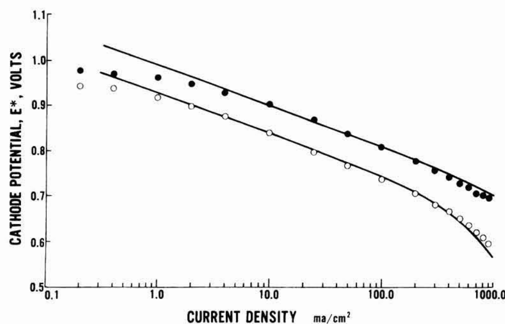

Fig. 22. Comparison of data of the present study with the calculated results of the cylindrical agglomerate model at 160°C in 96% H_3PO_4; 0.31 mg Pt/cm^2. ●, Oxygen; ○, air. Values of parameters used in the calculations: exchange current = 2.4×10^{-8} for oxygen; exchange current = 0.73×10^{-8} for air; Pt surface area = 70 m^2/g; agglomerate porosity = 0.60; agglomerate length = 0.0382 mm; agglomerate diameter = 1.6μ; tortuosity = 1.0; electrolyte film thickness = 0.20μ; electrolyte conductivity = 0.57 (ohm-cm)$^{-1}$; oxygen diffusivity-solubility product = 0.63×10^{-11} mole/cm-sec; density of carbon = 2.0 g/cm^3.

The values of the agglomerate diameter, porosity, and electrolyte film thickness for the supported platinum electrode were also reasonable considering the electron micrographs obtained for this type of electrode shown in Fig. 4. The agglomerate diameter appears to be somewhat small. This might be due to an effect of the carbon and/or Teflon on the diffusivity-solubility product of the oxygen in the electrolyte.

Again, a slight deviation between the predicted results using the model and the experimental data occurred above 0.9V. However, this might be expected in this case due to mixed potential effects caused by carbon, platinum, or impurity oxidation or perhaps a change in the catalytic properties of the platinum.

The fact that the cylindrical agglomerate model can be used to fit the experimental data for both the platinum black electrodes of Vogel and Lundquist and the supported platinum electrodes in this study does not confirm results obtained in this study but merely indicates that experimental data on both these types of electrodes can be rationalized using the results of this study. In all probability, the Tafel slope and exchange current for platinum black, platinum supported on carbon, and a flat platinum sheet are all the same, since the results obtained for platinum black and platinum supported on carbon are in such good agreement with the flat sheet results.

Conclusions

The following conclusions can be made from the results obtained in this study.

1. Platinum with an area as high as about 70 m^2/g when supported on carbon has approximately the same specific activity as a flat platinum sheet if the effect of electrode prepolarization is considered.

2. The specific activity of platinum black is most likely the same as that of a flat platinum sheet.

3. Crystallite size is relatively unimportant with respect to specific activity for oxygen reduction in the range of crystallite sizes studied and carbon does not interact significantly with the platinum.

4. The experimental data of Appleby are valid with respect to platinum activity in the potential range below 0.9V.

5. The mechanism for oxygen reduction is the same over a temperature range from 70° to 160°C for purified 85% phosphoric acid and is probably the same in both sulfuric and phosphoric acid. The Tafel slope varies as $RT/\mathbf{F}$.

6. Data above approximately 0.9V for platinum on carbon catalyzing pure oxygen reduction are confused by at least mixed potential effects and therefore cannot be used to obtain Tafel slope information for application to lower potential levels.

7. Data obtained for platinum black above approximately 0.9V indicate that possibly a change in mechanism for oxygen reduction may be occurring, perhaps through a change in the oxidation state of the surface.

8. Because the catalyst surface area for supported platinum determined using the electron microscope is larger than the electrochemical area and because the activity of the supported catalyst is somewhat lower than that anticipated using the data of Appleby, some of the catalyst in the supported platinum electrodes may be ineffective due to poor electronic or ionic paths.

Acknowledgments

The authors wish to thank Dr. A. Kaufman, M. Katz, and S. Organ for their assistance in the experimental phases of this work. The assistance of J. Kosinski in the theoretical studies and D. Pilney in the investigations with the electron microscope are also acknowledged.

Manuscript submitted Feb. 13, 1975; revised manuscript received May 16, 1975. This was Paper 40 presented at the New York, New York, Meeting of the Society, Oct. 13-17, 1974.

Any discussion of this paper will appear in a Discussion Section to be published in the June 1976 JOURNAL. All discussions for the June 1976 Discussion Section should be submitted by Feb. 1, 1976.

REFERENCES

1. W. M. Vogel and J. T. Lundquist, *This Journal*, **117**, 1512 (1970).
2. A. J. Appleby, *ibid.*, **117**, 328 (1970).
3. J. O'M. Bockris and A. Damjanovic, "The Mechanism and Electrocatalysis of Oxygen Reduction," Troisiemes Journees Internationales D'Etude Des Piles A Combustible, Brussels, 1969.
4. H. Angerstein-Kozlowska, B. E. Conway, and W. B. A. Sharp, *J. Electroanal. Chem.*, **43**, 9 (1973).
5. B. E. Conway and S. Gottesfeld, *J. Chem. Soc., Faraday Trans. I.*, **69**, 1090 (1973).
6. B. V. Tilak, B. E. Conway, and H. Angerstein-Kozlowska, *J. Electroanal. Chem.*, **48**, 1 (1973).
7. R. Brown and L. Horve, Paper 203, p. 109, The Electrochemical Society Extended Abstracts, Vol. I-5, Spring Meeting, Dallas, Texas, May 7-12, 1967.
8. J. Giner and C. Hunter, *This Journal*, **117**, 1124 (1969).
9. J. Kosinski, Paper 32, p. 90, The Electrochemical Society Extended Abstract Fall Meeting, Detroit, Michigan, Oct. 5-9, 1969.
10. D. A. J. Rand and R. Woods, *J. Electroanal. Chem.*, **47**, 353 (1973).
11. M. Paucirova, D. M. Drazic, and A. Damjanovic, *Electrochim. Acta*, **18**, 945 (1973).

Rate Capability and Electrochemical Stability of Carbon Fluorine Compounds in Organic Electrolytes

Herbert F. Hunger* and Joseph E. Ellison

Power Sources Technical Area, U.S. Army Electronics Technology and Devices Laboratory (ECOM), Fort Monmouth, New Jersey 07703

ABSTRACT

Polarization measurements of cathodes containing various carbon fluorine compounds, CF_n ($n = 0.24\text{-}1.5$), as the active depolarizer material were made in 1M $LiClO_4$-propylene carbonate at 298°K. The polarization (free of ohmic *iR* drop) was measured, using the periodically interrupted sine wave pulse current technique. The open-circuit potentials and polarization data were analyzed, considering their mixed potential character. The two major factors that influenced the data were the C/F ratio and the electrode compression pressure. With graphite fluorides, activation polarization was prevalent and Tafel behavior was observed ($b = 0.12$). The exchange currents were low, peaking at $n = 0.93$ with 10^{-22}A. From the exchange currents, the cathodic currents at the mixed potentials were computed. For $n = 0.93$, a value of about $7 \cdot 10^{-10}$A was obtained, indicating a depolarizer shelf life of about 10^6 years. Compounds with higher rate capabilities, such as polymeric, perfluorinated, and polycyclic hydrocarbons, show a very short shelf life by oxidizing rapidly the organic solvent. The experimental behavior of such compounds can be explained by the mixed potential theory. Shifts in open circuit, mixed potentials to more positive values are predicted for compounds with higher rate capability and can be observed experimentally.

The energy densities of lithium organic electrolyte batteries with graphite fluorides as depolarizers can reach 150 W-hr/lb; their rate capability, however, is limited to about 5-10 mA/cm² at room temperature. This limitation is mainly due to a relatively high polarization at the cathode at these current densities. The shape of the cathodic polarization curve indicates strong activation polarization (1). It would be desirable to decrease this overvoltage in order to obtain higher energy densities and rate capabilities in lithium batteries using carbon fluorine compounds as the cathodic material. Therefore, in our study, the polarization behavior of carbon fluorine compounds with various compositions and structures was investigated, but limited to a one solvent-electrolyte system.

Experimental

The electrochemical measurements and associated handling of cell materials were carried out in a dry lab in pure, dried argon or helium atmosphere. The water vapor level was between one and five parts per million.

Solvents and electrolytes.—The solvent employed in this investigation was propylene carbonate, purified by vacuum distillation. The electrolyte used in this study was one molar solution of anhydrous lithium perchlorate in propylene carbonate.

Depolarizer materials.—Graphite fluorides, covering the composition range from tetracarbon monofluoride to polycarbon monofluoride, were investigated as cathode materials. These materials were obtained from Rice University. Their preparations and purities have been described previously (2). Further, polymeric carbon fluorine compounds were investigated, such as the oxygen crosslinked polymers of perfluoro anthracene, perfluoro decacyclene, perfluoro phthalocyanine, and fluorinated paracyanogene. These compounds were prepared and characterized for the U.S. Army Electronics Command by Professor Lagow of MIT (3).

Preparation of electrodes.—The cathodes were prepared by a dry press technique. This involves preparing a dry cathodic depolarizer mixture of 80 weight per cent (w/o) depolarizer, 15 w/o graphite (spectroscopic grade), and 5 w/o Teflon powder. About 0.3g of the mixture were pressed into a highly porous nickel matrix of 10 cm² cross section. Both anode and reference electrode consisted of lithium foil pressed onto a nickel screen.

Electrochemical cell.—The electrochemical cell was assembled by placing the cathode, surrounded by a separator, between two lithium electrodes identical in size to the cathode. One of the lithium electrodes served as the anode and the other as the reference electrode. The cell design has been described in detail previously (1).

Electrochemical measurements.—Since the cathode polarization measurements included a substantial resistance polarization, it was essential to separate the resistance polarization component from the others. For that purpose, the periodically interrupted sine wave pulse current technique, invented by Kordesch and Marko, was chosen for polarization measurements free of the ohmic *iR* drop (4).

The circuit used in the measurements is shown in Fig. 1. The electrochemical cell C is connected with a load circuit (D_1) and two voltage measurement circuits (S_3 positions a and b). A gating switch circuit (D_2 and D_3) permits the cathode potential to be measured, free of the ohmic *iR* drop, during the brief

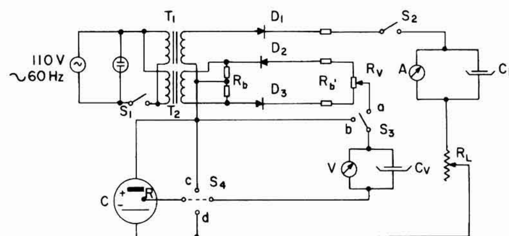

Fig. 1. Periodically interrupted sine wave pulse current circuit. Components: $T_1 = T_2 =$ 110V/24V, 1A. $D_1 =$ 50V, 1A. $D_2 = D_3 =$ 250V, 200 mA, $i_{rev} = 0.05\ \mu$A. $R'_b =$ 20 ohms, 35W each. $R'_b =$ 250 ohms, 38W each. $R_v =$ 50 ohms. $C_v = 10\ \mu$F, 150V. $C_1 = 100\ \mu$F, 500V.

* Electrochemical Society Active Member.

Key words: graphite fluorides, mixed potential, perfluoro anthracene, perfluoro decacyclene, perfluoro phthalocyanine.

period of current interruption (1/120 sec). The selection of the circuit components had to consider the higher cell voltages and the ohmic resistance characteristics of the lithium batteries which influence mainly the choice of the transformers (T_1 and T_2), the components in the gating switch circuit, and the condenser, C_V, parallel to the voltmeter. The latter had to be adjusted to the time constant of the voltage measurement circuit (S_3 position a).

Thus quasi steady-state current-cell voltage and current-cathode potential curves of lithium/graphite fluoride cells, including or excluding the ohmic *iR* drop, could be measured. In the case of polymeric carbon fluorine compounds as depolarizers, galvanostatic discharge curves were measured.

Results and Discussion

Standardization of cathode preparation.—Before a study of the kinetics of various graphite fluorides was started, the cathode preparation technique had to be optimized and standardized. It was found that the major two factors influencing the performance of the cathode were the carbon to fluorine ratio and the compression pressure applied in preparing the cathodes. The compression pressure was varied within the range of 400 to 30,000 lb/electrode. Using the dry press technique, a pressure of about 2000 lb/in.^{2} yielded graphite fluoride cathodes with the lowest polarization up to 5 mA/cm^2.

Mixed potential theory of CF_n reduction.—The key to the analysis of the polarization data was the mixed potential theory of CF_n reduction. The open-circuit potential of graphite fluoride cathodes is a mixed potential, the reduction of graphite fluoride being the cathodic reaction and solvent oxidation being the anodic reaction (1). The electrochemical behavior of carbon fluorine compounds is shown schematically in terms of the mixed potential theory in Fig. 2. E_{CF} is the potential of a carbon fluoride cathode *vs.* a lithium reference electrode, computed from thermodynamic data. It is numerically identical to the electromotive force of a corresponding lithium-carbon fluoride cell. The emf of such cells, covering the composition range from $CF_{0.24}$ to $CF_{1.13}$, have been determined recently by Professor Margrave and co-workers at Rice University (2). The values range from 5.23 to 4.56V at 298°K. Note that the potentials decrease with increasing fluorine content in the compounds. There are three current-potential curves shown in Fig. 2, covering three cases of CF kinetics, slow, medium, and fast. E_S is the oxidation potential of the organic solvent. The average potential of graphite electrodes in 1M $LiClO_4$-PC is 2.56V *vs.* lithium. Tiedemann has found that the potential of a completely discharged $(CF)_n$ electrode is approximately 2.5V *vs.* lithium (5). A_s is the solvent oxidation and C_s the solvent reduction curve.

The open-circuit potential of a CF electrode, *e.g.*, E_m, is a mixed potential and a function of its state of discharge (1). Experimental E_m values, ranging from 2.56 to 3.36V, have been observed with poly carbon monofluoride at 298°K. The variations are caused by the type of CF used and by the electrode compression pressure.

A mixed potential, E_m, is established when the cathodic current of CF reduction and the anodic current of solvent oxidation are equal. The open-circuit potential, E_m, is thus a function of the kinetics of the partial electrode processes (6, 7). According to the principle of the additive composition of all partial electrode processes, we should observe experimentally the interrupted curve, C_{exp}. The theoretical curve for CF reduction and the experimental curve are, however, practically identical between E_m and E_s due to the smallness of the solvent oxidation current.

CF_n cathode polarization data.—In Fig. 3, polarization data, free of ohmic *iR* drop, of graphite fluoride cathodes are shown. The polarization here is defined as the difference between the cathode potential, calculated from thermodynamic data, and the cathode potential at a given current measured *vs.* the lithium reference electrode. Each data point was taken after quasi steady state, defined by a change of less than ±5 mV/5 min, was reached. The average error in the polarization data, *e.g.*, for $CF_{0.93}$, for the 0.15 to 50 mA range was 38 mV or less than 1.8% at polarizations between 2.5 and 2.74V. At higher current densities, above 2 mA/cm^2 (20 mA), a slow, continuous increase in polarization with time was observed. In these cases, the initial data points taken are shown in the graph. The upper two curves (Fig. 3) are for white CF [dry press technique and wet preparation technique (1)] and the lower two curves for gray CF (dry press technique, two different metal current collectors).

A range of linear behavior with a slope of about 0.12V/decade of current can be observed. The deviations at higher currents from linearity could be due to blocking of parts of the inner surface area of the electrodes with reaction products, mainly lithium fluoride; the deposition will be proportional to current and time. Since no limiting currents have been observed up to 100 mA, any concentration polarization can be neglected due to its smallness.

Exchange currents of CF_n reduction.—From the linear part of the polarization curves, the exchange currents, i_o, for cathodic CF reduction could be computed, using the following equation

$$E_{CF} - E_i = 0.116 \log i_c - 0.116 \log i_o \quad [1]$$

Values of exchange currents for various graphite fluorides are shown in Table I. The highest exchange

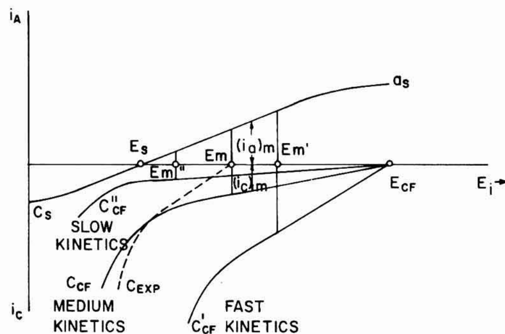

Fig. 2. Current-potential curves of carbon fluorine compounds and organic solvents.

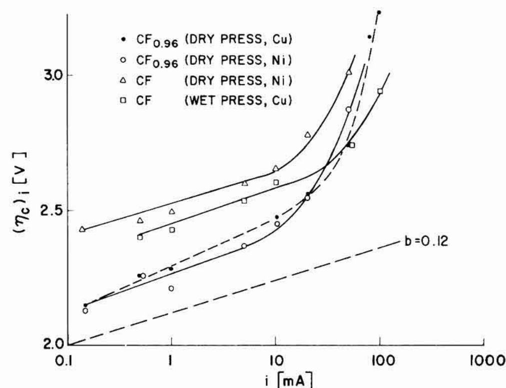

Fig. 3. Polarization data of CF_n cathodes free of ohmic *iR* drop. ● $CF_{0.93}$ (dry press technique, Cu collector), ○ $CF_{0.93}$ (d.p.t., Ni collector), △ CF (d.p.t., Ni collector), □ CF [wet preparation technique (1)] 1M $LiClO_4$-PC, 25°C.

ห้องสมุด กรมวิทยาศาสตร์

Table I. Exchange currents of graphite fluorides CF_n in 1M $LiClO_4$-PC at 298°K for about 2% discharge of the cathodes

n	i_o (A)	$(i_m)_e$ (A)	E_m (V)	τ (Y)
0.237	$3 \cdot 10^{-26}$			
0.55	$8.9 \cdot 10^{-23}$			
0.93	$1 \cdot 10^{-22}$	$6.9 \cdot 10^{-10}$	3.09	$3.05 \cdot 10^{+4}$
0.96	$2.2 \cdot 10^{-23}$			
1.0	$6.4 \cdot 10^{-24}$			
1.09	$3.6 \cdot 10^{-24}$	$3.39 \cdot 10^{-11}$	3.05	$9 \cdot 10^{+5}$

current was observed with $CF_{0.93}$. Considering the inner surface areas of the graphite fluorides (2), which range from 230 to 270 m^2/g, the exchange current density for gray CF should be in the order of $1.7 \cdot 10^{-28}$ A/cm^2 and that of white CF about $5.4 \cdot 10^{-30}$ A/cm^2; however, blocking of active, inner surface area by compression during electrode preparation has to lead to higher exchange current densities.

Electrochemical stability of CF cathodes.—From the exchange currents, the cathodic currents of CF_n reduction at the mixed potentials, $(i_m)_c$ (third column, Table I), could be computed via Eq. [2]

$$E_{CF} - E_m = 0.116 \log (i_m)_c - 0.116 \log i_o \quad [2]$$

For gray CF we obtain $(i_m)_c = 6.9 \cdot 10^{-10}$A. This value is significant in that it relates to the electrochemical stability of the CF cathode on open circuit. A cathodic current at the mixed potential of about 10^{-11}A corresponds to a depolarizer shelf life, τ, (last column, Table I) in the electrolyte of about 10^6 years.

It can be estimated that hypothetical compounds with a higher rate capability than gray CF, *e.g.*, with exchange currents of $(i_o)_{CF_n} = 10^{-12}$ or 10^{-7}A, would have, based on the computed $(i_m)_c$, a far shorter depolarizer shelf life in the electrolyte of about 3 years or 1 day, respectively.

In computing the depolarizer shelf life of such compounds from i_m, we have to consider the shift in E_m due to the faster kinetics of the CF_n reduction. E_m, i_m, and consequently τ, can be computed from the two equations [3] and [4] with two unknowns E_m and i_m

$$E_m - E_s = 0.12 \log i_m - 0.12 \log (i_o)_s \quad [3]$$

$$E_{CF_n} - E_m = 0.12 \log i_m - 0.12 \log (i_o)_{CF_n} \quad [4]$$

As mentioned earlier, E_s was found experimentally to average 2.56V. The exchange current of the solvent $(i_o)_s$ could be determined indirectly from i_m, *e.g.*, for $CF_{1.09}$, under assumption of activation control, using Eq. [3], E_m being the mixed potential of $CF_{1.09}$; $(i_o)_s$ was also determined directly by measuring the anodic oxidation of propylene carbonate at $CF_{1.09}$. With 1M $LiClO_4$-PC at 25°C, a Tafel slope of 0.12 was found and an $(i_o)_s$ of 10^{-16}A; $(i_o)_s$ determined indirectly was about 10^{-15}A.

E_{CF_n} can be estimated using Eq. [5] (2) and [6]

$$G^{\circ}_{298} = -(104.2n + 1.158) \text{ (kcal mole}^{-1}) \quad [5]$$

$$E^{\circ}_{CF_n} = G^{\circ}_{298}/n \cdot 23.053 \quad \text{(V)} \quad [6]$$

The polymeric carbon fluorine compounds, mentioned earlier, fall apparently into the category of high rate depolarizers by showing initially a far better kinetics than white CF, but also a strong reactivity with the organic solvent. Figure 4 shows the cathodic reduction of polymeric carbon fluorine compounds and of white CF. The discharge was performed galvanostatically at 1 mA/cm^2. In the figure the cathode potential measured *vs.* a lithium reference electrode is plotted *vs.* the discharge time in minutes. Oxygen crosslinked perfluoro anthracene, perfluoro decacyclene, perfluoro phthalocyanine, and fluorinated paracyanogene showed initially about 1V higher discharge potentials than poly carbon monofluoride. After a certain time, however, reactions between depolarizer and solvent consume the cathodes. Highly soluble depo-

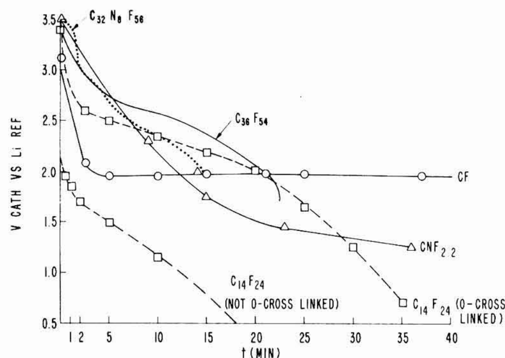

Fig. 4. Cathodic reduction of polymeric carbon fluorine compounds compared with CF (1 mA/cm^2). 1M $LiClO_4$-PC, 30°C. $C_{14}F_{24}$ perfluoro anthracene (oxygen crosslinked), $C_{36}F_{54}$ perfluoro decacyclene (oxygen crosslinked), $C_{32}N_8F_{56}$ perfluoro phthalocyanine (oxygen crosslinked), $CNF_{2.2}$ fluoro paracyanogene, CF poly carbon monofluoride.

larizers, such as oxygen crosslinked perfluoro anthracene, show inferior discharge behavior.

A more detailed explanation of the experimental behavior of these compounds is submitted: When the cathode is submerged for the first time in the electrolyte, reduction takes place initially at a high rate, corresponding perhaps to an $i_o = 10^{-7}$A, at a mixed potential of about 3.95V. For 100% bulk utilization of the depolarizer, a time of about 1 day would be required; for depletion of active species at the surface, however, far less time would be required. This depletion will change the kinetics to a slower one, *e.g.*, to an $i_o = 10^{-12}$A. A mixed potential of about 3.62V would be the consequence. This would approximately correspond to the starting points of our discharge experiments in Fig. 4. Drawing a cathodic current of 10^{-2}A at about 3.32V would result in a fast consumption of the remaining active depolarizer material which is indicated in Fig. 4 by a strong drop in discharge potential.

The mixed potential theory predicts a shift in E_m to more positive potentials for compounds with faster reduction kinetics (see Fig. 2). This could be observed experimentally in the case of oxygen crosslinked perfluoro anthracene, perfluoro decacyclene, perfluoro phthalocyanine, and fluoro paracycanogene. The mixed potentials of these compounds measured *vs.* a lithium reference electrode are given in Table II.

Such compounds could make excellent depolarizers with higher rate capabilities if solvents and electrolytes could be found that would be stable to oxidation by the compounds. The theoretical energy capacities of these compounds exceed those of graphite fluorides, 2050 W-hr/lb of cell reactants *vs.* 1785 W-hr/lb.

Manuscript submitted Nov. 13, 1974; revised manuscript received May 20, 1975. This was Paper 25 presented at the New York, New York, Meeting of the Society, Oct. 13-17, 1974.

Any discussion of this paper will appear in a Discussion Section to be published in the June 1976 JOURNAL. All discussions for the June 1976 Discussion Section should be submitted by Feb. 1, 1976.

Table II. Mixed potentials of polymeric carbon fluorine compounds in 1M $LiClO_4$-PC at 298°K vs. the lithium reference electrode

Compound	E_m (V)
$CF_{0.93}$	3.09
Oxygen crosslinked perfluoro	
Anthracene $C_{14}F_{24}$	3.46
Decacyclene $C_{36}F_{54}$	3.47
Phthalocyanine $C_{32}N_8F_{56}$	3.47
Fluoro paracyanogene $CNF_{2.2}$	3.58

Publication costs of this article were partially assisted by the U.S. Army.

REFERENCES

1. H. F. Hunger and G. J. Heymach, *This Journal*, **120**, 1161 (1973).
2. A. J. Valerga, R. B. Badachhape, G. D. Parks, P. Kamarchik, J. L. Wood, and J. L. Margrave, Final Report, Contract DAAB07-73-C-0056 (ECOM), Rice University, March 1974.
3. R. J. Lagow and J. L. Adcock, Final Report, Contract DAAB07-72-C-0166 (ECOM), MIT, May 1974.
4. K. Kordesch and A. Marko, *This Journal*, **107**, 480 (1960).
5. W. Tiedemann, *ibid.*, **121**, 1308 (1974).
6. K. J. Vetter, "Electrochemische Kinetik," p. 588, Springer-Verlag (1961).
7. C. Wagner and W. Traud, *Z. Elektrochem.*, **44**, 391 (1938).

High Conductivity Solid Electrolytes

Double Salts of Substituted Organic Ammonium Halides and Cuprous Halides

Anthony F. Sammells,* Jack Z. Gougoutas,[1] and Boone B. Owens*[,2]

Gould Incorporated, Gould Laboratories, St. Paul, Minnesota 55165

ABSTRACT

Copper solid electrolytes have been synthesized by the solid-state reaction between substituted organic ammonium halides and cuprous halides. High conductivity electrolytes were found with both high and low symmetry organic ammonium halides, indicating that high symmetry in the latter need not be necessary in this class of electrolytes. Initial experiments with these materials in galvanic cells and coulometers indicated some instability.

Many of the highly conducting solid electrolytes investigated over the past decade have been silver ion conductors. The most conductive of these, $RbAg_4I_5$, has a conductivity of 0.27 $ohm^{-1} \cdot cm^{-1}$ at ambient temperatures (1) and has found application in galvanic cells (2). Silver electrolytes have also been synthesized through compound formation between AgI and various substituted ammonium halides (4, 5) and also between AgI and sulfonium iodides (6). The single-crystal structures of certain of these unique phases have been investigated (7-11) to determine the structural features that permit fast ion diffusion in solids. It was observed that the iodide ions form face-sharing polyhydra (generally tetrahedra), with the silver ions situated within these polyhedra. On the average there are two or three vacant sites per silver ion, thus permitting ready diffusion through the faces of the polyhedra.

Because of the similar properties of Ag^+ and Cu^+ together with the much lower cost of copper compared to silver, it has been of considerable interest to synthesize copper electrolytes with ionic transport properties analogous to those of the above referenced silver electrolytes. Such materials were recently reported to exhibit ionic conductivities as high as 0.045 $ohm^{-1} \cdot cm^{-1}$ (12-13).

In the present investigation, following procedures similar to those of Takahashi, Cu^+ ion conducting solid electrolytes were synthesized by the combination of NN'-dimethyltriethylenediamine dibromide + cuprous bromide, NN-dihydrotriethylenediamine dibromide + cuprous bromide, and N-hydrohexamethylenetetramine chloride + cuprous chloride, in good agreement with the results of Takahashi *et al.* (12, 13).

The organic cations that are presumably stabilizing the high conductivity phase in the above three electrolytes have both high symmetry and a saturated cage-type structure. In order to determine whether ionic conduction is limited to the hydrohalides of triethylenediamine and hexamethylenetetramine and their derivatives, and investigate the relative importance of high symmetry, the cage-type structure, and the onium nitrogen atoms, we have investigated several other systems. Our choice of substituents for the most part has been empirical since no crystallographic structural information is available to suggest those molecular features which the organic moeity should possess in order to form an ionically conducting phase. The possibility of ionically conductive cuprous halide phases being stabilized by quinuclidine, quinuclidone, pyridinium, dimethylpiperizine, NN',NN'-diethylenedipyrilidinium, and 1-adamantanamine halides was investigated.

Conductivity measurements have been reported both at 1000 Hz and ∞Hz. Extrapolation to ∞Hz was made to eliminate the faradaic impedance ΔR, which may be proportional to the square root of frequency (14, 15).

$$\Delta R = kf^{-1/2}$$

where f is frequency and k a proportionality constant. The measured resistance R_m will contain both the bulk electrolyte resistance R and any faradaic impedance effects that may exist at the interface

$$R_m = R + \Delta R = R + kf^{-1/2}$$

The error caused by ΔR was minimized by extrapolating the measured resistance to infinite frequency.

The conductivity-temperature function was determined for some of these electrolytes and activation energies reported. The stability of these electrolytes under a potential was evaluated by fabricating galvanic cells with copper anodes and various cathodes, including $CuBr_2$, MoO_3, V_2O_3, tetrapropylammonium tribromide, tetrabutylammonium tribromide, and triethylenediamine dibromide.

Experimental

Electrolyte syntheses.—3-quinuclidone hydrochloride, quinuclidine hydrochloride, and 1-adamantanamine were obtained from Aldrich Chemical Company. Triethylenediamine was purchased from Eastman Kodak Chemical Company. Cuprous chloride and bromide were very carefully purified by recrystallization from the appropriate halogen acid, followed by wash-

* Electrochemical Society Active Member.

[1] Present address: Chemistry Department, University of Minnesota, Minneapolis, Minnesota 55455.

[2] Present address: Medtronic Incorporated, Minneapolis, Minnesota 55418.

Key words: copper ion diffusion, frequency measurements, symmetry, organic ammonium halides, activation energy, galvanic cells.

ing with glacial acetic acid, and ethanol. While still moist with ethanol, the cuprous halide was stirred with tetrahydrofuran and rapidly transferred to a round bottom flask, where the remaining solvent was removed under vacuum. After solvent removal the cuprous halides were not exposed to the atmosphere in any subsequent operation.

The electrolyte materials were synthesized under a nitrogen atmosphere by intimately mixing the appropriate mole quantities of cuprous halide and organic material in a round bottom flask, using sufficient ethanol to make a slurry. The ethanol was then vacuum distilled. After thorough washing and drying the materials were transferred to a dry box where they were pressed into pellets at 57,000 psi. These pellets were then heated under the conditions illustrated in Table I. After the solid-state reaction, the pellets were transferred to a dry box, ground up, and repressed at 57,000 psi into conductivity cells of the configuration Cu,E/E/Cu,E (E is the electrolyte). The electrodes consisted of powdered copper intimately mixed with electrolyte in the weight ratio 2:1. Some of the conductivity cells were annealed under high purity nitrogen to remove any excess halogen that may be present. However, attempts to anneal the electrolytes containing quinuclidine and 3-quinuclidone resulted in deterioration of these materials.

Synthesis of electrolyte components.—NN'-dimethyltriethylenediamine dibromide.—Methyl bromide (2 moles) was reacted with triethylenediamine (1 mole) in benzene. The product was recrystallized from tetrahydrofuran. [Br: found 51.70%, calculated 52.98% (13).] This material was also prepared from NN'-dimethylpiperidine and 1-2-dibromoethane.

NN'-dihydrotriethylenediamine dibromide.—Triethylenediamine was reacted with an excess of a 47% aqueous HBr solution. The solution was allowed to stir overnight; the product was recrystallized from EtOH/water. [Br: found 57.4%, calculated 58.39% (13).]

N-hydrohexamethylenetetramine chloride.—Hexamethylenetetramine was reacted with 1 mole equiv. of 47% aqueous HBr in ethanol and was recrystallized from ethanol. [Cl: found 19.37%, calculated 20.11% (12).]

Quinuclidine hydrobromide.—Quinuclidine hydrochloride was treated with 1M NaOH, stirred with $MgSO_4$, and then reacted with a slight excess of HBr. The product was recrystallized from ethanol. (Br: found 40.94%, calculated 41.66%.)

Quinuclidine methylbromide.—As above except treated with 3 moles methylbromide. The product was recrystallized from ethanol. (Br: found 37.70%, calculated 38.83%.)

3-Quinuclidone hydrobromide.—This material was synthesized by passing quinuclidone hydrochloride through an anion exchange resin (amberlite IR-45) and the product was recrystallized from ethanol. (Br: found 40.18%, calculated 38.46%.)

Pyridinium bromide.—This extremely hygroscopic salt was prepared by titrating an aqueous solution of pyridine with 47% aqueous HBr. After evaporation of the solvent, the solid was recrystallized from acetone/ethanol. (Br: found 45.17%, calculated 41.66%.)

NN'-dimethylpiperizine dihydrochloride.—NN'-dimethylpiperizine was treated with 2 moles of aqueous hydrochloric acid. Crystals were obtained by concentration of the solution and were recrystallized from ethanol. (Cl: found 34.74%, calculated 37.96%.)

NN',NN'-diethylenedipyrrolidinium dibromide.—Pyrrolidine was reacted with ethylenedibromide, the solution was clarified using NORITE (activated charcoal) and the product was recrystallized from iPrOH. [Br: found 45.28%, calculated 44.94% (16).]

Synthesis of cathode materials.—Tetramethylammonium tribromide.—Tetramethylammonium bromide was reacted with bromine in carbon tetrachloride. The excess bromine was pumped off.

Tetrabutylammonium tribromide.—Tetrabutylammonium was reacted in carbon tetrachloride with a 0.05 mole Br_2/CCl_4 solution (14).

Triethylenediamine dibromine complex of.—Triethylenediamine was dissolved in benzene and was stirred with excess bromine in benzene. The yellow product was filtered, washed with benzene, and air dried. The product was recrystallized from glacial acetic acid.

Experimental measurements.—Cell resistances were measured at frequencies between 500 and 20,000 Hz using a General Radio 1608A impedance bridge with an external Hewlett-Packard 209A oscillator. The measurements were made on cells maintained in an inert atmosphere. The cell voltages were measured with an HP3430A digital voltmeter. X-ray powder diffraction patterns were run on a GE XRD-6 x-ray spectrometer using $CuK\alpha_1$ lines.

Table I. Conductivity results

Electrolyte	Conductivity $ohm^{-1} \cdot cm^{-1}$ at 25°C				Electrolyte synthesis	Conductivity cell anneal
	1000 Hz		∞ Hz			
	Before anneal	After anneal	Before anneal	After anneal		
Quinuclidine-HBr-CuBr (87.5 m/o)	4.2×10^{-3}	1.3×10^{-3}	8.7×10^{-3}	3.0×10^{-3}	190°C 16 hr under vac	110°C 8 hr N_2 flow
Quinuclidine-MeBr-CuBr (87.5 m/o)	6.0×10^{-3}		1.6×10^{-2}		150°C 16 hr under vac	
Quinuclidine-HCl-CuCl (85 m/o)	1.8×10^{-4}		4.0×10^{-4}		160°C 16 hr under vac	
3-Quinuclidone-HBr-CuBr (80 m/o)	2.4×10^{-4}		3.0×10^{-4}		175°C 16 hr under vac	
3-Quinuclidone-HCl-CuCl (80 m/o)	2.6×10^{-3}		2.5×10^{-3}		120°C 16 hr under vac	
Pyridinium bromide-CuBr (87.5 m/o)	7.4×10^{-4}		3.3×10^{-3}		100°C under H_2	
NN'-dihydrotriethylenediamine dibromide-CuBr (87.5 m/o)		2.0×10^{-2}		6.5×10^{-2}	190°C 16 hr under vac	170°C 8 hr N_2 flow
NN'-dimethyltriethylenediamine dibromide-CuBr (94 m/o)	2.7×10^{-3}	6.5×10^{-3}		1.4×10^{-2}	190°C 16 hr under vac	170°C 8 hr N_2 flow
N-hydrohexamethylenetetramine chloride-CuCl (87.5 m/o)	5.4×10^{-4}	2.4×10^{-3}	2.5×10^{-3}	2.7×10^{-3}	120°C 16 hr under vac	120°C 8 hr N_2 flow
Dimethylpiperazine-2HCl-CuCl (87.5 m/o)	9.6×10^{-7}	3.3×10^{-7}			110°C 16 hr under vac	
NN',NN'-diethylenedipyrrolidinium dibromide-CuBr (87.5 m/o)		4.0×10^{-8}				110°C 8 hr N_2 flow
1-Adamantylamine-HCl-CuCl (80 m/o)	3.1×10^{-7}	1.2×10^{-7}			180°C 16 hr under vac	140°C 8 hr N_2 flow
Triethylenediamine-CuBr (90 m/o)		No conductivity			100°C 16 hr N_2 flow	
Triethylenediamine-CuCl (90 m/o)	1.3×10^{-7}				100°C 16 hr N_2 flow	

Results

The systems reported on are shown in Fig. 1. These are (I) quinuclidine hydrobromide-CuBr, (II) quinuclidine methylbromide-CuBr, (III) quinuclidine hydrochloride-CuCl, (IV) 3-quinuclidone hydrobromide-CuBr, (V) 3-quinuclidone hydrochloride, (VI) pyridinium bromide-CuBr, (VII) NN'-dihydrotriethylenediamine dibromide-CuBr, (VIII) NN'-dimethyltriethylenediamine dibromide-CuBr, (IX) N-hydrohexamethylenetetramine chloride-CuCl, (X) dimethylpiperizine dihydrochloride-CuCl, (XI) NN',NN'-diethylenedipyrrolidinium dibromide-CuBr, (XII) 1-adamantanamine hydrochloride-CuCl, (XIII) triethylenediamine-CuBr, (XIV) triethylenediamine-CuCl.

A typical frequency dependence for a conductivity cell resistance is shown in Fig. 2 for the electrolyte NN'-dimethyltriethylenediamine dibromide-CuBr [94 mole per cent (m/o)]. If we plot cell resistance values at 1 kHz against cell length, the resultant faradaic impedance, as represented by the intercept, is generally several ohms. However, by plotting the extrapolated conductivity values at ∞Hz against cell length, the intercept is at the origin, demonstrating that the impedance effect has been minimized, as shown in Fig. 3. All of our results for both 1 kHz and ∞Hz are summarized in Table I. The highest conductivity found was for NN'-dihydrotriethylenediamine chloride-CuBr (87.5 m/o) at 6.5×10^{-2} $ohm^{-1} \cdot cm^{-1}$ at ∞Hz, which is in reasonable agreement with the value of 4×10^{-2} $ohm^{-1} \cdot cm^{-1}$ at 1000 Hz reported by Takahashi.

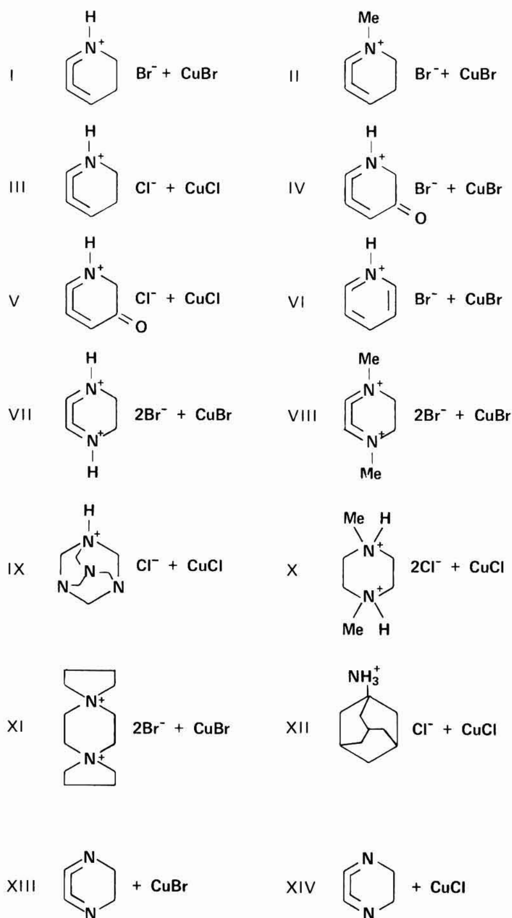

Fig. 1. Copper electrolyte systems investigated

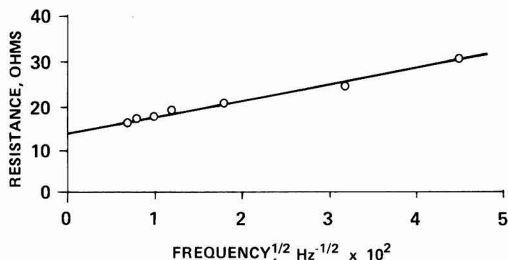

Fig. 2. Frequency dependence for dimethylenediamine dibromide + CuBr(94 m/o).

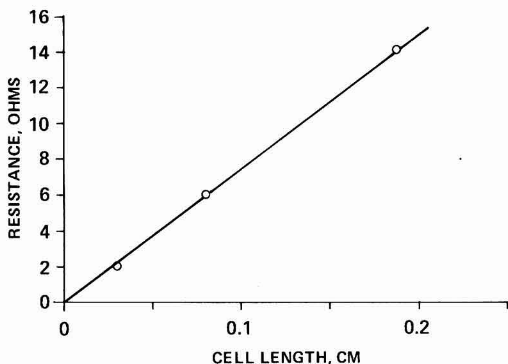

Fig. 3. Cell resistance *vs.* cell length at ∞Hz for dimethyltriethylenediamine dibromide + CuBr(94 m/o).

The composition dependence of the conductivity was determined for the more conductive systems investigated. The compositions at which maxima occurred are summarized in Table I. The synthesis temperatures chosen were those where new phase materials could be detected from x-ray patterns. The presence of the new phases was then correlated with directly measured conductivity values to find the synthesis temperature at which the most conductive samples were produced.

The optimized stoichiometries for maximum conductivity were quite distinct, but were generally not sharp.

The observed temperature dependence of the conductivity for quinuclidine hydrobromide-CuBr (87.5% m/o) over the temperature range 50° to −20°C is shown in Fig. 4. The slope corresponds to an activation energy of 2.7 kcal/mole. The activation energies observed in the present study varied from 2.7 up to 6.7 kcal/mole as shown in Table II.

X-ray powder diffraction patterns were routinely run on samples of optimized stoichiometry. All samples showed lines characteristic of the starting materials together with, in some cases, new phases, indicating that the phases were not optimized to equilibrium.

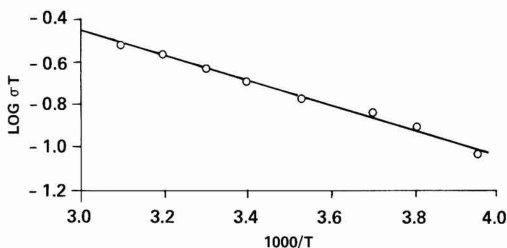

Fig. 4. Conductivity temperature dependence for quinuclidine hydrobromide + 87.5 m/o CuBr.

Table II. Activation energies for copper solid electrolytes

Electrolyte	ΔE, kcal/mole
Quinuclidine-HBr-CuBr (87.5 m/o)	2.68
Quinuclidine-MeBr-CuBr (87.5 m/o)	3.6
3-Quinuclidone-HBr-CuBr (80 m/o)	6.72
Pyridinium-HBr-CuBr (87.5 m/o)	4.19
NN'-dihydrotriethylenediamine dibromide-CuBr (87.5 m/o)	4.55
NN'-dimethyltriethylenediamine dibromide-CuBr (94 m/o)	5.7
N-hydrohexamethylenetetramine chloride-CuCl (87.5 m/o)	5.46

Table III. Galvanic cells investigated

System		Initial voltage, mV
Cu | Hexamethylenetetramine-HCl-CuCl	| Triethylenediamine dibromide	674
Cu | Hexamethylenetetramine-HCl-CuCl	| $Propyl_4NBr, Br_2$	618
Cu | Hexamethylenetetramine-HCl-CuCl	| $Butyl_4NBr, Br_2$	618
Cu | Hexamethylenetetramine-HCl-CuCl	| MoO_3	378
Cu | Hexamethylenetetramine-HCl-CuCl	| V_2O_5	423
Cu | Dihydrotriethylenediamine dibromide-CuBr	| Triethylenediamine dibromide	710
Cu | Hexamethylenetetramine-HCl-CuCl	| $CuBr_2$	672
Cu | 3-Quinuclidone-HCl-CuCl	| Triethylenediamine dibromide	581
Cu | 3-Quinuclidone-HCl-CuCl	| $Propyl_4NBr, B_2$	527
Cu | 3-Quinuclidone-HCl-CuCl	| $Butyl_4NBr, B_2$	592

To evaluate the utility of these copper electrolytes in solid-state galvanic cells, various cells were made. Initial voltages are reported in Table III. A load curve for the cell Cu/hexamethylenetetramine-HCl CuCl (87.5 m/o) $CuBr_2$ is shown in Fig. 5. During discharge or upon standing on open circuit, the electrolyte phase in our cells deteriorated and became black in appearance. There was a concurrent loss of cell voltage, possibly due to electronic conductivity in the electrolyte decomposition product.

The plating characteristics of copper in these materials was investigated for a simple coulometer cell. The plate, deplate cycle for the cell Cu/pyridinium bromide-CuBr (87.5 m/o) graphite is shown in Fig. 6.

Some preliminary work was performed on identification of the ionically conductive phase or phases present in these copper electrolytes by the use of single-crystal techniques. Single crystals of a conductive phase of pyridinium bromide-CuBr were prepared from an aqueous solution. A preliminary crystallographic survey of the single crystals suggested an orthorhombic unit cell (a = 11.8Å, b = 14.1Å, c = 13.1Å). The observed density of 3.178 g/cm³ and unit

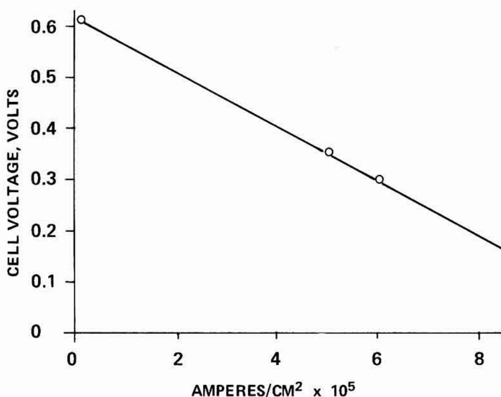

Fig. 5. Load curve for Cu/hexamethylenetetramine-HCl/$CuBr_2$ + CuCl(87.5 m/o).

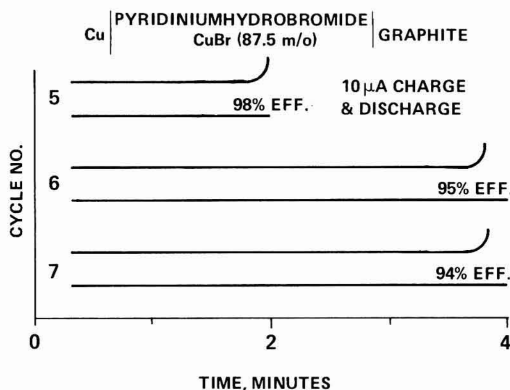

Fig. 6. Application in coulometers

cell volume agree with a unit cell containing 20 CuBr and 8 C_5H_6NBr.

Discussion

The present results indicate that copper ion conducting phases can be stabilized not only by substituted organic ammonium compounds of high symmetry (D_3h) as reported by Takahashi (12, 13) but also by species in which some lowering of the over-all symmetry occurs. High conductivity has been observed for double salts of copper halides with quinuclidine hydrobromide, quinuclidine methylbromide, and quinuclidine hydrochloride, where there is still a high symmetry organic ammonium halide, but one of the "onium" nitrogens of the NN'-dialkyltriethylenediamine halide has been removed. In fact, the conductivity at infinite frequency found for quinuclidine methylbromide-CuBr (87.5 m/o) was close to that observed in this laboratory for NN'-dimethyltriethylenediamine dibromide-CuBr (94 m/o), Table I. The molecular symmetry of quinuclidine may be C_{3y} or C_3, but it was clear that the cation need not contain rotational axes or mirror planes of symmetry perpendicular to the three-fold axis. It also followed that a doubly charged cation was not essential for the formation of a conducting phase.

Asymmetry was introduced into the quinuclidine structure by introduction of an oxygen atom at the three-position, giving the quinuclidone-type structure. High conductivity was found for 3-quinuclidone hydrochloride-CuCl (80 m/o) and 3-quinuclidone hydrobromide-CuBr (80 m/o), showing that highly symmetric organic nitrogen compounds are not necessary for the formation of highly conductive phases.

However, it is possible that the carbonyl group represents only a relatively small perturbation on the cage structure which, accordingly, may be axially disordered at 120° rotational intervals in the crystal structure of the double salt and thereby simulate three-fold symmetry. A crystallographic study of such possible positional disorder in the double salt would be required to clarify this possibility.

The formation of conductive phases with cations not having a cage structure was evaluated in the systems: dimethylpiperizine dihydrochloride-CuCl and NN', NN'-diethylenedipyrrolidinium dibromide-CuBr, the structures of which are shown in Fig. 1, No. X and XI, respectively. No significant conductivity was observed with either of these materials. One might infer from the low conductivity of these two materials that removal of the cage structure from a saturated species such as NN'-dimethyltriethylenediamine dibromide appears to prevent the stabilization of conductive phases. However, by analogy with previous work on silver conductors (8, 10) high conductivity was found with pyridinium bromide-CuBr (87.5 m/o) where the

organic cation has a planer aromatic ring and in particular, three-fold symmetry is absent.

The possible conductivity of the 1-adamantanamine hydrochloride-CuCl system (Fig. 1, No. XII) was investigated by analogy to the electrolyte N-hydrohexamethylenetetramine chloride-CuCl (87.5 m/o) (Fig. 1, No. IX). Conductivities only a little greater than 10^{-7} $ohm^{-1} \cdot cm^{-1}$ were achieved with the samples investigated.

From conductivity measurements the optimum Cu/substituted organic ammonium halide mole ratios were found to be 7:1 for CuBr-quinuclidine hydrobromide, CuBr-quinuclidine methylbromide, and CuBr-pyridinium bromide, close to 6:1 for CuCl-quinuclidine hydrochloride, and 4:1 for CuBr-3-quinuclidone hydrobromide and CuCl-3-quinuclidone hydrochloride. The conductive materials used in these investigations were not single phase, as determined by x-ray diffraction, and optimized stoichiometries may be somewhat contingent upon experimental details used for electrolyte synthesis. Further comment on the stoichiometry of the conductive phase or phases in these electrolytes must await single-crystal structural determinations.

The conductivity of an ionic conductor can be represented by $\sigma = n\mu q$ (17), where n is the concentration of migrating species, μ is the ionic mobility, and q is the charge on the migrating species. Assuming that a univalent copper ion is the migrating species in these electrolytes, q will be essentially constant. The concentration of ions n in these copper electrolytes will vary between one material and another, being dependent on how much ionically conducting phase is present. Therefore, to compare conductivity values between the more highly conductive copper electrolytes might be somewhat erroneous.

The mobility μ of such ionic conductors can be represented by (17)

$$\mu = \mu_0 e^{-\Delta E/kT}$$

where ΔE is the activation energy for ionic migration and the other symbols have their usual significance. The concentration of migrating species n will be difficult to predict in the absence of single-phase material; it may therefore be more meaningful to compare ΔE values obtained from the conductivity-temperature dependence than absolute conductivity values.

The lowest activation energies were found for electrolytes (Table II) stabilized by the quinuclidine structure. The conductivities of these electrolytes are comparable to those found for electrolytes stabilized by NN'-dihydro and dimethyltriethylenediamine dibromide. The activation energies of the latter materials were found to be higher than those of the quinuclidine-CuX electrolytes, which suggests that there may be more mobile copper ions in the latter materials.

The introduction of an oxygen double bond into the three-position of quinuclidine causing the possible loss of symmetry in the 3-quinuclidone increased the activation energy for copper migration from 2.7 kcal/mole for quinuclidine hydrobromide-CuBr (87.5 m/o) to 6.7 kcal/mole for 3-quinuclidone hydrobromide-CuBr (80 m/o). The optimum stoichiometric ratios are also changed from 7:1 to 4:1 indicating a different structure and possibly a different conduction mechanism. The electrolyte 3-quinuclidone hydrochloride-CuCl (80 m/o) was not stable at the temperatures used for temperature dependence measurements, however assuming an activation energy comparable to that found in 3-quinuclidone hydrobromide-CuBr (80 m/o) there must be a high concentration of mobile species available since a conductivity of 2.5×10^{-2} $ohm^{-1} \cdot cm^{-1}$ was recorded at ∞Hz.

These results indicate that high molecular symmetry in the substituted organic ammonium cations is not essential in achieving high conductivity, but does appear to give a lower ΔE value for copper ion migration in the solid phase. For example, the activation energy for NN'-dimethyltriethylenediamine dibromide-CuBr (87.5 m/o) is greater (5.7 kcal/mole) than for NN'-dihydrotriethylenediamine dibromide-CuBr (87.5 m/o) 4.55 kcal/mole), and quinuclidine methylbromide-CuBr (87.5 m/o) is greater (3.6 kcal/mole) than quinuclidine hydrobromide (2.68 kcal/mole). We tentatively conclude that introduction of a larger group on the onium nitrogen atom leads to larger ΔE values. However, the over-all conductivity will be contingent also on the number of migrating species available in the phase that is stabilized as indicated earlier.

All of the copper electrolytes were evaluated in galvanic cells and were observed to lose voltage upon standing on open circuit, with electrolyte deterioration, even when stored in a dry box under an argon atmosphere. With halide cathode materials the initially white electrolyte became black both upon standing and during discharge. This color change appears to be a direct chemical reaction. By pressing pellets of the configuration $CuBr_2$/electrolyte/$CuBr_2$ the initially white electrolyte was observed to become black upon standing, indicating that even in the absence of any voltage breakdown of the electrolyte, a direct chemical path was also available for reaction with the copper electrolyte. This chemical instability was only observed in the stabilized conductive electrolyte phases and not in the organic nitrogen halide compounds used for the electrolyte synthesis. No color change was observed in pellets $CuBr_2$/organic nitrogen halide/$CuBr_2$ upon extended standing. The electrolytes were also stable to copper since conducting cells Cu/electrolyte/Cu were stable over several months without evidence of chemical breakdown.

The chemical change taking place in galvanic cells containing halide cathode materials, probably involves a halide migration which could cause the formation of electron holes, and/or the formation of Cu^{2+} species in the electrolyte, thus explaining the loss of cell voltage. The presence of electron holes in cuprous halides containing an excess of halogen is well known (18, 19). Four cells of the configuration Cu/electrolyte/graphite + electrolyte were charged up initially to around 600 mV; these cells slowly began to lose their charge with the simultaneous decomposition of the electrolyte (detected by the color change), and finally held a voltage of around 350 mV for several months.

In cells using V_2O_5 or MoO_3 as cathode materials, the cell voltage similarly deteriorated with time; however, no electrolyte color change was observed. This indicates that voltage breakdown of the electrolytes is probably occurring leading to some electronic conduction path. Preliminary attempts using x-ray diffraction techniques to identify the electrolyte decomposition products were not conclusive.

The performance of these electrolytes in solid-state coulometers is illustrated by the cell Cu/pyridinium bromide-CuBr (87.5 m/o)/graphite (Fig. 6). The first few cycles charging and discharging at 10 μA showed high coulombic efficiencies, indicating that initially the materials were predominantly Cu^+ ion conducting; however, upon extended cycling the efficiency began to decrease, probably due to electrolyte breakdown caused by the voltage drop across the cell.

The fact that high ionic conduction has been found in copper electrolytes stabilized by substituted organic ammonium compounds of lower symmetry than previously reported, indicates that such electrolyte phase stabilization is more general than might have previously been thought. From the evidence presently available it would appear that these materials are somewhat unstable when applied in galvanic cells. Whether these copper electrolyte materials can find any useful applications in solid-state devices must await the syntheses or isolation of the phase or phases that are responsible for the ionic conduction, together with the necessary structural determination and stabilization of the electrolytes in cells.

Acknowledgment

The partial support of this investigation by the National Science Foundation (NSF Faculty Research Participation Project, Grant No. GZ-2939) and the assistance of Patricia M. Schultz who performed many of the technical measurements are gratefully acknowledged.

Manuscript submitted March 31, 1975; revised manuscript received June 4 1975. This was Paper 19 presented at the New York, New York, Meeting of the Society, Oct. 13-17, 1974.

Any discussion of this paper will appear in a Discussion Section to be published in the June 1976 JOURNAL. All discussions for the June 1976 Discussion Section should be submitted by Feb. 1, 1976.

Publication costs of this article were partially assisted by Gould Incorporated.

REFERENCES

1. D. O. Raleigh, *J. Appl. Phys.*, **41**, 1536 (1970).
2. a. B. B. Owens, J. S. Sprouse, and D. L. Warburton, 25th Power Sources Conference, 1972, p. 8.
   b. J. E. Oxley and B. B. Owens, Power Sources 3, D. H. Collins, Editor, Oriel Press, Boston (1970).
3. B. B. Owens, *This Journal*, **117**, 1536 (1970).
4. B. B. Owens, J. H. Christie, and G. T. Tiedemann, *ibid.* **118**, 1144 (1971).
5. B. B. Owens, in "Advances in Electrochemistry and Electrochemical Engineering," P. Delahay and C. W. Tobias, Editors, Vol. 8, p. 1-61, Wiley-Interscience, New York (1971).
6. J. H. Christie, B. B. Owens, and G. T. Tiedemann, Abstract 20, p. 53, The Electrochemical Society Extended Abstracts, Fall Meeting, New York, New York, Oct. 13-17, 1974.
7. S. Geller, *Science*, **157**, 310 (1967).
8. S. Geller and M. D. Lind, *J. Chem. Phys.*, **52**, 5854 (1970).
9. S. Geller, *Science*, **176**, 1016 (1972).
10. S. Geller and B. B. Owens, *J. Phys. Chem. Solids*, **33**, 1241 (1972).
11. S. Geller, P. M. Skarstad, and S. A. Wilber, *This Journal*, **122**, 332 (1975).
12. T. Takahashi, O. Yamamoto, and S. Ikeda, *ibid.*, **120**, 1431 (1975).
13. T. Takahashi and O. Yamamoto, *ibid.*, **122**, 83 (1975).
14. E. Warburg, *Ann.*, **6**, 125 (1901).
15. G. Jones and S. M. Christian, *J. Am. Chem. Soc.*, **57**, 272 (1935).
16. F. F. Blicke and E. B. Hatelling, *ibid.*, **76**, 2427 (1954).
17. W. Jost, "Diffusion in Solids, Liquids, and Gases," E. M. Laebl, Editor, Academic Press Inc., New York (1960).
18. C. Wagner, *J. Chem. Phys.*, **18**, 62 (1950).
19. J. B. Wagner and C. Wagner, *ibid.*, **26**, 1597 (1957).

On the Kinetics of the Breakdown of Passivity of Preanodized Aluminum by Chloride Ions

Z. A. Foroulis*,[1] and M. J. Thubrikar

Department of Metallurgy and Materials Science, New York University, New York, New York 10019

ABSTRACT

The kinetics of passivity breakdown and nucleation of pitting of preanodized aluminum by chloride ions has been investigated using aluminum supporting oxide films of reasonably well-known thickness and structure. The kinetics of passivity breakdown at the steady-state, critical pitting potential is influenced by chloride ion concentration, temperature, and oxide film thickness; it was found to be independent of solution pH in the range 5-10. It is postulated that passivity breakdown and nucleation of pitting at the critical pitting potential occurs by a process of Cl^- adsorption (assisted by the field at the oxide-solution interface) on the hydrated oxide surface and formation of a soluble, basic chloride salt with the lattice cation which readily goes in solution. This process of localized dissolution of the hydrated oxide film via formation of a soluble, basic, aluminum chloride salt once initiated is likely to continue in an "autocatalytic" fashion until the oxide is locally "penetrated" and dissolution of the substrate metal begins.

The breakdown of passivating oxide films on aluminum, by "aggressive" anions such as chlorides at sufficiently positive anodic potentials is frequently responsible for the failure of aluminum and its alloys in aqueous chloride solutions because it usually leads to severe pitting of the underlying metal. Several mechanisms for the breakdown process have been suggested (1-7). However, there is little experimental information on the kinetics of the oxide film breakdown process which could be used to establish the mechanism of pit nucleation of aluminum by chloride ions. Considerably more research is required to better understand the physical and chemical processes occurring during pit nucleation. In particular, there is considerable need to understand the role of surface films, Cl^- concentration, solution pH, and temperature on the kinetics of passivity breakdown and nucleation of pitting.

The work described in this report was undertaken to study the kinetics of pit nucleation of preanodized aluminum by chloride ions, as a function of Cl^- concentration, solution pH, and temperature. The purpose of prefilming of aluminum by anodization was to obtain oxide films of reasonably well-known thickness and structure.

Experimental

The electrodes, about 4-7 cm^2 total exposed area were cut from 99.99% pure aluminum. The electrode assembly was similar to the one described previously (8). Surfaces were abraded through 4-0 emery paper and then metallographically polished using 1 and 0.5μ alumina. This surface preparation produced a mirror like surface.[2] Following rinsing in distilled water,

* Electrochemical Society Active Member.
[1] An Adjunct Professor and also associated with Exxon Research and Engineering Company, Florham Park, New Jersey 07932.
Key words: aluminum, pitting, corrosion, passivity breakdown, kinetics.

[2] This type of surface preparation was essential for the microscopic observation of pits.

specimens were anodized using two different methods. One method involved constant current anodization in sulfuric acid using 15% w/v sulfuric acid (sp gr 1.84) for various times at 25 mA/cm^2 (20-21V) with a standard rate of stirring. Following anodization, the specimens were sealed in boiling distilled water. In general, the ratio of anodizing time to sealing time in boiling distilled water was 1:30. In some instances, however, longer times of sealing were also used. The unsealed films produced consisted of a thin barrier layer adjacent to the metal and a thick outer porous layer. The oxide film prior to sealing in water is essentially γ-Al_2O_3. During exposure in boiling water, sealing of pores due to hydration of γ-Al_2O_3 and formation of the less dense boehmite, AlO(OH), or $Al(OH)_3$ is well known (9-12). The sealing procedure gives an essentially pore free film (9). The over-all thickness of the oxide films produced by anodization was estimated from values reported by Hoar and Wood (9).

Another method of prefilming of aluminum specimens was constant voltage anodization in 3% ammonium tartrate. In this case different anodizing voltages were used in order to get different film thicknesses. Films formed in ammonium tartrate solution are much thinner, nonporous, and did not require sealing. The oxide films produced by anodization in ammonium tartrate are similar to the air formed oxides and consist essentially of γ-Al_2O_3. The thickness of oxides produced by anodizing in ammonium tartrate solutions were estimated from values reported by Hass (13).

Solutions for the kinetic studies of film breakdown and pit initiation were prepared from distilled water and reagent grade KCl, KOH, and H_2SO_4. The cell design was essentially identical to the one described previously (14). Solutions were deaerated by bubbling prepurified nitrogen prior and throughout each run. Additional purification was done by passing it through copper turnings heated at 500°C. Potential control was obtained by means of an electronic potentiostat. Potentials were measured against SCE using a vacuum tube millivoltmeter (high impedance). Current was measured by recording the potential drop across a standard resistor using a millivolt recorder. Temperature control was achieved either by means of a heat mantle fitted to the lower part of the cell or by using suitable cooling baths.

Since the aim of this investigation was to gain an understanding of the mechanism of nucleation of pitting, it was felt of particular significance to study the kinetics of film breakdown at the steady-state, critical pitting potential. The procedure was to anodically polarize the electrode, in steps of 10 to 20 mV,[3] after a rest period of a few minutes at the open-circuit potential. At each step the potential was kept constant at a given value, while the current was recorded continuously for as long as 24 hr and the electrode was then observed under a low power microscope for pitting. The potential at and above which pitting was observed was taken as the potentiostatic, critical pitting potential, E_c. It was also observed that at and above E_c, the current, after an initial induction period (τ) during which the current remained essentially constant, began and continued to increase with time, eventually reaching current values higher by two or more orders of magnitude. At potentials smaller than the critical, the current generally <1 $\mu A/cm^2$, remained essentially constant and pits were not observed. Reproducibility of the critical pitting potential was within about 10-15 mV. All potentials are reported with reference to the SCE.

To gain information regarding the kinetics of film breakdown and pit nucleation at the critical pitting potential, the induction time τ was determined experimentally as a function of Cl^- ion concentration, temperature, oxide film thickness, and solution pH. The induction time τ is defined as the initial period of time (generally a few minutes) at the critical pitting potential during which the anodic current (induction current) is very low and essentially constant, prior to a beginning of a continuous increase of current with time which eventually reaches current values higher than the induction current by two or more orders of magnitude as shown in Fig. 1.

[3] Prior to each potential setting, the electrode was subjected to new surface preparation (polishing, anodization, and sealing for specimens anodized in sulfuric acid).

The continuous increase of the over-all anodic current at the critical potential at times higher than τ is attributed to growth of minute pits initiated on a microscale during the induction time. As the minute pits grow the over-all, anodic current density, due to active metal dissolution at the very small pit or pits and the passive current passing through most of the electrode surface which remains passive, continues to increase with time as the size of pits grow and perhaps additional pits nucleate. The localized, anodic current density due to active metal dissolution at the small pit or pits is expected to be higher by several orders of magnitude as compared with the current density passing through the passive surface. It should be mentioned that pits could actually be observed under a low power microscope only after the electrode was maintained at the critical potential for an extended period of time beyond the induction time τ during which pits grew to sufficient size to be visible under the microscope.

In a typical experiment for the induction time determination, the preanodized aluminum electrode was introduced in the cell and its potential was set and maintained at the steady-state critical potential for pitting while the current was recorded continuously. The time required for the current to begin its sharp and continuous increase was measured as τ, the induction time for the oxide film breakdown and nucleation of pitting.

The measurement of the induction time τ for pit nucleation was not very reproducible. The poor reproducibility of the induction time for pit nucleation as seen by the spread of the experimental data points is probably due to several reasons, such as nonuniform thickness of the oxide film produced by anodization due to nonuniform current distribution on the specimen surface (edge effects), small variations in surface finish, and perhaps other oxide surface discontinuities. Since the induction time τ relates to the very precise process of current increase at the critical pitting potential, the relative accuracy of measuring τ is also affected by the uncertainty of 10-15 mV in reproducing the critical pitting potential (15). The reported, induction time data represent clearly defined values using specimens with carefully prepared surface finish, as described previously.

Results and Discussion

A typical experiment showing the variation of current with time at and below the critical pitting potential is shown in Fig. 1. The data were obtained with preanodized aluminum exposed to 3.0M KCl at 25°C.

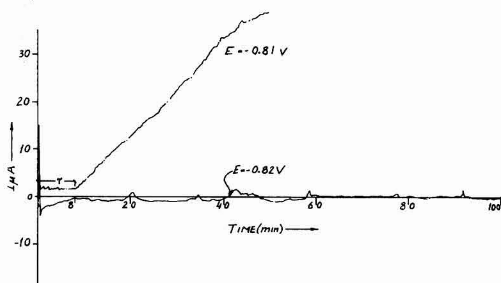

Fig. 1. Typical current-time curve for preanodized pure aluminum electrode potentiostated at −0.81 and −0.82V (SCE) in 3M KCl at 25°C.

The critical pitting potential in this case was $-0.81V$ (SCE) and the induction time, τ, for pit nucleation was about 8 min. At the lower potential of $-0.82V$ (SCE) the current remained relatively constant and very low and no pits were observed for up to 24 hr.

The dependence of the induction time on chloride ion concentration was measured at 25°C in the concentration range 0.01-3M KCl; the pH of these solutions was in the range 5.9-6.1. The data for a series of experiments with preanodized[4] aluminum are plotted in Fig. 2. The data show that the induction time for pit nucleation decreases from about 23 min in 0.01M KCl to about 4 min in 3M KCl. The slope, n, of the log $1/\tau$ *vs.* log C_{Cl^-} line is approximately $n \simeq -0.1$ in the concentration range 0.01-1M KCl. At higher chloride ion concentrations the induction time appears to decrease rapidly as indicated by the approximate slope of $n \simeq -0.9$ which was drawn through the available experimental points. One may question the relative accuracy of the slopes drawn through the data points; the significant thing is not the precise value of the slopes but rather the general conclusion drawn from the data that in low Cl^- concentrations there is a very weak dependence of τ on KCl concentration but in higher KCl concentrations there is a tendency for higher dependence of τ on Cl^- concentration.

Temperature as might be expected has also considerable influence on the rate of pit nucleation as indicated by data on the temperature dependence of τ plotted in Fig. 3. This figure shows an Arrhenius-type plot for the temperature variation of τ of preanodized aluminum in 0.1M KCl solution. The plot shows an apparent activation energy of about 6.7 kcal/mole for the pit nucleation process.

The solution *p*H in the range 5-10, at constant chloride ion concentration, was found to have no effect on the rate of pit nucleation, as measured by the induction time. This is shown with the data plotted in Fig. 4. These data were obtained with preanodized aluminum in 0.1M KCl in the *p*H range 5-10. Solution *p*H was adjusted as required with either H_2SO_4 or KOH.

In order to study the influence of oxide film thickness on the rate of film breakdown and pit nucleation, a series of experiments was carried out with oxide films of a broad thickness range. Most oxide films on aluminum were prepared by anodization in 15% H_2SO_4 followed by sealing in distilled water as described in the experimental section. This procedure produced oxide films in the thickness range 0.8 to about 40μ. Several oxide films of considerably smaller thicknesses, in the range of 260-1300Å, were also produced by anodization in 3% ammonium tartrate solution.

The dependence of the incubation time τ for pit nucleation on the oxide film thickness is shown in Fig. 5. The data show essentially a linear dependence of τ on oxide film thickness. The data plotted in Fig. 5 were obtained in 0.1 and 3M KCl solutions with aluminum preanodized in H_2SO_4 and sealed in distilled water and in 0.1M KCl solutions with aluminum preanodized in 3% ammonium tartrate solution.

Table I shows the dependence of the steady-state, critical pitting potential on the thickness and structure of the oxide film. The data show that the critical pitting potential of specimens covered with oxide films in the thickness range of 0.026-0.130μ is essentially the same within the ±10-15 mV (experimental error) of the average value. However, in the case of much

[4] Unless otherwise indicated, specimens were anodized for 1 min in 15% H_2SO_4 and sealed for 30 min in boiling distilled water.

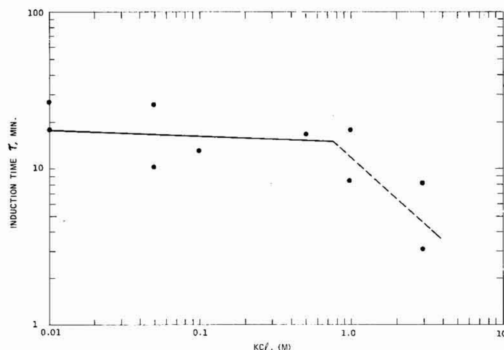

Fig. 2. Dependence of the induction time for pit nucleation on chloride ion concentration in the *p*H range 5.9-6.0 at 25°C. Preanodized pure aluminum.

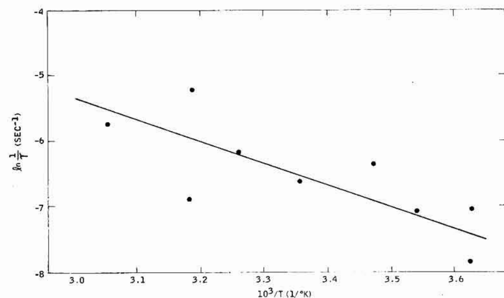

Fig. 3. Arrhenius-type plot for temperature dependence of induction time for pit nucleation. Preanodized aluminum, 0.1M KCl.

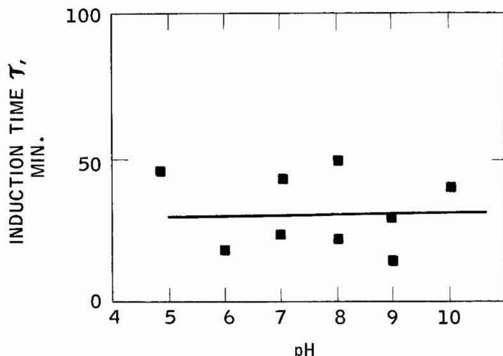

Fig. 4. Dependence of induction time for pit nucleation of preanodized aluminum in 0.1M KCl on solution *p*H.

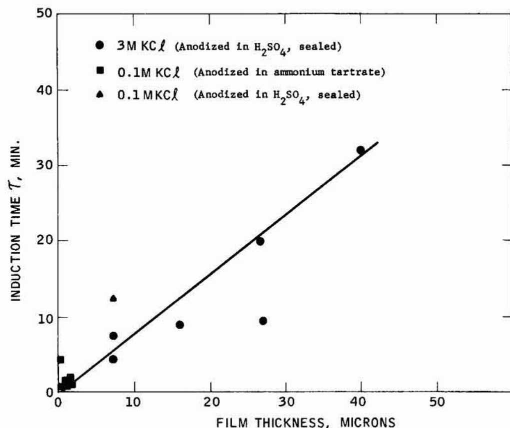

Fig. 5. Dependence of induction time for pit nucleation on oxide film thickness in 0.1 and 3M KCl, 25°C.

Table I. Steady-state critical pitting potentials, E_c vs. SCE

Electrolyte	Surface preparation	Oxide film thick-ness, μ	E_c, V (SCE)
0.1M KCl 25°C	Anodization in 3% ammonim tartrate	0.026	−0.73
0.1M KCl 25°C	Anodization in 3% ammonim tartrate	0.097	−0.72
0.1M KCl 25°C	Anodization in 3% ammonim tartrate	0.130	−0.71
0.1M KCl 25°C	As polished		−0.73
0.1M KCl 25°C	Anodization in 15% H_2SO_4 and sealed in boiling dist. H_2O	0.79	−0.68

higher oxide film thickness (about 0.79μ) there is clear evidence that E_c increases with oxide film thickness. The apparent increase in E_c with oxide film thickness suggests that with increasing oxide film thickness, due to potential drop (pd) within the oxide film, a higher applied anodic potential is required to attain the minimum pd across the oxide-solution interface which is required to achieve the penetration of Cl^- through the electric double layer at the oxide-solution interface and its adsorption on the hydrated oxide surface.

Following the arguments of Engell and Stolica (16), Hoar and Jacob (17), and Bogar and Foley (18), it is assumed that $1/\tau$ is an approximate estimate of the rate of the limiting process leading to pit nucleation of aluminum. Then the slope of the straight lines in Fig. 2 is interpreted as the order n of the rate-determining step during pit initiation with respect to the concentration of chloride ion in solution.

The very weak dependence of τ on chloride ion concentration in dilute chloride solution, as shown in Fig. 2, and the low apparent activation energy of about 6.7 kcal/mol (Fig. 3) suggest that in dilute chloride solutions the rate-determining step in the process of pit initiation is likely to be a diffusion or adsorption step. Lattice diffusion of chloride ions through the aluminum oxide film via lattice defects or by place exchange of oxide ions and chloride ions would be energetically consistent with the measured activation energy and the weak dependence of τ on C_{Cl^-}, but the diffusion rate itself would be much too slow to account for the induction time observed (19).

If we suppose that the relationship between the concentration of Cl^- adsorbed on the hydrated oxide surface and the bulk solution is that of a Freundlich adsorption isotherm, and assuming that pitting is initiated at the critical pitting potential when a critical concentration of Cl^- is established at one or more sites on the hydrated oxide surface, then $1/\tau$ should be related to the bulk chloride ion concentration C according to the Freundlich adsorption isotherm. The data plotted in Fig. 2 in dilute solutions follow such a functional relationship

$$\frac{1}{\tau} \simeq k_1 C^{1/n'} \simeq k_1 C^n$$

where k_1 and $1/n'$ are constants of a Freundlich-type isotherm and n is the stoichiometric factor described previously.

In higher chloride ion concentrations, the induction time apparently decreases much faster with chloride ion concentration as indicated by the approximate dotted line slope of about $n \simeq -0.9$. The stronger dependence of τ on the bulk chloride ion concentration in concentrated KCl solutions suggests that the rate-determining step in the over-all process of passivity breakdown changes from a step involving adsorption from solution on the hydrated oxide surface to that of a chemical reaction on the hydrated oxide surface which involves approximately one Cl^- per aluminum cation.

The stoichiometric factor n obtained in this study for the pit initiation process of aluminum is considerably smaller than the values of 2.5-4.5 reported by Hoar and Jacob (17) for the breakdown of passivity in 18-8 stainless steel by chloride ion in sulfuric acid solution of pH 2.05, in the potential range of 0.4-0.8V (SHE). These authors also found an apparent activation energy of about 60 kcal/mole for the breakdown of passivity in acidic solutions. Values of n in the range 3.0-11.1 were also reported by Foley and Bogar (18) for pit initiation of aluminum alloys in sulfuric acid solutions containing chloride ions in the pH range 0.0-3.5. Their data on the temperature dependence of the breakdown process give apparent activation energies in the range of 22.9 kcal in pH 0.0 and 12.0 kcal/mole in pH 6.08. Reasons for the considerable difference in stoichiometric numbers n and activation energies between the present study and those of Foley and Bogar (18), Hoar and Jacob (17), and Engell and Stolika (16) are not known. It is assumed, however, that this difference is probably caused by the considerable difference in pH of the solutions used in the various breakdown experiments, and the difference in alloy and passive film compositions. This explanation is consisent with the decreasing stoichiometric number and apparent activation energy reported by Foley and Bogar (18) with increasing solution pH for the passivity breakdown process of an aluminum alloy potentiostated at 0.18V (SCE) in sulfuric acid solution.

General Discussion

Several mechanisms for the action of chloride ions to initiate pitting corrosion have been suggested in the literature. These include: (*a*) Cl^- penetration of the protective oxide film which covers the metal surface through pores or other weak places (1, 20, 21), (*b*) competitive adsorption of Cl^- and oxygen or OH^- for sites on the metal surface (22, 23), (*c*) migration of chloride ions inward through the oxide lattice (4), (*d*) peptization of the oxide film by a strong negative charge caused by adsorbed anions (5) and by dynamic breakdown-repair mechanism (7). Aluminum provides a good opportunity to evaluate the influence of an oxide on the process of pit initiation since well-known methods are available for preparing oxide films of different thicknesses and structure by anodization.

The results of the present study provide considerable experimental evidence to test the various mechanisms for passivity breakdown and initiation of pitting in nearly neutral solutions by chloride ions.

Chloride ion migration through pores or other weak places in the oxide film (1, 20, 21) followed by competitive adsorption between chloride ions and adsorbed oxygen or hydroxyl ions at the metal/solution interface as a mechanism of pit initiation (22, 23) is an unlikely mechanism for several reasons. Migration of Cl^- through pores or other weak spots in the oxide film as the rate-determining step can be ruled out, since by treating the aluminum specimens as a porous electrode it can be shown (24) that the mass transport limiting current for a porous and a corresponding flat electrode are the same both being determined by mass transport in the hydrodynamic layer outside the electrode. Furthermore, it is considered unlikely that continuous pores through the oxide film to the bare aluminum surface are present in oxide films prepared by anodization in ammonium tartrate or in H_2SO_4 with subsequent sealing.

Competitive adsorption (22, 23) between chloride ions and adsorbed oxygen or OH^- on a bare metal surface is also considered an unlikely mechanism. There is abundant evidence that aluminum metal (even without a thick barrier-type film) in neutral solutions is covered with a thin persistent and fairly protective film of aluminum oxide (25). A dynamic passivity breakdown-repair mechanism (7) which attributes to the Cl^- the role of inhibiting repassivation rather than promoting passivity breakdown, cannot account for the observed increase in induction time τ with the thickness of the oxide film. The passivity breakdown-repair mechanism (7) conceptually is similar to the com-

petitive adsorption mechanism (22, 23) and assumes in essence competitive adsorption between Cl^- and OH^- (or H_2O) on the metal surface as the rate-limiting process of pit nucleation. If this were the rate-limiting process in pit nucleation, the induction time should be independent of the thickness of the oxide film (which must in some way be "penetrated" before Cl^- can adsorb on the bare metal surface). This, of course, is contrary to the data shown in Fig. 5, which indicate that the induction time increases with oxide film thickness.

Migration of chloride ions inward through lattice diffusion, as discussed previously, is much too slow to account for the induction time observed (19).

The kinetic data presented in this paper are consistent with a pit nucleation model (26) which involves field-assisted adsorption of chloride ions from solution on the hydrated oxide surface followed by oxide dissolution as the rate-determining steps in the process of passivity breakdown and pit nucleation of aluminum in nearly neutral solutions. The over-all passivity breakdown and nucleation of pits according to this model involves the following sequence of reaction steps: (*a*) adsorption of Cl^- on the oxide-solution interface under the influence of the electric field (at the oxide-solution interface) in competition with OH^- or H_2O molecules for surface sites on the hydrated oxide surface; (*b*) formation of a basic hydroxychloride aluminum salt with aluminum oxide cations on the hydrated oxide surface, which immediately separates from the oxide lattice and readily goes in solution.

It is suggested that a probable reaction describing formation of such a readily soluble basic chloride aluminum salt is reaction [2]

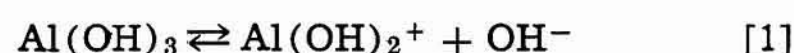

$$Al(OH)_3 \rightleftarrows Al(OH)_2^+ + OH^- \quad [1]$$

$$Al(OH)_2^+ + Cl^- \rightarrow Al(OH)_2Cl \quad [2]$$

Reaction [1] describes the ionization of the hydrated aluminum oxide surface in nearly neutral solution. This reaction accounts for the positive charge on the hydrated oxide surface as indicated by ζ potential measurements (27-29).

This process of field assisted Cl^- adsorption on the hydrated oxide surface and formation of a soluble aluminum chloride salt leading to localized oxide dissolution will have a high probability of repeating itself at the same site, since at constant anode potential the applied field at the oxide-solution interface will tend to be stronger at the "thinned" point of the oxide film. Thus, the process of localized dissolution of the oxide film via the formation of a basic chloride aluminum salt ($Al(OH)_2Cl$) is likely to continue until the oxide film is locally dissolved; once the oxide film is locally "dissolved," dissolution of the substrate metal begins and the anodic current density at the very small pit or pits increases by several orders of magnitude compared with the current density of the passivated surface.

Localized dissolution of the oxide (leading to pitting of the underlying metal), rather than general dissolution of the oxide film occurs at the critical pitting potential because of the "autocatalytic" character of the localized oxide film dissolution at the critical pitting potential. Once a critical concentration of chloride ions is adsorbed on a particular site on the hydrated oxide surface via this mechanism (26), and one or more, adjacent, aluminum oxide lattice cations are transformed to chloride-containing soluble salts, they are likely to immediately separate from the oxide cations in the lattice and go in solution.[5] The probability of this localized oxide dissolution to continue on the same sites is considerable because of the higher potential drop (pd) at the oxide-solution interface (under constant, applied anodic potential) expected on these sites.

This argument implies that preferential sites for pit initiation are likely to be areas of oxide surface defects such as scratch lines, voids or other surface flaws where the oxide thickness is smaller than in adjacent areas and therefore the pd across the oxide-solution interface is higher (30).

The question may be raised as to why the high field across the oxide film would not rapidly repair the film in areas where it is locally thinned by dissolution and thereby prevent film breakdown. The answer to this lies in the supposition that on the oxide-solution interface a competition exists between Cl^- and OH^- (or H_2O molecules) for oxide surface sites. Once oxide dissolution is initiated via the proposed mechanism, a high probability exists that as aluminum cations advance through the oxide film at the thinned points of the film (under the influence of the field across the oxide film) instead of oxide forming OH^- or H_2O molecules, they are likely to meet Cl^- and OH^- so that a high probability exists for formation of a readily soluble aluminum hydroxychloride salt rather than an insoluble aqueoaluminum complex required for oxide film repair.

In low chloride ion concentrations adsorption of chloride ions, from solution, on the hydrated aluminum oxide surface under the influence of the field at the oxide-solution interface is assumed to be the rate-determining step in the process of passivity breakdown. In higher chloride ion concentrations, the reaction step leading to formation and dissolution of the hydroxychloride aluminum salt on the hydrated oxide surface is likely to become the rate-determining step in the process of pit initiation.

The induction time for passivity breakdown and pit initiation according to the proposed mechanism is a direct measure of the rate of the localized dissolution of the passive aluminum oxide film via the sequence of Cl^- adsorption and formation of a readily soluble chloride containing aluminum salt (Eq. [2]).

On this basis, it is expected that the induction time τ for pit initiation should increase with the thickness of the oxide film. Data plotted in Fig. 5 on the dependence of the induction time for preanodized aluminum on oxide film thickness show that τ increases with oxide thickness following essentially a linear dependence.

The hypothesis in the proposed mechanism that a readily soluble, chloride-containing aluminum salt is locally formed on the solution side of the aluminum oxide surface, once the chloride ions under the influence of the applied anodic potential have penetrated the electric double layer at the oxide-solution interface and adsorbed on the hydrated oxide surface, is consistent with literature data (31, 32) indicating that hydrated aluminum oxides form soluble aluminum salts in acidic or nearly neutral aqueous solutions containing chloride ions.

Acknowledgment

The authors are pleased to acknowledge support of this research by the Ocean Engineering Research Program in the Department of Metallurgy and Materials Science of New York University, and the encouragement and support provided by Dr. H. Margolin.

Manuscript submitted Feb. 10, 1975; revised manuscript received June 2, 1975.

Any discussion of this paper will appear in a Discussion Section to be published in the June 1976 JOURNAL. All discussions for the June 1976 Discussion Section should be submitted by Feb. 1, 1976.

[5] It is worth noting that the solubility of hydrated aluminum oxide cations present in the film without the participation of the activating chloride ions is considerably lower; the very low rate of dissolution in this case is uniform thoughout the oxide surface.

REFERENCES

1. U. R. Evans, L. C. Bannister, and S. C. Britton, *Proc. Roy. Soc.*, **A131**, 366 (1931).
2. H. Bohni and H. H. Uhlig, *This Journal*, **116**, 906 (1969).

3. Ya. M. Kolotyrkin, *Corrosion*, **19**, 263t (1963).
4. T. P. Hoar, D. C. Mears, and G. P. Rothwell, *Corrosion Sci.*, **5**, 279 (1965).
5. T. P. Hoar, *ibid.*, **7**, 341 (1967).
6. M. A. Heine, D. S. Keir, and M. J. Pryor, *This Journal*, **112**, 24 (1965).
7. J. Zahavi and M. Metzger, in "Localized Corrosion," B. F. Brown, J. Kruger, and R. W. Staehle, Editors, p. 132, NACE, Houston (1975).
8. M. Stern and A. C. Makrides, *This Journal*, **107**, 782 (1960).
9. T. P. Hoar and G. Wood, *Electrochim. Acta*, **7**, 333 (1962).
10. J. E. Draley, S. Mori, and R. E. Loess, *This Journal*, **110**, 622 (1963).
11. J. E. Draley and W. E. Ruther, *ibid.*, **103**, 441 (1956).
12. S. Mori, R. E. Loess, and J. E. Draley, *Corrosion*, **19**, 165 (1963).
13. G. Hass, *J. Opt. Soc. Am.*, **39**, 532 (1949).
14. Z. A. Foroulis, *This Journal*, **113**, 532 (1966).
15. Z. A. Foroulis and M. J. Thubrikar, *Werkstoffe Korrosion*, **26**, 350 (1975).
16. H. Engell and N. Stolika, *Z. Physik. Chem. N.F.*, **20**, 113 (1959).
17. T. P. Hoar and W. R. Jacob, *Nature*, **216**, 1299 (1967).
18. F. D. Bogar and R. T. Foley, *This Journal*, **119**, 462 (1973).
19. A. E. Paladino and W. D. Kingery, *J. Chem. Phys.*, **37**, 457 (1962).
20. T. P. Hoar and U. R. Evans, *This Journal*, **99**, 212 (1952).
21. M. Streicher, *ibid.*, **103**, 375 (1956).
22. H. Leckie and H. Uhlig, *ibid.*, **113**, 1262 (1966).
23. Y. Kolotyrkin, *Corrosion*, **19**, 261t (1963).
24. R. deLevie, in "Advances in Electrochemistry and Electrochemical Engineering," Vol. 6, p. 329, P. Delahay and C. Tobias, Editors, John Wiley & Sons, Inc., New York.
25. M. J. Pryor, *Z. Elektrochem.*, **62**, 782 (1958).
26. Z. A. Foroulis, Presented at the 5th Internatinal Congress on Metallic Corrosion, Tokyo, Japan. Proceedings to be published by NACE; Z. A. Foroulis, *Werkstoffe Korrosion*, Submitted.
27. J. A. Yopps and D. W. Fuerstenau, *J. Coll. Sci.*, **19**, 61 (1964).
28. H. J. Modi and D. W. Fuerstenau, *J. Phys. Chem.*, **61**, 640 (1957).
29. V. C. P. Morphopoulos and H. C. Pareira, *Corrosion Sci.*, **7**, 241 (1967).
30. J. A. Richardson and G. C. Wood, *ibid.*, **10**, 313 (1970).
31. K. F. Lorking and J. E. O. Mayne, *J. Appl. Chem.*, **11**, 170 (1961).
32. E. A. Devuyst and I. H. Warren, in "Oxide-Electrolyte Interfaces," R. S. Alwitt, Editor, p. 112, The Electrochemical Society Softbound Symposium Series, Princeton, N. J. (1973).

Rate of Propagation of Growth Layers on Cubic Crystal Faces in Electrocrystallization of Silver

V. Bostanov, G. Staikov, and D. K. Roe*,[1]

Central Laboratory of Electrochemical Power Sources, Bulgarian Academy of Sciences, Sofia, Bulgaria

ABSTRACT

The advancement rate of mono- and polyatomic growth steps was measured on perfect, screw dislocation-free cubic faces of silver single crystals during electrocrystallization of silver. For low overvoltages, a linear dependence of the rate on overvoltage was found. It was established that the advancement rate of the steps depends on the surface conditions of the crystal face and is about two times larger on a "fresh" surface than on an "aged" one. It was also found that mono- and polyatomic steps advance with the same rate on a fresh surface. A polyatomic step is considered as a ledge composed of monoatomic steps. The ledge spacing of this composite step was estimated. On the basis of these experimental results as well as on the experimentally determined value of the exchange current of adatoms with metal ions of the electrolyte, it is concluded that the electrolytic deposition of silver in 6M solution of silver nitrate is carried out according to the direct transfer mechanism. The value of the exchange current of the edge atoms at the steps with ions of the electrolyte was determined to be $i_{o,st} = 200\ A \cdot cm^{-2}$ for an aged surface and $i_{o,st} = 370\ A \cdot cm^{-2}$ for a fresh surface.

The kinetics of growth of an equilibrium-form, close packed crystal face depends on the rate of advancement of the growth steps on its surface. The theory of electrocrystallization assumes two basic mechanisms of step growth offered by Volmer (1) and Brandes (2): the direct transfer mechanism and the surface diffusion mechanism. According to the first, the ionic transfer onto the crystal surface through the double layer occurs directly at the kink sites of the steps. The ions are discharged and incorporated simultaneously into the crystal lattice. According to the second mechanism the transfer is carried out on completely built areas of the surface. Here the ions discharge and remain adsorbed (adatoms) for a certain period of time.

* Electrochemical Society Active Member.

[1] Present address: Chemistry Department, Portland State University, Portland, Oregon 97207.

Key words: crystal growth, electrocrystallization, silver single crystal, growth layer propagation.

By surface diffusion the adatoms can reach the kink sites and be incorporated into the crystal lattice.

The dependence of the current density, i ($A \cdot cm^{-2}$), on the overvoltage, η, in the case of surface diffusion was derived for the first time by Lorenz (3) and has the form

$$i = i_{o,ad}[e^{\alpha zF\eta/RT} - e^{-(1-\alpha)zF\eta/RT}] \frac{\lambda_o}{x_o} \tanh \frac{x_o}{\lambda_o} \quad [1]$$

In this equation, $i_{o,ad}$ ($A \cdot cm^{-2}$) is the exchange current density of the adatoms with the metal ions of the electrolyte; $2x_o$ (cm) is the average distance between the monoatomic steps which can also be given by the total step length L_s ($cm \cdot cm^{-2}$) per unit area; λ_o(cm), the surface diffusion penetration, is defined by

$$\lambda_o = (zFD_s c^o_{ad}/i_{o,ad})^{1/2} e^{-\alpha zF\eta/2RT}$$

where D_s ($cm^2 \cdot sec^{-1}$) is the surface diffusion coeffi-

cient and c^{o}_{ad} (mol·cm^{-2}) the equilibrium adatom concentration.

In the case of direct transfer the dependence of the current density on overvoltage is described by a Volmer-type equation

$$i = i_{o,st}\delta L_s[e^{\alpha zF\eta/RT} - e^{-(1-\alpha)zF\eta/RT}] \quad [2]$$

here $i_{o,st}$ (A·cm^{-2}) is the exchange current density of the edge atoms of the monoatomic step with the metal ions of the electrolyte and δ (cm) is the width of an atomic row in the crystal lattice parallel to the step.

The normal velocity of step growth or the advancement rate of the step v (cm·sec^{-1}) and the current density are connected in the relation

$$v = iv_M/zFhL_s \quad [3]$$

where v_M (cm^3·mol^{-1}) is the molar volume and h (cm) is the height of a monoatomic step. For low overvoltages, under the assumption that the surface diffusion penetration is small as compared to the average step half-distance, $\lambda_o/x_o << 1$, from Eq. [1] and [2] one obtains a linear dependence of the current density on step length and overvoltage

$$i = \kappa L_s\eta \quad [4]$$

where the constant κ (ohm^{-1}·cm^{-1}) is given by

$$\kappa = i_{o,ad}2\lambda_o zF/RT \quad [5]$$

for surface diffusion, and

$$\kappa = i_{o,st}\delta zF/RT \quad [6]$$

for direct transfer. Under these conditions the advancement rate of the steps is linearly dependent on overvoltage

$$v = k_v\eta \quad [7]$$

where the advancement rate constant k_v (cm·sec^{-1}·V^{-1}) is given by

$$k_v = \kappa v_M/zFh \quad [8]$$

Experimental

The advancement rate of growth steps in electrocrystallization of silver was studied on perfect, dislocation-free, (100) crystal faces. These were obtained by the capillary method described in detail earlier (4, 5). The essence of the method is the electrolytic growth of a silver single crystal in a capillary along a definite crystallographic axis. If this axis is <100>, a (100) face would appear as a frontal face of the single-crystal filament. Under specified conditions of electrolysis, the face may fill up the whole cross section of the capillary. These conditions require high purity of the electrolyte, high concentration of silver ions, and, above all, modulation of the direct current of growth with an alternating 50 Hz current. At slow growth conditions of the single-crystal filament (20 mA·cm^{-2}) and a suitably chosen amplitude of the alternating current, the number of screw dislocations intersecting the front face gradually decreases and a perfect face can be obtained.

It was experimentally shown that dislocation-free (100) faces grow by two-dimensional nuclei (5), in agreement with the theory of crystal growth. The critical overvoltage for the nucleation process is about 6 mV, and if an overpotential lower than this value is applied, charge flow through the electrolytic cell is not observed. A potentiostatic pulse with suitable amplitude and duration (*e.g.*, 12 mV, 100 μsec) leads to the creation of only one nucleus. If after the pulse the face remains at a potential lower than the critical overvoltage, current flows through the cell, passing through a maximum and subsequently decreasing to zero. This current is connected with the growth of the newly formed monolayer and is proportional to the length of growing monoatomic step, in accordance with Eq. [4]. The value of the constant κ in this equation may be determined from the current-time curves following nucleation overvoltage pulses which produce different supersaturations. The round shape of the face complicates this task. The experiment is considerably simplified if the crystal face has the shape of an elongated rectangle.

Rate of Propagation and Form of Monoatomic Layers

The capillary method was developed using capillaries with round cross section. Crystal faces filling up the entire cross section and free of screw dislocations can also be obtained in capillaries with a rectangular cross section (*e.g.*, 400 × 100 μm) (6). At constant rate of growth of a monoatamic layer on a perfect face with rectangular form, a plateau should be expected in the current-time curve, since after a definite time interval a step would be advancing along the face with a constant length. This was experimentally confirmed and Fig. 1 represents three characteristic experimental current-time curves at constant overvoltage.

As shown in Fig. 2, the value of the growth current of a monoatomic step with constant length is linearly dependent on overvoltage, according to Eq. [4]. However, to determine exactly the constant κ in Eq. [4], one should know the step length. Besides on the capillary width, the step length depends also on the form of the monoatomic layer, or whether the layer is round or polygonized. If polygonized, it would also depend on the orientation of the layer, *i.e.*, on the orientation of the seed crystal with respect to the capillary cross section. In Fig. 2 the straight line a refers to the case when the long axis of the rectangular section of the capillary is parallel to the crystallographic direction <100>, and the straight line b, when this axis is parallel to the direction <110>. The slopes of both straight lines differ by $\sqrt{2}$. Therefore it can be concluded that

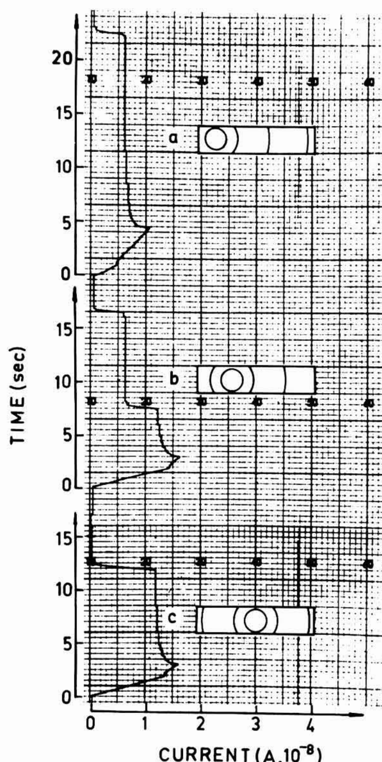

Fig. 1. Current-time curves at 3 mV overvoltage following a nucleation overvoltage pulse on a perfect (100) face with rectangular form (0.1 × 0.4 mm). The probable site of nucleation is schematically indicated in each case.

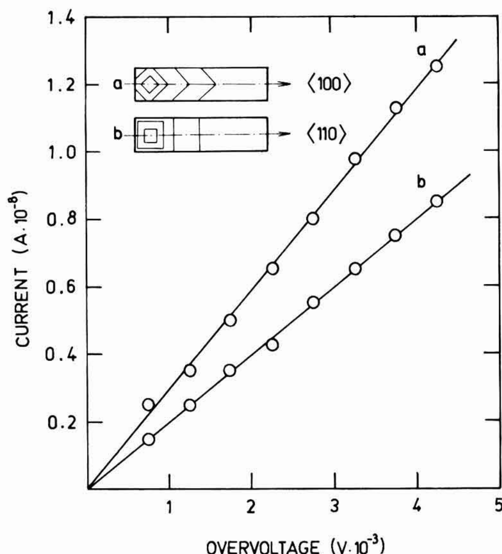

Fig. 2. The stationary value of the current (Fig. 1) as dependent on overvoltage, for two orientations of the seed crystal in respect to the rectangular cross section of the capillary: straight line a, the longitudinal axis of the cross section coincides with the direction 100; straight line b, with the direction 110.

the monoatomic layers are polygonized and have a square form and that the growth steps are parallel to the crystallographic direction <110>. So the step length is known and the constant κ in Eq. [4] can be exactly calculated. At 45°C and in 6M solution of $AgNO_3$ the value obtained is $\kappa = 2 \cdot 10^{-4}$ $ohm^{-1} \cdot cm^{-1}$. The advancement rate constant k_v can be obtained from this constant, according to Eq. [8] and is $k_v = 1.0$ $cm \cdot sec^{-1} \cdot V^{-1}$.

Rate of Propagation of Polyatomic Layers

On a dislocation-free (100) face the rate of propagation of polyatomic layers was now studied. Polyatomic layers sometimes originate after an overvoltage pulse having higher amplitude and longer duration (*e.g.*, 50-60 mV, several milliseconds).

At higher overvoltages a dislocation-free face grows according to the multinuclear, multilayer growth mechanism (7, 8). During the pulse action several tens of monoatomic layers are deposited on its surface. After the pulse the face surface has a complex relief, comprising several lattice planes. Under the action of a low overvoltage applied after the pulse, the face begins to flatten and the current drops slowly to zero.

The crystal face is generally expected to be homogeneous in respect to the process of two-dimensional nucleation. The surface becomes then randomly rough during and immediately after the pulse. In some cases, however, on a specific, more "active" center the nucleation proceeds with a higher rate resulting in a more pronounced hillock at this site. During the subsequent flattening this hillock gives the origin of a polyatomic front of growth. By means of the interference contrast device after Nomarski, this front, if sufficiently thick, is already visible under the microscope as a strip advancing on the face. The current accompanying the process during the flattening stabilizes to a stationary value proportional to the front length and thickness, Fig. 3. This growth front can be considered either as a single polyatomic ledge or as a composite step consisting of several monoatomic layers.

The advancement rate of such steps was measured as described below. After the stabilization of the current at the stationary value two flash light pictures

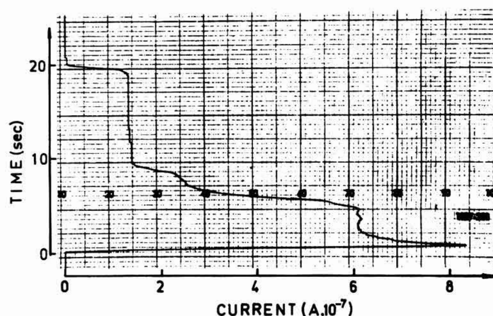

Fig. 3. Current-time curve following an overvoltage pulse with amplitude 60 mV and duration 5 msec on a perfect (100) face with rectangular form. The stationary value of the current results from the growth of a visible in the microscope polyatomic step retaining a constant length.

are taken in sequence on the same frame. With the first flash an electronic chronometer is triggered which is stopped by the second one. A picture made in this way is shown in Fig. 4. Two positions of the growth step are clearly fixed by the two consecutive flash exposures. The distance traveled by the step for the time interval between the flash exposures can be measured quite accurately. The time interval is indicated by the chronometer so that the rate of advancement of the step is directly determined. From the rate of advancement and the stationary value of the current (Fig. 3), the height of the polyatomic step is evaluated.

Using the interference contrast after Nomarski, steps higher than 10Å (equivalent to 5 monoatamic layers) can be visually detected, while steps above 30Å can be photographed, as shown in Fig. 4. It was also found that independently of their thickness, steps up to 80Å advance with the same velocity. A measurable decrease in the velocity is observed only for steps higher than 100Å. Figure 5 shows the dependence of the advancement rate of steps 30-80Å high on overvoltage. From the slope of the straight line the value of the constant k_v in Eq. [7], $k_v = 1.9$ $cm \cdot sec^{-1} \cdot V^{-1}$ is obtained. The value of k_v is roughly two times higher than the value obtained for monoatomic steps. This unexpected difference can be explained by the assumption that the polyatomic steps under the conditions of their creation advance on a "refreshed" surface. Immediately before their origination during the high amplitude pulse, several tens of monoatomic layers have been deposited on the face obviously refreshing the surface. This assumption is confirmed by the fact that if the surface prior to the creation of a mono-

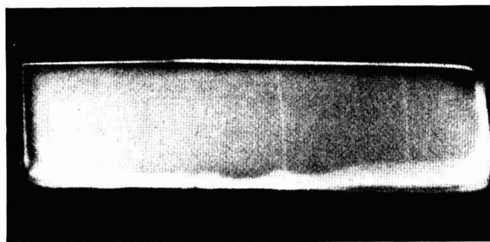

Fig. 4. Two overlapping flashlight photographs of a perfect (100) crystal face in a glass capillary with rectangular form of the cross section (0.1 × 0.4 mm). The two bright strips represent the polyatomic step with height 30Å advancing along the face in the moment of the first and the second photographs.

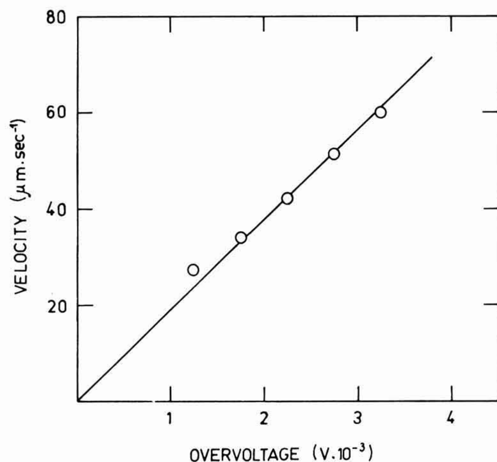

Fig. 5. The dependence of the rate of advancement of polyatomic steps up to 80Å high on overvoltage.

atomic layer is refreshed by a high amplitude pulse as described above, one obtains the curve a in Fig. 6, instead of the curve b observed on an aged surface. It is readily seen that the slope of curve a is nearly two times higher than that of curve b. From the slope of curve a one obtains $\kappa = 3.7 \cdot 10^{-4}$ ohm$^{-1}\cdot$cm^{-1}, and for k_v 1.9 cm$\cdot$sec$^{-1}\cdot$V^{-1} which is equal to the value found for a polyatomic step.

It is interesting to note that by the propagation of monoatomic layers the surface is not refreshed. Such a refreshing occurs only when more than several tens of layers are deposited simultaneously.

Ledge Spacing in a Composite Polyatomic Step

As already mentioned, a growing polyatomic step can be considered as a "train" of parallel monoatomic steps By means of the interference contrast device the polyatomic step is seen under the microscope as a darker or brighter thin strip. The width of the strip on this interferential picture is not related in a simple manner to the width of the step train.

The advancement rate of the polyatomic step at constant overvoltage is known. The step height is determined by the rate and the growth current. Then the average ledge spacing can be determined from the time required for disappearance of the ledge into the capillary wall which is strictly parallel to it. This time can be measured from the current drop to zero accompanying the ledge disappearance. As has been demonstrated, the ledges are parallel to the crystallographic direction <110> and advance toward the narrow capillary wall. To orientate the seed crystal so that the direction <110> is strictly parallel to these walls is a very difficult task. This difficulty can be overcome if, instead of in the capillary wall, the ledge is made to disappear in a crystal edge parallel to it. This can be easily achieved if the crystal face filling up the capillary cross section is grown for a specified time by a suitably modulated direct current at which its dimensions begin to decrease. Between the crystal face and the narrow capillary walls crystal edges and dislocation-free (111) faces of small dimensions appear. Figure 7 shows an experimental curve of the current drop recorded at the disappearing of a polyatomic step in a crystal edge. From the curve the average ledge spacing $2x_0$ at the step train is determined to 160Å.

It should be noted that the above estimation indicates the maximum possible value of the average ledge spacing. This distance can in fact be smaller because any deviation of the ledge from a straight line parallel to the edge increases the time of disappearance of the polyatomic steps. For example the curve in Fig. 7 can be obtained from a very steep polyatomic step curved in an arc with a radius of 2.5 mm, *i.e.*, with side wings advancing only 0.5 μm after the central part of the step. It is obvious that it is impossible to determine a curvature of this magnitude and hence it is excluded in the observation conditions of our case. In fact in many cases longer periods of ledge disappearance have been observed which are obviously connected with an already visible curvature or any other irregularity of the ledge.

Mechanism of Electrolytic Deposition of Silver

As shown above, on a "fresh" surface the monoatomic and all polyatomic steps with a height up to 80Å advance with one and the same rate. The average ledge spacing in some of the polyatomic steps does not exceed 160Å. From these two relevant experimental findings a conclusion elucidating the mechanism of electrolytic deposition of silver can be drawn.

The rate of advancement of the growth steps does not depend at all on the step distance if the metal ions are directly incorporated in kink sites along the steps. If the crystal lattice is built up by surface diffu-

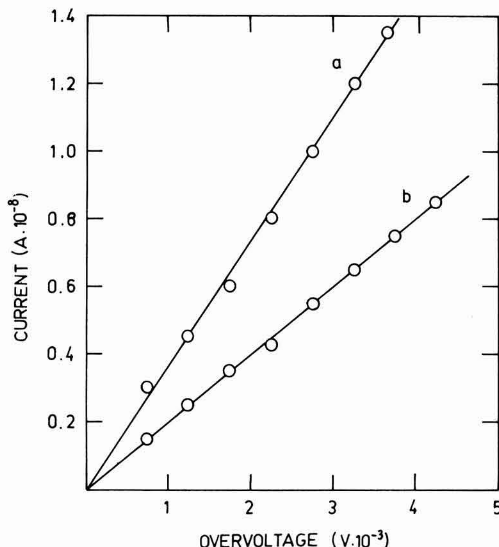

Fig. 6. Current (stationary value)-overvoltage curve at the growth of a monoatomic layer. The straight line a refers to a fresh surface; and b, to an aged surface.

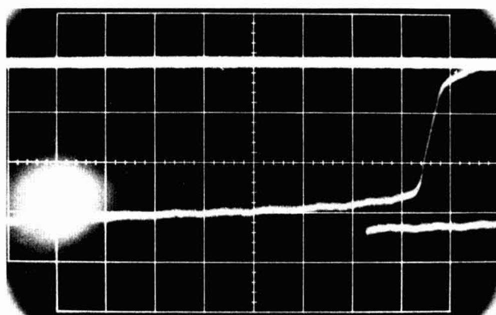

Fig. 7. Curve of current drop to zero, accompanying the disappearance of the polyatomic step in a crystal edge parallel to it. Height of the step, 61Å (30 monoatomic layers); rate of advancement, 48 · 10^{-4} cm · sec^{-1} (overvoltage 2.5 mV). Vertical sensitivity, 1 · 10^{-7} A ·cm^{-1}, time base, 20 msec · cm^{-1}.

sion of adatoms, the advancement rate of the steps does not depend on the distance between them only if the depth of the surface diffusion penetration is small compared to the average half-distance between the steps, $\lambda_o/x_o << 1$. Obviously, if one assumes the surface diffusion mechanism of deposition of silver, λ_o must be $\leqq 80$Å

The constant κ of Eq. [4] in the case of surface diffusion mechanism is given by Eq. [5] and contains $i_{o,ad}$ and λ_o. Under experimental conditions similar to ours, the exchange current $i_{o,ad}$ for crystal (100) face has been determined by high frequency impedance measurements on a perfect completely built up aged face and was found to be $i_{o,ad} = 0.06$ A·cm^{-2} (9). Preliminary impedance measurements carried out now on a fresh crystal face lead to the conclusion that the value of the exchange current of the adatoms is smaller than the one for aged surface. The value of λ_o is unknown but it is not larger than 80Å. If the constant κ is now evaluated with these values of $i_{o,ad}$ and λ_o, one obtains $\kappa = 3.5 \cdot 10^{-6}$ ohm^{-1}·cm^{-1} which is two orders of magnitude smaller than the one experimentally observed here. It follows therefore that the electrolytic deposition of silver occurs almost exclusively by direct incorporation. The contribution of the surface diffusion would not exceed 1%. From the experimentally found values of κ, according to Eq. [6], for the exchange current of the step edge atoms with metal ions in the electrolyte two values were found: $i_{o,st} = 200$ A·cm^{-2} for an aged surface and $i_{o,st} = 370$ A·cm^{-2} for a fresh one.

This conclusion pertaining to the mechanism of electrolytic deposition of silver was made by Vitanov, Popov, and Budevski (10) on the basis of: (*i*) the results of impedance measurements at high frequency on a (100) face, atomically smooth (9) and with a surface relief defined by spiral growth (10); (*ii*) the results of the experimental check of the theory of spiral growth by the electrocrystallization of silver of a (100) face (11). The value of the exchange current determined by these authors is $i_{o,st} = 170$ A·cm^{-2} and refers to an aged surface. This value is very close to the one $i_{o,st} = 200$ A·cm^{-2}, given here for the same surface.

Acknowledgment

The authors wish to thank Prof. Dr. E. Budevski for the helpful discussions throughout the course of this work. The participation of D. K. Roe was through the scientific exchange program between the Bulgarian Academy of Sciences and the National Academy of Sciences; this cooperative support is gratefully acknowledged.

Manuscript submitted April 14, 1975; revised manuscript received June 6, 1975.

Any discussion of this paper will appear in a Discussion Section to be published in the June 1976 JOURNAL. All discussions for the June 1976 Discusion Section should be submitted by Feb. 1, 1976.

REFERENCES

1. M. Volmer, "Das elektrolytische Kristallwachstum," Verlag Herman, Paris (1934).
2. H. Brandes, *E. Physik. Chem.*, **142,** 97 (1929).
3. W. Lorenz, *Z. Naturforsch.*, **9A,** 716 (1954).
4. V. Bostanov, A. Kotzeva, and E. Budevski, *Bull. Inst. Chim. Phys., Acad. Bulgare Sci.*, **6,** 33 (1967).
5. E. Budevski, V. Bostanov, T. Vitanov, Z. Stoynov, A. Kotzeva, and R. Kaishev, *Phys. Status Solidi*, **13,** 577 (1966); *Electrochim. Acta*, **11,** 1697 (1966).
6. V. Bostanov, R. Roussinova, and E. Budevski, *Chem.-Ing.-Techn.*, **45,** 179 (1973).
7. R. Armstrong and J. Harrison, *This Journal*, **116,** 328 (1969).
8. V. Bostanov, R. Roussinova, and E. Budevski, *ibid.*, **119,** 1347 (1972).
9. T. Vitanov, E. Sevastianov, V. Bostanov, and E. Budevski, *Elektrokhimiya*, **5,** 451 (1969); T. Vitanov, E. Sevastianov, Zdr. Stoinov, and E. Budevski, *ibid.*, **5,** 238 (1969).
10. T. Vitanov. A. Popov, and E. Budevski, *This Journal*, **121,** 207 (1974).
11. V. Bostanov, R. Roussinova, and E. Budevski, *Comm. Dept. Chem., Bulgare. Acad. Sci.*, **2,** 885 (1969).

Compensation of Ohmic Potential Interactions Occurring at Ring-Disk Electrodes

Mani Shabrang* and Stanley Bruckenstein**

Chemistry Department, State University of New York at Buffalo, Buffalo, New York 14214

ABSTRACT

Pseudocollection and inverse pseudocollection effects caused by potential drops at ring-disk electrodes can be eliminated by positive feedback. A potential proportional to a fraction of the disk electrode current is fed back to the ring electrode potentiostat, eliminating changes in ring potential and current that arise due to the variations of the disk electrode potential and current. Analogously, feedback of a potential proportional to a fraction of the ring current to the disk electrode potentiostat prevents variations of disk electrode potential and current that are due to the variations in ring electrode potential and current. The two positive feedback networks function independently and no *a priori* knowledge of the uncompensated resistance is required.

Many investigators have considered the problems of positive feedback compensation of the ohmic potential drop that exists in an electrochemical cell between the working and the reference electrode (1-10). Roe (11) and Nicholson (12) have summarized recent work on this subject while Smith (13) has reviewed work prior to 1972. In all these studies the ohmic potential drop occurred between the reference electrode and a single working electrode. Two working electrodes exist when a rotating ring-disk electrode (RRDE) is used, and some unique ohmic potential compensation problems can arise in an electrochemical cell having a RRDE.

Recently an equivalent circuit for the uncompensated primary resistances existing at a RRDE was proposed by us (14). The validity of this circuit was veri-

* Electrochemical Society Student Member.
** Electrochemical Society Active Member.
Key words: inverse pseudocollection effect, pseudocollection effect, uncompensated resistance, positive feedback.

fied, and the circuit is shown within the circled region of Fig. 1. Point T represents the tip of the Luggin capillary leading to the reference electrode. The tip's location in the electrochemical cell determines its effective position on three of the resistors making up the equivalent circuit. In this paper we are concerned with treating the case in which the tip lies on the R_C, the resistance that is common to the current path between the Luggin capillary tip and the two working electrodes, the ring and the disk. In Fig. 1, R_{aux} represents the resistor between the Luggin capillary tip and the auxillary electrode. The total uncompensated resistance between the capillary tip and the disk electrode is $R_C + R_D$, and is $R_C + R_R$ between the capillary tip and the ring electrode. E_D, E_R, and E_{Ref} represent the half-cell potentials of the disk, ring electrode, and reference electrode, respectively, and include all the impedances characteristic of the electrode processes that are occurring. I_D and I_R are the corresponding disk and ring electrode currents, and no current flows through the reference electrode.

Full compensation for the total uncompensated ohmic potential drops between the Luggin capillary and the ring and disk electrodes is not considered in this paper. Full compensation is an elusive concept when dealing with working electrodes that have nonuniform current distributions such as those that can exist at disk, ring, and other electrode geometries. Under such circumstances positive feedback circuitry cannot compensate for the nonuniform potential distribution that is inherent to the electrolysis cell.

The ohmic potential drop dealt with in this paper is associated with the flow of current through resistor R_C, the resistor common to the ring and disk electrodes. The pseudocollection effect (14) is the term we have used to represent the current phenomena occurring at the ring electrode produced as a result of varying uncompensated potential drops associated with a changing disk electrode current. Conversely, the inverse pseudocollection effect coresponds to the current phenomena produced at the disk electrode as a result of varying uncompensated ohmic potential drops produced by varying ring electrode currents.

Appropriate positive feedback compensation has the effect of repositioning the Luggin capillary at point O of Fig. 1 and thus eliminates the pseudocollection effect and the inverse pseudocollection effect. This kind of feedback compensation involves only partial compensation of the total ohmic potential drop and does not give rise to any of the conceptual difficulties associated with full compensation in the presence of a nonuniform current density, nor are there experimental problems of potentiostat stability which arise when full compensation of an ohmic potential drop at an electrode is attempted.

Experimental

Reagents.—Solutions of 0.01*M* sulfuric acid were prepared from triply distilled water and a Baker reagent grade sulfuric acid.

Cell.—The glass cell and the auxiliary equipment are described elsewhere (15, 16).

Electrodes.—The four electrodes used in the experiments were: electrode I, a platinum-ring platinum-disk with a diameter, d_1, of 7.6 mm and ring-inner diameter, d_2, of 8.0 mm and ring-outer diameter, d_3, of 8.4 mm; electrode II, a platinum-ring gold-disk with d_1 = 7.6 mm, d_2 = 8.0 mm, and d_3 = 11.0 mm; electrode III, a gold-ring platinum-disk with d_1 = 7.6 mm,

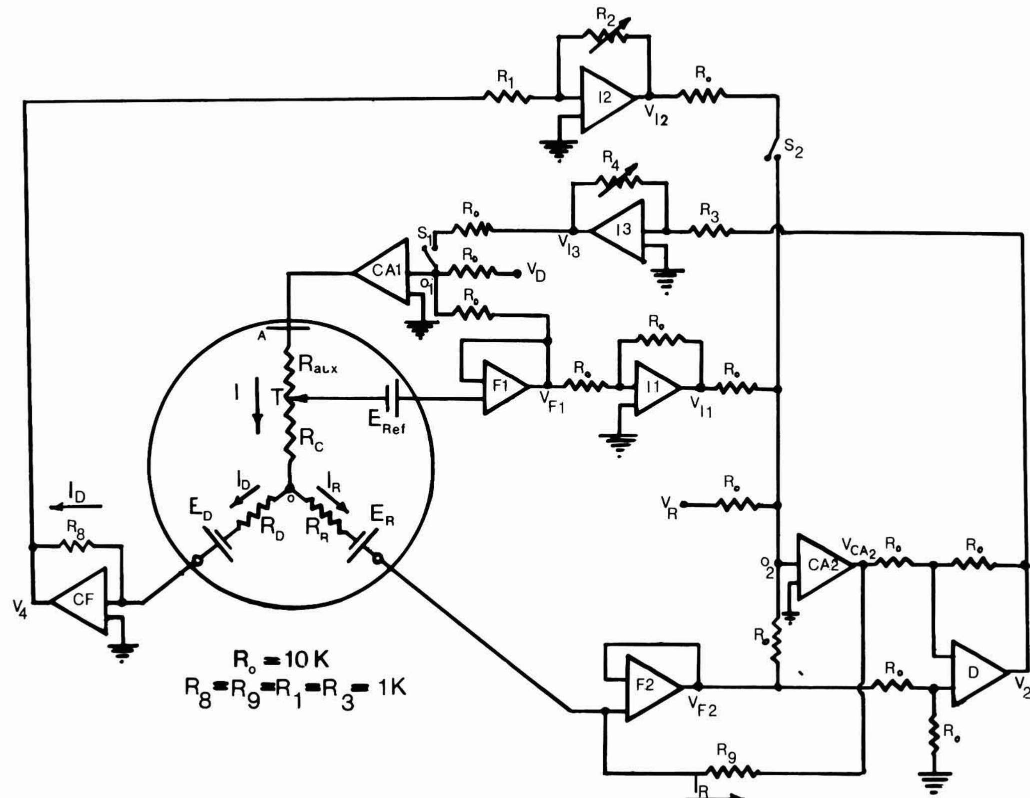

Fig. 1. Conventional four-electrode potentiostat with the additional positive feedback network. The equivalent circuit for the uncompensated ohmic resistance at ring-disk electrodes is enclosed by the circle.

$d_2 = 8.0$ mm, and $d_3 = 11.0$ mm; and electrode IV, a gold-ring gold-disk with $d_1 = 7.6$ mm, $d_2 = 8.0$ mm, and $d_3 = 8.4$ mm. Teflon was used as the insulating material for all electrodes.

These electrodes were electrochemically pretreated before each experiment, as discussed in Ref. (17), and were all polished to a final mirror finish using 0.05μ alumina on Buehler microcloth.

Instrumentation.—A conventional four-electrode analog instrument for independent potentiostatic control of the ring and the disk was used (18-20), and the *I-E* curves obtained were recorded on an EA1, X-Y-Y′ 1131 Variplotter, Model 141 A. Analog Devices operational amplifiers were used in the positive feedback networks.

The operational amplifier instrument for independent galvanostatic control of the ring and the disk used for the common resistance measurement is described elsewhere (14).

A Heathkit Model IG-18 function generator was used to supply the a-c signal.

All potentials were measured and reported *vs.* the saturated calomel electrode. Experiments were run at 25°C. The Luggin capillary was positioned, by eye, to lie on the axis of rotation, unless otherwise stated.

Theoretical

Four electrode potentiostat with finite cell resistance.—Consider Fig. 1, which includes the electronic schematic and the ring-disk electrode equivalent circuit. We intend to obtain the expression for the disk electrode potential *vs.* the reference electrode, $E_D - E_{Ref}$, and the ring electrode potential *vs.* the reference electrode $E_R - E_{Ref}$, in terms of various currents and cell resistances, and the voltages applied to control amplifiers CA1 and CA2. It is instructive to consider the original four electrode potentiostatic circuit first, *i.e.*, S-1 and S-2 open, before undertaking the analysis of circuit with positive feedback, since this analysis was not given earlier (18).

No-ohmic drop compensation.—Disk electrode.—If switches S-1 and S-2 are open, the circuit corresponds to a slightly modified version of the original by Johnson, Napp, and Bruckenstein (18). The various relations of interest in obtaining the disk potential control function are:

summing point restraint at CA1

$$V_{F1} + V_D = 0 \quad [1]$$

and the output of the voltage follower, F1

$$V_{F1} = E_D - E_{Ref} + I_D R_C + I_R R_C + I_D R_D \quad [2]$$

Defining

$$E_D^* \equiv E_{Ref} - E_D \quad [3]$$

we obtain

$$E_D^* = V_D + I_D(R_C + R_D) + I_R R_C \quad [4]$$

and we see that the disk potential contains an uncompensated ohmic resistance, R_C, through which the ring electrode current passes. Changes in the ring current will therefore produce changes in the disk potential even though V_D is held constant. The partial derivative

$$\left(\frac{\partial E_D^*}{\partial I_R}\right)_{I_D} = R_C \quad [6]$$

is a convenient measure of this resistance, which we term the inverse pseudocollection resistance.

Ring electrode.—The various relations of interest in obtaining the ring electrode potential control functions are the summing point restraint at CA2

$$V_{F2} + V_R + V_{I1} = 0 \quad [7]$$

the output of voltage follower 2

$$V_{F2} = E_D - E_R - I_R R_R + I_D R_D \quad [8]$$

the output of I1

$$V_{I1} = -V_{F1} \quad [9]$$

and the output of F_1 given by Eq. [2] above. Defining

$$E_R^* \equiv E_{Ref} - E_R \quad [10]$$

and solving for E_R^* using Eq. [2] and [7]-[9], yields

$$E_R^* = -V_R + I_R(R_C + R_R) + I_D R_C \quad [11]$$

Thus, we see that there is an uncompensated resistance through which the disk electrode current can affect the ring potential. This resistance R_C is given by

$$\left(\frac{\partial E_R^*}{\partial I_D}\right)_{I_R} = R_C \quad [12]$$

and is termed the pseudocollection resistance.

The pseudo and inverse pseudocollection resistances are identical, hence, the magnitude of the pseudo and inverse pseudocollection effects for a given value of R_C depend on slope of the current-potential curves at the ring and disk electrodes and the remaining uncompensated potential drops at these two indicator electrodes. For example, if the ring electrode is set on the rising portion of a current-potential curve, variations of the disk current produce changes in the ring electrode potential that can be accompanied by large relative changes in the faradaic current.

In addition, the double layer capacity at the ring and disk electrodes can play a significant, even major, role in the case where there are time-varying currents, *e.g.*, the sinusoidal variation of current through a rotating disk electrode (Albery papers) will produce a sinusoidal variation in the ring electrode potential and thus a double layer charging current. The treatment presented above was a d-c analysis, and for simplicity was not presented in a-c terms, although this extension is quite straightforward. The d-c analysis is also used below to discuss the positive feedback circuitry.

Compensation for R_C.—Disk electrode.—Assume switch S-1 is closed. Then Eq. [1] must be replaced by

$$V_{F1} + V_D + V_{I3} = 0 \quad [13]$$

where

$$V_{I3} = -V_2 \frac{R_4}{R_3} \quad [14]$$

and

$$V_2 = I_R R_9 \quad [15]$$

Using Eq. [13]-[15] and Eq. [8] and [13] yields

$$E_D^* = V_D + I_D(R_C + R_D) + I_R(R_C - R_4R_9/R_3) \quad [16]$$

for the relationship describing the disk potentiostat behavior. Hence, when

$$\frac{R_4R_9}{R_3} = R_C \quad [17]$$

the inverse pseudocollection effect vanishes. In practice, R_4 is increased from zero, and the magnitude of the effect is seen to decrease to zero and to change sign as R_4R_9/R_3 becomes greater than R_C.

Ring electrode.—Assume switch S-2 is closed at CA2, the summing point condition leads to

$$V_{F2} + V_R + V_{I1} + V_{I2} = 0 \quad [18]$$

instead of Eq. [7]. Also

$$V_{I2} = -\frac{R_2}{R_1} V_4 \quad [19]$$

and

$$V_4 = -I_D R_8 \quad [20]$$

Thus, using Eq. [18]-[20] along with Eq. [8]-[10] yields

$$E_R^* = -V_R + I_R(R_C + R_R) + I_D\left(R_C - \frac{R_2R_8}{R_1}\right) \quad [21]$$

Hence, compensation from the pseudocollection effects occurs when

$$\frac{R_2}{R_1} R_8 = R_C \quad [22]$$

Again, experimentally, partial or overcorrection (with change in sign) for the pseudocollection phenomena is observed by continuously varying R_2 from zero to larger values.

In both of the derivations for compensation of R_C, note that the position of S-2, when S-1 was closed, or S-1, when S-2 was closed. is irrelevant. The position of the other switch does not affect the statement of Eq. [2], which is common to both derivations even though the values of E_D, I_D, and I_R may be affected. Any change in these quantities is accounted for by the other relationships involved in the derivations. Therefore, one may elect to compensate for either the pseudo or inverse pseudocollection effect, or both, as the experimental needs dictate.

Discussion

Pseudocollection-faradaic processes.—As was shown earlier (14, 21-24) the current of a ring electrode which is potentiostated at "constant" potential can be affected by the currents that pass through the disk electrode. Figure 2 illustrates the pseudocollection phenomena strikingly. The platinum ring electrode has been potentiostated on the rising portion of the hydrogen evolution current (at -0.400V in 0.01*M* H_2SO_4). As the potential of the gold disk electrode is scanned at $\pm$ 130 mV/sec, the changing disk electrode currents produce a change in the ring electrode potential. Cathodic disk electrode currents produce more anodic ring electrode currents, and vice versa; as a result of decreasing or increasing the hydrogen evolution current. This result is consistent with the idea of a common uncompensated ohmic resistance, represented by R_C in Fig. 1. This result also indicates the difficulty in detecting an intermediate produced during nonsteady-state disk current conditions if the required ring electrode potential lies on the rising portion of a voltammetric wave, *e.g.*, either the solvent or supporting electrolyte decomposition.

One approach to eliminating the pseudocollection effect was suggested earlier by us (14). The position of the Luggin capillary in the cell determined the value of R_C, and thus by proper positioning (trial and error) the Luggin tip can be placed at point O of Fig. 1 (*i.e.*, $R_C = 0$). In fact if the capillary is brought extremely close to the electrode, the pseudocollection response reverses since the capillary is in effect located on R_D. The results of such an experiment in 0.01*M* H_2SO_4 is shown in Fig. 3. As the Luggin capillary is moved down the axis of rotation toward the disk electrode, the pseudocollection effect becomes smaller (curves b-d), vanishes (at curve e), and reappears with a reversed sign (curves f, g). This result is in accordance with the physical representation of the capillary tip, T in Fig. 1, moving toward point O, through point T and then down R_D toward E_D. Curve e, corresponding to complete compensation ($R_C = 0$), is produced when the capillary is very close to the electrode ($\leq$1 mm) and it requires some patience to locate this point exactly. There are a number of positions of the Luggin which give very little evidence of the pseudocollection effect, but there appears to be only one position that compensates for both the pseudo and inverse pseudocollection effect, which in our equivalent circuit corresponds to locating the capillary precisely at point O.

Figures 4 and 5 demonstrate the behavior of the compensation circuitry in Fig. 1. The faradaic ring electrode reaction in both cases is the evolution of hydrogen at the platinum ring electrode in a supporting electrolyte of 0.01*M* H_2SO_4. Figure 4 illustrates the case of no compensation (curve b) and over compensation (curve c) in which case there is a reversal in the appearance of the ring electrode current shape, as predicted by Eq. [22] when $R_2R_8/R_1 > R_8$. Note that severe overcompensation (by a factor of more than two) does not produce any instability in the circuit.

The circuit response in the vicinity of ideal compensation, *i.e.*, $R_2R_7/R_1 = R_C$, is shown in Fig. 5. Curve d shows no pseudocollection effect, while a $\pm 3\%$ change in the value of R_2 produces a visible pseudocollection response.

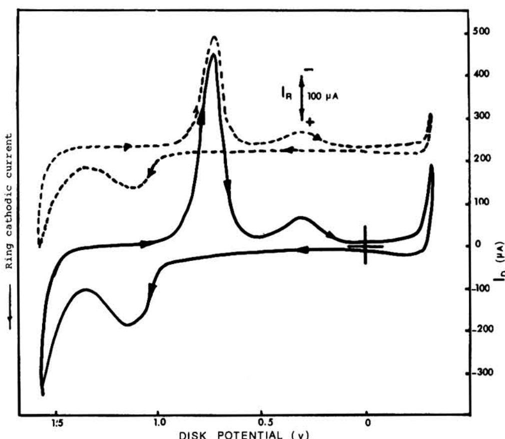

Fig. 2. Pseudocollection effect. 0.01*M* H_2SO_4 using electrode No. 2. Solid curve and dashed curve represent disk and ring voltammograms, respectively. The gold ring electrode is potentiostated at -0.400V, where $2H^+ + 2e$ occurs. Ring current offset arbitrarily from zero. Scan rate = 130 mV/sec; rotation speed = 2500 rpm. There is a trace of platinum left on the gold disk after polishing, and it is visible in the *I-E* curve at $\sim$ 0.4V.

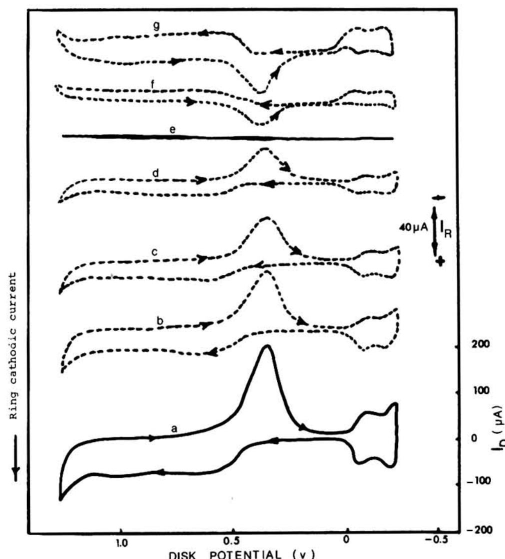

Fig. 3. Pseudocollection compensation by positioning of Luggin capillary. 0.01*M* H_2SO_4 using electrode No. 1. Solid curve and dashed curves represent disk and ring electrode voltammograms, respectively. Ring is potentiostated at -0.370V. All ring current curves are zero offset to allow for current due to $2H^+ + 2e = H_2$. Scan rate = 120 mV/sec; rotation speed = 2500 rpm. The approximate distance of the Luggin capillary tip from the plane of the rotating ring-disk electrode is 1 in., 6, 3, 2, and 1 mm, and a fraction of mm for curves b, c, d, e, f, and g, respectively. The tip has been positioned by eye, on the axis of rotation.

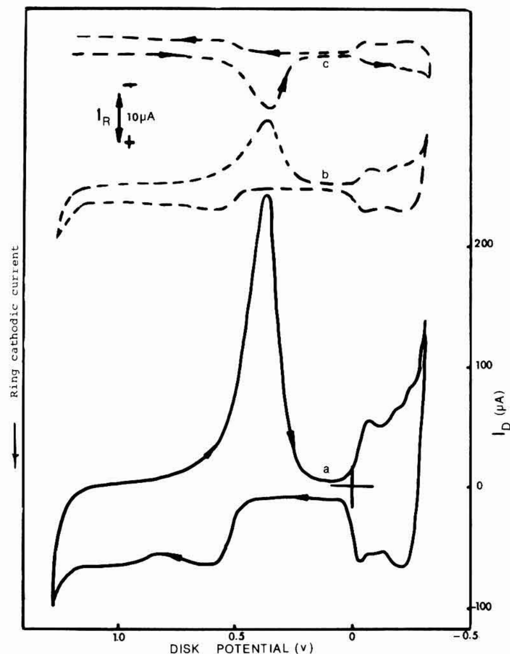

Fig. 4. Pseudocollection compensation by positive feedback. 0.01M H_2SO_4 using electrode No. 1. Solid curve and dashed curves represent disk and ring voltammograms, respectively. Ring is potentiostated at −0.325V. Ring current arbitrarily offset from zero. Scan rate = 130 mV/sec; rotation speed = 2500 rpm. The value of the resistor R_2 is 0 and 90 ohms for curves b and c, respectively.

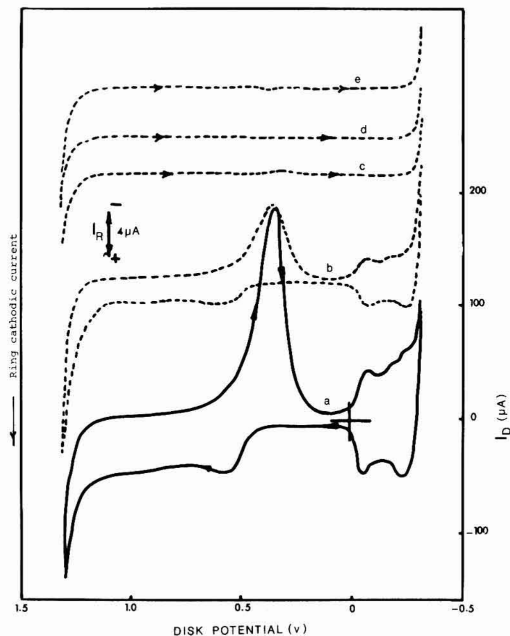

Fig. 5. Pseudocollection compensation by positive feedback. 0.01M H_2SO_4 using electrode No. 1. Solid curve and dashed curves represent disk and ring voltammograms, respectively. Ring is potentiostated at −0.300V. Ring current is arbitrarily offset from zero. Scan rate = 110 mV/sec. Rotation speed = 2500 rpm. R_2 = 0, 32, 33, and 34 for curves b, c, d, and e, respectively. The curves c, d, and e are recorded only when the disk potential is scanned in the cathodic direction.

The pseudocollection resistance ($R_2R_8/R_1 = R_C$) is readily found by varying R_2 and observing the ring electrode current trace in the potential region where the oxidized disk electrode is reduced. Table I presents the results of pseudocollection resistance measurements obtained by this procedure at five different locations of the Luggin capillary. Also listed in Table I are the corresponding values of R_C found using our earlier procedure (14). The agreement between these two methods is excellent.

Inverse pseudocollection.—Another test of the equivalent circuit was performed by interchanging the leads to the ring and disk electrodes, *i.e.*, the ring electrode to the input of F2. The effect of this change to position R_R at the input of CF and R_D at the input of F2. Thus varying the ratio R_2R_8/R_1 compensates the disk electrode potential for effects caused by ring electrode currents passing through R_C, *i.e.*, compensates for the inverse pseudocollection effect.

Table II lists the values of the inverse pseudocollection resistance found by the above procedure at three different locations of the Luggin capillary. Also listed are the values of the pseudocollection resistance found when the disk electrode lead was connected to CF and the ring electrode lead was connected to F2, *i.e.*, the original configuration. The agreement between the pseudo and inverse pseudocollection resistances found in this way is good.

Table I. Determination of pseudocollection resistance. 0.01M H_2SO_4. Rotation speed = 2500 rpm

Electrode No.	R_C (ohm) Method of Ref. (14)[a]	R_C (ohm) Using Eq. [22]
1	53	52
1	61	60
1	26	25
2	45	43
3	50	50
4	50	51

[a] Using Eq. [3].

Pseudo and Inverse Pseudocollection Effects: Double Layer Charging Currents

Albery (23) in his a-c studies at the ring-disk electrode noticed that an a-c ring electrode current flows in the ring electrode circuit even when only an a-c double layer charging current flows through the disk electrode and correctly ascribed this phenomenon to an uncompensated ohmic potential drop caused by the disk current flowing through a solution resistance that is coupled to the ring electrode. The equivalent circuit for this situation is shown in the circled region in Fig. 1 in which E_D and E_R should be considered to contain the double layer capacitances of the disk and ring electrodes. Our model contains the Albery *et al.* features and in addition predicts the reciprocal effects of current at one electrode on the other electrode's poten-

Table II. Comparison of pseudo and inverse pseudocollection resistances. Electrode No. 1, 0.01M H_2SO_4. Rotation speed = 2500 rpm

R_C (ohm) Pseudocollection resistance	R_C (ohm) Inverse pseudocollection resistance
42	45
53	55
55	56

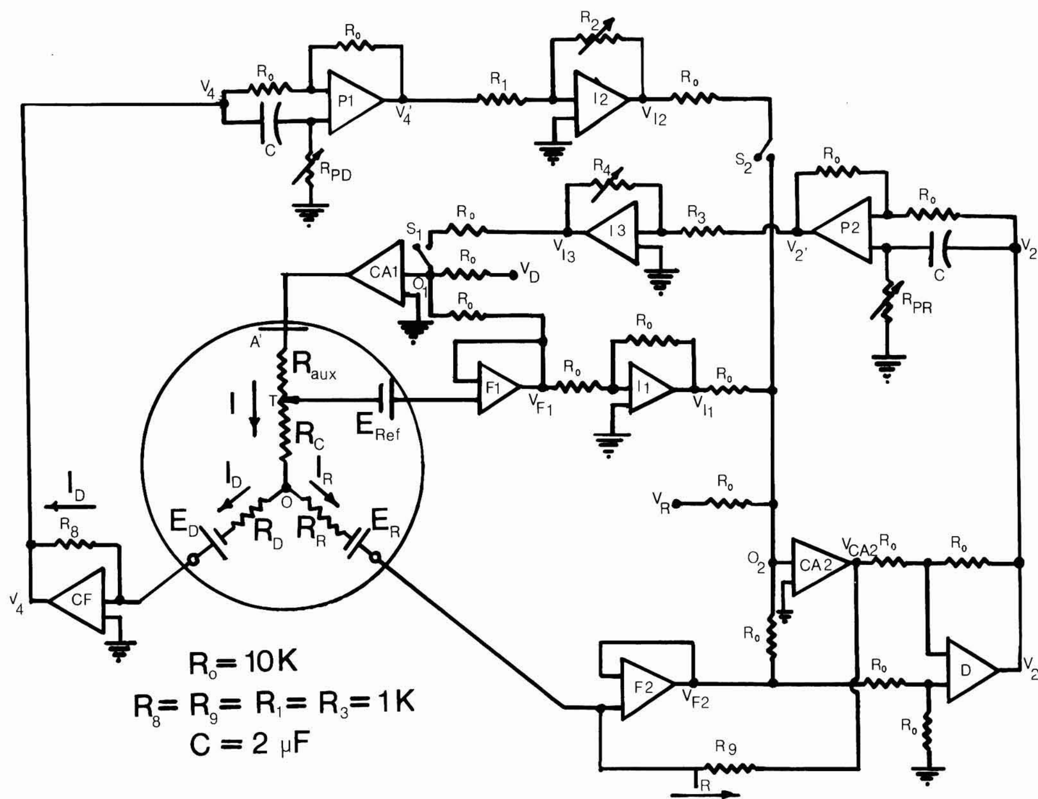

Fig. 6. The four-electrode potentiostat and the positive feedback circuitry with modification for a-c compensation. The equivalent circuit for the uncompensated ohmic resistances at ring-disk electrodes is enclosed by the circle.

tial. The a-c voltage fluctuation across the common resistance, R_C, of Fig. 1, produces potential fluctuations across the ring electrode double layer capacitance, and thus double layer charging currents at the ring electrode. Analogously, as is shown below, an inverse pseudocollection effect can be produced by an a-c current flowing at the ring electrode.

The ring and disk electrode currents involved in these capacitative pseudo and inverse pseudocollection effects are out of phase with each other as a result of the differing value of R_R, R_D, the ring electrode double layer capacitance and the disk electrode to double layer capacitance. Hence, the derivation leading to Eq. [17] and [22] would have to be suitably modified to account for this phase shift. This was not done, since it is seen that if the proper phase shifted fraction of I_D is fed back to the ring control amplifier CA2, the inverse pseudocollection effect can be eliminated. Similarly, by feeding back the appropriate phase shifted fraction of I_R to the disk control amplifier, the inverse pseudocollection effect can be eliminated. The circuit used to accomplish these results is given in Fig. 6, in which a phase shifting circuit P1 and P2 was introduced into the ring and disk current positive feedback loops. P1 and P2 are identical circuits, and have the property of unity gain at all frequencies, shifting the phase of an a-c signal from 180° to 360°, depending on values of the R_P's and C's and the frequency.

In an actual a-c pseudocollection compensation experiment, both R_2 and R_{PD} are adjusted until there is no a-c ring current in the absence of a faradaic process at the disk electrode. The analogous adjustment of R_4 and R_{PR} compensates for the a-c inverse pseudocollection effect.

The results of such a-c compensation experiments at 10, 100, and 200 Hz are given in Table III. The currents listed in parenthesis are the a-c pseudo or inverse pseudocollection currents. The values of R_2R_8/R_1 and R_4R_9/R_3 produce the resistance values necessary to produce the proper amplitude for compensation after adjusting the phase shift resistors, R_{PR} or R_C, as measured by the d-c method in which the faradaic currents flow through the ring and disk electrodes. R_C values measured in this way are given in the last column of Table III, and agree well in all pseudo and inverse pseudocompensation studies.

The positive feedback networks function completely independently of each other when the inverse pseudocollection effect is compensated according to Eq. [17], the pseudocollection phenomenon is unaffected, and visa versa when the condition of Eq. [22] is met. When the conditions of Eq. [17] and [22] are both met, both effects vanish.

Conclusion

The uncompensated common resistance R_C, between the reference electrode and the ring and disk electrodes can be a significant fraction of the uncompensated resistance found at ring-disk electrodes. Pseudo and inverse pseudocollection effects arise due to this common resistance. These effects can be completely eliminated, in both d-c and a-c experiments, by appropriate positive feedback networks, without any noticeable loss of dual potentiostat stability. The positive feedback networks used are our earlier equivalent circuit for the uncompensated resistances occurring at ring-disk electrodes (14) and the success of the positive feedback networks in eliminating pseudo and inverse

Table III. A-C pseudo and inverse pseudocollection compensation. 0.01M H_2SO_4. Rotation speed = 2500 rpm, electrode No. 1, C = 2 μF

Experiment type	Frequency (Hz)	E (mV)	E' (mV)	I_D (μA)	I_R (μA)	R_{PD} (k-ohm)	R_P (k-ohm)	R_2R_8/R_1 (ohm)	R_4R_8/R_8 (ohm)	R_C[c] (ohm)
Pseudo	10	400	0	1200	(15)	100		44		44
Pseudo	100	30	−300[a]	250	(100)	14		44		44
Pseudo	100	30	0	250	(100)	14		44		44
Pseudo	200	200	0	2000	(200)	33		44		44
Inverse[b]	200	80	0	(350)	600	35		46		44
Inverse	200	0	20	(20)	450		12		45	44
Pseudo	200	0	20	18	(170)	6		44		44
Pseudo	200	0	200	2000	(160)	55		45		44
Pseudo	100	10	−300[a]	70	(20)	10		36		37
Pseudo	100	200	−300[a]	1500	(360)	18		36		37
Pseudo	100	130	0	40	(120)	20		38		37
Inverse	100	0	130	(800)	36		20		38	37

[a] D-C values.
[b] Method of Table II.
[c] Procedure of Ref. (14), Eq. [3].

pseudocollection effects is considered to be a further test for the validity of the model.

Acknowledgment

This research was supported in part by Henry Woodburn Fellowship from S.U.N.Y.A.B. (M.S.) and by AFSOR Grant No. 505034A.

Manuscript submitted March 8, 1975; revised manuscript received May 28, 1975.

Any discussion of this paper will appear in a Discussion Section to be published in the June 1976 JOURNAL. All discussions for the June 1976 Discussion Section should be submitted by Feb. 1, 1976.

REFERENCES

1. G. Lauer and R. A. Osteryoung, *Anal. Chem.*, **38**, 1106 (1966).
2. E. R. Brown, T. G. McCord, D. E. Smith, and D. D. DeFord, *ibid.*, **38**, 1119 (1966).
3. A. A. Pilla, *This Journal*, **118**, 702 (1971).
4. C. Lamy and P. Malaterre, *J. Electroanal. Chem.*, **32**, 137 (1971).
5. D. Garreau and J. M. Saveant, *ibid.*, **35**, 309 (1972).
6. N. S. Sarma, L. Sankar, A. Krishnan, and S. R. Rajagoplan, *ibid.*, **41**, 503 (1973).
7. E. R. Brown, H. L. Hung, T. G. McCord, D. E. Smith, and G. L. Booman, *Anal. Chem.*, **40**, 1424 (1968).
8. E. R. Brown, D. E. Smith, and G. L. Booman, *ibid.*, **40**, 1411 (1968).
9. A. Bewick, *Electrochim. Acta.*, **13**, 825 (1968).
10. A. A. Pilla, *This Journal*, **116**, 1105 (1969).
11. D. K. Roe, *Anal. Chem. Rev.*, **46**, 8R (1974).
12. R. S. Nicholson, *ibid.*, **44**, 478R (1972).
13. D. E. Smith, *CRC Crit. Rev. Anal. Chem.*, **2**, 247 (1971).
14. M. Shabrang and S. Bruckenstein, *This Journal*, **121**, 1439 (1974).
15. D. C. Johnson and S. Bruckenstein, *ibid.*, **117**, 460 (1970).
16. D. T. Napp, Ph.D. Thesis, University of Minnesota (1967).
17. D. F. Untereker and S. Bruckenstein, *Anal. Chem.*, **44**, 1009 (1972).
18. D. T. Napp, D. C. Johnson, and S. Bruckenstein, *ibid.*, **39**, 481 (1967).
19. D. F. Untereker, Ph.D. Thesis, S.U.N.Y.A.B. (1973).
20. S. H. Cadle, Ph.D. Thesis, S.U.N.Y.A.B. (1972).
21. C. Gabrielli, M. Keddam, and H. Takenouti, *J. Chem. Phys.*, **4**, 737 (1972).
22. M. Shabrang, *This Journal*, **121**, 50C (1974).
23. W. J. Albery, A. H. Davis, and A. J. Mason, *Discussions Faraday Soc.*, **56**, 317 (1973).
24. B. Miller, Private communications.

Studies in Derivative Chronopotentiometry

II. Analysis of Multicomponent Systems

P. E. Sturrock* and B. Vaudreuil

School of Chemistry, Georgia Institute of Technology, Atlanta, Georgia 30332

and R. H. Gibson*

Department of Chemistry, University of North Carolina at Charlotte, Charlotte, North Carolina 28213

ABSTRACT

Instrumental compensation for diffusion current of prior steps is investigated for the derivative chronopotentiometry of multicomponent systems. This technique, in combination with the instrumental compensation and mathematical correction for charging current described in a previous paper (1) is applied to the analysis of multicomponent systems by standard addition and titration. As examples, an amount of 0.2 μmoles of cadmium was determined by standard addition in the presence of 100 μmoles of lead and an amount of 2 μmoles of cadmium was titrated with EGTA in the presence of 50 μmoles of copper.

Chronopotentiometry of solutions containing two or more electroactive substances which undergo consecutive electrode reactions suffers the inherent disadvantage that the faradaic current for the second and subsequent components is reduced by the amount of the residual diffusion current from the more easily

* Electrochemical Society Active Member.

Key words: current correction, standard addition, titration, DME.

electrolyzed components. This has the effect of increasing the transition times for the subsequent components. In addition, the shape of the chronopotentiogram for the second component is altered, thus complicating the relationship between transition time and the minimum of the dE/dt curve.

Previous attempts to correct the transition time of the latter component were based on theoretical concentration-transition time relationships derived by Delahay and Mamantov (2) for two consecutive processes and which were extended to multicomponent systems by Reilly *et al.* (3). Sturrock, Anstine, and Gibson (4) derived the theoretical potential-time relationships for multicomponent derivative chronopotentiometry. They found it is possible to evaluate τ for second and third components by using a computer prepared tabulation of a parameter which is dependent on $(dE/dt)_{min}$ for the component in question, and the sum of the transition times for the preceding waves.

The same authors proposed a standard addition type analysis to determine the concentration of the component in question. However, this type of analysis cannot be applied to very dilute solutions or to transition times much shorter than 3 msec because it is impossible to apply a Bard-type separation of faradaic and capacitative currents to correct for double-layer charging.

Bowman and Bard (5), working with stationary electrodes, were able to decrease the effect of a preceding wave by imposing a constant potential between the two waves for a measured time before applying the constant current for the chronopotentiometry of the second component. Extension of the potential step technique was undertaken in the present work in which all experiments were performed on a DME. If the prebias potential is applied for a long enough time, the diffusion current of the first component decays to a small and nearly constant value. If the chronopotentiometric current is applied at any time within the flat portion of the i *vs.* τ curve, the diffusion current can be considered to be constant over the short (1-50 msec) time span of the chronopotentiometric wave. The constant diffusion current, i_d, can be subtracted from the applied current to give the current going toward the faradaic process for the second component, i_f. The value of i_f is used with the observed transition time to calculate the $i\tau^{1/2}/C$ ratio for the second component. The chronopotentiometric constant is stated in terms of a corrected current, rather than a corrected transition time. If the value of i_f is known, or can be held constant, analytical applications are possible.

There are various methods, based on the Cottrell and Ilkovic equations of obtaining a value for i_d. The disadvantage of calculating instantaneous currents by the Ilkovic equation lies in the inaccuracies introduced by the use of so many measured parameters. To reduce the number of experimentally measured parameters involved, a new expression was derived in the course of this work combining the Cottrell and Sand equations. The concentration of electroactive substance in the bulk solution was expressed in terms of the Sand equation, then this expression was substituted for C in the Cottrell equation along with a factor, $\sqrt{7/3}$, to account for the expansion of the drop. The resulting equation is

$$i_d = (2/\pi)(7/3t)^{1/2} i\tau^{1/2} \qquad [1]$$

where t is the delay time (the length of time that the growing drop is subject to the prebias before the chronopotentiometric current is applied) and i and τ are obtained from a chronopotentiogram of the first component, without prebias, at time t in the drop life. Essentially, i_d for a single component is calculated from a single chronopotentiogram of that component.

In the course of this investigation, a simpler method was discovered to determine diffusion currents. A prebias potential beyond the first wave is maintained for time t, as the electrode drop grows, then upon switching to galvanostat mode, sufficient current is applied from a continuously variable calibrated source so that the prebias potential is maintained. Under such conditions, the applied current is equal to the diffusion current of the first species. If the applied current is less than the diffusion current, the concentration of electroactive species will increase at the electrode surface and the potential will change in accord with the Nernst equation. Likewise, if too large a current is applied the potential will move in the opposite direction. The diffusion current measured in this way is subtracted from the total current to the next drop of the DME to obtain i_f. A simpler method is to use an uncalibrated, variable current source adjusted to supply just the current necessary to equal the diffusion current and maintain the prebias potential. Then this current can be electronically added to the current, applied to the next drop of the DME so that nominally all the applied current is available for the second faradaic process. In a multicomponent situation where one is trying to measure a transition for a wave on top of several others, this method is superior to the use of the Sand-Cottrell calculation which can be applied only with difficulty to multicomponent systems. It is also superior to the application of the Ilkovic equation which involves summing the diffusion currents for each of the preceding waves. In the new instrumental method, the total residual diffusion controlled current is measured without regard to the number or magnitude of its components.

Experimental Verification of Applied Corrections

The validity of the various corrections proposed was tested on lead-cadmium solutions using potassium nitrate as the supporting electrolyte. The transition for the reduction of lead occurs at approximately −0.4V *vs.* SCE. The reduction wave for cadmium occurs at a potential about 0.2V more negative. Both metals are reduced reversibly, and neither species is known to be adsorbed on a mercury electrode.

Calculation and measurement of diffusion currents.—Diffusion controlled currents for lead were determined by four methods; direct measurement at −0.52V, Sand-Cottrell calculation, Ilkovic calculation based on $D^{1/2}$ obtained from derivative chronopotentiometry, and Ilkovic calculation based on polarographic literature value of $D^{1/2}$.

To 50 ml of 1M KNO_3 supporting electrolyte were added 2 ml portions of 2×10^{-2}M $Pb(NO_3)_2$. The solution was deaerated after each addition and allowed to become quiet. The delay time for switching from prebias to controlled current modes was 2.625 sec into the drop life. The diffusion current was measured by adjusting the calibrated main cathodic current control to exactly maintain the prebias voltage for a period of 50 msec, thus giving a horizontal trace on the oscilloscope. The magnitude of the applied current was read directly from the dial of the current control potentiometer.

To obtain data required for the Sand-Cottrell calculation derivative chronopotentiograms were run on the above solutions with the prebias at −0.2V. Values of $(dE/dt)_{min}$ for the lead wave were converted to transition times. Using delay time, t, equal to 2.625 sec, and combining numerical terms, the modified Sand-Cottrell equation (Eq. [1]) reduces to

$$i_{d(\text{in }\mu A)} = 0.600\ (i\tau^{1/2}) \qquad [2]$$

Experimental values of i and τ were used to calculate i_d for solutions with different lead concentrations.

The Ilkovic calculation was based on the following experimentally measured parameters

$D^{1/2} = 0.00290$ cm/sec$^{1/2}$, $t = 2.625$ sec,
$m = 2.393$ mg/sec, $C =$ (variable) mmoles/liter

Combining numerical terms, the Ilkovic equation reduces to

$$i_{d(\text{in } \mu A)} = 8.63C \quad [3]$$

When using a literature value of $D^{1/2}$ from polarographic data (6), Eq. [3] becomes

$$i_{d(\text{in } \mu A)} = 9.00C \quad [4]$$

The values of i_d obtained for lead solutions over a concentration range from $7.69 \times 10^{-4}M$ to $4.38 \times 10^{-3}M$ are summarized in Table I. Diffusion current is a linear function of concentration of the diffusing species. Values for diffusion currents calculated by the Sand-Cottrell and the Ilkovic equations based on chronopotentiometric $D^{1/2}$ values agree well. However, the diffusion currents obtained by direct measurement were consistently higher by about 6% and in close agreement with the Ilkovic calculation based on literature value of polarographic $D^{1/2}$ (6).

The discrepancy noted in Table I was thought to be due to the depletion of electroactive substance in the vicinity of successive drops. A semiquantitative evaluation of the magnitude of the depletion effect was obtained by examining the changes in successive chronopotentiograms of an electroactive substance as the depleted layer, resulting from a prebias, is replenished by continued diffusion after the prebias is switched off.

A cadmium solution ($1.1 \times 10^{-3}M$ in 1.0M KNO_3) was subjected to a prebias of $-0.76V$ until a steady-state diffusion current (10 μA) was observed at the usual delay time. Then the prebias was switched off manually to coincide as closely as possible to drop detachment. Derivative and conventional chronopotentiograms were run on the next four drops of the DME. With an applied current of 100 μA and an electrode area of 0.0290 cm^2, $\tau^{1/2}$ values were 0.128, 0.145, 0.152, and 0.153 $sec^{1/2}$. The increase in $\tau^{1/2}$ from the first to the fourth drop indicates a corresponding increase in the apparent concentration of cadmium at the electrode surface. Stated in another way, application of a prebias to a DME electrode results in a residual concentration polarization such that the concentration of electroactive species seen by the newly formed drop may be much less than the true bulk concentration. The directly measured diffusion currents presented in Table I were obtained after a steady state of depletion was reached. The same steady-state conditions were used in subsequent work. During the application of the prebias, the situation at the electrode is exactly the same as in polarography and one would expect the Ilkovic equation to be applicable provided polarographic values of $D^{1/2}$ are used.

No depletion effect was observed on any chronopotentiograms run normally, that is, without a prebias beyond the reduction potential for that substance. Chronopotentiograms on the first and subsequent drops were identical for single component systems. For multicomponent systems, with a prebias set between the reduction potentials of the different components, chronopotentiograms of the first few drops were not identical. Discrepancies between first and subsequent drops can be explained by considering the variation of current required to set up the diffusion layer for the more active component. As the current required to set up the diffusion layer decreases, the fraction of the total current which is used for the chronopotentiometric process increases. Once a steady state is reached in the diffusion of the more active component, the chronopotentiograms of the less active component will superimpose so that successive traces on a storage oscilloscope appear as one trace.

Table I. Lead diffusion currents

Conc. Pb (mmoles/liter)	Diffusion current (μA): Direct measurement	Sand-Cottrell calculation	Ilkovic calculation: Chronopotentiometric $D^{1/2}$	Ilkovic calculation: polarographic $D^{1/2}$
0.77	7.3	6.72	6.63	6.91
1.48	13.6	12.8	12.8	13.3
2.14	19.6	18.6	18.5	19.3
2.76	25.2	23.8	23.8	24.8
3.33	30.3	28.6	28.7	30.0
3.87	35.4	33.4	33.4	34.8
4.38	40.1	37.5	37.8	39.4

Contributions to the apparent diffusion current from charging the double layer of the growing drop at the prebias potential are insignificant. For a drop area change of 1% ($\Delta a = 0.0003$ cm^2) and a typical double-layer capacitance of 20 $\mu f/cm^2$, charging the double layer required approximately 0.006 μcoul/V. At a prebias of $-0.52V$ over a time of 50 msec, the required current would be

$$i = \frac{0.006\ \mu\text{coul} \times 0.1\text{V}}{0.05\ \text{sec}} = 0.012\ \mu A$$

This is insignificant compared to the magnitude of the diffusion currents reported in Table I.

Consistency of the chronopotentiometric constant for cadmium in the presence of lead.—A series of solutions which were $3.8 \times 10^{-6}M$ to $4.3 \times 10^{-3}M$ in cadmium and 2.0×10^{-3} in lead was prepared by adding portions of solutions which were $1.0 \times 10^{-3}M$ or $1.0 \times 10^{-4}M$ in cadmium and also $2.0 \times 10^{-3}M$ in lead and 1.0M in KNO_3 to a solution which was $2.0 \times 10^{-3}M$ in lead and 1.0M in KNO_3. A series of chronopotentiograms was run on these solutions using a prebias of $-0.52V$ and instrumental compensation for the lead diffusion current. The diffusion current was checked after each addition and was found to be invariant. The chronopotentiograms were run with and without instrumental double-layer compensation and the transition times measured with the derivative technique (1).

Three sets of chronopotentiometric constants were calculated: from the uncompensated (double-layer) and uncorrected data; from uncompensated (double-layer) data corrected according to Bard (7); and from data compensated (double-layer) instrumentally. The results are shown in Table II. Consistency was achieved for cadmium concentrations as low as $1.66 \times 10^{-5}M$ both by Bard corrections and by instrumental compensation. For Cd solutions on the order of $10^{-6}M$, Bard-corrected results were more consistent than were the instrumentally compensated results. The results from the latter were improved by applying Bard corrections; $i\tau$ *vs.* $C\tau^{1/2}$ plots of the instrumentally compensated data showed a residual double-layer effect of about 0.0036 μcoul. This is one-tenth the double-layer effect in the uncompensated data and becomes insignificant at concentrations of $10^{-5}M$ and higher, but it consumes significant portions of the very low currents used for lower concentrations.

The lowest current setting available on the instrument used was 1 μA. For a $3.8 \times 10^{-6}M$ cadmium solution using double-layer compensation, this lowest current yielded a τ of 7.73 msec, too near the lower limit imposed by the speed of the differentiator for an attempt to analyze more dilute solutions. There is reason to believe that with a lower applied current and a more sophisticated double-layer compensator, this concentration limit can be extended to the lower 10^{-6} range and perhaps beyond.

It should be emphasized that in these experiments the amount of lead present was 0.5-500 times the amount of cadmium. Consistency of $i\tau^{1/2}/aC$ was attained despite the large amounts of lead.

Application to Analysis

The concentration of an electroactive substance can be determined by chronopotentiometry by substituting experimental values for the other parameters into the Sand equation and solving for C. The value obtained, however, is subject to considerable error owing to the large number of variables used. Standard addition and titration methods offer a better approach. A series of chronopotentiograms is used to obtain data for the analytical curves.

Table II. Chronopotentiometric constants for cadmium in the presence of 2×10^{-3}M lead

	Uncompensated data					Instrumentally compensated data				
	Uncorrected			Bard-corrected		Uncorrected			Bard-corrected	
Conc. Cd (moles/liter)	i (μA)	τ (msec)	$\frac{i\tau^{1/2}}{aC}$	i_t (μA)	$\frac{i_t\tau^{1/2}}{aC}$	i (μA)	τ (msec)	$\frac{i\tau^{1/2}}{aC}$	i_t (μA)	$\frac{i_t\tau^{1/2}}{aC}$
4.29×10^{-3}	400	19.7	451.2	398.5	449.5	400	19.7	451.2		
3.15×10^{-3}	300	19.7	460.9	298.5	458.4	300	19.7	460.9		
1.37×10^{-3}	150	15.5	469.8	148.1	463.6	150	14.9	461.5		
7.4×10^{-4}	100	10.2	470.8	97.1	457.0	100	9.62	457.4		
5.83×10^{-4}	50	25.5	472.3	48.7	460.3	50	24.1	458.9		
3.62×10^{-4}	50	10.31	483.9	46.9	454.0	50	9.02	452.6		
1.89×10^{-4}	20	18.1	490.4	18.2	447.1	25	9.84	452.7		
1.42×10^{-4}	30	5.70	550.2	24.4	447.3	25	5.55	452.6		
9.09×10^{-5}	30	3.38	662.3	20.5	453.5	15	6.37	454.3		
6.25×10^{-5}	20	4.25	719.4	12.5	448.7	10	6.99	461.3		
3.22×10^{-5}	10	6.66	874.5	5.19	454.7	10	1.86	462.4		
1.66×10^{-5}	20	2.28	1982.4	4.43	439.1	2.0	12.74	469.1		
1.07×10^{-5}	30	1.35	3549.4	3.70	438.2	2.0	8.02	577.5	1.55	448.0
7.4×10^{-6}	20	1.99	4158.0	2.16	449.2	1.0	15.47	579.8	0.11	446.1
3.8×10^{-6}	20	1.92	7970.1	1.56	621.0	1.0	7.73	798.4	0.54	426.3

Note i = applied current; $a = 0.0290$ cm²; $i_t = i - B/\tau$; B for uncompensated data = 0.035 μcoul; B for compensated data = 0.0036 μcoul. Units for $\frac{i\tau^{1/2}}{aC}$ in $\frac{\mu\text{A-sec}^{1/2}\text{-liter}}{\text{cm}^2\text{-mmole}}$.

Constancy of the $i\tau^{1/2}/C$ ratio is a necessity if chronopotentiometry is to be used for standard addition or titrimetric determinations. Either instrumental compensation of double-layer charging or arithmetic corrections as described previously (1) can be used to assure the constancy of $i\tau^{1/2}/C$ over the range of concentration to be spanned during the titration or standard addition. Generally, instrumental compensation will yield values for τ that can be used directly in plotting an analytical curve.

Standard addition determinations.—For a standard addition determination it is essential that a plot of $i\tau^{1/2}$ *vs.* C (which is equivalent to a Bard-type plot of $i\tau$ *vs.* $C\tau^{1/2}$) intercept the C-axis at the point $C = 0$. If double-layer effects are not eliminated by compensation or corrections, the $i\tau^{1/2}$ *vs.* C line may be displaced upward, indicating a higher concentration of the substance than is actually present. As derived in an earlier paper on derivative chronopotentiometry of single component systems (8), double-layer charging can be corrected for by maintaining a constant value for current density and plotting $\tau^{1/2} - \tau_{res}/\tau^{1/2}$ on the ordinate. In order to create a perfectly linear plot, it is necessary to correct for dilution.

If the solution which is being determined contains two or more electroactive species, these species can be determined independently in the same solution. In this study, cadmium was determined in the presence of lead by using the prebias and diffusion current compensation techniques discussed above. As aliquots of a standard cadmium solution are added to the test solution, the concentration of lead present is decreased. Thus the lead diffusion current changes after each Cd addition, and the diffusion current must be checked and the compensation readjusted.

When a sufficient number of additions (3-5) has been made and data obtained for the cadmium standard addition curve, the prebias can be lowered to a potential below the lead wave and aliquots of a standard lead solution added, yielding data for the lead determination. A solution of several electroactive substances can be analyzed by this means as long as the reduction potentials for the substances are separated sufficiently for a prebias to be imposed between the waves.

It is important that the substance which is reduced at a more negative potential be determined first. The additional amount of that substance which remains in the solution as a result of the standard addition acts as supporting electrolyte and does not interfere when the more easily reduced species is determined. If, on the other hand, the more easily reduced species is determined first, the additional amount present in the test solution interferes in the determination of the less easily reduced species. The more of the former present, the more difficult it becomes to compensate for it.

Another precaution is worthy of note. To achieve the best precision, the amount of electroactive substance added in each increment should be of the same order of magnitude as the total amount of that substance initially present. Addition of considerably larger amounts greatly compresses the concentration axis and reduces the precision by which small amounts may be determined. If, on the other hand, the increments are much smaller than the amount to be determined, extrapolation over a long distance adds to the uncertainty of the result.

An example of a two component standard addition determination is presented in Fig. 1. Cadmium in the amount of 0.2 μmoles was determined, in the presence of 100 μmoles of lead, by derivative chronopotentiometry.

Titration using chronopotentiometric end point detection.—Cadmium can be titrated with EGTA ([ethylene bis(oxyethylenenitrate)] tetraacetic acid) in the presence of copper if an ammonia-ammonium buffer of *p*H 10 is used. The ammonia strongly complexes the copper and masks it for reaction with EGTA. The $Cd(NH_3)_4{}^{2+}$ complex is weaker and does react with the EGTA. End point detection is difficult, however, because copper interferes with metallo-chromic indicators such as Eriochrome Black-T which is routinely used for the EGTA titration of cadmium.

As EGTA complexes cadmium during the course of the titration, chronopotentiometry can be used to measure the decreasing concentration of uncomplexed cadmium.

As the concentration of cadmium decreases, double-layer effects become prominent. Bard corrections work well to deal with these effects. The τ measured by derivative means which occurs beyond the equivalence point is τ_{res}, the apparent transition time due to double-layer charging (8). It is constant at points well beyond the equivalence point where the concentration of cadmium not complexed by EGTA is essentially zero. If $\tau^{1/2} - (\tau_{res}/\tau^{1/2})$ is plotted *vs.* ml EGTA added, the portion of the titration curve beyond the equivalence point coincides with the x-axis. Thus the point where the extrapolated initial portion of the titration curve intersects the x-axis is taken as the end point.

If volume changes during the titration are significant, volume corrections must be applied, just as they are in the case of standard addition determinations. Chronopotentiometric end point determination lends itself to the use of concentrated titrant which can be added in small volume, eliminating the need for volume corrections. In the vicinity of the end point, titrant can be added in larger increments, so long as several

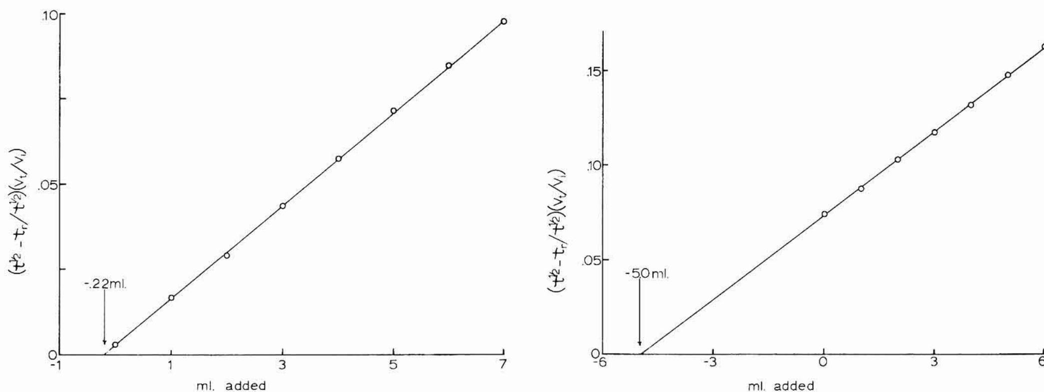

Fig. 1. Standard addition curves. (a, left). 0.2 μ moles of cadmium in presence of 100 μmoles of lead. Addition of 1.0 × 10^{-3} F $Cd(NO_3)_2$. 0.22 μmoles Cd found. (b, right). 100 μmoles lead. Additions of 1.0 × 10^{-2} F $Pb(NO_3)_2$. 100 μmoles lead found.

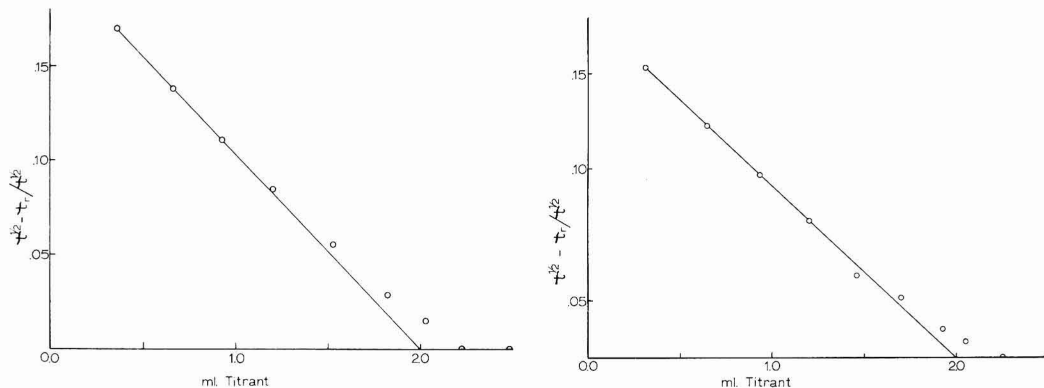

Fig. 2. Titration curves. (a, left). 2 μmoles of cadmium and no copper. (b right) 2 μmoles of cadmium and 50 μmoles of copper

points are obtained in the linear regions before and beyond the end point.

An EGTA solution was standardized against a standard cadmium solution using Eriochrome Black-T and an ammonia-ammonium nitrate buffer of *p*H 10. A series of identical solutions was made as follows: 1.00 ml standard Cd solution (2 μmoles Cd) was added to 5 ml buffer, 10 ml 1.0M KNO_3, and sufficient water to make 50 ml total. The concentration of Cd in these test solutions was 4.00 × 10^{-5}M. The EGTA titrant was determined to be exactly 1.00 × 10^{-3}M.

The same titration was performed using chronopotentiometry. The chronopotentiometric titration curve is presented in Fig. 2a. For this determination, electrode area = 0.02899 cm^2, current = 30 μA, and prebias = −0.66V. The cadmium-ammonia complex is reduced at −0.8V.

The same procedure was repeated on a new test solution, identical to the preceding one except for the presence of 50 μmoles copper. Diffusion current compensation was used to eliminate interference from the Cu. The titration curve is presented in Fig. 2b.

The results of the two cadmium titrations using chronopotentiometric end point detection are identical to the result of the series of titrations using Eriochrome Black-T, and demonstrate the feasibility of titrating multicomponent mixtures using chronopotentiometry.

Manuscript submitted March 24, 1975; revised manuscript received June 4, 1975.

Any discussion of this paper will appear in a Discussion Section to be published in the June 1976 JOURNAL. All discussions for the June 1976 Discussion Section should be submitted by Feb. 1, 1976.

Publication costs of this article were partially assisted by Georgia Institute of Technology.

REFERENCES

1. P. E. Sturrock, J. Hughey, B. Vaudreil, G. O'Brien, and R. Gibson, *This Journal*, **122**, 1195 (1975).
2. P. Delahay and G. Mamantov, *Anal. Chem.*, **27**, 478 (1955).
3. C. N. Reilley, G. W. Everett, and R. H. Johns, *ibid.*, **27**, 483 (1955).
4. P. Sturrock, W. Anstine, and R. Gibson, *ibid.*, **40**, 505 (1968).
5. J. Bowman and A. Bard, *Anal. Letters*, **1**, 533 (1968).
6. L. Meites, "Polarographic Techniques," p. 270, Interscience, New York (1955).
7. A. Bard, *Anal. Chem.*, **35**, 340 (1963).
8. P. Sturrock, G. Privett, and A. Tarpley, *J. Electroanal. Chem.*, **14**, 303 (1967).

The Frequency Response of Limiting Currents to Sinusoidal Speed Modulation at a Rotating Disk Electrode

Koichi Tokuda* and Stanley Bruckenstein*

State University of New York, Buffalo, New York 14214

and Barry Miller*

Bell Laboratories, Murray Hill, New Jersey 07974

ABSTRACT

When a sinusoidal modulation is superimposed on the rotation speed of a rotating disk electrode, the corresponding modulated current follows the Levich equation closely for sufficiently low ratios of the modulation frequency to the constant center rotational frequency. In this work, the frequency response of the modulated current (amplitude and phase) is derived for the general case and the results experimentally confirmed over a wide range of Schmidt numbers (230-2100 Sc) and modulation to rotational frequency ratios for the reduction of Fe^{+3} to Fe^{+2} in 1.0*M* H_2SO_4 over the temperature range 25°-85°C. Tables are given of the phase and amplitude factors which would be encountered for the normal range of both modulation and solution parameters.

In recent papers (1-6), we have considered various theoretical and experimental aspects of hydrodynamic voltammetry at the rotating disk (RDE) and ring-disk electrodes (RRDE). In these studies, the angular velocity of the RDE, ω, was programmed as a function of time, *t*, or current, *i*. With the exception of one study (4) involving step speed change, this work dealt with conditions for which the Levich equation always applied, *i.e.*, a quasi-steady state existed in which the concentration gradients adjacent to the RDE could be described adequately using the instantaneous angular velocity, ω, of the electrode and the von Kármán (7)-Cochran (8) approach. Recently, using the results of Benton (9), we considered the current transient produced by a step change in angular velocity, $\Delta\omega$, of a RDE held at a limiting current. After such a step change in ω, the fluid velocities in the region adjacent to the RDE adjust very rapidly from values characteristic of the initial velocity, ω_o, to those characteristic of the final velocity, $\omega_o + \Delta\omega$, while the concentration profiles adjust somewhat more slowly.

We consider here the problem of describing the limiting, convective-diffusion controlled current at a disk subjected to a rotational velocity program of the form

$$\omega^{1/2} = \omega_o^{1/2}(1 + \epsilon \cos \sigma t) \quad [1]$$

In Eq. [1]

$$\epsilon = \Delta\omega^{1/2}/\omega_o^{1/2} \quad [2]$$

and σ is the modulation frequency in radians/sec. In this paper, we refer to this class of techniques as sinusoidal hydrodynamic voltammetry (SHM) to distinguish it from other uses now being made of the term "hydrodynamic voltammetry (10)."

Equation [1] will describe the experimental situation for all values of ω_o, ϵ, and σ, including those for which the angular acceleration, $d\omega/dt$, is too high for the quasi-steady state assumptions used in our previous studies of a sinusoidal modulation of ω to apply. These broader experimental conditions will produce current responses deviating from those (5, 6) found for Levich-type conditions ($\epsilon\sigma$ small), *i.e.*, the current is not given by

$$i = i_{\omega_o} + \Delta i \cos \sigma t \quad [3]$$

where

$$\Delta i = i_{\omega_o} \Delta\omega^{1/2}/\omega_o^{1/2} = i_{\omega_o}\epsilon \quad [4]$$

and i_{ω_o} is the convective-diffusion limiting current at a constant angular velocity of ω_o.

Instead, as will be shown later, *i* is given by

$$i = i_{\omega_o} + \Delta i_1 \cos(\sigma t - \varphi_1) + \Delta i_2 \cos(2\sigma t - \varphi_2) + \dots \quad [5]$$

In our experiments we have determined Δi_1 and φ_1 by appropriate techniques and have therefore restricted the detailed theoretical analysis to the first harmonic term, *i.e.*, to the calculation of Δi_1 and φ_1 as a function of the Sc number. The results for the amplitude response are reported in terms of the dimensionless parameter *A*

$$A = \Delta i_1/\Delta i \quad [6]$$

where $A \to 1$ as $\sigma \to 0$.

The need to predict values of Δi_1 and φ_1 had been prompted by unpublished studies of certain applications of SHM. These results indicated the desirability of performing experiments at larger values of σ/ω_o than those to which we restricted the earlier work. For example, where potential scanning programs are used, higher modulation frequencies permit using higher scanning rates before undue distortion of Δi_1-*E* curves is found, shortening experiments, reducing sensitivity to impurity poisoning, and thus leading to a better response to convective-diffusion controlled reactions.

Excellent agreement between the theory for *A* and φ_1 and experiment has been found for the reduction of Fe^{+3} to Fe^{+2} in 1.0*M* H_2SO_4 over the temperature range 25°-85°C (230-2100 Sc).

Theoretical

The normal component of the fluid velocity, w_o, for an infinite disk rotating at constant angular velocity was first studied by von Kármán (7) and later by Cochran (8). After quasi-steady state is reached, w_o is given by

$$w_o = (\omega\nu)^{1/2} H_o(\eta) \quad [7]$$

where ν is the kinematic viscosity and

$$\eta = (\omega/\nu)^{1/2} z \quad [8]$$

For small η

$$H_o(\eta) = -0.51023\,\eta^2 + 0.33333\,\eta^3 - 0.10267\,\eta^4 + \dots \quad [9]$$

* Electrochemical Society Active Member.

Key words: hydrodynamic modulation, frequency dependence, convective-diffusion.

where the value of the second derivative of $H(\eta)$ with respect to η at $\eta = 0$ is the one given by Cochran (8).

Sparrow and Gregg (11) analyzed the analogous rotating disk problem for the case in which the angular velocity was a time dependent quantity. Their expression for the instantaneous normal component of the fluid velocity w, was obtained by a series expansion about the value found at quasi-steady state, *i.e.*

$$w = (\omega\nu)^{1/2}\{H_o(\eta) + \beta_1 H_1(\eta) + \beta_2 H_2(\eta) + \ldots\} \quad [10]$$

where

$$\beta_1 = (d\omega/dt)/\omega^2 \quad [11]$$

$$\beta_2 = (d^2\omega/dt^2)/\omega^3 \quad [12]$$

and the $H_i(\eta)$ are axial velocity functions that satisfy the equations

$$H_i(\eta) = \tfrac{1}{2} H_i''(0)\eta^2 = c_i\eta^2 \quad [13]$$

for all i values at small values of η.

The values of the $H_i(\eta)$ functions were given graphically (11) for $0 \leq \eta \leq 20$, and the values of $H_2''(0)$ were given in their Table I. However, the values of higher derivatives at $\eta = 0$ were not given. Using their Table I data, we obtain

$$c_0 = -0.51023$$
$$c_1 = 0.204835 \quad [14]$$
$$c_2 = -0.023112$$

and

$$w = -0.51023(\omega^3/\nu)^{1/2}z^2\{(1 - 0.65327\eta + 0.20121\eta^2) - 0.40144\beta_1 + 0.04530\beta_2\} \quad [15]$$

as a good approximation to w when $\beta_{i+1} \leq \beta_i$. Note that when $\beta_1 = \beta_2 = 0$, Cochran's result, as used by Newman (12), is obtained. It is therefore possible to solve the Levich problem for small oscillations in ω, given its time dependence.

As stated previously, the superposition of a sinusoidal $\omega^{1/2}$ modulation, $\Delta\omega^{1/2}$, about a constant value, $\omega_o^{1/2}$, is advantageous from the experimental viewpoint, and the problem we deal with assumes that

$$\omega = \omega_o(1 + \epsilon\cos\sigma t)^2 \quad [16]$$

It is also convenient to define

$$p = \sigma/\omega_o \quad [17]$$

Thus, the values of β_1 and β_2 are

$$\beta_1 = -2\epsilon p \sin\sigma t(1 + \epsilon\cos\sigma t)^{-3} \quad [18]$$

and

$$\beta_2 = -2\epsilon p^2\{\cos\sigma t + \epsilon(\cos^2\sigma t - \sin^2\sigma t)\}(1 + \epsilon\cos\sigma t)^{-6} \quad [19]$$

Substituting Eq. [18] and [19] into Eq. [15] and assuming $\epsilon << 1$ yields the expression for the instantaneous normal component of the fluid velocity

$$w = w_o\{1 + \epsilon(a_{01}\cos\sigma t + a_{10}\sin\sigma t) + \epsilon^2(a_{02}\cos 2\sigma t + a_{11}) + \ldots\} \quad [20]$$

where

$$w_o = -0.51023(\omega_o^3/\nu)^{1/2}z^2(1 - 0.65327\eta_o + 0.20121\eta_o^2)$$

$$a_{01} = (3 - 2.6131\eta_o + 1.0060\eta_o^2 - 0.090591p^2)/(1 - 0.65327\eta_o + 0.20121\eta_o^2)$$

$$a_{10} = 0.80288p/(1 - 0.65327\eta_o + 0.20121\eta_o^2) \quad [21]$$

$$a_{02} = (1.5 - 1.9598\eta_o + 1.0060\eta_o^2 - 0.04530p^2)/(1 - 0.65327\eta_o + 0.20121\eta_o^2)$$

$$a_{11} = (1.5 - 1.9598\eta_o + 1.0060\eta_o^2 - 0.13589p^2)/(1 - 0.65327\eta_o + 0.20121\eta_o^2)$$

and

$$\eta_o = (\omega_o/\nu)^{1/2}z$$

However, if $\epsilon < 1$ rather than $\epsilon << 1$, only the amplitude of the second harmonic expression in Eq. [20] will be in error, while the amplitude of the first harmonic with which we are experimentally concerned remains unchanged.

In order to obtain the time dependent convective-diffusion limiting current, the convective-diffusion equation

$$\frac{\partial C}{\partial t} = D\frac{\partial^2 C}{\partial z^2} - w\frac{\partial C}{\partial z} \quad [22]$$

must be solved for the boundary conditions

$$z = 0 : C = 0$$
$$z \to \infty : C \to C^\circ \text{ (bulk concentration)} \quad [23]$$

$w(z, t)$ given by Eq. [20] and [21] and for steady sinusoidal variations.

Taking into account the form of Eq. [20], a solution of the convective-diffusion equation is

$$C = C^\circ\ u(z, t) \quad [24]$$

where

$$u(z, t) = u_o(z) + \epsilon\{u_{01}(z)\cos\sigma t + u_{10}(z)\sin\sigma t\} + \epsilon^2\{u_{02}(z)\cos 2\sigma t + u_{20}(z)\sin 2\sigma t + u_{11}(z)\} + \ldots \quad [25]$$

Thus, we substitute Eq. [24] and Eq. [20] into Eq. [22], equate the coefficients of all terms having the same time dependence in the resulting expression, and obtain a set of ordinary differential equations involving functions of z. These equations are not written out here but may be simplified by using the dimensionless variable

$$\xi = \{0.51023(\omega_o^3/\nu)^{1/2}/3D\}^{1/3}z = 0.55405\ \text{Sc}^{1/3}\eta_o \quad [26]$$

where $\text{Sc}(\equiv \nu/D)$ is the Schmidt number, and they lead to the set of equations below where the various u's are functions of ξ and the primes represent differentiation with respect to ξ

$$u''_o - f(\xi)u'_o = 0 \quad [27]$$

$$u''_{01} - f(\xi)(u'_{01} + a_{01}u'_o) = bu_{10} \quad [28]$$

$$u''_{10} - f(\xi)(u'_{10} + a_{10}u'_o) = -bu_{01} \quad [29]$$

$$u''_{02} - f(\xi)(u'_{02} + a_{02}u'_o) = 2bu_{20} \quad [30]$$

$$u''_{20} - f(\xi)u'_{20} = -2bu_{02} \quad [31]$$

$$u''_{11} - f(\xi)(u'_{11} + a_{11}u'_o) = 0 \quad [32]$$

where

$$f(\xi) = -3\xi^2 + 3.5372\ \text{Sc}^{-1/3}\xi^3 - 1.9663\ \text{Sc}^{-2/3}\xi^4 \quad [33]$$

The quantity b is defined by

$$b = \{9\nu/(0.51023)^2D\}^{1/3}p = 3.2576\ \text{Sc}^{1/3}p \quad [34]$$

The boundary conditions become

$$\xi = 0 : u_0 = u_{01} = u_{10} = u_{02} = u_{20} = u_{11} = 0$$
$$\xi \to \infty : u_0 \to 1, u_{01}, u_{10}, u_{02}, u_{20}, \text{ and } u_{11} \to 0$$

It is readily shown that the form of Eq. [25] leads to a current of the form given by Eq. [5].

The limiting convective-diffusion current, i, is defined by

$$i = n\mathbf{F}\pi r^2 D(\partial C/\partial z)_{z=0} \quad [35]$$

or in terms of ξ

$$i = n\mathbf{F}\pi r^2 DC^\circ(d\xi/dz)(\partial u(\xi, t)/\partial\xi)_{\xi=0} \quad [36]$$

where r is the radius of the disk electrode. Combining Eq. [25] and [36] with Eq. [26] yields

$$i = i_{\omega_o} + i_{\omega_o}I(\infty)\epsilon a_1\cos(\sigma t - \varphi_1) + i_{\omega_o}I(\infty)\epsilon^2\{a_2\cos(2\sigma t - \varphi_2) + a_3\} + \ldots \quad [37]$$

where

$$a_1 = [\{u'_{01}(0)\}^2 + \{u'_{10}(0)\}^2]^{1/2} \quad [38]$$

$$\varphi_1 = \cos^{-1}\{u'_{01}(0)/a_1\} = \sin^{-1}\{u'_{10}(0)/a_1\} \quad [39]$$

$$a_2 = [\{u'_{02}(0)\}^2 + \{u'_{20}(0)\}^2]^{1/2} \quad [40]$$

$$\varphi_2 = \cos^{-1}\{u'_{02}(0)/a_2\} = \sin^{-1}\{u'_{20}(0)/a_2\} \quad [41]$$

$$a_3 = u'_{11}(0) \quad [42]$$

and

$$i_{\omega_0} = 0.6205 n\mathbf{F}\pi r^2 D^{2/3}\nu^{-1/6}\omega_0^{1/2}C^\circ\Gamma(4/3)/I(\infty) \quad [43]$$

The above value for i_{ω_0} is obtained by solving Eq. [27] to obtain

$$u_0(\xi) = I(\xi)/I(\infty) \quad [44]$$

where

$$I(\xi) = \int_0^\xi \exp\left[\int_0^\xi f(x)\,dx\right] d\xi$$

$$= \int_0^\xi \exp\,(-\xi^3 + 0.8843\mathrm{Sc}^{-1/3}\xi^4 - 0.3932\mathrm{Sc}^{-2/3}\xi^5)\,d\xi \quad [45]$$

and $I(\infty)$ is given by

$$I(\infty) = 0.89294 + 0.26610\mathrm{Sc}^{-1/3} + 0.12960\mathrm{Sc}^{-2/3} \quad [46]$$

which was obtained by Newman (12) for the correction of the Levich equation and holds for $\mathrm{Sc} \geqq 100$.

The experiments we have performed involve detecting the magnitude and phase of the current at the frequency used to modulate $\omega^{1/2}$; hence we need only solve Eq. [28] and [29] and we have postponed consideration of the behavior of the terms associated with the second harmonic.

Equations [28] and [29] were solved numerically (13) for various values of p in the range 0-1.0 and for selected values of Sc in the range 100-2100. In addition, A and ϕ_1 corresponding to specific experimental Sc values were calculated where required.

The effect of p on amplitude response for selected values of Sc is given in Table I, using the parameter A defined by Eq. [6].

By comparing the coefficients of the $\cos(\sigma t - \varphi_1)$ of Eq. [5] and [37] it is seen that

$$\Delta i_1 = i\omega_0 I(\infty)\epsilon a_1 \quad [47]$$

Substituting Eq. [47] and [46] into Eq. [6] yields

$$A = (0.89294 + 0.26610\mathrm{Sc}^{-1/3} + 0.12960\mathrm{Sc}^{-2/3})a_1 \quad [48]$$

The theoretical values of a_1 at constant p and Sc are calculated using the numerical values of $u'_{01}(0)$ and $u'_{10}(0)$ obtained through Eq. [28] and [29] and applying Eq. [38]. The phase shift φ_1 is calculated from Eq. [39] and is given in Table II.

In using Tables I and II, linear interpolation at low Sc values is not accurate. A more sophisticated interpolation technique or graphing of the tabulated values of A and φ_1 is necessary if an error less than that found experimentally is to be achieved.

In the above discussion, both the deviation of hydrodynamics from quasi-steady state and the simultaneous relaxation of the diffusion layer were taken into account. It is of interest to estimate the conditions under which the current response is controlled almost completely by convective-diffusion, *i.e.*, the conditions under which the hydrodynamic situation deviates by only a small percentage from quasi-steady state. Since we propose to obtain only an estimate for this condition, only the large Schmidt number limit for the normal velocity component, obtained from Eq. [15], will be used, *i.e.*

$$w = -0.51023[\{\omega(1 - 0.40144\beta_1 + 0.04530\beta_2)^{2/3}\}^3/\nu]^{1/2}z^2 \quad [49]$$

From Eq. [49] it is seen that small deviations of ω from quasi-steady state are approximately given by $2/3 \times 0.401\beta_1\omega$. Since the deviation in the percentage current error, α, is twice that in angular velocity, it follows that relationship between the error in ω and i is given by

$$\beta_1 = \frac{\dot\omega}{\omega^2} = -2p\frac{\sin\sigma t}{(1 + \epsilon\cos\sigma t)^3} \leqq 0.0187\alpha \quad [50]$$

Table I. Values of A for values of p and Sc

p	0.05	0.10	0.15	0.20	0.25	0.30	0.40	0.50	0.60	0.70	0.80	0.90	1.00
Sc													
100.0	0.9903	0.9626	0.9205	0.8687	0.8118	0.7535	0.6420	0.5447	0.4635	0.3970	0.3426	0.2982	0.2616
140.0	0.9872	0.9545	0.9057	0.8468	0.7836	0.7202	0.6028	0.5037	0.4233	0.3588	0.3070	0.2653	0.2314
200.0	0.9848	0.9458	0.8886	0.8215	0.7514	0.6829	0.5601	0.4604	0.3817	0.3200	0.2714	0.2329	0.2020
315.0	0.9809	0.9318	0.8623	0.7837	0.7047	0.6303	0.5030	0.4045	0.3296	0.2726	0.2288	0.1946	0.1677
400.0	0.9783	0.9230	0.8461	0.7612	0.6777	0.6008	0.4722	0.3753	0.3031	0.2490	0.2078	0.1768	0.1512
446.0	0.9784	0.9200	0.8395	0.7517	0.6664	0.5883	0.4593	0.3633	0.2923	0.2394	0.1994	0.1687	0.1448
600.0	0.9745	0.9066	0.8160	0.7203	0.6300	0.5496	0.4209	0.3281	0.2611	0.2122	0.1757	0.1480	0.1266
615.0	0.9741	0.9054	0.8139	0.7175	0.6269	0.5463	0.4177	0.3252	0.2586	0.2100	0.1739	0.1464	0.1252
800.0	0.9672	0.8888	0.7875	0.6843	0.5901	0.5111	0.3840	0.2952	0.2327	0.1877	0.1547	0.1298	0.1107
890.0	0.9639	0.8812	0.7758	0.6700	0.5745	0.4953	0.3694	0.2825	0.2217	0.1784	0.1467	0.1235	0.1053
1000.0	0.9630	0.8756	0.7658	0.6571	0.5603	0.4808	0.3560	0,2708	0.2119	0.1700	0.1396	0.1169	0.0996
1200.0	0.9606	0.8652	0.7483	0.6354	0.5369	0.4548	0.3325	0.2508	0.1950	0.1559	0.1276	0.1067	0.0912
1400.0	0.9557	0.8529	0.7299	0.6138	0.5170	0.4351	0.3151	0.2361	0.1828	0.1458	0.1192	0.0995	0.0846
1600.0	0.9537	0.8444	0.7162	0.5974	0.4972	0.4159	0.2984	0.2222	0.1714	0.1369	0.1112	0.0928	0.0792
1800.0	0.9506	0.8352	0.7024	0.5814	0.4809	0.4002	0.2850	0.2112	0.1630	0.1289	0.1050	0.0880	0.0748
2100.0	0.9475	0.8239	0.6851	0.5616	0.4608	0.3810	0.2688	0.1980	0.1517	0.1202	0.0979	0.0815	0.0692

Table II. Values of phase shift for values of p and Sc

p	0.05	0.10	0.15	0.20	0.25	0.30	0.40	0.50	0.60	0.70	0.80	0.90	1.00
Sc													
100.0	10.6	21.0	30.8	40.1	48.7	56.5	70.3	81.8	91.5	99.8	107.0	113.2	118.8
140.0	11.5	22.7	33.3	43.1	52.1	60.2	74.3	85.9	95.5	103.7	110.7	116.7	122.1
200.0	12.6	24.7	36.1	46.5	55.9	64.3	78.6	90.2	99.7	107.7	114.4	120.3	125.4
315.0	14.2	27.7	40.2	51.3	61.2	70.0	84.4	95.9	105.1	112.8	119.1	124.6	129.3
400.0	15.1	29.4	42.5	54.1	64.2	73.0	87.6	98.9	109.0	115.4	121.5	126.6	131.3
446.0	15.5	30.2	43.5	55.2	65.5	74.4	88.9	100.1	109.1	116.3	122.4	127.5	132.0
600.0	16.8	32.6	46.7	58.9	69.3	78.3	92.8	103.8	112.5	119.4	125.2	130.0	134.2
615.0	16.9	32.8	46.9	59.2	69.7	78.7	93.1	104.1	112.8	119.7	125.4	130.2	134.4
800.0	18.3	35.3	50.1	62.8	73.5	82.3	96.6	107.4	115.7	122.3	127.7	132.3	136.2
890.0	18.9	36.3	51.5	64.3	75.1	83.9	98.2	108.8	117.1	123.6	128.9	133.1	136.9
1000.0	19.5	37.4	52.8	65.8	76.6	85.4	99.5	110.0	118.1	124.4	129.6	133.9	137.6
1200.0	20.5	39.1	54.9	68.1	79.0	88.0	102.1	112.4	120.2	126.3	131.3	135.4	138.7
1400.0	21.4	40.7	57.0	70.4	81.0	90.0	103.9	113.9	121.5	127.4	132.2	136.2	139.6
1600.0	22.2	42.1	58.6	72.1	83.1	92.1	105.8	115.6	123.0	128.5	133.4	137.3	140.3
1800.0	23.0	43.4	60.2	73.8	84.7	93.7	107.3	116.9	123.9	129.7	134.2	137.6	140.9
2100.0	24.0	45.0	62.2	75.9	86.8	95.7	109.0	118.3	125.3	130.6	134.9	138.5	141.6

The maximum value of β_1, β_{max}, is

$$\beta_{max} = 2\epsilon p \frac{\sqrt{1 - \left(\frac{1 - \sqrt{1 + 24\epsilon^2}}{4\epsilon}\right)^2}}{\left(\frac{5 - \sqrt{1 + 24\epsilon^2}}{4\epsilon}\right)^3} = 2\epsilon p f(\epsilon) \quad [51]$$

so that the relationship between p, and ϵ and α is

$$2\epsilon p f(\epsilon) \leq 0.0187\alpha \quad [52]$$

Sparrow and Gregg (11) considered the problem of determining under what condition the shear stress would deviate by less than 5% from its quasi-steady state value and found that

$$\beta_1 \leq 0.0834$$

which, by comparison with Eq. [50], corresponds to an α of 4.5%.

Table III gives the values of p *vs.* selected ϵ's which cannot be exceeded if the deviation from hydrodynamic quasi-steady state is not to produce a current error exceeding 4.5%

The significance of Table III is merely that, within specified restrictions on p and ϵ, the total current is determined by convective-diffusion processes rather than by the coupling of convective-diffusion and a deviation from a hydrodynamic quasi-steady state.

Experimental

The motor drive and operational amplifier control systems have been described previously (3, 5). The entire system (mechanical plus electronic) bandwidth for modulation was examined by recording the motor tachometer's voltage amplitude and phase shift with respect to the driving waveform. The latter signal was the sum of a linear voltage ramp and a sinusoidal voltage of constant frequency and amplitude. The ramp voltage was selected to scan the center motor speed, ω_0, from 6.67 Hz (400 rpm) to above 125 Hz (7500 rpm).

Typical tracings of a-c motor reponse to this kind of program are shown in Fig. 1; *e.g.*, at a constant modulation (signal) amplitude of 3 $rpm^{1/2}$ and a frequency of 6 Hz, the tachometer amplitude agrees with the a-c driving signal to $\pm 1\%$ and the phase shift is constant within $\pm 1°$ at least up to a center speed of 84 Hz (>5000 rpm). The amplitude circuitry in the Dranetz Phasemeter automatically switches ranges during experiments since a constant $\Delta\omega^{1/2}$ at all speeds produces a-c voltages (related to $\Delta\omega$) which typically vary by a factor of more than four. The observed constant phase shift level in each trace is determined solely by modulation frequency, up to the rotational frequencies indicated by the roll-offs in Fig. 1.

All experiments were carried out with combinations of modulation frequency, amplitude, and center rotational speed frequency for which any amplitude and phase errors due to the above sources were well within $\pm 1\%$ and $\pm 1°$, respectively. Thus, correction of the modulated disk electrode current response for $\Delta\omega^{1/2}$ variations was eliminated, and a full-wave rectifier circuit was used to obtain the amplitude in Δi-experiments. In these experiments, the amplitude response Δi_1 was determined as a function of p. Extrapolations of the Δi_1 data to $p = 0$ yield the maximum amplitude response, and A values were calculated by dividing

Table III.

ϵ	p
0.01	$\leq$4.17
0.05	$\leq$0.825
0.1	$\leq$0.399
0.2	$\leq$0.176
0.3	$\leq$0.095

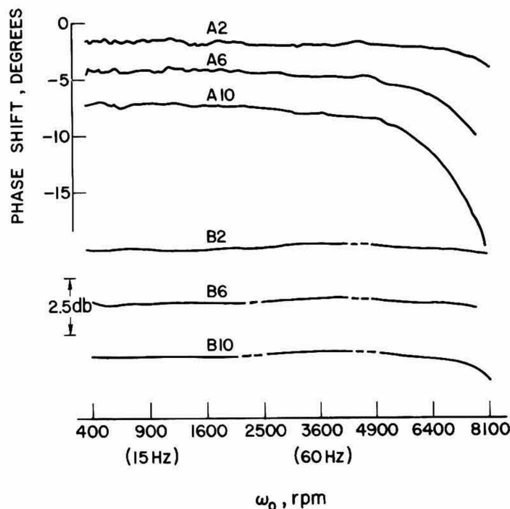

Fig. 1. A-C motor response to sinusoidal modulation. Curves A are phase shift, tachometer *vs.* signal; curves B are log of amplitude ratio, tachometer to signal. Signal amplitude set to constant $\Delta\omega^{1/2}$ of 3 $rpm^{1/2}$; center was scanned from low to high. Fixed frequency of modulation (Hz) indicated by number following A or B. Constant phase shift levels were, for A2, A6, and A10, respectively, $-1.6°$, $-4.3°$, and $-7.2°$, expressed as deviation from the theoretical 180° (no lag) shift. Amplitude plots arbitrarily displaced from common value; dashed regions indicate interruption of measurement due to ranging of phasemeter.

this value into the observed amplitude response at the various p values.

The phase shift of the sinusoidal Δi response relative to the $\Delta\omega$ tachometer output was continuously recorded with a Dranetz Model 305 Phasemeter equipped with a Model 3009A plug-in, after prefiltering each signal with matched 0.64-32 Hz two-pole bandpass amplifiers that introduced <0.5° of phase shift uncertainty. In a typical experiment, ω_0 was scanned from 400 to *ca.* 8000 rpm and back, and the φ data averaged to correct for a small hysteresis related to time constant effects. The experimental abscissas were converted to $p = \sigma/\omega_0$ values and the φ data were used without further reduction.

The electrochemical experiments were all carried out with a 0.313 cm^2 platinum disk electrode and a 2.17 mM Fe^{+3} – 1.0*M* H_2SO_4 solution, prepared from reagent chemicals and triply distilled (the last two from quartz) water. The Sc was varied by performing experiments at 10°C ± 0.5°C increments between 25° and 85°C. The supporting electrolyte kinematic viscosities, ν were determined with a Cannon-Fenske viscometer that was calibrated with water over the 25°-75°C range. The diffusion coefficients for Fe^{+3} were calculated at the various temperatures from the slopes of Levich plots (i_L *vs.* $\omega^{1/2}$) for the limiting current of Fe^{+3} reduction, utilizing the ν values determined independently above and Eq. [46]. Log plots of Sc, D, and ν *vs.* $1/T$°K are shown in Fig. 2.

All data in this paper were obtained at 0.00V *vs.* an unthermostated SCE. This potential was in the limiting current region over the 25°-85°C cell temperature range.

Results and Discussion

The phase shift, φ_1, of the modulated limiting disk current output, Δi_1, produced by $\omega^{1/2}$ modulation at the frequency $f = \sigma/2\pi$ Hz, was directly measured for the reduction of Fe^{+3} to Fe^{+2} in 1.0*M* H_2SO_4, using the constant modulation frequency-ω_0 variation technique described in the Experimental Section. The value of A, however, was, as noted, not calculated directly from the defined value of $\Delta i_1/\Delta i$ but rather from $\Delta i_1/$

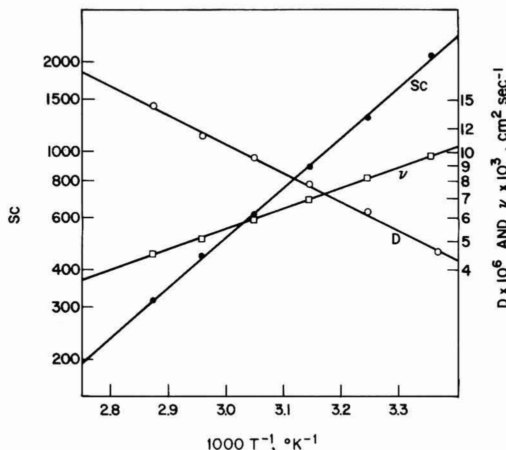

Fig. 2. Log plots of Sc, D, and ν vs. $1000/T°$ K.

$(\Delta i_1)_{p\to 0}$ where $(\Delta i_1)_{p\to 0}$ is the extrapolated value of Δi_1 at $p = 0$. Satisfactory agreement between $(\Delta i_1)_{p\to 0}$ and Δi has been established previously by us (5), and the present procedure cancels a number of possible sources of small determinate errors associated with the electronic instrumentation including bandpass, gain, and rectification efficiency.

Theoretical plots and experimental values of A and φ_1 as a function of p for three values of Sc (315, 890, and 2100) are given in Fig. 3 and 4. Other sets of data obtained for different Sc (not plotted) agree equally well with theory. The Sc range illustrated in Fig. 3 and 4 covers the great majority of aqueous solution cases that will be encountered.

Satisfactory experimental tests of the theory for A and φ_1 dependence on Sc for five constant p values from 0.2 to 0.6 are given in Fig. 5 and 6. The theoretical values of A and φ_1 for these particular Sc values may also be accurately obtained by graphical interpolation in the tables of A and φ_1 given earlier, assuring the general experimental usefulness of the tabulations.

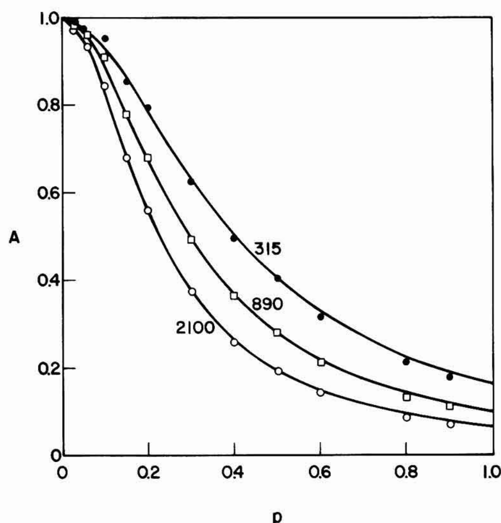

Fig. 3. Amplitude factor A as a function of p for Sc values of 315, 890, and 2100, as marked. Solid lines are theoretical, points are experimental.

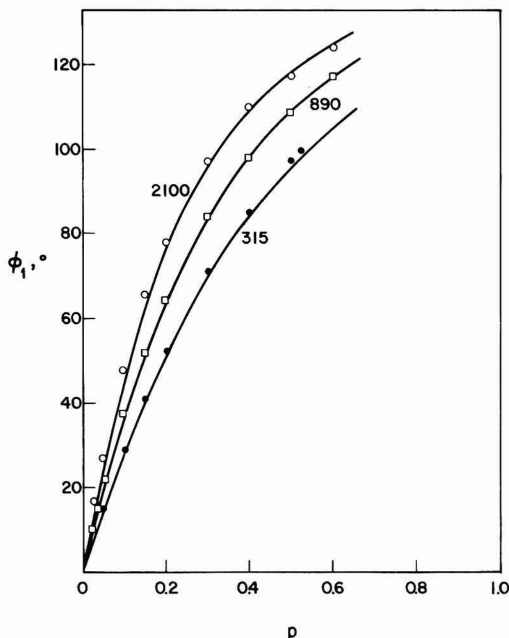

Fig. 4. Phase shift ϕ_1 as a function of p for Sc values of 315, 890, and 2100. Sc values marked. Solid lines are theoretical, points are experimental values.

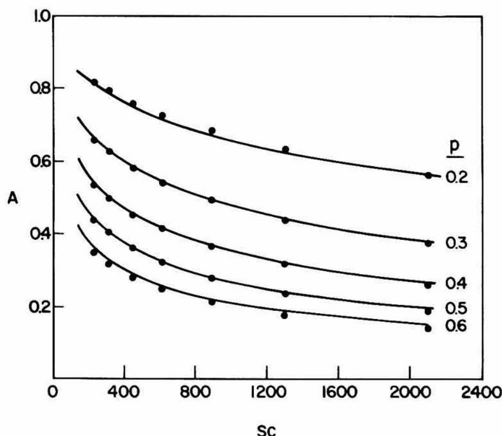

Fig. 5. Amplitude factor as a function of Sc at constant p. Values of p indicated at right of curves. Solid curves are theoretical, points are experimental.

The criteria of Table III, expressing maximum limits of p and ϵ for which the total current is essentially determined by convective-diffusion processes, have been exceeded in certain of our measurements by a factor of as much as three. Our theory explicitly takes into account the region in which convective-diffusion and hydrodynamics couple. Nevertheless, it was of significance to examine experimentally whether the $p\epsilon$ product at these levels, rather than just p alone, influenced the value of A in a given solution. Therefore, Δi_1 was measured as a function of $\Delta\omega^{1/2}$ under conditions of constant p, while $\Delta\omega^{1/2}$ was varied so that $p\epsilon$ was either always ≤ 0.04, exceeded 0.04 at an intermediate value of $\Delta\omega^{1/2}$, or was ≥ 0.04 for all $\Delta\omega^{1/2}$. We

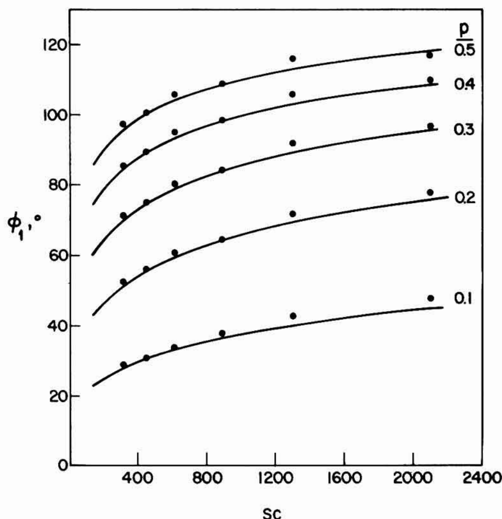

Fig. 6. Phase shift ϕ_1 as a function of Sc for constant p. Values of p indicated at right of curves. Solid curves are theoretical, points are experimental.

chose 0.04 simply as the approximate level of the $p\epsilon$ products collected in Table III.

These results for Fe^{+3} reduction in 1.0*M* H_2SO_4 are shown in Fig. 7. The points taken for $p = 0.2$ cover $p\epsilon$ from 0.004 to 0.03, those for $p = 0.4$ cover 0.012-0.093, and those for $p = 0.8$ cover 0.04-0.26. All three plots are linear and both the slope ratios (*A* ratios) and absolute *A* values are in satisfactory correspondence to the theory given above. Absolute *A* values were estimated in this case by determining Levich plots of i_{ω_0} *vs.* $\omega_0^{1/2}$ for various $\omega_0^{1/2}$ and comparing the slopes with those of the Fig. 7 plots. By combining Eq. [43] with Eq. [6], a definition of *A* related to this experimental approach is obtained, *i.e.*

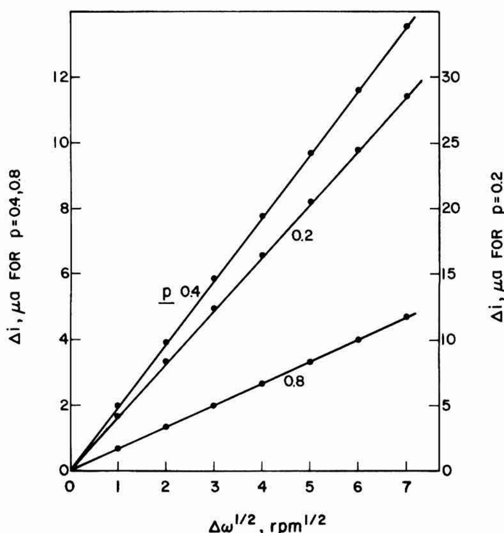

Fig. 7. Δi_1 as a function of $\Delta\omega^{1/2}$ at constant p values of 0.2, 0.4, and 0.8, as marked. Modulation frequency 6 Hz (all curves), center speed held at 30, 15, and 7.5 Hz. Abscissa is convertible to $p\epsilon$ values by multiplication by 0.00472, 0.0133, and 0.0377 for $p =$ 0.2, 0.4, and 0.8, respectively.

$$A = \frac{\Delta i_1}{\Delta\omega^{1/2}} \bigg/ \frac{i_{\omega_0}}{\omega_0^{1/2}} \qquad [53]$$

Hence, the slopes of the SHM data in Fig. 7, when divided by the slopes of the Levich plots, give the *A* values for the particular *p* values.

As far as the SHM technique is concerned, exceeding the $p\epsilon$ criterion for deviation from a hydrodynamic quasi-steady state by even a factor of six appears to have little detectable effect on $\Delta i_1 - \Delta\omega^{1/2}$ plots. This result, predicted by theory, has the significance for practical use of the SHM technique at higher modulation frequencies (larger *p*) that, to a large extent, much of the loss of current sensitivity associated with a decreasing *A* factor at higher *p* values may be compensated by a $\Delta\omega^{1/2}$ increase. At present, the practical limitations of this sort of approach appear to reside mostly in the amplitude and frequency response of the motor system.

The *A* and φ_1 functions are independent of the concentration of the electroactive species and its *n* value in the electrode process. This property suggests a method for determining the diffusion coefficient of an electroactive species without *a priori* knowledge of the *n* value (or concentration), as is required by RDE and other voltammetric steady-state diffusion layer techniques. From the *A* (or φ_1) *vs.* *p* data for an unknown system, Sc for the electroactive species can be determined by interpolation in Table II (or I). *D* can then be calculated from the readily determined kinematic viscosity of the solution. This value of *D* may be in error by ±10-15%, because of the combination of experimental error and relative insensitivity of the *A* or φ_1 *vs.* *p* function to some values of Sc. However, if i_{ω_0} and the electroactive solute's concentration are known, substituting these data and the estimate of *D* into Eq. [43] will permit determination of the integral value of *n*, and thence a precise value of *D*.

Application of the SHM technique to solutions containing two or more electroactive components leads to certain difficulties if phase sensitive detection is used to determine Δi_1. In such mixtures, each electroactive species has its unique value of Sc, and thus a corresponding phase shift. The detection of Δi_1 response for regions on the current-voltage curve involving simultaneous reduction (or oxidation) of more than one species is thus complicated by the varying phase shifts for each component. There are obvious experimental strategems to correct for this difficulty, *e.g.*, manual tuning of the phase shift for each of the components is feasible. However, the variation of phase angles as a function of Sc at constant *p*, as can be seen from Table I or Fig. 3, is not large. The phase angle effect is modest when compared to the phase angle setting accuracy requirements of lock-in amplifiers. Phase errors of ±10° are necessary for 1½% signal loss and, if the spread of Sc values is not extreme, errors due to this source will probably be small in most practical situations.

It should be noted that, if a tuned filter used to isolate the a-c response to SHM is followed by either full-wave rectification or RMS detection, the phase problem is completely avoided.

The theory presented here does not apply to the case of mixed electron and mass transfer control, which we have already considered for the $p \rightarrow 0$ limit (6). There are effects in those situations (further diminishing *A* and increasing φ_1) which require a more involved treatment.

Acknowledgments

Work done at the State University of New York at Buffalo was supported by the Air Force Office of Scientific Research through AFOSR Grant No. 74-2572 to the Research Foundation of the State of New York.

Manuscript submitted February 6, 1975; revised manuscript received June 13, 1975. This was Paper 397 presented at the Toronto, Canada, Meeting of the Society, May 11-16, 1975.

Any discussion of this paper will appear in a Discussion Section to be published in the June 1976 JOURNAL. All discussions for the June 1976 Discussion Section should be submitted by Feb. 1, 1976.

Publication costs of this article were partially assisted by Bell Laboratories.

REFERENCES

1. B. Miller and S. Bruckenstein, *This Journal*, **117**, 1032 (1970).
2. B. Miller, M. I. Bellavance, and S. Bruckenstein, *ibid.*, **118**, 1082 (1971).
3. B. Miller, M. I. Bellavance, and S. Bruckenstein, *Anal. Chem.*, **44**, 1983 (1972).
4. S. Bruckenstein, M. I. Bellavance, and B. Miller, *This Journal*, **120**, 1351 (1973).
5. B. Miller and S. Bruckenstein, *Anal. Chem.*, **46**, 2026 (1974).
6. B. Miller and S. Bruckenstein, *This Journal*, **121**, 1557 (1974).
7. Th. von Kármán, *Z. Angew. Math. Mech.*, **1**, 233 (1921).
8. W. G. Cochran, *Proc. Cambridge Phil. Soc.*, **30**, 365 (1934).
9. E. R. Benton, *J. Fluid Mech*, **24**, 781 (1966).
10. K. Tokuda and H. Matsuda, *J. Electroanal. and Interfac. Electrochem.*, **52**, 41 (1974).
11. E. M. Sparrow and J. L. Gregg, *J. Aerospace Sci.*, **27**, 252 (1960).
12. J. Newman, *J. Phys. Chem.*, **70**, 1327 (1966).
13. IBM Application Program, System/360 Scientific Subroutine Package, Version III, Programmer's Manual Program Number 360A-CM-03X, 5th ed, 1970.

Technical Note

The Cathodic Reaction of Iron Disulfide Electrode in KCl-LiCl Eutectic Electrolyte

Katsushi Abe and Takewo Chiku*

Toyota Central Research and Development Laboratories, Incorporated, 2-12, Hisakata, Tempaku-ku, Nagoya 468, Japan

The molten salt battery will be given more attention in the near future because of its high specific power and high specific energy. However, in the present state, there are various difficulties involving the battery construction, particularly the risk at high temperature operation from the use of liquid (1) or gaseous (2) active material as the positive electrode.

Vissers *et al.* (3) studied the molten salt secondary cells with iron sulfide as the positive material. This study was useful because it showed that there was no significant deterioration of electrical performance with cell operation.

Tomczuk, Martin, and Steunenberg (4,5) found that metal sulfides, such as nickel or cobalt sulfide, were solid-state materials that could serve as a positive electrode for a molten salt battery, and they proposed that the charge reaction of iron disulfide proceeds by three steps. The present authors have also examined various metal sulfides as solid-state active material for a battery with KCl-LiCl eutectic electrolyte.

It is the purpose of the present note to elucidate the discharge reaction of iron disulfide in KCl-LiCl eutectic electrolyte by a combination of the polarization character and x-ray diffration analyses.

Experimental

The test electrodes were prepared, as shown in Fig. 1, by putting a definite quantity of iron disulfide powder in a hole (3.2 mm diameter, about 3 mm depth) drilled in spectroscopic graphite rod (6 mm diameter, 150 mm length), then filling it with electrolyte salt powder; the lower part of the rod was fixed by baking Aremco alumina adhesive and glazed Pyrex to separate it from the electrolyte except the hole. To prevent iron disulfide from escaping, the hole was sealed by wind-

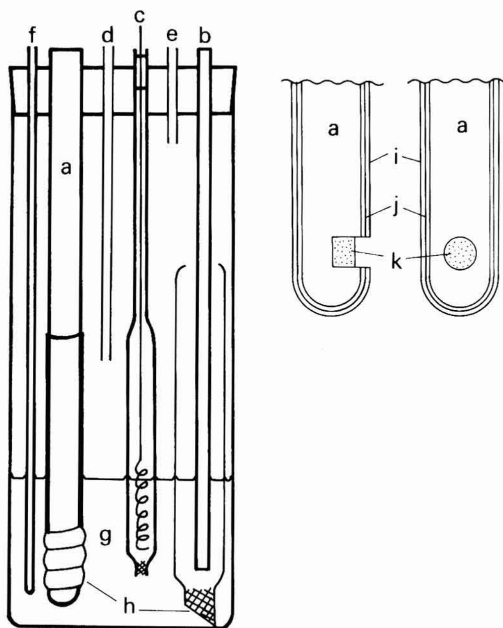

Fig. 1. Electrolysis cell and electrode construction. a, Graphite (test electrode); b, glassy carbon counterelectrode; c, reference electrode; d, Ar gas inlet; e, Ar gas outlet; f, thermocouple; g, KCl-LiCl eutectic; h, quartz wool; i, Pyrex glass seal; j, alumina adhesive; k, FeS_2 powder.

* Electrochemical Society Active Member.

Key words: iron pyrite, discharge reaction, molten salt electrolyte, high temperature cell.

ing the rod with quartz wool. The iron disulfide powder sample used in this study was a commercial pyrite (99.9% purity) containing only a trace of marcasite as shown by x-ray diffraction analysis.

The 58 mole per cent (m/o) LiCl-42 m/o KCl eutectic electrolyte was prepared by combining reagent grade lithium chloride and potassium chloride in a Pyrex vessel at 400°C, bubbling hydrogen chloride gas for about 1 hr and then high purity argon gas (O_2: ~1 ppm, dew point: −65°C) for several hours. A Pyrex tube 28 mm inner diameter and 150 mm height was used as the electrolysis cell; the anode and the cathode compartments were separated by quartz wool. Figure 1 shows a schematic representation of its construction. The iron disulfide electrodes were discharged and charged at 400°C in the electrolyte with glassy carbon as the counterelectrode. High purity argon gas was made to flow continuously over the electrolyte during the experiments. The electrode potential was measured against a Pt/0.01 mole $PtCl_2$ reference electrode with the supporting electrolyte.

The reaction products used for x-ray measurements were taken from the electrode at various stages of charge and discharge in the following way: The respective electrodes were removed from the circuit and cooled in argon atmosphere, the products extracted from the graphite rods were crushed and pulverized in the atmosphere, then were covered with a thin film of Mylar. No washing or drying procedures were performed so as to prevent any change in the chemical composition.

Results and Discussion

Discharge and charge characteristics.—Figure 2 shows potential/time curves for the iron disulfide electrode with the repetition of discharge and charge cycles at a constant current of 200 mA/cm². The potential curve obtained during the first discharge to −2.0V shows several steps, and similar steps also were obtained in the curve with the subsequent charge to −0.7V, in which open-circuit potential before the discharge was about −0.7V. When repeating the cycle, the corresponding curves have little change in the shapes and the discharge capacities, at least up to 40 cycles. There is an additional step at about −0.8V in the discharge curve. However, judging from the fact that the upper limit of the charging potential was equal to the open-circuit potential at the initial state, the open-circuit potential could not be that of iron disulfide itself.

Figure 3 shows the discharge and charge curves at a constant current density of 100 mA/cm² and open-circuit potentials in various discharge and charge states; a stationary value obtained about 30 min after the circuit was opened at each state served for the open-circuit potential. It is seen that both the open-circuit potential curves in the discharge and charge were composed of four steps, and they are in close agreement with each other. These results suggest that the discharge-charge reaction proceeds through four reversible processes. At this current density, the polarization curve in discharge also shows four distinct steps corresponding to those in the open-circuit potential curve, but the four steps grow less distinct as the discharge current increases.

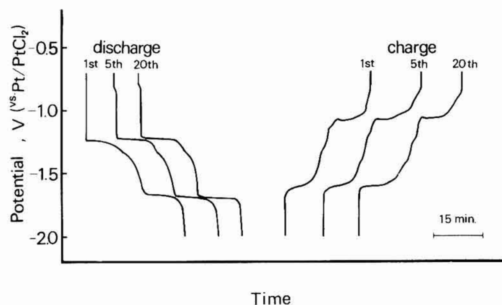

Fig. 2. Typical potential/time curves for FeS_2 electrode in discharge-charge cycling at a constant current density of 200 mA/cm².

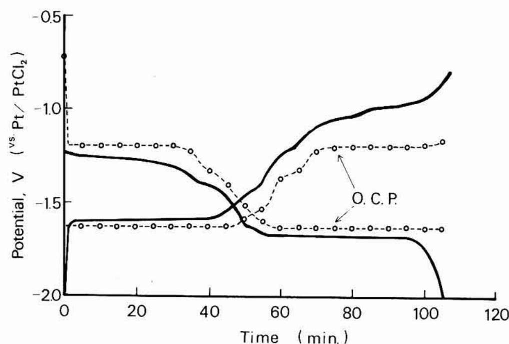

Fig. 3. Discharge-charge curves at a constant current density of 100 mA/cm² and open-circuit potentials in various discharge and charge states, for 20 mg FeS_2 at 400°C.

X-ray diffraction analyses.—Five electrodes, each containing 70 mg of iron disulfide, were placed in the discharge and charge states in the KCl-LiCl electrolyte. Three of them were partially discharged to −1.3, −1.6, or −2.0V at a current density of 50 mA/cm². The fourth electrode was completely discharged to −2.0V intermittently at 25 mA/cm². The last electrode was discharged to −2.0V at 100 mA/cm², then immediately recharged to −0.7V, the level of initial potential, at the same current density. X-ray diffraction analyses were carried out as a function of the depth of discharge. The results are summarized in Table I. As seen from the table, the starting material is pyrite containing a trace of marcasite. Phases gradually decrease with progressive discharge and are eventually exhausted at about −1.6V. At −2.0V, lithium sulfide and iron were observable as the final products. It is noted here that by recharging the electrode, the diffraction peaks of lithium sulfide and iron disappear accompanied by the reformation of pyrite together with a trace of pyrrhotite. However, many unknown peaks were present in the diffraction pattern at the partial discharge states. As shown in the last column

Table I. Results of x-ray diffraction analyses; Co-Kα, 2θ; 30° ~ 80°

No. of sample	Sampling potential (V)		Discharge state (%)	Identified material	Unknown peaks		
	Discharge	Charge					
—	—	—	0	Pyrite, Marcasite (trace) ↓ ↓			
1	−1.3	—	35	(Decrease) Marcasite ↓ ↙↓	(A) ↓	(B) ↓	
2	−1.6	—	40	(Not detected)	↓	Decrease	(C) ↓
3	−2.0	—	85	Li_2S, Fe	Increase ↓		Decrease
4	−2.0	—	100	Li_2S, Fe	Not detected		
5	(−2.0)	−0.7	3	Pyrite, $Fe_{1-x}S$ (trace)			

of Table I, the unknown peaks were divided into three groups denoted by A, B, and C, respectively. These classifications show a partial increase or decrease as the discharge takes place. To ascertain if said peaks may have been caused by atmospheric oxidation or hygroscopicity during the sample preparation, the same examination was carried out with the sample specially prepared in a high purity argon atmosphere. No change, however, was observed in the diffraction pattern.

The results suggest at least that the corresponding substances were formed with the discharge process and that they transform to a stable substance at the final stage. In fact, the unknown peaks disappeared at the complete discharge state, and lithium sulfide and iron, which are considered to be the final products, could only be detected. These results corroborate previous findings that suggested four reversible processes make up the discharge-charge reaction.

Acknowledgments

The authors wish to thank Dr. K. Nakajima of Toyota Central Research and Development Laboratories for his helpful suggestions during this study.

Manuscript submitted Jan. 27, 1975; revised manuscript received June 9, 1975.

Any discussion of this paper will appear in a Discussion Section to be published in the June 1976 JOURNAL. All discussions for the June 1976 Discussion Section should be submitted by Feb. 1, 1976.

Publication costs of this article were partially assisted by Toyota Central Research and Development Laboratories, Incorporated.

REFERENCES

1. L. A. Heredy, N. P. Yao, and R. C. Saunders, International Electric Vehicle Symp., Nov. 5-7, 1969, p. 325.
2. D. A. J. Swinkels, *This Journal*, **113**, 6 (1966).
3. D. R. Vissers, Z. Tomczuk, and R. K. Steunenberg, *ibid.*, **121**, 665 (1974).
4. Z. Tomczuk, A. E. Martin, and R. K. Steunenberg, Paper 53 presented at the Electrochemical Society Meeting, New York, N.Y., Oct. 13-17, 1974.
5. A. E. Martin, R. K. Steunenberg, and Z. Tomczuk, Paper 54 presented at The Electrochemical Society Meeting, New York, N.Y. , Oct. 13-17, 1974.

Erratum

In the paper "Electrochemistry of Multisulfur Heterocycles: Trithiocarbonates and Trithiocarbenium Ions" by P. R. Moses, J. Q. Chambers, J. O. Sutherland, and D. R. Williams which appeared on pp. 608-615 in the May 1975 JOURNAL, Vol. 122, No. 5, several bonds were omitted from the structure in Eq. [5]. The equation should read as follows:

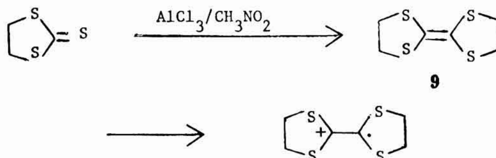

JOURNAL OF THE ELECTROCHEMICAL SOCIETY

SOLID-STATE SCIENCE
AND TECHNOLOGY

OCTOBER
1975

Role of Anodic Processes in the Electrolytic Coloration of Alkali Halides

M. T. Montojo[1] and F. Jaque

Departamento de Física, Universidad Autónoma, Cantoblanco, Madrid, Spain

and C. Sánchez

FEMSA, D.E.P. Investigación, Hnos. Garćia Noblejas No. 19, Madrid 17, Spain

ABSTRACT

An investigation has been made into the origin of Zone IV (1) of the current *vs.* time curves obtained during electrolytic coloration of alkali halides with a pointed cathode and a flat metallic anode mechanically pressed against the crystal. Zone IV is not intrinsic and is not due to the crystal volume itself, but is related to processes occurring in the crystal metallic anode interface. Whenever these processes are inhibited, *e.g.*, by using a vacuum evaporated metallic anode, Zone IV is suppressed and intrinsic current *vs.* time curves are obtained. These curves resemble those corresponding to space charge limited currents in insulators and semiconductors. The following anodic processes are mentioned: An electrical arc was produced in the thin and irregular gap between the crystal and the anodic plate. The intensity of the light emitted from this arc correlates with electrical current during Zone IV and the spectral distribution shows a complicated multipeak structure. The number and position of the peaks are quite independent of the alkali halide crystal, anodic material, and gas filling the furnace. Most of the spectrum peaks correspond fairly well in position to those of the air component discharge. The main characteristics of the arc are due to air (water vapor) adsorbed on the anodic crystal surface. A tentative explanation of how this electrical arc can determine the properties of Zone IV is proposed.

Electrolytic coloration has been extensively used as a procedure to create F-centers in alkali halides (2); the number of F-centers produced depending upon the experimental conditions. Experiments are usually carried out at constant temperatures (~350°-700°C) and applied voltages ($50\text{-}10^3$/V). Currently, a pointed cathode and a flat metallic anode machanically pressed against the crystal are used. Atmospheres surrounding the crystals are air, vacuum, or an inert gas.

The evolution of the electrical current through the crystal during the electrolytic coloration has been recorded in KCl and KBr (1, 3, 4). Figure 1 shows an example of this behavior in KBr single crystals. F-center density changes in a parallel fashion, as shown by the dashed curve, although a time lag exists. Four zones appear in the *i-t* curve. Zone I has been accounted for as being due to purely ionic transport (1, 4, 5). This process leads to the formation of an injecting contact at the cathode-crystal interface (6). Once this contact is formed electrons are injected from the pointed cathode into the crystal. Electronic current marks the start of Zone II. The kinetics of this zone in KCl has been explained by Heiland (3) and Karabascheff (7) as due to F-center diffusion. Equations describing the slope of this zone have also been proposed.

In spite of the wide use of electrolytic coloration, several questions relating to its physical mechanisms still remain open. Briefly, these questions relate to: (*i*) The appearance of Zone IV in KBr and KCl which corresponds to an enhancement of the electrical current and F-center density in the crystal. According to Heiland (3) Zone II should be followed by an equilib-

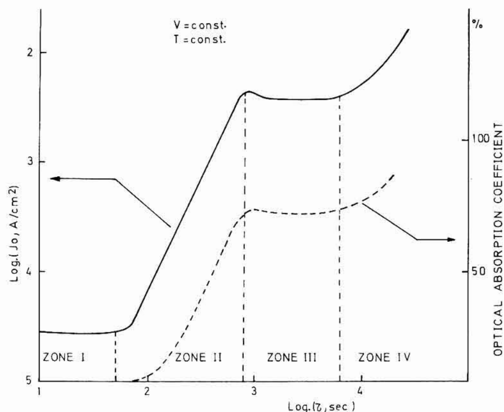

Fig. 1. Electrical current (continuous line) and F-center density (dashed line) *vs.* time during electrolytic coloration of KBr single crystals. [After Andreev *et al.* (1)].

[1] Also: C.I.D.A., Arturo Soria No. 289, Madrid, Spain.

Key words: solid electrolytes, injected carriers, color centers, dielectric breakdown.

rium stage (Zone III) in all cases, and Zone IV should never appear. (*ii*) The F-color cloud starts at the cathode and propagates through the crystal. Pisarenko (8) has observed a coloration starting at the region surrounding the anode after the conductivity increased in Zone IV in KCl crystals at temperatures between 250°-350°C.

Herein are reported some new experimental results in relation to these points. It is shown that Zone IV is exclusively due to processes occurring at the anode-crystal frontier. These processes can be inhibited, therefore suppressing Zone IV. They are responsible for the high current and high F-center concentrations that characterize Zone IV.

Experimental

A vacuum-sealed furnace was used to electrolytically color the crystals. Temperature was controlled with ±1°C and measured with a Chromel-Alumel thermocouple. Experiments were performed in either air, vacuum, nitrogen, or argon atmospheres. A pointed cathode (stainless steel, Pt) and a flat anode (tungsten, aluminum foils, and graphite) were used. In some experiments the anode was a vacuum-evaporated film.

A couple of quartz windows in the furnace allowed for luminescence measurements and photographing the crystals. A high intensity Bausch and Lomb monochromator and an EMI 9558 QB photomultiplier were used in the range 2500-4500Å. Single crystals of KBr, NaCl, KCl, KI, and CsI of ~ 10 × 5 × 5 mm were colored. Other experimental details are described in (4).

Results

In the process of electrolytically coloring KBr single crystals with a stainless steel pointed cathode and a tungsten foil anode mechanically pressed against the crystal, a light emission was detected. The samples were placed between the electrodes in the open air and the sample holder was then introduced into the furnace. Air was evacuated and nitrogen was let into the furnace at a pressure slightly higher than the atmospheric one. The sample was heated and once the working temperature (~350°-550°C) was stabilized, the electric field was turned on in order to color the crystal. Light emission was also measured with other crystals (KCl, KI, NaCl, and CsI), electrodes (platinum point, aluminum foils, and graphite), and atmospheres (air and argon).

Photographs taken during the coloration process proved that in all cases the light is generated at the anode-crystal frontier. The crystal is shown in Fig. 2 with a black line and the pointed cathode is at the top of the picture. The light emitted has a multipeak spectrum as shown in Fig. 3. The width of the lines

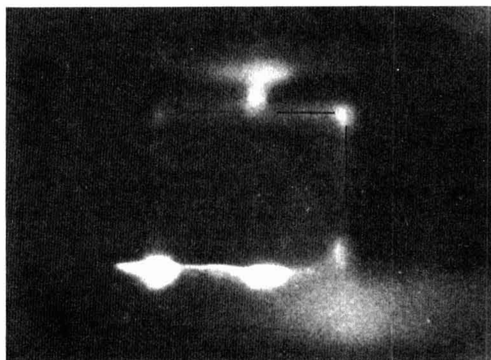

Fig. 2. Photograph of a KBr crystal during coloration in Zone IV shows light emission in the anodic region. The crystal is marked with a black line.

cannot be considered as a reliable datum due to the monochromator we used. The intensities of the lines were highly dependent on the experimental conditions and no systematic study of this point has been made.

In order to elucidate the possible origin of the electrical arc and the light emission, experiments were performed with different alkali halides, electrodes, and atmospheres. In all cases, the experimental procedure was that described above. The most relevant parameters from the obtained spectra were the peak positions. Table I shows some of the experimental results: the crystal, cathode and anode material, and the atmosphere used in each experiment are indicated. The main air component discharge is also quoted for comparison purposes. It is clear from the table that most of the peak positions are quite independent of the various crystals, electrodes, and atmospheres. In our experiments with KBr and KCl single crystals, we were able to obtain measurements only for wavelengths shorter than ~ 4700Å due to the emission of the furnace walls: A much lower temperature is required to color CsI than to color KBr and KCl. All the wavelengths in the table are affected by an error of ±50Å. At this point it is interesting to note that whenever a graphite anode was used, the peak intensities were much weaker than with an Al or W anode. Furthermore, with air filling the furnace the intensities of all the lines were considerably improved.

The intensity of the emitted light is a function of time during the coloration process: we never detected

Table I. Peak position wavelengths (Å) of the anodic emission spectra obtained by electrolytically coloring different alkali halides with several electrodes and atmospheres. The major lines of the air component discharge are also included. All the values are affected by an error of ±50Å.

Crystal Electrodes Atmosphere	CsI SS*-W Nitrogen	CsI Pt-Al Nitrogen	CsI Pt-W Nitrogen		KBr SS* graphite Nitrogen		KBr SS*-W Nitrogen	KBr Pt-Al Nitrogen	KBr SS*-W Argon	KCl SS*-W Nitrogen	Principal air Lines**
Peak positions (Å)	5865	5800	5880	5830							5888
	5680		5740	5656							5750
			5400	5304							5330
	4980	~5100	5020	5018							4969
		4750	4700								4705
	4650			4600	4660						4649
	4300	4300	4330	4292	4270	4300	4370				4349
	4040		4000	4028		4050	4090	4040			4070
		3900		3940	3900						3995
		3700	3770	3808	3750	3800	3810	3800	3760	3790	3749
		3600	3600	3610	3530	3570	3570	3580	3560	3590	
											3390
							3345	3380	3330	3350	3332
											3329
	This range has not been covered						3120	3140	3120	3100	3134
							2950				
							2810		2850		
									2750		2733
							2680	2600	2650		2678

* SS = stainless steel.
** Wavelength tables for spectrum analysis, Adam Hilger Ltd., London (1931).

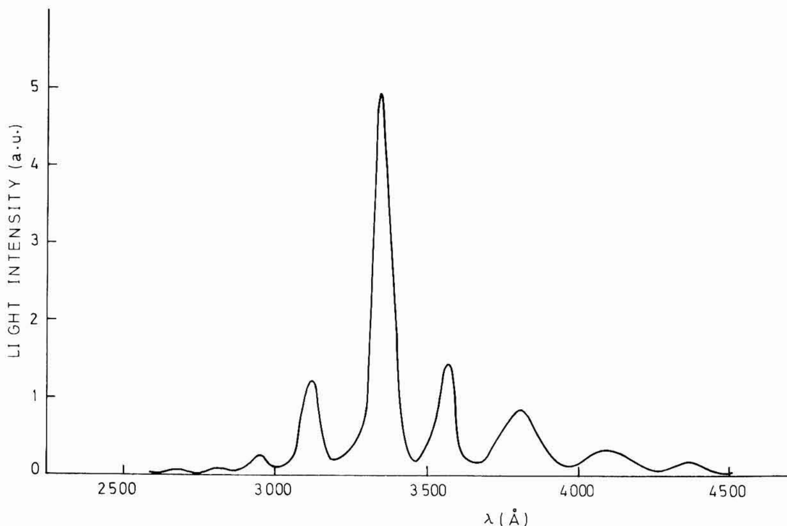

Fig. 3. Spectral distribution of light emitted during electrolytic coloration of KBr with a W foil as anode and nitrogen atmosphere.

light during Zone I of the coloration curve; a very weak emission was measured sometimes during Zone II and at other times during Zone III; but the emission of light was highly efficient during Zone IV. This behavior is depicted in Fig. 4(a) where the evolution of the electrical current (curve A) and the light intensity measured at $\lambda = 3570Å$ (curve B) during the electrolytic coloration of KBr are shown. A time lag between the current and light is observed initially; but in Zone IV both curves rise up proportionally as represented in Fig. 4(b). This behavior appears in all the materials we have studied. The slope of the straight line and the value of the electrical current when there is no light intensity are a function of the experimental conditions, but are more affected by the applied electric field and the sample temperature. It was also noted that at temperatures below 500°C the F-coloration originating at the cathode during Zone II is very weak, but on reaching Zone IV a dense line of coloration from the anode propagates through the crystal and begins its dielectric breakdown when it joins the cathode.

Discussion

It is clear from Fig. 2 that the emission of light during Zone IV of the current-time curve is due to processes occurring in the crystal-anode interface. All the experimental results already described were obtained by using a metallic anodic plate mechanically pressed against the sample; the conventional method used to electrolytically color alkali halides. The experimental procedure followed in all cases was that described above.

It is also evident that a close parallelism exists between the electrical behavior in Zone IV and the anodic processes responsible for the light emission. In order to examine this parallelism more closely, the anodic contact was changed. Crystals with vacuum (10^{-6} Torr)-evaporated metallic (Au, Al) anodes were prepared. The rest of the experimental procedure was as previously described: The same stainless steel or platinum pointed cathode was used. While coloring the crystal with these new anodes, the electrical current passing through the sample was recorded. Curve A in Fig. 5(a)

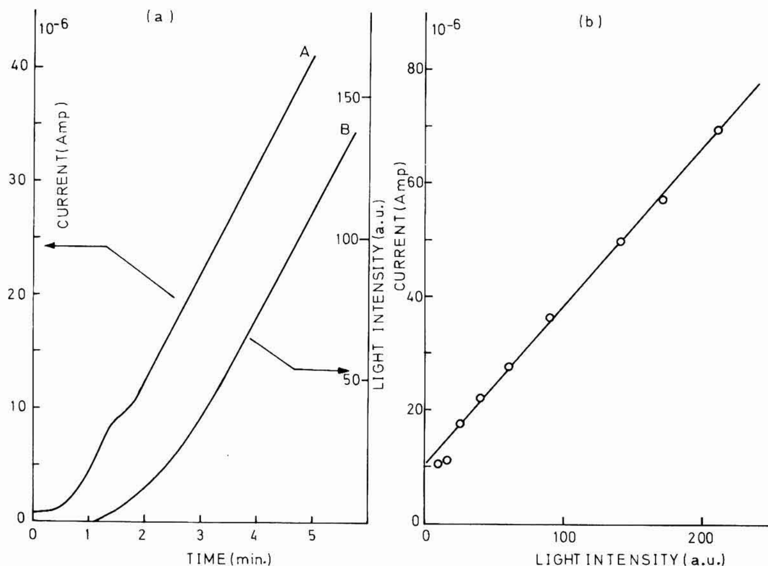

Fig. 4. (a). Electrical current (curve A) and light intensity at $\lambda = 3570Å$ (curve B) during electrolytic coloration of KBr at $T = 422°C$, $V = 600V$. (b) Relationship between current and light intensity.

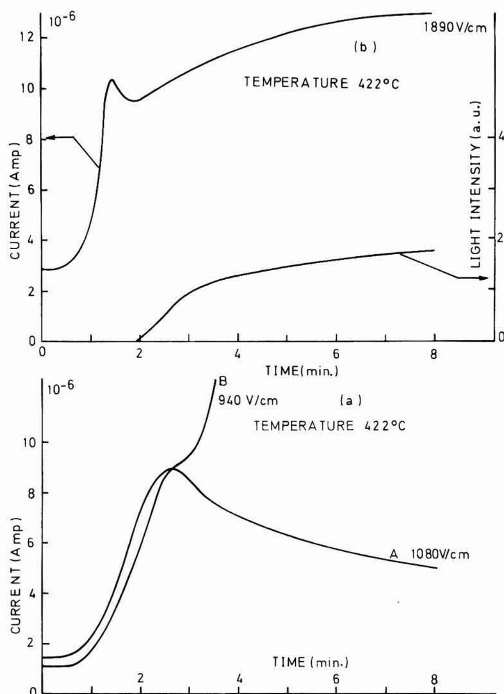

Fig. 5. (a). Electrical current during electrolytic coloration of KBr with a vacuum-evaporated Al film as anode (curve A). Curve B is shown for comparison purposes and has been obtained with a tungsten plate. (b). Shows the effect of increasing the voltage to higher values than those commonly used in our experiments. The anode was a vacuum-evaporated film.

represents the results obtained. At the same time it must be emphasized that no light emission was detected along the whole coloration process. It is clear from Fig. 5(a) that Zone IV does not appear. The electrical current follows Zones I and II, reaches a maximum, and finally decreases; the difference between the maximum and the final steady value of the current being a function of the applied voltage and the crystal temperature. From these experiments it was concluded that Zone IV of the curves is not intrinsic and is due to the processes occurring in the crystal-anode interface while electrolytically coloring alkali halides by conventional means. If these phenomena are inhibited, at least partially, Zone IV disappears. The anodic processes are not totally avoided by using vacuum evaporated anodes as can be seen from Fig. 5(b) where the applied voltage has been increased to much higher values than those commonly used in these experiments. Current again increases, leading to a very reduced Zone IV. At the same time, a very slight light emission is detected [Fig. 5(b)] proving that both light emission and electrical current in Zone IV have the same origin. For comparison purposes a typical curve obtained with a tungsten foil anode mechanically pressed against the crystal at the same temperature is shown as curve B in Fig. 5(a).

It is worthwhile to note that curve A in Fig. 5(a) closely resembles those obtained in insulators and semiconductors (9) whenever space charge controlled mechanisms are operating. Results regarding the role played by these mechanisms in the electrolytic coloration of alkali halides will be published elsewhere.

As to the physical nature of the processes occurring in the crystal-anode interface, it is clear from Table I that the peak positions of the emission spectra are widely independent of the crystals, electrodes, and gas filling the furnace. On the other hand, a very narrow correspondence (within the experimental error) exists between these values and those shown by the principal lines of the air component discharge (last column of Table I). These two experimental facts, and the evidence that on using vacuum-evaporated anodes there is no light emission, lead to the suggestion that the air (essentially water vapor) adsorbed in the anodic crystal face during the cleaving and the storing of the samples plays a major role in all the described phenomena. This water vapor is probably desorbed during the heating of the sample and retained in the thin and irregular gaps between the crystal and the anodic plate due to the overpressure of the nitrogen (or argon) introduced in the furnace. As a consequence, the main characteristics of the emission spectra correspond to those of the air component discharge. A confirmation of this hypothesis was obtained by the following experiments: with the same primitive flat anode (tungsten or aluminum foils), the crystal holder was introduced into the furnace and the crystal heated in a dynamic vacuum (without introducing inert gas) up to the working temperature, then the vacuum was maintained for some time (~1 hr) before letting nitrogen or argon in. With this procedure we tried to partly eliminate the water vapor adsorbed in the crystal surface. On applying the electric field to color the crystal, curves similar to curve A in Fig. 5(a) are obtained and no light emission exists. Whenever the water vapor retained in the gaps between the crystal and the metallic anode is removed, Zone IV disappears and there is no luminous phenomena. Not all the observed phenomena are due exclusively to this water vapor, no doubt there is some influence from the gas filling the furnace and the electrode materials, but these should be rather small in comparison with the contribution of the adsorbed water vapor.

Regarding the origin of the electrical arc in the crystal anode interface, no clear conclusion can be obtained from these results. According to the shape of the curve in Fig. 1 it can be suggested that during Zone II a high negative space charge accumulates at the crystal anodic face and a very high electric field is produced through the narrow gaps between the crystal and the anode. This suggestion has some experimental support in that the arc appears either during or at the end of Zone II.

Finally, the means by which the electrical arc in the anodic face can give place to Zone IV of the curves should be discussed. The whole process appears to be very complicated, and some speculation seems unavoidable. Our results suggest that water vapor molecules desorbed from the anodic face of the crystal are decomposed by the arcing, and oxygen ions react with the metal plate to produce oxides. In fact, the area of the anodic foil in contact with the crystal shows a very dark stain, clear evidence of a chemical reaction. On the other hand, the principal emission lines that were measured correspond to those of the second ionization of oxygen. One possible mechanism for this decomposition could be

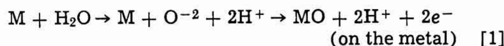

$$M + H_2O \rightarrow M + O^{-2} + 2H^+ \rightarrow MO + 2H^+ + 2e^- \quad \text{(on the metal)} \quad [1]$$

although the whole process must be much more complicated and other quantitative combinations are possible. M signifies the anodic metal (W, Al, Mo). Reactions like Eq. [1] have been observed in different metallic surfaces under the action of an electric arc (10).

In order to account for the high value of electrical current in Zone IV, it is plausible to think that protons liberated in the arc region are injected into the crystal under the electric field existing in the gap. Their high mobility should produce a considerable contribution to the electrical current. Phenomena parallel to those we are discussing now have been shown to take place in some glasses when atmospheric moisture is present (11). Further experimental work is needed before all these possible mechanisms can be confirmed.

The final conclusion in relation to the electrolytic coloration process is that only Zones I, II, and III are intrinsic; Zone IV is not due to the crystal itself. From our results it appears that water vapor adsorbed in the anodic face of the crystal plays an important role in relation to Zone IV of the curve. But it is not yet possible to determine the exact processes taking place in the electrical arc at the anode region.

Acknowledgments

The authors gratefully recognize "Ayudas Manuel Aguilar" which partly supported this work. Fruitful discussions with the members of C-IV (U.A.M.) have been a continuous encouragement.

Manuscript submitted July 1, 1974; revised manuscript received May 23, 1975.

Any discussion of this paper will appear in a Discussion Section to be published in the June 1976 JOURNAL. All discussions for the June 1976 Discussion Section should be submitted by Feb. 1, 1976.

Publication costs of this article were partially assisted by FEMSA.

REFERENCES

1. G. A. Andreev, G. B. Semushkin, and A. N. Tsikin, *Soviet Phys. Solid State*, **9**, 2564 (1968).
2. J. J. Markham, "F-centers in Alkali Halides," Academic Press, Inc., New York (1966).
3. G. Heiland, *Z. Physik*, **127**, 144 (1950).
4. M. T. Montojo and C. Sánchez, *J. Phys. Chem. Solids*, **35**, 1437 (1974).
5. N. Paramo and C. Sánchez, *J. Phys. Soc. Japan*, **30**, 1106 (1971).
6. M. T. Montojo and C. Sánchez, *Solid State Commun.*, **14**, 485 (1974).
7. N. Karabascheff, *Z. Physik*, **118**, 718 (1942).
8. V. F. Pisarenko, *Soviet Phys. Solid State*, **3**, 2184 (1962).
9. M. A. Lampert and P. Mark, "Current Injection in Solids," Academic Press Inc., New York (1970).
10. G. Amsel, in "Physics of Solid Electrolytes," J. Hladik, Editor, p. 133, Academic Press Inc., London (1972).
11. K. Hughes and J. O. Isard, *ibid*, p. 368.

The Transport of Chromium in Cr_2O_3 Scales in Sulfidizing Environments

G. Romeo,*[,1] H. S. Spacil,* and W. J. Pasko

Research and Development Center, General Electric Company, Schenectady, New York 12301

ABSTRACT

The diffusivity of chromium in Cr_2O_3 scales formed during the oxidation of chromium at 900°-1000°C appears to increase by several orders of magnitude when an initially present oxide scale is exposed to sulfur-bearing atmospheres at low oxygen partial pressure. As a result chromium sulfide scales grow on both sides of the preexisting oxide layer. The transition from oxidation to sulfidation corresponds to a change from parabolic to linear weight gain, indicating that the sulfide growth is controlled by a constant rate of supply of chromium through the oxide to the outer oxide-sulfide interface, under fixed experimental conditions. The sulfidation rate increases with sulfur partial pressure, indicating that chromium transport in the oxide is affected by changes in the defect structure of Cr_2O_3 induced by the presence of sulfur. A model is proposed in which sulfur enters the oxide as an electron donor, thereby increasing the concentration of chromium vacancies and interstitials.

Hot corrosion phenomena of gas turbine superalloys frequently result in the formation of mixed oxide/sulfide scales. Sulfidation has been reported as due to the reaction of the alloy surface with sodium sulfate deposits, considering the sulfate, with a very low sulfur activity, as the only source of sulfur (1). However, the presence of sulfur at an activity above the equilibrium value for sulfide formation would provide an additional mechanism for accelerated corrosion. Such high sulfur activities could arise from local reducing conditions in an otherwise oxidizing environment (2). Internally precipitated sulfides are frequently observed under Cr_2O_3 scales formed on Ni-base alloys. It is then possible that a mechanism involving the transport of sulfur across these scales from a high activity source is responsible for the presence of sulfide particles. The diffusion of sulfur in polycrystalline Cr_2O_3 has been studied by Seybolt (3), who reported a tracer diffusion coefficient of about 1.5×10^{-10} cm²/sec at 1000°C. No mechanism was proposed for the migration of sulfur species through the oxide. A recent paper by Chang *et al.* (4) on the diffusion of S^{35} in hot-pressed α-Cr_2O_3 reported a diffusion coefficient for S^{35} varying from 5.1×10^{-11} to 5.2×10^{-10} cm²/sec in the temperature range 700°-1050°C.

* Electrochemical Society Active Member.
[1] Present address: General Electric Company, Vallecitos Nuclear Center, Pleasanton, California 94566.

Key words: sulfidation, chromium diffusion, chromium oxide.

In a previous publication (5) we have reported preliminary results on the sulfidation kinetics and scale morphologies of chromium specimens preoxidized and subsequently exposed at 900°C to 10% H_2S-H_2 gas mixtures. This paper summarizes the results of further experiments in which the sulfidation of preoxidized chromium was studied at different partial pressures of sulfur.

Experimental

Rectangular specimens of high purity "iochrome" (99.997%) approximately $1.5 \times 0.7 \times 0.15$ cm were cut from a cast ingot. After a suspension hole was drilled in each, these were wet ground through 600 grit silicon carbide paper and cleaned with acetone and methanol. Finally, their dimensions were measured with a micrometer.

Reaction kinetics were determined by following the weight gain of a specimen with a spring balance, the basic design of which has been described in a previous publication (6). Some modifications were made to this equipment in order to run experiments at low sulfur pressures. These could be attained by bubbling argon or a carbon monoxide/argon mixture through a flask containing molten sulfur. The flask was immersed in a silicone oil bath which was held at temperatures controlled within 1°C. Argon was used as an inert carrier

for sulfur, while carbon monoxide could provide a reducing environment. Gas mixtures of composition ranging from 0.001-10 volume per cent (v/o) hydrogen sulfide in hydrogen were also used as a source of sulfur. Linde commercial mixtures of "ultra high purity" gases were employed directly or appropriately diluted with hydrogen for this purpose. When the sulfur bath was used, the vapor pressure of S_2 was known from the temperature of the bath; by assuming saturation of the argon carrier, the S/CO ratio in the final gas mixture could be specified. With either H_2S-H_2 or CO-S_2 mixtures, the equilibrium sulfur partial pressure can be found by employing thermodynamic data for the relevant species. For the latter mixtures, formation of COS, CO_2, and SO_2 must be considered. Data from the JANAF Tables were used for this purpose (7).

Prior to each sulfidation run the chromium specimen was oxidized isothermally with oxygen at atmospheric pressure at temperatures of 900° or 1000°C, the latter value being chosen to allow the formation of thicker oxide layers. The oxygen flow was then stopped, the reaction cell was purged with argon, and the furnace temperature was adjusted to a value of 900°C prior to sulfidation, with the exception of a few runs carried out at 800° and 1000°C. The temperature of 900°C was chosen for its relevance to gas turbine operations.

After completion of each run the specimens were mounted in epoxy resin and cross-sectioned for metallographic examination and microprobe analysis of the scale. Also, after some runs the scale composition was identified by the Debye-Scherrer method.

Results

As reported elsewhere (5), a dramatic change in reaction rate and mechanism took place when a previously oxidized chromium specimen was exposed to a sulfur-containing atmosphere. Figure 1 shows that the weight gain curve of a specimen exposed directly to a 10% H_2S-H_2 gas mixture at 900°C followed a parabolic rate law, with a rate constant of 52 mg^2-cm^{-4}-min^{-1}, in quite good agreement with the value 92 mg^2-cm^{-4}-min^{-1} reported by Strafford and Hampton for the sulfidation of chromium at 925°C with a 30% H_2S-H_2 gas mixture (8). Figure 2 shows the weight gain curve of a specimen preoxidized and subsequently exposed at 900°C to the 10% H_2S-H_2 gas mixture. In the latter instance, switching from an oxidizing to a sulfidizing atmosphere brought about a change from a parabolic to a linear rate law after an incubation period.

Figure 3 shows an example of scale structure formed after a complete preoxidization and sulfidation run (No. 4 in Table II). Chromium sulfide can be formed on both sides of the oxide layer initially present, with the outer portion of the sulfide scale much thicker than the inner portion. Although the initial compactness of the oxide layer has been altered by the growth of the inner chromium sulfide layer, a fairly uniform layer of chromium oxide exists between the chromium sulfide scales.

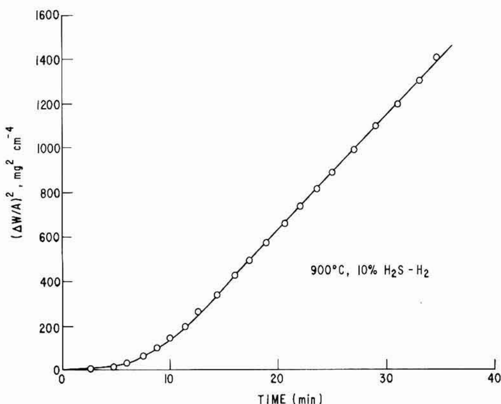

Fig. 1. Parabolic plot of weight gain vs. time for the sulfidation of chromium at 900°C with a 10% H_2S-H_2 gas mixture.

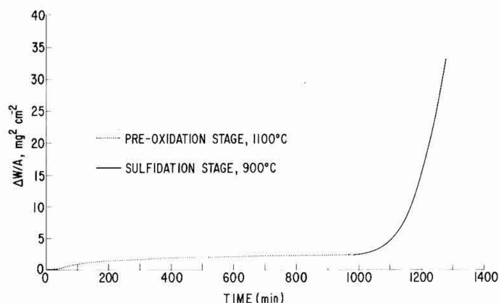

Fig. 2. Weight gain of a chromium specimen first exposed to oxygen at 1 atm and 1100°C, then to a 10% H_2S-H_2 gas mixture at 900°C.

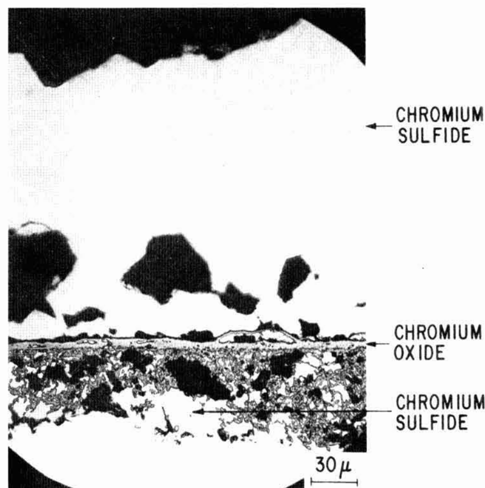

Fig. 3. Scale structure of a chromium specimen preoxidized and subsequently exposed for 20 hr to a 0.1% H_2S-H_2 gas mixture at 900°C.

Table I summarizes the values of the linear rate constant k_l obtained during sulfidation for three different thicknesses of pregrown oxide. The sulfidation was carried out in each case at 900°C in a 10% H_2S-H_2 gas mixture. The corresponding weight gain curves have been reported previously (5).

To verify the lower limits of sulfur pressure at which sulfidation does not take place on a preoxidized chromium specimen, similar experiments were also carried out in a much lower range of sulfur pressures. The experimental conditions and linear rate constants are

Table I. Linear rate constants in sulfidizing atmosphere of 10% H_2S-H_2

No.	Oxidation temperature (°C)	Weight of oxide at end of oxidation (mg × cm^{-2})	k_l (sulfidation) (mg × cm^{-2} × min^{-1})
1	900	0.6	0.50
2	1100	2.3	0.23
3	1200	3.2	0.11

Table II. Linear rate constants in low sulfidizing atmospheres

No.	Oxidation temper- ature (°C)	Weight of oxide at end of oxidation (mg × cm^{-2})	Atmosphere composi- tions (v/o)	k_l (sulfidation) (mg × cm^{-2} × min^{-1})
			H_2S-H_2	
1	1000	2.7	0.001	—
2	1000	1.6	0.05	0.01
3	1000	1.6	0.1	0.06
4	900	1.1	0.1	0.09
5	900	0.5	0.2	0.09

summarized in Table II. Figure 4 shows the corresponding weight gain curves, in which time zero is the time at which the sulfidizing mixture was introduced into the reaction cell. Again, after an incubation period which varied with the thickness of the pregrown oxide, sulfidation took place in all cases according to an approximately linear rate law, except for run No. 1 of Table II.

A similar weight gain curve was obtained when the sulfidation stage was carried out using a reacting gas mixture of carbon monoxide bubbled through a sulfur melt held at 175°C. The purpose of this experiment was to observe whether a decrease in oxygen activity in the reacting gas mixture due to a reducing agent other than hydrogen would result in a comparable sulfidation mechanism. Indeed the corresponding weight gain curve, labeled with an asterisk in Fig. 4, followed the same trend as the curves obtained with H_2S-H_2 atmospheres. However, the morphology of the corrosion product was different in this case, as shown in Fig. 5. X-ray and microprobe analysis identified the outer layer of the scale as Cr_3S_4, the dark layer underneath it as a mixture of sulfides and carbides of chromium, and the innermost layer as primarily chromium together with chromium oxide and carbide particles. Saturation of the carrier gas with sulfur was more difficult to accomplish, and the vapor pressure of sulfur in the gas may have been below the nominal value of 10^{-3} atm corresponding to the temperature of the sulfur bath.

Discussion

The equilibrium phases that would be expected at 900°C in the Cr-O-S system are shown in Fig. 6, which is the stability diagram for this system in terms of the chemical potentials of oxygen and sulfur. These chemical potentials are given by $\mu_X = RT \ln p_{X_2}^{1/2}$, where X represents either oxygen or sulfur and p_{X_2} is the equilibrium partial pressure of O_2 or S_2. Data on sulfide stability were obtained from Young *et al.* (9), except for CrS, where an average of data from Young *et al.* with that of Hager and Elliott (10) was used. Data on

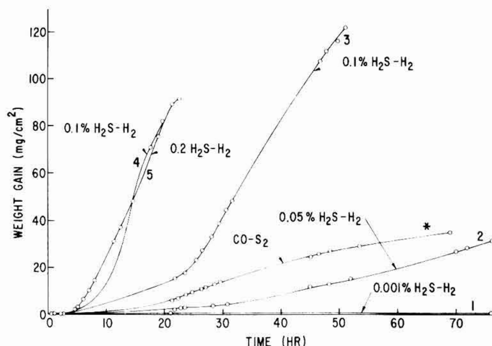

Fig. 4. Weight gain curves of chromium specimens preoxidized and subsequently sulfidized at 900°C with H_2S-H_2 gas mixtures of different composition. The experimental conditions corresponding to the curves labeled with numerals are listed in Table II. The curve labeled with an asterisk corresponds to a sulfidation stage carried out with a CO-S_2 gas mixture.

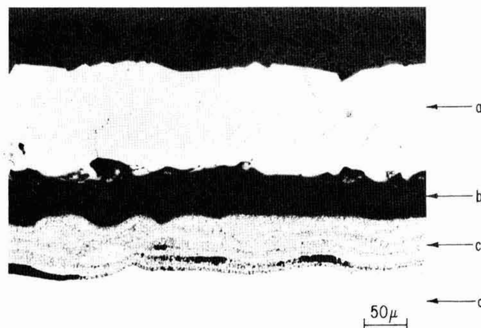

Fig. 5. Scale structure of a chromium specimen preoxidized and exposed at 900°C for about 70 hr to a CO-S_2 gas mixture: a, chromium sulfide (Cr_3S_4); b, mixture of sulfides and carbides of chromium; c, mixture of chromium with some oxides and carbides; d, chromium.

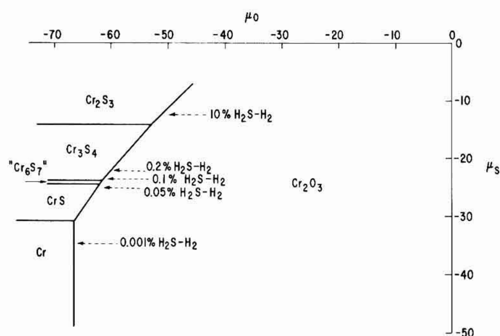

Fig. 6. Stability diagram of the Cr-O-S system at 900°C (μ_O, μ_S in kcal/mole).

oxide stability were taken from Elliott and Gleiser (11). The phase "Cr_6S_7" represents an average of data for the phases Cr_5S_6 and Cr_7S_8 reported by Young *et al.*; the equilibrium S_2 pressures for these two phases in equilibrium with CrS and Cr_3S_4, respectively, are sufficiently close to allow treating them as one phase for the present purpose.

Figure 6 also shows the sulfur potentials corresponding to the various H_2S-H_2 compositions of Tables I and II. It is immediately apparent from this figure that the lowest composition of 0.001% H_2S is thermodynamically incapable of forming any sulfide. Thus run No. 1 of Table II would be expected to show no sulfide formation. All other compositions, however, can lead to sulfide formation at oxygen potentials below that of oxide/sulfide equilibrium. Since sulfide was formed, it can be presumed that the oxygen contents of the sulfidizing atmospheres were sufficiently low to satisfy this condition. Direct measurements of the oxygen potential in the sulfidizing atmospheres employed for the experiments summarized in Table I showed that this requirement was met (5).

Figure 3 shows that the oxide scale remains relatively intact during sulfidation even though Fig. 4 would predict conversion of the oxide to sulfide under any combination of sulfur and oxygen potentials that lead to sulfide formation. Since this conversion does not occur appreciably during the sulfidation time periods employed, it can be concluded that transport of oxygen through the external sulfide layer formed during sulfidation is very slow. Further, the linear growth of the sulfide at a rate which is low compared to direct sulfidation (see Fig. 2) suggests that Cr trans-

port through the oxide layer is the limiting step during sulfidation. Thus a probable "reaction path" for the sulfur and oxygen potentials across the reaction products of a specimen during sulfidation is shown in Fig. 7, which is a simplified version of Fig. 6 that does not distinguish between the various chromium sulfides. Point A represents the gas/external sulfide layer interface, point B the external sulfide layer/oxide layer interface, point C the oxide layer/internal sulfide layer interface, and point D the internal sulfide layer/metal interface. Since the sulfidation rate in the presence of an oxide layer is much less than that of direct sulfidation, the sulfur potential gradient in both sulfide layers has been assumed to be nearly zero. Most of the sulfur potential drop then occurs across the oxide layer as shown in Fig. 7.

The mechanism of Cr transport in Cr_2O_3 has not been determined unambiguously. This oxide is a p-type semiconductor, but its electrical conductivity at relatively high oxygen pressures is nearly independent of oxygen pressure, indicating a lack of any strong reaction between O_2 and electron holes (12). The oxidation rate of Cr metal to Cr_2O_3 is likewise essentially independent of oxygen pressure in a similar pressure range, indicating that while Cr diffusion under such conditions may involve a defect mechanism, the defect concentration is not determined by a defect-O_2 reaction (13). Thus Hauffe and Block have proposed that the principal defects in Cr_2O_3 are Cr vacancies, Cr interstitials, and electron holes, formed in accordance with the equilibrium (12)

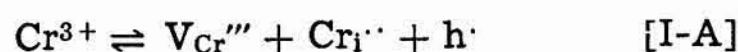

$$Cr^{3+} \rightleftharpoons V_{Cr}''' + Cr_i^{\cdot\cdot} + h^{\cdot} \quad \text{[I-A]}$$

where Cr^{3+} is a normal Cr ion on a cation site, V_{Cr}''' is a triply charged (negative) Cr vacancy, $Cr_i^{\cdot\cdot}$ is a doubly charged (positive) Cr interstitial, and $h^{\cdot}$ is a positively charged electron hole.

Kassner *et al.* studied the oxidation of Cr metal and the tracer diffusion of Cr^{51} in Cr_2O_3 at the low equilibrium oxygen pressures generated by H_2-H_2O mixtures (14). They observed an oxygen partial pressure dependence of the oxidation rate and of the tracer diffusion coefficient which led them to propose that the principal defects in Cr_2O_3 are Cr vacancies and electron holes formed in accordance with the equilibrium

$$1/2\, O_2 \rightleftharpoons O^{--} + 2/3\, V_{Cr}''' + 2h^{\cdot} \quad \text{[I-B]}$$

where O^{--} is a normal O ion on an anion site.

The presence of other cations in Cr_2O_3 would be expected to affect the oxidation rate of Cr metal if these cations were either electron donors or electron acceptors. Reactions [I-A] and [I-B] both indicate that such cations would modify the intrinsic hole concentration and thus Cr diffusivity through changing Cr defect concentration. This effect has been demonstrated

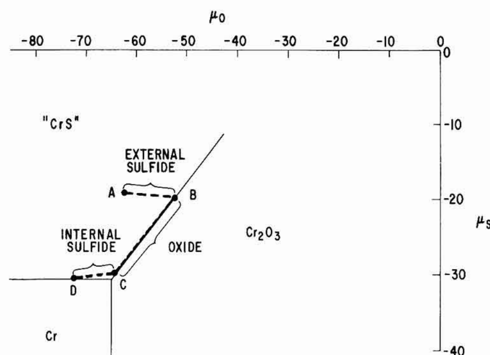

Fig. 7. Schematic reaction path in the Cr-O-S system during sulfidation at 900°C.

as a change in oxidation rate (15). If sulfur were an electron donor in Cr_2O_3, it would likewise be expected to increase the Cr diffusivity in the oxide through decreasing the hole concentration and consequently increasing the Cr defect concentration as either reaction [I-A] or [I-B] are shifted to the right. Konev *et al.* have proposed that sulfur enters NiO as S^- ions rather than S^{--} ions (16). Wagner and his co-workers have also suggested that S^- ions may be the form in which sulfur generally enters into solution in most oxides (4). The sulfur could act as an electron donor according to the equilibrium

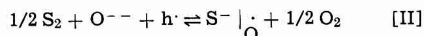

$$1/2\, S_2 + O^{--} + h^{\cdot} \rightleftharpoons S^- |_O^{\cdot} + 1/2\, O_2 \quad \text{[II]}$$

where $S^- |_O^{\cdot}$ is a singly ionized sulfur ion on an anion site, and is thus a singly charged (positive) defect with respect to the anion lattice.

The equilibrium constants for reactions [I-A], [I-B], and [II] can be expressed in terms of x_V, x_i, x_h, and x_S which are, respectively, the mole fractions of Cr vacancies, Cr interstitials, electron holes, and singly ionized sulfur ions on anion sites. These equilibrium constants will also involve the oxygen and sulfur activities, which are defined as $a_O = p_{O_2}{}^{1/2}$ and $a_S = p_{S_2}{}^{1/2}$. It can be noted that the chemical potentials are then given by $\mu_X = RT \ln a_X$, where X represents either oxygen or sulfur, allowing the activities corresponding to specific phase equilibria to be obtained from Fig. 6.

From reaction [II], the value of x_S is obtained as $x_S = K_{II}(a_S/a_O)x_h$, where K_{II} is the equilibrium constant for reaction [II]. We will assume that in the H_2-H_2S gas mixtures considered in the following analysis that the oxygen activity is sufficiently low to cause $K_{II}(a_S/a_O)$ to be much greater than unity. The vacancy concentrations corresponding to reactions [I-A] and [I-B] can then be obtained as

$$x_V = K(a_S{}^{1/3}/a_O{}^{1/3}) \quad \text{[1-a]}$$

and

$$x_V = K(a_S{}^{3/4}/a_O{}^{3/8}) \quad \text{[1-b]}$$

where K in each instance represents some combination of the equilibrium constants $K_{I\text{-}A}$ and K_{II} or $K_{I\text{-}B}$ and K_{II}. If reaction [I-A] is assumed to take place, then $x_i = x_V$ and Cr transport could occur either through interstitial or vacancy defects. Whether reaction [I-A] or [I-B] is assumed to prevail, however, a Cr defect concentration gradient could exist across the sulfur-containing Cr_2O_3 layer during sulfidation to act as a driving force for Cr transport through this layer.

The sulfur and oxygen activities on each side of the Cr_2O_3 layer during sulfidation of any specimen used in the present work can be obtained from Fig. 6, assuming that a reaction path such as that shown schematically in Fig. 7 applies to the sulfidation process. A general form of Eq. [1-a] or [1-b] is

$$x_D = K(a_S{}^f/a_O{}^g) \quad \text{[2]}$$

where x_D is the Cr defect concentration, whether vacancies or interstitials. The outward molar flux of Cr through the Cr_2O_3 layer is then given by the proportionality relationship

$$\Gamma_{Cr} \propto (x_{D,B} - x_{D,C})/m \quad \text{[3]}$$

where Γ_{Cr} is the Cr flux, m is the mass per unit area of the oxide layer, and the subscripts B and C refer to the external sulfide/oxide interface and the oxide/internal sulfide interface, respectively (cf. Fig. 7). Assuming that the linear sulfidation is due primarily to the formation of the external sulfide layer of composition Cr_xS_y, the linear rate constant for sulfidation is given by the proportionality relationship

$$k_l \propto ((y/x)/m)\phi \quad \text{[4]}$$

where the factor ϕ is defined as

$$\phi = (a_{S,B}/a_{S,C})^f (a_{O,C}/a_{O,B})^g - 1 \quad [5]$$

Since k_l, the ratio y/x, and m are experimentally accessible, they can be consolidated into a single parameter, using Eq. [4], defined by

$$k = (x/y) m k_l \quad [6]$$

Thus the value of k should be proportional to ϕ for any run, or the value of k/ϕ should be constant for all runs in which sulfide was formed at a single temperature of 900°C. The ratio k/ϕ was calculated for each of the runs of Tables I and II. Values for $a_{S,C}$ and $a_{O,C}$ were taken as those corresponding to the $Cr/CrS/Cr_2O_3$ equilibrium of Fig. 6, and remain the same for all runs. Values for $a_{S,B}$ and $a_{O,B}$ as well as for x and y were those corresponding to the appropriate Cr_xS_y/Cr_2O_3 equilibrium of Fig. 6 at the sulfur potential level indicated by the dashed line for each H_2-H_2S composition. Since the absolute magnitude of the ratio k/ϕ has no significance, the value of the ratio was normalized using the average values obtained in arbitrary units of each set of runs treated. Three pairs of values of the exponents f and g were used: $f = 0$ and $g = 0$; $f = 1/3$ and $g = 1/3$; $f = 3/4$ and $g = 3/8$. These represent, respectively, an absence of any influence of sulfur or oxygen on Cr defect concentration, a Cr defect concentration established according to Eq. [1-a], and a Cr defect concentration governed by Eq. [1-b].

Table III summarizes the normalized k/ϕ ratios obtained for each pair of exponents. Averages and variances are also presented. Since the average must be unity for the normalized k/ϕ ratio, the variances are direct indications of how well the three assumed models for the influence of sulfur on Cr diffusivity fit the experimental observations. Either of the models involving the presence of sulfur as an electron donor gives a better fit than the assumption of no interaction between sulfur and Cr defects. It is thus proposed that sulfur enters Cr_2O_3 as an electron donor, thereby reducing the electron hole concentration. This reduction leads to an increase in Cr defect concentration through reactions similar to [I-A] or [I-B]. Such a general model can be qualitative only at present, but it is suggested that a parameter containing an equilibrium constant and both sulfur and oxygen activities, in the form given by Eq. [2], describes the effect of sulfur on the Cr defect composition.

An enhanced Cr diffusivity in Cr_2O_3 due to the presence of sulfur could be either a grain boundary or volume effect. It is not possible to distinguish between these two types of mechanism at this time. Factors which may contribute variations in linear sulfidation rate are deviations from the nominal gas compositions, differences in Cr_2O_3 layer grain size as a result of different oxidation temperatures, and partial disruption of the Cr_2O_3 layer during sulfidation. Thus no more detailed analysis of the data appears warranted.

The single test undertaken with a CO-S_2 mixture (Fig. 4) was performed to show that the observed enhancement of Cr transport through Cr_2O_3 during sulfidation was not uniquely dependent on the use of H_2 to achieve the low oxygen potentials that thermodynamically allow sulfide formation. Figure 5 indicates that the Cr_2O_3 layer was at least partially converted to one or more Cr carbides during this run. While not conclusively demonstrating that neither hydrogen nor carbon is affecting defect equilibria, the result shows that hydrogen is not unique and that the sulfur itself is most probably responsible for the enhanced diffusivity of Cr in Cr_2O_3 exposed to sulfur at low oxygen potentials. Since the reaction products of the specimen were not the same as those of other tests, no attempt was made to treat this test quantitatively.

Table III. Values of ratio of sulfidation parameter defined by Eq. [6] to sulfur and oxygen activity function defined by Eq. [5]. The designation of each run corresponds to numbering in Tables I and II.

Run	$(k/\phi)/(\overline{k/\phi})$		
	$f = 0$, $g = 0$	$f = 1/3$, $g = 1/3$	$f = 3/4$, $g = 3/8$
I-1	1.44	1.32	0.59
I-2	2.52	2.30	1.03
I-3	1.66	1.50	0.68
II-2	0.12	0.20	0.61
II-3	0.52	0.70	1.75
II-4	0.53	0.70	1.80
II-5	0.25	0.29	0.57
Average	1.00	1.00	1.00
Variance	± 0.89	± 0.75	± 0.55

Conclusions

Exposure of preoxidized Cr to an ambient atmosphere of sufficiently high sulfur potential and low oxygen potential results in the linear growth of Cr sulfide on both sides of the Cr_2O_3 layer formed during oxidation. Most of the sulfide growth takes place in the external sulfide layer by transport of Cr through the relatively intact Cr_2O_3 layer which is metastable as a result of limited oxygen transport through Cr sulfides. The sulfidation rate in this situation reflects a much higher Cr diffusivity in the Cr_2O_3 than would be expected in the absence of sulfur. A model for the defect equilibria in Cr_2O_3 exposed to sulfur can be formulated, in which sulfur enters the oxide as an electron donor, thereby increasing the concentration of Cr defects.

Acknowledgment

The technical support of the Materials Characterization Operation staff of the General Electric Research and Development Center is gratefully acknowledged.

Manuscript submitted July 22, 1974; revised manuscript received April 22, 1975. This was Paper 184 presented at the San Francisco, California, Meeting of the Society, May 12-17, 1974.

Any discussion of this paper will appear in a Discussion Section to be published in the June 1976 JOURNAL. All discussions for the June 1976 Discussion Section should be submitted by Feb. 1, 1976.

Publication costs of this article were partially assisted by General Electric Company.

REFERENCES

1. J. A. Goebel, F. S. Pettit, and G. W. Goward, *Met. Trans.*, **4**, 261 (1973).
2. D. W. McKee and G. Romeo, *ibid.*, **4**, 1877 (1973).
3. A. U. Seybolt, *Trans. Met. Soc. AIME*, **242**, 752 (1968).
4. D. R. Chang, R. Nemoto, and J. B. Wagner, Jr., *Met. Trans.*, In press.
5. G. Romeo and H. S. Spacil, in "High Temperature Gas-Metal Reactions in Mixed Environments," S. A. Jansson and Z. A. Foroulis, Editors, p. 299, *TMS-AIME* (1973).
6. G. Romeo, W. W. Smeltzer, and J. S. Kirkaldy, *This Journal*, **118**, 740 (1971).
7. JANAF Thermochemical Tables, Second Edition, D. R. Stull and H. Prophet, Editors, Nat. Bur. of Standards, Washington, D.C. (1971).
8. K. N. Strafford and A. F. Hampton, *J. Less Common Metals*, **21**, 305 (1970).
9. D. J. Young, W. W. Smeltzer, and J. S. Kirkaldy, *This Journal*, **120**, 1121 (1973).
10. J. P. Hager and J. F. Elliott, *Trans. AIME*, **239**, 513 (1967).
11. "Thermochemistry for Steelmaking," Vol. 1, J. F. Elliott and M. Gleiser, Editors, Addison-Wesley Publishing Co., Reading, Mass. (1960).
12. K. Hauffe and J. Block, *Z. Phys. Chem.*, **198**, 232 (1951).
13. W. C. Hagel, *Trans. ASM*, **56**, 583 (1963).
14. T. F. Kassner, L. C. Walters, and R. E. Grace, in "Thermodynamics," Proc. Symposium on Thermodynamics, Vol. II, organized by IAEC/IUPAC, p. 357, IAEC (1966).
15. C. S. Tedmon, Jr. and W. C. Hagel, *This Journal*, **115**, 147 (1968).
16. V. N. Konev, V. N. Cherbotin, N. V. Suntsov, and L. I. Startseva, *Zashchita Metal.*, **6**, 448 (1970), available as Consultants Bureau Translation UDC 620.193.5 (1970).

The Deposition of Tin Oxide Films from a D-C Glow Discharge

D. E. Carlson

RCA Laboratories, Princeton, New Jersey 08540

ABSTRACT

Tin oxide films have been deposited on soda-lime-silicate glass using a d-c glow discharge in atmospheres of $Sn(CH_3)_4$ and O_2, and $SnCl_4$ and O_2. The sodium ions were removed from the surface of the glass during the film deposition by forcing the current to pass through the heated glass substrates. Film properties were studied as a function of atmospheric composition, current density, and deposition time.

Many investigators (1-12) have reported the deposition of thin films on various substrates using a-c and d-c glow discharges in appropriate gases or vapors (typically at a pressure of 0.1-10 Torr). The glow discharge breaks chemical bonds and promotes complex reactions in the gas or gas mixture, and the films result from the deposition of certain reactive components on substrates in the vicinity of the discharge.

Most of the published work involves films deposited on substrates placed in rf or microwave glow discharges. This technique has been used to produce films of organic polymers (2, 3), silicon oxides (4, 5), silicon nitride (5, 6), aluminum oxide (7), amorphous silicon (8, 9), etc. (9, 10). The substrate may or may not be heated depending on the type of film desired.

Much less work (11, 12) has been reported on the deposition of films from a d-c glow discharge. The scarcity of work in this area has been attributed to poor reproducibility of film composition and contamination of the film due to sputtering effects (1, 4). However, the present study shows that good quality tin oxide films can be produced on the cathode in a d-c discharge and that the sputtering action of the discharge can be controlled. Moreover, the d-c technique is simple in practice and readily allows the uniform deposition of thin films over large areas. An additional benefit is gained in the deposition of films on glass substrates since the glass surface will be either ion-depleted (13, 14) or proton-exchanged (15) during the deposition. In either case, the removal of alkali ions from the glass surface allows high quality films to be deposited (14).

Experimental Procedure

The apparatus used in the present study is depicted schematically in Fig. 1. The major components of the system were a vacuum bell jar, a mechanical vacuum pump, and a high voltage d-c power supply (5 kV, 5A). A heating plate was located in the center of the bell jar on a thin-walled, fused silica pedestal. Power for the heater was provided by coupling through an isolation transformer to a variable auto-transformer.

For glass substrates, the bottom was first painted with a conductive coating such as Ag or graphite so that at elevated temperatures the current passed through the glass. The substrate to be coated was then placed on the heating plate with the negative lead (0.005 in. Pt wire) from the power supply in electrical contact with the bottom of the substrate. That part of the negative lead not under the substrate was electrically shielded with a fused silica tube.

The anode was a metal sheet (usually Pt) placed ~2 cm above the substrate. The ceramic spacers that held the anode were several cm to either side of the substrate so that they were outside of most of the glow discharge region. A limiting resistor (10^5 ohm, 100W) was used to stabilize the discharge. The current was monitored by measuring the voltage drop across a 10^3 ohm resistor.

The system was evacuated to a pressure of ~5 mTorr with the substrate hot (200°-550°C) before any gases or vapors were admitted. The procedure for admitting vapors such as tetramethyltin ($Sn(CH_3)_4$) was to freeze a vial of $Sn(CH_3)_4$ in liquid nitrogen while pumping on it. Once a pressure of ~5 mTorr was attained, the sample was warmed until the desired vapor pressure was achieved. The appropriate gases or vapors were sequentially bled into the system, and the pressure during each admission was monitored with a thermocouple vacuum gauge. Since the thermocouple gauge was calibrated for air, a McLeod vacuum gauge was used to measure the pressure after each admission. The total pressure was in the range of 0.5-2.0 Torr for most of the film depositions.

The minimum voltage for deposition of uniform films was determined by adjusting the applied voltage so that the negative glow of the discharge covered the entire cathode substrate. This is the beginning of the regime for the abnormal fall of potential near the cathode (16). Operating at this voltage assures a uniform deposition while minimizing sputtering effects. Increasing the voltage beyond this value will increase the deposition rate, but eventually sputtering effects will decrease the rate and may even prevent film deposition. Normally, a constant current density was maintained during the film deposition. The applied voltage had to be increased during the deposition when a glass substrate was used. (As the depleted region in the glass increased in thickness, the resistance increased.)

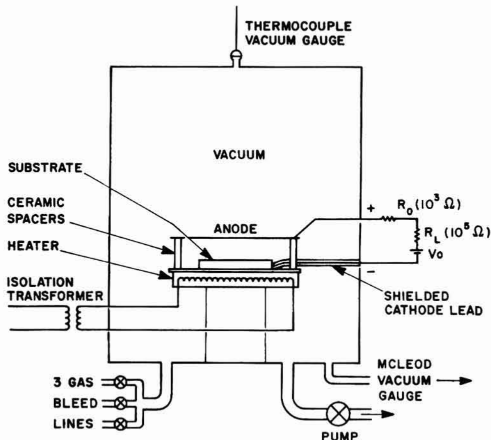

Fig. 1. Schematic diagram of the apparatus used for film deposition from a d-c glow discharge.

Key words: glass, semiconductor, ion-depletion.

The films could be deposited in patterns by using either insulating or conducting masks. Insulating masks perturbed the field distribution in the discharge and generated borders that were not sharp, *i.e.*, the film thickness increased gradually up to a distance of a few mm from the edge of the mask. Conducting masks did not affect the field distribution, and the film edges were sharp to within a few microns. When glass substrates were used, Na was removed from the glass surface beneath both the depositing film and the conducting mask.

Since the edges of the cathode substrates were high field regions, the film thickness varied near the edges. Uniform deposition over the entire substrate was achieved by placing another cathode material around the edges of the substrate. This effectively moved the high field regions of the cathode out beyond the edges of the substrate. For uniform deposition, the total pressure was maintained at $\lesssim 1$ Torr since the discharge tended to localize at higher pressures.

The thickness of various films was measured with a stylus profilometer (Bendix Linear Pilotor, Type RLC). The surface resistivity was measured with an RCA VoltOhmyst or a Keithley Electrometer (Model 610C) after painting parallel stripes on the surface of the film with air-drying Ag paint. The transmission of visible light was measured with a Cary spectrophotometer (Model 14R).

Results and Discussion

Tin oxide films were deposited on soda-lime-silicate glass[1] substrates using d-c glow discharges in vapors of $Sn(CH_3)_4$ and oxygen, and in vapors of $SnCl_4$ and O_2. The inclusion of the glass substrate in the electrical circuit caused the glass surface to be either ion-depleted (13, 14) (for a discharge in $SnCl_4$ and O_2) or proton-exchanged (15) (for a discharge in $Sn(CH_3)_4$ and O_2) during the film deposition. The Na ions were typically removed from the glass surface to a depth of ~2000Å. The removal of Na ions from the glass surface during the deposition gave rise to sodium-free films with excellent optical and electrical properties. Moreover, the Na-depleted region is little affected by thermal treatment below the transformation temperature of the glass (~510°C), so the films should remain Na free during any subsequent thermal processing below this temperature. (The thermal stability of the ion-depleted region is due to the removal of the nonbridging oxygen ions (13) during the film deposition.)

Figure 2 shows how the volume resistivity of films deposited in a discharge of $Sn(CH_3)_4$ and O_2 depended on the composition of the atmosphere. The current density and treatment time were held constant, and the thickness of the films increased as the ratio of $Sn(CH_3)_4$ to O_2 was increased (from 350Å at a ratio of 0.10 to 1250Å at a ratio of 0.23). When the ratio of $Sn(CH_3)_4$ to O_2 was small ($\lesssim 0.10$), the films were fairly resistive ($\rho > 10^{-2}$ ohm-cm). When the ratio of $Sn(CH_3)_4$ to O_2 was large (~0.23), the films were also resistive and acquired a yellowish coloration and became less scratch-resistant. The coloration is probably due to an oxygen deficiency in the films; only ~0.2 atomic per cent (a/o) of C was found in these colored films. When the optimum ratio was selected, films with resistivities of $\sim 3 \times 10^{-3}$ ohm-cm were obtained; these films had a surface resistivity of ~400 ohm/□ (~750Å thick) and an average light transmission as compared to uncoated glass of ~87% (over the wavelength range of 3500-6500Å). Approximately 0.5 a/o of C was present in the most conductive films.

These films were relatively insensitive to thermal cycling and exhibited only 10-20% reduction in conductivity after baking for 24 hr at 400°C in air. (Baking for 1 hr at 550°C caused a decrease of 50%.) If the conduction were due only to donor states arising from

[1] Approximate composition by weight per cent (w/o): 73 w/o SiO_2; 13.5 w/o Na_2O; 9 w/o CaO; 4 w/o MgO; 0.2 w/o Al_2O_3.

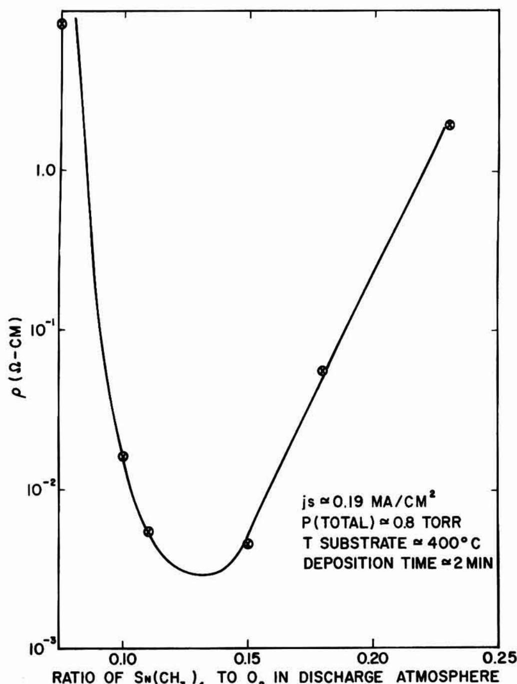

Fig. 2. Volume resistivity of tin oxide films as a function of the ratio of $Sn(CH_3)_4$ to O_2 in the discharge atmosphere.

oxygen vacancies, the resistivity should have increased by more than an order of magnitude (17,18). One possibility is that donor levels are created by the presence of OH groups in the tin oxide structure. The glow discharge is expected to produce OH groups because of the large number of hydrogen atoms per $Sn(CH_3)_4$ molecule and the large per cent of O_2 in the initial discharge atmosphere (~88% O_2).

Figure 3 shows how the film thickness and the surface resistivity varied with time for a discharge in $Sn(CH_3)_4$ and O_2. The deposition rate was ~1200 Å/min for the first 15 sec and slowed to ~225 Å/min after 1 min. The average volume resistivity decreased from $\sim 4 \times 10^{-2}$ ohm-cm at 15 sec to $\sim 10^{-2}$ ohm-cm at 4 min. The composition or stoichiometry of the film varied with thickness since the percentage of Sn in the discharge atmosphere decreased with time.

Figure 4 shows how the surface resistivity of films formed from a discharge in $Sn(CH_3)_4$ and O_2 varied with current density. For low current densities, the deposition rate increased as the current density increased. As the current density (or cathode fall potential) became larger, the deposition rate decreased due to the influence of sputtering. At large current densities ($\gtrsim 1.0$ mA/cm^2), film deposition did not occur and the glass surface was slowly sputter etched.

Tin oxide films were deposited on glass substrates at temperatures as low as 200°C using a d-c glow discharge in $Sn(CH_3)_4$ and O_2. These films can be deposited at temperatures much lower than with chemical vapor deposition (CVD) ($\gtrsim 375$°C) (17) because the discharge dissociates the molecules and drives the positive ions to the substrate with appreciable kinetic energies (~10-100 eV depending on the deposition parameters). Thus, the positive ions arriving at the substrate are on the order of 10^3 times "hotter" than the substrate.

The average light transmission and volume resistivity of the best films deposited at 250°C were com-

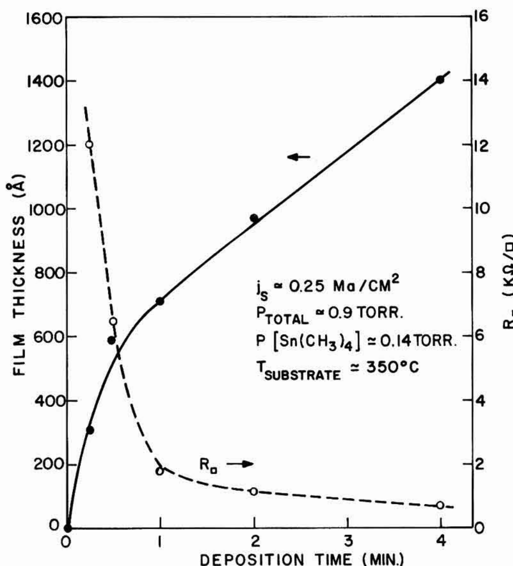

Fig. 3. Thickness and surface resistivity of tin oxide films as a function of deposition time.

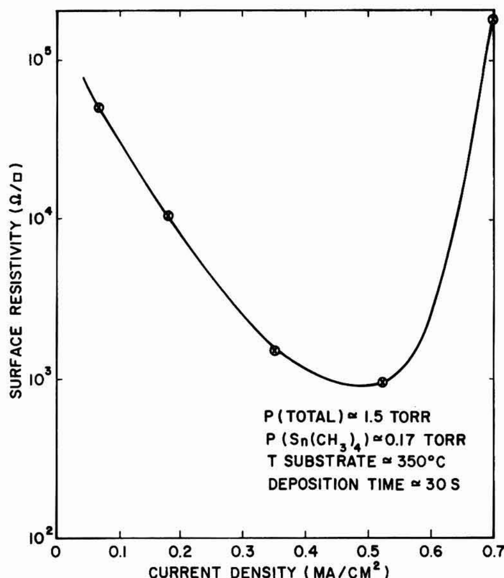

Fig. 4. Surface resistivity of tin oxide films as a function of current density.

parable to those deposited at 400°C. However, the films deposited at lower temperatures appeared to be slightly less scratch-resistant.

As the deposition temperature was reduced, the highest conductivity films were produced at decreasing ratios of $Sn(CH_3)_4$ to O_2. For example, at a deposition temperature of 400°C, the ratio was ~0.13 (Fig. 2), while at 250°C the ratio was ~0.04. A larger ratio was probably necessary at higher temperatures to compensate for the thermal decomposition of some of the $Sn(CH_3)_4$ in the vicinity of the heater coils.

By admitting $SbCl_5$ to an atmosphere of $Sn(CH_3)_4$ and O_2, films with volume resistivities as low as 1.7 $\times 10^{-3}$ ohm-cm were produced. The variation of volume resistivity with varying amounts of $SbCl_5$ in the atmosphere is shown in Fig. 5. Mass spectrometry (solids) showed that the most conductive film contained ~0.33 a/o of Cl and less than 0.06 a/o of Sb. The average light transmission for this film was ~90%.

SnO_2 films were also made from glow discharges in $SnCl_4$ and O_2. For depositions at 400°C, a current density of ~0.2-0.5 mA/cm² was applied for 2 min. The ratio of $SnCl_4$ to O_2 was typically 0.3-0.5 ($P_{total} \simeq 0.8$ Torr) and was not as critical as in the case of $Sn(CH_3)_4$ and O_2 (Fig. 2).

The most conductive films made from a discharge in $SnCl_4$ and O_2 had a resistivity of $\sim 1.5 \times 10^{-3}$ ohm-cm. These films only showed a 20-40% increase in resistivity after baking for 24 hr at 400°C in air. (Baking for 1 hr at 550°C caused a 70% increase.) The doping must be caused mainly by substitutional incorporation of chlorine (18, 19) since mass spectrometry (solids) showed that the films contained ~1 a/o of Cl. However films that are halogen-doped during spray deposition do not usually show the stability to thermal cycling in air that the discharge-produced films do. For example, films formed by spraying solutions of stannic bromide on hot fused silica showed an order of magnitude increase in resistivity after baking in air for 24 hr at 400°C (20). Films made by spraying stannic chloride solutions on hot glass show similar thermal degradation in air. The films produced by a d-c glow discharge may be more dense than those produced by spraying, and thus halogen diffusion may be reduced in the discharge-produced films.

Electron diffraction by reflection has shown that discharge-produced films have a crystallite grain size less than 100Å for deposition temperatures below ~400°C. The grain size was slightly larger in films produced from discharges in $SnCl_4$ and O_2 than those from $Sn(CH_3)_4$ and O_2 for the same deposition temperature.

In conclusion, the present study shows that a d-c glow discharge in the appropriate atmosphere can be

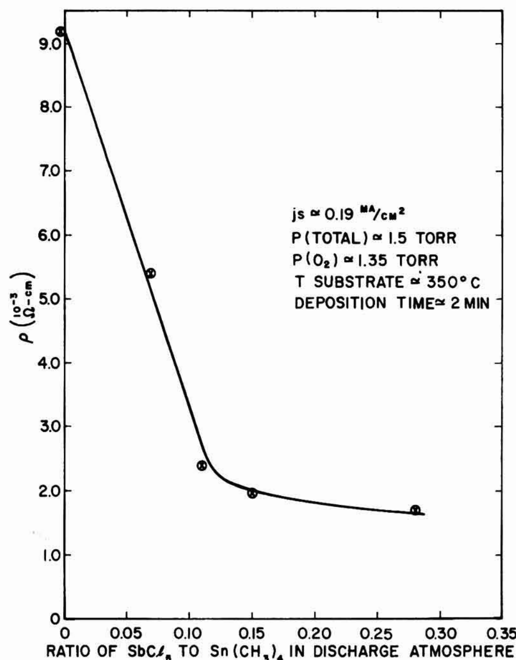

Fig. 5. Volume resistivity of doped tin oxide films as a function of the ratio of $SbCl_5$ to $Sn(CH_3)_4$ in the discharge atmosphere.

used to deposit good quality, tin oxide films on the surface of a soda-lime-silicate glass.

Acknowledgments

The author thanks P. J. Zanzucchi for making the optical transmission measurements and E. M. Botnick for providing the mass spectrometry (solids) data.

Manuscript received Feb. 6, 1975; revised manuscript received June 12, 1975.

Any discussion of this paper will appear in a Discussion Section to be published in the June 1976 JOURNAL. All discussions for the June 1976 Discussion Section should be submitted by Feb. 1, 1976.

Publication costs of this article were partially assisted by RCA Laboratories.

REFERENCES

1. A. M. Mearns, *Thin Solid Films,* **3,** 201 (1969).
2. J. Goodman, *J. Polymer Sci.,* **44,** 551 (1960).
3. F. J. Vastola and J. P. Wightman, *J. Appl. Chem.,* **14,** 69 (1964).
4. L. L. Alt, S. W. Ing, Jr., and J. H. Alexander, *This Journal,* **110,** 465 (1963).
5. R. J. Joyce, H. F. Sterling, and J. H. Alexander, *Thin Solid Films,* **1,** 481 (1967/1968).
6. R. C. G. Swann. R. R. Mehta, and T. P. Cange, *This Journal,* **114,** 713 (1967).
7. H. Katto and Y. Koga, *ibid.,* **118,** 1619 (1971).
8. H. F. Sterling, J. H. Alexander, and R. J. Joyce, *Le Vide,* p. 80 (1966).
9. H. F. Sterling and R. C. G. Swann, U. S. Pat. 3,655,438 (1972).
10. J. Goodman, U. S. Pat. 3,239,368 (1966).
11. H. Pagnia, *Phys. Status Solidi,* **1,** 90 (1961).
12. B. G. Carbajal III, *Trans. Met. Soc. AIME,* **236,** 364 (1966).
13. D. E. Carlson, *J. Am. Ceram. Soc.,* **57,** 291 (1974).
14. D. E. Carlson, K. W. Hang, and G. F. Stockdale, *ibid.,* **57,** 295 (1974).
15. D. E. Carlson, *ibid.,* **57,** 461 (1974).
16. F. M. Penning, "Electrical Discharges in Gases," The Macmillan Co., New York (1957).
17. J. Kane, H. P. Schweizer, and W. Kern, Paper 15 RNP presented at Electrochemical Society Meeting, San Francisco, California, May 12-17, 1974.
18. C. A. Vincent, *This Journal,* **119,** 515 (1972).
19. J. A. Aboaf and V. C. Marcotte, *ibid.,* **120,** 701 (1973).
20. H. Kim and H. Laitinen, presented at 76th Annual Meeting of the American Ceramic Society, 1974; *Am. Ceram. Soc. Bulletin,* **53,** 342 (1974).

Microstructural and Electrical Properties of Thin PtSi Films and Their Relationships to Deposition Parameters

R. M. Anderson and T. M. Reith

IBM System Products Division, East Fishkill Facility, Hopewell Junction, New York 12533

ABSTRACT

The intimate relationships among the microstructure, electrical characteristics, and deposition parameters of thin PtSi films deposited on {001}, {011}, and {111} Si wafers are discussed. PtSi morphology and crystallinity fall into several distinct categories, according to substrate surface preparation, deposition conditions, heat-treatment, and electrical performance. *In situ* sputter cleaning before PtSi deposition and formation gives better films. Also, the microstructure and sheet resistance of PtSi are strongly affected when deposition and formation are followed by heat-treatment at temperatures from 400° to 950°C.

PtSi films have recently been the subject of much investigation because of their usefulness in forming near-ideal ohmic and Schottky contacts to both n- and p-type Si (1, 2). The crystallography and morphology of PtSi films have received considerable attention (3-8), as have the kinetics of their formation (9-12). This paper discusses the intimate interrelations of the microstructure of thin PtSi films, their electrical properties, and their dependence on deposition conditions.

Experimental

Preparation of samples.—In the present study we have examined both sputter- and e-beam-deposited PtSi films, although we have concentrated on the former. For the sputter-deposited films, an oil diffusion-pumped vacuum system with a Pt target 30 cm in diameter was used. It had provisions for *in situ* rf sputter cleaning and d-c sputtering of Pt. A Pt-coated stainless steel substrate holder resting on a Cu block with an embedded heating element enabled us to heat the wafers to 450°C before, during, or after Pt deposition (Fig. 1). The *in situ* sputter cleaning, when performed and unless otherwise indicated, was for 2 min at an rf power of 100W and an Ar pressure of 10 mTorr. Figure 2 shows the amounts of Si and SiO_2 removed as a function of time and rf power. The curves were obtained by sputter etching bare and thermally oxidized 3.2 cm Si wafers, which were partially masked with chromium to create a step in the surface. The step height was subsequently measured by use of a Talystep apparatus.

Extrapolation of the appropriate curves indicates that, for 2 min at 100W of rf power, about 75Å of SiO_2 and 175Å of Si are removed. The Pt was d-c sputter deposited with a 2 kV potential applied to the target and at 40-50 mTorr of Ar pressure unless otherwise noted. Various heat-treatments were used to form the PtSi, either *in situ* or externally in dry, flowing N_2. After PtSi formation, any unreacted Pt was removed in aqua regia at 60°-65°C. An oil diffusion-pumped vacuum system with a 180° four-pocket Cu-hearth e-beam source was used for the evaporated PtSi films. The pressure in the deposition system was $1\text{-}5 \times 10^{-6}$ Torr during all evaporations. A spiral-wound tungsten wire heater was used to heat the substrates to ~300°C during deposition. The PtSi was formed externally in dry N_2, and unreacted Pt was stripped in aqua regia.

Key words: electron microscopy, platinum-silicon, electrical measurements.

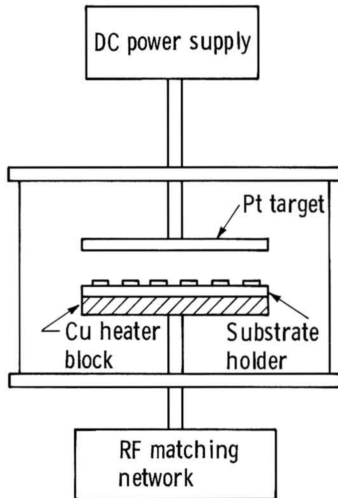

Fig. 1. Pt sputtering system

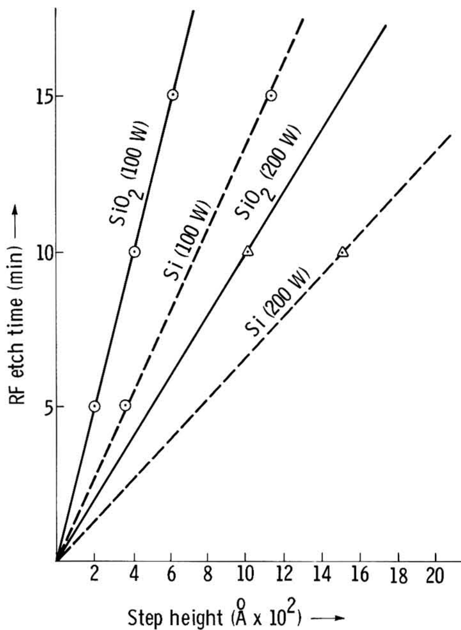

Fig. 2. RF etch time

To examine the dependence of PtSi microstructure on the dopant level and species of the Si on which it is formed, and the stability of the compound as a function of high heat-treatment temperature, 500Å of Pt was sputter deposited on the entire surface of several 3.2-cm Si wafers that had been diffused with either boron or arsenic to various dopant concentrations. After the wafers were cleaned by rf sputtering, the Pt was d-c sputter deposited as described previously. The substrates were heated to 450°C during the Pt deposition to form PtSi *in situ*. Any unreacted Pt that may have been present was removed in hot aqua regia. The sheet resistance of films was measured as a function of dopant and anneal by use of an in-line four-point probe apparatus. No attempt was made to convert the measurements into resistivity units, because there was some uncertainty about the total thickness of the PtSi. As before, all heat-treatments subsequent to the *in situ* PtSi formation at 450°C were done in dry, flowing N_2. The resulting microstructures were then examined by transmission electron microscopy (TEM).

To examine the effects of *in situ* rf sputter cleaning, bare 10-20 ohm-cm As-doped Si wafers, 3.2 cm in diameter, were sputter etched for 5 min at 100 and 500W of rf power. These specimens were analyzed by transmission electron microscopy, reflection electron diffraction (RED), low-angle-Laue, Berg-Barrett surface topography, and electron microprobe methods to determine whether any microstructural changes could be induced on the Si surfaces as a result of the *in situ* sputter cleaning. Also, some of the device structures described earlier were sputter cleaned for 15 min at rf power levels of 100 and 200W and examined by scanning electron microscopy (SEM) and electron microprobe analysis to determine whether SiO_2 can be back sputtered from the areas surrounding the opened contacts onto the exposed Si in these contacts by the sputter-cleaning operation. All sputter cleaning performed was either of longer duration or at higher power than would normally be used and hence represented an extreme condition.

Electrical testing procedure.—By use of the test structure shown in Fig. 3, the specific contact resistance of the various PtSi-Si contacts formed was measured. Since the only point in common between the current and voltage loops is the PtSi-Si contact, the measured voltage drop is that which occurs across the PtSi-Si interface, if spreading resistances are neglected. The test structures were defined by standard photolithographic methods. To simulate a typical "base" contact, boron was diffused into 10-20 ohm-cm phosphorus-doped <001> Si wafers. After reoxidation, the measured junction depth was about 0.5 μm, and the surface concentration was 2.4×10^{19} atoms/cm³. To simulate a typical "emitter" contact, slightly smaller cuts were opened photolithographically on half the devices through the reoxidized SiO_2 above the "bases" and an arsenic diffusion was done. After reoxidation, the junction depth was approximately 0.25 μm, and the surface concentration was 1.1×10^{21} atoms/cm³. To complete the structures, contact holes 0.05 mm in diameter were etched to expose the doped Si surfaces. After PtSi deposition and formation, 1000Å of Cr and 10,000Å of

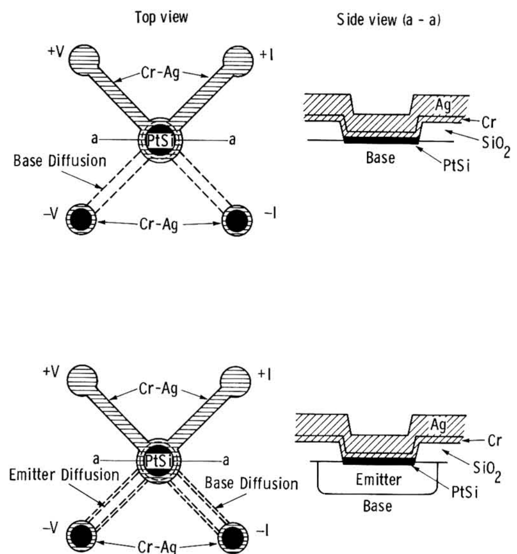

Fig. 3. Electrical test structure

Ag were evaporated through a molybdenum mask 0.1 mm thick to facilitate electrical probing. Unlike Al, Cr (13, 14) will not react with PtSi until temperatures well above those typically encountered in semiconductor device processing are reached. This fact was confirmed by four-point probe resistivity measurements and particle backscattering analysis. All measurements of contact resistance were made with a constant-current source and a digital voltmeter. Finally, HCl was used to stripe the Cr-Ag metallization to expose the electrically characterized PtSi contacts for subsequent TEM analysis.

Transmission electron microscopy specimen preparation.—The electrically characterized wafers were scribed and broken up into specimens, each containing one device, of a size that would fit the specimen holder of the JEM 200A electron microscope. After appropriate masking, the Si was thinned from the backside of the specimen down to the intermetallic film in a mixture of $HF\text{-}HNO_3\text{-}CH_3COOH$ (1:2:3). Specimens were thinned further, as required, in a Commonwealth ion milling machine.

Results

Microstructure vs. electrical properties.—At this point it would be well to stop and look at what "good" and "bad" PtSi microstructures are like. As we have learned, the key to "good" and "bad" microstructures lies in the cleanliness of the Si surface before Pt deposition. Pt deposited on a clean Si surface will begin to form a satisfactory PtSi film during deposition or subsequent heat-treatments, even without substrate heating. Unreacted Pt on Si films are due primarily to the presence of a contamination layer between the Pt and the Si which prevents the formation of PtSi, even after extensive heat-treatments. Quite often, especially with thin (<150Å) initial Pt depositions, the as-deposited Pt films are not fully coalesced and do not become so after subsequent heat-treatment. Selected area electron diffraction (SAD) of thin, poor Pt on Si films shows randomly oriented Pt diffraction rings superimposed on Si reflections. Subsequent heat-treatment brings no change; the Pt has not reacted with the Si, and the SAD patterns still show Pt rings and Si substrate spots.

For thicker initial Pt depositions on randomly and unintentionally contaminated Si, the as-deposited Pt films still do not fully coalesce. After heat-treatment these films undergo simultaneous grain growth and void enlargement, producing lacelike Pt films on Si. Whenever the initial Pt deposition fails to show a preferred orientation to the Si wafer, the microstructure observed after heat-treatment is poor, and no PtSi phase forms. Where the contamination film is itself incomplete, allowing islands of more or less continuous PtSi to form, the stress evolved as the PtSi phase shrinks during formation dissipates itself through void enlargement. One obvious observed consequence of the failure to form PtSi over contaminated Si is that when the aqua regia etch for unreacted Pt is applied, the film disappears. Where PtSi forms in islands, the unreacted Pt over contaminated Si is etched away. Any subsequent metallurgy forms a "capacitor," with the contaminant film as a very leaky "dielectric." Moreover, the metallurgy contacts the Si because of the circular channel of bare Si exposed around the islands of PtSi (opened up by shrinkage of the PtSi phase). No electrical data were taken on the very poor Pt on Si films discussed above, because no PtSi phase formed.

The contamination film on the Si was analyzed by x-ray microprobe and ESCA methods. It consists primarily of oxygen (as SiO_2) and carbon films, 50-100Å thick. It builds up in the perimeters of contacts. ESCA has also shown the presence of a thin SiO_2 film (<100Å thick) on top of freshly prepared PtSi films. Heat-treating the PtSi films in air instead of nitrogen results in a surface containing less platinum and more oxygen. The etching in aqua regia may promote the formation and growth of the thin SiO_2 film on the PtSi. This phenomenon has been observed by other investigators (15).

When Pt is deposited on clean Si, but not heat-treated *in situ* or later, the electron microscope shows a continuous Pt film with a very strong <111> preferred orientation to the Si substrate. As was mentioned earlier, this strong orientation is a good indication that a satisfactory PtSi film will form upon heat-treatment. When these films are heated *in situ* in the electron microscope while being recorded in the SAD mode on 16-mm motion picture film, it is possible to edit frames from the sequence and index the SAD patterns. By this method we find that the phases formed are $Pt + Si \rightarrow Pt_3Si \rightarrow Pt_2Si \rightarrow PtSi$. The complete reaction occurs in approximately 20 sec at 450°C. Often one or more rings from the Pt_2Si phase remains in the PtSi phase diffraction pattern despite prolonged heat-treatment.

PtSi films <500Å thick, deposited or heat-treated in the range of 400°-850°C, can have several different morphologies, each with its own associated crystallography and, as will be shown later, concentration of dopant in the substrate. For Si substrates that are less than atomically clean, or high concentrations of Si dopant, we see a continuous, polycrystalline PtSi film, randomly oriented to the Si and having high-angle grain boundaries separating grains that are randomly oriented toward each other. Figure 4a is typical of such a PtSi film. For very clean Si substrates and intrinsic-to-moderate Si dopant levels, the PtSi film is heteroepitaxial to the Si substrate and consists of very small nodules of PtSi, having a high degree of orientation toward each other and separated by discontinuities, or voids, 20-150Å wide. This important result indicates that PtSi, by itself, could not be used as an effective diffusion barrier to prevent interaction between the subsequently deposited device interconnective metal and the substrate. Figure 4b is an example of such a film on a <001> Si substrate; the SAD pattern in the insert exhibits anomalous symmetry, greater than two-fold. These two morphologies are extremes; many morphologies may be observed between these limits.

The results for microstructure *vs.* electrical performance are summarized in Table I. Here the specimens observed are divided into groups as functions of deposition conditions. The specific contact resistance data in the table are the statistical means of the data for the specimens in any particular group. Any difference between the forward and reverse values gives a measure of the contact's departure from ohmic behavior. When an occasional sample in one of the superior

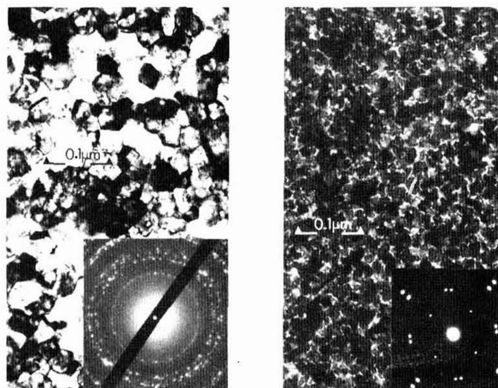

Fig. 4. PtSi morphology: extremes. Corresponding diffraction patterns are shown in the insets. (a, above left) High-angle grain-boundaries; sample is described in Table I, I (base). (b, above right) PtSi nodules; sample is described in Table I, III (base).

Table I. PtSi properties related to deposition parameters

Group	Substrate preparation	Heat-treatment	Diffusion	Specific contact resistance: forward, reverse (ohm-cm^2 × 10^{-5})	Morphology	Crystallinity
I	Chemical cleaning plus sputter cleaning, performed *in situ*	450°C *in situ* during Pt deposition; substrates cooled *in vacuo*	Base	5.48, 6.29	Nodules (300A), taken as definitive. Internodule voids, 10-50A. Buildup of larger, thicker nodules in contact hole perimeter (Fig. 5a)	Type A pattern, taken as definitive
			Emitter	0.406, 0.507	Nodules (210A). Internodule voids, 10-50A. Nodules have textured surface or internal structure, build up in perimeter	Type A pattern
Ia	Same as I	Same as I	Base	13.6, 13.4	As above except discontinuity in perimeter 2000-3000A wide, exposing bare Si	Type A pattern in PtSi
			Emitter	0.528, 2.64	Same as base	Type A pattern in PtSi
Ib	Same as I	Same as I	Base	19.1, 19.1	As in group Ia, plus scallops in edge of PtSi area (Fig. 5b)	As in group Ia
			Emitter	0.812, 1.22	Same as base	
II	Same as I	450°C for 20 min *in situ* after deposition	Base	15.2, 15.0	PtSi as in groups I, Ia, and Ib on different samples with no change in contact resistance	Type A pattern mixed with regions of type B pattern
			Emitter	0.771, 0.771	Same as base plus an occasional large void, 500-1000A	Same as base
III	Chemical cleaning	550°C for 30 min externally in clean furnace	Base	17.5, 17.7	High-angle g.b.* Some large voids. Perimeter effects as in group II	Type C pattern
			Emitter	1.68, 1.68	Same as base	Same as base
IIIa	Same as I	Same as III	Base	13.4, 13.2	Mixed nodules and high-angle g.b., porous	Type B patterns mixed with type C; some unreacted Pt
			Emitter	0.446, 1.91	Same as base but more porous	Type C pattern plus some unreacted Pt
IV	Chemical cleaning	Same as III, but in a contaminated furnace**	Base	102, 81.2	High-angle g.b. Large grains, some voids, etching damage, perimeter effects	Poly PtSi plus unreacted Pt
			Emitter	40.6, 40.6	Same as base; contamination evident	Same as base
Effect-of-thickness samples	Same as I	550°C for 30 min in clean furnace	Base	16.1, 16.1	Two-layer film; nodules next to substrate, and very porous, very small grain layer above (Fig. 5c)	Type A pattern next to substrate; broad, diffuse Pt rings above
			Emitter	1.81, 1.02	Same as base except that nodule layer was thinner	Same as base
Evaporated Pt-I	Chemical cleaning; deposition at 300°C	Same as effect-of-thickness samples	Base	12.4, 12.2	Same as groups Ia and Ib	Same as group Ia
			Emitter	0.790, 0.821	Same as group Ia	Same as group Ia
Evaporated Pt-II	Same as evaporated Pt-I	Same as effect-of-thickness samples	Base	24.8, 24.6	High-angle g.b.;* two-layer structure; etch damage (Fig. 5d)	Poly PtSi below; broad, diffuse Pt rings above
			Emitter	12.03, 11.42 (when PtSi film is present)	Same as base; or, for some samples, Pt did not react with Si and was etched off during the aqua regia step	Same as base or no film at all

* g.b. = grain boundary.
** The furnace was intentionally contaminated with oxygen.

specimen groups had electrical data more typical of one of the contaminated groups, and electron microscopy confirmed the presence of a contaminated or anomalous microstructure, the data for such specimens are presented in a separate statistical subgroup in the table.

For brevity, codes were adopted. In the morphology section, "high-angle g.b." refers to the first limiting case, described above, of a continuous, random, polycrystalline PtSi film with high-angle grain boundaries. "Nodules" refers to the second limiting case of highly oriented, heteroepitaxial, small, discontinuous nodules (lacking grain boundaries) of PtSi; the width of the void between modules is specified in the table. "Poly PtSi"refers to a diffraction pattern of randomly oriented PtSi phase with no preferred orientation. A "type A pattern" is a single-crystal PtSi diffraction pattern consisting of one diffraction zone.[1] A "type B pattern" is a mixture of two or more PtSi diffraction zones, and a "type C pattern" is a mixture of one or more diffraction zones with polycrystalline PtSi rings. The morphology types are illustrated in Fig. 4a and b. For comparison, Table I includes data from thicker sputtered specimens and from films e-beam evaporated and subsequently heat-treated.

Some of the points brought forth in the table merit detailed discussion. The contact perimeter effects that distinguish groups I, Ia, Ib, and II from one another and are illustrated in Fig. 5a and b are due to different degrees of cleanliness in the contact holes combined with the volume contraction, about 500Å, associated with the formation of the PtSi phase. Even when the contacts are sputter cleaned *in situ* before Pt deposition, microanalysis methods often disclose an increased level of chemical etchant residues within 5000Å of the SiO_2 step-down to the Si around the perimeter of the contact hole. When this contamination is present, the Pt immediately adjacent to the SiO_2 step fails to react with the Si, with the result that the aqua regia strip leaves a ring of exposed Si around the contact, as in Ia, or a ring plus scallops, as in Ib. The group I samples occur when the sputter cleaning effectively eliminates the contaminating residue. *In situ* heat-treatment of group II samples in the electron microscope reveals that the Pt on the walls and the top of the SiO_2, having no Si to react with, rapidly diffuses down to feed the reaction in the contact hole perimeter, yielding thicker PtSi nodules in the perimeter. This phenomenon is observed only for sputtered Pt samples in which edge coverage of the oxide step-down is very good. The group II PtSi films had a somewhat poorer heteroepitaxy than the group I films, with an apparently concomitant insensitivity of the specific contact resistance to perimeter effects.

The formal Discussion section will deal with the nodular plus void morphology we attribute to pure PtSi. We believe that the high-angle g.b. morphology is a manifestation of PtSi formed in the presence of low levels of surface contamination that prevents the PtSi from becoming heteroepitaxial to the Si. For PtSi films more than 300-400Å thick, we often see remnants of the Pt_2Si diffraction pattern mixed with diffraction patterns of types A, B, and C. *In situ* heat-treatment in the electron microscope has shown that when the substrate conditions are appropriate for the

[1] The diffraction zone of the pattern is a function of the Si substrate orientation and will be identified along with the n-fold anomalies of the diffraction patterns in the Discussion section.

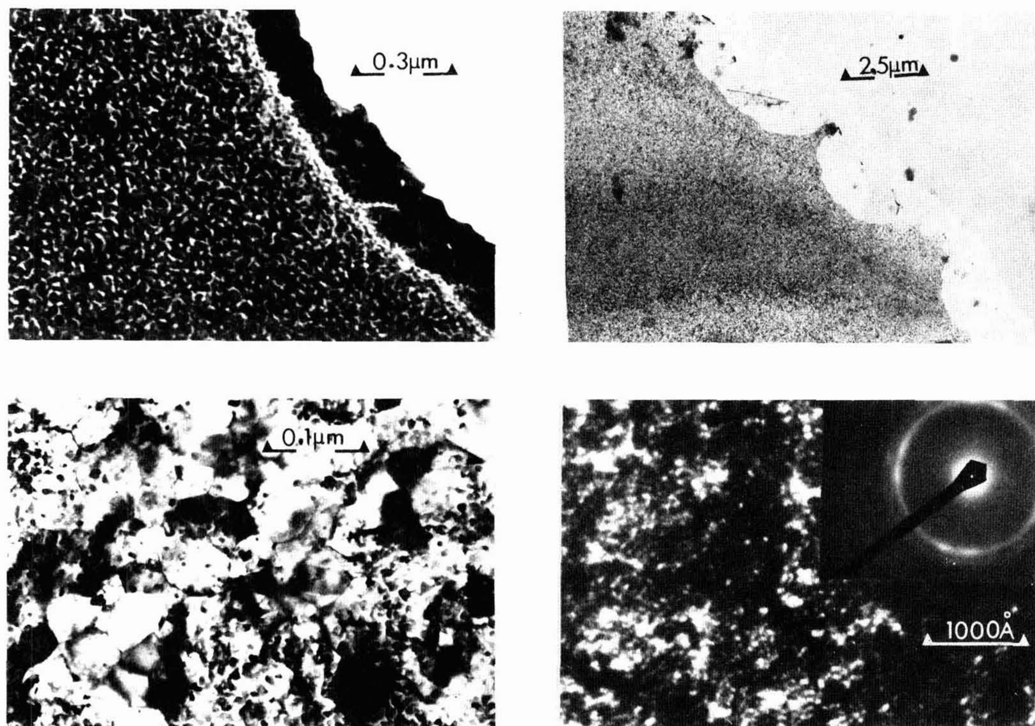

Fig. 5. Anomalies in morphology of PtSi. (a, top left) Buildup of thicker grains of PtSi in perimeter of contact. (b, top right) Opened-up contact perimeter with scallops. (c, bottom left) Remnants of nodule layer beneath recrystallized Pt_xSi_y. (d, bottom right) Porous Pt with diffraction pattern showing diffuse Pt rings.

formation of high-angle g.b. PtSi, heat-treatment at a temperature of over 500°C for more than 1 or 2 min may induce void growth.

The "effect-of-thickness" samples introduce a new morphological type: the two-layer film. The two discrete layers are detected visually in the transmission and scanning electron microscopes and by their different chemical etching behavior. Both layers yield Pt and Si spectra in energy and wavelength dispersion studies in the x-ray microprobe. As is mentioned in Table I, the layer adjacent to the Si substrate has a nodular morphology that often compares well with the group II samples. The top layer has a very slow etch rate and has a spongelike morphology consisting of grains 50-75Å in size in a matrix that is about 50% small grains and 50% voids. Electron diffraction patterns from the top layer are indexed as fcc Pt, but the Pt rings are very broad and diffuse. On this evidence, we identify the top layer as porous Pt, an etching residue.[2]

For these samples, the heteroepitaxial PtSi nodules are diffusion limited to a maximum thickness of 200-500Å before, presumably, stoichiometric deficiencies cause the PtSi to renucleate in a randomly oriented polycrystalline morphology, as has been observed on unetched specimens. Figure 5c depicts a thick sample that has been thinned from below; the remnants of the nodules can be seen under the large renucleated Pt_xSi_y $(x > y)$ grains. This Pt_xSi_y is attacked by the aqua regia etch to produce porous Pt (Fig. 5d). The thickness of Pt_xSi_y/porous Pt is maximized, for a given Pt thickness, by poor contact hole cleaning and/or higher concentrations of B or As dopants in the Si, as is discussed later.

PtSi formed from evaporated Pt presents a study in contrasts. The evaporated Pt group I samples, which are typical of most of the evaporated Pt-PtSi examined, compare very favorably with sputtered samples of groups Ia and Ib. In all cases, evaporated Pt contacts exhibited deleterious contact perimeter effects. When evaporated Pt-PtSi contacts are made in large lots, with no intentional changes in deposition parameters, electrical tests occasionally reveal wafers with high specific contact resistances. TEM analysis of these wafers reveals the microstructure identified as evaporated Pt group II in Table I. The morphology and crystallinity of evaporated Pt samples in group II combine the worst features of sputtered group IV and the effect-of-thickness samples. Often the perimeter discontinuity expands to the center of the contact, leaving only a small region of PtSi.

The authors believe that the poor quality of the microstructures in the evaporated Pt samples in group II is directly attributable to contamination of the Si contacts. Support for this belief comes from ESCA and SEM/Auger analysis, which reveals higher levels of carbon that presumably are due to residues of chemical cleaning and photoresist left before deposition. Often the high contact resistance of evaporated Pt group II samples can be lowered somewhat by additional heat-treatment before the aqua regia etch. Heat-treatments of up to 2 hr at 550°C were used. This is additional, indirect evidence of contact contamination; one can assume that hydrocarbons in the contacts are breaking down and allowing the Pt to react with the Si.

Dopant C_o dependence.—During our analysis of PtSi thin films, we noted that the microstructure of the PtSi films is sensitive to the dopant species and surface concentration in the underlying Si substrate. As was noted in the section on preparing specimens, the dopant-C_o-dependence PtSi was formed on the seven wafers listed in Table II. The Si dopant species and the range of dopant concentrations were chosen with the aim of encompassing all of the Si-dopant possibilities germane to the production of viable contacts. The 2.0×10^{15} boron wafer is taken as the intrinsic Si case. Sheet resistances were measured on the as-deposited films and after the external heat-treatments as listed in Table II. The heat-treatments were performed after the unreacted Pt strip, to prevent any unreacted Pt present from adding to the volume of PtSi phase formed during the deposition *in situ* heat-treatment. The drop in sheet resistance observed after the heat-treatment at 750° or 850°C is due to the expansion of the heteroepitaxial film via the partial consumption of the thin polycrystalline PtSi (or porous Pt) film overlying the heteroepitaxial nodules. We postulate not that the sheet resistance is lower because of the more perfect microstructure of the PtSi films, but rather that the electrical properties of the films are degraded as the increased heat-treatment temperature drives the finite amount of Pt deeper into the Si at the expense of the stoichiometry of the PtSi films. The films heat-treated at 950°C have been completely recrystallized. The PtSi is now completely randomly oriented polycrystalline, with high-angle grain boundaries and no voids. Paralleling Sinha's findings (8), the polycrystalline PtSi film is covered with discontinuous clusters of agglomerated large grains of PtSi protruding from the smooth film. Note in Table II that the complete absence of stoichiometric heteroepitaxial PtSi in the 950°C samples is invariably accompanied by an increase in sheet resistance.

Space does not permit us to include representative micrographs and diffraction patterns for all of the combinations of Si dopants and heat-treatments reported in Table II. Let us start with the intrinsic (2.0×10^{15}B) Si sample. The as-deposited, two-layer PtSi film has a complete nodule layer over the Si and an incomplete poly PtSi/porous Pt film over the nodules. After heat-treatment at 750°C, there is much less poly PtSi/porous Pt in evidence; after heat-treatment at 850°C, there is none at all in discrete areas on the intrinsic Si. The morphology of the film after the heat-treatment at 950°C consists of protruding large PtSi grains on randomly oriented continuous PtSi film.

The most obvious effect of increasing the Si dopant in the substrate is to improve the coverage of the as-deposited samples by poly PtSi/porous Pt. The As 1.0×10^{19} sample was covered about as well as the intrinsic Si sample, about 50%. On the other hand, the As 1.0×10^{20} and the B 4.0×10^{18} as-deposited samples were 70-90% covered over the heteroepitaxial nodules. At higher dopant levels of either species in Si, the nodules were completely covered with poly PtSi/porous Pt. The microstructural effects of heat-treatment of all the as-deposited films parallel the sequence described for intrinsic Si: at 750° or 850°C the poly PtSi/porous Pt loses its identity as a discrete film, and at 950°C it recrystallizes. The only exception to the general trend was that the As 1.0×10^{21} sample heat-treated at 850°C was partly recrystallized.

Effect of in situ sputter cleaning on the silicon surface.—We have stressed the importance of contact hole

Table II. Sheet resistance (ohm/sq) of PtSi as a function of dopant concentration and heat-treatment. All heat-treatments lasted 1 hr

Dopant	Heat-treatment, °C	Dopant concentration (cm^{-3})		
		2×10^{15}*	5×10^{18}	4×10^{19}
Boron	As deposited	13.50	0.721	0.697
	750	9.36	0.493	0.694
	850	6.50	0.546	0.659
	950	6.86	0.497	0.689
		1×10^{19}	1×10^{20}	1×10^{21}
Arsenic	As deposited	12.74	5.14	4.51
	750	7.67	4.41	4.20
	850	6.90	4.37	4.36
	950	7.74	5.54	5.47

* Taken as the intrinsic case.

[2] A porous reaction occurs when an intermetallic alloy, consisting of a noble metal and a nonnoble metal, is etched: the noble metal is leached from the alloy lattice, leaving the noble metal in a highly disordered state. The remnant lattice will produce a diffraction pattern consisting of broad, diffuse lines. The porous metal product has a spongelike morphology and is not amenable to further etching.

cleanliness on the microstructure of the subsequently deposited PtSi film. We have shown that *in situ* sputter cleaning before Pt deposition produces improved PtSi films and minimizes or eliminates contact perimeter effects. In this section we deal with the side effects of *in situ* sputter cleaning. Specifically, are the SiO_2 surrounding the contacts, and Pt from the nearby Pt fixtures, being backsputtered into the contacts during the cleaning?

TEM analysis of the 100W and 500W sputtered wafers showed contrast effects on the Si that were found to be associated with a rough surface morphology, very small dislocation loops, or the nucleation of a foreign material on the Si surface. Electron diffraction patterns showed single-crystal Si reflections, polycrystalline Si rings, and a ring pattern indexed as Pt.

A part of each sample was analyzed by reflection electron diffraction analysis (RED), comparing the center of the wafer with observations out to the edge. RED showed polycrystalline Si rings, Pt rings, and one ring identified as PtSi on the sample that had not been heat-treated. The only Si single-crystal reflections seen were very weak; this indicates that the thickness of the polycrystalline Si is nearly as great as the depth to which the electron beam from the RED apparatus penetrates into the substrate, about 300Å. The Pt reflections were broadened; this, in turn, indicates that the Pt is very thin. Both the polycrystalline Si and the Pt were more intense near the edges of the wafers than at the centers. Neither the thin polycrystalline Si nor the Pt showed in a low-angle Laue x-ray photograph. A Berg-Barrett surface topograph revealed no surface damage, within the limit of resolution of this method.

In view of the diffraction results, the samples were given a heat-treatment designed to clear up the ambiguity in the TEM observations of the surface. A heat-treatment would cause nucleated Pt to form PtSi with a resolvable size and/or any Si defects, such as dislocation loops, to grow to analyzable dimensions. After a heating cycle that peaked at 750°C after 30 min, TEM revealed isolated islands of PtSi with a strong PtSi <110> orientation relationship normal to the Si. No polycrystalline Si was detected.

For corroboration, the 500W sample was analyzed in the x-ray microprobe for Pt as a step function of distance from the center of the wafer to its edge. Pt was detected from the center out to the edge; its concentration was lowest at the center and peaked approximately 5 mm from the edge. The total counts at each step were low, indicating a very thin layer.

By use of the ESCA and Auger/SEM methods and the x-ray microprobe, we searched for backsputtered SiO_2 in the contact windows that had been sputter cleaned *in situ*. All three analyses confirmed that oxygen and/or SiO_2 were present, along with carbon, in the contact holes. However, the amount of contamination was very close to the above method's detectability limits and to the amount of SiO_2/carbon present on control samples that had not been sputter etched; hence the few monolayers of contamination that we see may well be native oxide films grown on the Si after sputter etching and artifactual carbon contamination induced in the analyzing instrumentation.

Apparently, then, the effect of rf sputter cleaning the Si wafer, if we neglect SiO_2 and carbon contamination, is to introduce a thin layer of polycrystalline Si on the surface (which is probably caused by backscattering or reflection of sputter-etched Si falling back on the surface) and to backscatter some Pt from the Pt-coated sputter-etching cathode and the nearby Pt d-c sputter-deposition cathode. When the samples were heat-treated, the Pt reacted preferentially, with the polycrystalline Si consuming it in the formation of PtSi. No dislocation loops or other line defects were observed in the Si. Although twins and other remnants of the existence of the polycrystalline Si layer could be expected in the heat-treated samples, none was observed.

The presence of backscattered Pt on the Si is desirable (16). The amount and distribution of it can be controlled by manipulation of the sputtering conditions.

The formation of a polycrystalline Si layer is probably not harmful. In fact, it may speed the formation of the PtSi phase.

Excessive sputter etching may produce an amorphous Si layer on top of the polycrystalline Si; however, we found no evidence of such a layer.

Discussion

PtSi diffraction anomalies.—The anomalous greater than twofold symmetry observed in diffraction patterns taken of orthorhombic PtSi was explained in earlier works (11-13). There we identified the epitaxial relationship of PtSi on {100} Si to be PtSi $(1\bar{1}0)$ parallel to Si (001) and PtSi [001] parallel to Si [110]. The fourfold symmetry arises from double positioning of PtSi [001]'s on the two cubic <110> of the surface in neighboring PtSi nuclei.

In an illustration, we see that the PtSi on the {100} Si diffraction pattern in Fig. 6a exactly matches the computer plot in Fig. 6b. The computer plot was made by first drawing a PtSi $[1\bar{1}0]$ zone (asterisks) and then

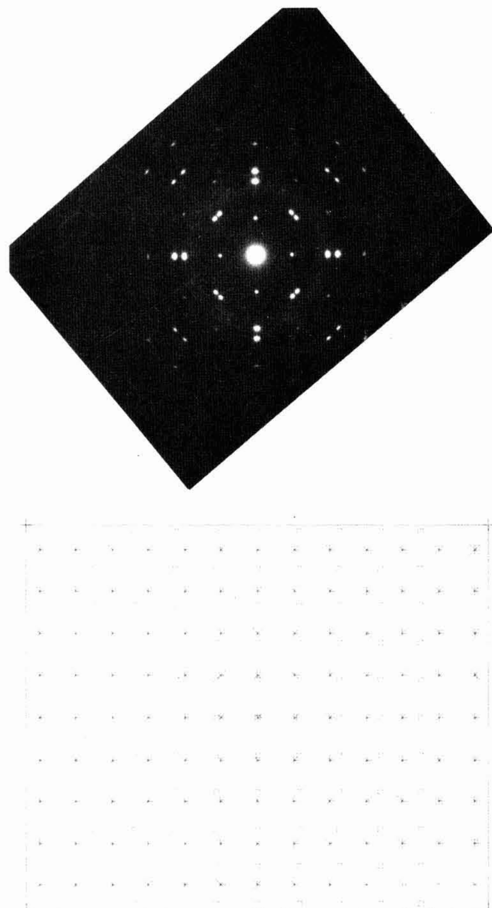

Fig. 6. Comparison of {100} diffraction pattern and computer plot for PtSi on {001} Si. (a) Diffraction pattern. (b) Computer plot, containing two PtSi [110] zones plotted with a 90° mutual rotation.

redrawing the same [1$\bar{1}$0] zone (squares) after a 90° rotation about the common zone normals. The same explanation applies to the anomalous threefold diffraction patterns observed for PtSi on {111} Si wafers. In this case the PtSi (010) is parallel to the Si (111), and the PtSi [010] is triply positioned on three equivalent <224> of the Si. In Fig. 7 a diffraction pattern and a computer plot are compared as before except that the computer plots the PtSi [010] zone twice after two 60° rotations. The nonmatching reflections plotted by the computer are structure-factor-forbidden PtSi reflections that are present in the [010] zone. Figure 7a also contains oriented Pt_2Si reflections.

For completeness, we have also investigated the epitaxial relationships of PtSi formed on {011} Si substrates. The 150Å of PtSi was formed *in situ* during sputtering with conditions the same as those which produce type A PtSi. The blanket samples exhibited a type A nodule morphology. The diffraction patterns exhibited greater than twofold symmetry, but it was obvious that more than one crystallographic zone was present in the patterns. Figure 8a depicts the morphology of PtSi on {011} Si, and Fig. 8b shows the corresponding diffraction pattern. The heteroepitaxial relationships, obtained from Fig. 8b, are as follows:

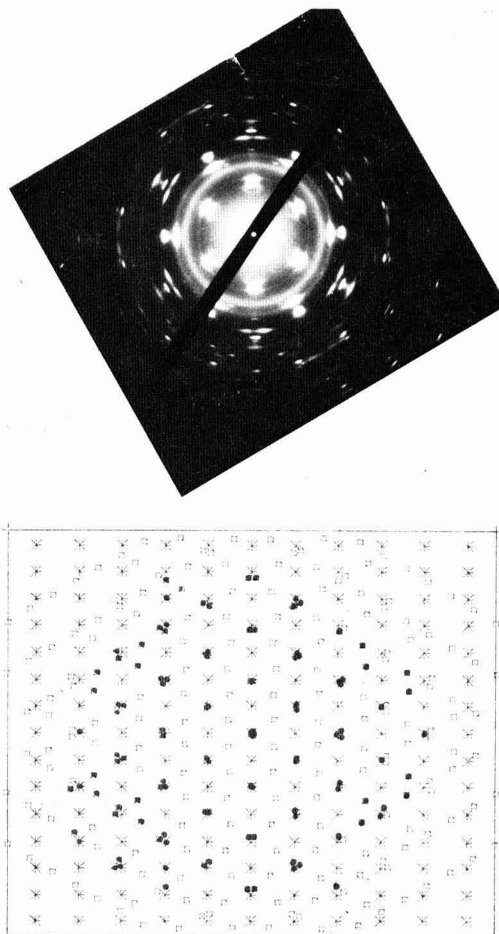

Fig. 7. Comparison of {111} diffraction pattern and computer plot for PtSi on {001} Si. (a) Diffraction pattern, which contains a Pt_2Si reflection that also shows anomalous symmetry. (b) Computer plot, containing three PtSi [010] zones plotted with 60° mutual rotations.

PtSi on {011} Si

Major orientation—double positioning of

PtSi (133) | | Si (011)
PtSi [30$\bar{1}$] | | Si [0$\bar{2}$2]

Coexisting minor orientations

(a) PtSi (120) | | Si (011)
PtSi [00$\bar{2}$] | | Si [0$\bar{2}$2]

(b) PtSi (011) | | Si (011)
PtSi [$\bar{1}$1$\bar{1}$] | | Si [400]

The samples with PtSi on {011} Si were also used to find a solution for another electron diffraction puzzle observed on {001} and {111} Si. When a thin type A film is observed in SAD mode over a thin wedge of Si tilted into perfect zonal orientation, clusters of satellite reflections are formed around the Si matrix diffraction spots (Fig. 9a). Multiple diffraction effects, superlattice formation, and film formation on twinned Si surface regions were suggested as mechanisms for the satellite spot formation (17). Silicon twins primarily across (111) planes; the {011} samples, which have two (111) planes perpendicular to the surface, are ideal vehicles to test the twinning argument.

The assumption of twinning across the two (111) traces in Fig. 9a accounts for all of the anomalous reflections in what appears to be an n/3 relationship to the Si reflections. The close-by satellite reflections are not accounted for in this manner; they are presumed to arise from a combined multiple-diffraction-twinning mechanism, not yet determined, involving the substrate and the heteroepitaxial film. Analogous satellite arrangements for {001} and {111} substrates are seen in Fig. 9b and c.

The one significant conclusion drawn from the identification of the twin reflections in Fig. 9a is that local regions of the Si surface bear twin relationships to one another. Therefore, PtSi films formed heteroepitaxially on one region of Si will bear a twin relationship to PtSi formed on a neighboring, twinned region of Si. This in turn leads to an alternative argument to account for the greater than twofold symmetries observed in PtSi diffraction patterns. For example, the major asymmetry of Fig. 8b, ascribed to double positioning of {133} PtSi zones, could be equivalently produced by forming {133} PtSi over twinned regions of Si. Unfortunately, the Si planes over which the PtSi {133} must be mirrored are the Si (011) and (001), which have not been observed to be Si twinning axes. An attempt to extend the twinning argument to account for the high symmetry of PtSi on {001} and {111} Si wafers is also unsuccessful because the assumption of twinning over the previously reported [111], [123], and [511] Si twinning axes cannot account for the anomalous symmetry.

With the epitaxial relationships established, we can explain the observed morphology of thin, clean, epitaxial PtSi in thicknesses from 100 to 500Å. For PtSi on Si {100} wafers, we would expect an epitaxial PtSi film consisting of grains of PtSi abutting with 90° grain boundaries. Contrary to expectation, the morphology of such a film (Fig. 10a) consists of small disconnected nodules of PtSi with random shapes. This morphology probably arises because large misfit energies make neighboring PtSi nuclei with 90° rotations between PtSi <001> directions unable to coalesce during film deposition or recrystallization.

By carefully tilting a PtSi film on a {100} Si specimen in the goniometer stage of the electron microscope, it was possible to extinguish the PtSi reflections and leave one Si (400) reflection in a selected-area electron diffraction pattern. The Si (400) reflection was used to produce a high-magnification dark-field micrograph (Fig. 10b) of the area seen in Fig. 10a. Here the internodule regions are illuminated. This establishes that the epitaxial PtSi nodules are surrounded by un-

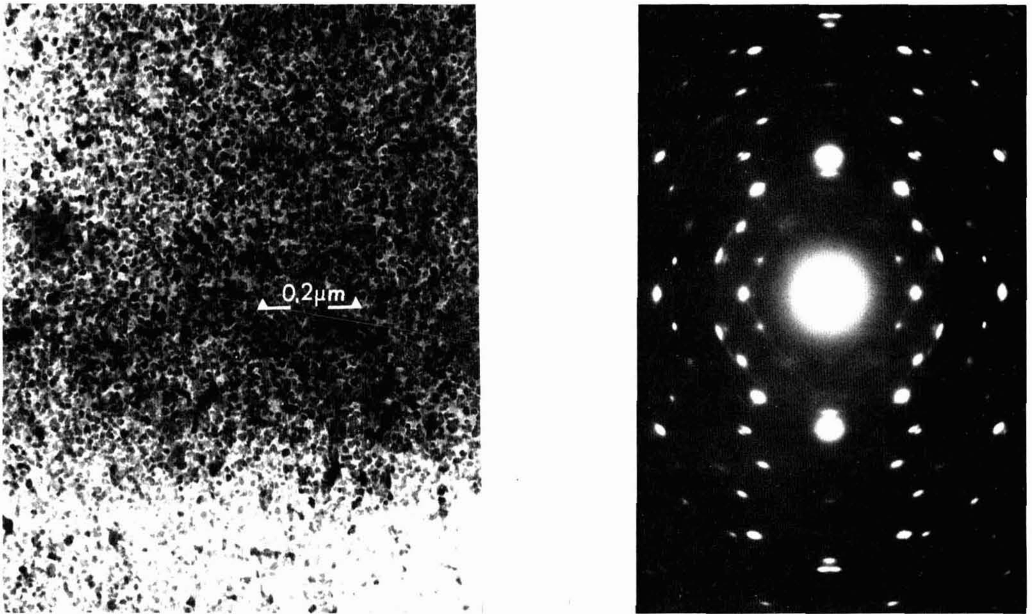

Fig. 8. PtSi on {011}. (a, above left) Nodule morphology. (b, above right) Corresponding diffraction pattern, containing two PtSi [133] zones rotated 180° plus minor orientations.

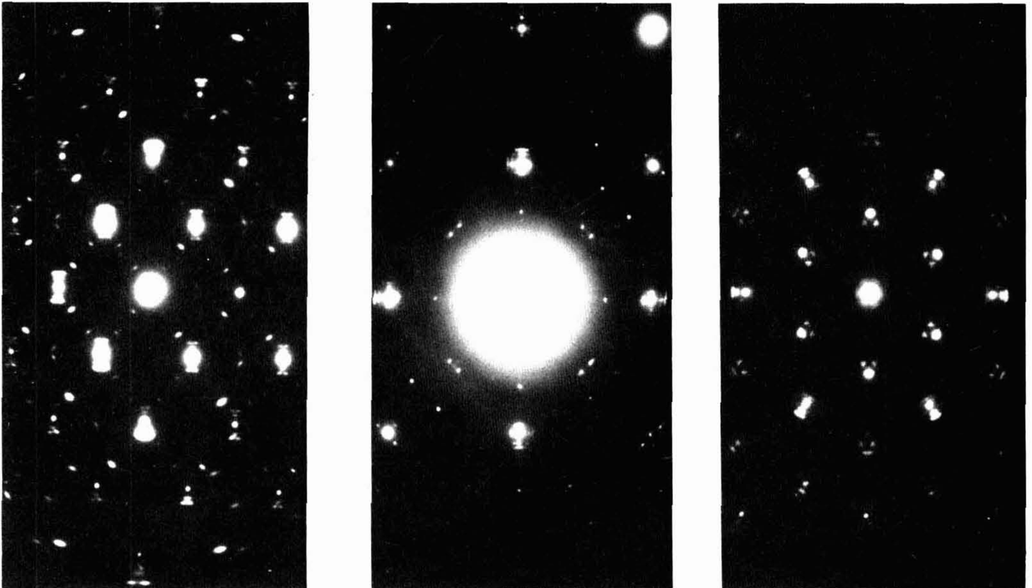

Fig. 9. Extra reflections observed when thin PtSi over Si is brought to perfect Si zonal orientation. (a, above left) {011} Si. (b, above middle) {001} Si. (c, above right) {111} Si.

reacted Si channels approximately 20-30Å wide. Apparently the misfit energy associated with the coalescence of two PtSi nodules oriented 90° with respect to each other overcomes the driving force of the intermetallic phase formation, leaving, presumably, very highly stressed, unreacted Si between nodules.

The same explanation applies to the identical epitaxial PtSi morphology observed on {111} and {110} Si wafers.

Relationship of electrical properties of morphology and crystallinity.—Clearly, the best electrical contacts, *i.e.*, the lowest in specific contact resistance and the closest to ohmic behavior, produce single-crystal PtSi diffraction patterns consisting of one diffraction zone (type A). Morphologically, such structures consist of heteroepitaxial PtSi nodules 200-500Å in diameter separated by voids of 10-50Å, as shown in Fig. 10a. Not surprisingly, the PtSi microstructure that yields the

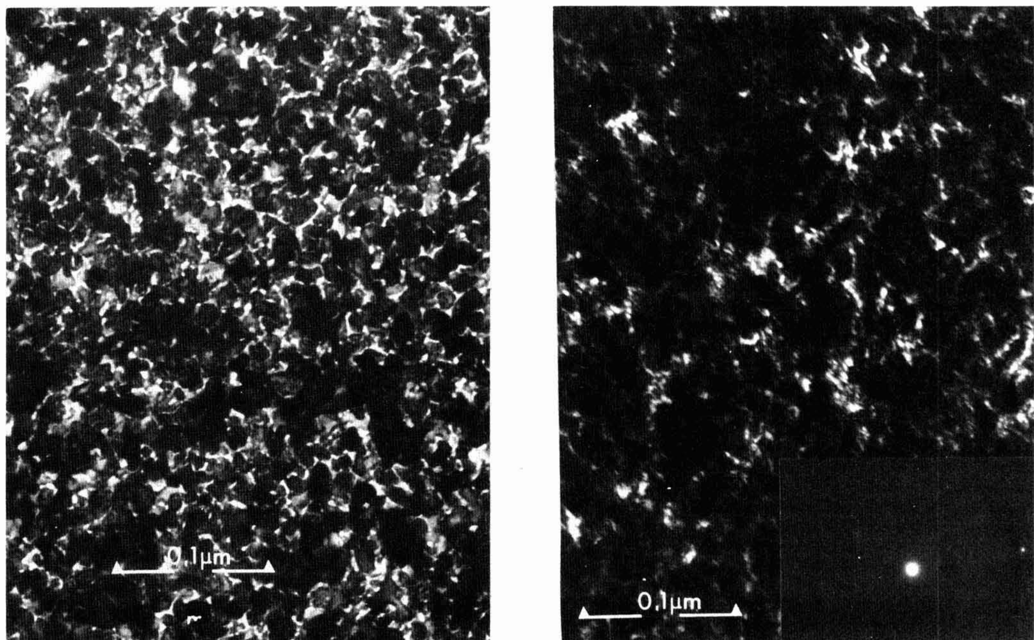

Fig. 10. Unreacted Si between PtSi nodules. (a, above left) Bright-field micrograph. (b, above right) Companion dark-field micrograph taken by use of a Si (400) reflection.

best electrical base contacts also gives the best emitters. Type A PtSi, therefore, appears to be the best from a pragmatic as well as an esthetic point of view.

Relationship of microstructure to deposition conditions.—We have found that the best PtSi films could be formed most consistently by sputter depositing at elevated substrate temperature (~450°C) after *in situ* sputter cleaning. Heat-treating *in situ*, but after rather than during the deposition, produced microstructurally and electrically better contacts than heat-treating externally in a flowing dry N_2 furnace, even with the furnace 100°C higher in temperature. Both methods, however, are inferior to *in situ* heating during deposition.

Chemical cleaning plus *in situ* sputter cleaning also gave consistently better results than chemical cleaning alone. No direct comparison of *in situ* sputter-etched sputter-deposited PtSi and *in situ* sputter-etched, e-beam-evaporated films was made, but sputter depositing should be better, if only because it covers the perimeters of the contact holes better. Perimeter coverage is an extremely important factor when the PtSi is used on lightly doped n-type Si to form a rectifying (Schottky) contact, in which edge effects play a dominant role in reverse-bias operation.

Conclusions

A number of conclusions can be drawn from this study:

1. A direct relationship has been established between the microstructural and the electrical properties of PtSi thin films. We are now able to predict with certainty, by only a microstructural examination, when a PtSi contact will be electrically acceptable. Conversely, we have related unsatisfactory electrical performance to specific microstructures ,which are in turn related to certain deposition conditions; this finding makes it possible to adjust microstructures on the production line on the basis of electrical data.

2. A direct relationship has been established between PtSi deposition parameters and microstructural properties (and hence electrical properties). The best PtSi films, microstructurally and electrically, are formed by sputter depositing Pt while continuously forming PtSi *in situ* at approximately 450°C on Si that has been rf sputter cleaned *in situ*.

3. Sputter cleaning forms a thin layer of polycrystalline Si and deposits a small amount of unreacted Pt on the surfaces of the Si contacts. Neither effect is detrimental; in fact, the formation of polycrystalline Si may aid in the efficient, uniform formation of PtSi.

4. A PtSi film more than 200-500Å thick has two layers. The layer next to the Si substrate often compares well to the best single-layer PtSi. The top layer, after etching, has been identified as "porous Pt" and is poorer microstructurally than the layer beneath. A porous reaction occurs in intermetallic alloys of a noble metal and a nonnoble metal when the latter is leached from the lattice, leaving the noble metal in a highly disordered state.

5. The microstructure and the electrical sheet resistance of a PtSi thin film are sensitive to the dopant species and surface concentration of the Si on which the film is formed, and to subsequent heat-treatment in the range from 750° to 950°C. For a given heat-treatment, the best microstructures are observed on the lowest doped Si, and the lowest sheet resistances on the highest doped Si. For films formed on Si with any dopant species and surface concentration, sheet resistance decreases in the 750°-850°C range, but increases at 950°C because discontinuous clusters of large PtSi grains form and any stoichiometric heteroepitaxial PtSi is completely destroyed.

Manuscript submitted April 24, 1975; revised manuscript received June 12, 1975.

Any discussion of this paper will appear in a Discussion Section to be published in the June 1976 JOURNAL. All discussions for the June 1976 Discussion Section should be submitted by Feb. 1, 1976.

Publication costs of this article were partially assisted by IBM Corporation.

REFERENCES

1. D. Kahng and M. P. Lepselter, *Bell System Tech. J.*, **44**, 1525 (1965).

2. M. P. Lepselter, *ibid.*, **45**, 233 (1966).
3. R. M. Anderson and S. Dash, EMSA Proc., p. 120 (1969).
4. R. M. Anderson, EMSA Proc., p. 518 (1972).
5. G. A. Walker, R. C. Wnuk, and J. E. Woods, *J. Vacuum Sci. Technol.*, **7**, 543 (1970).
6. F. B. Koch and P. B. Byrnes, Paper 191 presented at Electrochemical Society Meeting, Atlantic City, N.J., Oct. 4-8, 1970; *This Journal*, **117**, 262c (1970).
7. H. N. S. Lee, F. B. Koch, and W. R. Costello, Paper 70 presented at Electrochemical Society Meeting, Washington, D.C., May 9-13, 1971; *This Journal*, **118**, 72c (1971).
8. A. K. Sinha, R. B. Marcus, T. T. Sheng, and S. E. Haszko, *J. Appl. Phys.*, **43**, 3637 (1972).
9. H. Muta and D. Shenoda, *ibid.*, **43**, 2913 (1972).
10. A. Hiraki, M.-A. Nicolet, and J. W. Mayer, *Appl. Phys. Letters*, **18**, 178 (1971).
11. T. Kawamura, D. Shenoda, and H. Muta, *ibid.*, **11**, 101 (1967).
12. J. M. Poate and T. C. Tisone, *ibid.*, **24**, 8 (1974).
13. H. H. Hosack, *ibid.*, **21**, 256 (1972).
14. H. H. Hosack, *J. Appl. Phys.*, **44**, 8 (1973).
15. M. J. Rand, *This Journal*, **120**, 685 (1973).
16. J. L. Vossen, J. J. O'Neill, Jr., K. M. Finlayson, and L. J. Royer, *RCA Rev.*, **31**, 2, 293 (1970).
17. G. Das, Private communication.

An ESCA Study of the Oxide at the $Si\text{-}SiO_2$ Interface

R. A. Clarke,[1] R. L. Tapping[2], M. A. Hopper,[*,3] and L. Young[*]

Department of Electrical Engineering and Department of Chemistry, The University of British Columbia, Vancouver, British Columbia, Canada

ABSTRACT

Thermally grown oxide films on silicon were investigated using ESCA (electron spectroscopy for chemical analysis). Evidence was obtained which confirmed previous indications from other techniques that there is a transition layer of about 15 or 20Å thickness next to the silicon. In this layer the oxide changes from SiO close to the silicon to SiO_2 in the rest of the film.

The silicon/silicon oxide interface has a part in controlling the rate of thermal oxidation of silicon (1). Conversely, the atomic arrangement at this interface (which is important in determining several electrical properties of MOS systems) is itself affected by the variables of the oxidation process (2). The aim of the present work was to see what information could be obtained about the composition of the oxide near the interface with ESCA. Using this method, the shift of the 2p electron levels in silicon atoms, due to changes in the chemical environment of silicon atoms in oxide of different oxygen content, was observed. Confirmation of previous evidence from various techniques [including helium ion backscattering (3), secondary ion spectroscopy (4, 5), and optical reflectance (6, 7)] was obtained showing that there is a silicon-rich layer near the interface.

Experimental Procedures

The x-ray source of the Varian IEE-16 photoelectron spectrometer produces $h\nu = 1254$ eV photons. Absorption of a photon raises an electron from the 2p level of the silicon. Neglecting any loss of energy in escaping from the material. the kinetic energy E_k of the freed electron would be $E_k = h\nu - E_b$ where E_b is the difference in energy between the vacuum level and the 2p level. Electrons thus released will not be collected by the detector if the potential difference across the intervening vacuum is of appropriate sign and slightly greater than E_k/e (where e = magnitude of charge on electron). For this condition to exist, the observable difference in Fermi levels between the two electrodes and their work functions is related by $(E_F{}^d + \phi^d) - (E_F{}^s + \phi^s) = E_k$, where d refers to the detector and s to the specimen. Consequently

$$E_b = h\nu - (\phi^d - \phi^s) - eV$$

where V is the applied voltage (sample positive). Rather than estimate the work function difference, the energy calibration of the electron spectra was accomplished by taking the binding energy of some other known observable level. Either a film of gold was deposited on the sample and the higher energy Au 4f level was taken as 87.5 eV or the 2p line of the bulk silicon was used as a reference. The latter can, of course, be used only if the oxide is not too thick to prevent the escape of electrons from the substrate. Located with respect to the above gold standard, this level was found to be 99.5 ± 0.3 eV for the n-type 10 ohm-cm material which we used. Different values of the energy of the silicon peak were observed for different doping densities (*e.g.*, 98.9 ± 0.2 eV for degenerate p-type silicon and 99.9 ± 0.2 eV for degenerate n-type silicon). This is expected since the work function of the silicon is, of course, changed by doping. In this work we are interested in shifts of the level due to silicon atoms in the oxide. To circumvent complications due to doping as well as to band-bending, all bulk silicon peaks used as a reference were arbitrarily taken as having an absolute energy of 98.9 eV.

The silicon samples were commercially polished n-type (111)-oriented 10 ohm-cm material. They were cleaned by immersion in 1:1 H_2O_2-H_2SO_4, 4:1:1 H_2O-H_2O_2-HCl, and dilute HF and were oxidized in steam or pure oxygen in a quartz furnace tube.

The thickness of the oxide films was estimated using ellipsometry. For very thin films on silicon, thickness and refractive index differences cannot readily be distinguished using ellipsometry. The thicknesses were calculated using 1.458 for the refractive index of the oxide at 6328Å, which was the value found for thicker "dry" oxides. For very thin films of low oxygen content, and also for "wet" oxides, this index will, of course, be slightly in error.

For the ESCA measurements the oxide was removed from the back surface with HF and silver paste was

* Electrochemical Society Active Member.
[1] Present address: Garrett Manufacturing Company, 40 Voyager Court North, Rexdale, Ontario, Canada.
[2] Present address: Chalk River Nuclear Laboratories, Atomic Energy of Canada Limited, Chalk River, Ontario, Canada.
[3] Present address: Xerox Research Centre of Canada, Mississauga, Ontario, Canada.
Key words: silicon, ESCA, oxidation, thin films.

used to mount pieces of wafer on the gold-plated brass specimen holders.

Since fluorine is a likely contaminant and would cause a shift in the peaks, a search was made but no detectable signals were found from any of the fluorine orbitals. The pressure in the ESCA system was typically 2×10^{-7} Torr.

Results and Discussion

Spectra from silicon with not too thick an oxide contained two peaks, as illustrated in Fig. 1. The lower energy peak is due to silicon atoms in the substrate. The higher energy peak is due to silicon atoms in the oxide and, as shown in Fig. 1, the energy of this "oxide" peak depends on how the oxide was prepared and on its thickness.

The solid curve in Fig. 1 was obtained with a specimen from which oxide had been removed with HF immediately before insertion in the ESCA system. It is believed to have had about 5Å of oxide giving an unresolved peak at 102 eV. Three features of the ESCA spectra will be discussed. These are (*i*) the ratio *P* defined as the "oxide" peak height divided by the sum of the "oxide" and "silicon" peak heights, (*ii*) the line width of the "oxide" signal, and (*iii*) the energy shift between the "oxide" and the "substrate" peaks.

By defining the quantity *P* in terms of peak height rather than peak area it is possible to avoid the problem of deconvolving the rather closely spaced oxide and bulk silicon peaks. While not the ideal approach, this definition allows the general trends to be observed as shown in Fig. 2 where *P* is plotted as a function of oxide thickness for dry and wet oxides. The so-called escape depth from any material was taken to be that depth at which probability of escape of an excited electron is $1/e$ of its value at the surface (8). In silicon (8) this depth was calculated to be 20 ± 5Å. An analysis of Fig. 2 indicates that the escape depth from the oxide is somewhat greater than this. The figure also shows a significant difference between "wet" and "dry" oxides, presumably due to inclusion of H_2O or OH in the former. This difference merely implies less silicon in a thin film containing water than in one not containing water but of equal thickness as determined by ellipsometry assuming the same refractive index.

Figure 3 shows spectra of three films: (*i*) 16Å dry oxide, (*ii*) 16Å grown in O_2 bubbled through water at 95°C, and (*iii*) 29Å grown in steam. All gave the same *P*. Clearly the line width is larger when there is more water in the oxidation ambient. The increased width, however, is insufficient to account for the extra silicon required to provide an oxide of 29Å.

Figure 4 shows the energy of the oxide peak as a function of film thickness for films grown in dry oxygen at different temperatures. Also shown are data for films etched back in buffered HF to the thickness show from an initial 150Å (produced at 900°C). The figure shows data referred to the substrate silicon peak and also data referred to the gold level. In both cases, the oxide peak shifts with increasing thickness in the direction which, as shown below, corresponds to a change from SiO to SiO_2. Because of the limited escape depth of electrons, the ESCA technique samples only the outer part of the thicker films. However, the etch-back data show that these thicker films have an SiO-like layer near the silicon, similar in composition to the initial thin layers.

To calibrate the shift of position of the ESCA "oxide" peak as a function of composition, measurements were made on powdered fused silicon dioxide and on pow-

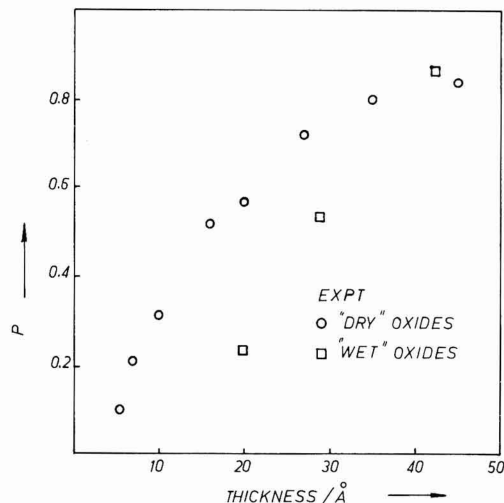

Fig. 2. Ratio *P* of the "oxide" signal to the total signal as functions of thickness for "wet" and "dry" oxides.

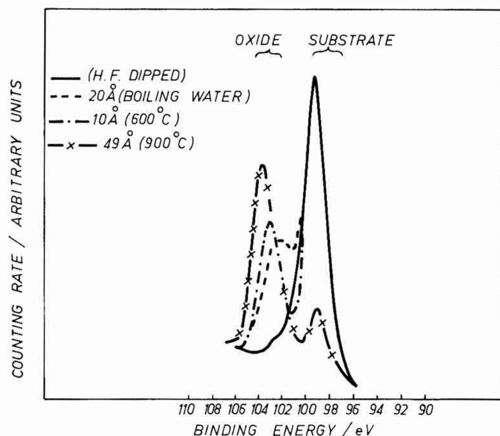

Fig. 1. ESCA spectra for silicon 2p electrons, indexed to gold, obtained with silicon wafers with thin film of oxide prepared in the ways shown inset.

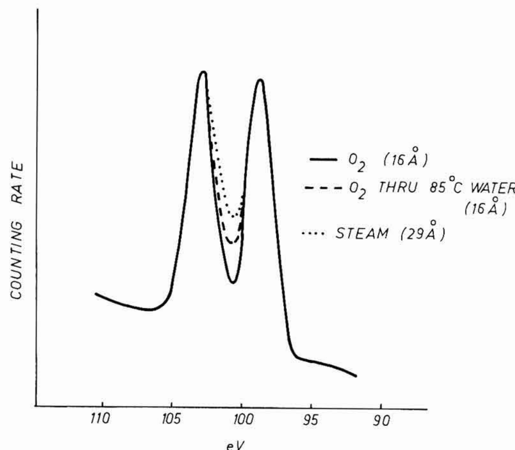

Fig. 3. Oxide and substrate peaks showing increasing linewidth of oxide peak in going from ——— 16Å dry oxide to - - - - - 16Å of oxide grown in O bubbled through H_2O at 95°C to . . . . . . 29Å of oxide grown in steam.

dered Linde Corporation "silicon monoxide." It is, of course, well known that SiO is not a stoichiometrically well-defined compound. As a further complication, our ESCA studies showed that our samples of the Linde product contained a small amount of elemental silicon. The spectra of SiO_2 and "SiO" powders are shown in Fig. 5. The order of line positions is reversed from that reported by previous authors (9). However, the theory developed later shows that the order observed by us is to be expected.

One source of error in ESCA measurements is the build-up of charge on insulating samples. Some tests were made to see if charging was occurring. A technique (10) was used in which a gold layer evaporated onto both the powder and the supporting metal block. Charging, if it occurs, is indicated by an asymmetry of the gold line. No charging was observed with the "SiO" or with the oxide-coated silicon wafers. About 0.8V of charging was observed with the SiO_2 powder. The difference between the gold-referenced data and the silicon-referenced data in Fig. 4 are believed due to band-bending effects rather than to charging.

A theoretical treatment is now given which allows the observed differences in energy and line width between the ESCA peaks for "SiO" and SiO_2 to be accounted for, and which, in fact, allows predictions to be made of these quantities for oxide of arbitrary composition, SiO_x. The theory is based on an analysis of the structure of the amorphous forms of SiO_x due to Philipp (6). He noted that the tetrahedral configuration of oxygen around the silicon atoms in SiO_2 is

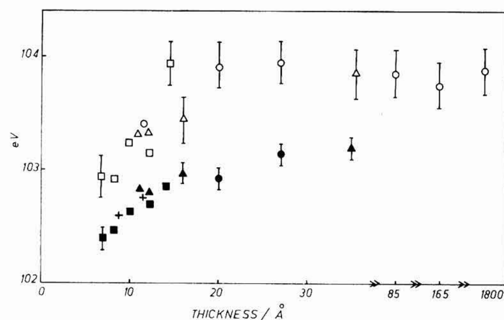

Fig. 4. "Oxide" peak energy as function of oxide film thickness. Open symbols, referred to gold peak; solid symbols, referred to substrate peak. □ and ■ grown at 600°C; △ and ▲ grown at 750°C; ○ and ● grown at 900°C; + etched back from films greater than 150Å thickness.

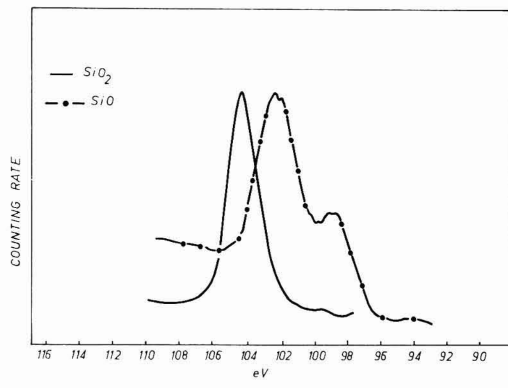

Fig. 5. ESCA spectra for bulk powders —— SiO_2 and –●– SiO. Energies referred to gold peak.

maintained in SiO_x except that some silicons replace oxygen, the average tetrahedron containing not four oxygens but $(4 - y)$ oxygens and y silicons (with a relation implied between x and y). Any given individual tetrahedron must be one of five kinds (*i.e.*, with $y = 0$, 1, 2, 3, or 4). The proportions of each of the five kinds are shown in Table I for different values of x in SiO_x. Considering only nearest-neighbor interaction, the chemical shift in the 2p level of a given silicon atom will depend on which of the five types of tetrahedron it has around it. It should be understood that the observed peaks represent a superposition of contributions from individual atoms, but that these contributions produce a single peak; the spectrometer does not resolve separate peaks from atoms in each type of tetrahedral coordination. The greater line width found in Fig. 5 with SiO as compared to SiO_2 is, for example, explained in that, in the former, all 5 tetrahedra are present, whereas only one type is present in SiO_2. Also, the shift for SiO will be expected to be less than of SiO_2, as we observed.

From the above theory it should be clear that homogeneous materials of formula SiO_x can be simulated, for the purposes of ESCA, by making heterogeneous mixtures of SiO_2 and "SiO" and hence varying the relative concentrations of each type of tetrahedron so as to produce an averaged peak corresponding to that given by any required homogeneous oxide with $1 < x < 2$.

Figure 6(a) and 6(b) shows the energy and width of the composite line observed with mixtures of various mole fraction χ of Linde "SiO." These confirm the direction of shift in peak energy and line width seen with the separate powders. The lines labeled "theory" in Fig. 6 were calculated for hypothetical SiO_x with x corresponding to a homogeneous oxide of the same over-all composition as our mixtures of "SiO" and SiO_2 The separation between "SiO" and SiO_2 was taken as 1.5 eV and the observed line widths for the separate powders were used together with the proportions of the types of tetrahedra from Table I.

Agreement between theory and experiment in Fig. 6 is substantially improved if the presence of elemental silicon in the Linde "SiO" is taken into account. Based on the height ratio of the two peaks in the "SiO" spectra of Fig. 5, it can be shown that the true values of χ_{SiO} for the mixture are ~20% lower than the values shown. With this correction, for instance, the mole fraction at which equal oxide signal magnitude are obtained from each component of the mixture is seen to be χ ~0.67 both experimentally and theoretically. It should be noted that this is greater than the value of 0.5 that might have been expected for such a condition if one assumed the "SiO" structure contained only a single tetrahedral form as is the case with SiO_2.

Oxide-coated wafers with graded oxide composition would give a line corresponding to some average composition of SiO_x where the averaging process would involve the escape depth. It can be inferred, therefore, from Fig. 4 that the outer 50Å of silicon oxide layers on silicon approaches SiO_2 in composition only for oxide thickness >50Å. The continuing presence at all thicknesses of a thin (15-20Å) transition layer at the oxide-silicon interface of "average" composition SiO

Table I. Proportion of 5 possible tetrahedron types in oxides of various Si to O atom ratios*

	SiO_2	$SiO_{1.5}$	SiO	$SiO_{0.5}$	Si
Si—(O_4)	1.0000	0.3164	0.0625	0.0039	0.0000
Si—(SiO_3)	0.0000	0.4219	0.2500	0.0469	0.0000
Si—(Si_2O_2)	0.0000	0.2109	0.3750	0.2109	0.0000
Si—(Si_3O)	0.0000	0.0469	0.2500	0.4219	0.0000
Si—(Si_4)	0.0000	0.0039	0.0625	0.3164	1.0000

* H. R. Philipp, *J. Phys. Chem. Solids*, 32, 1935 (1971).

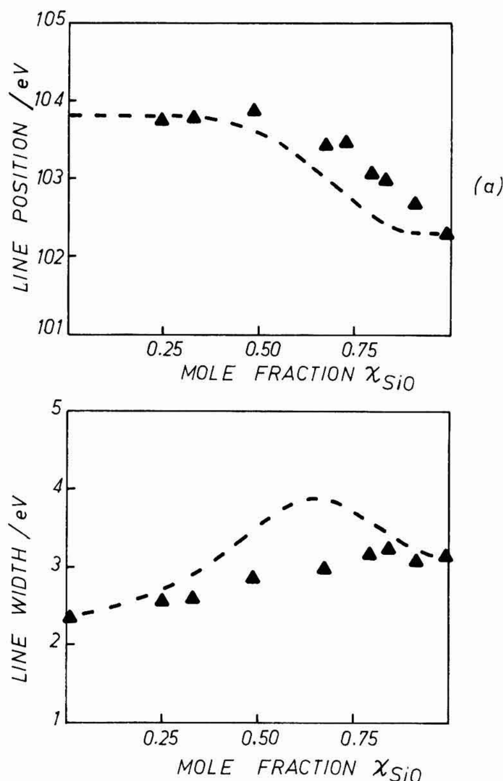

Fig. 6. Points are observed (a) peak energies and (b) line widths for mixtures of SiO and SiO_2 powders. Lines are calculated as discussed in text.

would account for energy shifts in the oxide peaks observed for oxides <50Å.

Conclusions

ESCA studies of the 2p electron spectral line of silicon atoms in thermally grown silicon oxides showed that the width and energy of this line varies with oxide thickness and oxidation ambient. For oxides less than 40Å in thickness, the width of the line increased and the binding energy decreased with decreasing film thickness and with increasing water vapor content in the oxidizing ambient. No effect was found of oxidation temperature and oxide thickness before etchback. Comparison between thermal oxide data and data obtained with mixtures of "SiO" and SiO_2 shows that the oxide at the interface of the Si-SiO_2 structure has the form SiO_x with x increasing from 1 to 2 with increasing distance from the silicon surface up to about 20Å. The transition region is thicker for the steam grown oxides but is of more uncertain Si:O ratio because of the probable presence in the oxide of OH or H_2O. The shifts in the peaks for oxides of different compositions were discussed using Phillip's model for the structure of oxides of the form SiO_x.

Acknowledgments

We thank Professors C. A. McDowell and D. Frost for the use of the ESCA system and for their interest and helpful comments. The work was supported by the CRC (DSS Contract Serial No. OSU4-0180) and the NRC of Canada. R. A. Clarke, R. L. Tapping, and M. A. Hopper thank the University of British Columbia for teaching Post Doctoral Fellowships.

Manuscript submitted Dec. 12, 1974; revised manuscript received April 21, 1975.

Any discussion of this paper will appear in a Discussion Section to be published in the June 1976 JOURNAL. All discussions for the June 1976 Discussion Section should be submitted by Feb. 1, 1976.

Publication costs of this article were partially assisted by the University of British Columbia.

REFERENCES

1. B. E. Deal and A. S. Grove, J. *Appl. Phys.*, **36**, 3770 (1965).
2. A. G. Revesz and K. H. Zaininger, *R C A Rev.*, **29**, 22 (1968).
3. T. W. Sigmon, W. K. Chu, E. Lugujjo, and J. W. Mayer, *Appl. Phys. Letters*, **24**, 105 (1974).
4. A. Benninghoven, *Surface Sci.*, **35**, 427 (1973).
5. A. Benninghoven and S. Storp, *Appl. Phys. Letters*, **22**, 170 (1973).
6. H. R. Philipp, *J. Phys. Chem. Solids*, **32**, 1935 (1971).
7. H. R. Philipp, *J. Appl. Phys.*, **43**, 2835 (1972).
8. C. J. Powell, *Surface Sci.*, **44**, 29 (1974).
9. R. Norberg, H. Brecht, R. G. Albridge, A. Fahlman, and J. R. Van Wazer, *Inorg. Chem.*, **9**, 2469 (1970).
10. D. J. Hnatowich, J. Hudis, M. L. Perlman, and R. C. Ragaini, *J. Appl. Phys.*, **42**, 4883 (1971).

Formation and Properties of Porous Silicon and Its Application

Y. Watanabe, Y. Arita, T. Yokoyama, and Y. Igarashi

Musashino Electrical Communication Laboratory, Nippon Telegraph and Telephone Public Corporation, Musashino-shi, Tokyo, Japan

ABSTRACT

Preparation, properties, and applications of porous silicon film were investigated. Silicon single crystal is converted into porous silicon film by anodization in concentrated hydrofluoric acid at currents below the critical current density. When an n-type silicon was anodized, the silicon surface was illuminated to generate holes which were necessary for this anodic reaction. The growth rate of the film, from n-type silicon, was larger than that from p-type silicon in this experimental condition. The crystalline structure was the same as that of silicon single crystal. A new isolation technique for bipolar integrated circuits was proposed by making use of the properties of the film such that it can be formed several microns thick and oxidized easily to form an insulator. The main feature of the technique is that it provides a means to form thick insulating film inlaid through the n-type epitaxial layer without prolonged heat-treatment. A preliminary experiment was carried out to test the practical usage of the technique.

With the increasing usage of silicon integrated circuits, their fabrication techniques have developed remarkably. However, many problems are left for each fabrication process. Improvement of the isolation process for bipolar integrated circuits is one of the most important and difficult problems. The conventional diffusion method for isolation has various parasitic effects. In addition, the spreading of the isolation region due to sideways diffusion limits the integration density.

Recently, many new structures for isolation have been proposed. Some of them have been considerably successful in avoiding the above mentioned effects. One typical example is the isoplanar technique, in which passive oxide layers are substituted for the usual diffused layers. In this partial oxidation method, however, prolonged heat-treatment is necessary to form thick silicon dioxide films. In the bipolar integrated circuits, the intense heat-treatment has serious problems. For example, when a buried collector exists, the additional diffusion of the buried impurities toward the surface may affect the breakdown characteristics of the fabricated devices.

The authors have also been investigating the isolation technique in silicon integrated circuits and have found a new technique (1) called the IPOS technique. IPOS is an abbreviation of insulation by oxidized porous silicon. The IPOS technique is roughly divided into two processes. The first one is a selective anodization of a silicon epitaxial wafer in hydrofluoric acid. The parts of silicon, where isolation layers are to be formed, are converted into porous silicon, which seems to be the same as the thick anode film reported by Turner and others (2, 3). The other process is a subsequent heat-treatment in oxidizing atmosphere. The porous silicon film can easily be oxidized to a thick insulating film because of its porosity and active nature. Through these processes, isolated islands of silicon single crystal, similar to those of the isoplanar technique, can be formed without long heat-treatment.

There are also two approaches in applying IPOS to the isolation of bipolar integrated circuits, namely n-type method and p-type method. They are shown in Fig. 1. In the former method, the n-type epitaxial layer is directly converted into porous silicon film under illumination. In the latter method, the film is anodized after acceptor diffusion is carried out, as in the usual diffusion isolation. Since the p-type silicon is anodized at lower forming voltage than n-type silicon, only the diffused p-type regions are converted without mask and illumination.

Key words: silicon, IC, porous, anodize, isolation.

This paper describes preparation, properties of the porous silicon film, and isolation process of the n-type method.

Experimental

Preparations and properties of porous silicon films.—Porous silicon films were prepared by anodization of the silicon single crystals in 48% concentrated hydrofluoric acid under constant current densities. The cathode was the platinum.

Since positive holes are necessary for the reaction to occur (2), hole generation was induced by xenon lamp illumination to anodize n-type silicon. The light intensities were 10 ~ 60 mW/cm^2. P-type silicon was anodized without illumination.

At first the growth rates of the porous silicon films were measured with respect to both p-type and n-type silicons. Next, measurements of apparent specific gravities by volumes and weights, observations of film structure by scanning electron microscope, and weight change measurements in an oxidizing atmosphere were performed.

Preparation of samples for testing isolation characteristics.—The structures of the sample is shown in Fig. 2. N on P silicon epitaxial wafers were used. The thicknesses of the n-type epitaxial layers and p-type substrates were, respectively, 2 ~ 4μ and 200μ, and the

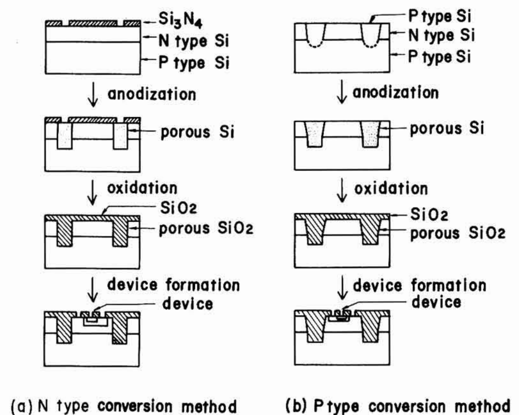

Fig. 1. Two IPOS processes

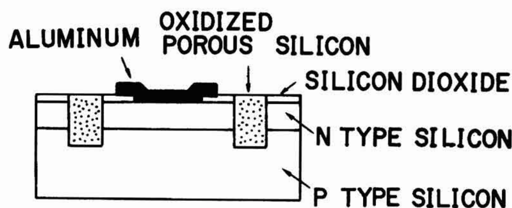

Fig. 2. Structure of the sample for measuring isolation characteristics.

resistivities of the former and the latter were 0.3 ohm-cm and 0.3 ~ 30 ohm-cm, respectively.

For selective formations of porous silicon films to make isolated islands, silicon nitride films were used as hydrofluoric acid-proof mask patterns. The 1500Å thick nitride films were deposited on the wafers by the vapor phase reaction of silane and ammonium, and then were partially removed by the usual photolithographic etch process. On anodization, the silicon portions, where the nitride films had been removed, were converted into porous silicon films.

In order to obtain films of uniform thickness, aluminum films were formed on the back of the wafers by vacuum evaporation to act as equipotential low resistivity contact layers. Moreover, acid-proof wax was coated over the aluminum films to prevent current flow from the films to hydrofluoric acid.

After anodization, wax, aluminum films, and nitride films were removed. The wafers were washed in hot phosphoric acid and boiled in water to improve the film properties. Subsequently, they were heated in a wet oxygen atmosphere to convert the porous silicon films into insulators. Heating was done for 30 min at 1100°C.

The above processes form islands of n-type epitaxial silicon, isolated from each other by the oxidized porous silicon and p-n junctions. Conventional silicon planar technology may then be applied to fabricate the integrated circuits. In this experiment, a metallization process was followed to make ohmic contact directly to the island for testing the isolation properties by the n-type method.

Electrical characteristics measurements.—To investigate the isolation characteristics of the samples, leakage currents and capacitances were measured. As the isolation characteristics in this case are reduced to those of the reverse biased mesa diodes, their d-c leakage currents and capacitances were measured. The frequency used for measuring the capacitances was 1 MHz. All measurements were made at room temperature.

Results and Discussion

Porous silicon film preparation and properties.—Figure 3 shows the relation between the growth rates and the anodizing current densities. The growth rates for n-type silicon were larger than those for p-type silicon for equal current densities.

Though the growth rates were not proportional to the current densities, the total amount of dissolved silicon was proportional to the total electric charge. On the other hand, the film thickness increased in proportion to the square root of the anodizing time. One of these relations is shown in Fig. 4.

The specific gravity of the porous film depends on the anodizing condition. Figure 5 shows the relation of the specific gravities and the current densities. In the case of p-type silicon, specific gravities decreased with current densities. For n-type silicon, however, maxima appeared at about 40 mA/cm² and they decreased with increasing light intensities.

Pore diameters at the sample surface were smaller than 10Å for both p-type and n-type silicon. Those of the inner part of the film were 10 ~ 10,000Å. A cross-sectional view of porous silicon prepared from n-type

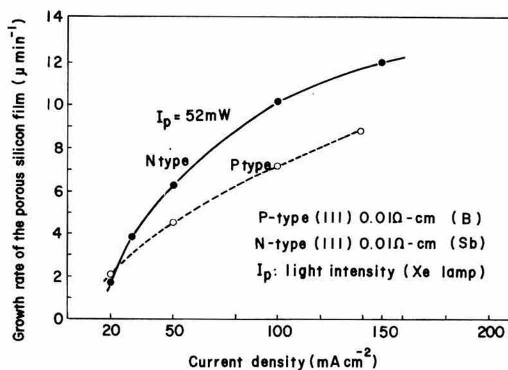

Fig. 3. Relation between growth rate and current density

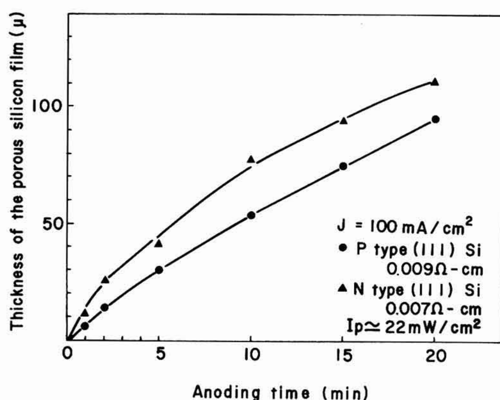

Fig. 4. Relation between the porous silicon thickness and anodizing time.

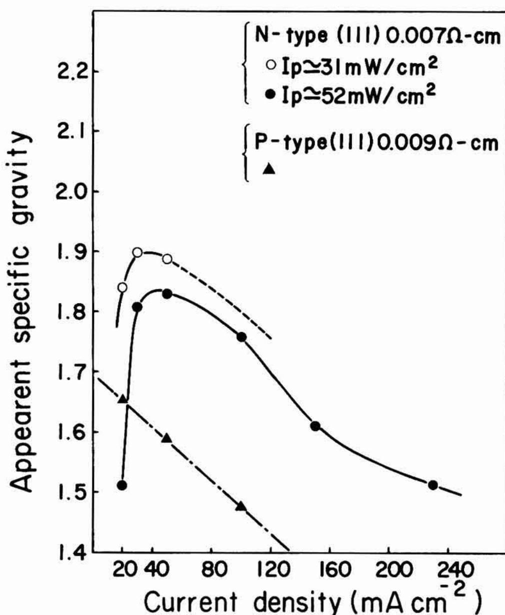

Fig. 5. Relation between apparent specific gravity and anodizing current density of porous silicon film.

silicon with low donor density at small current density is shown in Fig. 6. In this case, the pore diameter was about 1μ. At the surface of the film, however, the pores were very fine.

It is interesting that the crystal structure of the porous silicon was the same as that of the silicon single crystal. This fact was confirmed by x-ray diffraction and electron diffraction. The films are probably a mixture of the unreacted original silicon crystal and the silicon that was the product of the disproportionation reaction of silicon difluoride proposed by Turner (2).

The porous silicon is oxidized very rapidly in oxygen or steam at elevated temperatures. This was confirmed by infrared absorption spectrum and the weight change measurement. Figure 7 shows the relation between weight change of a wafer in which the porous silicon film was formed during oxidation in oxygen at 1000°C and the oxidation time. Most of the weight change occurred in a very short time and, thereafter, no remarkable change was found. This implies that the greater part of silicon in the film was oxidized within a few minutes. There are two reasons why the oxidation velocity is very large. One is the existence of many pores in the film; oxygen and steam can penetrate through the pores. The other is the nature of the film constituents.

Isolation processes.—Figure 8 shows a comparison of the original isolation pattern with the porous silicon pattern. Figure 8(a) is one of the original mask patterns. The width of the isolation zone is 6μ. Figure 8(b) is the porous silicon pattern formed using the above mentioned mask pattern. In this case, the thickness of the film was 6μ. It was observed that sideways spreading of the anodized zone occurred beyond the original zone. The ratio of the spreading width to the thickness of the porous film was about 7:10. This ratio was the same in other anodizing conditions and it is slightly smaller than that of the diffusion isolation.

A cross-sectional view of the isolation region is shown in Fig. 9. In this picture the nail-like line across the n-type layer is the isolation region. When the width of the isolation zone is large, the anodic reaction seems to proceed more rapidly at the edge of the region than at the inner part, due to the current concentration effect.

Current densities suitable for forming proper quality porous films were 200 ~ 400 mA/cm². Proper quality means that the films could be easily oxidized sufficiently deep compared with the thickness of the epi-

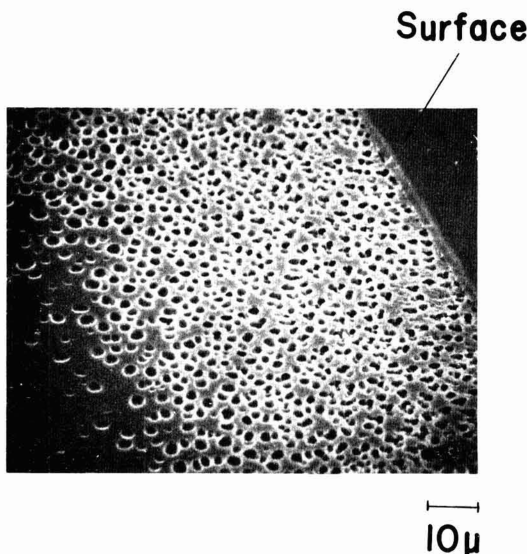

Fig. 6. Cross-sectional view of porous silicon film observed by SEM (×5000). Sample was bevelled at an angle of 5°.

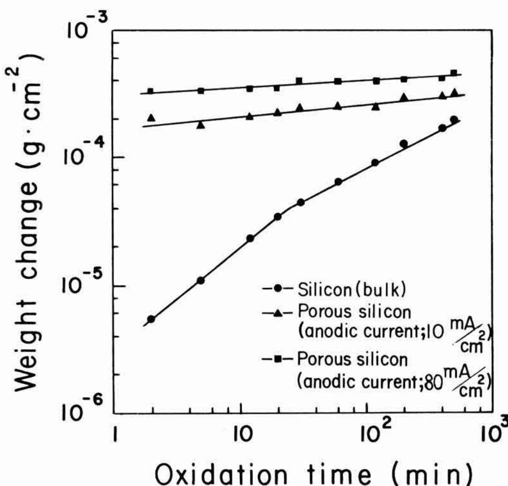

Fig. 7. Relation between weight change and oxidation time at 1000°C in wet oxygen.

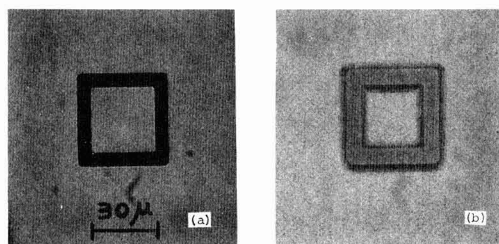

Fig. 8. Isolation pattern. (a) Original mask pattern. Isolation width, 6μ. Inside area, 900μ². (b) Porous silicon pattern formed by using a pattern (a). Thickness was 6μ.

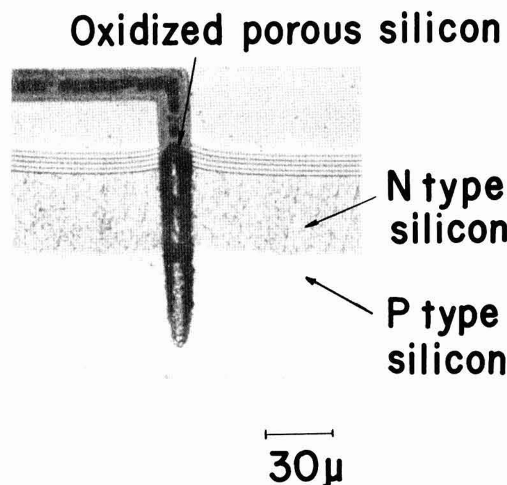

Fig. 9. Cross-sectional view of the isolation region bevelled at an angle of 5°.

taxial layers and have flat surfaces after the oxidation process.

Below 100 mA/cm^2 it was difficult to obtain films that were converted into a high resistivity insulator. This fact is probably in connection with the specific gravities and the pore diameters. On the other hand, at current densities over 500 mA/cm^2 peeling off of the oxidized film occurred and a large surface roughness was observed. In particular, it was marked at the edges of the isolation regions.

Heat-treatment in a wet oxygen atmosphere at 1100°C for 30 min was sufficient to make the porous film prepared at the above mentioned current densities insulating. Under this condition, silicon dioxide film of 0.5μ thick was grown on silicon single crystal. On the other hand, porous silicon films greater than 5μ thick were wholly oxidized as was verified by measurements of leakage currents. There was still slight unevenness at the surface of the oxidized porous silicon. Figure 10 shows a typical example of the surface observed by scanning electron microscopy. The unevenness was also measured by Talystep. It has been confirmed that the interconnecting metallization and photolithographic processes were not affected by this unevenness because their heights were less than 0.5μ and the slopes were gradual. When single crystal silicon is oxidized, the volume of the oxide is about two times that of the original crystal. In the case of the porous film, the ratio of the volume increase is very small because of the porous nature.

Electrical characteristics.—A typical current voltage relation between two islands is shown in Fig. 11. The apparent breakdown voltage was about 210V. This value was larger than that of the diffusion isolation whose breakdown voltage was about 60V, limited by the epitaxial layer resistivity. However, if the isolation process by the IPOS technique were successfully carried out, higher breakdown voltage determined by the resistivity of the substrate of the wafer should be realized. Accordingly, it is considered that the breakdown in this case occurred at the damaged p-n junction parts that were adjacent to the oxidized porous silicon. More detailed leakage current behavior of the same sample is shown in Fig. 12. The current was smaller than 1×10^{-8}A at applied voltages below 100V and increased gradually with increasing voltage. This value is slightly larger than that of diffusion isolation. Most of the leakage current was considered to flow at the same place where breakdown occurred. Leakage of this order does not prevent practical use of IPOS for bipolar integrated circuits. However, in the isolation of the MOS integrated circuits, smaller leakage currents are desired. It is probable that further reduction can be achieved by improving the fabricating processes.

Leakage currents were reduced with the reduction of substrate resistivities. For example, a sample with the substrate resistivity of 0.3 ohm-cm showed an order of 10^{-11}A at 10V.

The relation between capacitances and bias voltages of the sample was measured and the result is shown in Fig. 13. The capacitance was inversely proportional to the cube root of the voltage. This is the same relationship as that of the graded p-n junction. Figure 14 shows the capacitances of two different areas. These

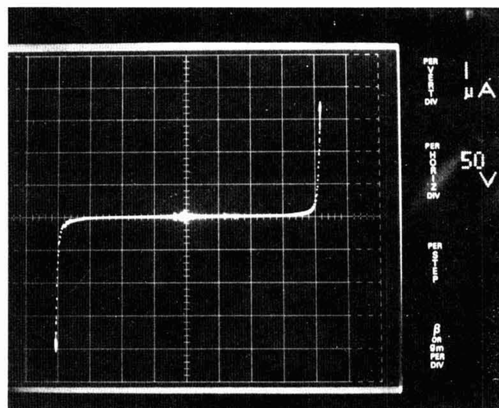

Fig. 11. Current/voltage relation between two islands. Epitaxial layer: 2μ, 0.3 ohm-cm, n-type. Substrate: 200μ, 30 ohm-cm, p-type.

Fig. 10. Surface of isolation region, observed by SEM

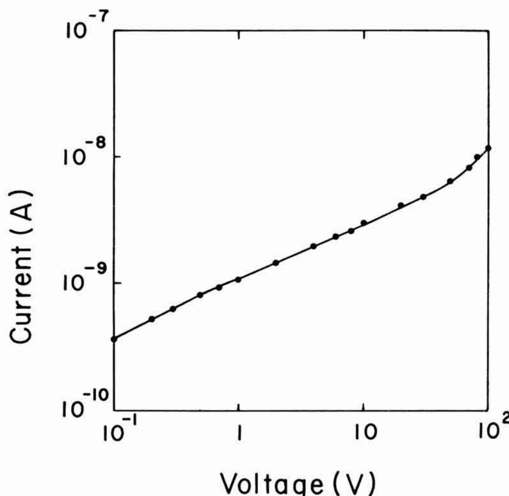

Fig. 12. Current/voltage relation between an island and substrate. Epitaxial layer: 2μ, 0.3 ohm-cm, n-type. Substrate: 200μ, 30 ohm-cm, p-type. Area of island: 10,000μ^2.

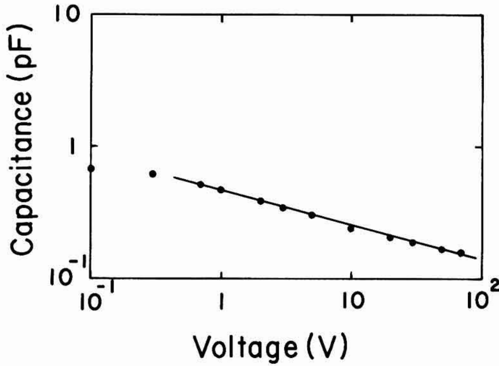

Fig. 13. Capacitance/voltage relation between an island and substrate. Epitaxial layer: 2μ, 0.3 ohm-cm, n-type. Substrate: 200μ, 30 ohm-cm, p-type. Area of island: 10,000μ^2.

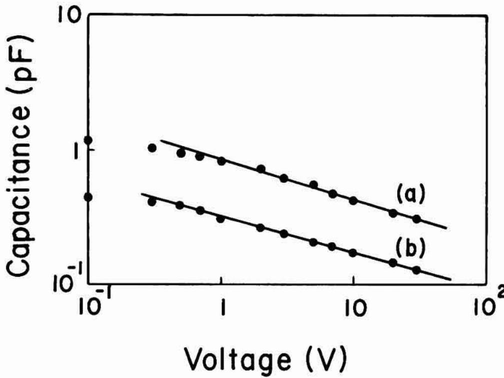

Fig. 14. Capacitance/voltage relations between an island and substrate. Epitaxial layer: 2μ, 0.3 ohm-cm, n-type. Substrate: 200μ, 5 ohm-cm, p-type. Area of islands: (a) 10,000μ^2, (b) 3600μ^2.

values agree exactly with the estimated values from the areas of the islands and the substrate resistivities.

From these data, the capacitances of the oxidized porous silicon layers can be considered negligible. It implies that the isolations of small capacitances can be realized using the IPOS technique because the isolation capacitances are only due to the p-n junctions between n-type epitaxial layers and p-type substrates.

As described above, the n-type method IPOS technique can be advantageously applied to bipolar integrated circuits isolation. Though the experimental result concerned only samples whose epitaxial layers were 2μ thick, the same results have also been obtained for those above 4μ thick.

Conclusion

A thick porous silicon film retaining a flat surface was prepared by anodization of silicon single crystal in hydrofluoric acid. The silicon surface was illuminated when the n-type silicon was anodized. The growth rate of the film from n-type silicon was larger than that from p-type silicon. Apparent specific gravity and pore diameter of the film on n-type silicon were affected by the current density and donor density. The crystalline structure of the film was the same as that of silicon single crystal.

The film was oxidized very rapidly in oxidizing atmospheres. A preliminary attempt was made to apply the porous silicon film to bipolar integrated circuits isolation. An oxidation step at 1100°C for 30 min was sufficient to make an insulating film 4μ thick. Small excess leakage current was observed in the sample. Capacitance/voltage relation was similar to that of a graded p-n junction, $C \alpha V^{-1/3}$.

The IPOS technique may be applicable to fabricating not only bipolar integrated circuits, but also MOS integrated circuits. Some problems still remain to be resolved. For example, a lower leakage current is desired for application to MOS devices.

Acknowledgments

The authors would like to thank Dr. T. Suzuki and Dr. K. Ono for their helpful guidance.

Manuscript submitted Oct. 31, 1974; revised manuscript received April 30, 1975. This was Paper 117 presented at the Boston, Massachusetts, Meeting of the Society, October 7-11, 1973.

Any discussion of this paper will appear in a Discussion Section to be published in the June 1976 JOURNAL. All discussions for the June 1976 Discussion Section should be submitted by Feb. 1, 1976.

Publication costs of this article were partially assisted by the Nippon Telegram and Telephone Public Corporation.

REFERENCES

1. Y. Watanabe and T. Sakai, *Rev. Elec. Commun. Lab.*, **19**, 899 (1971).
2. D. R. Turner, *This Journal*, **105**, 402 (1958).
3. A. Uhlir, *Bell System Tech. J.*, **35**, 333 (1956).

Temperature Dependence of Characteristics of Plastic Film Thermoelectrets

K. Ikezaki, K. Wada, and I. Fujita

Department of Instrumentation, Faculty of Engineering, Keio University, Yokohama, Japan

ABSTRACT

The initial charge and its decay characteristics of Teflon FEP thermoelectrets have been investigated at different polarizing and storage temperatures. The decay of the electrets strongly depends on the polarizing temperature T_p even when they are stored under the same conditions. For low polarizing temperatures, the initial charge is fairly large but it decreases as the polarizing temperature increases. After it reaches a minimum value at $T_p \simeq 100°C$, it increases again with T_p. On the other hand, for low T_p the residual charge which is measured 60 min after polarization, is small in spite of the fairly large initial charge and it increases with T_p. From these experimental results, it is concluded that the polarizing temperature plays an essential role for charge stability in electrets. Observed temperature dependence of the initial charge and its decay characteristics are discussed briefly.

Recently plastic film thermoelectrets have been investigated owing to the practical interest in the electret microphone (1). For several plastic film electrets, the time variation of the surface charge was studied as a function of the storage temperature for estimating the lifetime of electrets (2).

Usually, most of the values of surface charge densities reported in the literature are order of $10^{-9} \sim 10^{-10}$ coulomb/cm^2. In these electrets with relatively low charge densities, effects of molding and stripping charges also become important (3,4). In these electrets charge reversal often takes place. The effect of storage temperature on the charge reversal was investigated for various electret materials (5, 6). Pillai *et al.* (3,7) investigated the effect of polarizing temperature on initial charge and its decay characteristics for polyvinylchloride and polyvinylacetate electrets. The importance of polarizing temperature and electric field is also pointed out in the thermoelectrets of polyvinylchloride and polymethylmethacrylate (8). Recently, Perlman and Unger (9) studied the polarizing temperature effect on charge trapping in Teflon film electrets with the use of the thermally stimulated current technique (10). They reported that both molecular motion and thermal excitation are important for charge release. With the use of the thermally stimulated current technique, Takamatu and Fukada also studied the polarizing temperature effect (11, 12).

For practical purpose, however, it is desirable to produce electrets having large charge density, and to study forming conditions for good electrets is useful not only for deeper understanding of basic mechanisms of electret phenomena but also for practical application of electrets. To get a practical film electret with large homocharge, several techniques have been developed (2, 13, 14). In the present paper, initial charge and its decay characteristics are studied in thermoelectrets of Teflon FEP film which are polarized at various polarizing temperatures with use of the technique of dielectric insert (14).

Experimental

The electret material used in this investigation is a film of Teflon FEP (copolymer of tetrafluoroethylene and hexafluoropropylene) of 12μ in thickness. A film sample and a disk of soda glass (0.75 mm thick) metallized on one face were placed between brass electrodes of a polarizing holder. As shown in Fig. 1, this glass disk was inserted between the sample and the negative electrode in order to obtain an electret with a large homocharge without arcing during the polarization process (14).

Electrets were obtained as follows: a sample was heated to a polarizing temperature T_p and then a polarizing voltage V_p (800V) was applied across the electrodes. After 10 min under the electric stress at the temperature of T_p, the sample was cooled down to room temperature under the same electric stress. The cooling process took about 40 min. In order to exclude a confusing contribution of unstable charges which stay on the surface of electrets, after polarization all electrets were kept for 5 min between brass electrodes short-circuited, and then the net surface charges were measured by the vibrating electrode method developed by Reedyk and Perlman (15). The decay characteristics of the surface charges for various storage temperatures were observed as a function of storage time t_s by measuring the surface charges of electrets which were stored in free (unshort-circuited) at a temperature of T_s.

Results

The time variations of the surface charge were investigated for the samples which were polarized at various temperatures. Since the decay of the charge on the anode surface of the sample was almost the same as that of the cathode except for some irregular behavior, the charge on the cathode surface was chiefly investigated.

The net surface charge observed in this study was a homocharge and the charge reversal did not take place.

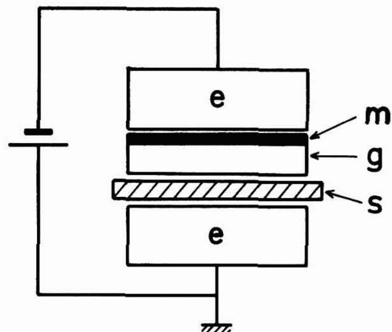

Fig. 1. Electrode assembly. e, Brass electrode; g, glass disk; m, metal layer.

Key words: Teflon FEP, polarizing temperature, initial charge, residual charge.

Observed values of the initial surface charge scattered from sample to sample even when the electrets were produced under the same conditions, and the electrets slightly differed in their decay characteristics. Therefore, normalized decay curves were determined from the several measurements as shown in Fig. 2. For various polarizing temperatures, the normalized decay curves are shown in Fig. 3 and 4. As is seen from these figures, the decay characteristics of Teflon FEP electrets are nonexponential and they strongly depend on T_s and T_p. Mean values of the initial charge densities on the anode and cathode surfaces, $\sigma_+(0)$ and $\sigma_-(0)$, and their mean errors are presented in Fig. 5. Their values were determined by taking averages of 12-34 samples which were polarized under the same conditions (12 samples for $T_p = 60°C$, 34 for $T_p = 80°C$, 26 for $T_p = 110°C$, 25 for $T_p = 140°C$, and 14 for $T_p = 180°C$). In Fig. 5, the values of $\sigma_-(60)$ defined as residual charge on the cathode surface after storage of 60 min at T_s, are also plotted against T_p for various storage temperatures. These values of the residual charge were determined from the mean values of $\sigma_-(0)$ and the normalized decay curves.

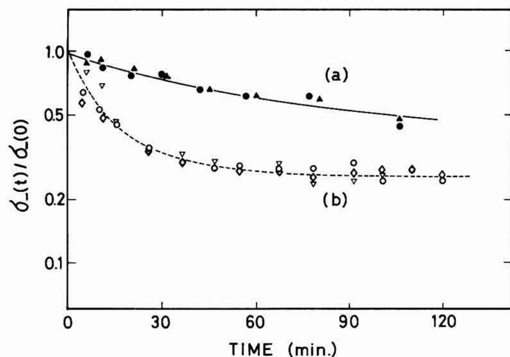

Fig. 2. Normalized decay curve of surface charge on the cathode side of Teflon FEP thermoelectrets. Curve (a), $T_p = 180°C$, $T_s = 100°C$ $V_p = 800V$. Curve (b), $T_p = 60°C$, $T_s = 80°C$, $V_p = 800V$.

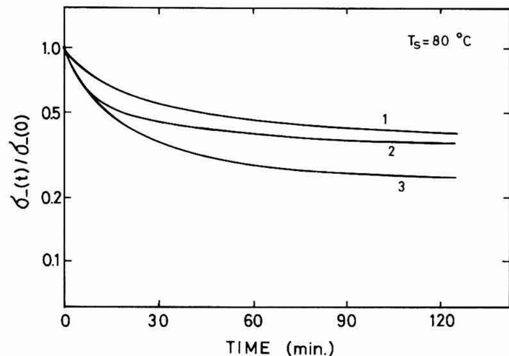

Fig. 3. Normalized decay curves of surface charge on the cathode side of Teflon FEP thermoelectrets stored at 80°C. Curve 1, $T_p = 140°C$; curve 2, $T_p = 80°C$; curve 3, $T_p = 60°C$.

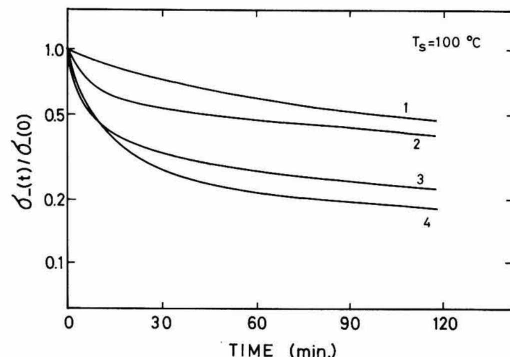

Fig. 4. Normalized decay curves of surface charge on the cathode side of Teflon FEP thermoelectrets stored at 100°C. Curve 1, $T_p = 180°C$; curve 2, $T_p = 110°C$; curve 3, $T_p = 80°C$; curve 4, $T_p = 60°C$.

Discussion

In electrets there are two kinds of surface charge (16), a homocharge and a heterocharge. The heterocharge is due to the volume polarization and it decays more rapidly as compared with the homocharge in many electrets (17). The electrets which are produced with a suitable dielectric insert as in this study, have a large homocharge (2, 13, 14). This homocharge is thought to be due to the discharge in the air gap between the sample and the polarizing electrodes (18-22). The charge produced by this discharge is then trapped by the various trapping sites in the sample. In real electrets there are many kinds of traps. The kinds of traps and the trap densities depend on several factors such as the physical and chemical properties of the material used and the polarizing conditions of electrets. In addition to these facts, in real electrets the heterocharge may be present. Therefore, the decay characteristics of the surface charge become complicated and cannot be expected to obey strictly a simple exponential function. In many electrets, however, the decay form is found to be quasiexponential: After decay has taken place for some time, the subsequent decay can be expressed by a simple exponential curve (17).

For our Teflon FEP electrets, it is found from Fig. 2-4, that the decay curves of the surface charge consist of two components: an initial fast decay component and the subsequent, slow and somewhat exponential component. Similar decay curves have been reported in the electrets with high homocharge (2, 13). As is

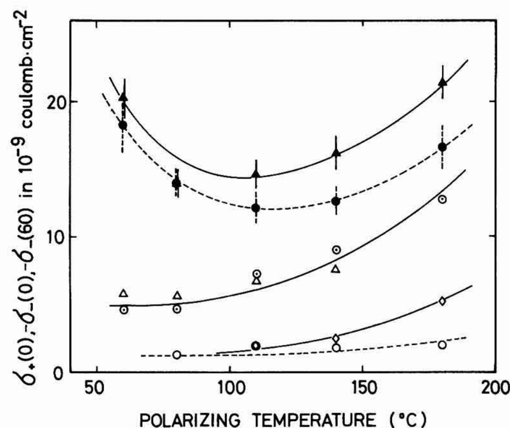

Fig. 5. Effect of polarizing temperature on the initial and residual surface charge densities of Teflon FEP thermoelectets. ●, $\sigma_+(0)$; ▲, $\sigma_-(0)$; △, $\sigma_-(60)$ at $T_s = 80°C$; ⊙, $\sigma_-(60)$ at $T_s = 100°C$; ◇, $\sigma_-(60)$ at $T_s = 120°C$; ○, $\sigma_-(60)$ at $T_s = 150°C$; where, $\sigma_+(0)$ and $\sigma_-(0)$ are initial charge densities on the anode and the cathode surfaces, respectively, and $\sigma_-(60)$ is residual charge density on the cathode surface which is measured after storage of 60 min at various storage temperatures.

seen from Fig. 2-4, relative values of these components vary depending on T_s and T_p. In general, the fast component is more remarkable in electrets polarized at low T_p and stored at high T_s than in electrets polarized at high T_p and stored at low T_s. This T_p-dependence of the charge trapping was recently investigated by Perlman and Unger (9). They observed that the curves of thermally stimulated currents in electro-electrets of Teflon vary depending on the polarizing temperature and the current spectra shift toward higher temperature with increasing sample temperature during polarization. This peak shift in thermally stimulated current spectra was also observed by Takamatu and Fukada (11, 12). They found that there are two kinds of peaks in thermally stimulated current spectra in polyvinylidenfluoride, polyethylene, and polytetrafluoroethylene thermoelectrets. For one kind of peaks, the peak position does not depend on polarizing temperature and it locates at low temperatures (most of these peaks appear below 0°C). For the other kind of peaks, the peak position is T_p-dependent and peaks appear at the temperature several degrees higher than that of polarizing temperature. From these facts it is suggested that polarizing temperature plays an essential role for charge trapping in electrets.

Figure 5 shows T_p-dependence of the initial charges. It is almost the same on both anode and cathode sides but the surface charge on the cathode side is slightly larger. In Teflon FEP electrets, negative charges seem to be more stable than the positive. The initial charges on both sides have large values for low T_p and they decrease as T_p increases. After the charges have minimum values at $T_p \simeq 100°C$, they increase again with T_p and have large values for high T_p. On the other hand, the residual charge becomes large with increasing T_p.

In our electrets, the homocharge is thought to be produced by the following process (18, 19): Applying a voltage between electrodes increases the field in the air gap. Eventually, this field will exceed the breakdown strength of the air gap and the spray discharge will occur. The homocharge deposition by this spray discharge continues until the surface density of the deposited charge attains a certain threshold value which reduces the field in the gap below breakdown and quenches the discharge. In order to discuss qualitatively the observed T_p-dependent initial charges and their decay characteristics, we make an assumption for simplicity that there are two kinds of charge traps in our electrets, low energy traps and relatively deep traps. Then, a part of the homocharges produced by the spray discharge is held in the two kinds of traps, σ_1 in shallow traps and σ_2 in deep traps. The remainder of the spray charges contributes to a forming current or to an unstable charge σ_0 which stays on the surface of the sample and easily escapes while the electret is kept for 5 min between the electrodes short-circuited or handled prior to measurements. Since the quenching of the discharge in the air gap is determined only by the threshold value of the deposited charge and it does not depend on the kind of traps in which the charge falls, just after polarization the total value of $\sigma_0 + \sigma_1 + \sigma_2$ is thought to be constant and independent of T_p as long as the polarizing voltage remains constant.

Observed T_p-dependent behavior of the electrets is explained as follows on the basis of an idea that the relative values of σ_0, σ_1, and σ_2 vary depending on T_p.

For electrets polarized at low temperatures, the charge trapped in the shallow traps predominantly contributes to the initial charge. Therefore, at high storage temperature the detrapping rate from the shallow traps is large and the surface charge rapidly decreases in the initial part of the decay. In this case the residual charges are small in spite of the large initial charge.

For electrets polarized at high temperatures, emission probability from the shallow traps increases and the equilibrium net trapping rate by the shallow traps decreases. For this reason the unstable charge σ_0 may be large and the initial charge becomes small.

When the polarizing temperature T_p is much higher, the contribution from the charge held in the shallow traps becomes smaller and smaller due to increase of detrapping probability, but the charges released from the shallow traps migrate much more easily at high T_p and are retrapped more easily by the deeper traps. As a result, the charge held in the deep traps contributes much more to the threshold charge density which quenches the spray discharge. Therefore, the initial charge becomes large again and the residual charge also increases with T_p. In this case the initial rapid decay is not observed.

The charge retrapping was reported by Sessler and West (13). From analysis of thermally stimulated currents, they found that charges in polyethyleneterephthalate and Teflon FEP electrets are subjected to considerable retrapping. This charge retrapping is also supported from the following experiment. Two kinds of electrets were polarized under the same V_p and T_p but different polarizing time t_p, 3 hr and 10 min, respectively. Figure 6 shows charge decay curves of these electrets. As is seen from Fig. 6, the initial charge of the electrets polarized with applying V_p for 3 hr is larger than the electrets polarized with applying V_p for 10 min, and these two kinds of electrets show quite different decay characteristics. In the electrets with t_p of 3 hr, no initial rapid decay is observed and the residual charge is larger. As the polarizing time increases, emitted charges from the shallow traps have much more chance to be retrapped by the deeper traps, so that the unstable component σ_0 decreases and the ratio of σ_2 to σ_1 becomes large even when the values of V_p and T_p are kept constant. This results in a larger initial charge and no initial rapid decay, as is found for the electrets with a long t_p in Fig. 6.

Although the detailed natures of the two kinds of traps are not clear at this stage, the charge σ_1 may be loosely bound on the surface of an electret and decay chiefly by surface recombination. On the other hand, it is found from Fig. 5 that, when T_s is 120° or 150°C, the values of the residual charges decrease abruptly in comparison with the cases of T_s = 80° and 100°C. This suggests that the deep traps may be associated with the motion of the main chain of Teflon FEP because the glass transition temperature of the film is about 130°C (23).

Summary

The observed results are summarized as follows.

1. The initial charge density and its decay charac-

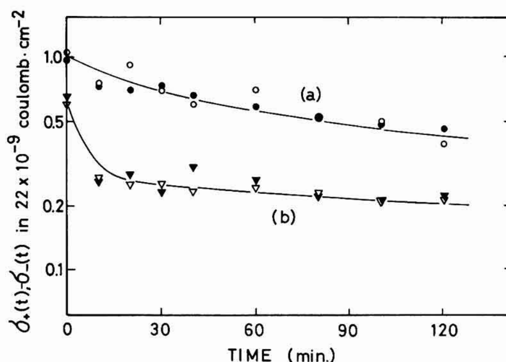

Fig. 6. Effect of polarizing time on charge decay of Teflon FEP thermoelectrets (average over 3 electrets). The storage temperature T_s is 100°C. Curve (a), t_p = 3 hr, T_p = 75°C, V_p = 800V. Curve (b), t_p = 10 min, T_p = 75°C, V_p = 800V. ○, ▽, Surface charge densities on the anode surface. ●, ▼, Surface charge densities on the cathode surface.

teristics of Teflon FEP thermoelectrets strongly depend not only on the storage temperature but also on the polarizing temperature.

2. The decay curves of the electrets are nonexponential and they consist of two components, a fast decay component and a slow component.

3. For electrets polarized at relatively low T_p, the fast decay component becomes remarkable. In this case the surface charge is predominantly held in shallow traps and the residual charge density is small in spite of its large initial charge density.

4. As the polarizing temperature increases, the initial charge density decreases and it has a minimum value when the polarizing temperature is around 100°C.

5. For electrets polarized at T_p higher than about 100°C, the relative amount of the charge trapped by deep traps becomes large, and both initial and final charges increase with T_p.

6. To get a stable electret, the polarizing temperature should be high enough to produce many deep trapping sites and the polarizing time should be long enough for charge retrapping by deeper traps.

Acknowledgment

The authors wish to thank Messrs. J. Nakamura, K. Okazaki, and Y. Suzuki of the Research and Development Department, Aiwa Company, Limited for their technical help.

Manuscript submitted Oct. 15, 1974; revised manuscript received April 30, 1975.

Any discussion of this paper will appear in a Discussion Section to be published in the June 1976 JOURNAL. All discussions for the June 1976 Discussion Section should be submitted by Feb. 1, 1976.

Publication costs of this article were partially assisted by Keio University.

REFERENCES

1. G. M. Sessler and J. E. West, *J. Acoust. Soc Am.*, **40**, 1433 (1963).
2. M. M. Perlman and C. W. Reedyk, *This Journal*, **115**, 45 (1968).
3. P. K. C. Pillai, V. K. Jain, and G. K. Vig, *ibid.*, **116**, 836 (1969).
4. G. G. Wiseman and G. R. Feaster, *J. Chem. Phys.*, **26**, 521 (1957).
5. B. Hilczer, B. Blaszyk, and S. Goderska, *Phys. Status Solidi*, **23**, 419 (1967).
6. J. Handerek and R. Wilk, *Acta Phys. Polon.*, **29**, 623 (1966).
7. P. K. C. Pillai and V. K. Jain, *J. Phys. D., Appl. Phys.*, **3**, 829 (1970).
8. M. Latour, *Compt. Rend.*, **272**, *serie B*, 469 (1971).
9. M. M. Perlman and S. Unger, *Appl. Phys. Letters*, **24**, 579 (1974).
10. C. Bucci, R. Jieschi, and G. Guidi, *Phys. Rev.*, **148**, 816 (1966).
11. T. Takamatu and E. Fukada, *Rept. Inst. Phys. Chem. Res. (Tokyo)*, **45**, 1 (1969).
12. T. Takamatu and E. Fukada, *ibid.*, **45**, 73 (1969).
13. G. M. Sessler and J. E. West, *J. Appl. Phys.* **43**, 922 (1972).
14. K. Ikezaki, I. Fujita, K. Wada, and J. Nakamura, *This Journal*, **121**, 591 (1974).
15. C. W. Reedyk and M. M. Perlman, *ibid.*, **115**, 49 (1968).
16. B. Gross, *Phys. Rev.*, **54**, 57 (1940).
17. H. J. Wintle, *J. Acoust. Soc. Am.*, **53**, 1578 (1973).
18. B. Gross, *J. Chem. Phys.*, **17**, 886 (1949).
19. B. Gross, *Brit. J. Appl. Phys.*, **1**, 259 (1950).
20. J. W. Wild and J. D. Stranathan, *J. Chem. Phys.*, **27**, 1055 (1957).
21. R. A. Draughn and A. Catlin, *This Journal*, **115**, 391 (1968).
22. J. Roos, *J. Appl. Phys.*, **40**, 3135 (1969).
23. Plastic Handbook, S. Maruhashi, R. Oda, and M. Imoto, Editors, p. 461, Asakura shoten, Tokyo (1969).

The Formation and Structure of Anodic Films on Beryllium

M. T. Shehata* and Roger Kelly*

Institute for Materials Research, McMaster University, Hamilton, Ontario, Canada, L8S 4M1

ABSTRACT

The present, as well as previous, work on the anodizing of Be confirms that most electrolytes yield films characterized by one or more of being porous, being subject to extensive dissolution, or being crystalline. This includes electrolytes based on the following: aqueous KOH, a CrO_3-HNO_3 mixture, aqueous Na_2CO_3, $(C_2H_5)_2HPO_4$, a $(C_2H_5)_2SO_4$-H_2SO_4 mixture, acetic acid. Significantly different results are obtained with ethylene glycol which is saturated with Na_2HPO_4 or KH_2PO_4 or both Na_2HPO_4 and Na_2SO_4. The films are then nonporous, as shown by scanning electron microscopy. They are formed with negligible dissolution, as follows by implanting the Be with 30-keV Kr^{85} before anodizing and noting the loss of activity during anodizing. They are nominally amorphous, as inferred by reflection electron diffraction, though crystallize to hexagonal BeO at a temperature lying somewhere below 300°C. It will be shown in a subsequent paper that the films formed in an ethylene-glycol-based electrolyte can be quantitatively removed and that Be can therefore be microsectioned.

Anodic films on metals are often classified as porous or nonporous. Nonporous films, which are the more usual, are normally found to form in electrolytes in which the oxide has a low solubility, and to grow until they reach an almost limiting thickness which, for a given time scale, is proportional to the applied potential. They are characterized by a high resistivity and by conduction which is mainly ionic in character. Nonporous films are often amorphous though there are many exceptions, including Sn (1) and Zr (2, 3) in general and Mo (4), Ta (4, 5), Ti (3, 5), U (6), V (4), and W (4) under particular conditions.

On the other hand, electrolytes in which the oxide is somewhat soluble are occasionally found to support the growth of porous films which increase more or less indefinitely in thickness while the applied potential varies slightly or not at all. They are characterized by a low resistivity. Though normally described as "crystalline," they are variously amorphous [Al anodized at room temperature (5)] or crystalline [Be (7, 8), probably Sn (9, 1)].

* Electrochemical Society Active Member.
Key words: beryllium, anodization, thin films, anodic sectioning.

Films formed on Be have invariably been found to show one or more of the characteristics of a porous film. Thus no films at all were obtained with some dilute aqueous electrolytes (7, 8). Those formed with HNO_3, CrO_3, or mixed CrO_3-HNO_3 were crystalline (7, 8) and had thicknesses up to ~400 nm (7) or more (10). Those formed with ammonia in ethylene glycol appeared to have had a low resistivity and to have been subject to dissolution (7, 8), while use of 0.5M Na_2CO_3 resulted in crystalline films (11).

The object of the present work was to attempt to form anodic films on Be which, unlike those of previous work, were simultaneously nonporous, formed with minimal or no dissolution, and nominally amorphous. This goal was achieved, such that films could be formed under conditions when the potential drop across the film was about 19×10^8 V/m and the efficiency at 30V for fixed current was 0.95 ± 0.02. Beryllium can thus be made to anodize in a similar manner as with most other metals (Table I). The formation of such films is in principle of importance in the understanding of anodic oxidation from an electrochemical point of view, but we regard it of greater interest to work on diffusion or on ion-solid collisions. It leads first of all to a microsectioning technique, thence to the possibility of studying diffusion and ion depth distributions in Be (12). It leads secondly to the possibility of studying secondary particle emission from BeO in a manner similar to what was done with Al_2O_3 (13).

Experimental

The specimens used throughout this work were polycrystalline Be foils with dimensions of approximately $25 \times 12.5 \times 0.25$ mm and with purities claimed to be 99.5%. They were obtained from Ventron Corporation (Alpha Products). After an initial polishing with a series of increasingly fine SiC papers, the specimens were given further treatment consisting either of chemical polishing [in 5 weight per cent (w/o) sulfuric acid, 75 w/o phosphoric acid, 7 w/o chromic acid, and 13 w/o water] or else of mechanical polishing using 6 μm and 1 μm diamond paste with kerosene as a lubricant. For experiments where reproducible flat surfaces were required, the specimens were finally anodized and sectioned 5 times. The anodizings were carried out at 50V in ethylene glycol which is saturated in both Na_2HPO_4 and Na_2SO_4 and will be subsequently called "electrolyte A." The sectionings were accomplished by exposing the films to 10% KOH for 1 min (12). Such treatment may be assumed to remove submicroscopic irregularities, though this matter will be investigated explicitly in work now underway.

All anodizings were performed at room temperature (~22°C) using a power supply such that limits to both the current and potential could be preset (Hewlett-Packard Model 6186B). The cathode was made of platinum gauze in the form of a cylinder with an inside diameter of 25 mm. Potentials refer to the total value from anode to cathode rather than to the value across the oxide film. For electrolyte A and a current of 3 mA/cm^2 these values differ by ~5V (as determined using a Ni wire near the Be as a probe), though with none of the results to follow is this of importance. The anodizings were carried out in unstirred electrolytes and without protection from air, and the electrolytes were therefore discarded after 5 or 6 anodizings or 1 hr, whichever came first.

The extent of metal dissolution during anodizing was determined using a depth-distribution technique due to Giani (1). Kr^{85}, which is beta-active, was implanted in Be at 30 keV to a dose of 2×10^{15} $ions/cm^2$, and the activity was noted before and after anodizing. The experimental depth distribution of such an implant is shown in Fig. 1 (12) and enables the retained activity fraction to be expressed as a depth. Such a depth is a lower limit to the metal loss during anodizing the lower-limit aspect entering due to the possibility of film formation by outward migration of Be, thence to a burying of the marker in the manner shown by Pringle (14) for Ta.

Table I. Comparison of fields and efficiencies for anodizing various metals

Metal	Electrolyte	Field to form a 50-V film (10^8 V/m)	Efficiency at constant current of 2 or 3 mA/cm^2	Ref.
V	Mainly acetic acid	2.8	0.95	19, 23
Mo	Mainly acetic acid	2.9	0.95	17, 23
Nb	Aqueous	3.4	~1.0[a]	16, 24
Zr	Aqueous	4-6	0.50	25
W	Mainly acetic acid	4.6	0.96	16, 23
Ta	Aqueous	6.2-6.6	0.99	20
Al	Aqueous	8.7-9.1	0.90	20
Be	Electrolyte A	19.0	0.95 ± 0.02	here, Eq. [1]

[a] Not for constant current.

Results

Dilute aqueous electrolytes.—It was concluded by Levin (8) that no film at all is formed on Be in 1% H_2SO_4 or 1% KOH, though 1% HNO_3 led to crystalline BeO if the current density was high enough. Survey experiments undertaken in the course of the present work have largely confirmed these results, except for an indication of film formation with 1% KOH. This follows from the *V-t* and *I-t* behavior (Table II).

To provide new information on the use of dilute aqueous electrolytes the depth-distribution technique was applied. Unacceptable extents of metal dissolution during anodizing were revealed (Table II).

CrO_3-HNO_3.—A CrO_3-HNO_3 mixture consisting of 200 g/liter of CrO_3 in 10% HNO_3 is known to yield crystalline films with Be which grow in thickness linearly with time while the current remains constant (7,8). Anodic films have also been obtained using as electrolyte 20% aqueous CrO_3 (10, 15). The results were interpreted in terms of the initial formation of a nonporous layer of small but constant thickness fol-

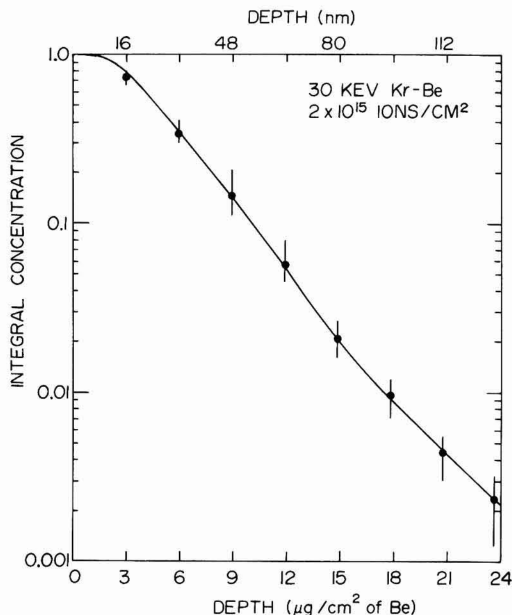

Fig. 1. Integral depth-distribution curve for 30-keV Kr in polycrystalline Be as determined by anodic sectioning (12). Such a curve enables retained activity fractions, *i.e.*, integral concentrations, to be expressed as depths.

Table II. V-t behavior, I-t behavior, and dissolution for the anodization of Be
(Present potential 30V with 1% KOH, 50V otherwise)

Electrolyte	Final potential (V)	Time to reach preset potential (min)	Initial current (mA/cm^2)	Final current (mA/cm^2)	Total anodizing time (min)	Fraction of Kr implant which is retained	Inferred loss of Be[b] (nm)
1% H_2SO_4	~0	Never	20	20	5	<0.003	≥120
1% HNO_3	~3	Never	20	20	5	0.15 ± 0.01	≥50
1% KOH	30	4	20	3	10	0.07 ± 0.02	≥60
CrO_3-HNO_3 mixture	~3	Never	30	30	2	0.19 ± 0.05	≥40
0.5M Na_2CO_3	50	6	10	0.4	15	0.13 ± 0.03	≥50
$(C_2H_5)_2HPO_4$	50	14.5	5	4.5	20	<0.01	≥90
$(C_2H_5)_2SO_4$-H_2SO_4 mixture	50[a]	0.3[a]	20	~20	10	<0.01	≥90
Mainly acetic acid	50	0.5	10	1	15	0.06 ± 0.01	≥60
Electrolyte A	50	0.3	3	10.35	1.5	0.986 ± 0.006	≥1

[a] The voltage rose to 50V in 0.3 min and then fell slowly to 30V by 10 min.
[b] Deduced from the preceding column with the help of Fig. 1.

lowed by a thick film which could be shown to be porous.

We have undertaken a limited number of additional experiments using the CrO_3-HNO_3 electrolyte of Ref. (7, 8). The *V-t* behavior, as shown in curve A of Fig. 2 and also in Table II, suggests (though does not prove) that thick, porous films are formed. The extent of porosity was investigated explicity by means of scanning electron microscopy. The results, given in Fig. 3 show clearly the porous nature of the films, the scale of the porosity being 100-1000 nm. The extent of metal dissolution during anodizing was determined by the depth-distribution technique and found to be significant (Table II)).

In conclusion, the anodic films formed on Be with the CrO_3-HNO_3 electrolyte of Ref. (7, 8) have none of the properties which were desired regarding porosity, dissolution, and structure.

Na_2CO_3.—Heusler (11) was able to form films on Be with an electrolyte consisting of 0.5*M* Na_2CO_3. The films were crystalline, could be formed up to a thickness of ~250 nm (at 200V), and were accompanied by oxygen evolution.

We have sought to obtain additional information on the use of 0.5*M* Na_2CO_3. The *V-t* and *I-t* behavior, as shown in curve B of Fig. 2 and also in Table II, suggests (though does not prove) that nonporous films result. The extent of porosity was again investigated by scanning electron microscopy. The results, given in Fig. 4, show that the films are mainly nonporous, but with evidence for both local and general dissolution. Metal dissolution during anodizing occurred to a significant extent (Table II).

The use of 0.5*M* Na_2CO_3 as the electrolyte for anodizing Be is thus unsatisfactory in the present context for two reasons: the dissolution and the crystallinity. Porosity, on the other hand, is not a problem.

Nonaqueous electrolytes.—An indication that nonaqueous electrolytes may be of interest with Be is found in work by Kerr and Wilman (7). They established, using a 25 g/liter solution of ammonia in ethylene glycol, that 30 nm thick amorphous films could be

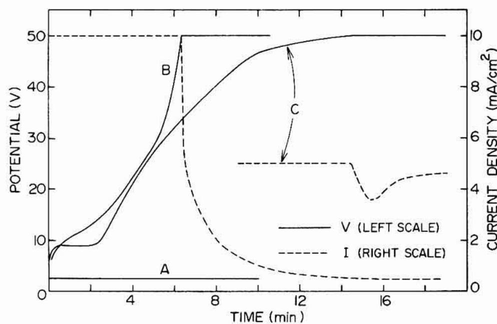

Fig. 2. Typical *V-t* and *I-t* curves for the anodization of Be in CrO_3-HNO_3 (curve A, always 30 mA/cm^2), 0.5*M* Na_2CO_3 (curve B), and $(C_2H_5)_2HPO_4$ (curve C). Solid lines: *V-t*, with potential as in scale at left. Dashed lines: *I-t*, with current as in scale at right.

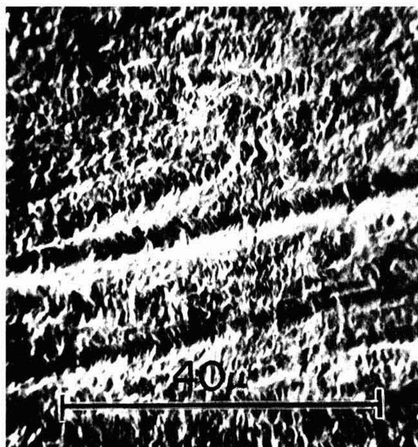

Fig. 3. Scanning electron micrographs with different magnifications of film formed by anodizing Be in CrO_3-HNO_3 for 2 min at 30 mA/cm^2. The films are markedly porous, the scale of the porosity being 100-1000 nm.

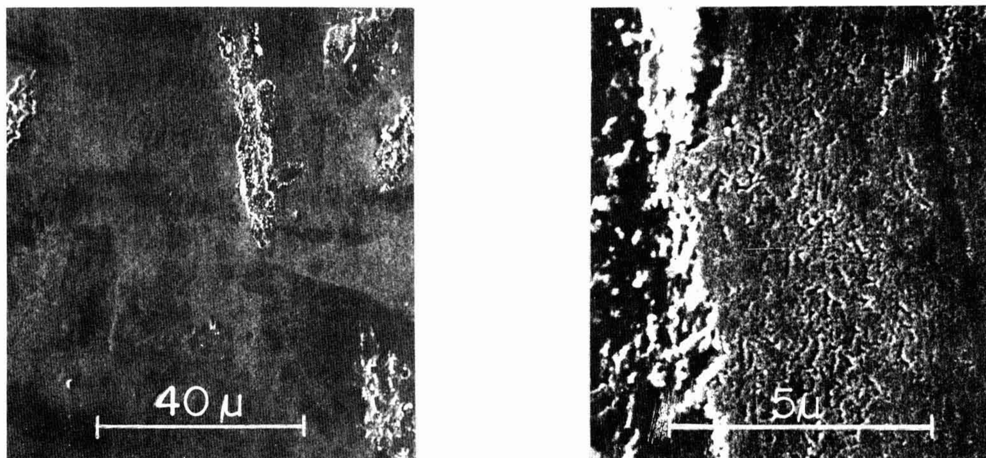

Fig. 4. Scanning electron micrographs with different magnifications of film formed by anodizing Be in 0.5M Na_2CO_3 for 15 min with a preset current of 10 mA/cm^2 and a preset potential of 50V. The films are mainly nonporous, though show features suggestive of both local and general dissolution.

formed. Unfortunately, the current remained roughly constant, as if the films were not insulating or alternatively were dissolving.

In the present work we have investigated nonaqueous electrolytes of four types.

(i) $(C_2H_5)_2HPO_4$. Anodizing Be in diethyl phosphate results in a *V-t* curve suggestive of a nonporous film but an *I-t* curve leading to the converse conclusion (curve C of Fig. 2 and also Table II). To gain further information, the extent of metal dissolution during anodizing was determined and found to be unacceptably high (Table II).

(ii) $(C_2H_5)_2SO_4$-H_2SO_4. A mixture of 75% $(C_2H_5)_2SO_4$ and 25% H_2SO_4 has been successfully used in the anodic sectioning of Nb and Ta (16). Anodizing Be in this electrolyte results in *V-t* and *I-t* curves of nonideal type (Table II). The electrolyte is implied by this to be unsatisfactory, and this conclusion was confirmed by finding similar metal dissolution to occur during anodizing as with diethyl phosphate (Table II).

(iii) Acetic acid. An acetic-acid based electrolyte, consisting of acetic acid, $Na_2B_4O_7 \cdot 10H_2O$, and water, is one of the few which permits Mo (17) and V (18,19) to be anodized. Its use with Be appeared at first sight encouraging in view of the *V-t* and *I-t* behavior (Table II); however, unacceptable metal dissolution occurs (Table II).

(iv) Ethylene glycol. More satisfactory results were obtained with ethylene glycol which has been saturated with certain salts. As seen in Fig. 5, the choice of Na_2CO_3 (curve A) or Na_2SO_4 (curve B) as the salt is unsatisfactory owing to the low value of dV/dt, whence an implied low efficiency. The choice of Na_2HPO_4 (curve C) or KH_2PO_4 or both Na_2HPO_4 and Na_2SO_4 (curve D and also Table II), however, results in *V-t* and *I-t* curves similar to those found when nonporous films are formed on Nb, Ta, V, or W (16, 19). We will subsequently refer to the electrolyte consisting of ethylene glycol saturated with both Na_2HPO_4 and Na_2SO_4 as "electrolyte A".

Anodizing efficiency with electrolyte A.—Experiments of two kinds were done to determine the anodizing efficiency with electrolyte A. First of all, Be thicknesses inferred by integrating *I-t* curves with expanded time scales, such as those shown in curves A and B of Fig. 6, were compared with true Be thicknesses obtained gravimetrically by stripping the films in 10%

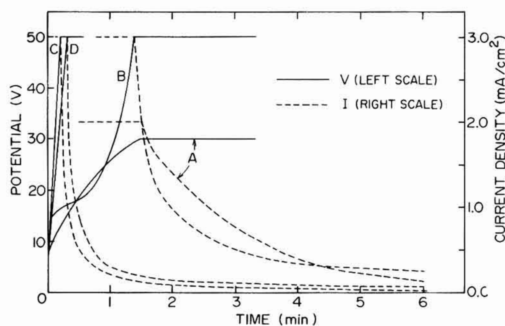

Fig. 5. Typical *V-t* and *I-t* curves for the anodizing of Be in ethylene-glycol-based electrolytes. Curve A: ethylene glycol saturated with Na_2CO_3 (abnormally low *dV/dt*). Curve B: ethylene glycol saturated with Na_2SO_4 (abnormally low *dv/dt*). Curve C: ethylene glycol saturated with Na_2HPO_4 (no anomalies). Curve D: ethylene glycol saturated with both Na_2HPO_4 and Na_2SO_4 (electrolyte A, no anomalies). Solid lines: *V-t*, with potential as in scale at left. Dashed lines: *I-t*, with current as in scale at right.

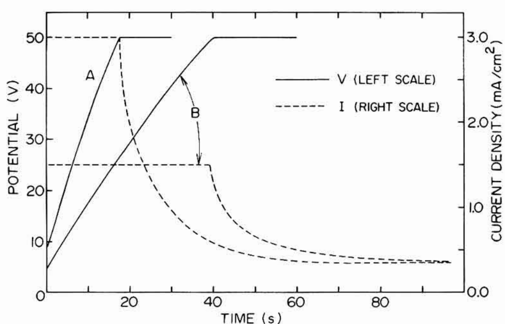

Fig. 6. Like curve D of Fig. 5 but plotted with an expanded time scale. An appropriate analysis of such curves is shown to yield the anodizing efficiency for conditions both of constant current and of constant current followed by constant potential.

Table III. Anodizing efficiency for Be using electrolyte A

Preset potential (V)	Anodizing time (sec)	Charge passed[a] (C/m^2)	Be thickness from Faraday's law[b] ($\mu g/cm^2$ of Be)	True Be thickness from Eq. [1] ($\mu g/cm^2$ of Be)	Anodizing efficiency
25	55	454 ± 10	2.12 ± 0.05	1.50 ± 0.08	0.71 ± 0.04
50	65	920 ± 30	4.29 ± 0.14	2.90 ± 0.15	0.68 ± 0.04

[a] Given by the total area under I-t curves as in Fig. 6 for an initial current density of 3.0 mA/cm^2. Repeated 3 times for each present potential.
[b] Calculated assuming an efficiency of 1.00.

KOH for 1 min. The true thicknesses are shown elsewhere (12) to be given by the relation

$$\text{thickness} \approx 0.1 + (0.056 \pm 0.003) \times V \ \mu g/cm^2 \text{ of Be} \quad [1]$$

which is valid provided the preset current is 3 mA/cm^2 and the current is allowed to drop, following the attainment of the preset potential, for 45 sec. The results, summarized in Table III, indicate an efficiency of ~0.7, valid for conditions of fixed current followed by fixed potential.

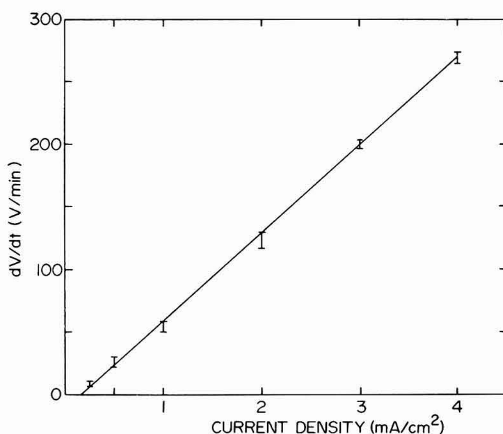

Fig. 7. dV/dt at 30V vs. I for the anodization of Be in electrolyte A. Given that dV/dt is proportional to the ionic current as in Eq. [2], these curves serve to separate the total current of 3 mA/cm^2 into an ionic part of 2.85 ± 0.05 mA/cm^2 and a nonionic part of 0.15 ± 0.05 mA/cm^2.

The dependence of dV/dt on the total current I can be used to estimate the efficiency under conditions of fixed current. The basic relation, which remains valid even if (as in the present work) the IR drop in the electrolyte is not corrected for, is

$$\frac{dV}{dt} \propto i_1 = k(I - i_2 - i_3) \quad [2]$$

where i_1 is the ionic current, i_2 is the electronic current (which usually causes oxygen evolution), and i_3 is the current leading to film dissolution (20). Accordingly, a second group of experiments was carried out. The primary data were as in Fig. 6, and from these plots of dV/dt at 30V vs. I as in Fig. 7 were constructed. The intercept with the current axis represents the nonionic current density, namely

$$i_2 + i_3 = 0.15 \pm 0.05 \ mA/cm^2 \quad \text{(at 30V)}$$

when I is 3 mA/cm^2. The efficiency follows as 0.95 ± 0.02 and is thus markedly greater for fixed current than for fixed current plus potential. This result is understandable if it is remembered that the contribution of $i_2 + i_3$ will depend on the total anodizing time (19) and the times were ~15 sec at fixed current but 65 sec at fixed current plus potential.

A slight curvature in the rising portions of the curves in Fig. 6 will be noted. We have not studied this effect in detail and therefore cannot say whether it is due to a change (with V or t) of the field in the anodic film or of the efficiency. The discrepancy between $i_2 + i_3 = 0.15$ mA/cm^2 and the leakage current in Fig. 6, 0.35 mA/cm^2, becomes less for longer times.

Porosity, dissolution, and crystallinity with electrolyte A.—Figure 8 shows scanning electron micrographs obtained for a film formed on Be and electrolyte A. Comparison with Fig. 3 and 4 suggests a significant freedom from porosity.

The depth-distribution technique showed that the metal dissolution during anodizing was essentially zero (Table II). Electrolyte A differs in this respect from all others that were examined. Stated in other terms, the dissolution current, i_3, is evidently less important than the electronic current, i_2, in lowering the anodizing efficiency to ~0.7 for conditions of fixed current plus potential.

Figure 9a shows a reflection electron diffraction pattern typical of a film as formed with electrolyte A.

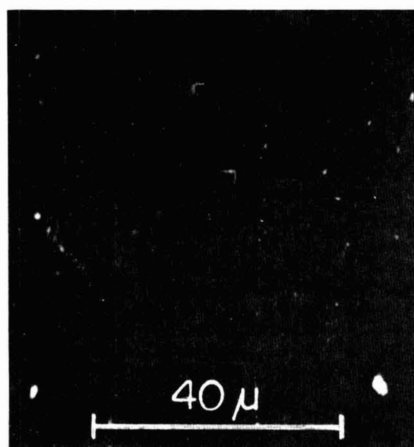

Fig. 8. Scanning electron micrographs with different magnifications of film formed by anodizing Be in electrolyte A for 1.5 min with a preset current of 3 mA/cm^2 and a preset potential of 50V. The films are significantly free from porosity.

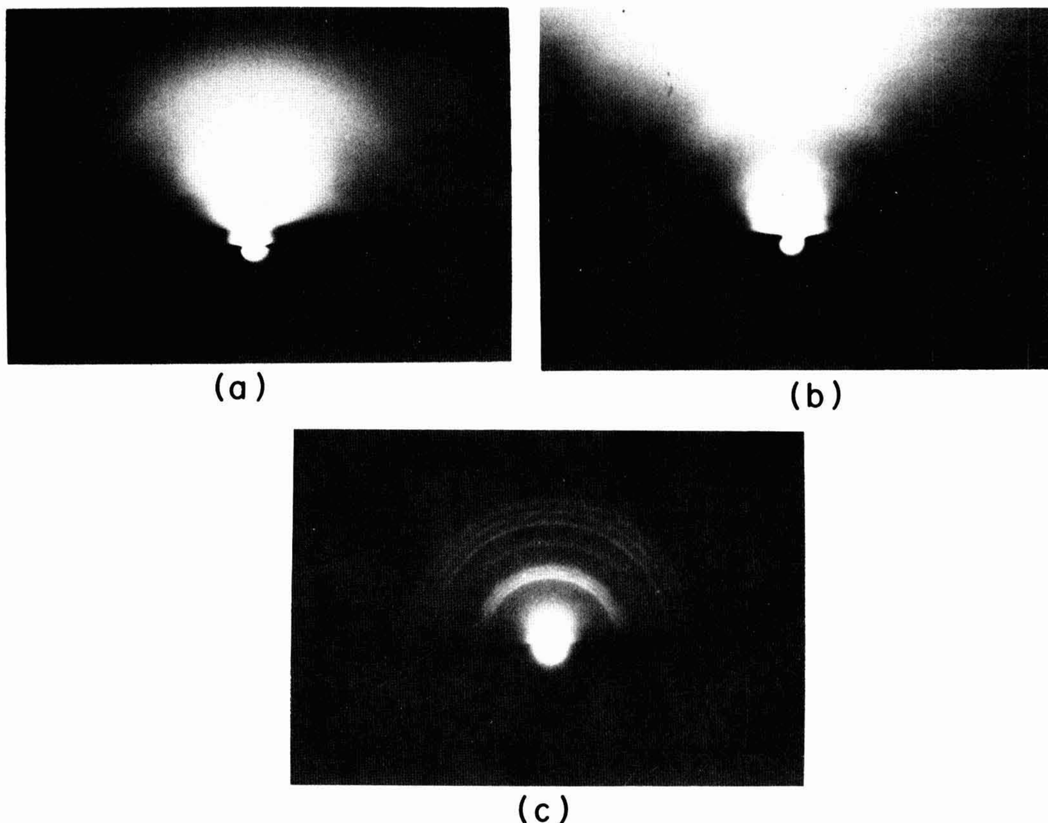

Fig. 9. Reflection electron diffraction patterns taken at 60 or 80 kV of film formed by anodizing Be in electrolyte A for 1.5 min with a preset current of 3 mA/cm^2 and a preset potential of 50V. Image (a): as-formed film, showing halos such as are conventionally ascribed to an amorphous structure though can also arise from microcrystallites having sizes of 1-2 nm. Image (b): film heated for 30 min in a vacuum of 1×10^{-4} Pa at 300°C, showing the halos to have split into diffuse rings. Image (c): film heated for 30 min in vacuum at 600°C, showing sharp rings identifiable as hexagonal BeO.

The film is nominally amorphous. After heating the films for 30 min in a vacuum of about 1×10^{-4} Pa at 300°C (Fig. 9b) or 600°C (Fig. 9c), the diffraction patterns revealed increasing degrees of crystallinity, such that the heating at 600°C led to overt polycrystallinity. The rings were identifiable as those of hexagonal BeO.

Discussion and Conclusions

Type of film.—The results presented here have shown that the behavior of Be with regard to anodizing is much like that of Al (5) and Sn (1, 9). Porosity, dissolution, and crystallinity can be varied almost at will depending on the electrolyte, with over-all results as in Table IV. The most interesting electrolytes would appear to be those consisting of ethylene glycol saturated with Na_2HPO_4 or KH_2PO_4 or both Na_2HPO_4 and Na_2SO_4 (electrolyte A). The *V-t* and *I-t* behavior suggested that a voltage-dependent limiting film thickness was obtained (Fig. 5 and 6). The films were found to be nonporous (Fig. 8) and dissolution to be undetectable (Table II). The films were nominally amorphous, with a crystallization temperature lying somewhere below 300°C and with the crystallization product consisting of hexagonal BeO (Fig. 9). Their structure thus more nearly resembled the chemically precipitated BeO studied by Kerr (21) than the anodic films obtained in previous work (7, 8, 11). Anion incorporation in the anodic film from the electrolyte, such as that demonstrated with Ta (16, 22) may or may not have played a role and will be investigated in subsequent work.

Anodizing efficiency.—The anodizing efficiency using electrolyte A was determined in two ways: from Faraday's law and from dV/dt. Use of the former gave a value of ~0.7, valid for conditions of fixed current

Table IV. Summary of Be anodizing

Electrolyte	Film?	Current at fixed potential	Porous?	Dissolution?	Crystallinity
1% H_2SO_4 or 1% HNO_3	No	Constant		Yes	
1% KOH	Yes	Falls slowly		Yes	
CrO_3-HNO_3 mixture	Yes	Constant	Yes	Yes	Crystalline (7)
0.5M Na_2CO_3	Yes	Falls rapidly	No	Yes	Crystalline (11)
$(C_2H_5)_2HPO_4$	Yes	Nearly constant		Yes	
$(C_2H_5)_2SO_4$-H_2SO_4 mixture	Yes	Constant or nearly constant		Yes	
Mainly acetic acid	Yes	Falls rapidly		Yes	
Electrolyte A	Yes	Falls rapidly	No	No	Nominally amorphous

followed by fixed potential. Use of dV/dt gave a value of 0.95 ± 0.02, valid at 30V for fixed current. Efficiencies of less than unity will arise whenever electronic current, i_2, or dissolution current, i_3, play a role. The lack of dissolution (Table II) shows that i_2 is the more important in the present case. We attribute this role of electronic current to the relatively low thicknesses of the anodic films formed on Be (Eq. [1]) such that the resulting fields across the films are higher than with most other metals (Table I).

Anodic sectioning of Be.—The present work constitutes the first instance in which Be has been anodized under controlled conditions, the important feature being the choice of electrolyte. We will in a subsequent paper (12) treat the converse of film formation, namely the quantitative removal of films. This leads first of all to a microsectioning technique, thence to the possibility of studying diffusion and ion depth distributions in Be. We note in this connection that Be is a particularly interesting material for depth-distribution work in view of its low mass. Film removal also has a purely electrochemical interest, in that it leads to explicit information on efficiencies such as that in Table III.

Acknowledgment

This research was supported by a grant from the National Research Council, Ottawa, Canada.

Manuscript submitted March 7, 1975; revised manuscript received June 16, 1975.

Any discussion of this paper will appear in a Discussion Section to be published in the June 1976 JOURNAL. All discussions for the June 1976 Discussion Section should be submitted by Feb. 1, 1976.

Publication costs of this article were partially assisted by McMaster University.

REFERENCES

1. E. Giani and R. Kelly, *This Journal*, **121**, 394 (1974).
2. P. H. G. Draper and J. Harvey, *Acta Met.*, **11**, 873 (1963).
3. D. G. Brandon, J. Zahavi, A. Aladjem, and J. Yahalom, *J. Vacuum Sci. Technol.*, **6**, 783 (1969).
4. M. R. Arora and R. Kelly, Submitted to *J. Mater. Sci.*
5. R. A. Harrington and H. R. Nelson, *AIMME, Inst. Metals Div.*, **137**, 62 (1940).
6. O. Flint, J. J. Polling, and A. Charlesby, *Acta Met.*, **2**, 696 (1954).
7. I. S. Kerr and H. Wilman, *J. Inst. Metals*, **84**, 379 (1955-1956).
8. M. L. Levin, *Trans. Faraday Soc.*, **54**, 935 (1958).
9. R. Kerr, *J. Soc. Chem. Ind.*, **57**, 405 (1938).
10. R. M. Al'tovskii, A. G. Fedotova, M. I. Urazbaev, and S. I. Korolev, *Prot. Metals*, **5**, 172 (1969).
11. K. E. Heusler, *Ber. Bunsengesellschaft*, **67**, 943 (1963).
12. M. T. Shehata and R. Kelly, Submitted to *Rad. Effects.*
13. R. Kelly and K. Kerkdijk, *Surface Sci.*, **46**, 537 (1974).
14. J. P. S. Pringle, *This Journal*, **120**, 398 (1973).
15. A. I. Vol'fson, N. E. Markova, V. V. Chernyshev, V. N. Lebedev, and V. V. Vavakin, *Prot. Metals*, **9**, 321 (1973).
16. M. R. Arora and R. Kelly, *Electrochim. Acta*, **19**, 413 (1974).
17. M. R. Arora and R. Kelly, *This Journal*, **119**, 270 (1972).
18. R. G. Keil and R. E. Salomon, *ibid.*, **15**, 628 (1968).
19. M. R. Arora and R. Kelly, *ibid.*, **120**, 128 (1973).
20. J. Siejka, J. P. Nadai, and G. Amsel, *ibid.*, **118**, 727 (1971).
21. I. S. Kerr, *Acta Cryst.*, **9**, 879 (1956).
22. G. Amsel, C. Cherki, G. Feuillade, and J. P. Nadai, *J. Phys. Chem. Solids*, **30**, 2117 (1969).
23. M. R. Arora, Ph.D. Thesis, McMaster University (1974).
24. N. Q. Lam and R. Kelly, *Can. J. Phys.*, **48**, 137 (1970).
25. A. Charlesby, *Acta Met.*, **1**, 340 (1953).

Photoluminescence of Epitaxial ZnSe Layers Grown on Ge

F. Chernow, G. F. Ruse, and G. W. Eldridge

Department of Electrical Engineering, University of Colorado, Boulder, Colorado 80302

ABSTRACT

The epitaxial growth of ZnSe on (100) Ge using the close-spaced transport process is described. Substrate temperature of 575°C and source temperatures of 675°C yield 10μ single-crystal layers in 10 hr. The Ge substrate provides a nonreplenishable, chemical transport agent and the epitaxial layer thickness is limited to approximately 10μ. As-grown epitaxial layers show excellent photoluminescence structure at 77°K. As-grown layers exhibit high resistivity, annealing in Zn vapor at 575°C reduces the resistivity to 10-100 ohm-cm. Zinc vapor annealing quenches the visible photoluminescence.

The literature on the epitaxy of ZnSe on Ge is relatively large. Growth techniques include vacuum deposition (1-3), chemical vapor transport (4), close-space vapor transport (5), and close-space, chemical vapor transport (5). The pair of semiconductors is particularly attractive for electronic applications such as transistors with wide bandgap emitters (6, 7) due to the small lattice mismatch and low concentration of interface states achievable (8). Vacuum-deposited layers exhibit strain and adhesion problems that may make them unacceptable for devices (1, 2). Chemical transport techniques lead to incorporation of substantial halogen concentrations which create donors and comparable densities of deep acceptors (4, 5, 9). The close-spaced growth process using pure H_2 gas and undoped ZnSe sources minimizes doping and compensation in a configuration that is inherently clean and efficient (10).

The present work was motivated by a need to prepare ZnSe substrates suitable for ion-implanted electroluminescent devices. Required characteristics include morphography adequate for ion implantation,

Key words: close-spaced transport.

low doping to minimize the dose required for compensation, and high luminescence efficiency. Layers grown using the close-space technique were examined for morphology and macroscopic uniformity, behavior under Zn vapor annealing, and photoluminescence structure. Photoluminescence measurements provide information on both the defect structure of the ZnSe layer and a suggestion of its electroluminescence potential. Little has been reported on the photoluminescence of ZnSe epitaxial layers and the reported results are somewhat disappointing (4).

Experimental Procedure

Growth system.—The close-space transport system employed in this work is shown in Fig. 1. This configuration is similar to that described by Hovel and Milnes (5). The insert in Fig. 1 shows the actual growth region. The high purity quartz crown establishes the source to substrate separation and aids in controlling the vapor pressure over the substrate. Slots cut in this crown provide access for the flow gas. Several variations in the access area were used, but no dependence of the growth behavior on this area could be determined. The source and substrate are clamped by high purity, low porosity carbon blocks which act as absorbers heated by external 600W tungsten-iodide lamps. These susceptors are supported by high purity quartz tubes. Thermocouples inserted in these tubes are used to monitor the temperatures of the susceptors and control the power to the lamps. Dual, digital, set point indicators, current modulators, and SCR power circuits control the substrate temperature (T_{sub}) and the source-substrate temperature difference (ΔT). Rapid response with little or no overshoot and temperature control of better than 1°C was easily achieved.

A gas flow and mixing system was designed to accommodate HCl chemical transport growth as well as the work described here. It was constructed of Monel, Type 316 stainless steel, and inert plastics. This system

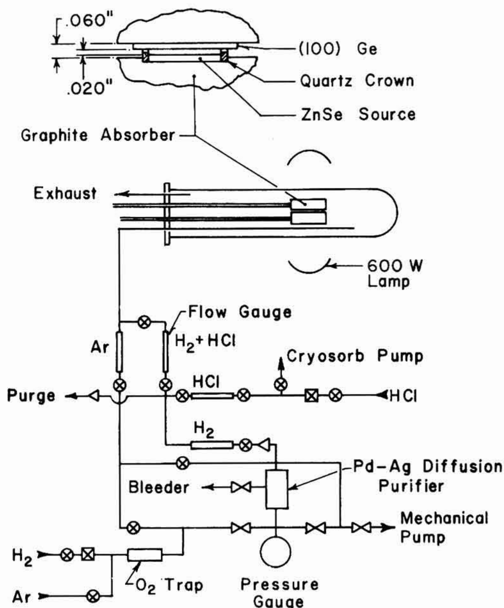

Fig. 1. ZnSe growth system. Graphite absorbers are 1½ in. diam × 7/16 in. thick; Ge substrates are 1/2 in. square, and the ZnSe growth region is 0.34 in. in diameter. Gases are vented through bubblers to prevent back diffusion. For H_2 + HCl growths pure H_2 flows through the Ar flow gauge and a large fraction of the initial H_2 + HCl mixture is dumped at the purge port in order to obtain low HCl concentrations.

was made leak tight to within the 10^{-10} atm-cm^3/sec sensitivity of a helium leak detector. The hydrogen flow gas used during the growths was palladium-diffusion purified. Electronic grade HCl and prepurified argon were employed. Argon was used as a continuous flushing gas when the systems were not in use. (Several glass envelope-susceptor systems were constructed; each system was used exclusively for particular substrate and flow gas combination except where it is noted otherwise.) Systems were open to the atmosphere for source or substrate replacement for a few minutes at most. Prior to growth, the growth region was baked at 350°C in flowing H_2 for a minimum of 1 hr.

Substrate and source preparation.—Substrates were prepared from 2/3 mm thick, (100) oriented germanium wafers. The Ge was nominally undoped (40-100 ohm-cm, p-type). The dependence of epitaxial layer morphography on substrate surface structure was complicated by selective Se etching of the Ge during growth. The best results in terms of ZnSe uniformity and surface morphology were obtained when the substrates were mechanically polished using 1μ Al_2O_3 and then etch polished using concentrated NaOCl on a low nap pad (11). This produces optically flat, scratch-free Ge surfaces. A final etch in dilute I_2-HF to remove 3-5 mils was used to reduce surface damage resulting from the polishing procedure.

Since the close-space transport is very efficient, approximately twenty 10μ thick growths can be made before the source-substrate gap changes appreciably. The work described here is the result of two separate source charges of which each were used twenty times. Sources were prepared from two, separate, high purity, melt grown, ZnSe single crystals purchased from Eagle-Picher Industries. Both crystals had high dark resistivity and both contained numerous grain boundaries. Emission spectroscopy analysis of the as-received crystals revealed an impurity concentration of 540 ppm (500 ppm Si, 20 ppm Fe) in the first crystal and an impurity concentration of 70 ppm (50 ppm Si, 20 ppm Fe) in the second crystal. These emission spectroscopy estimates exclude copper which was measured by atomic absorption at 87 and 0.4 ppm, respectively. The first crystal was ground down to ~50μ grains to form a "crushed-crystal" source. The second crystal was cut and polished to fit the quartz crown to form a "single-crystal" source. Surface damage and contamination were removed by etching in H_2SO_4-$K_2Cr_2O_7$ in the latter case (12). No chemical analysis was performed on the completed sources.

Analysis techniques.—Surface morphography was observed using a 27-1250× microscope with a Nomarski phase-contrast attachment. The front surface of the ZnSe layer was always examined; in some cases the ZnSe layer was removed by etching in 5% bromine in methanol to permit examination of the Ge substrate for etching by Se vapor during growth (5). Samples were cleaved for microscopic examination to determine the thickness of the ZnSe layers. Uniformity of both the growth and substrate etching were also noted. Crystallinity of the ZnSe layers was examined using Laue x-ray reflection and glancing, high energy, electron diffraction techniques. As a consequence of the thin layers ($\leq$10μ) and good lattice match, the x-ray data is dominated by reflections from the substrate.

Several samples were annealed in a Zn vapor atmosphere at 575°C. No attempt was made to protect the Ge substrate from attack by the Zn vapor, and this precluded annealing in liquid Zn (5). The samples were placed in high purity quartz ampuls with a weighed quantity of metallic Zn (99.9995% pure) sufficient to achieve the Zn_l-Zn_g equilibrium at the annealing temperatures while minimizing the quantity of excess, liquid Zn (13, 14). The ampuls were evacuated to 10^{-6} Torr and sealed. Annealing was performed for times between 1 and 36 hr. The ampuls were inserted into a

preheated furnace and quench-cooled upon removal. Annealed samples were examined for cracks and peeling which would indicate stress and adhesion problems. Four terminal resistivity measurements were performed, and the ZnSe layer was etched back in steps and the resistivity measurement repeated to determine the uniformity of the induced conductivity.

Ultraviolet-stimulated luminescence measurements were performed to assess the quality of the ZnSe epitaxial layers. Samples were clamped to a cold finger in an evacuated Dewar and held at liquid nitrogen temperature. Light from a high pressure, 100W mercury lamp was filtered (Corning No. 7-51) to remove visible components and focused on the sample. The spectrum was resolved using a double pass monochromator and detected using a photomultiplier with an S-10 photocathode. None of the spectra were corrected for system response.

Experimental Results

Growth.—T_{sub} and ΔT were varied from 550° to 800°C and 5° to 125°C, respectively, to determine optimum growth conditions. Optimum conditions for this case are defined as best surface morphography, best crystal structure, with acceptable growth rate. The optimum conditions were $T_{sub} = 575°C$, $\Delta T = 100°C$ at a hydrogen flow of 300 cm³/min.

Ten micron thick films were grown in 10 hr under optimum conditions. Increasing T_{sub} leads to severe pitting of the Ge substrate while almost no pitting was observed under optimum conditions. There is always evidence of Ge etching in the area where the quartz crown makes contact with substrate. At the inside diameter of the crown, erosion reaches depths of a few microns. This erosion decreases continuously toward the outside diameter where isolated, square etch pits are found. No etching is observed outside the crown except in the immediate neighborhood of the slots. Decreasing ΔT increases substrate pitting as well as reducing the growth rate. For $T_{sub} = 575°C$, ΔT must be greater than 50°C for the ZnSe thickness to exceed the erosion depth of the substrate. As T_{sub} is increased, ΔT must also be increased for this condition to be met. Increasing ΔT above 125°C leads to faceting and macroscopic nonuniformity of the layer but HEED and x-ray analysis indicated that all the epitaxially grown films were single crystal.[1] T_{sub} must exceed 500°C to achieve usable growth rates.

It has not been possible to define a ZnSe growth rate for this configuration. Increasing the growth time from 10 to 20 hr does not increase the layer thickness by more than 20%. Similar evidence for saturation of the layer thickness is found when the growth time is reduced. Any conclusions, however, must be qualified due to a ±20% uncertainty in the layer thickness under supposedly identical conditions.

The first series of growths were performed using the crushed crystal source. A Nomarski photograph of the ZnSe layer produced in run No. 12 is shown in Fig. 2a. The source had been used for 54 hr growing time prior to this run without replenishment. Earlier runs show projecting yellow needles as well as the uniform epitaxial layer. The density of dendritic needles decreases continuously to zero over the first 75 hr of source use. There also appears to be some improvement in the uniformity of the continuous layer with each succeeding growth.

Figure 2b is a Nomarski photograph of a ZnSe layer produced using the single-crystal source after 144 hr of prior use. In contrast to the powder source results, dendritic growth appears in only the first epitaxial layer and no further systematic changes occur in the morphography of the epitaxial layers.

[1] Experiments were performed to determine the growth rate for the single crystal to polycrystal transition at the optimum substrate temperature. Addition of 0.6% HCl leads to a growth rate of 30 μ/hr and induces this transition. This agrees with a linear extrapolation of the transition data for ZnSe epitaxy on (100) Ge presented by Calow *et al.* (2).

Fig. 2a. Surface of ZnSe epitaxial layer grown from the crushed-crystal source: Nomarski phase contrast; calibration marks correspond to 5μ.

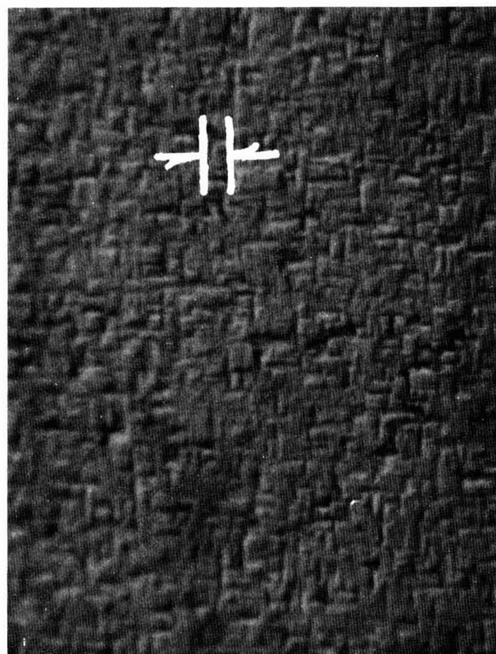

Fig. 2b. Surface of ZnSe epitaxial layers grown from the single-crystal source: Nomarski phase contrast; calibration marks correspond to 5μ.

Photoluminescence.—Figure 3 shows the visible photoluminescence spectra of a series of ZnSe layers

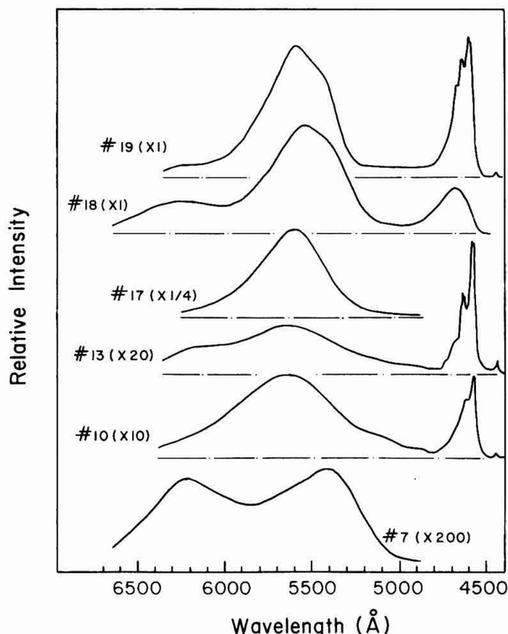

Fig. 3. Luminescence of ZnSe layers grown from a crushed-crystal source. The numbers in parentheses are the scaling factors used to multiply the intensity of the original data in preparing this figure. The relationship between run number and the accumulated hours of source use is No. 7, 20 hr; No. 10, 39 hr; No. 13, 65 ½ hr; No. 17, 107 hr; No. 18, 119 hr; and No. 19, 131 hr. Run No. 17 employed a GaAs substrate.

grown using the crushed-crystal source. The chronological sequence of the growths is indicated by the run number; all of these growths were performed with approximately optimal parameter values. There is also a reduction in dendritic growth in this progression. The dendritic growth was brushed off the sample prior to taking the spectra shown in Fig. 3. Etching to remove any residue of the dendrites did not alter the spectra.

The evolution of the luminescence from layer to layer using the same source is too complex to be described completely by Fig. 3. The epitaxial layers grown when the source is new are of relatively poor quality and the luminescence is characterized by a broad, weak line peaking between 5900 and 6100Å. As the source is used, epitaxial layers exhibit a 5400Å line of increasing intensity followed by the gradual appearance of a line at 6240Å and simultaneous decrease in the intensity of the 6000Å line (No. 7). In turn, the 6240Å line decays and what appears to be an unresolved pair of lines at ~6000 and ~5625Å grows in intensity. Still later growths from the same source result in epitaxial layers that exhibit a reduction in intensity of the 6000Å line with no change in the 5625Å line. Appearance of the blue emission band at 4560-4720Å and the line at 4450Å occurs with extinction of the 6000Å band (No. 10). Continued use of the source leads to epitaxial layers that show increased intensity and better resolution in the blue emission band (No. 13).

Run No. 17 was performed on a GaAs substrate. A 5μ epitaxial ZnSe layer was grown on the (100) GaAs substrate in 10 hr. T_{sub} and ΔT were maintained at 575° and 100°C, respectively. In contrast to normal procedure, neither the growth tube nor the ZnSe source were changed. Figure 3, No. 17 shows substantial intensity enhancement and line width reduction of the 5625Å line. No other lines were observed in the spectrum. Run No. 17 was followed by additional growths on germanium substrates using the same source and growth tube. The 6240Å red band and a structureless blue band reappears in No. 18. Figure 3, No. 19 indicates a return to the spectrum shown in Fig. 3, No. 13. Later runs show that the return to the original spectra is erratic and slower than might appear from the data appearing in Fig. 3, No. 18 and 19.

Figure 4 details the behavior of the blue emission. The phonon-assisted emission series seen in the run No. 13 sample has been identified as resulting from a free to bound transition by Dean and Merz (15). The LO phonon energy implied is 30.5 $\pm$ 1 meV in agreement with published results (15, 16). The blue emission band for the run No. 18 sample is typical of ZnSe with high Al and Na concentrations (16). The line at 4450Å is a combination of unresolved I_1, I_2, and I_x lines (17).

ZnSe layers grown from single-crystal sources show similar luminescence spectra with notable exceptions. The structure of the blue emission changes in an erratic manner from growth to growth and never develops the detail observed in the spectra of the epitaxial layers grown from the powdered source. The 4450Å line is observed in all epitaxial layers from the onset of use of the source. Layers grown during the initial runs show the ~5600Å band and blue emission in the 4560-4720Å range is absent. The broad 6000Å emission band may appear alone or with a line at approximately 5400Å. Other epitaxial layers exhibit a 6240Å emission band appearing with a line peaking anywhere between 5600 and 5400Å. The 4560-4720Å blue emission is present only when the 6000Å band is absent. Luminescence intensity in epitaxial layers grown from both sources is comparable.

Although growth of ZnSe epitaxial layers using HCl as a chemical transport agent is not the subject of this paper, some reference to the luminescent spectra obtained is useful. Layers grown using single-crystal sources and less than 0.1% HCl in H_2 show a green emission band centered at 5300Å. At higher HCl concentrations the layers show a broad 6000Å band and the blue emission is either structureless and very weak or absent. The photoluminescence spectra indicate no persistent contamination of the ZnSe source as a result of using HCl. Cutting off the HCl flow yields epi-

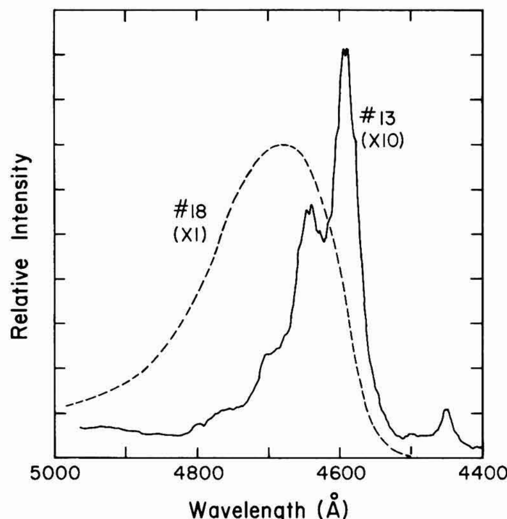

Fig. 4. Detail of blue luminescence of ZnSe layers. The spectra of the layer obtained from run No. 13 is typical of those obtained from runs No. 12 through No. 16. Run No. 18 was preceded by one run on a GaAs substrate. The numbers in parentheses are scaling factors for the data as defined in Fig. 3.

taxial layers showing 6240 and 5400Å emission bands and good blue emission in the following growth.

Sources used in HCl also show ~6200 and ~5400Å emission bands but do not show either intense or highly structured blue emission. Examination in regions with and without exposed grain boundaries shows that most of the emission originates at the grain boundaries. Small shifts in the peak wavelengths and changes of the line width of both the 6200 and 5400Å band demonstrate that the higher intensity observed at grain boundaries is not due to scattering. Unused source wafers do not exhibit uniform luminescence intensity or structure except that blue emission is usually not present. Sources used in H_2 only show a single, weak luminescence band peaking at 5400Å.

Zinc annealing.—All as-grown epitaxial layers exhibit resistivities greater than 10^8 ohm-cm as measured with a four-point probe. Uncertain junction isolation between the n-type epitaxial layer and the p-type substrate sets this value as a lower limit. Annealing in saturated Zn vapor at 575°C for 18 hr reduces the resistivity to 10-100 ohm-cm. Etching studies indicate that the conductivity modification is uniform throughout the epitaxial layer thickness. Similar changes are observed upon annealing ZnSe source crystals under the same conditions. These results are typical of bulk ZnSe (15). In contrast to bulk ZnSe crystals annealed under these conditions, ZnSe epitaxial layers grown on Ge by H_2 transport show no visible photoluminescence at 77°K. Etching experiments demonstrate that this absence persists throughout the layer. Annealing in saturated Zn vapor at 575°C for times such that the resistivity is reduced to the 10^4 ohm-cm range results in a fourfold reduction in luminescence intensity and broadening of the blue emission lines.

It might be hypothesized that photoluminescence is killed by a deep trapping and recombination center. Hovel has reported a Ge-ZnSe heterojunction switching device that depends on the presence of deep traps (18). Measurements on these annealed samples do not show switching behavior strongly suggesting that deep traps are not present.

Annealed samples did not exhibit lifting or cracking. In contrast to other ZnSe-Ge epitaxy studies employing different deposition techniques and/or thickness, this work did not show an adhesion or stress problem that can be revealed by annealing.

Discussion

Approximately 10μ thick ZnSe layers can be grown on (100) Ge using the close-space technique without using a chemical transport agent. Nonlinearity in the growth rate confirms Hovel and Milnes' observation that Ge itself acts as a chemical transport agent (15). Hovel and Milnes also obtained no growth on GaAs (B surface) under conditions similar to those used here; *i.e.*, $T_{sub} = 590°C$, $\Delta T = 110°C$, and 0.02% HCl in H_2. (HCl should increase the growth rate but we have not observed measurable increases at this low concentration.) In contrast, a 5μ thick ZnSe layer was obtained ($T_{sub} = 575°C$, $\Delta T = 100°C$, and pure H_2) on (100) GaAs using a source that had been used for repeated growths on Ge. Although conditions are not identical, the most probable explanation for the discrepancy is persistent Ge contamination of the source powder. Parker *et al.* obtain Ge concentrations of 50-100 ppm in ZnSe epitaxial layers grown by HBr transport on ~500°C Ge substrates (4), and Hovel and Milnes demonstrate that this Ge is provided by Se rather than halogen etching of the substrate (5). It must be concluded that under optimum growth conditions, when there is no visible etching under the ZnSe layer, the $GeSe_x$ concentration is replenished via etching at the quartz crown-substrate interface. Etching in only this region implies very low Zn and ZnSe mobility on the substrate surface and very fast reaction of H_2Se with the exposed Ge. Slightly higher substrate temperature at this interface may also enhance the selectivity of the etching.

Gradual changes in the morphography of layers grown from the crushed-crystal source and absence of similar changes in layers grown from the single-crystal source can be explained by several models. The large surface area of the crushed-crystal source, uncertain thermal contact, and latent heat of vaporization may cooperate to yield supersaturation and dendritic and atypical growth. Morphography improves as smaller grains are consumed or "fused" together to reduce the surface area and improve thermal contact. It is also possible that the ZnSe source surface must equilibrate at nonstoichiometric Zn and Se concentrations in order to achieve stoichiometric deposition. The higher impurity concentration of the crushed-crystal source may have an adverse effect on morphography. Crushing ZnSe also exposes grain boundary surfaces and the impurity concentration on these surfaces is expected to be higher than the bulk. Repeated sublimation from these surfaces may lead to successively purer epitaxial layers.

The photoluminescent spectra of the best epitaxial layers is superior to both that previously reported for epitaxial layers (9, 19) and the source crystals employed in this work. "Superior" in this case refers to the dominance and structural detail achieved in the blue emission region. Blue emission has been identified with Na acceptors (16), but the origin of Na has not been established in this case. Emission spectroscopy reveals no Na in the ZnSe sources and 2 ppm Na in the graphite absorbers. The Ge substates were not analyzed.

The consistent reduction of the long wavelength emission of layers grown from the crushed-crystal source and the erratic behavior of this emission in layers grown from the single-crystal source suggests that with the exception of the 5625Å line these lines are associated with chemical impurities originating preferentially from grain boundaries in the source. An abnormally high concentration of chemical impurities at grain boundaries is expected and examination of the source luminescence confirms a higher concentration of optically active defects at grain boundaries. Crushing the source exposes these high impurity concentration regions so they are sublimed and incorporated in the early grown epitaxial layers. Single-crystal sources release these impurities for incorporation as sublimation and preferential sublimation at grain boundaries exposes impurity pockets. This model requires that these impurities do not both diffuse freely along the grain boundaries and sublime preferentially at the source surface.

Only speculative identifications can be made as to the specific origin of the long wavelength lines. The luminescence band at 6000Å is thought to be equivalent to the self-activated blue luminescence center in ZnS (20). The S-10 photocathode response distorts the luminescence data in this wavelength range. Correction for the S-10 response brings the center wavelength and the linewidth of the 6000Å band into agreement with the self-activated emission band reported by Jones and Woods (21). This center has been suggested to consist of a Zn vacancy associated with a halogen or a Group III donor (22). Appearance of this line in layers grown in high HCl concentrations suggests the halogen donor is responsible.

Cu has been associated with emission bands at approximately 5300 and 6300Å (19, 22-24). Aven and Halstead observed green emission in compensated ZnSe:Cu:Cl and red emission in ZnSe:Cu:Al containing excess Cu (22). Cl does not appear to be optically active in the former case while an optically active Cu-Al complex appears to form in the latter case (22, 25). Similar processes may lead to the 5300Å band in layers grown using low HCl concentration and reappearance of the 6240Å band after contamination of the growth apparatus with Ga (19). Correction for the

S-10 photocathode response bring the center wavelength and the linewidth of the 6240Å band into agreement with the copper-red emission band reported by Jones and Woods (21). The relative behavior of layers grown from the two sources is not consistent with the initial Cu concentrations, however.

Both the 5625Å line in layers grown from the crushed crystal and the 5600-5440Å line in layers grown from the single crystal appear to be the so-called yellow self-activated luminescence (26, 27). Variability in the peak in the latter case is thought to be due to a varying defect concentration.

The ZnSe source material used for this study is similar to that employed by Dean and Merz and by Chatterjee *et al.* in regard to both electrical and photoluminescent behavior (15, 16). Prior to Zn vapor annealing the epitaxial layers also exhibited similar photoluminescent behavior. The initial conductivity of the epitaxial layers and their response to Zn vapor annealing is also similar. Dean and Merz annealed their ZnSe samples in Zn vapor to create or enhance the Q and $Q^{F \rightarrow B}$ emission lines (15). This procedure should reduce the Zn vacancy concentration. Chatterjee *et al.* indicate that Na substituting for Zn is responsible for the Q emission series (16). The presence of substitutional Na must be accompanied with a reduction in Zn vacancies if the blue emission is to be enhanced. If not, the deeper Zn vacancies would tend to dominate the photoluminescence and lead to longer wavelength emission. The epitaxial layers show no visible photoluminescence when Zn is vapor annealed to achieve similar electrical properties. This implies either that a killer center involving Ge impurities is formed or that the optically active centers are gettered by the substrate.

Approximately 75 hr of firing the source powder at the growth temperature is an impractical method for stabilizing and purifying the source material. Even this preparation does not achieve surface morphography comparable to that obtained using a single-crystal source. It is possible that prefiring single-crystal sources in liquid zinc would make these sources more uniform and achieve some purification by a solvent extraction process (28).

Some form of chemical analysis of the epitaxial layers would have been helpful in explaining the luminescence data. The luminescence is a complex function of the concentrations of more than one chemical species in general, and these concentrations may lie in the range of 1 ppm or less in ZnSe (27).

Manuscript submitted Feb. 14, 1975; revised manuscript received May 27, 1975.

Any discussion of this paper will appear in a Discussion Section to be published in the June 1976 JOURNAL. All discussions for the June 1976 Discussion Section should be submitted by Feb. 1, 1976.

Publication costs of this article were partially assisted by The University of Colorado.

REFERENCES

1. J. T. Calow, S. J. T. Owen, and P. W. Webb, *Phys. Status Solidi*, **28**, 295 (1968).
2. J. T. Calow, D. L. Kirk, and S. J. T. Owen, *Thin Solid Films*, **9**, 409 (1972).
3. A. San, *J. Appl. Phys.*, **44**, 523 (1973).
4. S. G. Parker, J. E. Pinnell, and L. N. Swink, *J. Phys. Chem. Solids*, **32**, 139 (1971).
5. H. J. Hovel and A. G. Milnes, *This Journal*, **116**, 843 (1969).
6. H. Kroemer, *Proc. IRE*, **45**, 1535 (1957).
7. H. J. Hovel and A. G. Milnes, *IEEE Trans. Electron Devices*, **ED-16**, 766 (1969).
8. A. G. Milnes and D. L. Feucht, "Heterojunctions and Metal-Semiconductor Junctions," Academic Press, New York (1972).
9. S. G. Parker, *J. Cryst. Growth*, **9**, 177 (1971).
10. F. H. Nicoll, *This Journal*, **110**, 1165 (1963).
11. A. Reisman and R. Rohr, *ibid.*, **111**, 1425 (1964).
12. V. S. Park, C. R. Geesner. and B. K. Shin, *Appl. Phys. Letters*, **21**, 567 (1972).
13. R. E. Honig, *RCA Rev.*, **23**, 567 (1962).
14. P. Goldfinger and M. Jeunchemme, *Trans. Faraday Soc.*, **59**, 2851 (1963).
15. P. J. Dean and J. L. Merz, *Phys. Rev.*, **178**, 1310 (1969).
16. P. K. Chatterjee, A. J. Rosa, and B. G. Streetman, *J. Luminescence*, **8**, 176 (1973).
17. A. Rosa, Private communication.
18. H. J. Hovel, *Appl. Phys. Letters*, **17**, 141 (1970).
19. C. Auzary Roindessault and F. Lebourg, *Compt. Rend. Acad. Sci. Paris*, **272**, 691 (1971).
20. J. S. Prener, and D. J. Weil, *This Journal*, **106**, 409 (1959).
21. G. Jones and J. Woods, *J. Luminescence*, **9**, 389 (1974).
22. M. Aven and R. Halstead, *Phys. Rev.*, **137A**, 228 (1965).
23. G. B. Stringfellow and R. H. Bube, *Phys. Rev.*, **171**, 903 (1968).
24. L. Yz. Markovskii, I. A. Mironov, and Yu. S. Ryzhkin. *Bull. Acad. Sci. USSR*, **33**, 887 (1969).
25. S. G. Parker and J. E. Pinnell, *Trans. Met. Soc. AIME*, **245**, 541 (1969).
26. S. Iida, *J. Phys. Soc. Japan*, **26**, 1140 (1969).
27. S. Iida, *ibid.*, **25**, 177 (1968).
28. M. Aven and H. H. Woodbury, *Appl. Phys. Letters*, **1**, 53 (1962).

Poly(Vinyl Arene Sulfones) as Novel Positive Photoresists

M. J. Bowden and E. A. Chandross

Bell Laboratories, Murray Hill, New Jersey 07974

ABSTRACT

The synthesis and photosensitivities of a number of copolymers of sulfur dioxide and various arylethylenes are described. Irradiation with ultraviolet light causes chain scission and increases the solubility of these polymers; thus they function as positive photoresists.

All commercial positive photoresists appear to depend on the same photochemical process, *viz.*, the rearrangement and hydration of a quinone diazide to form a carboxylic acid which solubilizes the resist in mild alkali (1). Process operations using these materials have not been entirely satisfactory. The resist solutions are complex mixtures and batch to batch variation in properties can make developing procedures unsatisfactory. Positive resists have limited chem-

Key words: polysulfones, positive resist, photoresist.

ical resistance to etching solutions and are readily soluble in alkaline etchants. Certain difficulties also arise when positive resists are used in conjunction with gallium arsenide substrates since the substrate is attacked by the developing solution, leading to marked undercutting of the resist and attendant loss of resolution.

We have investigated a new type of positive photoresist, analogous to the recently described electron-sensitive olefin-sulfur dioxide copolymers,

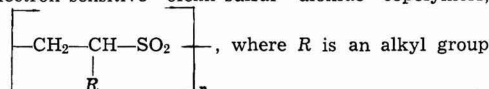

(2). This group of polymers does not absorb ultraviolet light in a useful region of the spectrum ($\lambda > 250$ nm) and it is not possible to sensitize photodegradation. We thought that polysulfones containing $R =$ aromatic hydrocarbon should show photochemical cleavage of the benzylic carbon-SO_2 bond. Related photochemical reactions are known for cyclic sulfones (3). We have found that the copolymers of arylated olefins, such as styrene, and sulfur dioxide are sensitive to ultraviolet light that is absorbed by the hydrocarbon moiety and that these copolymers function as positive photoresists with useful differential solubility.

Styrene is known to form a 2:1 copolymer with sulfur dioxide under certain conditions (4). We chose this material for our initial studies and found it to be sensitive to ultraviolet light absorbed by the pendant benzene rings (*ca.* 265 nm). The solubility of this polymer is increased by irradiation, indicating that chain scission is the principle mode of degradation as in the electron beam resists; thus it functions as a positive photoresist. The sensitivity is rather low because the absorbance is weak and lies in a region where there is relatively little output from the high pressure mercury arc lamp.

In order to increase the photosensitivity of this type of polymer we replaced some or all of the benzene groups with larger aromatic hydrocarbon systems having greater ultraviolet absorbance at somewhat longer wavelength. The systems studied are summarized in Table I. The sensitivity presumably depends not only on the aforementioned factors but also on the inherent instability of the polymer and the mechanism of photodecomposition.

The most promising member of this class of compounds was a terpolymer based on styrene, acenaphthylene and SO_2, whose sensitivity was about 500 mj cm^{-2} for ultraviolet light in the wavelength region 200-400 nm. This paper reports a more detailed investigation of the properties of this resist.

The photochemical reaction appears to proceed most readily from the excited singlet state as triplet sensitization, *e.g.*, benzophenone was extremely inefficient. This may reflect the energy required to break the carbon-SO_2 bond which is comparable to the triplet energy of the naphthalene group (60 kcal $mole^{-1}$). These polymers decompose at elevated temperatures and the photochemical reaction may be a hot ground state thermal reaction.

The acenaphthylene section of the polymer contains the grouping —CH—CH—SO_2 which has the aryl group

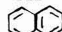

attached to two atoms of the main chain. We believe that the increased sensitivity of this polymer over the related vinylnaphthalene polymer is due to the strain introduced by the five-membered ring of the acenaphthylene group.

Experimental

Poly(styrene-acenaphthylene sulfone) (PASS).—A solution of acenaphthylene (8.75g, 0.057 mole) in freshly distilled styrene (30g, 0.29 mole) containing azobisisobutyronitrile (0.1g) and dimethylformamide (5 ml) was degassed by several freeze-thaw cycles. Sulfur dioxide (*ca.* 50g, 0.8 mole) was added and the flask was sealed. It was immersed in a water bath at 50°C for 72 hr. The polymer was precipitated by pouring the viscous mixture into a large excess of methanol. It was redissolved in dioxane and reprecipitated into methanol and then dried under vacuum at room temperature.

The elemental analyses of various batches of the polymer are given in Table II. The u.v. absorption spectrum is shown in Fig. 1. Acenaphthene groups in the polymer are responsible for the absorption in the 290 nm region and their concentration can be determined from the u.v. spectrum.

Sensitivity.—The polymers were dissolved in Kodak Photoresist Thinner (methoxyethyl acetate) and films were spun on Si/SiO_2 substrates using a Headway photoresist spinner. Films were baked for 30 min at 200°C. The films were irradiated through a mask with collimated light from a 200W high pressure mercury arc source. The light was filtered through a Corning 7-54 filter which transmits the 220-400 nm region of the spectrum. The intensity, measured with a thermopile, was 20 mW cm^{-2} at the resist surface.

Following exposure, the irradiated areas of the film were spray-developed with a 60 (dioxane)/40 (isopropyl alcohol) mixture. This developer did not attack the remaining film.

Resolution was checked by exposing the resist through a contact mask and developing the image as described. The resist was then postbaked (30 min at 200°C) and the substrate was etched in buffered HF.

Results and Discussion

Polymerization.—Styrene and sulfur dioxide form a 2:1 copolymer under the conditions used in our experiments. The addition of acenaphthylene (AcN) markedly reduces the over-all polymerization rate. Elemental analyses of the terpolymer indicated that acenaphthylene is incorporated into the chain in either —Sty—AcN—SO_2— or —Sty—Sty—AcN—SO_2— sequences interspersed between the —$(Sty)_2$—SO_2 sequences of the normal copolymer. The marked retarda-

Table I. Properties and exposure parameters of poly(vinyl arene sulfones)

Name	Monomer formula	(Vinyl arene / SO_2) copolymer	ϵ	λ max (nm)	Sensitivity (jcm^{-2})
Poly(styrene sulfone)	CH = CH_2	2	200	265	18.4
Poly(4-vinylbiphenyl sulfone	CH = CH_2	2	16,000	250	6.0
Poly(1-vinylnaphthalene sulfone)	CH = CH_2	This material was not further investigated since yields were very low			
Poly(styrene-co-acenaphthalene sulfone)*	CH = CH	2 (25 mole % AcN)	7,000 200	290 320	<0.50

* Acenaphthalene did not form a homopolysulfone. Attempts were also made to synthesize the polysulfone from N-vinylcarbazole but were unsuccessful.

Table II. Analysis of PASS samples*

Sample No.	Initial mole feed composition sty/AcN/SO_2	Initiation	C (%)	H (%)	S (%)	%AcN (u.v. spectrum)	Comments
2	3/1/15	tBuOOH at 0°C	70.12 (71.6	6.18 5.65	11.48 11.3)	14 (13.4)	2/1 copolymer with approximately every 8th styrene unit replaced by an AcN unit
3	3/1/15	AIBN at 50°C	75.87 (75.86	5.77 5.74	9.10 9.19)	23 (22)	5/2 copolymer with approximately every 5th styrene unit replaced by an AcN unit
4	5/1/15	AIBN at 50°C	72.92 (73.6	6.05 5.65	10.27 10.26)	20.8 (19.5)	11/5 copolymer with 2 AcN units per 11 vinyl arene units

* Values shown in parentheses are theoretical values based on assumed composition.

tion of the over-all rate indicates a kinetically unfavorable addition reaction to acenaphylene and of the acenaphthylene radical to SO_2. Thus the reaction must be carried out at moderate temperatures in order to obtain reasonable yields of product. The upper limit will, however, be determined by reversibility of the addition of SO_2 (ceiling temperature considerations) which tends to reduce its incorporation into the polymer. The rate retardation by acenaphthylene also results in a substantial reduction in molecular weight. This, alone, reduces the photosensitivity which is dependent on the rate of separation of molecular weight distributions; this rate is dependent on the initial molecular weight (5).

We found that cationic homopolymerization could sometimes occur readily in these systems but that it could be suppressed by the addition of small amounts of dimethylformamide. The amide was added routinely to avoid this undesired side reaction.

Film properties.—It was observed that, upon spray developing the exposed areas of the substrate, the unexposed areas developed a "frosted" appearance after extended spraying. This was not observed in the exposed areas which developed normally. Microscopic examination of the frosted regions showed that a myriad of semimicro cracks had developed in the film. In several cases, the film had markedly pulled away, exposing large areas of substrate. Some photomicrographs of these regions are shown in Fig. 2. This effect was only observed in films with thickness > 300 nm. At thicknesses ≤ 300 nm, the resists developed normally, leaving the unexposed film completely intact.

Several reasons may be advanced for this phenomenon. It was thought that the effect could be due to residual stress in the film which was not annealed during prebaking (the resists were initially prebaked at 100°C). It is generally considered advisable to prebake above the glass transition temperature in order to remove residual stress from the film. The T_g, as measured by differential thermal analysis, was found to be 186°C. Thermal degradation of the resist did not occur until 275°C. TGA and DTA analysis results are shown in Fig. 3. Some decrease in the tendency of the resist to crack was observed on increasing the prebaking temperature to 200°C but it was never entirely eliminated.

It appears that the reason for cracking of the film lies in the extreme brittleness of the film. It was not even possible to cast a film on mercury for infrared

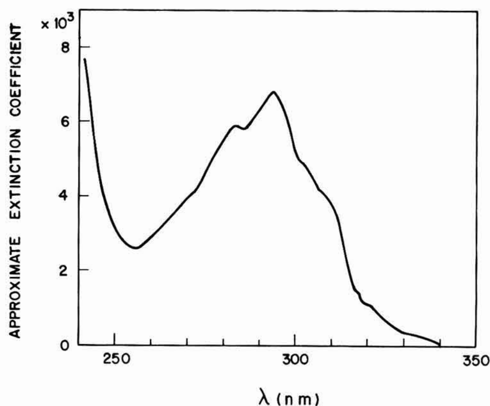

Fig. 1. U.V. absorption spectrum of poly(acenaphthalene styrene) sulfone.

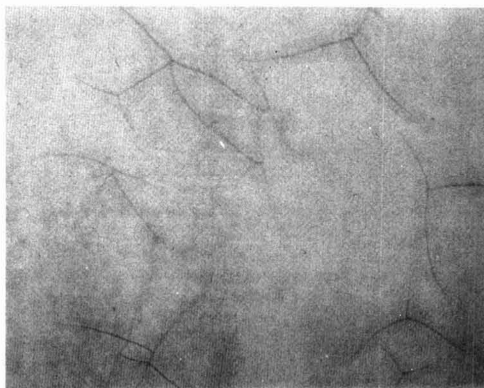

Fig. 2. Micrograph of "frosted" unirradiated regions of developed film showing development of microcracks.

Fig. 3. TGA and DTA curves for PASS

measurement without the film breaking up during the final states of solvent evaporation.

Accordingly, attempts were made to "plasticize" the film by incorporating other groups into the polymer chain. The most practical approach was to attach groups to the *para* position of the polystyrene units in the chain. A typical approach is outlined below

$$CH=CH_2C_6H_4CH_2Cl \; [I] + RO^-Na^+ \rightarrow CH=CH_2C_6H_4CH_2OR \; [II] \qquad R = C_5H_{11}, C_8H_{17}$$

These films did not crack under prolonged spraying by developing solutions. Unfortunately, the polymer derived underwent cross-linking during u.v. irradiation, presumably through cleavage of the ether bond and cross-linking to another chain.

It may be possible to obviate the cracking problem by increasing the molecular weight of the initial polymer. The addition of acenaphthylene to the mixture of styrene and SO_2 markedly reduces the over-all rate of polymerization and degree of polymerization of the resultant mixture. Reasonable yields of PASS were obtained where the initial mole ratio of styrene to acenaphthylene was 5/1. Acenaphthylene did not form a polysulfone by itself.

Resist evaluation.—The following results were obtained using sample PASS No. 4 which is a 11/5 copolymer of vinyl aryl groups/SO_2 with two acenaphthalene units per eleven vinyl aryl groups. Evaluation was made on films of 300 nm thickness.

As can be seen in Fig. 1 acenaphthene absorbs strongly at 294 nm with a tail extending out to 330 nm. Exposures were accordingly made through the Corning 7-54 filter which transmits the 220-400 nm region of the spectrum. The sensitivity under these conditions was 500 mJ cm^{-2}. It was found that the sensitivity of the polymer film was unaltered by a 1 mm Pyrex filter (cutoff $\lambda \sim 285$ nm). When the absorption peak of acenaphthene is matched against the ouptut of the Hg lamp, it appears that the photochemical reaction is primarily due to the Hg line at 313 nm. Since more than half of the light passed by the 7-54 filter lies outside the polymer absorption band, the sensitivity at this wavelength is <200 mJ cm^{-2}. This may be compared with a value of ~ 60 mJ cm^{-2} for the AZ positive photoresists (6).

PASS is an excellent etching mask against buffered HF. Some patterns etched in SiO_2 are shown in Fig. 4.

Fig. 4. Micrographs of test patterns etched in SiO_2

Conclusions

The major drawback to these resists is the region of the spectrum over which they absorb. Admittedly, they are sensitive enough, but they only use a small fraction of the output of the Hg lamp. In addition, one would need to use quartz optical systems for collimating the light, etc. However, for those special situations where current available materials are unsatisfactory, as in the patterning of gallium arsenide, it is felt these resists offer a viable alternative.

It would obviously be desirable to extend the sensitivity into the 365 nm region of the ultraviolet where the lamp output is high and glass optics are usable. Studies directed toward this goal are underway.

Acknowledgments

We thank Mrs. A. H. Schiebel for synthesizing the alkoxystyrene monomers, H. Bair for the DTA measurement, and E. D. Feit for the use of his irradiation apparatus.

Manuscript submitted May 22, 1974; revised manuscript received Oct. 10, 1974.

Any discussion of this paper will appear in a Discussion Section to be published in the June 1976 JOURNAL. All discussions for the June 1976 Discussion Section should be submitted by Feb. 1, 1976.

Publication costs of this article were partially assisted by Bell Laboratories.

REFERENCES

1. A. A. Lamola and N. J. Turro, "Energy Transfer and Organic Photochemistry," p. 371, John Wiley and Sons, New York (1969).
2. M. J. Bowden and L. F. Thompson, *J. Appl. Polymer Sci.*, **17**, 3211 (1973).
3. M. P. Cava, R. H. Schlessinger, and J. P. Van Meter, *J. Am. Chem. Soc.*, **86**, 3173 (1964).
4. K. J. Ivin and J. B. Rose, *Adv. Macromol. Chem.*, **1**, 335 (1968).
5. M. J. Bowden, *J. Polymer Sci.*, **49**, 221 (1975).
6. M. S. Htoo, *Photo Sci. Eng.*, **12**, 169 (1968).

Comparison of Group IV and VI Doping by Implantation in GaAs

D. Eirug Davies, J. K. Kennedy, and C. E. Ludington

Air Force Cambridge Research Laboratories, Air Force Systems Command, Bedford, Massachusetts 01730

ABSTRACT

Factor important in attaining higher n-type conductivity on implanting GaAs have been investigated. These are reflected in a comparison of Group IV and VI dopants where the difference in behavior can be ascribed to the different sublattice occupation. The importance of Ga outdiffusion with SiO_2 encapsulated layers is seen on incorporating Ga within the oxide prior to initiating any heat-treatment. For sulfur, the electrical activity is doubled by the presence of the oxide gallium. Such an oxide is detrimental for implanted Si^+ layers and indicates that some Ga outdiffusion is desirable. Presumably the same applies and inadvertently occurs with the traditionally simpler p-type implants. The annealing of S^+ and Se^+ implants with a dose-dependent, optimum annealing temperature differs significantly from Si^+ which requires higher annealing for comparable doping. The advantage gained by implanting Group VI dopants at elevated temperatures is not as pronounced with Si and in this respect Si resembles the p-type dopant Zn which does not exhibit any strong dependence on implantation temperature.

One of the limiting factors in GaAs technology is the difficulty of forming thin, heavily doped n-type regions. In diffusion, problems can arise in working with arsenic overpressures and through many of the dopants reacting chemically with the GaAs wafer surface. When the dopants are introduced by implantation, it is difficult to get a substantial fraction electrically active and uncompensated. Details of early implantation work have been given by Allen (1) while more recent results are summarized by Eisen (2).

Both Group IV and VI elements can be used for n-type doping in GaAs. While Group VI elements are n-type dopants on the As sites, Group IV elements are amphoteric and in contrast exhibit n-type conductivity on the Ga sites. Thus, implanted Group IV and VI ions might be expected to behave somewhat differently and particularly during postimplantation annealing.

An area that has received considerable attention in investigating n-type implants is surface encapsulation. Such a layer is required to prevent thermal erosion that otherwise occurs during annealing. The simplest dielectric to apply is SiO_2 and though it fulfills its initial intent of containing the arsenic, Ga will outdiffuse into the oxide (3). While this Ga loss may be detrimental for Group VI dopants, a certain concentration of Ga vacancies so formed could conceivably benefit Si and other Group IV dopants.

All Group VI dopants exhibit better conductivity when implanted at elevated temperatures, in addition to the usual postimplantation annealing. Foyt *et al.* (4) reported the most efficient Se doping as occurring at the upper end of the room temperature to 500°C range investigated. Better Te doping was obtained by Harris *et al.* (5) when implanting at 150°C rather than at room temperature. For S, an increase in utilization as dopants occurs ~150°C (6), coinciding with the temperature required to avoid lattice disorder (7), and no further improvement occurs at higher temperatures (up to 500°C). As no significant reduction in compensation occurs on implanting hot (6), the inferior room temperature results are attributed to the failure of these ions when so implanted to act as substitutional dopants on the arsenic sublattice. Thus, Group IV elements would not necessarily exhibit the same behavior with regard to implantation temperature in becoming n-type dopants on Ga sites. In this respect, Si or Sn might be expected to follow p-type dopants such as Zn which does not show any great dependence on implantation temperature (8, 9).

Here, S, Se, and Si have been implanted with the intent of comparing and contrasting their annealing behavior. Earlier work on compensation has indicated that even though annealing occurs at 225° and 525°C, this compensation arising from irradiation defects is still only partially recovered at least up to 600°C (10). As a consequence, any n-type doping regardless of the dopant implanted will require annealing to well over 600°C. Annealing temperatures used on this study range from 700° to 900°C. The influence of Ga loss into SiO_2 has been investigated by the use of oxides containing an initial quantity of Ga prior to any outdiffusion. Some implants have also been annealed using Si_3N_4 and AlN instead of SiO_2. Finally, the implantation temperature dependence of Si, taken as representative of the Group IV dopants, is compared to the Group VI dopant behavior.

Key words: GaAs doping, implantation, surface encapsulation.

Experimental

Epitaxial GaAs grown by the hydride vapor phase method has been used in the present work. It is grown 2° off the <100> direction and to a thickness of 1-1½ μm. The doping is held $\lesssim 10^{15}$ cm^{-3} and will have negligible effect compared to the implanted conductivity to be investigated. Any dependence of the implanted electrical activity on the initial material is minimized by confining the work to this epitaxial material which is grown as required under near identical conditions. In contrast, some earlier Si implants into chrome-doped bulk GaAs exhibited carrier concentrations and mobilities that were only around 75% of what is generally attainable with the epitaxial layers.

The SiO_2 used as a surface encapsulant is spun on from an alcohol solution.[1] Following an HF cleaning treatment the oxide is applied and spun at 3000 rpm. The oxide is baked at 180°C and film thicknesses are generally ~1700Å. The gallium-SiO_2 layers are similarly applied using oxides meant primarily to be Ga sources for diffusion into silicon and containing Ga to concentrations of 10^{21} cm^{-3}. The Si_3N_4 and AlN are sputtered on (using targets of the same composition and not reactively). The AlN contains considerable oxide while the Si_3N_4 is relatively pure. Wafer deterioration becomes physically apparent with the oxide encapsulation after heat-treatment to 875°-900°C. Si_3N_4, on the other hand, can withstand temperatures up to at least 925°-950°C.

The encapsulating layers are generally applied prior to implantation and so protect the GaAs during both implantation and postannealing. Most of the S^+ implants to be reported were carried out at 500°C while temperatures within the 200°-300°C range were used for both Se and Si. It should be noted that as there is no advantage in implanting S^+ at 500°C rather than at 200°-300°C (6), the lower temperatures should also be preferred for S^+ (and particularly if implanting prior to applying the surface encapsulant were required).

All the implants have been performed at 1 MeV. Other than one series of S^+ implants at 3×10^{14} cm^{-2} a dose of 10^{14} cm^{-2} has been used throughout. SiH^+ has been implanted instead of Si^+ to avoid contamination from other mass 28 species. Annealing is carried out in a nitrogen ambient for 10 min. For performing Hall measurements tin contacts are alloyed into the implanted layer and no contracting problems are encountered at the dose levels mentioned.

Results

Table I compares the electrical activity resulting from sulfur implants when SiO_2 containing Ga, "pure" SiO_2, and Si_3N_4 are used as the encapsulants. The variation in implantation temperature (170°-360°C) should have minimal effect on the resulting activity. All the samples were implanted to a dose of 10^{14} cm^{-2} and then similarly annealed at 825°C for 10 min. It will be observed that the highest active concentration is given by the Ga-SiO_2 encapsulated layer, indicating that the presence of Ga has a direct bearing on the resulting activity. Si_3N_4, though better than straight SiO_2, does not at present measure up to Ga-SiO_2. Some implants were also undertaken with AlN as the protective layer but the corresponding activity was much lower with only 1-2 $\times 10^{13}$ cm^{-2} becoming electrically active. It should be borne in mind that as no information has been obtained on the relative effectiveness of the encapsulants in retaining the as-implanted distributions, the increase in integrated (sheet) concentrations may also reflect some profile widening.

[1] Commercially available from Emulsitone, Whippany, New Jersey.

Table I. Doping efficiency of 10^{14} S^+ cm^{-2} implants annealed at 825°C with different encapsulants

Encapsulant	$T_{impl.}$ (°C)	R_s (ohm/□)	μ(cm²/V-sec)	N_S(cm^{-2})
Ga-SiO_2	360	51	3100	4.0×10^{13}
	170	57	2750	4.0×10^{13}
Si_3N_4	240	81	3100	2.5×10^{13}
SiO_2	299	99	3150	2.0×10^{13}
	240	127	2050	2.4×10^{13}

The annealing temperature of 825°C used in Table I is near the optimum annealing temperature for 10^{14} cm^{-2} S^+ implants. This can be seen in Fig. 1 where both the sheet carrier concentration and the mobility are shown as a function of annealing temperature. The maximum concentration of 3.6×10^{13} cm^{-2} is lower than the 4×10^{13} cm^{-2} value given in Table I for similarly capped (Ga-SiO_2) implants. The reduction presumably arises from the 500°C implantation temperature used in Fig. 1 and which is marginally close to the onset of a deterioration in activity that occurs on implanting at temperatures $\gtrsim$ 500°C (6).

The improvement in mobility at 750°-800°C despite the accompanying rise in free carrier concentration suggests that considerable defect annealing is occurring. Relocation of S onto substitutional sites alone would lead to increased impurity scattering and a reduction in mobility. The maximum mobility of 3000 indicates a high degree of damage recovery. These mobilities correspond to 10^{18} cm^{-3} doping in bulk GaAs.

It is presumed that the fall off in conductivity that occurs above 825°C is surface related. The activity still attainable at higher temperatures for Si_3N_4 encapsulated Te implants (7) suggests that certain dielectrics may not be as restrictive as SiO_2 in this respect. More clarification is required, however. The same optimum annealing feature is followed at higher doses as can be seen in Fig. 2 for a 3×10^{14} cm^{-2} dose level. At 800°C both the carrier concentration and mobility are close to what was obtained from the 10^{14} cm^{-2} implant with similar annealing. The mobility then falls to reflect the higher active carrier concentration and, despite using similarly applied Ga-SiO_2, the optimum annealing condition of 800°-825°C in Fig. 1 shifts to 850°-875°C.

Similar annealing features are exhibited by Se^+. This is shown in Fig. 3 where Se^+ has been implanted to doses of 10^{14} cm^{-2} at 250°C and annealed with SiO_2 containing Ga. The highest activity occurs at the same annealing temperature seen in Fig. 1 with sulfur. The mobilities are generally lower than those already observed for sulfur and what can be obtained from Si^+ implants.

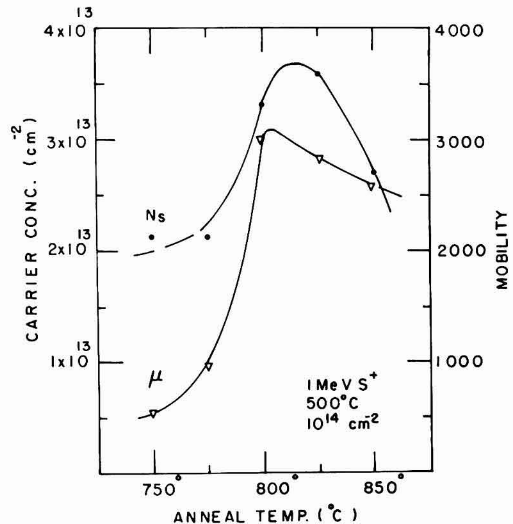

Fig. 1. Dependence of the sheet carrier concentration and mobility on annealing temperature for sulfur encapsulated with Ga-SiO_2.

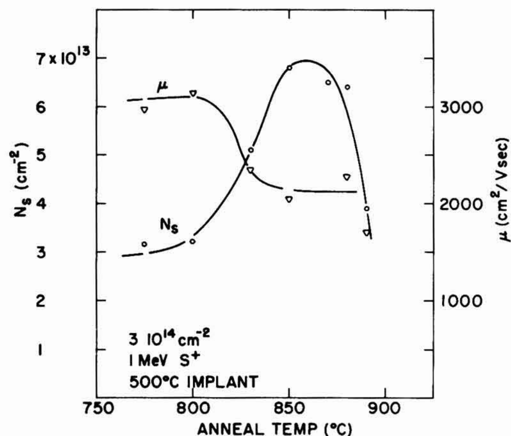

Fig. 2. Annealing of sulfur showing the higher temperatures required for the heavier 3×10^{14} cm^{-2} dose level.

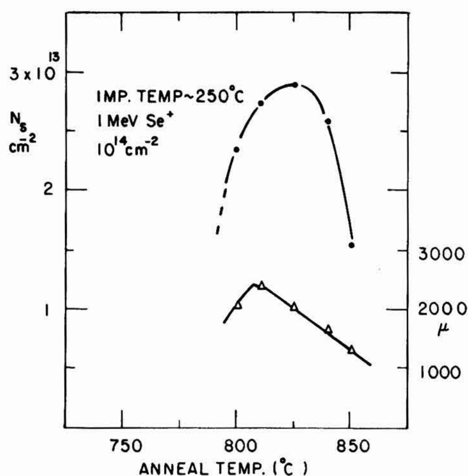

Fig. 3. Annealing of selenium-implanted layers passivated with Ga-SiO_2.

Turning to Group IV dopants, the influence of various dielectric coatings on the annealing of Si^+-implanted layers is shown in Table II. Doses of 10^{14} cm^{-2} were implanted at 250°-300°C and then annealed to 800°C. Contrary to the behavior with S^+, the presence of Ga within the oxide now becomes detrimental to achieving high electrical activity. It thus appears again that Ga-SiO_2 reduces the out-diffusion of Ga but here, unlike with S^+, such an out-diffusion seems desirable. The Si_3N_4 and AlN annealed layers are intermediate between the two oxide extremes.

Table II. Doping efficiency of 10^{14} Si^+ cm^{-2} implants annealed at 800°C with different encapsulants

Encapsulant	$T_{Impl.}$ (°C)	R_s (ohm/□)	μ(cm²/V-sec)	N_S(cm⁻²)
Ga-SiO_2	260	496	2100	0.6×10^{13}
	300	340	2300	0.8×10^{13}
AlN	290	149	3000	1.4×10^{13}
	250	142	2600	1.7×10^{13}
Si_3N_4	270	139	2500	1.8×10^{13}
SiO_2	290	99	3000	2.1×10^{13}
	240	87	3000	2.4×10^{13}

The 800°C annealing for the implants of Table II is not the most ideal for Si. This is illustrated in Fig. 4 where it can be seen that Si does not exhibit the 800°-825°C optimum temperature observed earlier with both S^+ and Se^+ at the same 10^{14} cm^{-2} dose. These Si^+ implants, at 220°-240°C, were annealed using Ga-free SiO_2. The sheet carrier concentrations up to 3.6×10^{13} cm^{-2} (R_s = 52 ohm/□) are limited by the temperature which the oxide can withstand and which presently is ~900°C. Possibilities for improvement include overcoating the oxide with a nitride layer which would withstand higher temperatures or going to an oxynitride layer which may allow some Ga out-diffusion.

The corresponding mobilities together with those of other Si^+ layers annealed with various oxides including As-SiO_2 are shown in Fig. 5. An improvement occurs at ~825°C but this stage is not as pronounced as that seen ~775°C with S^+ (Fig. 1).

The effect of implantation temperature on S, Se, and Si layers can be seen in Table III. All ions have been implanted above 150°C as well as at room temperature. The sulfur results are taken from earlier work (6) while those for Se are in agreement with Foyt *et al.*

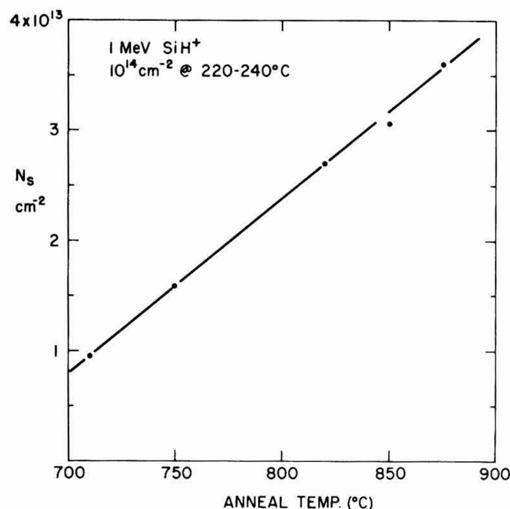

Fig. 4. Annealing of silicon with SiO_2 as the encapsulant

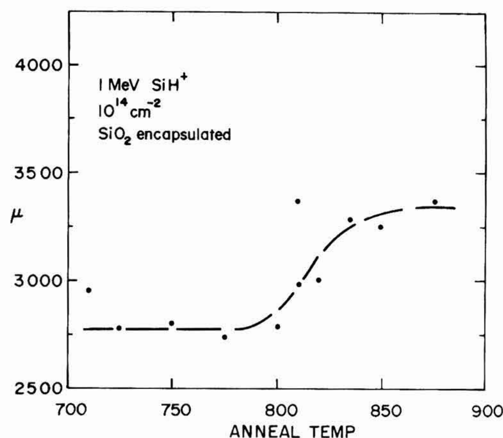

Fig. 5. Dependence of mobility on annealing for silicon implanted layers.

Table III. Effect of implantation temperature on S^+, Se^+, and Si^+ electrical activity

Ion	$T_{Impl.}$ (°C)	T_{Anneal} (°C)	Encapsulant	μ(cm^2/V-sec)	N_S(cm^{-2})	Heated N_S / R.T. N_S
S	360	825°	Ga-SiO_2	3100	4.0×10^{13}	2.5
	20	825°	Ga-SiO_2	3000	1.6×10^{13}	
Se	280	825°	Ga-SiO_2	2050	2.9×10^{13}	3.2
	20	825°	Ga-SiO_2	1650	0.9×10^{13}	
Si	235	825°	As-SiO_2	2750	2.2×10^{13}	1.2
	20	825°	As-SiO_2	2700	1.9×10^{13}	
Si	295	810°	SiO_2	3000	2.3×10^{13}	1.3
	20	810°	SiO_2	3350	1.8×10^{13}	

(4). The most significant factor is the relative insensitivity of Si to implantation temperature. It is clear that Si becomes substitutional more readily than the Group VI dopants when implanted at room temperature.

The comparatively lower activity in Table III that is shown for Si^+ arises through annealing at similar temperatures to the S^+ and Se^+ layers rather than at the more ideal higher temperatures indicated by Fig. 4. Both SiO_2 and As-SiO_2 have been used in annealing these Si^+ implants. It may be noted that incorporation of As within the oxide does not produce any improvement comparable to that obtained for S with Ga-SiO_2. It appears that As loss is not a problem, in agreement with Gyulai *et al.* (3) who established from backscattering measurements that Ga alone out-diffuses through SiO_2.

In summary, significant differences arise in the behavior of implanted S^+ or Se^+ and Si^+. These differences are attributed to Group VI and Group IV dopants occupying different sublattice sites. Incorporation of Ga into SiO_2 resulted in a marked improvement with S^+ implants but was detrimental to achieving high conductivity with Si. It is concluded from such behavior that the gallium within the oxide at least partially inhibits the gallium loss from the wafer surface. Further, some Ga loss seems desirable in the case of Si^+ and presumably the same applies and inadvertently occurs on implanting Group II p-type dopants which can in general be more readily rendered electrically active (2). The annealing characteristics of S and Se with an optimum annealing temperature contrast sharply with Si which requires higher annealing temperatures to achieve similar doping levels. Finally, the substantial difference in the electrical activity resulting from implanting Group VI elements at room temperature and $\gtrsim 150°C$ does not apply to Si. In this respect Si resembles Zn which does not exhibit any strong dependence on implantation temperature.

Acknowledgment

We would like to thank Dr. Genser of Emulsitone for valuable advice on the use of spin on oxides. The technical assistance of M. Deane and J. Hawley with sample preparation is gratefully acknowledged.

Manuscript submitted March 5, 1975; revised manuscript received June 9, 1975.

Any discussion of this paper will appear in a Discussion Section to be published in the June 1976 JOURNAL. All discussions for the June 1976 Discussion Section should be submitted by Feb. 1, 1976.

Publication costs of this article were partially assisted by Air Force Cambridge Research Laboratories.

REFERENCES

1. R. M. Allen, "European Conference on Ion Implantation," p. 126, Peter Peregrinus Ltd. (1970).
2. F. H. Eisen, Presented at Fourth Int. Conf. on Ion Implantation, Osaka, Japan, 1974.
3. J. Gyulai, J. W. Mayer, and I. V. Mitchell, *Appl. Phys. Letters*, **17**, 332 (1970).
4. A. G. Foyt, J. P. Donnelly, and W. T. Lindley, *ibid*, **14**, 372 (1969).
5. J. S. Harris, F. H. Eisen, B. Welch, J. D. Haskell, R. D. Pashley, and J. W. Mayer, *ibid.*, **21**, 601 (1972).
6. D. E. Davies, S. Roosild, and L. Lowe, *Solid State Electron.*, **18**, 733 (1975).
7. F. H. Eisen, J. S. Harris, B. Welch, R. D. Pashley, D. Sigurd, and J. W. Mayer, in "Ion Implantation in Semiconductors and Other Materials," B. L. Crowder, Editor, p. 631, Plenum Press, New York (1973).
8. V. M. Zelevenskaya, G. A. Kachurin, N. B. Pridachin, and L. S. Smirnov, *Soviet Phys.-Semiconductors*, **4**, 1529 (1971).
9. Y. Yuba, K. Gamo, K. Masuda, and S. Namba, *Japan J. Appl. Phys.*, **13**, 641 (1974).
10. D. E. Davies, J. K. Kennedy, and A. C. Yang, *Appl. Phys. Letters*, **23**, 615 (1973).

Vapor-Phase Etching and Polishing of Gallium Arsenide Using Hydrogen Chloride Gas

Rajaram Bhat,* B. Jayant Baliga,,[1] and Sorab K. Ghandhi†**

Electrical and Systems Engineering Department, Rensselaer Polytechnic Institute, Troy, New York 12181

ABSTRACT

Vapor-phase etching of (100) and ($\bar{1}\bar{1}\bar{1}$) GaAs substrates has been conducted in HCl-H_2-AsH_3 gas mixtures. Specular surfaces, suitable for epitaxy, were obtained for substrates doped with Cr, Te, Si, and Zn when the substrates were etched at temperatures above 870°C. It is shown that the etching reaction is mass-transport limited at these temperatures for both (100) and ($\bar{1}\bar{1}\bar{1}$) surfaces. At lower temperatures, faceting results from the unequal etch rates for the different orientations. Etch rates of 0.02-14 μm/min were obtained in this study.

The capability for *in situ* etching of substrates has often been incorporated in systems for vapor-phase epitaxy to insure a clean and damage-free surface prior to growth. It is an inherent feature of gallium arsenide epitaxial systems utilizing arsenic trichloride but details of the etching step are not available. Lin, Chou, and Miller (1) have studied the vapor-phase etching of ($\bar{1}\bar{1}\bar{1}$) and (100) gallium arsenide using hydrogen-water vapor mixtures. Shaikh, Chou, and Donaghey (2) have studied hydrogen chloride etching of (100) gallium arsenide in a hydrogen-arsine ambient. The emphasis in their study was on the modeling of the mass transfer process to account for the etch rates observed experimentally. HCl etching of Si-, Te- and Sn-doped (100) GaAs surfaces has been studied by Moon and James (3) using Auger electron spectroscopy but no details of the surface morphology were published.

In this paper we wish to report studies conducted on the vapor-phase etching of a variety of gallium arsenide substrates using anhydrous hydrogen chloride gas in a hydrogen and arsenic ambient. High quality surfaces, with etch rates ranging from 0.02-14 μm/min, were obtained for (100) and ($\bar{1}\bar{1}\bar{1}$) substrates, at temperatures exceeding 870°C. The etching reaction for all orientations was mass-transport limited at these temperatures. Under these conditions the partial pressure of arsenic did not significantly influence the etch rate or surface morphology, provided sufficient arsenic was present to prevent decomposition.

Experimental Conditions

Apparatus.—Etching was carried out in a 50 mm ID, 37 cm long, rf heated, horizontal quartz tube. A 50 by 25 by 13 mm graphite susceptor, coated with pyrolytic graphite, was placed approximately 16 cm from the input end of the reaction chamber, at an angle of 7° to the direction of gas flow. Temperature was monitored using a Pt/Pt-13% Rh thermocouple enclosed in a quartz sheath and inserted into the susceptor. The temperature was verified using infrared pyrometric measurements. Gases were delivered to the reaction chamber through stainless steel tubing, except in the case of HCl where Monel tubing was used to minimize contamination. The apparatus was similar to the one used for the growth of III-V compounds (4).

Gases.—The purity of the hydrogen chloride gas was found to have considerable effect on the quality of the etched surface. Electronic grade hydrogen chloride gas obtained from Matheson Gas Products[2] resulted in poor surfaces under all experimental conditions. Similar difficulties have been reported by Amick, Roth, and Gossenberger (5) in the etching of germanium. Etching with electronic grade HCl, diluted to 1% in six-nines purity hydrogen,[3] gave excellent results. The arsine gas used in this investigation was either a 2% mixture in five-nines purity hydrogen[2] or a 10% mixture in six-nines purity hydrogen.[3] Ultrahigh purity hydrogen,[2] passed through a deoxidizer and molecular sieve,[4] was used as the carrier gas.

Substrates.—Most experiments were performed with boat-grown, *(100) oriented, Te-doped GaAs as the* substrates.[5] Some investigations were also conducted using boat-grown (100) Cr- and Zn-doped[5] GaAs, ($\bar{1}\bar{1}\bar{1}$) Te-doped,[6] Zn-doped,[6] Cr-doped,[6] and Si-doped[7] GaAs substrates. All wafers were obtained chemimechanically polished on one side. The wafers were degreased in methanol, etched in Caro's etch [$10H_2SO_4$ (97%):$1H_2O_2$ (30%):$1H_2O$] for 2 min at room temperature, rinsed in deionized water, and blown dry in filtered air after a final rinse in methanol. This procedure ensured a featureless, damage-free surface prior to *in situ* etching. More elaborate cleaning procedures, such as successive boiling in trichloroethylene, acetone, and methanol were attempted with no significant improvement in the quality of the etched wafer.

Procedure.—Substrates measuring 5 by 6 mm were placed centrally on the susceptor. The system was first purged with prepurified argon (2 liters/min) for 15 min, followed by a 5 min purge with ultrahigh purity hydrogen (3 liters/min). The susceptor was then heated to the etching temperature after introducing the required amount of arsine to prevent decomposition of the GaAs substrate. Substrates were maintained in hydrogen for 15 min at the etching temperature. This step served to remove traces of oxide on the gallium arsenide substrates and resulted in improving the quality of the etched surfaces. HCl gas was then introduced at the desired rate of flow and the substrates were usually etched for 2 min. The system was maintained at the etching temperature for 3 min, after the HCl gas was shut off. Typical flow rates were 3-18 ml/min for arsine gas,[8] 250-8100 ml/min for hydrogen, and 0.1-5 ml/min for HCl gas.[8] Typical etch rates ranged from 0.02-23 μm/min at 900°C.

* Electrochemical Society Student Member.
** Electrochemical Society Active Member.
† Electrochemical Society Life Member.
[1] Present address: General Electric Company, Research and Development Center, Schenectady, New York 12301.
[2] Matheson Gas Products, East Rutherford, New Jersey 07073.
Key words: vapor etching, vapor polishing, gallium arsenide, hydrogen chloride gas, epitaxy.

[3] Precision Gas Products, Inc., Rahway, New Jersey 07065.
[4] The use of a Pd-diffuser did not result in any improvement in the quality of the etched wafers.
[5] Electronic Materials Corporation Pasadena, California 91107.
[6] Texas Materials Laboratory, Inc., Garland, Texas 75041.
[7] Supplied by Dr. W. Tantraporn, General Electric Company, Schenectady, New York 12301.
[8] In this paper, flow rates for AsH_3 and HCl are all quoted in terms of the actual arsine and hydrogen chloride content of the diluted gas.

Etch rate definition and determination.—Figure 1 shows the decrease in substrate thickness with increasing etch time for a typical etching experiment. The decrease in GaAs substrate thickness is seen to be a linear function of time, for times less than approximately 5 min. The deviation from linearity for etch times greater than 5 min is due to the loss of planarity of the substrates. Based on these considerations, it was decided that all measurements of etch rate would be made for an etch period of 2 min. Since the etch rate was constant for this period, it was defined in terms of the substrate thickness removed per unit time. The change in substrate thickness was obtained gravimetrically.

Experimental Results

Temperature.—The effect of temperature on etch rate was determined for (100) and $(\bar{1}\bar{1}\bar{1})$ oriented, Te-doped GaAs substrates using a flow of 900 ml/min of hydrogen, 3 ml/min of arsine, and 2 ml/min of HCl gas. Under these conditions, the etching reaction of (100) GaAs substrates was mass-transport limited at temperatures above 850°C and kinetically controlled below this temperature with an activation energy of 1.25 eV/molecule. The etching reaction of the $(\bar{1}\bar{1}\bar{1})$ GaAs substrates was mass-transport limited at temperatures above 870°C and kinetically controlled below this temperature with an activation energy of 1.85 eV/molecule. As expected, equal etch rates were observed at temperatures above 870°C, as shown in Fig. 2. [The data in Fig. 2 have not been corrected for the change in linear velocity with temperature (6)].

Surfaces of both (100) and $(\bar{1}\bar{1}\bar{1})$ GaAs substrates etched below 870°C became increasingly faceted, with the simultaneous formation of either etch pits or hillocks,[9] due to the unequal etch rates for different substrate orientations. Above 870°C, where the etch rates for the different orientations were equal, etched (100) and $(\bar{1}\bar{1}\bar{1})$ substrate surfaces were featureless, as seen in the photomicrographs of Fig. 3 and 4.[10]

Chemical polishing of semiconductor substrates occurs when the etch rate for all crystallographic orientations is equal. This is achieved when the etching reaction is mass-transport limited, provided that the adsorption of the etchant on the substrate surface is independent of perturbations present on the surface (7).

[9] Distinguished by scanning electron microscopy.
[10] In this paper, all photomicrographs were taken using the Nomarski interference contrast technique.

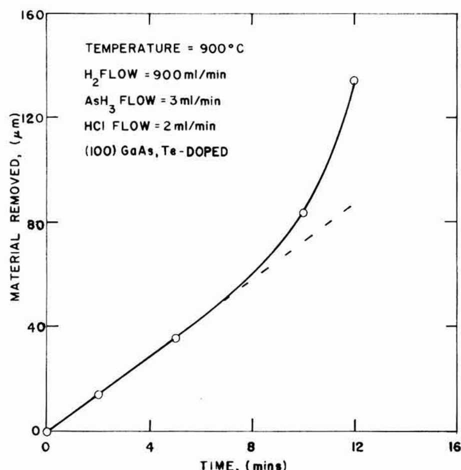

Fig. 1. Change in thickness of the wafers as a function of time

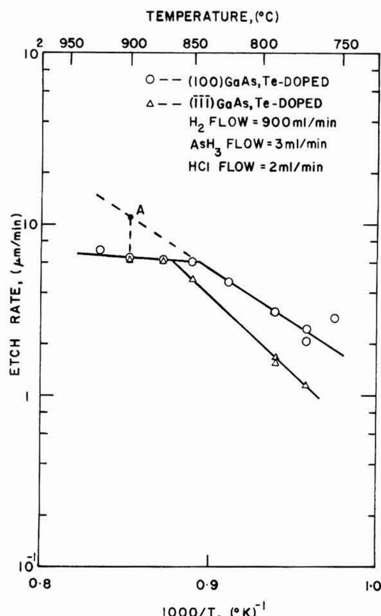

Fig. 2. Effect of substrate temperature on etch rate

The latter condition is apparently met during the vapor-phase etching of GaAs by HCl gas.

Hydrogen flow.—Figure 5 shows the variation of etch rate with hydrogen flow at 900°C for (100), Te-doped GaAs. In these experiments, the arsine and HCl gas flow was varied in proportion to the hydrogen flow to keep their partial pressures constant at 3.3×10^{-3} atm and 2.22×10^{-3} atm, respectively. It is seen that the etch rate varies linearly as the square root of the hydrogen flow for flows below 2.5 liters/min. This is because the etch rate varies directly with the rate of transport of HCl atoms to the substrate under mass-transport limited kinetics. This rate of transport varies directly with the boundary layer thickness at the substrate, and hence as the square root of the hydrogen flow under laminar flow conditions. At higher flows the etch rate saturates at 10.7 μ/min. This independence of etch rate at high hydrogen flow indicates the etching mechanism has become kinetically limited. If the data representing kinetically controlled etching shown in Fig. 2 is extrapolated to 900°C (point A), the value of the etch rate obtained is indeed the same as the observed saturated value.

The rate of transport of As to the GaAs surface decreases with decreasing hydrogen flow due to the increase in the boundary layer thickness. Consequently, substrate decomposition can be expected to occur at low hydrogen flows. This was indeed found to be the case for hydrogen flow rates below 0.45 liter/min. Verification of this fact was carried out by heating substrates under the above conditions without performing HCl etching. Surfaces of the HCl etched and the heated substrates were found to have similar features for identical hydrogen flow rates.

Arsine flow.—The effect of arsine flow on etch rate and surface quality under mass-transport limited conditions was investigated at 900°C using a hydrogen flow of 900 ml/min. It was found that at least 3 ml/min of arsine was required to prevent the decomposition of the substrate. For arsine flows between 3 and 18 ml/min, there was no appreciable change in surface quality, and the etch rate did not change within experimental error. Under similar flow conditions at 790°C,

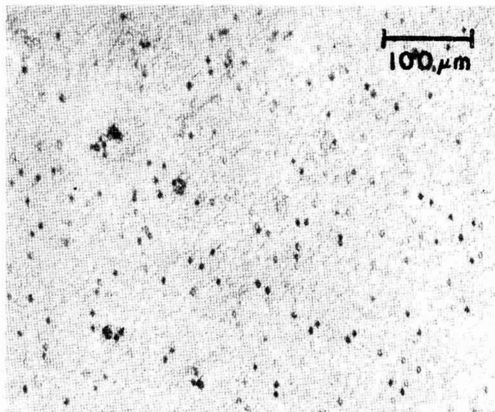

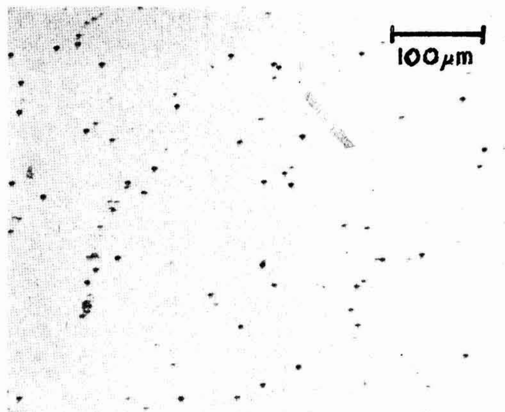

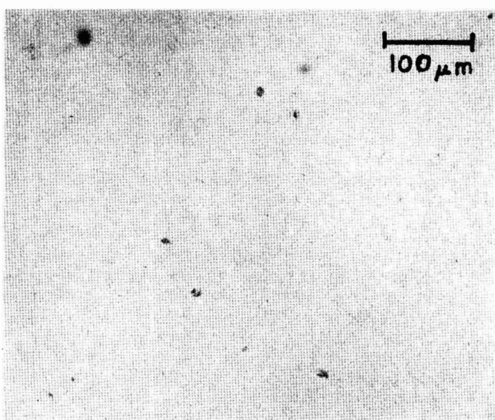

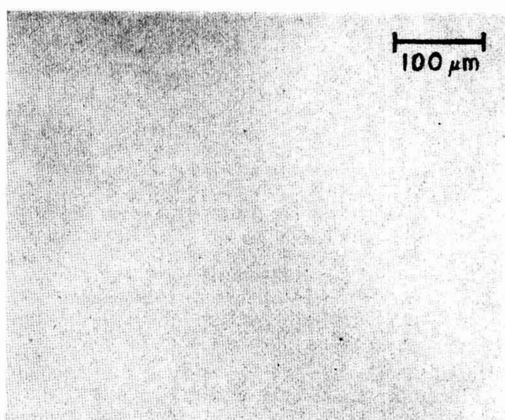

Fig. 3. Effect of temperature on the surface morphology of (100) Te-doped GaAs etched at (a, top left) 750°C, (b, top right) 825°C, (c, bottom left) 850°C, and (d, bottom right) 900°C.

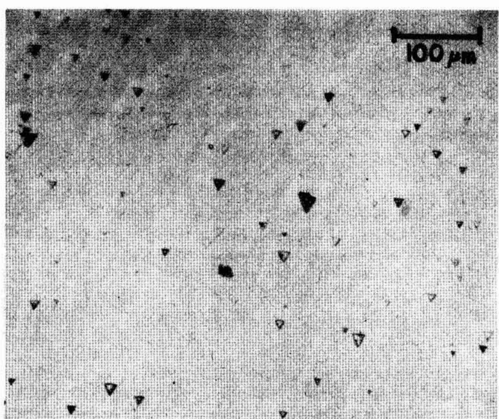

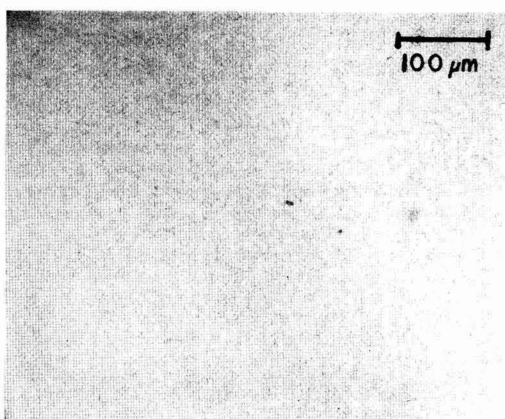

Fig. 4. Effect of temperature on the surface morphology of $(\bar{1}\bar{1}\bar{1})$ Te-doped GaAs etched at (a, left) 790°C and (b, right) 900°C

where the etching was kinetically controlled, the etch rate was found to decrease with increasing arsine flow.

HCl flow.—Figure 6 shows the etch rate of (100), Te-doped GaAs substrates as a function of the HCl gas flow. These experiments were conducted at a temperature of 900°C using a total hydrogen flow of 900 ml/min and an arsine flow of 3 ml/min. The etch rate was found to vary superlinearly with HCl concentration. Similar nonlinear dependence of the etch rate on etchant gas flow, under mass-transport limited conditions, has been observed in the vapor-phase etching of Si (8, 9) and Ge (6). Ideally, under mass-transport

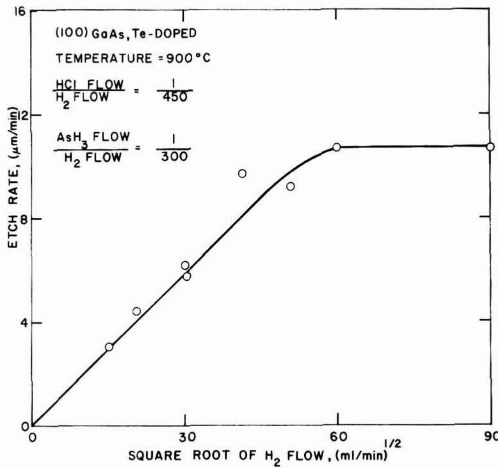

Fig. 5. Effect of hydrogen flow on etch rate

limited conditions, the etch rate should vary parabolically with the etchant concentration at low etchant partial pressures (9).

Orientation and dopant type.—The etch rate and the surface quality of (100) and $(\bar{1}\bar{1}\bar{1})$ GaAs substrates with different dopants were also evaluated. The etch rate observed for Zn- and Cr-doped (100) and Si-,[11] Zn-, and Cr-doped $(\bar{1}\bar{1}\bar{1})$ GaAs substrates, under both mass-transport limited and kinetically controlled conditions, was the same as for their Te-doped counterparts. Therefore, the etch rate is insensitive to the type of dopant incorporated in the GaAs.

[11] Si-doped (100) GaAs was not available to us at the time this investigation was carried out.

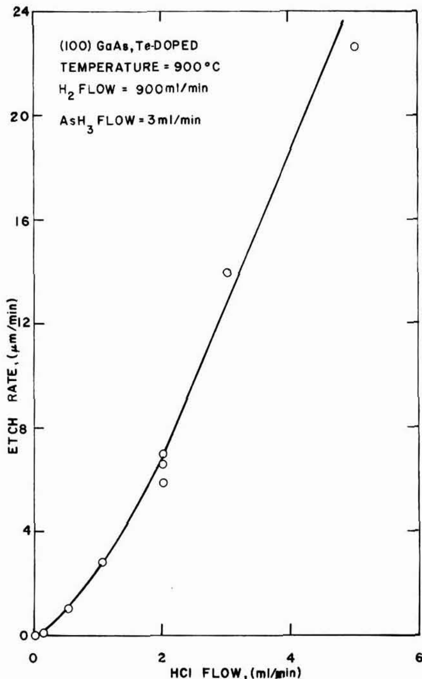

Fig. 6. Effect of HCl gas flow on etch rate

All substrates etched at 900°C using a hydrogen flow of 900 ml/min, arsine flow of 3 ml/min, and a HCl gas flow of 2 ml/min were specular to the unaided eye. However, the quality of etched (100) Cr-doped and $(\bar{1}\bar{1}\bar{1})$ Si- and Cr-doped GaAs substrate surfaces was inferior to those obtained with Te- and Zn-doped GaAs substrates under microscopic examination (Fig. 7). This

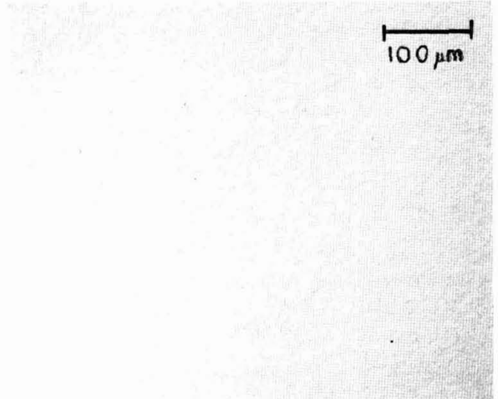

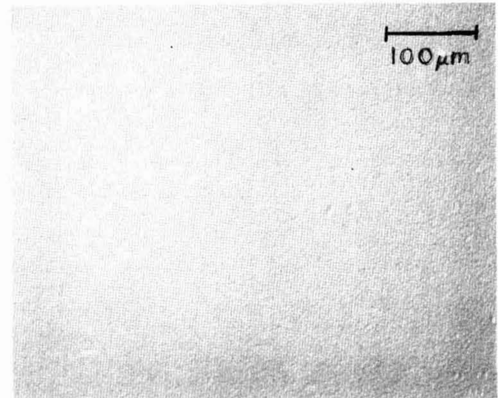

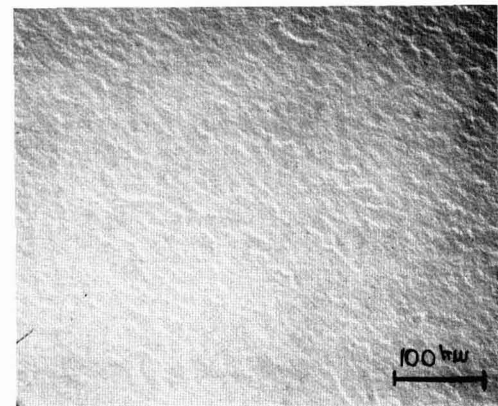

Fig. 7. Surface mor hology of etched (a, top) Si-doped, $(\bar{1}\bar{1}\bar{1})$ GaAs, (b, center) Cr- oped, (100) GaAs, and (c, bottom) Cr-doped, $(\bar{1}\bar{1}\bar{1})$ GaAs substra .s. Temperature 900°C, H_2 flow 900 ml/min, AsH_3 flow 3 ml/min, HCl gas flow 2 ml/min.

difference in etching behavior is believed to be due to greater inhomogeneities in the doping and dislocation densities in Cr- and Si-doped substrates.

Conclusions

Vapor-phase HCl etching of GaAs substrates can be performed to yield specular surfaces, suitable for epitaxy, with etch rates ranging from 0.02 to 14 μm/min, for (100) and $(\bar{1}\bar{1}\bar{1})$ Cr-, Te-, Zn-, and Si-doped GaAs substrates. A necessary condition for obtaining specular surfaces is that all orientations have the same etch rate. This condition is achieved at sufficiently high temperatures where the etch rate is mass-transport limited for all orientations. The quality of etched (100) and $(\bar{1}\bar{1}\bar{1})$ Si- and Cr-doped substrate surfaces was inferior to those obtained for Te- and Zn-doped GaAs substrates.

Acknowledgment

This work was partly supported by Grant No. GK-31332 from the National Science Foundation. The authors are indebted to Dr. W. Tantraporn for providing the Si-doped gallium arsenide and to Ms. R. Rafun for assistance in manuscript preparation.

Manuscript submitted March 24, 1975; revised manuscript received May 9, 1975.

Any discussion of this paper will appear in a Discussion Section to be published in the June 1976 JOURNAL. All discussions for the June 1976 Discussion Section should be submitted by Feb. 1, 1976.

Publication costs of this article were partially assisted by Rensselaer Polytechnic Institute.

REFERENCES

1. C. Lin, L. Chow, and K. L. Miller, *This Journal*, **117**, 407 (1970).
2. S. A. Shaikh, H. K. Chou, and L. F. Donaghey, Abstract 151, p. 364, Electrochemical Society Extended Abstracts, Spring Meeting, San Francisco, Calif., May 12-17, 1974.
3. R. L. Moon and L. W. James, *This Journal*, **120**, 581 (1973).
4. B. J. Baliga and S. K. Ghandhi, *ibid.*, **121**, 1642 (1974).
5. J. A. Amick, E. A. Roth, and H. Gossenberger, *RCA Rev.*, **24**, 473 (1963).
6. A. Reisman and M. Berkenblit, *This Journal*, **118**, 812 (1965).
7. H. C. Gatos and M. C. Lavine, *ibid.*, **107**, 427 (1960).
8. G. A. Lang and T. Stavish, *RCA Rev.*, **24**, 488 (1963).
9. W. H. Shepherd, *This Journal*, **112**, 988 (1965).

Chemical Processes in Vapor Deposition of Silicon

I. Deposition from $SiCl_2H_2$ and Etching by HCl

Vladimir S. Ban* and Stephen L. Gilbert

RCA Laboratories, Princeton, New Jersey 08540

ABSTRACT

Chemical processes occurring in the vapor deposition of silicon from $SiCl_2H_2$ and in the etching of silicon by HCl were studied by means of a mass spectrometer coupled to the CVD reactor. This setup was successfully used for the qualitative and quantitative analysis of the composition of the vapor phase in the Si-Cl-H system. Species found in the vapor phase were H_2, HCl, $SiCl_2$, $SiCl_2H_2$, $SiCl_3H$, and $SiCl_4$, and their partial pressures were measured as a function of temperature, value of the Cl/H ratio, and of the chemical nature of the initial gaseous mixture entering the reactor. The experimentally determined partial pressures were compared with the equilibrium partial pressures of vapor species, calculated from the newest thermochemical data for the Si-Cl-H system. On the basis of these results we discuss the nature and the extent of chemical processes in systems studied.

The chemical vapor deposition (CVD) of thin layers of silicon is among the most important processes in the electronic industry. For this purpose, various Si-containing gases are used, *e.g.*, SiH_4 or various chlorosilanes such as SiH_3Cl, SiH_2Cl_2, $SiHCl_3$, and $SiCl_4$. Typically, a mixture consisting of approximately 1% of Si-containing gas and 99% of carrier gas, usually H_2 or He, is introduced into the CVD reactor, where it comes into contact with substrates placed on a hot susceptor. The deposition of a layer of Si then takes place on these substrates through chemical reactions, the nature of which depends on experimental conditions, such as temperature, partial pressures and nature of the gaseous mixture, reactor geometry, etc. The purpose of this article is to discuss our studies of chemical processes leading to the deposition of Si. In particular, we studied the deposition of Si from $SiCl_2H_2$ as well as the reverse of this process, *i.e.*, the HCl etching of Si. Dichlorosilane, $SiCl_2H_2$, is becoming an increasingly important starting material for the deposition of Si-layers (1).

* Electrochemical Society Active Member.
Key words: mass spectrometry, CVD, thermodynamics, kinetics.

In general, CVD processes in any system can be understood through the chemical thermodynamics of that system. Thermodynamical calculations should in principle yield information on the feasibility of CVD processes, possible efficiencies of these processes, and on the expected structure and composition of the product. However, in order to apply thermodynamics correctly, one has to know the following about the systems: (*a*) the composition of the condensed and gaseous phases under all experimental conditions; (*b*) the magnitude and the nature of possible kinetic effects, the existence of which may determine the applicability of thermodynamics to the system in question; and (*c*) a set of reliable and consistent thermochemical data should be available.

In growth of Si from $SiCl_2H_2$ and in etching of Si by HCl, the pertinent system is Si-Cl-H. Thermodynamical calculations were applied to this system previously (2, 3). These calculations predicted the composition of the vapor phase, as well as the efficiency of the deposition of Si under various experimental conditions. However, neither the applicability of thermodynamics to the system nor the results of cal-

culations were experimentally verified. One could therefore suspect that the actual situation in the CVD reactor is perhaps different from the situation predicted by calculations. In this paper, we present results of the experimental qualitative and quantitative determination of the composition of the vapor phase and, in view of these results, discuss the applicability of thermodynamics to the system. The experimental and the calculated values of partial pressures are compared, and the nature and the extent of deviations from thermochemical equilibrium, *i.e.,* the role of kinetics, are assessed.

The determination of the composition of the vapor phase was done by means of a time-of-flight mass spectrometer connected directly to the CVD reactor. This method was successfully employed in studies of CVD of various III-V compounds (4-6).

Instrumental

Although the essential part of the mass spectrometer-CVD reactor setup has been described previously (4), we shall briefly review the main points as well as describe modifications made for the study of the Si-Cl-H system.

The reactor used in our studies is a tubular reactor with hot walls, similar to the reactor used in synthesis of III-V materials. This reactor is quite different from reactors normally used in deposition of Si-films, but it nevertheless enabled us to study the pertinent chemical processes. The deposition of Si took place either on the quartz wall of the reactor or on the layer of Si deposited there in previous experiments. Similarly, the HCl also reacted with this deposit in the etching experiments. The residence time of the gas phase as well as the Si area exposed to the gas phase was larger than in the normally used horizontal reactor used for CVD of Si. This should actually facilitate the attainment of chemical equilibrium in the system without altering the nature of reactions. The reactor was heated by a 4-segment tubular furnace. Measurements described here were done in the temperature range of 800°-1300°K. The length of the hot zone could be varied by switching one or two of the segments off. Gases were fed into the reactor through a combination of calibrated Fischer and Porter flow meters and Matheson electronic mass flow transducers. In this way, it was possible to introduce known amounts of $SiCl_2H_2$, HCl, H_2, or He into the reactor, and create a starting mixture of desired composition. There are also provisions for usage of $SiCl_3H$ and $SiCl_4$ in the reactor, but this will be described in another publication.

The reactor is connected to the mass spectrometer via a small quartz capillary. In this way, it is possible to sample hot vapor from the reactor under normal CVD conditions, *i.e.,* 1 atm and temperatures of over 1000°C. The capillary is maintained at the temperature of the sampled gas and since it is made from the same material, *i.e.,* quartz, as the reactor, no interactions different from those in the reactor would occur in the capillary. The capillary reduces pressure from 1 atm in the reactor to 10^{-5} Torr in the mass spectrometer. From it emanates a stream of hot gas directly into the ion source of the mass spectrometer. Since a mean free path at the pressure of 10^{-5} Torr is much longer than the distance between the capillary and the ion source (*ca.* 12 cm), most molecules enter the source without undergoing any interactions in the area between the capillary and the source. We therefore believe that the sample entering the mass spectrometer is representative of the gaseous phase in the CVD reactor. The mass spectrometer can be calibrated for quantitative studies. One can introduce into the reactor gaseous mixtures where partial pressures of constituents are known, *e.g.,* mixtures of $SiCl_2H_2$ and H_2, or HCl, $SiCl_2H_2$ and H_2, and then relate peak intensities in the mass spectra to corresponding partial pressures.

Schematic representation of the mass spectrometer-reactor combination is given in Fig. 1.

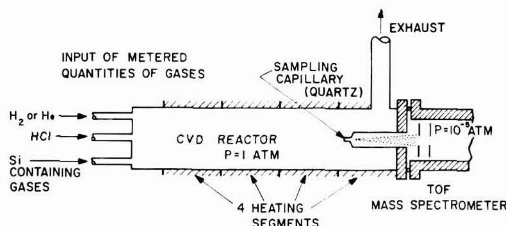

Fig. 1. Schematic representation of the system mass spectrometer-CVD reactor.

Thermodynamical Calculations

Calculations of equilibrium partial presures of vapor species in the Si-Cl-H system have been done by several authors (2, 3, 7) and we shall describe the method only briefly. Basically, one deals with a 3-component system, where the gaseous phase is in equilibrium with the solid phase, *i.e.,* silicon. Therefore, according to the Gibbs rule, the system has three degrees of freedom. These are pressure, temperature, and a compositional variable Cl/H. This Cl/H ratio remains constant throughout the deposition process because neither Cl nor H atoms are added or removed from the system during the deposition (or etching) of Si. Its value is determined by partial pressures of gases in the initially introduced mixture. From the previously referenced works, we learned that the following eight species are most abundant in the Si-Cl-H system: H_2, HCl, SiH_4, SiH_3Cl, SiH_2Cl_2, $SiHCl_3$, $SiCl_4$, and $SiCl_2$. Other possibly existing species, such as Cl, Cl_2, Si_2Cl_6, etc., would be present in negligible amounts only. In order to calculate equilibrium partial pressures of the eight species mentioned above, one must have a set of eight independent, generally nonlinear equations, which specify relationships between these species. Six of these equations represent chemical equilibria between species

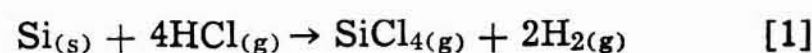

$$Si_{(s)} + 4HCl_{(g)} \rightarrow SiCl_{4(g)} + 2H_{2(g)} \quad [1]$$

$$K_{p(1)} = \frac{P_{SiCl_4} \cdot P^2_{H_2}}{a\text{Si} \cdot P^4_{HCl}}$$

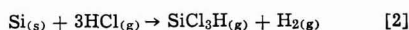

$$Si_{(s)} + 3HCl_{(g)} \rightarrow SiCl_3H_{(g)} + H_{2(g)} \quad [2]$$

$$K_{p(2)} = \frac{P_{SiCl_3H} \cdot P_{H_2}}{a\text{Si} \cdot P^3_{HCl}}$$

$$Si_{(s)} + 2HCl_{(g)} \rightarrow SiCl_2H_{2(g)} \quad [3]$$

$$K_{p(3)} = \frac{P_{SiCl_2H_2}}{a\text{Si} \cdot P^2_{HCl}}$$

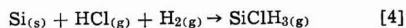

$$Si_{(s)} + HCl_{(g)} + H_{2(g)} \rightarrow SiClH_{3(g)} \quad [4]$$

$$K_{p(4)} = \frac{P_{SiClH_3}}{a\text{Si} \cdot P_{HCl} \cdot P_{H_2}}$$

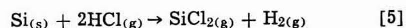

$$Si_{(s)} + 2HCl_{(g)} \rightarrow SiCl_{2(g)} + H_{2(g)} \quad [5]$$

$$K_{p(5)} = \frac{P_{SiCl_2} \cdot P_{H_2}}{a\text{Si} \cdot P^2_{HCl}}$$

$$Si_{(s)} + 2H_{2(g)} \rightarrow SiH_{4(g)} \quad [6]$$

$$K_{p(6)} = \frac{P_{SiH_4}}{a\text{Si} \cdot P^2_{H_2}}$$

The activity of Si is represented by a; $a = 1$.

The remaining two equations specify the Cl/H ratio and state that the total pressure in the system is 1 atm

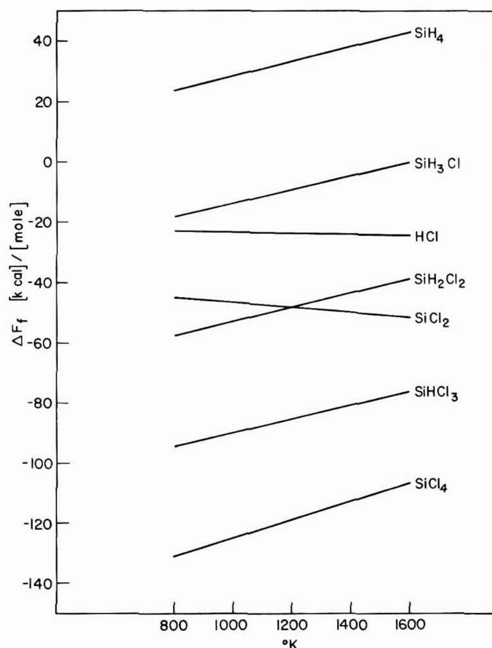

Fig. 2. Free energies of formation of important gaseous species in the Si-Cl-H system in the temperature interval of 800°-1600°K.

10^{-3}, 10^{-2}, 10^{-1}, and 10^{0}; the temperature was varied from 800° to 1600°K, in increments of 200°K. Results of calculations are given in Table I.

Thermodynamical calculations can also be used to determine the theoretical efficiency of the deposition process. The efficiency can be defined as

$$\eta = \frac{[\mathrm{Si/Cl}]_{\mathrm{in}} - [\mathrm{Si/Cl}]_{\mathrm{eq}}}{[\mathrm{Si/Cl}]_{\mathrm{in}}}$$

where $[\mathrm{Si/Cl}]_{\mathrm{in}}$ is the ratio of Si to Cl atoms in the starting mixture, and $[\mathrm{Si/Cl}]_{\mathrm{eq}}$ is this ratio in the equilibrium mixture. A negative value of η means that etching of Si is taking place in the system.

Experimental Results

Mass spectra of chlorosilanes.—Since the determination of the mass spectra of Si-containing gases in our setup is being reported elsewhere (9), we only briefly discuss this topic here. Vapor species in the reactor were identified by means of the attached mass spectrometer. The analysis is complicated by the fact that mass spectra of various chlorosilanes should be quite similar, due to the fragmentation of parent molecules by the ionizing electrons. We determined mass spectra of $SiCl_4$, $SiCl_3H$, $SiCl_2$, and $SiCl_2H_2$ in our experimental setup. A mixture containing 1% of these gases in He or H_2 (this change produces no difference in spectra) was introduced into the reactor and mass spectra were taken at room temperature, where no chemical reactions which would change the mixture occurred. The observed intensities of major peaks in these mixtures did not differ by more than 15%, thus indicating that our experimental setup is about equally sensitive for all chlorosilanes. Mass spectra of $SiCl_2$ were deduced from the high temperature mass spectrometry of $SiCl_4$-He mixtures where the only present vapor

$$\mathrm{Cl/H} = \frac{4P_{\mathrm{SiCl_4}} + 3P_{\mathrm{SiCl_3H}} + 2P_{\mathrm{SiCl_2H_2}} + 2P_{\mathrm{SiCl_2}} + P_{\mathrm{SiClH_3}} + P_{\mathrm{HCl}}}{2P_{\mathrm{H_2}} + P_{\mathrm{SiCl_3H}} + 2P_{\mathrm{SiCl_2H_2}} + 3P_{\mathrm{SiClH_3}} + P_{\mathrm{HCl}} + 4P_{\mathrm{SiH_4}}} \quad [7]$$

and

$$P_{\mathrm{SiCl_4}} + P_{\mathrm{SiCl_3H}} + P_{\mathrm{SiCl_2H_2}} + P_{\mathrm{SiClH_3}} + P_{\mathrm{SiCl_2}} + P_{\mathrm{SiH_4}} + P_{\mathrm{HCl}} + P_{\mathrm{H_2}} = 1 \quad [8]$$

Of course, when growing Si from a mixture of $SiCl_2H_2$ and H_2 partial pressures of all other species are initially equal to zero.

In order to find values of $K_{p(1\text{-}6)}$, the most convenient data to have are free energies of formation, ΔF_f, of all species in the temperature interval of interest. Values of ΔF_f of all species were calculated from thermochemical data for the Si-Cl-H system recently collected by Hunt and Sirtl (3). Figure 2 shows values of ΔF_f *vs.* temperature in the form of the so-called Ellingham diagrams (8).

Once values of K_p's were known, we calculated the equilibrium partial pressures of all eight species, using a simple iterative method on a time sharing computer. In these calculations, the Cl/H ratio was set to be

species were $SiCl_4$, $SiCl_2$, and He. Mass spectra of $SiClH_3$ were not determined, but as the calculations have shown, this should be a scarce species, and besides, using the analogy with other chlorosilanes, one could deduce its mass spectra with a fair degree of accuracy.

In determination of these spectra, 70 eV ionizing electrons were used. No corrections due to differences in ionization cross section of various species, possible mass discrimination of the instrument, etc., were applied, since we were primarily interested in the relative intensities of various peaks under our experimental conditions. Mass spectrum of $SiCl_4$ agrees reasonably well with the published data (10). Mass spectra of SiH_4, HCl, and H_2 are known. Results of the determination of mass spectra of $SiCl_4$, $SiCl_3H$, $SiCl_2H_2$, and $SiCl_2$ are graphically represented in Fig. 3. From the relative intensities of various peaks, one can calculate relative abundances of various species in the

Table I. Calculated values of equilibrium partial pressures (in atmospheres) of vapor species in the Si-Cl-H system

T, °K	Cl/H	H_2	HCl	$SiCl_4$	$SiHCl_3$	SiH_2Cl_2	SiH_3Cl	SiH_4	$SiCl_2$
1000	10^{0}	6.28×10^{-1}	1.52×10^{-2}	2.74×10^{-1}	8.01×10^{-2}	2.70×10^{-3}	5.05×10^{-5}	2.55×10^{-7}	1.99×10^{-4}
1000	10^{-1}	9.39×10^{-1}	1.07×10^{-2}	3.03×10^{-2}	1.88×10^{-2}	1.34×10^{-3}	5.33×10^{-5}	5.70×10^{-7}	6.62×10^{-5}
1000	10^{-2}	9.90×10^{-1}	5.40×10^{-3}	1.74×10^{-3}	2.26×10^{-3}	3.39×10^{-4}	2.83×10^{-5}	6.34×10^{-7}	1.59×10^{-5}
1000	10^{-3}	9.98×10^{-1}	1.67×10^{-3}	1.55×10^{-5}	6.58×10^{-5}	3.22×10^{-5}	8.78×10^{-6}	6.45×10^{-7}	1.50×10^{-6}
1200	10^{0}	6.0×10^{-1}	5.80×10^{-2}	2.61×10^{-1}	7.36×10^{-2}	2.92×10^{-3}	5.95×10^{-5}	3.43×10^{-7}	5.01×10^{-3}
1200	10^{-1}	9.18×10^{-1}	3.97×10^{-2}	2.44×10^{-2}	1.54×10^{-2}	1.37×10^{-3}	6.23×10^{-5}	8.02×10^{-7}	1.53×10^{-3}
1200	10^{-2}	9.83×10^{-1}	1.50×10^{-2}	4.30×10^{-4}	7.72×10^{-4}	1.94×10^{-4}	2.52×10^{-5}	9.22×10^{-7}	2.03×10^{-4}
1200	10^{-3}	9.98×10^{-1}	1.98×10^{-3}	1.26×10^{-7}	1.74×10^{-6}	3.38×10^{-6}	3.37×10^{-6}	9.49×10^{-7}	3.49×10^{-6}
1400	10^{0}	5.37×10^{-1}	1.38×10^{-1}	2.16×10^{-1}	5.99×10^{-2}	2.63×10^{-3}	5.75×10^{-5}	3.64×10^{-7}	4.62×10^{-2}
1400	10^{-1}	8.81×10^{-1}	8.63×10^{-2}	1.22×10^{-2}	8.89×10^{-3}	1.03×10^{-3}	5.88×10^{-5}	9.77×10^{-7}	1.10×10^{-2}
1400	10^{-2}	9.81×10^{-1}	1.85×10^{-2}	2.07×10^{-5}	7.84×10^{-5}	4.71×10^{-5}	1.40×10^{-5}	1.21×10^{-6}	4.52×10^{-4}
1400	10^{-3}	9.98×10^{-1}	1.98×10^{-3}	2.66×10^{-9}	9.56×10^{-8}	5.44×10^{-7}	1.53×10^{-6}	1.25×10^{-6}	5.13×10^{-6}

Total system pressure = 1 atm ± 1 × 10^{-5}.

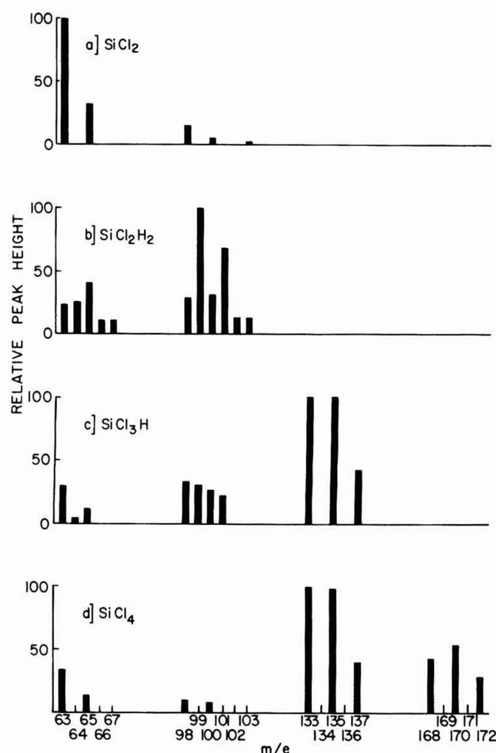

Fig. 3. Relative abundances of peaks in mass spectra of (a) $SiCl_2$; (b) $SiCl_2H_2$; (c) $SiCl_3H$; and (d) $SiCl_4$. The most abundant peak in each spectra is assigned a value of 100.

vapor phase; *i.e.*, one can perform the qualitative and the quantitative analysis of the vapor phase in the reactor.

Determination of partial pressures.—The qualitative and quantitative analysis results in determination of partial pressures of all detected species. Effects of temperature and of the Cl/H ratio, as well as possible effects of the nature of starting mixture on values of partial pressures of various species were studied. Measurements were done at 1000°, 1200°, and 1300°K; Cl/H ratios of 10^{-2}, 10^{-1}, and 10^0 were used. Mixtures with identical values of Cl/H ratio were prepared in two ways: by mixing pure $SiCl_2H_2$ with H_2, or by mixing the appropriate amounts of $SiCl_2H_2$ and HCl with H_2. The exact amounts mixed are given in Table II. In this way the effect of the nature (*i.e.*, of the presence or the absence of HCl) of starting mixture on the composition of the vapor phase could be studied. In cases of Cl/H = 10^0, either pure $SiCl_2H_2$ or pure HCl were introduced into the reactor. Of course, the deposition of Si will occur in the former, and the etching of Si will occur in the latter case, but the composition of the vapor phase in contact with solid Si should nevertheless be the same, providing that chemical equilibrium has been established.

Table II. Amounts of gases used to prepare starting mixtures

Cl/H	Symbol in Fig. 4	$SiCl_2H_2$, cm³/min	HCl, cm³/min	H_2, cm³/min
0.01	○	20	0	2000
0.01	●	20	20	2970
0.1	△	200	0	1800
0.1	▲	100	100	1350
1.0	□	200	0	0
1.0	■	0	200	0

Mass spectra of initial mixtures at room temperature contained only peaks characteristic for the gases comprising the mixture in question. At elevated temperatures new peaks appeared indicating the appearance of new species in the vapor phase. Under our experimental conditions, the following species were found to exist in appreciable amounts: H_2, HCl, $SiCl_2$, $SiCl_2H_2$, $SiCl_3H$, and $SiCl_4$. Species such as $SiClH_3$ and SiH_4 were not detected; Si_2Cl_6 was detected but only in very small amounts. The last three species were therefore ignored in the quantitative determination of partial pressures. When different Si-containing species coexist in the vapor phase, some of the peaks in the mass spectra comprise contributions from more than one species. For example, if the relative intensity of the peak with $m/e = 133$ is 100 and the relative intensity of the peak with $m/e = 170$ is only 25, one concludes that this gas mixture contains $SiCl_4$ (as evidenced by the existence of the peak at $m/e = 170$) and also $SiCl_3H$, because ratio of intensities of peaks with $m/e = 133$ and $m/e = 170$ is larger than in the mass spectrum of pure $SiCl_4$ (see Fig. 3) This means that some other species must contribute to the peak with $m/e = 133$. From Fig. 3 it is obvious that this can be only $SiCl_3H$. The relative amounts of $SiCl_4$ and $SiCl_3H$ can be obtained in this way. Once the relative amounts of $SiCl_4$ and $SiCl_3H$ are known, one proceeds to determine the relative amount of $SiCl_2H_2$ by substracting the contribution of $SiCl_3H$ to the peak with $m/e = 99$. The relative amount of $SiCl_2$ is determined from the intensity of peak at $m/e = 63$, after substracting contributions from $SiCl_4$, $SiCl_3H$, and $SiCl_2H_2$ to this peak. After the above procedure is completed, one obtains ratios of partial pressures of $SiCl_3H$, $SiCl_2H_2$, and $SiCl_2$ respective to the partial pressure of $SiCl_4$. We shall illustrate this on the previously given example, where relative intensity of $m/e = 133$ was 100, and of $m/e = 170$ was 25, respectively. The contribution of the $SiCl_4$ spectrum to the peak at $m/e = 133$ can be obtained by multiplying the ratio of relative intensities of $m/e = 133$ and $m/e = 170$ in the pure $SiCl_4$ spectrum with the relative intensity in the spectrum of the mixture

$$\frac{I_{133(SiCl_4)}}{I_{170(SiCl_4)}} \times I_{170(mix)} = \frac{100}{53} \times 25 = 47.2$$

The contribution of $SiCl_3H$ to the peak at $m/e = 133$ can be obtained by subtracting 47.2 from 100, *i.e.*, its contribution is 52.8. Since partial pressures of species are proportional to mass spectrometric intensities, one has

$$\frac{47.2}{52.8} = \frac{P_{SiCl_4}}{P_{SiCl_3H}} = 0.89$$

and one can express P_{SiCl_3H} in terms of P_{SiCl_4}

$$P_{SiCl_3H} = 1.12\, P_{SiCl_4}$$

This procedure can be repeated for $SiCl_2H_2$ and $SiCl_2$, so that partial pressures of these species are also expressed in terms of P_{SiCl_4}.

The partial pressure of HCl was determined through direct calibration. Intensities of HCl peaks in the mass spectra were measured at temperatures of interest in mixtures containing only HCl and H_2 in known proportions. Since Si was not present in these experiments, no reaction could occur in the reactor and measured HCl intensities can be directly correlated with the partial pressure of HCl.

Now one can proceed with calculations of actual values of partial pressures of $SiCl_4$, $SiCl_3H$, $SiCl_2H_2$, $SiCl_2$, and H_2 from mass spectrometric data. Partial pressures must satisfy Eq. [7] and [8]. Expressing partial pressures of all present chlorosilanes in terms of P_{SiCl_4} and neglecting mass spectrometrically nondetectable species, Eq. [7] and [8] can be written as

$$\frac{\text{Cl}}{\text{H}} = \frac{4P_{SiCl_4} + 3aP_{SiCl_4} + 2bP_{SiCl_4} + 2cP_{SiCl_4} + P_{HCl}}{2P_{H_2} + aP_{SiCl_4} + 2bSiCl_4 + P_{HCl}} \quad [9]$$

and

$$P_{SiCl_4} + aP_{SiCl_4} + bP_{SiCl_4} + cP_{SiCl_4} + P_{HCl} + P_{H_2} = 1 \quad [10]$$

where *a*, *b*, and *c* are mass spectrometrically obtained ratios connecting partial pressure of $SiCl_4$ with partial pressures of $SiCl_3H$, $SiCl_2H_2$, and $SiCl_2$, respectively.

Since P_{HCl} is known from calibration experiments, we deal with the system of two linear equations containing two unknowns, *i.e.*, P_{H_2} and P_{SiCl_4}. After solving for P_{H_2} and P_{SiCl_4} one obtains P_{SiCl_3H}, $P_{SiCl_2H_2}$, and P_{SiCl_2} from known values of *a*, *b*, and *c*, respectively.

In Fig. 4(a)-(e), the experimentally determined partial pressures of vapor species are compared with calculated partial pressures at corresponding temperatures and Cl/H values. Lines represent the temperature variation of calculated partial pressures of pertinent species; Cl/H $= 10^0$ for the top line, Cl/H $= 10^{-1}$ for the middle, and Cl/H $= 10^{-2}$ for the bottom line. Square symbols are to be compared with the top line, triangular symbols with the middle, and circular symbols with the bottom line. Open symbols represent values of partial pressures in mixtures where HCl was not initially present; the full symbols represent partial pressures in mixtures where HCl was initially present. The reproducibility of these data from experiment to experiment is about $\pm 20\%$.

Discussion

In this section we discuss the nature and the extent of chemical reactions occurring in the system. From the presence of H_2, HCl, $SiCl_2$, $SiCl_2H_2$, $SiClH_3$, and $SiCl_4$, one can conclude which reactions occur.

The drop of partial pressure of entering $SiCl_2H_2$ and the appearance of HCl in the system infers the following reaction (reverse of reaction [3]) by which the deposition of Si occurs

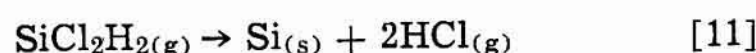

$$SiCl_2H_{2(g)} \rightarrow Si_{(s)} + 2HCl_{(g)} \quad [11]$$

The HCl created in this way reacts with the Si deposit to form other thermodynamically stable species; $SiCl_4$, $SiCl_3H$, and $SiCl_2$ are formed via reactions [1], [2], and [5], respectively. Reactions of equilibration between various vapor species can be also considered, *e.g.*

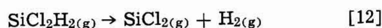

$$SiCl_2H_{2(g)} \rightarrow SiCl_{2(g)} + H_{2(g)} \quad [12]$$

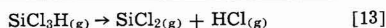

$$SiCl_3H_{(g)} \rightarrow SiCl_{2(g)} + HCl_{(g)} \quad [13]$$

$$SiCl_{4(g)} + Si_{(s)} \rightarrow 2SiCl_{2(g)} \quad [14]$$

$$SiCl_{4(g)} + H_{2(g)} \rightarrow SiCl_3H_{(g)} + HCl_{(g)} \quad [15]$$

It is possible to draw some conclusions about the mechanism and the kinetics of the above reactions by referring to Fig. 4(a)-(e). The comparison of calculated with equilibrium partial pressures shows that deviations from equilibrium exist, but their nature varies from species to species. In almost all instances P_{SiCl_2} and $P_{SiCl_2H_2}$ are higher than their equilibrium values; P_{HCl} is also higher except for Cl/H $< 10^{-1}$. On the other hand, P_{SiCl_4} is almost always lower than the equilibrium value, and P_{SiCl_3H} is also lower for $T > 1000°K$. From these observations, one can conclude that the creation of species which require more HCl molecules to form (*i.e.*, reactions [1] and [2]) proceeds slower than the creation of species which require less HCl (*i.e.*, reactions [3] and [5]). This suggests a dearth of HCl molecules at the Si surface, which could be caused either by the poor transport of HCl to the surface or by the poor adsorption of HCl at the surface. The increase of P_{HCl} by the addition of pure HCl to the gas phase increases the transport of HCl to the surface, but nevertheless, the relative abundance of vapor species does not change significantly. At higher Cl/H ratios one observes that the abundance of HCl in the vapor is higher than equilibrium data predict. This points toward the poor adsorption of HCl on silicon surface. The consequence is that species requiring more HCl for their formation (*i.e.*, $SiCl_3H$ and $SiCl_4$) will form less readily than species such as $SiCl_2$, which need only two HCl molecules for their formation. Recently, Robinson and Goldsmith obtained Si growth from mixtures of $SiCl_2H_2$ and HCl, where HCl content was so high that thermodynamic calculations predicted etching of Si rather than its growth (11). This indicates that in their system the reaction of HCl with Si also did not reach equilibrium.

The incomplete dissociation of $SiCl_2H_2$ (reaction [3]) could also contribute to the relatively high $P_{SiCl_2H_2}$. It is also possible that reaction [12] occurs in the system. This reaction is thermodynamically more feasible at our experimental temperatures than other homogeneous gas reactions, *i.e.*, reactions [13], [14], and [15]). Most likely, neither reactions [13], [14], and [15], nor their reverse reactions occur to a significant extent in our system. If they did occur, one would observe a strong dependence of P_{SiCl_4} and P_{SiCl_3H} on the presence of free HCl in the reactor. This has not been observed. We thus conclude that events on the Si surface were the principal factor in determining the composition of the vapor phase. A similar conclusion was reached by crystal growers, who consider Si deposition up to about 1250°K as surface kinetics controlled (12, 13). Our mass spectrometric data indicate that these deviations from thermochemical equilibrium also reflect themselves in the composition of the vapor phase. Nevertheless, all major species predicted by thermodynamic calculations have been detected, and in most cases, their measured partial pressures are of the same order of magnitude as the equilibrium values.

It was already mentioned that one can calculate the efficiency of the Si deposition process by comparing values of Si/Cl ratio in the initial mixture with the Si/Cl in the equilibrium mixture at some given temperature. The efficiency obtained in this way is the theoretical efficiency of the Si-deposition process. The comparison of the initial Si/Cl ratio with the Si/Cl ratio determined from mass-spectrometric values of partial pressures yields the experimental efficiencies. The Si/Cl ratio is defined by the following equation

$$\frac{\text{Si}}{\text{Cl}} = \frac{P_{SiCl_4} + P_{SiCl_3H} + P_{SiCl_2H_2} + P_{SiClH_3} + P_{SiH_4} + P_{SiCl_2}}{4P_{SiCl_4} + 3P_{SiCl_3H} + 2P_{SiCl_2H_2} + P_{SiClH_3} + 2P_{SiCl_2} + P_{HCl}} \quad [16]$$

Of course, in the initial mixtures, only $P_{SiCl_2H_2}$ and P_{HCl} (when present) should be considered; in the determination of the value of Si/Cl from the experimental data, the partial pressures of undetected species such as $SiClH_3$ and SiH_4 are considered to be equal to zero. In Table III, the experimental and the theoretical efficiencies are listed. Efficiencies are expressed in terms of percentage of the introduced Si converted into the solid Si. From data in Table III, it can be seen that, in general, the experimental efficiencies are significantly lower than theoretical ones in cases of lower temperatures and Cl/H values. The experimental efficiencies approach theoretical values with increasing temperatures and Cl/H values. In some cases, they are even higher than the theoretical efficiencies. This can be explained by the already discussed low rates of the HCl-Si interaction. If the deposition of Si from $SiCl_2H_2$ proceeds at higher rates than the back-etching of the deposit by HCl, a net accumulation of Si larger than the equilibrium amount will occur, leading to the observed higher than theoretical efficiencies. This is consistent with data in Ref. (11).

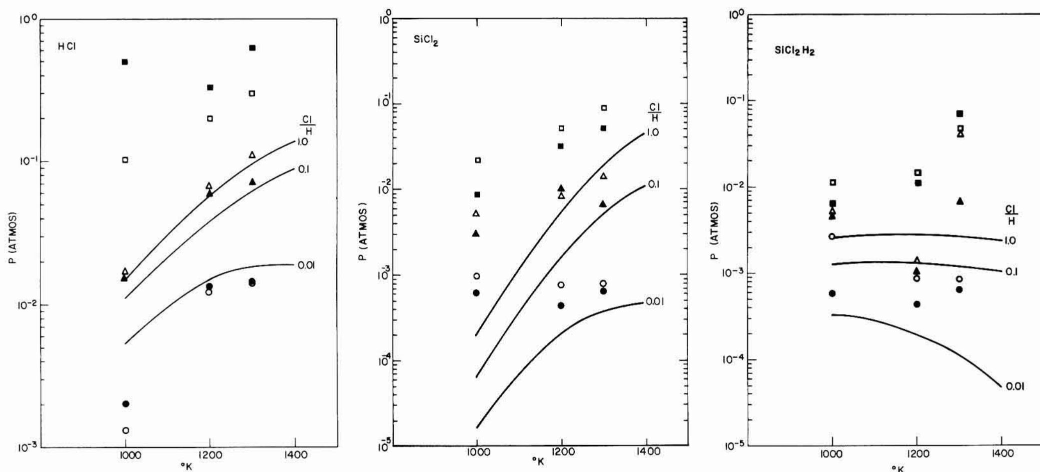

(a) Comparison between the calculated and experimental pressure of HCl.

(b) Comparison between the calculated and experimental pressure of $SiCl_2$.

(c) Comparison between the calculated and experimental pressure of $SiCl_2H_2$.

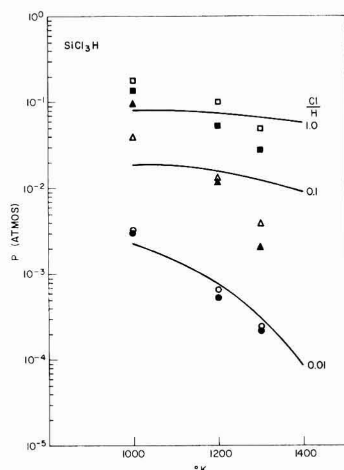

(d) Comparison between the calculated and experimental pressure of $SiCl_3H$.

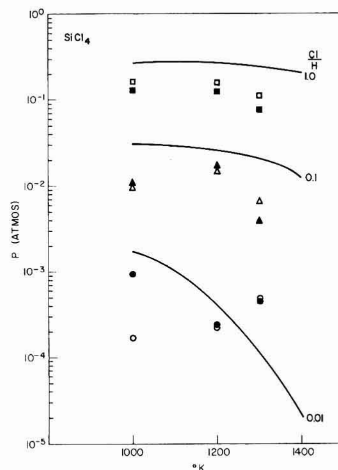

(e) Comparison between the calculated and experimental pressure of $SiCl_4$.

Fig. 4. Comparison between the calculated and the experimental partial pressures of detected species. Lines represent calculated temperature variations of partial pressures with Cl/H value as a parameter. Square symbols are to be compared with the top line (Cl/H $= 10^0$), triangular symbols with the middle (Cl/H $= 10^{-1}$), and circular symbols with the bottom line (Cl/H $= 10^{-2}$). Full symbols represent partial pressures in mixtures where HCl was initially present; the open symbols represent partial pressures in mixtures where HCl was not initially present.

In experiments where pure HCl was introduced into the reactor (*i.e.*, Cl/H $= 10^0$), the etching of the previously deposited Si occurred. The efficiency of etching can be obtained by comparing the experimentally determined amount of Si in the gas phase with the corresponding calculated amounts. Such comparison yields that the HCl-etching is 80, 64, and 71% efficient at 1000°, 1200°, and 1300°K, respectively. This again confirms the observation that the extent of HCl-Si interaction is lower than calculated.

Summary and Conclusions

The presented study of the chemical processes in deposition of Si from $SiCl_2H_2$ and of etching of Si by HCl is summarized in this section.

1. The mass spectrometer-CVD reactor setup has been successsfully used for the qualitative and quanti-

Table III. Comparison of theoretically and experimentally determined efficiencies of Si deposition from $SiCl_2H_2$

Cl/H	Presence of HCl in initial mix	1000°K Theor. η	1000°K Exp. η	1200°K Theor. η	1200°K Exp. η	1300°K Theor. η	1300°K Exp. η
0.01	No	55.9	25.0	83.6	73.6	91.1	76.0
0.01	Yes	33.8	9.8	75.4	73.2	86.6	70.9
0.1	No	47.1	39.2	54.8	58.9	60.3	67.1
0.1	Yes	20.6	5.3	32.2	35.4	40.4	54.9
1.0	No	47.4	44.8	48.8	48.8	49.4	49.1

tative analysis of the vapor phase in the Si-Cl-H system.

2. Mass spectra of $SiCl_4$, $SiCl_3H$, $SiCl_2H_2$, and $SiCl_2$ have been determined.

3. Species found in the vapor phase were H_2, HCl, $SiCl_2$, $SiCl_2H_2$, $SiCl_3H$, and $SiCl_4$, and their partial pressures were measured as a function of temperature, value of the Cl/H ratio, and of the chemical nature of the initial gaseous mixture entering the reactor.

4. The equilibrium partial pressures of all vapor species present in the Si-Cl-H system were calculated from the newest and most consistent set of thermochemical data available.

5. The comparison between the calculated and the experimentally determined partial pressures indicates that there are certain deviations from the thermochemical equilibrium which reflect themselves in the composition of the vapor phase. Notably, partial pressures of HCl, $SiCl_2$, and $SiCl_2H_2$ tend to be higher, and partial pressures of $SiCl_3H$ and $SiCl_4$ lower than the corresponding equilibrium partial pressures. Nevertheless, under most of our experimental conditions (particularly when $T > 1200°K$), the measured and the calculated partial pressures were of the same order of magnitude. The equilibrium calculations thus provide useful information on the composition of the vapor phase and on the deposition and etching of Si, although the complete equilibrium situation has not been established.

6. The main chemical reactions occurring in the reactor are summarized by the following scheme

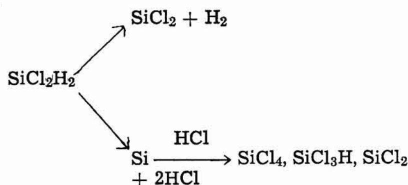

The incoming $SiCl_2H_2$ decomposes either to $SiCl_2$ through a loss of two H atoms or to Si through a loss of two HCl molecules; other species are then formed by the HCl-Si interaction.

7. From the nature and the extent of the deviations from the equilibrium, one concludes that their possible causes are the retarded HCl adsorption on Si and the incomplete dissociation of $SiCl_2H_2$.

8. The calculated and the experimentally determined efficiencies of the deposition and etching processes were compared and found to be similar when $T > 1000°K$ and $Cl/H > 10^{-2}$.

Acknowledgments

The authors gladly acknowledge helpful and informative discussions with D. Richman, N. Goldsmith, and G. Cullen.

Manuscript submitted Oct. 29, 1974; revised manuscript received June 2, 1975.

Any discussion of this paper will appear in a Discussion Section to be published in the June 1976 JOURNAL. All discussions for the June 1976 Discussion Section should be submitted by Feb. 1, 1976.

Publication costs of this article were partially assisted by RCA Corporation.

REFERENCES

1. N. Goldsmith and P. H. Robinson, *RCA Rev.*, **34**, 358 (1973); W. C. Benzing, A. E. Ozias, and H. B. Bradley, Paper 75 presented at Electrochemical Society Meeting, Washington, D. C., May 9-13, 1971.
2. R. F. Lever, *IBM J. Res. Develop.*, **8**, 460 (1964).
3. L. P. Hunt and E. Sirtl, *This Journal*, **119**, 1741 (1972).
4. V. S. Ban, *ibid.*, **118**, 1473 (1971).
5. V. S. Ban, *J. Crystal Growth*, **17**, 19 (1972).
6. V. S. Ban and M. Ettenberg, *J. Phys. Chem. Solids*, **34**, 1119 (1973).
7. L. P. Hunt and E. Sirtl, in "Chemical Vapor Deposition, Second International Conference," J. M. Blocher, Jr. and J. C. Withers, Editors, The Electrochemical Society Softbound Symposium Series, New York (1970).
8. H. J. T. Ellingham, *J. Soc. Chem. Ind.*, **63**, 125 (1944).
9. V. S. Ban, *Mat. Res. Bull.*, **10**, 81 (1975).
10. "Index of Mass Spectral Data," ASTM Committee E-14 on Mass Spectrometry, Philadelphia, Pa. (1969).
11. P. H. Robinson and N. Goldsmith, *J. Electron. Mat.*, **12**, 313 (1975).
12. J. Bloem, in "Semiconductor Silicon 1973," p. 180, H. R. Huff and R. R. Burgess, Editors, The Electrochemical Society Softbound Symposium Series, Princeton, N.J. (1973).
13. E. Sirtl, L. P. Hunt, and D. H. Sawyer, *This Journal*, **121**, 919 (1974).

Chemical Processes in Vapor Deposition of Silicon

II. Deposition from $SiCl_3H$ and $SiCl_4$

Vladimir S. Ban*

RCA Laboratories, Princeton, New Jersey 08540

ABSTRACT

Chemical processes occurring in the vapor deposition of silicon from $SiCl_3H$ and $SiCl_4$ were studied by means of a mass spectrometer coupled to the CVD reactor. Species identified in the vapor phase were H_2, HCl, $SiCl_2$, $SiCl_2H_2$, $SiCl_3H$, and $SiCl_4$. Their partial pressures were measured at temperatures of 1000°, 1200°, and 1300°K; the Cl/H value was 10^{-1}. Values of these partial pressures were compared with the calculated equilibrium partial pressures for the Si-Cl-H system, as well as with partial pressures determined in the deposition of Si from $SiCl_2H_2$. On the basis of the obtained results, we discuss the nature and the extent of chemical processes occurring during the deposition of Si from $SiCl_4$ and $SiCl_3H$.

In the preceding paper of this series (1), the chemical processes occurring in the deposition of Si from $SiCl_2H_2$ and in the HCl-etching of Si were discussed. The topic of the present paper is chemical processes occurring in the deposition of Si from $SiCl_3H$ and from $SiCl_4$. Both of these gases are important sources for the deposition of Si on the industrial scale.

In principle, the deposition of Si from all chlorosilanes should proceed in identical manner, because in all cases one deals with the Si-Cl-H system. The rate and the efficiency of the deposition, as well as the composition of the vapor phase should be uniquely determined by specifying the temperature, the total pressure, and the Cl/H ratio in the system, providing that the thermochemical equilibrium has been established. In reality, however, significant differences in the rate and the efficiency of Si deposition from various chlorosilanes have been observed (2). This implies that certain deviations from the thermochemical equilibrium occur, and that the nature of the input gas affects the deposition.

We studied possible causes and the extent of these effects by experimentally determining the composition of the gas phase by means of a mass spectrometer in a manner described previously (1). The deposition from $SiCl_3H$ and from $SiCl_4$ are compared with the deposition from $SiCl_2H_2$ discussed in Ref. (1). Values of the experimentally determined partial pressures will also be compared with the previously calculated equilibrium partial pressures of vapor species in the Si-Cl-H system (1). On the basis of these comparisons, we shall discuss chemical processes occurring during the Si deposition and the effect of the nature of the input chlorosilanes on these processes.

Experimental

The mass spectrometer-CVD reactor combination has been described in Ref. (1). Controlled amounts of $SiCl_3H$ or of $SiCl_4$ were introduced into the reactor by means of the Tylan Source I Vaporizer Controller. The $SiCl_3H$ and $SiCl_4$ were drawn from 50-lb tanks. Gases were of semiconductor grade purity and supplied by the M&T Chemicals Inc. The Matheson electronic mass flow transducers were used to introduce known amounts of carrier gases, such as H_2 or He, into the reactor. Therefore, partial pressures of Si-containing gases in the input mixtures were known.

The composition of initial mixtures was adjusted so that Cl/H $= 10^{-1}$. For the case of $SiCl_3H$-H_2 mixture, the Cl/H ratio is given by the following expression

$$Cl/H = \frac{3P_{SiCl_3H}}{P_{SiCl_3H} + 2P_{H_2}} \qquad [1]$$

* Electrochemical Society Active Member.

Key words: mass spectrometry, CVD, thermodynamics, kinetics.

The corresponding expression for the $SiCl_4$-H_2 mixture is given by

$$Cl/H = \frac{4P_{SiCl_4}}{2P_{H_2}} \qquad [2]$$

In the above expressions, P_{SiCl_3H}, P_{SiCl_4}, and P_{H_2} are the partial pressures of these gases at their entrance into the reactor. The $SiCl_3H$-H_2 mixture was prepared by combining flows of 100 cm^3/min of $SiCl_3H$ with 1450 cm^3/min of H_2. In the case of $SiCl_4$-H_2 mixture, 132 cm^3/min of $SiCl_4$ was mixed with 2640 cm^3/min of H_2.

The effect of replacing H_2 by He as a carrier gas was also studied. For this purpose, 132 cm^3/min of $SiCl_4$ was mixed with 2640 cm^3/min of He. Partial pressures of gases in this mixture will be compaerd with partial pressures in the mixtures containing H_2.

Results

Following the method described in Ref. (1), one can determine the qualitative and the quantitative composition of the vapor phase by means of a mass spectrometer. Briefly, various vapor species can be identified by their characteristic mass spectra. Values of partial pressures can then be determined from the mass spectrometrically measured relative amounts of various species and the specified Cl/H ratio and the total pressure in the system, which is 1 atm. Vapor species detected in the Si-Cl-H system, when either $SiCl_3H$ or $SiCl_4$ was used in the initial mixture, were: HCl, $SiCl_2$, $SiCl_2H_2$, $SiCl_3H$, $SiCl_4$, and H_2. In the Si-Cl-He system, only $SiCl_2$, $SiCl_4$, and He were detected. In Table I, the experimentally determined par-

Table I. Experimental partial pressures of vapor species in $SiCl_2H_2$-H_2, $SiCl_3H$-H_2, and $SiCl_4$-H_2 mixtures (Cl/H $= 10^{-1}$ in all cases) and their comparison with the calculated equilibrium partial pressures for the Si-Cl-H system

Temperature, °K	Species	P_p (atm) (Eq.)	P_p (atm) ($SiCl_2H_2$)	P_p (atm) ($SiCl_3H$)	P_p (atm) ($SiCl_4$)
1000	HCl	1.1×10^{-2}	1.7×10^{-2}	1.4×10^{-2}	1.9×10^{-3}
	$SiCl_2$	6.6×10^{-5}	5.2×10^{-3}	4.0×10^{-3}	$<10^{-5}$
	$SiCl_2H_2$	1.3×10^{-3}	5.2×10^{-3}	3.6×10^{-4}	$<10^{-5}$
	$SiCl_3H$	1.9×10^{-2}	3.6×10^{-2}	1.6×10^{-2}	1.2×10^{-2}
	$SiCl_4$	3.0×10^{-2}	9.8×10^{-3}	1.2×10^{-2}	3.8×10^{-2}
	H_2	0.939	0.9268	0.954	0.9478
1200	HCl	4.0×10^{-2}	6.5×10^{-2}	4.2×10^{-2}	2.8×10^{-2}
	$SiCl_2$	1.5×10^{-3}	8.5×10^{-3}	1.1×10^{-2}	2.8×10^{-3}
	$SiCl_2H_2$	1.4×10^{-3}	1.4×10^{-3}	1.1×10^{-3}	$<10^{-5}$
	$SiCl_3H$	1.5×10^{-2}	1.3×10^{-2}	1.0×10^{-2}	1.8×10^{-2}
	$SiCl_4$	2.4×10^{-2}	1.4×10^{-2}	2.2×10^{-2}	2.5×10^{-2}
	H_2	0.918	0.900	0.914	0.9256
1300	HCl	6.4×10^{-2}	1.1×10^{-1}	8.4×10^{-2}	6.4×10^{-2}
	$SiCl_2$	5.0×10^{-3}	1.4×10^{-2}	1.8×10^{-2}	1.7×10^{-2}
	$SiCl_2H_2$	1.3×10^{-3}	6.6×10^{-3}	5.3×10^{-3}	5.3×10^{-3}
	$SiCl_3H$	1.2×10^{-2}	4.0×10^{-3}	5.7×10^{-3}	3.9×10^{-3}
	$SiCl_4$	2.0×10^{-3}	6.5×10^{-3}	1.1×10^{-2}	1.7×10^{-2}
	H_2	0.8977	0.8589	0.876	0.8721

Table II. Comparison of the experimentally measured with the calculated equilibrium partial pressures of vapor species detected in the $SiCl_4$-He mixtures; Cl/He = 0.2, T = 1000°, 1200°, and 1300°K

	1000°K		1200°K		1300°K	
Species	P_{eq} (atm)	P_{exp} (atm)	P_{eq} (atm)	P_{exp} (atm)	P_{eq} (atm)	P_{exp} (atm)
$SiCl_2$	1.15×10^{-4}	$>10^{-5}$	2.6×10^{-3}	7.3×10^{-3}	9.34×10^{-3}	1.2×10^{-2}
$SiCl_4$	4.74×10^{-2}	4.8×10^{-2}	4.61×10^{-2}	4.4×10^{-2}	4.27×10^{-2}	4.1×10^{-2}
He	0.95268	~0.95240	0.95127	0.94890	0.94796	0.95873

tial pressures of vapor species present in the $SiCl_2H_2$-H_2, $SiCl_3H$-H_2, and $SiCl_4$-H_2 mixtures as well as the calculated equilibrium partial pressures in the Si-Cl-H system are listed. For all cases, Cl/H ratio is 10^{-1}; pressure values for temperatures of 1000°, 1200°, and 1300°K are listed. In Table II we compare the equilibrium and the experimentally determined partial pressures in the Si-Cl-He system at the above temperatures.

Discussion and Conclusions

Results listed in Table I permit one to compare the deposition of Si from various chlorosilanes. There are some noticeable differences. At $T = 1000°K$, most of the $SiCl_4$ remains undecomposed, and practically no deposition of Si occurs. This is consistent with the relatively high stability of $SiCl_4$ in comparison with other chlorosilanes (1) and with the observed lower growth rate of Si from $SiCl_4$ (2). Differences between the deposition from $SiCl_2H_2$ and from $SiCl_3H$ are smaller. With increasing temperatures, the values of pressures of vapor species become more similar for all three chlorosilanes and also closer to the calculated equilibrium partial pressures. In other words, the system approaches thermochemical equilibrium. However, at $T = 1300°K$, one still notices differences between the equilibrium and the experimental partial pressures. In particular, partial pressures of species containing two or less chlorine atoms (*i.e.*, HCl, $SiCl_2$, and $SiCl_2H_2$) tend to be higher than their equilibrium values, while partial pressures of $SiCl_3H$ and $SiCl_4$ tend to be lower than their equilibrium values. It is not clear whether the partial pressure of the incoming $SiCl_4$ indeed drops below its equilibrium value, or if this small deviation (~15%) is caused by the uncertainties of temperature measurement and/or of the thermochemical data used. Similar results have been reported in Ref. (1), and results described here provide some additional information which basically supports our previous discussion, where we concluded that the adsorption of HCl on the Si surface is retarded. In the case of growth of Si from $SiCl_4$ which occurs via the following reaction

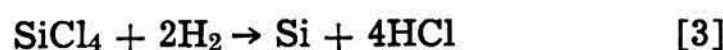

$$SiCl_4 + 2H_2 \rightarrow Si + 4HCl \quad [3]$$

four molecules of HCl are supplied. It seems that their residence time at the Si surface is short and that they desorb easily. This would lead to the relatively smaller probability of forming, say, $SiCl_3H$ where three molecules of HCl are needed

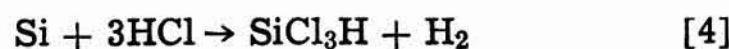

$$Si + 3HCl \rightarrow SiCl_3H + H_2 \quad [4]$$

than of forming $SiCl_2$ or $SiCl_2H_2$ where only two molecules of HCl are needed

$$Si + 2HCl \rightarrow SiCl_2H_2 \quad [5]$$

or

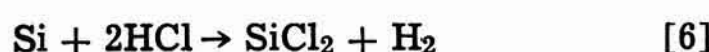

$$Si + 2HCl \rightarrow SiCl_2 + H_2 \quad [6]$$

Nevertheless, all of the above reactions occur and the resultant partial pressures of all vapor species at $T > 1200°K$ are never more than a factor of 3 or 4 apart from the equilibrium partial pressures.

The equilibrium partial pressures in the Si-Cl-He were calculated by employing the following system of three equations

$$P_{SiCl_4} + P_{SiCl_2} + P_{He} = 1.0 \quad [7]$$

$$\frac{Cl}{He} = \frac{4P_{SiCl_4} + 2P_{SiCl_2}}{P_{He}} = 0.2 \quad [8]$$

and

$$SiCl_{4(g)} + Si_{(s)} \rightarrow 2SiCl_{2(g)}; \; k_p = \frac{P^2_{SiCl_2}}{aSi \cdot P_{SiCl_4}} \quad [9]$$

The first of these equations specifies the total pressure in the system, the second one the Cl/He ratio, and the third one the chemical reaction involving the Si-containing gaseous species. In Eq. [9], aSi represents the activity of solid silicon; $a\text{Si} = 1.0$. Values of k_p at 1000°, 1200°, and 1300°K were calculated from thermochemical data given in Ref. (1).

The results of these calculations are given in Table II, along with the experimentally determined partial pressures of $SiCl_2$, $SiCl_4$, and He. An inspection of Table II shows that $SiCl_4$ does not react at $T \leq 1000°K$. At higher temperatures, significant amounts of $SiCl_2$ are detected, indicating that reaction [9] takes place. At 1200° and 1300°K the observed partial pressures are relatively close to the equilibrium pressures. Again, the P_{SiCl_4} appears to be slightly below the equilibrium value, but the extent of these deviations is smaller than the uncertainty in experimental temperatures and thermochemical data. Both P_{SiCl_2} and P_{SiCl_4} are considerably higher than the corresponding pressures in the Si-Cl-H system. This is so because, due to the absence of hydrogen, species such as $SiCl_2H_2$, $SiCl_3H$, and HCl cannot form. It is quite probable that in the Si-Cl-H system, where reactions such as [4], [5], and [6] are possible, reaction [9] occurs to a smaller extent.

Finally, we shall discuss the efficiencies of the Si deposition from $SiCl_3H$ and from $SiCl_4$. These efficiencies can be obtained by comparing the Si/Cl ratios of the initial mixture with ratios at elevated temperatures. The same method was used in Ref. (1). In Fig. 1, the experimentally obtained efficiencies (full lines) are compared with the deposition efficiencies available under the equilibrium conditions (dotted lines). These efficiencies give the amount of Si deposited as percentages of Si introduced into the system. One notices that in the case of $SiCl_3H$, the experimental efficiencies run close to the theoretical efficiencies. In the case of $SiCl_4$, the theoretical and experimental efficiencies are significantly lower. At $T < 1100°K$, actual etching of the previously deposited Si takes place when $SiCl_4$-H_2 mixture with $Cl/H = 10^{-1}$ is introduced into the system. Of course, in the Si-Cl-He system, etching occurs at all temperatures via the reaction [9]. The upper curves in Fig. 1 represent the theoretical and the experimental efficiencies of the deposition of Si from $SiCl_2H_2$. These results are taken from the previous paper and indicate that for the given temperature and Cl/H ratio of the initial mixture, $SiCl_2H_2$ is the most efficient source of Si among the chlorosilanes examined.

The presented work could be summarized as follows:

1. Chemical processes in the deposition of Si from $SiCl_3H$-H_2 and $SiCl_4$-H_2 mixtures with $Cl/H = 10^{-1}$ were examined by the mass spectrometer at temperatures of 1000°, 1200°, and 1300°K.

2. Vapor species detected at elevated temperatures were H_2, HCl, $SiCl_2$, $SiCl_2H_2$, $SiCl_3H$, and $SiCl_4$; their partial pressures were measured and compared with partial pressures detected in $SiCl_2H_2$-H_2 mixtures and

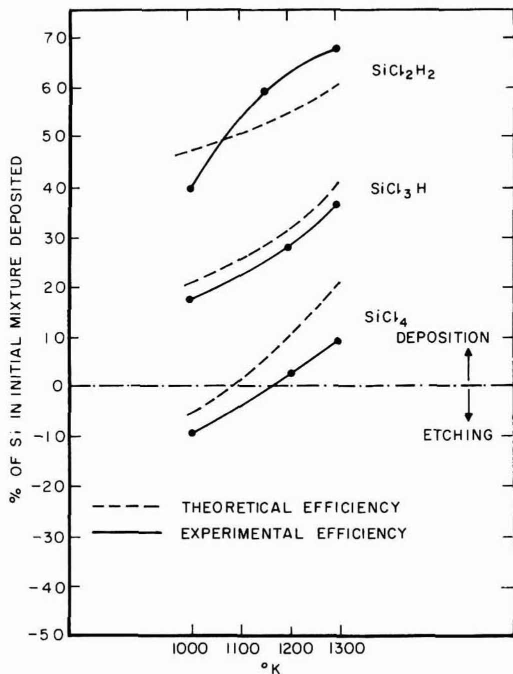

Fig. 1. Theoretical and experimental efficiencies of deposition of silicon from $SiCl_2H_2$, $SiCl_3H$, and $SiCl_4$ in temperature interval of 1000°-1300°K; Cl/H = 10^{-1} in all cases.

with the calculated equilibrium partial pressures.

3. In the Si-Cl-He system, $SiCl_4$, $SiCl_2$, and He were present in the vapor and their partial pressures were measured and compared with the calculated equilibrium partial pressures for this system.

4. Measured values of partial pressures indicate that there are some significant deviations from the thermochemical equilibrium in the system, especially at lower temperatures where $SiCl_4$ remains largely undecomposed; at $T > 1200$°K, partial pressures resemble more closely the equilibrium partial pressures, particularly in the Si-Cl-He system.

5. The calculated and experimentally determined efficiencies of the deposition of Si from $SiCl_2H_2$, $SiCl_3H$, and $SiCl_4$ were compared and found to decrease in order η-$SiCl_2H_2$ > η-$SiCl_3H$ > η-$SiCl_4$.

Acknowledgments

The author acknowledges helpful discussions with D. Richman, N. Goldsmith, G. W. Cullen, and M. Ettenberg.

Manuscript submitted Oct. 29, 1974; revised manuscript received June 2, 1975.

Any discussion of this paper will appear in a Discussion Section to be published in the June 1976 JOURNAL. All discussions for the June 1976 Discussion Section should be submitted by Feb. 1, 1976.

Publication costs of this article were partially assisted by RCA Corporation.

REFERENCES

1. V. S. Ban and S. L. Gilbert, *This Journal*, 122, 1382 (1975).
2. F. C. Eversteyn, *Philips Res. Rept.*, 29, 45 (1974).

A Solid-State Galvanic Cell Study of the Ti_2O_3,Ti_3O_5 Equilibrium

Ronald G. Sommer*[,1] and E. David Cater

Department of Chemistry, University of Iowa, Iowa City, Iowa 52242

ABSTRACT

The chemical potential of oxygen of the coexisting phases Ti_2O_3,Ti_3O_5 was found to be given by $\Delta\overline{G}_{1/2\,O_2}$ (Ti_2O_3,Ti_3O_5) = −86,030 + 15.30T(K) ± 180 cal (1 std dev.) from a study of the cell Nb,NbO/YDT [7.5 weight per cent (w/o) yttria]/Ti_2O_3,Ti_3O_5 between 1022° and 1495°K. In the evaluation of the data obtained for the above cell the relationship $\Delta G°_f$(NbO) = −99,870 + 21.51T(K) ± 150 cal (1 std dev.) which was determined from a study of the cell Nb,NbO/YDT (15 w/o yttria)/Fe,Fe_xO between 1089° and 1426°K was used. The data for Ti_2O_3,Ti_3O_5 correlate well with calorimetric measurements at lower temperatures and vaporization studies at higher temperatures.

This paper presents a study of the equilibrium chemical potential of oxygen in the coexisting solid phases Ti_2O_3,Ti_3O_5 from 1022° to 1495°K by a galvanic cell technique. For convenience idealized formulas are utilized in this paper for the various solid phases except where their actual nonstoichiometric compositions are of interest. The solid phases in the Ti-O system are of considerable interest because of the wide range of nonstoichiometry and unusual defect ordering near O/Ti = 1 (1, 2) and the multitudinous array of phases Ti_nO_{2n-1} based on crystallographic shear in the composition range O/Ti from 1.667 to 2.00 (1, 3, 4). At the time this work was begun thermodynamic data from calorimetric measurements were available for presumably stoichiometric TiO, Ti_2O_3, Ti_3O_5, and TiO_2 [references summarized in JANAF (5)]. Knudsen cell and mass spectrometric studies at temperatures above about 1700°K had explored the nature and thermodynamics of the vaporization processes (6-8) of the phases from O/Ti = 1.0-2.0. Several thermodynamic discrepancies and uncertainties existed in the literature, arising from uncertainties regarding effects of nonstoichiometry and heats of transition. Equilibrium gravimetric studies involving gas-solid equilibria have

* Electrochemical Society Active Member.
[1] Present address: Corning Glass Works, Sullivan Park, Corning, New York 14830.
Key words: thermodynamics, titanium oxides, niobium monoxide, yttria-doped thoria.

been reported for systems with O/Ti ratios greater than 1.67 (Ti_3O_5), but this technique has not been successfully applied to systems with the low oxygen potentials found in O/Ti < 1.67 (9, 10).

The present work was undertaken to provide thermochemical information on the intermediate oxide phases Ti_2O_3 and Ti_3O_5 by an equilibrium technique, in the range of temperatures between the calorimetric and vaporization studies and at lower oxygen potentials than could be explored with gravimetric techniques. Of particular interest was the question of whether the calorimetric data on stoichiometric materials were valid when extrapolated to higher temperatures where the coexisting phases might exhibit significant nonstoichiometry.

The use of solid oxide electrolyte galvanic cells for the direct determination at elevated temperatures of the chemical potential ($\Delta\overline{G}_{1/2\,O_2}$) or partial pressure ($P_{O_2}$) of oxygen of two phases which coexist in some metal-oxygen system is by now well known (11, 12). Prior to the recently published, extensive study of the Ti-O system with yttria-doped thoria (YDT) electrolyte cells by Suzuki and Sambongi (9), the two-phase region Ti_2O_3,Ti_3O_5 had not been investigated via this technique, although a galvanic cell study of the adjoining two-phase region Ti_3O_5,Ti_4O_7 had been performed by Vasil'eva and Shaulova, along with studies on higher oxide phases (13). A measurement of the difference in oxygen potential of the electrodes "Ti,TiO" and "TiO,Ti_2O_3" with a calcia-stabilized zirconia (CSZ) electrolyte cell attempted by Hoch *et al.* (14) was of questionable value because of incorrect assumptions about the Ti-O phase diagram and the useful region of CSZ. In the region O/Ti > 1.6, emf and gas-solid equilibrium studies have been surveyed by Suzuki and Sambongi (9) and critically reviewed by Merritt *et al.* (10).

The determination of $\Delta\overline{G}_{1/2\,O_2}$ for the region Ti_2O_3,Ti_3O_5 has been carried out in this laboratory via a study of the cell Nb,NbO/YDT (7.5 w/o yttria)/Ti_2O_3,Ti_3O_5. Although the equilibrium partial pressures of oxygen exhibited by these electrodes, on the order of 10^{-25} and 10^{-22} atm at 1000°C, respectively, are very low, Etsell (15) indicates that the average ionic transport number ($\bar{t}_i$) of the YDT electrolyte for such a cell is greater than 0.99 at 1000°C.

A preliminary investigation of the cell Nb,NbO/YDT (15 w/o yttria)/Fe,Fe_xO (x indicates the boundary composition of iron-saturated wüstite) was performed in order to evaluate the emf apparatus and redetermine $\Delta G°_f$(NbO). The majority of the emf data that have been reported for this cell are in excellent agreement (16, 17).

Experimental

Materials used in preparing electrodes were niobium and niobium pentoxide powders, both of 99.8% purity, and titanium powder of 99.5% purity from A. D. MacKay, Inc., hydrogen-reduced iron powder of Fisher Certified Reagent grade (labeled "95.8%" via an analysis which did not include oxygen), Matheson, Coleman, and Bell reagent grade iron oxide (Fe_2O_3) of 99% purity, and Baker Analyzed Reagent titanium dioxide powder, whose analyzed-for impurities totaled 0.0581%. X-ray powder diffraction was used to identify phases present in electrode and electrolyte materials.

Dense, ⅛ in. thick, ½ in. diameter disks of metal-to-oxide mole ratio 5:1, pressed at 3 kbar, functioned as the electrodes in the Nb,NbO//Fe,Fe_xO cell. The NbO phase was prepared by sintering the appropriate mixture of Nb,Nb_2O_5 at 1300°C for 12 hr in an inductively heated tungsten crucible within an evacuated quartz-walled chamber. The Fe,Fe_xO electrode was generated *in situ* from an Fe,Fe_2O_3 disk by holding the cell at 750°C overnight prior to any emf measurements.

The coexisting phases Ti_2O_3,Ti_3O_5 were prepared by vacuum sintering the appropriate mixture of Ti + TiO_2 at 900°-1500°C for 12 hr. The O/Ti ratio was found to be 1.63 both before and after use, by combustion in air at 1000°C to a product taken to be stoichiometric TiO_2. A mechanically sound Ti_2O_3,Ti_3O_5 disk could not be made, so the Ti_2O_3,Ti_3O_5 powder was packed into a flat-bottomed, 7.5 w/o YDT tube to function as the upper electrode in the Nb,NbO//Ti_2O_3,Ti_3O_5 cell. The tube had a nominal wall thickness of 1/16 in. and outside diameter of ½ in. A new electrolyte disk and the previously used Nb,NbO electrode completed the cell.

Powders obtained by crushing Zircoa (Zirconium Corporation of America, Solon, Ohio) slipcast YDT electrolyte tubes were used in preparing electrolyte disks of nominal composition 7.5 and 15 w/o yttria. Isaacs (18) has discussed the impurity level of such YDT. The disks were pressed at 3 kbar and densified by sintering in vacuum at 2000°C for 4 hr followed by firing in air at 1200°C. Disks of ½ in. diameter and ⅜ in. thickness, of densities 9.2 and 7.2 g/cm³ [103 and 92% of theoretical density (19)] were obtained.

The 7.5 w/o YDT tubes received from Zircoa were found by x-ray diffraction to contain detectable amounts of a second phase identified as thoria. However, the second phase was not detected in the electrolyte disks prepared by us.

The emf apparatus is shown in Fig. 1. A cell was supported in the inductively heated tantalum furnace tube and electrical contact to each electrode was made by a disk of platinum foil to which the bead of a platinum, platinum-10% rhodium thermocouple was attached. All insulators and cell supports were of recrystallized alumina. Springs at the top and bottom pushed the assembly together. A second concentric tantalum tube within the furnace tube shielded cells from the high frequency field. The environment of the cell and furnace was a clean dynamic vacuum, routinely 10^{-6} Torr.

A Rubicon precision potentiometer alone, or in combination with a Cary Model 31-CV vibrating reed electrometer, with appropriate filtering (14, 20) to remove high frequency signals, was used to measure emf's. No interference by the high frequency field was observed in cell emf measurements reported here. Cells containing the Ta,Ta_2O_5 electrode had been found to display high emf's within this apparatus when the induction coil was energized (20), presumably because of rectification by tantalum oxide films on tanta-

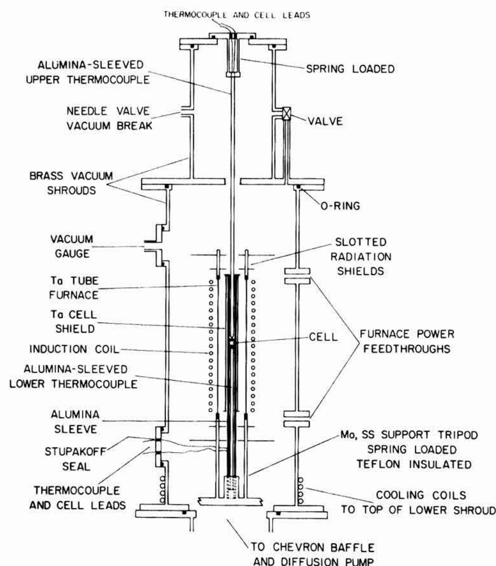

Fig. 1. High temperature inductively heated emf apparatus

lum. Temperatures have an estimated precision of ± 1° and uncertainty of ± 4°. The latter estimate includes an observed temperature gradient of from zero degree at 1100°K to 4° at 1400°K. Two runs were made with each cell. The emf data were taken after equilibration at temperatures both sequentially increased and decreased. Equilibration times were from 1.3 to 25.6 hr with the majority less than 3 hr. Both cells were still operating excellently after a total time at 900°K or above of approximately one week.

Apparently reversible, and clearly reproducible, emf's were displayed by the cells. Somewhat less scatter in the cell emf's, and also distinctly shorter equilibration times, were evident above about 1250°K. The Fe,Fe_xO electrode of the cell Nb,NbO/YDT/Fe,Fe_xO literally welded itself to the electrolyte disk, with staining of the YDT occurring to a depth of 80 μm. Others (21, 22) have previously reported similar phenomena. An electron microprobe study was made of a section sliced perpendicularly through the Fe,Fe_xO-YDT interface. Although the study was somewhat inconclusive due to excitation of the elements by secondary x-rays produced within the sample, no convincing evidence was obtained for diffusion of Fe into the electrolyte or Y into the Fe,Fe_xO disk. No gradient of Y, Fe, or O was detected near the interface and no evidence was found for formation of other phases such as the $YFeO_3$ reported by Worrell (21).

In the study of Ti_2O_3,Ti_3O_5, considerable coloration was developed by the YDT. However, no evidence was obtained for formation of any new phase such as, for example, $YTiO_3$ (23).

Results and Discussion

The data obtained in this laboratory for the cells Nb,NbO/YDT (15 w/o yttria)/Fe,Fe_xO and Nb,NbO/YDT (7.5 w/o yttria)/Ti_2O_3,Ti_3O_5 are plotted, respectively, in Fig. 2 and 3.

The raw data for the cell Nb,NbO//Fe,Fe_xO from 1089° to 1426°K when fit by an unweighted least squares analysis yield

$$E(\text{obs, mV}) = (797.9 \pm 5.6) - (0.1312 \pm 0.0044)T(\text{K}) \quad [1]$$

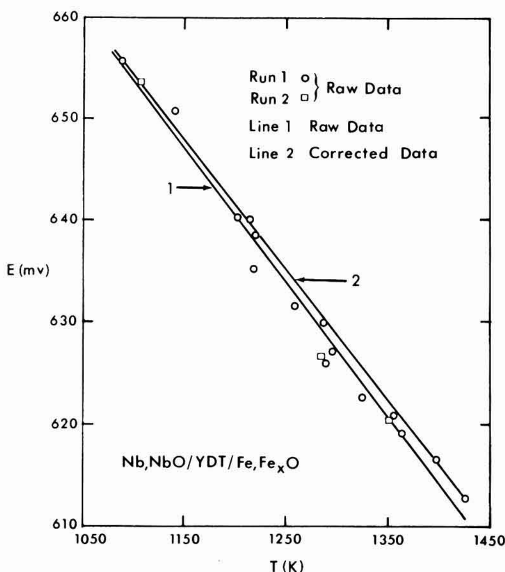

Fig. 2. Emf of cell Nb,NbO/YDT(15 w/o yttria)/Fe,Fe_xO vs. temperature. Line 1, least squares fit to data as measured (Eq. [1]); line 2, least squares fit to data adjusted for solubility of O in Nb (Eq. [2]).

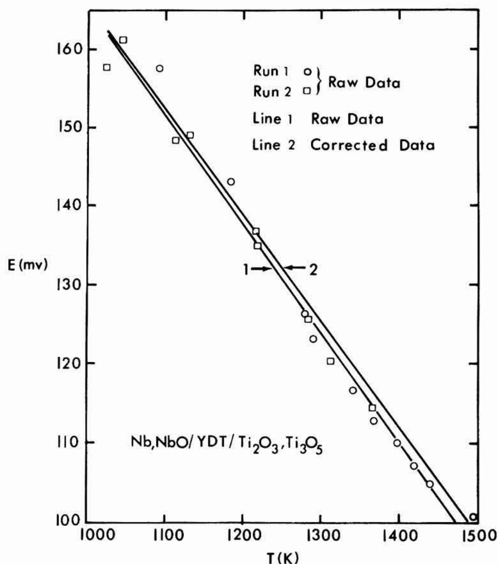

Fig. 3. Emf of cell Nb,NbO/YDT (7.5 w/o yttria)/Ti_2O_3,Ti_3O_5 vs. temperature. Line 1, least squares fit to data as observed (Eq. [7]); line 2, least squares fit to data adjusted for solubility of O in Nb (Eq. [8]).

To obtain the standard free energy of formation of NbO, the emf data were corrected point by point for the solubility of oxygen in niobium, giving

$$E(\text{corr, mV}) = (794.3 \pm 5.7) - (0.1275 \pm 0.0044)T(\text{K}) \quad [2]$$

Uncertainties in slopes and intercepts in these and subsequent equations are standard deviations. The emf's have standard deviations about the line of ±1.7 and ±1.8 mV in [1] and [2], respectively. The correction for oxygen solubility was made by using Bryant's solubility data (24) and assuming that Henry's law is valid for oxygen dissolved in niobium, while Nb obeys Raoult's law. Thus

$$E(\text{corr}) = E(\text{obs}) - (RT/n\mathbf{F}) \ln X_{\text{Nb}} \quad [3]$$

This correction amounts to at most 1.8 mV at 1426°K.

Correspondingly, from the Nernst relation $\Delta G = -n\mathbf{F}E$

$$\Delta G°_{1/2\ O_2}(\text{cell}) = (-36{,}640 \pm 260) + (5.88 \pm 0.20)T(\text{K}) \pm 80 \text{ cal} \quad [4]$$

The value of Faraday's constant **F** was taken to be 23.061 cal/mV-equiv. Using the relationship for the free energy of formation of the iron-rich wüstite phase from 873°-1600°K derived by Steele and Alcock (25) from the work of Darken and Gurry (26)

$$\Delta G°_f(Fe_xO) = -63{,}235 + 15.63T(\text{K}) \pm 125 \text{ cal mole}^{-1} \quad [5]$$

it was found that

$$\Delta G°_f(\text{NbO}) = -99{,}870 + 21.51T(\text{K}) \pm 150 \text{ cal mole}^{-1} \quad [6]$$

for 1089°-1426°K.

Tabulated in Table I are values of $\Delta G°_f$(NbO) which were calculated from the above relationship, from a study representative of the literature on the same cell, that of Ignatowicz and Davies (27), values from Worrell's results (21) based on cells different from the one studied here, along with those published by JANAF Thermochemical Tables (17). Also tabulated for comparison are values of $\Delta\overline{G}_{1/2\ O_2}$ for the coexisting

Table I. Comparison of ΔG°_f(NbO) from this work with literature values

	ΔG°_f(NbO, kcal)			
	1100°K	1200°K	1300°K	1400°K
This work (1089°-1426°K)	−76.21	−74.06	−71.91	−69.76
Worrell (21) (1050°-1300°K)				
1. $NbO,NbO_2//NbO_2,Nb_2O_{4.8}$	−76.79	−74.65	−72.50	(−70.36)*
2. Nb,NbO//NbO,NbO_2	−76.18	−74.02	−71.87	(−69.71)*
Ignatowicz and Davies (27)** (1073°-1373°K)	−76.18	−74.11	−72.03	(−69.95)*
JANAF (17))	−76.46	−74.39	−72.33	−70.28
$\Delta\overline{G}_{1/2\,O_2}$(Nb,NbO), this work	−76.19	−74.02	−71.85	−69.98

* Parentheses indicate ΔG°_f at temperature outside of experimental range.
** Corrected as herein for the solubility of oxygen in niobium.

phases Nb,NbO calculated from Eq. [1] and [5]. Worrell's first relationship was derived from $\Delta G^\circ_f(NbO_2)$ (28) and $\Delta G^\circ_f(Fe_xO)$ (29) obtained from reviews in the literature along with data from the cells $NbO_2,Nb_2O_{4.8}//Fe,Fe_xO$ and $NbO,NbO_2//NbO_2,Nb_2O_{4.8}$. His second relationship was derived from the same $\Delta G^\circ_f(NbO_2)$ (28) and data from the cell Nb,NbO//NbO,NbO_2. JANAF (17) has adopted $\Delta H^\circ_{f,298}$ based on the average of those from seven equilibrium (emf) studies. Five of these, including that of Ignatowicz and Davies (27), were of the cell Nb,NbO//Fe,Fe_xO. Worrell's data (21) for the cell Nb,NbO//Ta,Ta_2O_5 were also used. It is evident that the values tabulated for ΔG°_f(NbO) in Table I agree within better than 1% for 1100°-1400°K. Note that $\Delta G^\circ_f(Fe_xO)$ of Steele and Alcock (25) and that adopted by Blumenthal and Whitmore (29), which was used by Worrell (21) and by Ignatowicz and Davies (27), agree within 33 cal in this range. JANAF (17) has tabulated $\Delta G^\circ_f(Fe_{0.947}O)$, incorrectly implying a constant lower phase boundary composition for wüstite (26, 30), which are approximately 100 cal more negative than the other data. Giddings and Gordon (30, 31) in presenting the latest analysis on oxygen activities and phase boundaries of wüstite and of the use of Fe,Fe_xO electrode, prefer the equation for $\Delta G^\circ_f(Fe_xO)$ of Rizzo *et al.* (32), which gives values at 1100° and 1400°K, respectively, 220 and 80 cal more positive than those chosen here.

The excellent agreement of our results for ΔG°_f(NbO) with those in the literature is taken as evidence that our apparatus and technique are giving valid results, and that the Nb,NbO electrode is a suitable reference for measurements on Ti_2O_3,Ti_3O_5.

The raw data for the cell Nb,NbO//Ti_2O_3,Ti_3O_5 from 1022° to 1495° plotted in Fig. 3 were fit by unweighted least squares to obtain

$$E(\text{obs, mV}) = (303.6 \pm 5.0) - (0.1382 \pm 0.0040)T(\text{K}) \quad [7]$$

while the data corrected for the solubility of oxygen in niobium via Eq. [3] fit the relationship

$$E(\text{corr, mV}) = (300.1 \pm 5.0) - (0.1346 \pm 0.0040)T(\text{K}) \quad [8]$$

The standard deviation of E about the lines in [7] and [8] is ± 2.3 mV. Correspondingly

$$\Delta G^\circ_{1/2\,O_2}(\text{cell}) = (-13{,}840 \pm 230) + (6.21 \pm 0.18)T(\text{K}) \pm 110 \text{ cal} \quad [9]$$

and

$$\Delta\overline{G}_{1/2\,O_2}(Ti_2O_3,Ti_3O_5) = -86{,}030 + 15.30T(\text{K}) \pm 180 \text{ cal} \quad [10]$$

for 1089°-1426°K. For internal consistency our Eq. [6] for ΔG°_f(NbO) was used in deriving this equation.

Tabulated in Table II are values of $\Delta\overline{G}_{1/2\,O_2}$ (Ti_2O_3,Ti_3O_5) which were calculated from the above relationship, from the graphically presented emf data of Suzuki and Sambongi (9) for the cell $TiO_{1.6}//Cr,Cr_2O_3$, and from the recently revised JANAF Thermochemical Tables (17) for Ti_2O_3(c) and $Ti_3O_5(\beta)$. Suzuki and Sambongi have published the only previous study of Ti_2O_3,Ti_3O_5 by emf techniques. They used the cells $TiO_{1.6}$/YDT/Cr,Cr_2O_3 and Ta,Ta_2O_5/YDT/$TiO_{1.6}$ in a flowing argon atmosphere from 940° to 1740°K. Here, $TiO_{1.6}$ represents several compositions in the range $1.560 < O/Ti < 1.648$ in the Ti_2O_3,Ti_3O_5 two-phase region. They intercompared their Ta,Ta_2O_5 and Cr,Cr_2O_3 reference electrodes directly by means of the cell Ta,Ta_2O_5/YDT/Cr,Cr_2O_3, and both were measured against Fe,Fe_xO from 990° to 1520°K. Unfortunately their emf data and thermodynamic results for the Ti-O system are presented only graphically and they give no indication of how the lines in their figures were drawn among the data points. Their Eq. [20] for $\Delta G^\circ_f(Fe_xO)$ taken from Ref. (20) contains two typographical errors. Numerous inconsistencies exist among their figures and equations. By carefully measuring their published figures and deriving equations from these measurements, we obtained the following equation which we believe to be the best representation of their data for the Ti_2O_3,Ti_3O_5 equilibrium

$$\Delta\overline{G}_{1/2\,O_2}(Ti_2O_3,Ti_3O_5) = -86{,}418 + 15.82T(\text{K}) \text{ cal} \quad [11]$$

As shown in Table II, our free energies and those of Suzuki and Sambongi (9) for oxygen in Ti_2O_3,Ti_3O_5 are in excellent agreement. This supports the validity of both sets of measurements, because different reference electrodes, physical arrangements, and equilibration procedures were employed. Above 1773°K their emf's rapidly dropped because of reaction of the $TiO_{1.6}$ electrode and YDT electrolyte pellets.

The data in Table II calculated from the JANAF Tables (17) for Ti_2O_3(c) and $Ti_3O_5(\beta)$ are derived principally from calorimetric measurements on stoichiometric material. Our emf results agree well (within about 1% in $\Delta\overline{G}_{O_2}$) with these. JANAF (α-Ti_3O_5 table) (17) notes that the graphical emf data of Suzuki and Sambongi and "the authors' self-consistent data for the reference couples" yield ΔH and ΔS for the reaction

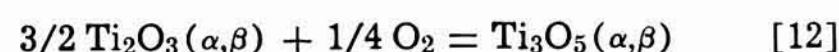

$$3/2\, Ti_2O_3(\alpha,\beta) + 1/4\, O_2 = Ti_3O_5(\alpha,\beta) \quad [12]$$

consistent with JANAF's adopted values. In addition, third law values of ΔH°_{298} for reaction [12], calculated from Suzuki and Sambongi's data, were in agreement with combustion calorimetric data.

Two further comments should be made in comparing the emf results to the JANAF data. First, use of the JANAF table for $Fe_{0.947}O$ with the emf data would reduce the small differences of Table II by approximately 0.1 kcal per ½ mole O_2. Secondly, $\Delta\overline{G}_{1/2\,O_2}$ for the reference electrode Cr,Cr_2O_3 obtained in Suzuki and Sambongi's work (9) is systematically more positive than the data adopted for that system obtained by JANAF (17) by about 800 cal from 1000° to 1500°K. JANAF apparently did not use the emf work of Suzuki and Sambongi in drawing up their Cr_2O_3 tables, although Suzuki and Sambongi's data on Ti_2O_3,Ti_3O_5 were used by JANAF. However, both we and Suzuki and Sambongi have referenced our cells ultimately to the same free energies for Fe,Fe_xO (25) so that their Cr,Cr_2O_3 and our Nb,NbO couples are in a sense only intermediate standards. JANAF (17) utilized other data of Suzuki and Sambongi's taken with the Cr,Cr_2O_3 reference electrode in drawing up tables for Ti_4O_7. Suzuki's oxygen potentials for oxide pairs in $1.67 < O/Ti < 2.0$ are in agreement with those determined by Merritt *et al.* (10) near 1300°K.

It appears from our results that the upper phase boundary (upb) composition of the Ti_2O_3 phase in equilibrium with the Ti_3O_5 phase from 1089° to 1426°K is not appreciably different from the stoichiometric composition. This is inferred because oxygen potentials we obtained from the equilibrium mixtures agree with those calculated from JANAF (17) for the stoichio-

Table II. Comparison of chemical potential of oxygen in Ti_2O_3,Ti_3O_5 from this work with literature values

	$\Delta\overline{G}_{1/2\,O_2}(Ti_2O_3,Ti_3O_5$, kcal)					
	1000°K	1100°K	1200°K	1300°K	1400°K	1500°K
This work (1022°-1495°K)	(−70.73)*	−69.20	−67.67	−66.14	−64.61	(−63.08)*
Suzuki and Sambongi (9) (940°-1740°K)	−70.60	−69.02	−67.43	−65.85	−64.27	−62.69
JANAF (17)	−71.13	−69.66	−68.11	−66.51	−64.88	−63.24

* Parentheses indicate $\Delta\overline{G}_{1/2\,O_2}(Ti_2O_3,Ti_3O_5)$ at temperature outside of experimental range.

metric compounds. Ti_3O_5 was shown to be a line phase by Merritt *et al.* (10) near 1300°K from their gas-solid equilibration studies. Vaporization studies above 1800°K by Gilles and Wahlbeck and their co-workers (6-8) showed that Ti_3O_5 vaporizes congruently at the stoichiometric composition, and the reported partial pressures of oxygen for Ti_3O_5 and Ti_2O_3,Ti_3O_5 are compatible with the JANAF extrapolation of lower temperature data for the two stoichiometric compounds. Hence it appears that the upb of Ti_2O_3 deviates little from the ideal composition up to the melting point, and that the phase width $1.49 \leq O/Ti \leq 1.51$ suggested by Andersson *et al.* (33) is not unreasonable and may be too generous.

This conclusion is in marked contrast to the range $1.425 < O/Ti < 1.585$ around Ti_2O_3, shown by Suzuki and Sambongi in their Fig. 14 from 1273° to 1873°K. Their suggested composition range was deduced from a statistical thermodynamic argument patterned after Anderson (34), but the defect model they used is physically unrealistic, the calculated upb is richer in oxygen than $TiO_{1.56}$, one of their two-phase mixtures, the P_{O_2} values at the TiO_{1+x}-Ti_2O_3 phase boundary used in their calculations are probably (15) too low for valid measurement using YDT, and the resulting P_{O_2} at the proposed upb is inconsistent with either our or their emf data. Their suggested composition range for Ti_2O_3 is thus unrealistic.

In conclusion it seems reasonable to accept the thermodynamic data for Ti_2O_3 and Ti_3O_5 as tabulated by JANAF (17), because this recent compilation successfully correlates calorimetric, emf, and vaporization data over a very large range of T and P_{O_2}.

More precisely stated, the JANAF tabulation presents smoothed enthalpy, entropy, and free energy functions from somewhat discordant calorimetric measurements (35, 36), extrapolated to higher temperatures. These may be combined with free energy data from high temperature equilibrium (emf and vaporization) studies to obtain $\Delta H°_{298}$ for the solids which agree satisfactorily with the calorimetric values. However, if P_{O_2} is to be calculated, we recommend direct use of the high temperature equilibrium data, for example, our Eq. [10]. This is because a discrepancy of $\pm 1\%$ in $\Delta\overline{G}_{1/2\,O_2}(Ti_2O_3,Ti_3O_5)$ at, say, 1300°K corresponds to ± 14 mV in cell potential, or $\pm$ 50% in P_{O_2}.

One remaining source of discrepancy between the emf and tabulated data is the transition from α to β Ti_3O_5 at 450° $\pm$ 20°K, for which JANAF (17) estimates $\Delta H°_t = 3.17 \pm$ kcal mole^{-1}, because of some uncertainty in the drop calorimetric measurements (35, 36) and a DTA study (37).

Acknowledgments

This paper is based on a thesis submitted to the University of Iowa by Ronald G. Sommer in partial fulfillment of the requirements for the Ph.D. degree, December 1974, and was reported in part at the 10th Midwest Regional Meeting of the American Chemical Society, Iowa City, November 1974. The work was supported in part by the USAEC through contract AT(11-1)-1182 with the University of Iowa and in part by the National Science Foundation under grant No. GP-33457. We are greatly indebted to Mr. Yasuyuki Ishikawa for translating the article by Suzuki and Sambongi. Dr. F. D. Ingram and Mary Jo Ingram of the Department of Physiology and Biophysics kindly performed the microprobe analysis of our samples.

Manuscript submitted Feb. 24, 1975; revised manuscript received May 19, 1975.

Any discussion of this paper will appear in a Discussion Section to be published in the June 1976 JOURNAL. All discussions for the June 1976 Discussion Section should be submitted by Feb. 1, 1976.

Publication costs of this article were partially assisted by Corning Glass Works.

REFERENCES

1. P. G. Wahlbeck and P. W. Gilles, *J. Am. Ceram. Soc.*, **49**, 180 (1966).
2. D. Watanabe, O. Terasaki, A. Jostens, and J. R. Castles, *J. Phys. Soc., Japan*, **25**, 292 (1968); "The Chemistry of Extended Defects in Non-Metallic Solids," L. Eyring and M. O'Keeffe, Editors, p. 238, North-Holland, Amsterdam, (1970).
3. S. Andersson and co-workers, *Acta Chem. Scand.*, **11**, 1641, 11653 (1957), and numerous later papers.
4. L. A. Bursill and B. G. Hyde, *Prog. Solid State Chem.*, **7**, 177 (1972).
5. JANAF Thermochemical Tables, Dow Chemical Co., NSRDS-NBS-37, U.S. Govt. Printing Office (1971).
6. P. W. Gilles, K. D. Carlson, H. F. Franzen, and P. G. Wahlbeck, *J. Chem. Phys.*, **46**, 2461 (1967), review older data and establish the general picture. Subsequent data are discussed in Ref. (7,8).
7. P. J. Hampson and P. W. Gilles, *ibid.*, **55**, 3712 (1971).
8. H. Y. Wu and P. G. Wahlbeck, *ibid.*, **56**, 4534 (1972).
9. K. Suzuki and K. Sambongi, *Tetsu To Hagane*, **58**, 1579 (1972), *Chem. Abstr.*, **77**, 169559q (1972). English translation by R. G. Sommer and Y. Ishikawa (1973).
10. R. R. Merritt, B. G. Hyde, L. A. Bursell, and D. K. Philp, *Phil. Trans. Roy. Soc. London*, **A274**, 627 (1973).
11. K. Kiukkola and C. Wagner, *This Journal*, **104**, 308 (1957).
12. K. Kiukkola and C. Wagner, *ibid.*, **104**, 379 (1957).
13. I. A. Vasil'eva and E. Yu. Shaulova, *Russ. J. Phys. Chem.*, **43**, 1713 (1969); **45**, 1141 (1971).
14. M. Hoch, A. S. Iyer, and J. Nelken, *J. Phys. Chem. Solids*, **23**, 1463 (1962).
15. T. H. Etsell, *Z. Naturforsch.*, **27a**, 1138 (1972).
16. T. H. Etsell and S. N. Flengas, *Chem. Rev.*, **70**, 339 (1970).
17. JANAF Thermochemical Tables, Dow Chemical Co. Midland, Mich.: Ti_2O_3(c) 6-30-73, Ti_3O_5 (α,β) 12-31-73, Ti_4O_7(c) 12-31-73, Cr_2O_3(c) 12-31-73, and NbO(c) 12-31-73 to appear in 1975 in *J. Chem. Phys. Ref. Data.*
18. H. S. Isaacs, *This Journal*, **119**, 455 (1972).
19. E. C. Subbarao, P. H. Sutter, and J. Krizo, *J. Am. Ceram. Soc.*, **48**, 443 (1965).
20. R. G. Sommer, Ph.D. Thesis, University of Iowa (1974).
21. W. L. Worrell, "Thermodynamics," Vol. 1, p. 131, International Atomic Energy Agency, Vienna (1966).
22. M. F. Lasker and R. A. Rapp, *Z. Phys. Chem. N.F.*, **49**, 198 (1966).
23. G. P. Shreikin and G. V. Bazuev, *Russ. J. Inorg. Chem.*, **18**, 155 (1973).

24. R. T. Bryant, *J. Less-Common Metals*, **4**, 62 (1962).
25. B. C. H. Steele and C. B. Alcock, *Trans. Met. Soc. AIME*, **233**, 1359 (1965).
26. L. S. Darken and R. W. Gurry, *J. Am. Chem. Soc.*, **67**, 1398 (1945).
27. S. Ignatowicz and M. W. Davies, *J. Less-Common Metals*, **15**, 100 (1968).
28. H. L. Schick, Fifth Progress Report (Sept. 15, 1963), Arco-Everrett Report, RAD-SR-63-183.
29. R. N. Blumenthal and D. H. Whitmore, *J. Am. Ceram. Soc.*, **44**, 508 (1961).
30. R. A. Giddings and R. S. Gordon, *ibid.*, **56**, 111 (1973), and references given therein.
31. R. A. Giddings and R. S. Gordon, *This Journal*, **121**, 793 (1974).
32. H. F. Rizzo, R. S. Gordon, and I. B. Cutler, Proc. Nat. Bur. Standards Symp. on Mass Transport in Oxides, Oct. 1967, NBS Special Publication 296, pp. 129-142 (1968).
33. S. Andersson, B. Collen, U. Kuylenstierna, and A. Magneli, *Acta Chem. Scand.*, **11**, 1641 (1957).
34. J. S. Anderson, *Proc. Roy. Soc. London*, **A185**, 69 (1946).
35. F. Naylor, *J. Am. Chem. Soc.*, **68**, 1077 (1946).
36. N. P. Slyusar, A. D. Krivorotenko, E. N. Fomichev, A. A. Kalashnik, and V. P. Bondarenko, *Teplofiz. Vysokikh Temperatur, Akad. Nauk SSSR*, **11**, 213 (1973).
37. C. N. R. Rao, S. Ramdas, R. E. Loehman, and J. M. Honig, *J. Solid State Chem.*, **3**, 83 (1971).

Mechanisms of Decomposition of Organochromium Compounds in the CVD Process. Cycloheptatriene Chromium Tricarbonyl

T. J. Truex, R. B. Saillant, and F. M. Monroe

Ford Motor Company, Dearborn, Michigan 48121

ABSTRACT

A general method for studying the decomposition of organometallic compounds in the low temperature chemical vapor deposition (CVD) process is described. Gas chromatographic and mass spectral analyses have been used to identify volatile by-products from CVD reactions and determine their relationship to deposit composition. The technique, in conjunction with ^{13}C labeling experiments, has been used to determine the mechanism of decomposition of cycloheptatriene chromium tricarbonyl [$(C_7H_8)Cr(CO)_3$]. $(C_7H_8)Cr(CO)_3$ pyrolyzes at temperatures $> 300°C$ to give deposits containing mainly chromium and carbon with small amounts of oxygen present. Reactions involving the CO ligands, including CO disproportionation, make only minor contributions to deposit composition with the majority of deposited carbon ($>85\%$) resulting from reactions involving the cycloheptatriene ring. The use of thermogravimetric analysis and differential scanning calorimetry to screen potential CVD compounds is described.

We have undertaken a program to evaluate the use of organometallic compounds in the low temperature chemical vapor deposition (CVD) process for two reasons: to develop general methods for studying the mode of decomposition of these compounds, and to determine the detailed mechanism(s) of decomposition of selected organochromium compounds.

The use of new organometallic compounds (1) for low temperature ($< 550°C$) CVD provides the potential of depositing metals, oxides, carbides, or nitrides on light metals, glass, and other materials not resistant to glow temperatures. The development of this process depends upon an understanding of the relationship between process variables (chemical and physicochemical) and deposit compositions and properties (2). In particular, an understanding of the mechanisms of decomposition of organometallic compounds could explain the origins of deposit compositions and conceivably indicate ways to control these compositions.

Several organochromium compounds have been used in the past to deposit chromium, chromium carbide, and/or chromium oxide by the CVD process. Lander and Germer (3) and also Owen and Webber (4) studied the decomposition of chromium hexacarbonyl, $Cr(CO)_6$. Deposits containing varying amounts of Cr, Cr_3C_2, and Cr_2O_3 were obtained depending upon reaction conditions. Decompositions using the bis(arene)-chromium(O) compounds, bis(benzene)chromium(O) **1** (5), and bis(cumene)chromium(O) **2** (6) also produced carbide deposits of varying compositions. Of the latter two systems, the bis(cumene)chromium(O) compound has been the most extensively studied. It decomposes at substrate temperatures between 325° and 550°C producing chromium carbide deposits containing 8-12 weight per cent (w/o) carbon. Mechanistic studies on this compound have been precluded due to the unavailability of pure starting material. Chemical decomposition of commercially available bis(cumene)chromium(O) in this and other laboratories (7) reveals that it is a mixture of bis(arene)chromium(O) compounds containing benzene, cumene, diisopropylbenzenes, and triisopropylbenzene. Recently there has been a report of the preparation of pure bis(cumene)-chromium(O) (8) which we hope to utilize for the preparation of pure samples for mechanistic studies.

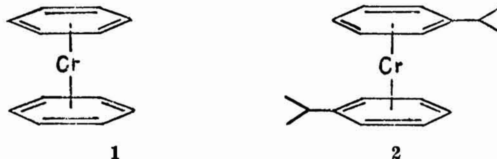

A third class of organochromium complexes which has received little attention as a potential source of CVD compounds is the arene chromium tricarbonyls **3** (9). These compounds are of particular interest for mechanistic studies because they incorporate structural features of both the $Cr(CO)_6$ and bis(arene)-chromium(O) systems. Thus, decomposition studies of these systems could reveal reactions involving the CO

Key words: chemical vapor deposition, organochromium, deposit composition, DTA/DSC analyses.

ligands leading to oxide and/or carbide formation as suggested for the metal hexacarbonyls of Cr, Mo, and W (3) and/or carbide formation from decomposition of the arene ligands as implied from results on the bis(arene)chromium(O) systems (5, 6).

3 4

Differential thermal analysis (DTA), differential scanning calorimetry (DSC), and preliminary plating studies on a series of arene chromium tricarbonyl compounds (*vide infra*) had also indicated that cycloheptatriene chromium tricarbonyl **4** (10) was a promising candidate for study. It is only slightly air-sensitive under ambient conditions, but thermally decomposes at temperatures > 300°C. It is easily sublimed at 70°C and 1.0 mm pressure.

Results are reported on the mechanism of decomposition of cycloheptatriene chromium tricarbonyl. In addition, general procedures for studying the decomposition of organometallic compounds are presented.

Experimental Procedure

Chemicals.—All organometallic compounds were obtained from Strem Chemicals Incorporated, Beverly, Massachusetts. Comparison of observed melting points, solution infrared, nmr, and mass spectra with literature data indicated all compounds were pure as received.

Apparatus and procedure.—A diagram of the experimental apparatus is shown in Fig. 1. The glass (Pyrex) or aluminum substrate was attached to a graphite block which was heated inductively. The substrate temperature was recorded by a thermocouple imbedded in the block. The pressure was measured with a thermocouple gauge. Condensable gaseous by-products were collected in cold traps at liquid N_2 (−196°C), Dry Ice/acetone (−76°C), or ice-methanol (~ −20°C) temperatures. Noncondensable gaseous by-products were collected in a 1 liter evacuated glass bulb and then pumped via a Toeppler pump into a 50 cm^3 volume.

DTA and DSC were performed under an N_2 atmosphere using a du Pont Model 900 analyzer.

The condensable by-products in the CVD reactions were analyzed by separating the components using a gas chromatograph interfaced with a mass spectrometer. These analyses were done at Shrader Analytical and Consulting Laboratories, Incorporated, Detroit, Michigan.

Fig. 1. Schematic diagram of apparatus for studying the mechanisms of decomposition of organometallic compounds.

Mass spectral analyses of the noncondensable gaseous by-products were performed using an Aero Vac Model AVA/61 residual gas analyzer. This instrument was calibrated for intensity *vs.* partial pressure for samples of air, CO, CO_2, H_2, CH_4, and C_2H_4.

Deposit compositions were determined by electron microprobe analyses.

In a typical plating run the following procedure was used. The reaction vessel was charged with the plating compound, the substrate/graphite holder was attached and the apparatus evacuated to the desired pressure. The induction furnace was then turned on and the substrate heated to the plating temperature. After the substrate temperature was stabilized, a preheated oil bath was placed around the bottom of the reaction vessel causing the complex to sublime. The condensable by-products were collected in the cold trap as described above. Noncondensable gases were collected in a 1 liter evacuated flask as described previously. All of the experiments with cycloheptatriene chromium tricarbonyl were done with a sublimation temperature of 70°C and a pressure of ~0.3 mm Hg on glass (Pyrex) or aluminum substrates.

^{13}CO labeling experiment.—The ^{13}CO exchange reaction described below is similar to that used to prepare the substituted compounds $(C_7H_8)Cr(CO)_2X$, where X is triphenylphosphine or triphenylphosphite (11). 6.84g (30 mmole) of cycloheptatriene chromium tricarbonyl was dissolved in 150 ml of degassed cyclohexane (distilled under N_2 from CaH_2). This was placed in a Vycor reaction vessel, with care taken to exclude air, and attached to a vacuum line. After several freeze-thaw cycles under vacuum, 100 cm^3 at 0.7 atm of 90% enriched ^{13}CO (Stohler Isotopes Incorporated) was introduced. The exchange reaction was allowed to proceed at room temperature under 3500Å irradiation for 36 hr. The reaction was then stopped, the solution frozen, and the gases above it replaced with a fresh supply of 90% enriched ^{13}CO (100 cm^3 at 0.5 atm). The reaction was then allowed to proceed an additional 36 hr under the same conditions as above. At the end of this period the gases above the solution were again replaced with a fresh supply (350 cm^3 at 0.36 atm) and irradiation continued for a final 36 hr. The solution was filtered under N_2 and the product isolated by evaporation *in vacuo*. The extent of enrichment was determined by mass spectroscopic analysis. The parent ion region was analyzed for increases due to ^{13}CO-containing species and the ratio of ^{13}CO and ^{12}CO was determined by analysis of the $m = 29$ and $m = 28$ peaks. The reaction can be followed qualitatively by monitoring the appearance and growth of a ^{13}CO stretching band at 1855 cm^{-1} (cyclohexane solvent) in the infrared spectrum. Two samples of labeled compound were prepared; one contained 7.5% ^{13}CO and the other 8.7% ^{13}CO.

Results and Discussion

Selection of potential CVD compounds.—The quick and systematic evaluation of potential CVD compounds is a continuing problem for new materials. DTA and DSC show promise as reliable screening techniques which provide sublimation and decomposition data. A linear correlation was observed, Fig. 2, when the initial decomposition temperatures were plotted against the minimum plating temperatures[1] under CVD conditions. The less-than-unity slope results from the difference between the DTA/DSC measurements and our criterion for "initial plating." These data led to the study of cycloheptatriene chromium tricarbonyl. In the future, these DTA/DSC studies will be extended to a number of other classes of compounds to determine if the observed correlation persists.

Experimental procedure and rationale.—Figure 3 represents the interaction between product and process

[1] For CVD this is necessarily qualitative and arbitrary. For our purposes it is the minimum substrate temperature at which a uniform opaque deposit forms during 30 min of reaction time.

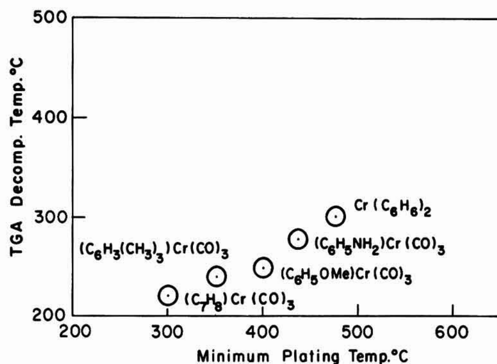

Fig. 2. Plot of DTA/DSC decomposition temperature vs. minimum CVD decomposition temperature.

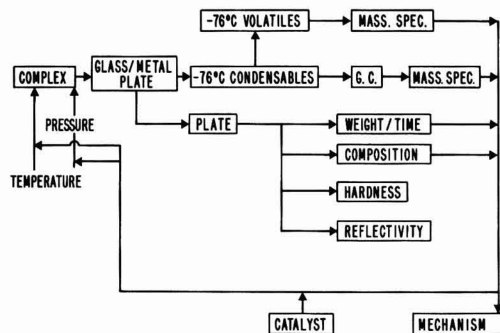

Fig. 3. Schematic representation of relationship between products and process variables in the CVD process.

variables. In this study we have controlled the pressure, and the substrate and sublimation temperatures. For a given set of these variables a deposit is formed which can be analyzed for different properties, some of which are shown. The property of interest for this study was coat composition. The reaction by-products can be experimentally separated into condensables and noncondensables by varying trap temperatures and analyzed as described in the experimental section. This procedure allows the correlation of deposit properties (composition) and reaction by-products with plating compound and variables from which a mechanism can be deduced.

The principle behind this approach is mass balance. Thus, a change in deposit composition must be accompanied by corresponding variations (molecular and/or concentration) in reaction by-products. Isotopic labeling has also been used in the present study to complement mass balance information and unambiguously identify specific carbon sources.

Results of decomposition studies on cycloheptatriene chromium tricarbonyl ($(C_7H_8)Cr(CO)_3$).—$(C_7H_8)Cr(CO)_3$ is a slightly air-sensitive red crystalline solid which must be stored in an inert atmosphere but can be handled in air for short periods of time without noticeable decomposition. Its volatility is high enough that adequate sublimation rates are obtained at temperatures ≥70°C. Rapid pyrolysis of $(C_7H_8)Cr(CO)_3$ occurs at temperatures ≥300°C. The temperature range which produces uniform, smooth, continuous, adherent, mirror-bright films is 350°-450°C. Below 350°C some spontaneous peeling of the film from Pyrex glass substrates is observed (this problem has not been encountered with aluminum substrates) and above 500°C formation of a black sooty material in the reaction chamber indicates that some of the vapor decomposes before it reaches the hot substrate. Although all deposition studies were conducted at a sublimation temperature of 70°C and a pressure of 0.3 mm Hg, it is probable that the optimum substrate temperatures will change as a function of other variables. We have not explored this possibility in detail but have instead chosen to vary substrate temperature while holding all other variables constant in an attempt to simplify the mechanistic analysis. The substrate temperature range studied was 300°-600°C.

The deposited films were analyzed for Cr, C, and O by electron beam microprobe analyses. The results show that deposits formed from $(C_7H_8)Cr(CO)_3$ decomposition in the 300°-600°C range contain mainly chromium and carbon with smaller amounts of oxygen. Average chromium and carbon contents [atomic per cent (a/o)] as a function of temperature were as follows:

300°C	63.6 a/o Cr	28.4 a/o C
400°C	62.4 a/o Cr	32.5 a/o C
500°C	58.8 a/o Cr	36.0 a/o C
600°C	59.1 a/o Cr	32.1 a/o C

Although quantitative oxygen analyses were not performed on all samples, in the analyzed samples oxygen accounted for the remainder of the film. In addition, no foreign elements other than chromium, carbon, or oxygen were detected in any of the films. These results show a fairly uniform composition throughout the temperature range with somewhat higher oxygen contents at both extremes of temperature. A poorly defined x-ray pattern was obtained for one deposit laid down at 600°C. The pattern could be associated with Cr_7C_3 although some known lines were absent. All other film deposits were amorphous. This type of behavior has been noted previously in chromium carbide films deposited at low temperatures (6b) where it was observed that annealing leads to crystallization. This has not been tried with films produced by $(C_7H_8)Cr(CO)_3$ decomposition since the major interest has been in as-deposited films. Of primary interest is the source of the deposited carbon and oxygen found in these films.

The variation in condensable by-products foɪ $(C_7H_8)Cr(CO)_3$ decomposition in the temperature range 300°-600°C is shown in Fig. 4. The relative proportion of the major component, cycloheptatriene, steadily decreases as the deposition temperature is increased. However, the relative proportions of benzene, toluene, cycloheptadiene, and styrene increased with temperature. The benzene and cycloheptadiene concentrations pass through maxima at ~500°C. This may indicate secondary reactions involving decomposition of these compounds above 550°C. Benzene decomposition has been noted in other CVD studies at temperatures >500°C (5b).

The major component of the noncondensable by-products was CO, with the second largest component being H_2 [~10-15 molecular per cent (m/o) of the noncondensable gas fraction]. Minor components of methane and ethylene were observed together with trace amounts of CO_2 (0-2 m/o) and C_2 and C_3 hydrocarbons. It was noted that the relative compositions of the noncondensable by-products do not vary in a significant manner throughout the 300°-600°C temperature range.

The appearance of the different chemical species found in the condensable by-products implies that the net chemical reactions presented in Fig. 5 are taking place during decomposition. Only benzene formation involves a loss of carbon and is therefore a possible source of deposited carbide. The other reactions involve no net change in carbon or, as in the case of styrene, the addition of one carbon atom. The carbon loss through benzene formation is ~7-10 a/o between 300°-400°C and ~20-30 a/o at decomposition temperature >450°C. Since styrene formation, and the associated carbon addition in this reaction is ~0-2 m/o throughout the decomposition temperature range, the

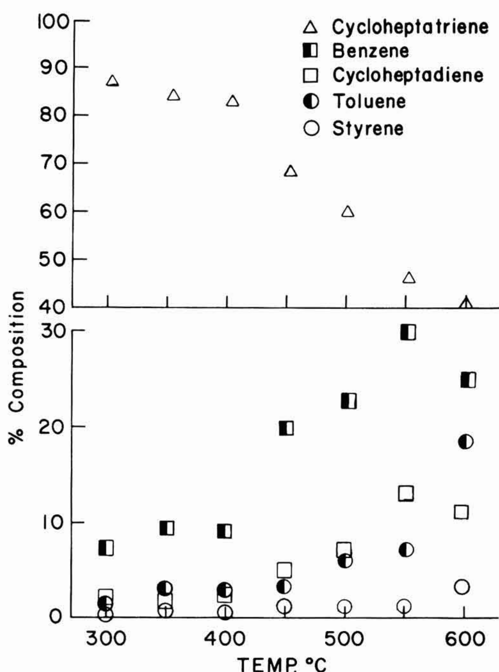

Fig. 4. Variation of condensable by-products for $(C_7H_8)Cr(CO)_3$ decomposition in the temperature range 300°-600°C.

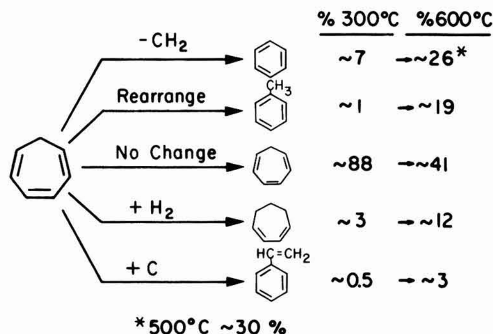

Fig. 5. Chemical reactions implied by the formation of condensable by-products in $(C_7H_8)Cr(CO)_3$ decomposition

majority of the carbon freed in the benzene reaction is available for carbide formation. Thus, below 400°C the benzene reaction can account for ~25-30% of the deposited carbon and above 400°C it can account for ~55-95% of deposited carbon.

The noncondensable gas results provide a complement to the condensable by-product conclusions. First, the absence of considerable amounts of CO_2 indicates that the CO disproportionation reaction proposed as a source of carbon formation in the decomposition of other carbonyl containing organometallics (3) is not significantly operative. This does not completely rule out participation of CO in deposit formation by some reaction pathway other than disproportionation. This point will be raised again during discussion of results from ^{13}C labeling experiments. The second point involves the large H_2 component seen in the noncondensable gas fraction. This implies that considerable reaction involving cycloheptatriene is taking place. Part of this is explained by the benzene formation reaction mentioned previously, but this will not account for all of the H_2 observed, especially below 400°C. This, together with the absence of lower hydrocarbons ($<C_6$), suggests that some total degradation of cycloheptatriene is taking place.

Definitive information on the relative participation of CO and cycloheptatriene in deposit formation has been provided by ^{13}C labeling experiments. ^{13}CO labeled cycloheptatriene chromium tricarbonyl was used for deposition studies at 300°, 400°, and 500°C (runs at 600°C were precluded due to interference from gas phase decomposition). The deposits from these runs were then combusted and the CO_2 given off collected and analyzed mass spectrometrically to determine the $^{13}CO_2/^{12}CO_2$ ratio. The results of these experiments are shown in Table I together with the calculated per cent of observed carbide formation coming from reactions involving CO. These data show that the fraction of carbide formation due to CO was a maximum of ~13% at 400°C with average values of 7.3% at 300°C, 10.0% at 400°C, and 2.0% at 500°C. These results confirm the conclusions drawn from the noncondensable gas analyses. Specifically, CO participation in carbide formation is small compared to that of cycloheptatriene. The presence of 5-9 a/o oxide in the deposits could arise from reaction of the oxygen atom in CO with deposited chromium, or from the presence of residual O_2 in the system which has a background pressure of ~1μ.

Conclusions

As part of an over-all program to determine mechanisms of decomposition of organometallic compounds, a study of the decomposition of cycloheptatriene chromium tricarbonyl has been made. $(C_7H_8)Cr(CO)_3$ decomposes at substrate temperatures of ≳300°C to form deposits on glass and aluminum substrates containing mainly chromium and carbon, with lesser amounts of oxygen present. Mechanistic studies utilizing comparisons of deposit compositions and condensable and noncondensable by-products analyses and ^{13}CO labeling studies allow the following conclusions concerning $(C_7H_8)Cr(CO)_3$ decomposition:

(*i*) Reactions involving CO account for less than 13% of deposited carbon in the deposition pressure and temperature ranges studied.

(*ii*) The majority of deposited carbide comes from the cycloheptatriene ring. Two specific reactions appear to account for this. First, transformation of cycloheptatriene into benzene with loss of a carbon atom and one molecule of hydrogen. This reaction is operative to only a minor extent at low temperatures, but at >450°C it can account for ~55-95% of the deposited carbide. Second, total degradation of cycloheptatriene into carbon and hydrogen. This reaction must be operative throughout the temperature range 300°-600°C, but below 450°C it produces the majority of the carbide formed (~70-75%). It should be noted that in separate experiments pure cycloheptatriene was found not to decompose under the deposition conditions used here. This implies that complexation to chromium activates decomposition, or an initially formed chromium deposit catalyzes the decomposition.

(*iii*) Several other reactions of cycloheptatriene which do not contribute to deposit formation were observed. These included formation of toluene, cycloheptadiene, and styrene.

Table I. ^{13}C labeling experiment results

Deposition temperature, °C	Per cent ^{13}CO in $(C_7H_8)Cr(CO)_3$	Per cent ^{13}C in deposit (range)	Per cent of deposited carbon from CO (range)
300	7.5	1.57(1.49-1.67)	7.3(6.1-8.9)
400	7.5	1.74(1.56-1.92)	10.0(7.2-13.0)
500	8.7	1.25(1.10-1.35)	2.0(0.0-3.3)

(*iv*) The presence of small amounts of oxygen in the films suggests some reaction of deposited chromium with oxygen from CO and/or background O_2 in the reaction system.

This study demonstrates the utility of the experimental approach used in determining mechanisms of decomposition of organometallic compounds in the CVD process. In the future these studies will be extended to other arene chromium tricarbonyl compounds and also other classes of organometallic compounds with the goal of developing thermodynamic models for the prediction of decomposition mechanisms of these systems.

Acknowledgments

The authors would like to thank Barbara Bergman and Jack Tabock of the Technical Services Department of the Ford Scientific Research Staff for performing the DTA and electron microprobe analyses, respectively.

Manuscript submitted Dec. 26, 1974; revised manuscript received May 27, 1975. This was Paper 307RNP presented at the Boston, Massachusetts, Meeting of the Society, Oct. 7-11, 1973.

Any discussion of this paper will appear in a Discussion Section to be published in the June 1976 JOURNAL. All discussions for the June 1976 Discussion Section should be submitted by Feb. 1, 1976.

Publication costs of this article were partially assisted by the Ford Motor Company.

REFERENCES

1. F. G. A. Stone and R. West, *Advances in Organometallic Chemistry*, Vol. 1 (1964); Vol. 11 (1973), Academic Press, New York.
2. K. H. Bloss and H. Lukas, *Electrodeposition and Surface Treat.*, **2**, 47 (1974).
3. J. J. Lander and L. H. Germer, *Metals Technol.*, **14**, TP 2259 (1947); *Metal Ind.*, (London), **71**, 459, 487 (1947).
4. B. B. Owen and R. T. Webber, *Metals Technol.*, **15**, TP 2306 (1948).
5. (a) M. Tsutsui and C. J. Marsel, Air Force Cambridge Reserach Laboratories, ARCRL-64-934, Bedford, Massachusetts (1964).
   (b) B. D. Nash, T. T. Campbell, and F. E. Block, *U.S. Bur. Mines, Rept. Invest. 7112*, Washington, D.C. (1968).
6. (a) R. Tomono, E. Yagi, and Y. Togashi, *Kinzoku Hyomen Gitjutsu (J. Metal Finishing Soc. Japan)* **16**, 210 (1965).
   (b) J. E. Knap, B. Pesetsky, and F. N. Hill, *Plating*, **53**, 772 (1966).
7. Y. A. Sorokin and G. G. Petukhov, *J. Gen. Chem. USSR*, **35**, 2123 (1966).
8. R. Middleton, J. R. Hull, S. R. Simpson, C. H. Tomlinson, and P. L. Timms, *J. Chem. Soc., Dalton Trans.*, 120 (1973).
9. R. L. Pruett, *Prep. Inorg. Reactions*, **2**, 187 (1965).
10. E. W. Able, M. A. Bennett, R. Burton, and G. Wilkinson, *J. Chem. Soc.*, 4559 (**1958**).
11. W. P. Anderson, W. G. Blenderman, and K. A. Drews. *J. Organomet. Chem.*, **42**, 139 (1972).

Theoretical Aspects of the Peltier Effect on the Temperature Distribution in Crystal Grown by the Czochralski Technique

S. Vojdani, A. E. Dabiri, and M. Tavakoli

Materials and Energy Research Center, Arya-Mehr University of Technology, Tehran, Iran

ABSTRACT

A theoretical treatment is given for the temperature distribution in a Czochralski system with and without the presence of the Peltier effect. The effect of Peltier heating on the crystal diameter during growth is also considered. The results indicate that the Peltier current necessary to control a given diameter of a crystal during intermediate stages of growth is dependent on T_c, the crucible temperature, and h_c, the height of crucible above the melt.

Recently the use of the Peltier effect has been reported for the control of the diameter of pulled Ge crystals (1). The effect has also been used in connection with modulation of dopant segregation in Czochralski-grown InSb (2). The Peltier effect is produced at the solid-liquid interface without time lag and can be reversed by reversing the current through the crystal.

Some theoretical attempts have been made to determine the solid-liquid interface shape (3) and the temperature distribution in the axial direction of a crystal and the melt in a Czochralski crystal growth system (4, 5) by solving computationally the steady-state heat transfer equation. In such computations the convective processes in the melt are generally ignored. In practice crystal rotation in Czochralski technique is introduced to provide a forced convection flow in the liquid, which tends to isolate the interface from thermal convection in the bulk liquid.

The objective of this paper is to investigate theoretically the effect of Peltier heating at a solid-liquid interface on such parameters as temperature distribution in the solid and the melt, temperature gradients in the solid and the melt, and in particular the control of crystal diameter.

Key words: crystal growth, Peltier effect, temperature distribution in solid, Czochralski technique.

Theoretical Method

The crystal growth arrangement used for the present analysis is shown schematically in Fig. 1.

Assumptions made in solving the heat transfer equation are as follows: (*i*) The heat loss from the crystal and the melt is only through radiation. (*ii*) Convection in the melt is neglected. (*iii*) Joule heating due to the Peltier current in the crystal and the melt for normally used current densities ($\sim$20 A-cm^{-2}) is neglected (6).[1] (*iv*) Thickness of the crucible wall is neglected. (*v*) The interface is assumed to be planar.

[1] The resistivity of the solid Ge, ρ_s, at the melting point is $\sim 10^{-3}$ ohm-cm; that of the liquid, ρ_L is about 1/5 this value. Assuming a normally used current density ($\sim$ 20 A-cm^{-2}), the Peltier heat at the interface is 1.7 W-cm^{-2} while the Joule heat in the solid and the liquid within 5 mm of the interface is 0.2 and 0.04 W-cm^{-2}, respectively.

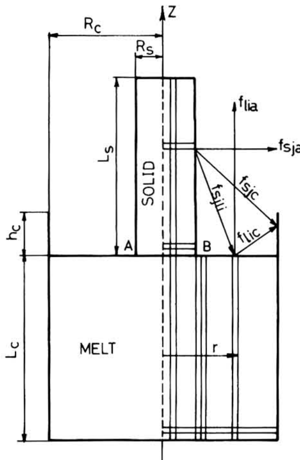

Fig. 1. Schematic diagram of crystal growth arrangement (L_c = 5 cm, L_s = 5 cm, R_c = 2.5 cm, R_s = 1 cm).

Assuming that the steady-state condition for the temperature distribution in the crystal and the melt is governed by the Laplace equation, and using the notation in the Appendix 1, we have

$$\frac{\partial^2 T}{\partial r^2} + \frac{1}{r}\frac{\partial T}{\partial r} + \frac{\partial^2 T}{\partial Z^2} = 0 \quad [1]$$

Subject to the following boundary conditions:
On the crystal axis by symmetry we have

$$\frac{\partial T}{\partial r} = 0 \quad [2]$$

On the crystal side surfaces

$$-K_s \left(\frac{\partial T}{\partial r}\right)_{sj} = q_{sj} \quad [3]$$

where q_{sj} is the net heat flux radiated from a point j on the side surface of the crystal and is given by

$$q_{sj} = \epsilon_s\sigma \left[\sum_{i=1}^{n} \epsilon_l f_{sjli}(T_{sj}^4 - T_{li}^4) + \epsilon_c f_{sjc}(T_{sj}^4 - T_c^4) + f_{sja}(T_{sj}^4 - T_a^4) \right] \quad [4]$$

In the above expression f's are the geometry factors between any two points in the growth arrangement as shown in Fig. 1. The exact calculation of the geometry factors are given in Appendix 2.

Furthermore

$$-K_s \left(\frac{\partial T}{\partial Z}\right)_{Z=L_s} = q_{ti} \quad [5]$$

where q_{ti} is the net heat flux radiated from a point i on the top surface of the crystal and is given by

$$q_{ti} = \epsilon_s\sigma (T_{si}^4 - T_a^4) \quad [6]$$

on the melt free surface

$$-K_l \left(\frac{\partial T}{\partial Z}\right)_{Z=0} = q_{li} \quad [7]$$

where q_{li} is the net heat flux radiated from a point i on the free surface of the liquid and is given by

$$q_{li} = \epsilon_l\sigma \left[\sum_{j=1}^{m} \epsilon_s f_{lisj}(T_{li}^4 - T_{sj}^4) + \epsilon_l f_{lic}(T_{li}^4 - T_c^4) + f_{lia}(T_{li}^4 - T_a^4) \right] \quad [8]$$

and on the solid-liquid interface we have

$$-K_s \left(\frac{\partial T}{\partial Z}\right)_{Z=0} = -K_l \left(\frac{\partial T}{\partial Z}\right)_{Z=0} + LG + Q_P \quad [9]$$

where Q_P is the heat flux given to the interface by the Peltier heating current and is given by

$$Q_P = \alpha I_P T_m \quad [10]$$

Finally on the point A and B of Fig. 1

$$T = T_m$$

Solving Eq. [1] computationally with the above-mentioned boundary conditions, the following results can be obtained: (*i*) temperature distribution inside liquid and solid with and without Peltier effect, (*ii*) temperature gradients inside solid and liquid with and without Peltier effect, (*iii*) crucible temperature for a desired diameter with a given h_c (it should be noted that T_c is not taken as a boundary condition), (*iv*) the amount of Peltier current required to keep the diameter constant (with a given initial h_c), and (*v*) the crucible temperature changes required to keep the diameter constant with a given initial h_c.

Results

As an example Ge has been chosen. The following representative values were used: T_a = 300°K, T_m = 1210°K, $\epsilon_l = \epsilon_s$ = 0.2, K_s = 0.24 W-cm^{-1} deg^{-1}, K_l = 0.71 W-cm^{-1} deg^{-1}, $L = 2.16 \times 10^3$ joule cm^{-3}, R_c = 2.5 cm, L_c = 5 cm, R_s = 1 cm, L_s = 5 cm, ϵ_c = 1, $\alpha = 7 \times 10^{-5}$ V deg^{-1}, and G = 1 mm min^{-1}.

Figures 2 and 3 show the temperature distribution and the temperature gradient along the axis of a 5 cm long crystal with and without application of Peltier heating current. With Peltier current employed (24 A-cm^{-2}) no detectable change is observed in temperature distribution or temperature gradient along the axis of the crystal. However when the Peltier current is applied, the T_c must be lowered in order to have the same diameter. Lowering T_c especially for $h_c \geq 2$ cm has the effect of reducing the temperature difference between the bottom of the crucible and the melt surface along the axis of the crucible. This should tend to reduce convection in the melt. Since even in the presence of Peltier effect and crystal rotation, convection in the melt cannot be completely removed, the result in Fig. 4 can only be approximate. Another effect noticed was the movement of the interface toward the crystal upon the application of Peltier heating.

Control of diameter by Peltier heating.—Figure 5 shows the variation of Peltier current with crystal length for different values of h_c. The curves show that to keep the diameter constant during growth, for a fixed h_c (and therefore T_c), the Peltier current must be increased continuously. The saturation effect seen over longer crystal lengths is related to small variations on total radiation losses from the crystal as the length of the crystal increases. This is shown as a plot of Q_s *vs.* length of the crystal in Fig. 6. It is important to note that the Peltier effect does not change the radiation losses. However since the total area of a crystal increases, therefore the net radiation losses increase and the Peltier effect must compensate this increase of loss. The effect of increasing h_c for a fixed crystal diameter is shown to lower the Peltier current. This is due to decrease of net radiation from the crystal with increasing h_c.

Control of diameter by changing T_c.—Another way to control the diameter of the crystal during growth is to program T_c instead of Peltier current. Figure 7 shows the variation of T_c to keep the diameter of Ge constant with different h_c's.

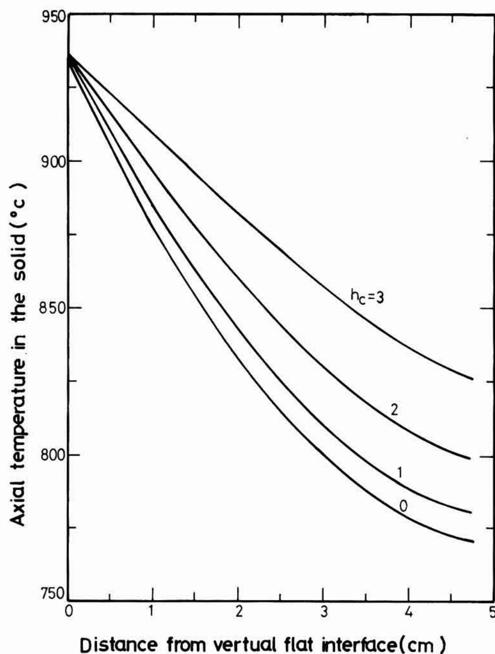

Fig. 2. Axial temperature distribution in the solid vs. distance from virtual flat interface.

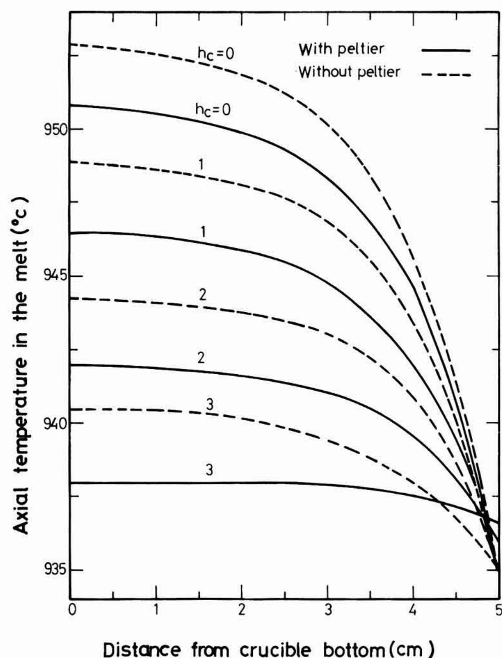

Fig. 4. Axial temperature distribution in the melt vs. distance from crucible bottom.

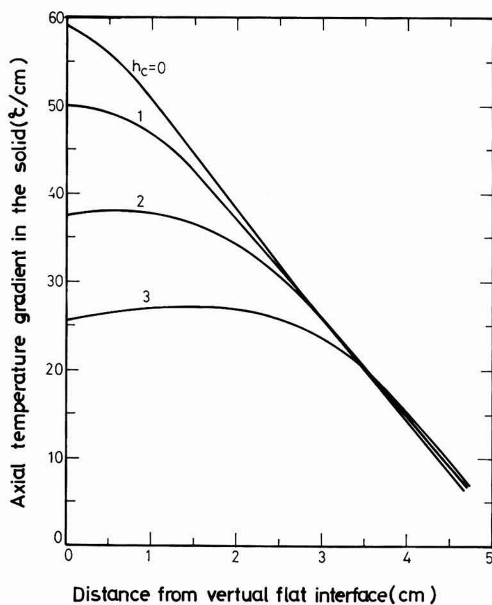

Fig. 3. Axial temperature gradient in the solid vs. distance from virtual flat interface.

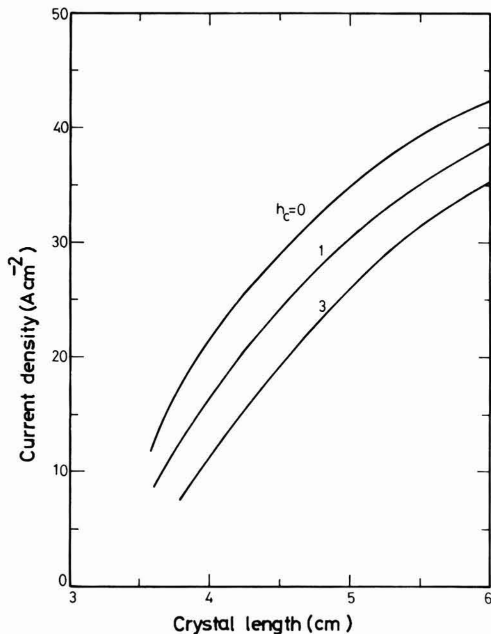

Fig. 5. Variation of current density vs. crystal length to control the diameter of the crystal at 2 cm for different h_c.

Conclusion

From the curves shown in Fig. 2-7 it has been demonstrated clearly that:

(*a*) The Peltier heating effect caused at the interface has no appreciable effect on the temperature distribution or gradients in the crystal.

(*b*) For a given diameter and T_c for every h_c the path of increasing the Peltier current to keep the diameter constant can be predicted. It must be noted that for large crystal diameters to keep the Peltier current

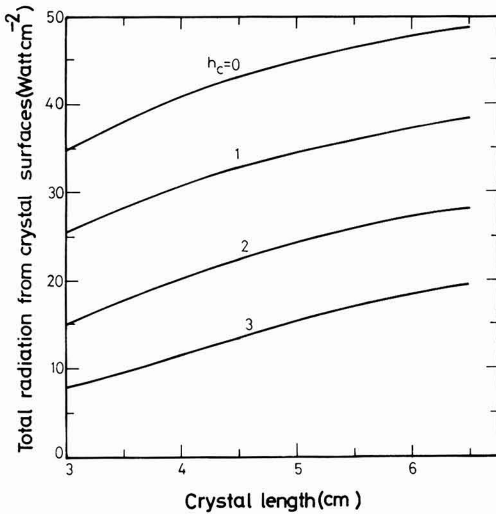

Fig. 6. Variation of total radiation from crystal surfaces with crystal length.

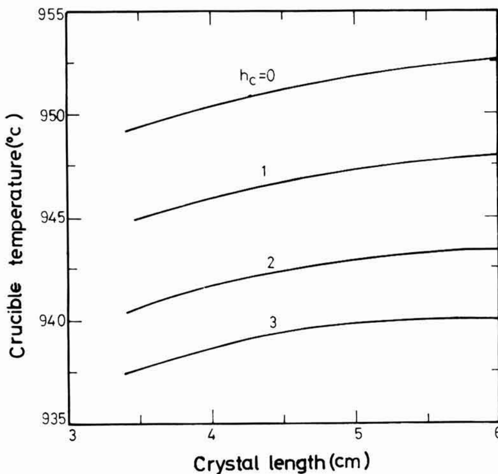

Fig. 7. Variation of crucible temperature with crystal length to control the diameter of the crystal at 2 cm for different h_c.

relatively low for diameter control, higher h_c (essentially an after heater) should be used. The Peltier current necessary for controlling the diameter saturates after, a certain length, a result which is known experimentally.

(c) The same control of crystal diameter can be obtained by changing T_c during growth. This is the process generally used in practice.

Manuscript submitted Dec. 11, 1974; revised manuscript received April 25, 1975.

Any discussion of this paper will appear in a Discussion Section to be published in the June 1976 JOURNAL. All discussions for the June 1976 Discussion Section should be submitted by Feb. 1, 1976.

Publication costs of this article were partially assisted by Arya-Mehr University of Technology.

Appendix 1

1. Geometry factor	f
2. Rate of crystallization	G
3. Height above melt surface	h_c
4. Peltier current	I_p
5. Liquid thermal conductivity	K_l
6. Solid thermal conductivity	K_s
7. Latent heat of fusion	L
8. Crucible height	L_c
9. Crystal length	L_s
10. Heat flux	q
11. Peltier heat	Q_p
12. Radial coordinate	r
13. Crucible radius	R_c
14. Crystal radius	R_s
15. Temperature	T
16. Atmosphere temperature	T_a
17. Crucible temperature	T_c
18. Melting point	T_m
19. Axial coordinate	Z
20. Difference between absolute Seebeck coefficients of solid and liquid	α
21. Liquid resistivity	ρ_L
22. Solid resistivity	ρ_s
23. Emissivity	ϵ
24. Stefen-Boltzmann constant	σ

Appendix 2

Calculation of Geometry Factors

1. $f_{li\to b}$.—The problem is to find the geometry factor of a point *li* on the melt-free surface and an annulus *b*. This can be obtained by differentiating $f_{li\to ss}$ (ss denotes solid surface) with respect to Z. $f_{li\to ss}$ is the same as $f_{d\to ss}$. Considering the relations between geometry factors we have

$$2\pi\rho d\rho f_{d\to ss} = 2\pi R_s L_s f_{ss\to d} \quad \text{[A-1]}$$

or

$$f_{d\to ss} = \frac{R_s L_s}{\rho d\rho} f_{ss\to d}$$

but

$$f_{ss\to d} = \frac{\partial f_{ss\to ls}}{\partial \rho}$$

where ls is the subscript for liquid-free surface. From definition of geometry factor, we may write

$$f_{ss\to ls} + f_{ss\to 5} + f_{ss\to(3+4)} = 1$$

but $f_{ss\to ls} = f_{ss\to 5}$ and therefore

$$f_{ss\to ls} = \tfrac{1}{2}\,(1 - f_{ss\to(3+4)}) \quad \text{[A-2]}$$

but

$$f_{ss\to(3+4)} = \frac{R_c}{R_s} f_{(3+4)\to ss}$$

and $f_{(3+4)\to ss}$ is given by (7)

$$f_{(3+4)\to ss} = \frac{R_s}{R_c}\left\{1 - \frac{1}{\pi}\left\{\cos^{-1}\frac{L_s^2 - R_c^2 + R_s^2}{L_s^2 + R_c^2 - R_s^2} - \frac{1}{2R_sL_s}\left[\sqrt{(L_s^2 + R_c^2 + R_s^2) - 4R_s^2R_c^2}\,\cos^{-1}\frac{R_s(L_s^2 - R_c^2 + R_s^2)}{R_c(L_s^2 + R_c^2 - R_s^2)} + (L_s^2 - R_c^2 + R_s^2)\sin^{-1}\frac{R_s}{R_c} - \frac{\pi}{2}(L_s^2 + R_c^2 - R_s^2)\right]\right\}\right\} \quad \text{[A-3]}$$

Substituting Eq. [A-3] into Eq. [A-2], and using Eq. [A-1], we get

$$f_{d\to ss} = f_{li\to ss} = \frac{1}{2\pi}\left[\cos^{-1}\left(-\frac{R_s}{\rho}\right) - \frac{L_s^2 + \rho^2 - R_s^2}{\sqrt{(L_s^2 + \rho^2 + R_s^2) - 4R_s^2\rho^2}}\cos^{-1}\frac{R_s^2(L_s^2 - \rho^2 + R_s^2}{(L_s^2 + \rho^2 - R_s^2)}\right] \quad \text{[A-4]}$$

2. $f_{li \to 3}$.—According to Fig. 8, $f_{li \to 3}$ could be approximated by the following equation

$$f_{li \to 3} = f_{d \to 3} = 1 - f_{d \to 6} - f_{d \to x} \quad \text{[A-5]}$$

but

$$f_{d \to 6} = \frac{\partial f_{7 \to 6}}{\partial \rho} d\rho$$

and $f_{7 \to 6}$ is given by (7)

$$f_{7 \to 6} = \frac{h_c^2 + \rho^2 + R_c^2 - \sqrt{(h_c^2 + \rho^2 + R_c^2)^2 - 4\rho^2 R_c^2}}{2R_c^2}$$

$f_{d \to x}$ could be evaluated from Eq. [A-4] where L_s is replaced by x. $\left(x = \frac{h_c}{R_c + \rho} (\rho - R_s) \text{ if } x < L_s \text{ and } x = L_s \text{ when } x \geq L_s\right)$.

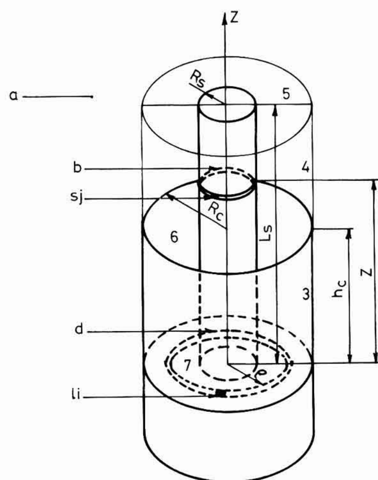

Fig. 8. Schematic diagram of crystal growth arrangement used for calculation of geometry factors.

3. $f_{li \to a}$.—The geometry factor of a point *li* on the melt-free surface and the atmosphere is given by

$$f_{li \to a} = 1 - f_{li \to 3} - f_{li \to ss} \quad \text{[A-6]}$$

4. $f_{sj \to d}$.—The problem is to find the geometry factor of a point *sj* on the crystal side and an annulus *d* on the melt-free surface. This can be obtained by differentiating $f_{sj \to ls}$ which is given by (7)

$$f_{sj \to ls} = \frac{1}{2\pi} \left\{ \cos^{-1} \frac{Z^2 - R_c^2 + R_s^2}{Z^2 + R_c^2 - R_s^2} - \frac{Z}{R_c} \left[\frac{Z^2 + R_c^2 - R_s^2}{\sqrt{(Z^2 + R_c^2 + R_s^2)^2 - 4R_c^2 R_s^2}} \cos^{-1} \frac{R_s (Z^2 - R_c^2 + R_s^2)}{R_c (Z^2 + R_c^2 - R_s^2)} - \cos^{-1} \frac{R_s}{R_c} \right] \right\} \quad \text{[A-7]}$$

5. $f_{si \to 3}$.—This could be obtained by the following equations

$$f_{sj \to 3} = f_{sj \to 6} - f_{sj \to ls} \quad (\text{if } L_s > h_c)$$

The value of $f_{sj \to 6}$ is obtained from Eq. [A-7] if Z is replaced by $Z - h_c$. And if $L_s < h_c$, then

$$f_{sj \to 3} = 1 - (f_{sj \to 6} + f_{sj \to ls})$$

6. $f_{sj \to a}$.—

$$f_{sj \to a} = 1 - (f_{sj \to ls} + f_{sj \to 3})$$

REFERENCES

1. S. Vojdani, A. E. Dabiri, and H. Ashoori, *J. Crystal Growth*, **24/25**, 374 (1974).
2. M. Lichtensteiger, A. F. Witt, and H. C. Gatos, *This Journal*, **118**, 1013 (1971).
3. W. R. Wilcox and R. L. Duty, *J. Heat Transfer. ASME*, **88C**, 45 (1966).
4. K. Akiyama and J. Yamaguchi, *J. Appl. Phys.*, **33**, 1899 (1962).
5. T. Arizumi and N. Kobayashi, *J. Crystal Growth*, **13/14**, 615 (1972).
6. W. G. Pfann, K. E. Benon, and J. H. Wernick, *J. Electronics*, No. 2, 597 (1957).
7. H. Leuenberger and R. A. Person, Am. Soc. Mech. Engrs., No. 56-A-144, 1 (1956).

Technical Note

Mass Spectrometric Analyses of Vapor in Chemical Vapor Deposition of Alumina

Sin-Shong Lin

Army Materials and Mechanics Research Center, Watertown, Massachusetts 02172

Current interest in improving techniques to fabricate a thick layer of translucent to transparent polycrystalline alumina with superior optical properties prompted the present investigation of the vapor phase composition in the preparation of alumina. Previous studies (1-3) relied mostly on analyses of deposits after the completion of a run. The present study extracts gaseous species directly from the deposition reaction, which may furnish basic information concerning vapor molecules existing in the reaction. The sampling of vapors from the process is accomplished by direct injection of these species from the hot furnace into vacuum followed by mass spectrometric detection. Thus the knowledge gained from vapor constituents of the reaction together with examination of the deposits provides valuable information in understanding the chemical deposition process.

Figure 1 shows a block diagram of the sampling device for the chemical vapor deposition of aluminum oxide by hydrolysis-oxidation of aluminum chloride. The experimental arrangement consists of gas inlet lines, a miniature chemical vapor deposition furnace, and a three-stage differential pumping system including a quadrupole mass filter and a modulated beam mechanism. Aluminum chloride is prepared by passing chlorine-hydrogen mixture in a 1:3 ratio over molten aluminum, and water vapor-oxygen mixture in a 1:4 ratio is obtained by bubbling oxygen through water at room temperature. Hydrogen as a carrier gas in the first mixture, reacts with oxygen at temperatures of the deposition to produce more water. Excess oxygen is used to avoid incomplete oxidation of the aluminum chlorides, and water is added not only to serve as a reactant but also to improve transparency of deposited materials. For the deposition reaction, these two gas mixtures are separately introduced into the hot furnace at the same flow rate. The initial flow rates of these gases are in the range of 2-5 cm^3/min.

The miniature furnace is built on the flange of the first chamber of the vacuum system as indicated on Fig. 2. The core of the furnace consists of two high-purity closed-end alumina tubes of ½ and ¼ in. OD in a concentric configuration. On the tip of each tube an orifice is drilled on the axial line. The orifice diameter of the ¼ in. tube is fixed at 0.006 in. and that of the outer ½ in. tube is either 0.04 or 0.06 in. A spacer or collar, cut from a ⅜ in. OD alumina tubing in lengths from ⅜ to ¼ in. is inserted between these two tips to define a hot reaction zone and to serve as a substrate. The spacing between the tips can be reduced to the position of an intimate contact to examine varying extents of the interaction. The heating element is molybdenum wire of a 0.03 in. diameter wound directly around the outer combustion tube. For uniform heating, the winding begins from the orifice edge and extends about 4 in. along the length of the tube. At least two layers of zirconia felt are wrapped around the heating element as insulation. The cylindrical water jacket and the water channel flange are located outside the felt to circulate cooling water. A Pt-10% Rh/Pt thermocouple is placed inside the inner tube near the tip to record temperature and to regulate the heating alternating current supplied to the furnace. The vacuum system, as shown on the right side of Fig. 1, consists of three chambers individually evacuated by three pumping assemblies. The vacuum in the first chamber was maintained at 2×10^{-4} Torr or lower so that a molecular beam could be formed for sampling. The quadrupole mass spectrometer manufactured by Extranuclear Laboratories, Inc., has a high efficiency detection and is designed to operate in a mass range 0-4000 amu. The theory and practice of this sampling technique has been summarized by Milne and Greene (4), and the operation of the present system is given elsewhere (5, 6).

Provision was made to establish and to monitor pressures and flow rates of the reactant gases. The wet oxygen was introduced axially into the furnace through the core of the inner combustion tube and the chlorine-hydrogen mixture was fed into the furnace through the annulus between the inner and the outer combustion tubes. Aluminum metal was placed about 1 in. from the tip of the combustion tube in the annular space so that it melted and reacted with chlorine at temperatures above 600°C to provide aluminum

Key words: aluminum chloride hydrolysis, aluminum chloride oxidation, aluminum-chlorine reaction.

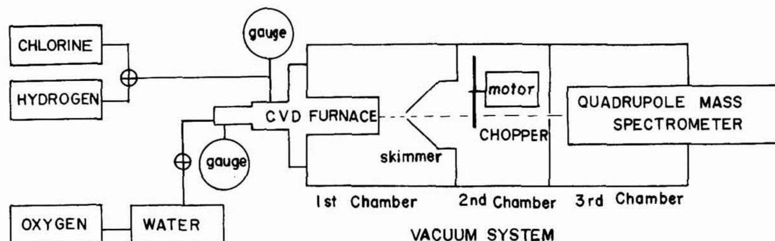

Fig. 1. Block diagram of CVD sampling device.

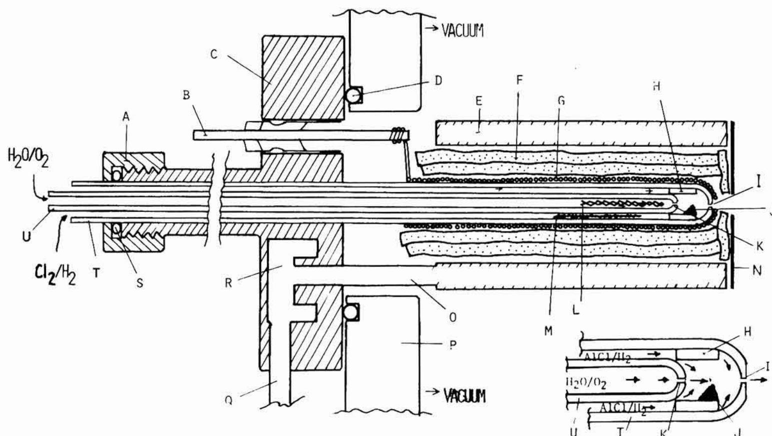

Fig. 2. Chemical vapor deposition furnace assembly, cross sectional view. Legend: A, quick coupling; B, electric feedthrough; C, vacuum flange; D, O-ring; E, cylindrical water jacket; F, zirconia felt; G, molybdenum heating wire; H, spacer or substrate; I, outer orifice; J, alumina deposit; K, inner orifice; L, Pt-10%Rh/Pt thermocouple; M, aluminum metal; N, tantalum heat shield; O, stainless steel tube; P, vacuum wall of the first chamber; Q, inlet and outlet water tubes; R, water channels; S, O-ring seal; T, ½ in. OD alumina combustion tube; U, ¼ in. OD alumina combustion tube. The enlarged sketch of the reaction zone and the two orifices is shown on the right lower corner, and the direction of gas flows is indicated by arrows.

chloride vapors. Since the metal was not placed in a boat, the surface area of molten aluminum tended to decrease after a period of reaction. The experiments were carried out at temperatures from 800°-1400°C, and the pressures of both gaseous mixtures in the furnace were 50-100 mm Hg initially. The pressure of the reaction zone is estimated to be in the range of a few mm Hg. During the run, the Cl_2/H_2 passage tended to clog gradually due to the formation of Al_2O_3 and the displacement of molten aluminum. Consequently the flow rate decreased and the source pressure increased. Alumina deposits resulting from the interaction of the two mixtures were found mostly on the inner cylindrical surface near the exit end of the spacer. All vapors including reactants and products were exhausted into vacuum through the outer orifice for detection. The run was terminated after either the source pressure had reached 1 atm from clogging or a period of 6 hr had elapsed. At the end of a run, gases were shut off and furnace was allowed to cool. The entire furnace was then disassembled and the substrate was separated from the combustion tube.

The extent of the interaction between aluminum and chlorine was examined first. The study was carried out by passing a chlorine-argon mixture over aluminum at temperatures up to 1400°C. Mass spectra were recorded continuously with rising temperatures. The gas-solid reaction begins somewhere around 300°C, and the products from the reaction depend on the surface area of aluminum and the partial pressure of the reactant. Ion species of Cl^+, unreacted Cl_2^+, $AlCl^+$, $AlCl_2^+$, $AlCl_3^+$, $Al_2Cl_5^+$, and a trace of $Al_2Cl_6^+$ were observed at low temperatures. The ions resulting from the dimer, Al_2Cl_6 diminish in abundance as the temperature rises to 900°C. At this temperature all ions containing two Al atoms disappear and no chlorine ions are detected. As the temperature is increased further, $AlCl^+$ becomes more abundant. Finally at temperatures above 1000°C, the monochloride ion becomes the predominant species and in most cases is the only major reaction product observed. The substitution of hydrogen for argon in the gas mixture did not change the reaction products except to produce HCl. Typical abundances of ions observed in the mass spectra are listed in the first half of Table I. The variation of the ion intensities of observed species with the partial pressure of chlorine-argon at 1365°C is illustrated in Fig. 3. At the high end of the chlorine pressure, the chlorine-rich ions are abundant, and at the low end $AlCl^+$ is a dominant ion species.

Prior to the deposition experiments, vapor species existing in argon carrier gas over $AlCl_3$ powders were

Table I. Relative abundances of ion species present in aluminum-chlorine reaction and chemical vapor deposition process of alumina. The magnitudes of signals are obtained directly from strip charts and computer printouts without corrections for the sensitivity and efficiency of the detector. Due to variations in the experimental conditions, the data represent only relative ion intensities in a run

Reaction	Run No.	Gas mixture	Temperature / Pressure	Relative ion intensity											
				H^+ H_2^+	OH^+ H_2O^+	Al^+	N_2^+ (a)	O_2^+	Cl^+	HCl^+	$AlCl^+$	Cl_2^+	$AlCl_2^+$	$AlCl_3^+$	$Al_2Cl_5^+$
Al + Cl_2	111772	Ar/Cl_2 =16/10	475°C 155 mm Hg	—	—	20	—	—	15	—	14	1.2	60	25	16
Al + Cl_2	020773	Ar/Cl_2 =15/15	600°C 175 mm Hg	—	—	18	—	—	11	15	21	1	58	29	1.5
Al + Cl_2	020873	Ar/Cl_2 =20/10	870°C 200 mm Hg	—	—	10	—	—	10	—	9	0.3	30	15	2.5
Al + Cl_2	112873	Ar/Cl_2 =20/10	1300°C 200 mm Hg	—	—	43	—	—	14	—	69	—	23	7	—
CVD of alumina	030774	(d)	1200°C	(b)	153	—	79	870	642 (c)						
CVD of alumina	030574	(d)	1000°C	(b)	116	—	147	1230	92 (c)						
CVD of alumina	041974	(d)	1200°C	47	135	—	75	995	867 (c)						

(a) N_2 is present due to leaks in the H_2O/O_2 inlet line.
(b) Ion intensities of H^+ and H_2^+ are not recorded.
(c) Sum of HCl^+ and Cl^+ ion intensities.
(d) Ratios of gas mixtures; H_2O/O_2 = 1/4 and Cl_2/H_2 = 1/3, see text for details.

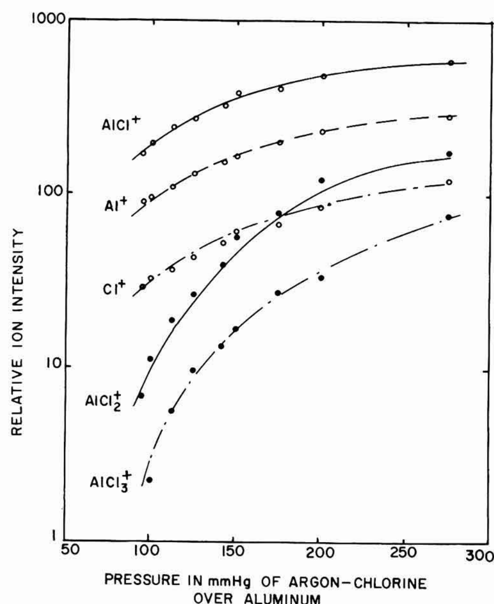

Fig. 3. Relative abundances of vapor ion species in aluminum-chlorine reaction at 1365°C. The data are taken from run 112872, Ar/Cl_2 ratio = 2/1, electron ionization energy = 40 eV, no correction is made for the detection efficiency. The fragmented ions are Al^+ and Cl^+ from AlCl, and $AlCl_2^+$ from $AlCl_3$.

also examined. At low temperatures up to 400°C, $Al_2Cl_5^+$ is the most abundant species, but at 1200°C, only $AlCl^+$ and $AlCl_2^+$ ion molecules exist and are equally abundant.

The mass spectra obtained during the deposition reaction at temperatures of 900°-1400°C reveal only the presence of H^+, H_2^+, O^+, OH^+, H_2O^+, O_2^+, Cl^+, and HCl^+ ions. The typical distribution of ion species is tabulated in the second half of Table II. The relative abundances may vary from run to run due to variation and fluctuation in the experimental conditions. In general there were no ions containing aluminum present, which indicated that the deposition reaction was nearly complete. During the experiments, the mass spectrometer was used repeatedly to scan up to mass 1000 amu to acertain that no large mass ion or cluster ion was present in the deposition system. If there was a high mass ion present, the abundance must be less than 10^{-5} of the most abundant species in the spectra.

Under the condition of the present experiments, the chemical vapor deposition of alumina from aluminum-chloride/hydrogen and water/oxygen is predominantly a heterogeneous process in contrast to the earlier report (3) that vapor phase homogeneous nucleation might take place. If vapor phase homogeneous nucleation had occurred, it would proceed via the random growth of small condensed aggregates and clusters of vapor molecules. The present result reveals the absence of aluminum-oxygen molecular species which are presumably the precursors of the aggregates and clusters, and Al_2O_3 nuclei in vapor phase. One might question the ability of the spectrometer to detect large microparticles from electron impact ionization processes. Since the existence of AlO^+ and Al_2O^+ ion species detected by the spectrometer has been reported (7, 8), there is no reason to suspect that the clusters of Al-O species would not have been detected if they had been present in the system in excess of 10^{-5} of the most abundant species. Perhaps large microcrystals dissociate into Al^+ and large neutral fragments upon electron impact ionization, but this is highly improbable.

Table II. Free energy changes of reactions between aluminum chlorides and water/oxygen in deposition of Al_2O_3 at various temperatures

	Reaction	Free energy change in kcal-mole⁻¹ 1300°K	1500°K	1700°K
[1]	$2AlCl(g) + H_2O(g) + O_2(g) = Al_2O_3(s) + 2HCl(g)$	−235.4	−217.3	−199.5
[2]	$2AlCl(g) + 3H_2O(g) = Al_2O_3(s) + 2HCl(g) + 2H_2(g)$	−151.4	−138.7	−126.4
[3]	$2AlCl(g) + 3/2\ O_2(g) = Al_2O_3(s) + Cl_2(g)$	−228.4	−206.9	−185.9
[4]	$2AlCl_3(g) + 3H_2O(g) = Al_2O_3(s) + 6HCl(g)$	−77.1	−77.8	−78.6

Examples of polycrystalline alumina deposits obtained from this study are shown in Fig. 4. These deposits were obtained from the CVD process under similar experimental conditions except for temperature, which was found to have a dominant influence over the textures of the deposits. The presence of whiskers grown on surfaces of the deposit at T = 1100°C (Fig. 4c) suggests that the surface nucleation is an important reaction mechanism.

The major vapor molecule from the aluminum-chlorine reaction at the present deposition temperature and pressure is AlCl. The exhaust gases from the CVD process of Al_2O_3 are HCl, Cl,[1] O_2, H_2O, and H_2. The over-all deposition reaction should be written according to existing vapors as

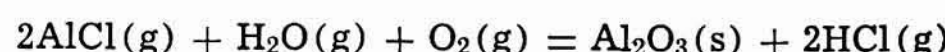

$$2AlCl(g) + H_2O(g) + O_2(g) = Al_2O_3(s) + 2HCl(g) \quad [1]$$

and

$$2AlCl(g) + 3H_2O(g) = Al_2O_3(s) + 2HCl(g) + 2H_2(g) \quad [2]$$

[1] The Cl^+ ion intensity was greater than could be accounted for by HCl fragmentation; the monatomic chlorine probably resulted from dissociation of unreacted Cl_2.

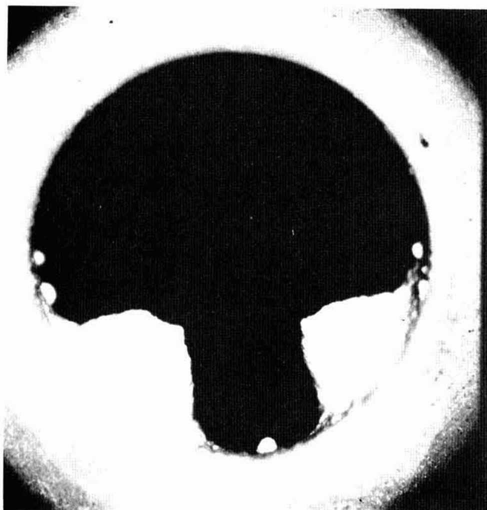

Fig. 4. Microphotographs (×7) of Al_2O_3 polycrystalline deposits obtained from chemical vapor deposition process. The deposits are grown on the cylindrical inner surface of the substates cut from a ⅜ in. OD alumina tube under same gaseous reactants.
a. White polycrystalline deposits obtained at 900°C. The similar white deposits were also obtained at temperatures above 1300°C and below 900°C.

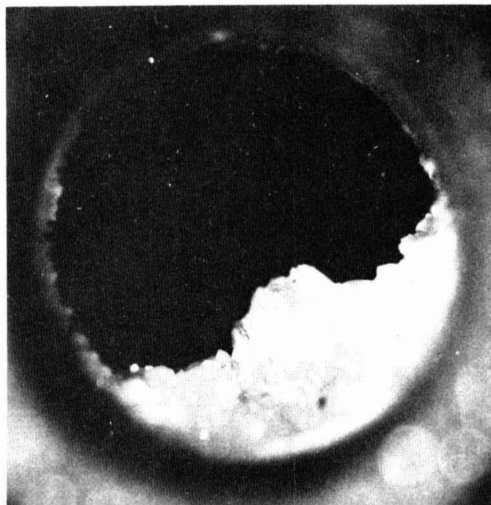

b. Opaque to transparent alumina obtained at 1000°C.

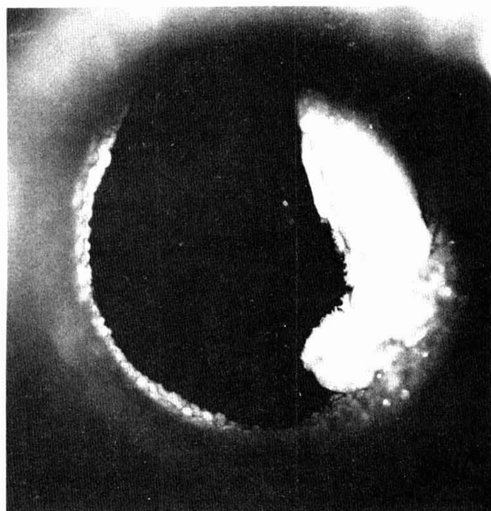

c. Whiskers on surfaces of opaque deposits obtained at 1200°C.

These reactions occur at the surfaces of substrates and/or Al_2O_3 crystals. The reaction

$$2AlCl(g) + 3/2\,O_2(g) = Al_2O_3(s) + Cl_2(g) \quad [3]$$

is thermodynamically feasible, but the formation of Al_2O_3 from this reaction is neither observed by the previous work (3) nor in this investigation. Table II tabulates the free energy changes of reactions leading to the formation of alumina. For the CVD of Al_2O_3 the first two reactions are both possible. The free energy change of reaction [1] is more negative than that of reaction [2], and reaction [1] seems to be kinetically more favorable because it requires fewer molecules to yield Al_2O_3 on the substrate surfaces. In reaction [1], oxygen is essential in the formation of Al_2O_3. The earlier report (3) proposed the over-all reaction in which $AlCl_3$ is the only major Al-containing reactant

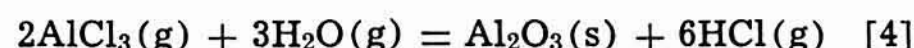

$$2AlCl_3(g) + 3H_2O(g) = Al_2O_3(s) + 6HCl(g) \quad [4]$$

It would have been of interest to duplicate the conditions of the earlier work at higher pressures (3) to confirm the importance of $AlCl_3$ in the reaction; however the very small orifice [*e.g.*, 0.01 cm (5)] necessary to isolate the high pressure region would have plugged with Al_2O_3 almost immediately, making measurements impossible.

At least, judging from analyses of vapor species in the present deposition data and associated experiments, the existence of AlCl molecule at the high temperature of the CVD process is highly probable. Furthermore, nonequilibrium kinetics in the chlorine-aluminum reactions could lead to AlCl vapor formation.

Competitive heterogeneous and gas-phase nucleation reactions leading to the formation of Al_2O_3 are believed to take place in the CVD process. The surface reaction is more favorable in the present experiments. Vapor phase nucleation is almost impossible because of fairly low pressures used in the present investigation. Perhaps vapor phase nucleation would have prevailed in the CVD system at much higher pressures.

Manuscript submitted Aug. 23, 1974; revised manuscript received June 2, 1975.

Any discussion of this paper will appear in a Discussion Section to be published in the June 1976 JOURNAL. All discussions for the June 1976 Discussion Section should be submitted by Feb. 1, 1976.

Publication costs of this article were partially assisted by The Department of the Army.

REFERENCES

1. P. S. Schaffer, *J. Am. Ceram. Soc.*, **4B**, 508 (1965).
2. R. Ellis, Raytheon Research Division, Contract DA-19-066-AMC-318(X), Final Report, AMMRC CR67-08(F), September 1968.
3. P. Wong and McD. Robinson, *J. Am. Ceram. Soc.*, **53**, 617 (1970).
4. T. A. Milne and F. T. Greene, in "Advances in High Temperature Chemistry," LeRoy Eyring, Editor, Vol. 2, p. 107, Academic Press, New York, London (1969).
5. S.-S. Lin, *Rev. Sci. Instr.*, **44**, 516 (1973).
6. S.-S. Lin, Army Material & Mechanics Research Center, AMMRC TR 73-9, March 1973.
7. K. J. D. MacKenzie, *J. Brit. Ceram. Soc.*, **58**, 83 (1968).
8. K. R. Thompson, *High Temp. Sci.*, **5**, 62 (1973).

Brief Communications

Low Temperature Thermal Oxidation of Silicon by Dry Oxygen Pressure above 1 Atm

R. J. Zeto,* C. G. Thornton,* E. Hryckowian, and C. D. Bosco

U.S. Army Electronics Technology and Devices Laboratory (ECOM), Fort Monmouth, New Jersey 07703

It is widely recognized that the cost, reliability, and performance of integrated circuit devices are adversely affected by the large number of process-induced chemical and physical defects that result from high processing temperatures in the range 950°-1250°C. High thermal oxidation temperatures may also destroy specific desired impurity distributions achieved in previous processing steps. Consequently, there is strong motivation for developing an oxidation process that can produce gate, field, and other masking and passivating oxides at lower processing temperatures for silicon integrated circuit devices. It is also desirable that reduced oxidation temperatures be achieved by a dry oxidation method since problems due to oxide defects and contamination may be more serious for oxides prepared by wet oxidation. Although the use of high pressure steam (1) has long been known as a method for achieving low temperature thermal oxidation, attractive electrical characteristics have not been reported and the method is not generally used. On the other hand, it is known (2) that the oxidation of silicon is accelerated by dry oxygen partial pressures to 1 atm, but to our knowledge there are no oxidation data reported for dry oxygen pressures above 1 atm. On the basis of these considerations, dry pressure-oxidation of silicon is a logial possibility for achieving improved electrical properties *via* accelerated oxide growth and reduced oxidation temperatures.

The purpose of this communication is to report the initial results of experiments which demonstrate that dry pressure-oxidation, P-OX, significantly reduces the required oxidation temperatures of semiconductor silicon used for integrated circuit devices. The rate of oxidation of arsenic-doped (111) silicon at 800°C, 140 atm dry oxygen pressure was measured and compared with conventional (2, 3) thermal oxidation methods. The results are shown in Fig. 1. It is evident that oxide growth by 140 atm dry P-OX at 800°C is faster than either 1 atm dry or wet oxidation at 800°C, and is comparable to 1200°C dry oxidation at 1 atm. The 400°C reduction in dry oxidation temperature by the application of only 140 atm oxygen pressure is remarkable. Since 140 atm pressure (2060 psi) is less than the pressure supplied in conventional pressurized gas cylinders that are widely used and ordinarily handled, the technique is expected to be amenable to practical utilization.

The experimental oxidation system is readily assembled from commercially available components. It consists of a pressurized cylinder of oxygen gas, an oxygen gas pump, a vacuum pump, a cold-seal pressure vessel of the type used for hydrothermal crystal growth, an external resistance furnace, and stainless steel pressure lines. Rectangular samples, 8 × 10 mm, were cut from a 1 in. silicon wafer and positioned in a quartz sample holder at the bottom of a 9 in. quartz tube (Amersil T08) that lined the inside of a 0.5 in. ID pressure vessel (Rene 41 alloy). The pressure-oxidations were conducted in a closed system with separate substrates for each experiment. Temperature and pressure were maintained within ±2°C and ±10 atm, respectively, during the course of the oxidations. Oxide thickness was measured with a Rudolph RR100 ellipsometer. The over-all uncertainty in thickness ranged from ±20Å for thin oxides to a maximum of ±200Å for some of the thicker oxides.

Special attention was given to the potential role of water vapor in the P-OX kinetics shown in Fig. 1. Scientific Gas Company electronic grade oxygen gas, 99.998% minimum purity, less than 3 ppm water vapor, and less than 1 ppm hydrocarbons as methane, was used. The stated moisture level was verified by measurements with a Panametrics Model 2000 hygrometer with a cell probe rated for operation to 5000 psi. Less than 14 ppm H_2O was measured in the exit gas from several overnight experiments. Using an identical hygrometer sensor element, Irene (4) recently compared the thermal oxidation kinetics of silicon at 1 atm oxygen pressure for conditions of less than 1 ppm water vapor *vs.* 20-30 ppm water vapor. This data for (111) silicon at 800°C is shown in Fig. 2 for comparison with the 800°C/140 atm P-OX data. With the ordinate scale used, both of Irene's cases are encompassed by the indicated points in Fig. 2. It was, therefore, concluded that the accelerated oxidation observed in the P-OX experiments was due to the effect

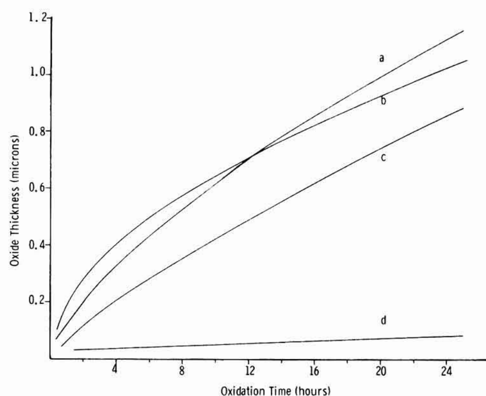

Fig. 1. Comparison of thermal oxidation conditions for (111) silicon: (a) 140 atm dry pressure-oxidation at 800°C, (b) 1 atm dry oxidation at 1200°C, (c) 1 atm steam oxidation at 800°C, (d) 1 atm dry oxidation at 800°C.

* Electrochemical Society Active Member.

Key words: silicon oxidation, dry oxygen pressure, oxide growth, MOS properties, passivation.

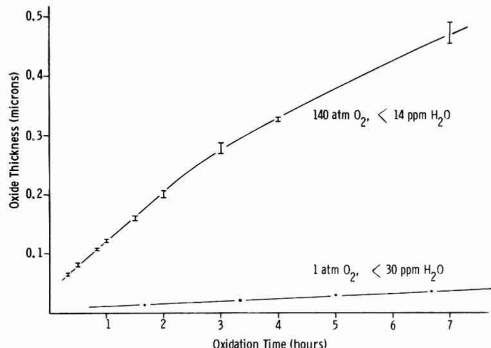

Fig. 2. Comparison of oxidation rate and moisture conditions for 800°C/140 atm P-OX and 800°C/1 atm (4) thermal oxidation of (111) silicon.

of dry oxygen pressure rather than moisture. For the P-OX conditions stated in Fig. 2, the oxide growth rate was linear between 650-2500Å with a value of about 14 Å/min.

Oxides for a wide range of applications in integrated circuit devices can be obtained at reduced temperatures by dry pressure-oxidation. A 1200Å gate oxide can be grown in 1 hr at 800°C/140 atm. Exploratory 3 hr oxidations at other temperature/pressure conditions yielded 4700Å at 800°C/500 atm and 16,000Å at 900°C/500 atm. Additional data on dry pressure-oxidation kinetics and detailed information on the P-OX experimental system will be reported.

According to the model of Deal and Grove (2), the thermal oxidation of silicon is initially reaction-rate limited at the oxide-silicon interface followed by diffusion control of the oxidant through the oxide. The corresponding coefficients in the oxidation equation $x_o^2 + Ax_o = B(t + \tau)$ are given in Table I for oxidation by 1 atm and 140 atm oxygen pressure at 800°C. Both the parabolic, B, and linear, B/A, rate constants are one to two orders of magnitude larger for 140 atm dry oxidation, indicating that both of these stages of the oxidation process are accelerated by pressures above 1 atm. The pressure variation of the coefficients, however, indicates that the pressure-oxidation mechanism is not completely described by

Table I. Coefficients for the dry thermal oxidation of (111) silicon according to $x_o^2 + Ax_o = B(t + \tau)$ for 1 atm (2) and 140 atm oxygen pressure at 800°C.

Oxidation pressure (atm)	A (μ)	B (μ^2/hr)	B/A (μ/hr)	τ (hr)
1	0.37	0.0011	0.0030	9.0
140	1.03	0.100	0.097	0.45

the model. The coefficient A is not independent of pressure, and neither the parabolic nor the linear rate constants are proportional to pressure. The pressure-oxidation mechanism will be examined as additional P-OX data are determined.

A pressure vessel was recently put into operation to evaluate the MOS properties of samples prepared by the dry P-OX of 1 in. silicon wafers using clean-room conditions and state-of-the-art procedures. Evaporated aluminum dots were used for electrical contact, and conventional capacitance-voltage measurements were made. MOS structures from initial experiments showed negligible (<0.1V) shift in flatband voltage under bias temperature stress and Q_{ss} values in the range 3-8 $\times$ 10^{10} cm^{-2}. These samples were (111) phosphorus-doped 1-5 ohm-cm silicon with 1000Å oxides prepared by 800°C/150 atm dry P-OX. Previous program effort was directed at an assessment of the dry pressure-oxidation kinetics, and for MOS properties exploratory experiments without clean-room conditions were made at 140 atm, 700°-800°C, with 8 $\times$ 10 mm samples of arsenic-doped silicon. Q_{ss} values in the range 2-7 $\times$ 10^{11} cm^{-2} were obtained, and under bias temperature conditions gross shifts in flatband voltage typical of alkali ion contamination were not present. These results indicate that significant benefits may be transferred to electrical properties by reduced temperature dry oxidation. Experimental conditions and procedures are currently being investigated to optimize electrical properties.

The characteristics of P-OX are advantageous for the preparation of oxide-isolated silicon devices with reduced impurity redistribution during dielectric isolation. This application of P-OX for bulk silicon and silicon-on-sapphire is currently under study. Initial results are promising and are reported separately (5).

Acknowledgments

The authors are indebted to G. J. Iafrate and S. Marshall for helpful discussions and advice, and E. Kostyk and J. Harthman for sample preparation.

Manuscript received Feb. 27, 1975.

Any discussion of this paper will appear in a Discussion Section to be published in the June 1976 JOURNAL. All discussions for the June 1976 Discussion Section should be submitted by Feb. 1, 1976.

Publication costs of this article were partially assisted by the U.S. Army Electronics Technology and Devices Laboratory.

REFERENCES

1. M. M. Atalla, in "Proceedings of the Conference on Elemental and Compound Semiconductors," H. Gatos, Editor, Interscience Publishers, New York (1960).
2. B. E. Deal and A. S. Grove, *J. Appl. Phys.*, **36**, 3770 (1965).
3. "Integrated Silicon Device Technology, Volume VII: Oxidation," p. 49, Research Triangle Institute, Durham, North Carolina (1965).
4. E. A. Irene, *This Journal*, **121**, 1613 (1974).
5. S. Marshall, R. J. Zeto, and C. G. Thornton, *This Journal*, **122**, 1411 (1975).

Dry Pressure Local Oxidation of Silicon for IC Isolation

S. Marshall, R. J. Zeto,* and C. G. Thornton*

U.S. Army Electronics Technology and Devices Laboratory (ECOM), Fort Monmouth, New Jersey 07703

This communication reports the use of dry pressure-oxidation (P-OX) for obtaining oxide-isolated device structures in both bulk silicon and epitaxial silicon on sapphire (SOS). Dry P-OX is a new low temperature oxidation technique which, compared with conventional dry thermal oxidation, reduces required oxidation temperatures as much as 400°C for equivalent oxide film growth. It has been shown, for example, that oxidation of silicon by 140 atm dry oxygen at 800°C is comparable to 1 atm dry oxidation at 1200°C (1).

Localized oxide isolation of silicon devices in integrated circuits utilizes silicon nitride as an oxidation mask (2). In the present work two structures were examined, one in which the Si_3N_4 was deposited directly on the silicon surface and one in which a 500-1000Å conventional thermal oxide was grown prior to the nitride deposition. The nitride was grown by the SiH_4-NH_3 process and was defined by supplemental CVD masking and etching in phosphoric acid. When the intermediate oxide layer was used, silicon areas were exposed by HF etching. The local oxidation process with dry P-OX was explored under a variety of experimental conditions, *i.e.*, 700°-880°C, 140-500 atm oxygen pressure, and oxidation times of 3-24 hr. Optimum pressure-temperature-time conditions have not yet been determined, but at 850°C and 250 atm, the average oxidation rate was about 17 Å/min for <100> silicon. For <111> silicon the rate was 47 Å/min at 850°C and 500 atm. Scanning electron microscopy (SEM) was utilized to reveal the morphology of the P-OX structures.

The application of P-OX to dielectric isolation in bulk silicon and SOS devices is illustrated in Fig. 1, where the nitride mask has been applied directly to the surface of the silicon. Figure 1(a) shows the required oxidized structure as achieved in bulk material by the dry P-OX process at oxidation temperatures where undesired impurity redistribution effects are very small. The oxide thickness is 1μ and was grown in 3½ hr at 850°C and 500 atm. In Fig. 1(b) the oxide extends completely through the 1 μm epitaxial silicon layer of an SOS structure, thus effecting dielectric isolation of adjacent silicon elements. In this case, the oxide happened to be grown in 23 hr at 850°C, 250 atm. A more optimum set of conditions can obviously be chosen from available data (1).

Following the P-OX treatment the structures were well defined, lateral oxidation under the nitride mask was negligible, and cracks in the nitride film were absent. The use of a chromate dislocation etch (3) failed to reveal significant nitride induced defects in the cleaved low temperature pressure oxidized structures examined. This observation is contrasted with results reported in Ref. (2) where application of the nitride directly to the silicon surface resulted in severe dislocation damage under higher temperature oxidation. Thus, an intermediate oxide "buffer" layer may not be needed to avoid undesirable defects at the silicon-nitride interface.

Local pressure oxidation of silicon using a more conventional nitride/oxide/silicon structure is illustrated in Fig. 2(a) and 2(b) for bulk silicon and SOS, respectively. It is evident from a comparison of Fig. 1 and 2 that lateral oxidation underneath the nitride mask is much more pronounced in the presence of an intermediate oxide layer, an observation originally reported by Appels and Paffen (4) for silicon oxidized at 1 atm. The shape of the oxide edge is similar to that reported by Powell *et al.* (5) for silicon oxidized in steam. The experimental conditions for bulk silicon and SOS are the same as reported above for Fig. 1.

The degree of lateral oxidation has an important bearing on device design since lateral oxidation establishes a minimum size for adjacent isolated structures. This point is illustrated in Fig. 3 in which the lateral oxide growth undermines the original 8.5μ width of the nitride mask. The ratio of lateral oxidation L to isolation oxide thickness t for the specific P-OX sample shown in Fig. 2(a) (<111> Si, 500 atm,

* Electrochemical Society Active Member.

Key words: pressure oxidation, selective oxidation, dielectric isolation, SOS.

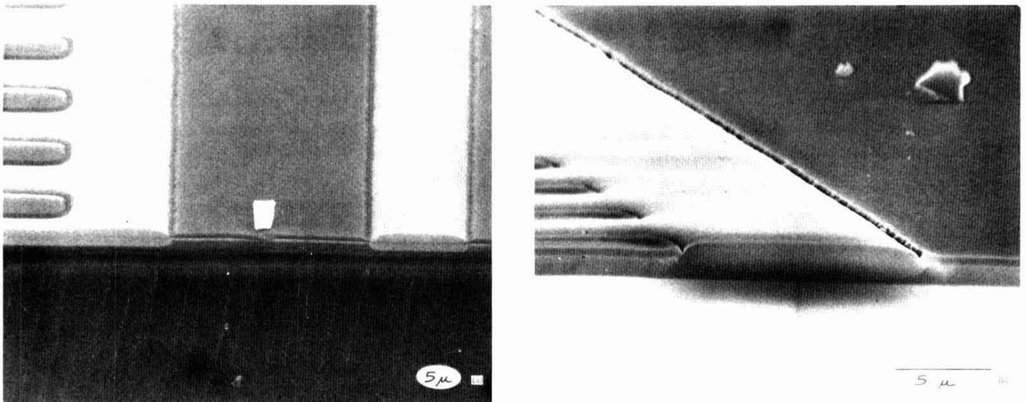

Fig. 1. Dry pressure-oxidation of nitride on silicon structures: (a) Bulk <111> silicon showing 1 μm oxide (light) and masking nitride (dark); (b) 1 μm <100> SOS showing complete dielectric isolation.

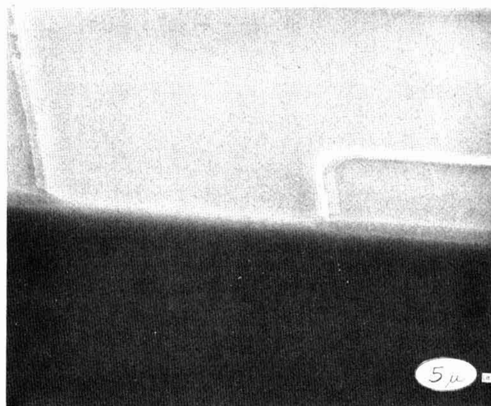

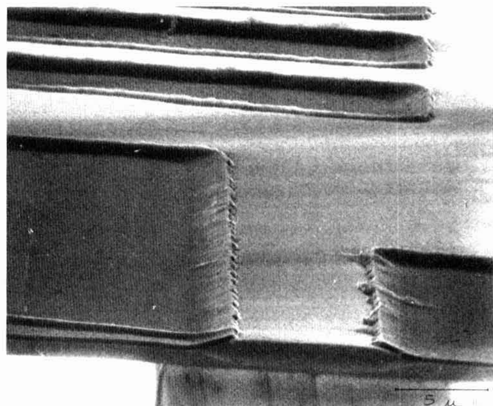

Fig. 2. Dry pressure-oxidation of nitride on thermal oxide on silicon structures: (a) bulk <111> silicon showing 1 μm pressure oxide; (b) 1 μm <100> SOS with 2700Å of silicon remaining. The extent of lateral oxidation is much greater than for the nitride-oxide structures of Fig. 1.

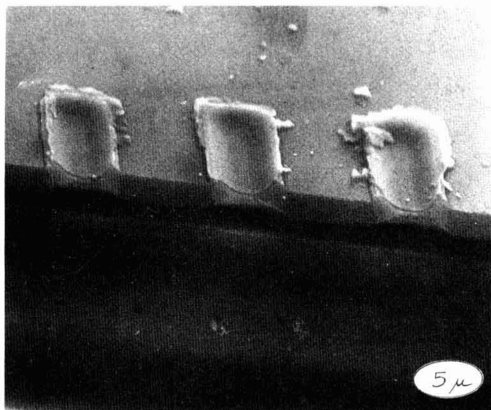

Fig. 3. LOCOS structure showing the limit imposed on device geometry by lateral oxidation beneath the nitride mask. Center to center pad spacing is 12 μm. The initial mask consisted of 8.5 μm wide nitride bars separated by 3.5 μm spaces. The nitride was deposited on 1000Å thermal oxide on bulk (111) silicon.

850°C) is 2.8. For comparison, a ratio of 3.3 is calculated from the data of Powell *et al.* (5) (steam oxidation at 60 atm, 675°C). The P-OX L/t ratio is 2.2 for the <100> SOS sample of Fig. 2(b) (250 atm, 850°C). For equivalent conditions with nitride/oxide/silicon structures it would be expected that the L/t ratio would be higher for high pressure steam due to the high solubility and diffusivity of water in the initially present oxide layer. For either process, selective etching of the silicon prior to the pressure oxidation, as described in Ref. (4) will decrease the oxidation time needed to achieve oxide isolation, reduce the lateral oxidation, and result in a desirable planar surface topography.

Subsequent work in this area will investigate in greater detail the effect of P-OX conditions on the generation of surface defects in nitride masked structures. Consideration will also be given to the oxidation kinetics of the nitride masking film and to the evaluation of "P-OX device" characteristics.

Acknowledgments

The authors are indebted to Mr. C. Cook for the SEM analysis and for many helpful discussions. They also wish to thank Ms. J. Harthman, Mr. A. Rogel, and Mr. E. Hryckowian for the preparation of the experimental samples.

Manuscript received Feb. 24, 1975.

Any discussion of this paper will appear in a Discussion Section to be published in the June 1976 JOURNAL. All discussions for the June 1976 Discussion Section should be submitted by Feb. 1, 1976.

Publication costs of this article were partially assisted by the U.S. Army Electronics Technology and Devices Laboratory.

REFERENCES

1. R. J. Zeto, E. Hryckowian, C. D. Bosco, G. J. Iafrate, R. W. Brower, and C. G. Thornton, Paper 206 presented at Electrochemical Society Meeting, New York, New York, Oct. 13-17, 1974.
2. J. A. Appels *et al.*, *Philips Res. Rep.*, **25**, 118 (1970).
3. B. M. Berry, "Integrated Silicon Device Technology," Vol. XII, p. 52, Air Force Avionics Laboratory (1966).
4. J. A. Appels and M. M. Paffen, *Philips Res. Rep.*, **26**, 157 (1971).
5. R. J. Powell, J. R. Ligenza, and M. S. Schneider, *IEEE Trans. on Electron Devices*, **ED-21**, 636 (1974).

New Method of Manufacturing Sintered-Type Aluminum Solid Electrolytic Capacitor

Sadao Okuma

Department of Applied Science, Tokyo Electrical Engineering College, Tokyo, Japan

The sintered-type aluminum solid electrolytic capacitor has been prepared by a new method, where first either nitrogen or hydrogen gas at 1 atm is used during the sintering of the aluminum powder to form the porous anode, and second either ammonium dihydrogen phosphate or ammonium borate solution is used during the anodization to form the dielectric.

The capacitors prepared by this method gave better characteristic properties than other electrolytic capacitors.

The preparation of the aluminum-sintered anode has been said to be difficult, because aluminum unlike tantalum easily forms a hard oxide at sintering temperature.

The author could prepare the aluminum-sintered anode in this experiment based upon the assumption that adequate sintering would take place in the gaseous atmosphere mentioned above.

This makes us suppose that the aluminum-sintered body has a large surface area with a suitable porous property and the interior surface can be converted to a good dielectric film by the usual anodization techniques.

Consequently, for the manufacture of the sintered-type aluminum solid electrolytic capacitor on this study, it has been understood that both ammonium dihydrogen phosphate as the forming solution and hydrogen gas as the sintering atmosphere gave better dielectric properties, respectively.

If the manufacturing steps are considered, the new method used in this study would be much simpler than the normal vacuum sintering method.

This communication reports a comparison of the characteristic properties with the ones obtained in this study.

Experimental

Materials.—99.98-99.99% pure aluminum powder was obtained from commercial sources. Particle sizes of the aluminum powder were 20, 35-150, 150-200, and 200 mesh, respectively. The binder used for sintering was less than 1 weight per cent (w/o). Gaseous atmosphere during sintering was at about 1 atm pressure. The forming solution was either 3% ammonium borate solution or 0.3% ammonium dihydrogen solution.

Apparatus.—The characteristic properties of the dielectric substance were measured by a Universal Bridge which was manufactured by Yokogawa Electrical Manufacturing Company.

Procedure.—The compacting pressure was either 0.1 ton/5 mm diameter or 0.2 ton/5 mm diameter. The size of the compact was 5 mm diameter by about 5 mm high. The sintering was at 600°C for about 120-180 min in each gas as mentioned above.

The anodization was performed at a constant current of 50 mA until 150V was reached, and the voltage was maintained at 150V until the current dropped to 2 mA.

The total formation time was 120 min. After formation the anodized pellet was washed for 60 min with water, and then dried at 500°C for 60 min.

Manganese dioxide, produced from thermal decomposition of a highly concentrated manganous nitrate solution at 300°C for 60 min, was used to form the interior semiconductor contact.

Finally, colloidal carbon was spread on the coated anode, dried, coated with silver paint, and dried at 500°C for 60 min.

Results and Discussion

Table I shows the characteristic properties for the sintered-type aluminum solid electrolytic capacitor manufactured in this study.

In spite of fact that the dielectric constant of aluminum oxide is lower than other dielectric of metal oxide, the sintered-type aluminum solid electrolytic capacitor obtained in this study gave a capacitance of 0.5-7.4 μ**F**.

The capacitance per unit weight of the aluminum solid electrolytic capacitor is 2-40 μ**F**/g. Then anodization voltage to form the aluminum capacitors is much higher than the tantalum, niobium, or zirconium capacitors, and consequently the anodic oxide film is much thicker. Consequently, it can be said that this method was effective enough for the preparation of the dielectric substance.

The dissipation factor of the aluminum capacitor was somewhat inferior to other capacitors; however, it was considered that it might be lowered to some extent by eliminating the naturally formed aluminum oxide. This proposal has not yet been tried. Instead further comparisons were made using either hydrogen or nitrogen gas as the sintering atmosphere and either ammonium dihydrogen phosphate or ammonium borate solution as the forming solution.

First, the dielectric film was formed using each forming solution and then transformed into the sintered-type aluminum solid electrolytic capacitor ac-

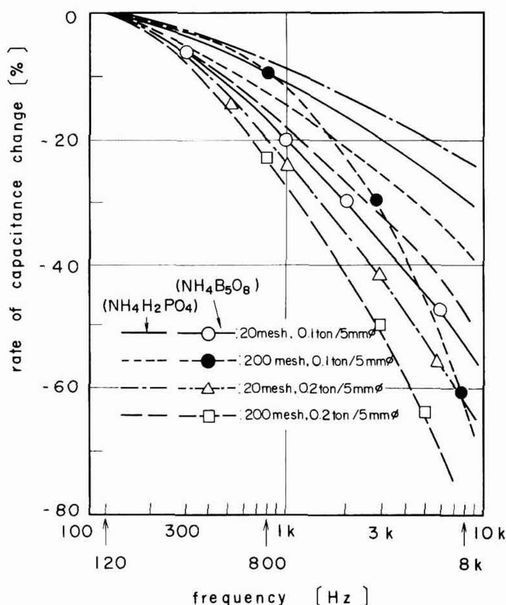

Fig. 1. *Rate of capacitance change vs. frequency at 20°C (N_2 atmosphere).*

Key words: aluminum, capacitor, sintered-type, solid, dielectric.

Table I. Comparison of various solid electrolytic capacitors at 20°C

Anode	Form	Etching done·none	Gaseous atmosphere to sintering	Forming solution	Density (g/cm³)	Forming voltage (V)	Capacitance (μF)	Capacitance Area (μF/cm²)	Capacitance Volume (μF/cm³)	Capacitance Weight (μF/g)	Dissipation factor (%)	Leakage* current $\left(\frac{\mu A}{\mu F - V}\right)$
Al	Foil	Done	—	Ammonium borate $NH_4B_5O_8$	2.7			5.0 2.7 0.6			10 8 6	0.07 0.05 0.03
Al in this study	Sintered	None	Nitrogen	Ammonium borate $NH_4B_5O_8$	1.4 ~ 1.8	150	1.6 ~ 7.4	1.6 ~ 7.4	16 ~ 75	11 ~ 40	13 ~ 40	0.16 ~ 0.21
			Nitrogen	Ammonium dihydrogen phosphate $NH_4H_2PO_4$	1.4 ~ 1.8	150	0.5 ~ 2.5	0.5 ~ 2.5	4.6 ~ 25	2 ~ 20	11 ~ 25	0.16 ~ 0.21
			Hydrogen	Ammonium dihydrogen phosphate $NH_4H_2PO_4$	1.5 ~ 1.8	150	0.5 ~ 1.6	0.5 ~ 1.6	5.6 ~ 1.7	4 ~ 11	7.5 ~ 13	0.16 ~ 0.21

* Measured at 4-6V.

cording to above procedure. The characteristic properties of these capacitors were measured.

Figure 1 gives the rate of capacitance change *vs.* frequency (at 20°C) of capacitors prepared in the sintering atmosphere of nitrogen gas as a function of the compacting pressure. Consequently, the element formed from ammonium dihydrogen phosphate solution is better than the one produced from ammonium borate solution.

Figure 2 shows the rate of capacitance and the dissipation factor of the capacitors made in a sintering atmosphere of hydrogen gas.

From these results, hydrogen gas was considered a better sintering atmosphere for it gave more stable dielectric characteristic properties than those prepared in nitrogen (1-3).

Conclusion

This study was carried out with the purpose of increasing the capacitance and the improvement of other characteristic properties of the dielectric substance.

The sintered-type aluminum solid electrolytic capacitors were prepared using either nitrogen or hydrogen gas as the sintering atmosphere and either ammonium borate or ammonium dihydrogen phosphate solution of the forming solution. Measurements were made of the characteristic properties of these capacitors.

The following conclusions can be made:

1. The anode in the capacitor has a large surface area with sufficient porosity to impregnate with manganous nitrate solution.
2. The dissipation factor is somewhat less satisfactory. However, it may be possible to improve it by a surface pretreatment before anodization.
3. Hydrogen gas as the sintering atmosphere and ammonium dihydrogen phosphate solution as the forming solution, each gave better dielectric properties than nitrogen gas and ammonium borate solution.
4. The new method used in this study would be more useful in the industrialization of the sintered-type aluminum solid capacitor than the vacuum mechanism method used hitherto.

Acknowledgment

The author wishes to thank Dr. Gisaku Ohara of Tokyo Electrical Engineering College for his actual

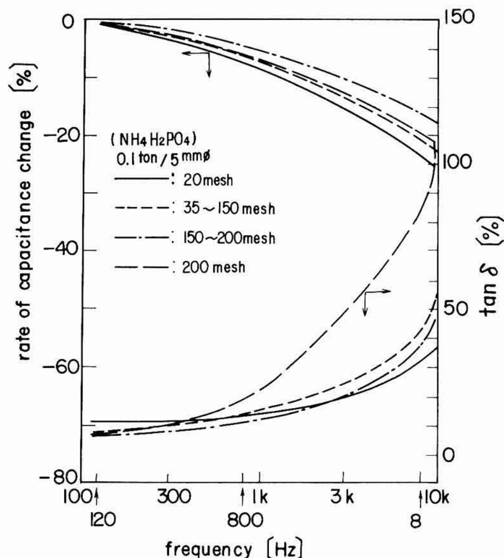

Fig. 2. Rate of capacitance change and dissipation factor vs. frequency at 20°C (H_2 atmosphere).

instruction in this study, and Mr. Hozui Okubo and Mr. Tomihiro Nemoto of the same college for their cooperation in submission of this paper.

Manuscript submitted Oct. 31, 1974; revised manuscript received June 13, 1975.

Any discussion of this paper will appear in a Discussion Section to be published in the June 1976 JOURNAL. All discussions for the June 1976 Discussion Section should be submitted by Feb. 1, 1976.

Publication costs of this article were partially assisted by Tokyo Electrical Engineering College.

REFERENCES

1. S. Okuma and T. Nemoto, *J. Metal Finishing Soc. Japan*, **23**, 204 (1972).
2. S. Okuma and T. Nemoto, *ibid.*, **24**, 376 (1973).
3. S. Okuma, *ibid..* **24**, 626 (1973).

THE ELECTROCHEMICAL SOCIETY, INC.

The Electrochemical Society is an international organization of individuals and companies concerned with or interested in materials sciences.

OBJECTIVES

1. The advancement of the theory and practice of electrochemistry, electrometallurgy, electrothermics, electronics, solid state, and allied subjects.
2. To encourage research and the reporting of such research for the dissemination of knowledge in the field of electrochemistry and solid state.
3. To insure the availability of adequate training in the field of electrochemistry for chemists, engineers, metallurgists, physicists, and solid-state investigators.

BENEFITS OF MEMBERSHIP

1. Assurance of keeping abreast of the latest scientific developments in your particular fields of interest.
2. Enjoyment of personal association with fellow scientists and engineers in the professions.
3. Opportunity to contribute to the advancement of the science and application of electrochemistry and solid state in your areas of interest.
4. Stimulation of interdisciplinary exchanges.

DIVISIONS

The activities of the Society are carried on by its nine Divisions as follows:

Battery
Corrosion
Dielectrics and Insulation
Electrodeposition
Electronics (Including Semiconductors and Luminescence)
Electrothermics and Metallurgy
Industrial Electrolytic
Organic and Biological Electrochemistry
Physical Electrochemistry

SECTIONS

Local Sections of the Society have been organized in the following cities and regions:

Boston
Chicago
Cleveland
Columbus
Detroit
Indianapolis
Midland (Michigan)
Metropolitan New York
National Capital Area
Niagara Falls
North Texas
Ontario-Quebec
Pacific Northwest
Philadelphia
Pittsburgh
Rocky Mountain
San Francisco
Southern California-Nevada
South Texas

JOURNAL OF THE ELECTROCHEMICAL SOCIETY

REVIEWS AND NEWS

OCTOBER 1975

Science and Technology—The New Challenges[1]

W. G. Schneider

National Research Council Canada, Ottawa, Ontario, Canada

RN

Science and technology today have attained a fairly high degree of maturity and scientific research has become highly institutionalized. These developments have evolved largely during the decades following World War II. During this period we have seen unprecedented advances in both science and technology. However, as we look to the future there are serious concerns whether the new challenges now facing the nations of the world can be adequately dealt with by simple linear extrapolations. Both the nature and the longer term implications of the new challenges will demand greater R&D initiatives and much greater adaptability by the scientific community than it has been accustomed to in the past.

The new realities.—As we approached the 70's a number of problem areas, which had been formerly of only minor concern, rapidly developed to a degree where they have now become of major concern both nationally and internationally. Some of these areas have reached near crisis proportions. What is equally clear is that many of these problems are closely interrelated and that they have serious long-term implications for man's well-being on this planet.

That having been said, I should make clear at the outset that I do not share most of the "doom and gloom" prophecies with respect to man's survival. Recognizing the problems and their implications, man also has the necessary intelligence, capability, and adaptability to act rationally and to manage his affairs so as to ensure his future well-being. As a result of the broad advances in science and technology over the past few decades, we are in a much stronger position to face up to these challenges, to devise new solutions, and to develop optional technologies for new strategic approaches. This is not to suggest that national and world problems will be solved by science and technology alone, but rather that science and technology will be needed as essential aids in the alleviation of and solutions to such problems.

Because the new challenges I refer to also imply possible serious consequences in the long term as well as in the short term, I prefer to call them the new realities. To be realist rather than alarmist, it is nevertheless appropriate to raise the question whether, in view of past inertia, the nations of the world, as well as the scientific community, have the conviction and the will to respond actively and comprehensively to the new realities.

To be more explicit, I would like to start with the following list of topics which have been identified as problem areas in many countries and which relate directly to our major concerns: (*i*) energy, (*ii*) food, (*iii*) housing and urban problems, (*iv*) industrial development (goods and services, employment), (*v*) environment, (*vi*) materials (resources) and materials recycling, (*vii*) transportation and communications, (*viii*) health, (*ix*) disarmament and peace, (*x*) economic, scientific, and technical aid to less developed countries, (*xi*) oceans, (*xii*) space.

This list is not intended to be in any particular order of importance or priority nor is it necessarily complete. Others might be added, such as economic stability (including trade, monetary problems, inflation, etc.), social justice, public safety and security. These are indeed explicit areas of concern. To some degree also they are implicit in the above list.[2]

In recent years much of the rhetoric on science policies has been concerned with relating scientific research to national goals. In the first instance, that is, without further elaboration, such goals are generally stated in very broad terms, as follows: food, shelter, prosperity, health, peace and security, justice and social welfare.

These could equally well be a statement of international goals. In essence, they reflect basic human needs and no country could long survive if such needs were not met to some minimum standard. When we compare these basic needs with the longer list of topics above, there is a striking overlap and resemblance.

There are several other distinguishing features of the longer list of twelve topics:

(*i*) Most of these areas have become more important or critical in recent years and are likely to be of on-

[1] This is the Electrochemical Society Lecture delivered at the Toronto, Canada, Meeting of the Society, May 12, 1975.

[2] The problem of population should properly be considered as part of the new reality. However, it would seem to belong more in the social or moral domain than in the domain of science and technology.

going concern in future. Frequently a particular topic forms the unique mission of a ministry of national governments.

(*ii*) There is a high degree of inter-connection between these problem areas.

(*iii*) Most of these problem areas are now also of international concern.

(*iv*) All depend heavily on applications of science and technology and will require considerably more R&D investment in future.

To this audience, there is no need to elaborate in detail on each of these topics but certain features are worth mentioning.

Energy.—Although the finite supply of fossil fuels had been frequently pointed out, it took the recent oil embargo to bring home to us an awareness of this fact, as well as of our excessive dependence (and therefore also vulnerability) on this form of energy. Past R&D investments in nuclear energy have provided an alternative form of energy. Other sources of energy will also have to be developed especially from renewable resources.

Food.—Ultimate shortages of food, especially cereals and protein had also been foreseen. The green revolution gave hope of buying time but made heavy demands on fertilizer supplies. Increased food demands were due in part to population increase and in part due to nutritional upgrading of substandard diets. The world now faces the double challenge of increasing food supply while conserving energy, including fertilizers.

Housing and urban problems.—The concerns relating to low-cost housing and a complex of urban problems are well known. The need for energy conservation, for environmental preservation, and for waste and materials recycling are added dimensions.

Industrial development.—In the past, economic viability of a private enterprise could be virtually assured if it had an efficient technology, good management and adequate market access. The ground rules are rapidly altering. Future enterprises will also be required to take into account and be accountable for social costs, environmental costs, energy costs, and material costs. It is doubtful whether many of today's technologies will be able to meet all criteria, and these technologies may have to be modified or alternate techologies may have to be developed. Such new technologies may not necessarily be large-scale technologies. Employment opportunity is an additional factor of growing importance.

Environment.—With today's numerous environmental concerns and risks, it is clear much more basic knowledge and understanding will be required to make environmental impact analyses with confidence. Indeed many environmental risks now of concern were detected only recently as a result of highly sensitive analytical techniques made possible by recent scientific advances.

Materials (resources) and materials recycling.—This is an area which will obviously continue to be science and technology intensive. The new parameters are likely to be energy conservation, materials conservation, substitution, and recycling.

Transportation and communications.—These are the essential service networks required by any nation (and among nations) to move people, goods, and information. Their importance to modern societies has grown enormously with a strong demand for new technologies. Future transportation systems will be required to meet stringent energy consumption standards, environmental acceptability, and urban standards. Electronic communications systems will be required with greater load handling capabilities and as a partial substitute for paper communications.

Health.—With R&D in the health sciences already at a substantial level, new emphasis is likely to be directed toward preventive medicine and health delivery systems.

Disarmament and peace.—This is a topic which requires special comment. At one time referred to as the War Department of national governments, it is currently called the Defense Department. In the new realities, it might better be called the Disarmament and Peace Department. On the one hand we need to question whether present defense theories and postures are becoming outmoded, and on the other hand whether the nations of the world can continue to condone the high wastage of capital, energy, and materials under the guise of defense. Accepting that every nation has a right to defend itself, and that what is regarded as an adequate defense bears an international relativity, the only feasible way to de-escalate mounting defense costs is through mutual and collective agreements among nations. A first goal in this direction must be a total ban on nuclear weapons together with verifiable and enforceable safeguards. The failure to contain the so-called nuclear club and the failure of the Nuclear Non-Proliferation Treaty should now be ample warning that we are drifting along a dangerous course and that a whole new positive approach is needed.

What does all this have to do with science and technology? Today's highly sophisticated defense systems are, of course, heavily dependent on science and technology. It is sometimes suggested that scientists in all countries should refuse to work on weapons technology. Unless a total moratorium could be guaranteed and enforced, such a tactic would be impractical and totally unacceptable, since it would place scientists in an untenable situation of having their motives questioned as unpatriotic. A much more positive approach has a better chance to succeed. An example of this was the contribution made by scientists in developing sensitive detection systems for nuclear explosions anywhere in the world, which led to the acceptance of the partial ban on nuclear tests. Obviously, rather sophisticated safeguard systems would have to be devised to achieve a high level of confidence and an acceptable agreement to ban nuclear weapons. This could be an area of active international collaboration and, if scientists of many countries worked together toward such a common purpose, the chances of success would be greatly enhanced. Such a combined effort could also help to influence attitudes and foster a better climate of understanding and trust. There would appear to be little hope of general disarmament until the problem of nuclear weapons and their delivery systems is resolved on a world scale.

I am not sure whether this is a practical suggestion or not. But I think the scientific community in all countries must seriously ask itself whether there is not some positive role or some new approach which could contribute to the ultimate resolution of this problem. Progress made in the other problem areas I have mentioned may well be negated or diverted unless there is also much more rapid progress toward disarmament and peace.

Economic, scientific, and technical aid to less developed countries.—This is an enormous problem, and in spite of a great deal of discussion and good intentions, relatively little progress has been made in reducing the wide disparities between have and have-not countries. It is now widely recognized that to achieve a more stable world community, this gap must be narrowed substantially and more rapidly than has been achieved until now. The difficulties are well known. More effective action programs, together with possible new approaches, are now urgently needed.

Oceans and space.—These are both areas of growing importance. Here, too, the international and political problems are well known and remain to be resolved. It is also clear that the exploitation of the world's

oceans and outer space for the benefit of mankind will require substantial R&D investments.

Implications for science and technology.—How can the scientific community play a more active role in seeking solutions to the above list of problem areas? These are formidable and highly complex problems. Ultimate solutions must of course seek to resolve simultaneously the socio-economic and political aspects. However, with better technological solutions and more technological options available these aspects become much more tractable.

A related question frequently posed is: How can I as an individual scientist or engineer contribute? What research should I do? What research is needed? This points up a major difficulty. Before we can start looking for answers and solutions by doing research, it is necessary to be clear what the question is. Has the question related to a problem been adequately defined and validated? Who should frame the questions and who is best able to do so?.

Such uncertainties, of course, do not arise when we are talking about basic research, but for the major problem areas of concern, they are highly relevant. The fact that these difficulties persist could mean that we lack a sufficient understanding of the problem areas to be able to define the significant questions amenable to research, or that in relation to the questions, we lack promising ideas worth researching, or simply that we have not yet developed adequate ways and means to focus our best talents and capabilities on these problems. Each of these possibilities is no doubt pertinent in particular instances.

Central to these issues is the role of government and its interface modes with the scientific research community. Research and development activities organized on a national scale largely grew out of government initiatives during the last war to mobilize scientific resources for the war effort. A cadre of peer scientists worked closely with various government departments and agencies to evaluate key problems and to formulate significant research requirements. A system for funding research projects through grants and contracts was devised. This system, with but minor modifications, was carried over into peacetime and continues today. Accordingly, government had taken on a major central role not only in funding mission research, but also basic research.

It is also worth noting that during the last war many scientists set aside their own research programs and became primarily problem solvers. What was especially impressive was the effective way in which basic scientists, given strong motivation, successfully became applied scientists and engineers. After the war most of these researchers went back to their prewar pursuits.

During the past thirty years government-funded R&D expanded very substantially. During this period of high affluence and expectation, we have lacked the same strong sense of focus, and the clear articulation of urgent problem areas that was so evident during the war. In this situation and with the rapid buildup of universities and academic research, science tended to become more inward-looking. However, as I mentioned earlier, during this period there had also been very impressive advances in science and technology, and in research capability, which require no defense, and which constitute essential and strategic resources for our future endeavors.

If scientists are to be in a position to respond more effectively to contribute toward the solution of key problem areas, there will need to be a more articulate identification of needs and longer-term objectives by governments. Science policy studies in recent years have attempted to deal with these issues. However, many of these attempts became more preoccupied with structures, budgets, and methodologies, that is, the "how" rather than with matters of substance such as what we should be doing, and why, and relative priorities. It should now be clear that dealing with the latter cannot be accomplished by an external group of planners working in isolation and out of contact with the real world. Action programs of the kind we are considering here can only be developed by having knowledgeable and well-informed scientists working in close consultation and collaboration with government policymakers and decisionmakers.

I am encouraged that we are now beginning to move more positively in this direction and that some of the results of these efforts will soon become apparent. As an example of this approach, many countries, including Canada, are well on the way to developing an integrated national energy R&D program. A similar articulation of objectives and R&D needs and opportunities in other major problem areas is in prospect and is needed to focus our R&D efforts and to permit the scientific community to contribute more effectively to these efforts.

On the other hand, there are also impediments arising from science itself which may inhibit more effective R&D participation on the part of individual scientists. These are matters scientists themselves must take under their purview for they are in the best position to effect changes that are deemed necessary or desirable. These matters touch on the structure and functioning of science as it has evolved over the years.

The strong discipline-orientation of science is usually seen as a handicap because of the apparent mismatch between discipline-oriented research and problem-oriented research. Historically, the development of science took place largely in universities, where it was closely coupled with academic programs. Scientific disciplines were simply a convenience to delineate manageable fields of study. As such, they also became the basis of organizational structures. Our university departments, our scientific societies, and our scientific publications all have a strong discipline basis.

I do not mean to imply that this discipline orientation is now outmoded. In fact, I believe it has served us extremely well and there is at present no obviously superior system to replace it. However, we now also recognize it is not self-sufficient and that other systems, in parallel or in series, will be needed to complement it.

It may be noted that even in basic science as knowledge advanced there has been a considerable blurring of disciplinary boundaries. Modern electrochemistry is an example of this. So are also disciplines such as biology and earth sciences. Numerous hybrid disciplines have also come into being, with their own scientific societies and their own research journals. This fragmentation, particularly of the scientific literature, has been a matter of some concern. On the other hand, there have also been some recent countervailing developments where a related number of scientific societies have joined together in a federation to pursue their common purposes. Examples are the Canadian Federation of Biological Societies and the Canadian Geoscience Council.

As scientific research has become more institutionalized over the years it has also tended to institutionalize its own system of incentives and rewards. Younger scientists sometimes assert that they would like to engage in problem-oriented research, but are concerned whether this might jeopardize their future scientific career. They contend that obtaining research grants and job promotions based on peer review virtually demand a continuous flow of published papers. This is easier to achieve by continuing to research the researchable in a particular specialty than by attempting to pioneer a new field which has as yet no recognized peers and where a research investment of several years may be required before publishable results emerge. There is no doubt that these concerns exist and a better system of incentives and merit recognition will need to be developed.

Looking to the future, what is the R&D picture likely

to be ten or twenty years from now? Because of the gravity of a number of the problems of ongoing national concern, and because of the potential contribution science and technology are capable of making toward alleviating these problems, it is likely that substantially increased R&D expenditures will be made in these areas. This, of course, must be conditional on the availability of competent research manpower in each of these areas as well as promising research ideas. The mounting of significant programs will also require more integrated and cooperative projects with closer collaboration between the government, industry, and university sectors.

In the government and industry sectors the problem of discipline mismatch is a minor one since research teams built around competent specialists required for particular research projects are readily formed. It does, however, pose serious problems in universities where research projects tend to follow disciplinary lines. Indeed, the extent to which universities should engage in mission or problem-oriented research remains a matter of active debate. In view of the many other pressures now being exerted on universities, this is a further question the universities will have to resolve for themselves.

If there are to be substantial new research expenditures in the major problem areas it is likely that a large proportion of new Ph.D. graduates emerging from universities will be required in these areas. This further underscores current discussions as to the most appropriate Ph.D. programs for the future. This is also a matter for which universities have primary responsibility.

In speculating about the future it also seems reasonable to assume there will be no cutback on the present level of effort in basic research to offset in part an increased level of effort in problem-oriented research. But such comparisons may well amount to a somewhat meaningless kind of bookkeeping. In the first place, the value of basic research is no longer in question and the need to support basic research is well recognized by government. The question is only "how much" is needed. New programs in problem-oriented research are very likely to create a demand for more basic research in particular areas. However, this may not necessarily amount to added effort in basic research since the new earmarked research dollars will also be competing for the talents and time of existing researchers in basic research. Accordingly, we may expect the future course of basic research to be strongly influenced by increased R&D effort in the major problem areas. Whether this is beneficial or not in the long term we can only speculate since there is no way of predicting in advance where new opportunities or knowledge gaps are likely to arise.

Finally, I would like to emphasize again the international dimensions of some of the major problem areas. These will demand a more active international cooperation than we have had in the past. Science, because of its universality and the many common links it has already established, provides us with a favorable and strategic base on which to build. Successful cooperation at this level can also serve to foster better mutual understanding, trust, and confidence, thereby facilitating ultimate resolution of the more difficult social and political problem areas.

In summary, the challenges which now face the nations of the world will demand new initiatives and responses from the scientific research community as well as from governments. Both government and the scientific community will need to develop better collaborative interfaces and new approaches in their respective roles. Present day science and technology are in a strong position to contribute significantly to the alleviation of the major problem areas of growing national and international concern. These will demand greater leadership and the focused efforts of highly competent scientists and engineers. In such endeavors we truly serve to further the common ideals and promise of science, namely, the betterment of human life on earth and of all mankind.

SECTION NEWS

Chicago Section

Symposium and Workshop on Advanced Battery Research

The Chicago Section of The Electrochemical Society and the Argonne National Laboratory will jointly sponsor a symposium and workshop on Advanced Battery Research at Argonne National Laboratory, Argonne, Ill., March 22-24, 1976.

Papers are solicited for the two day workshop sessions which will focus on experimental developments in advanced, high energy secondary batteries. Topics such as cell chemistry and materials, electrode design, and cell and battery design will be covered in four sessions. The workshop concept has been chosen to promote extensive interaction and information exchange among the participants.

The first day of the symposium features an overview by invited speakers on the state of the art in secondary batteries in the U.S., Japan, and Europe.

For further information, please contact: The Symposium Committee, c/o Robert K. Steunenberg, Chemical Engineering Division, Argonne National Laboratory, 9700 S. Cass Avenue, Argonne, Ill. 60439; phone (312) 739-7711, ext. 3912 or 3684.

DIVISION NEWS

Electrodeposition Division

Symposium on Selective Plating

The Electrodeposition Division is planning a symposium on Selective Plating for the Fall 1976 Society Meeting in Las Vegas, Nevada. Selective plating is a very active field these days especially where precious metals are involved such as gold. This symposium will present a broad overview of the science and technologies involved in selective plating of all types. It will also provide a forum for presentation of new work which contributes new knowledge or new technology to the general topic of selective plating.

Papers are solicited for the symposium on such topics as: chemical and mechanical masking; fluid flow masking; anode shape effects and techniques; plating cell design theory and techniques; electroless plating; and selectively catalyzed surfaces.

Suggestions and inquiries should be sent to Symposium Co-Chairmen: Dennis R. Turner, Bell Laboratories, 600 Mountain Ave., Murray Hill, N.J. 07974 or Warren R. Doty, Udylite Corp., 21441 Hoover Rd., Detroit, Mich. 48234.

NEW MEMBERS

It is a pleasure to announce the following new members of The Electrochemical Society as recommended by the Admissions Committee and approved by the Board of Directors in September 1975.

Active Members

Armstrong, J., Tigard, Or.
Buynoski, M. S., Mountain View, Ca.
Dundas, H. J., Livonia, Mi.
Frankiewicz, T. C., Lexington, Ma.
Hamby, D. C., McMinnville, Or.
Keramidas, V. G., Murray Hill, N. J.
Malbon, R. M., San Pedro, Ca.
McMillan, F. J., Tempe, Az.
Pludek, V. R., Calgary, Alta., Canada

Student Members

Cahen, G. L., Jr., Charlottesville, Va.
Kim, J.-S., Stanford, Ca.
Song, K. S., Philadelphia, Pa.

Life Membership

Oldham, K. B., Peterborough, Ont., Canada

Reinstatement

Griffin, R. A., Sheridan Park, Ont., Canada

Notice to Authors for Washington, D.C. Meeting

The 75-word abstracts for the Washington, D.C. Meeting of the Society, May 2-7, 1976, must be received by Society Headquarters on or before December 1, 1975. Extended abstracts are due on or before January 1, 1976. These deadlines must be adhered to in order for a paper to be considered for inclusion in the meeting program. Further details appear in the Call for Papers, pages 349C-352C of This Journal.

Three $1000 Electrochemical Society Summer Fellowship Awards to be Granted

The Electrochemical Society will offer three fellowship awards for qualified graduate students for the summer of 1976. Each award will have a stipend of $1000 and its purpose is to assist the student to continue his graduate work during the summer months in a field of interest to The Electrochemical Society. These awards are to be known as The Edward Weston Fellowship Award, The Colin Garfield Fink Fellowship Award, and The Joseph W. Richards Fellowship Award.

Candidates' qualifications: "Each award shall be made without regard to sex, citizenship, race, or financial need. They shall be made to graduate students pursuing work between the degrees of B.S. and Ph.D., in a college or university in the United States or Canada, and who will continue their studies after the summer period. A previous holder of an award is eligible for reappointment."

Qualified graduate students are invited to apply for these fellowship awards. Applicants must complete an application form and supply the following information.

1. A brief statement of educational objectives.
2. A brief statement of the thesis research problem including objectives, work already accomplished, and work planned for the summer of 1976.
3. A transcript of undergraduate and graduate academic work.
4. Two letters of recommendation, one of which should be from his research adviser.
5. Successful recipients of fellowships shall agree not to hold other appointments or other fellowships during the summer of 1976.

Application forms are available from the Chairman of the Fellowship Awards Subcommittee, to whom completed applications and letters of recommendation should be sent: Professor H. B. Herman, Department of Chemistry, the University of North Carolina at Greensboro, Greensboro, North Carolina 27412.

Deadline for receipt of completed applications will be January 1, 1976, and award winners will be announced on May 1, 1976.

Section News 341C
Division News 341C
New Members 341C
ECS Summer Fellowship Awards To Be Granted 341C
Acheson Medal Award To Be Granted 342C
News Items 342C
Obituary 343C
Book Reviews 343C-346C
Positions Available 347C
Positions Wanted 347C
Call for Papers—Washington, D.C. Meeting 349C-352C

Acheson Medal Award

The Edward Goodrich Acheson Medal is awarded biennially for outstanding contribution to the objectives, purposes, or activities of The Electrochemical Society. It is a major Award of the Society, and it consists of a gold medal and bronze replica, plus a sum of $2,000.

Nominations for the next Award, which will be presented in the fall of 1976, are invited from the membership of the Society. The nominee need not be a member of the Society to qualify, nor are distinctions to be made with regard to sex, citizenship, race, or residence. Nominations must be accompanied by suitable supporting materials and should be provided in their entirety to the Chairman of the Honors and Awards Committee in ten copies (in case of difficulty, the Society's Headquarters Office can be requested to prepare the copies).

It is desired that nominations be in the hands of the Committee not later than March 1, 1976.

Following is a list of those who have received the Acheson Award since its establishment in 1928:

Edward G. Acheson*—1929
Edwin F. Northrup*—1931
Colin Garfield Fink*—1933
Frank J. Tone*—1935
Frederick M. Becket*—1937
Francis C. Frary*—1939
Charles F. Burgess*—1942
William Blum*—1944
H. Jermain Creighton*—1946
Duncan A. MacInnes*—1948
George W. Vinal*—1951
J. W. Marden—1953
George W. Heise*—1954
Robert M. Burns—1956
William J. Kroll—1958
Henry B. Linford—1960
C. L. Faust—1962
Earl A. Gulbransen—1964
Warren C. Vosburgh—1966
Francis L. LaQue—1968
Samuel Ruben—1970
Charles W. Tobias—1972
Cecil V. King—1974

Please address all nominations to the Chairman of the Honors and Awards Committee, Erik M. Pell, Xerox Corporation, Xerox Square (W105), Rochester, N. Y. 14644.

* Deceased

NEWS ITEMS

International Symposium on Industrial Electrochemistry

The Society for the Advancement of Electrochemical Science and Technology, India, will be organizing an international symposium on Industrial Electrochemistry during November 1976 at Madras, India. The symposium will last for four days, during which a maximum of 60 papers, both invited and contributed, will be presented. Industrial visits and exhibitions are also planned.

The topics that are proposed to be covered are: new developments in power sources; electro-inorganic and organic chemical industries; electrowinning and refining of metals; engineering aspects of electrochemical systems, scale-up and optimization; pollution control; industrial electrocoatings; semiconductors; bioelectrochemistry; and economics (country and regional surveys).

For further details please contact: The Secretary, SAEST, Karaikudi 623006, India.

Positions Wanted

Society members of any class may, at no cost and for the purposes of professional employment, place not more than three identical insertions per calendar year, not to exceed 8 lines each. Count 43 characters per line, including box number, which the Society will assign.

Notice to Members

Society Headquarters will mail during October, dues bills for 1976. These are special IBM cards which must be returned in the envelope provided with the bill.

As your 1976 membership begins with January 1976, it is suggested that you forward your dues payment promptly.

International Symposium on Solid Ionic and Ionic-Electronic Conductors

An International Symposium on Solid Ionic and Ionic-Electronic Conductors is to be held in Rome on September 1-3, 1976. The symposium will include papers on the fundamental aspects and the practical applications of solid conductors characterized by ionic and mixed ionic-electronic conductivity. A short abstract should be submitted to each of the following by December 31, 1975: Professor B. Scrosati, Secretary, Organizing Committee, Istituto di Chimica Fisica ed Elettrochimica, University of Rome, Italy; Dr. B. B. Owens, Chairman, Scientific Committee, Medtronic, Inc., 3055 Old Highway Eight, Minneapolis, Minnesota 55418 U.S.A.; and Professor T. Dickenson, Electrochemistry Research Laboratory, Department of Physical Chemistry, The University, Newcastle upon Tyne NE1 7RU, England. The complete text of those papers accepted is desired in English, ready for offset printing, by April 30, 1976.

American Electroplaters' Society, Inc.

The American Electroplaters' Society, Inc., is sponsoring a special symposium on Design and Finishing of Printed Wiring and Hybrid Circuits, which will be held at the Fort Worth Hilton Inn, Fort Worth, Texas, January 21-22, 1976.

The main themes will be: design and fabrication of printed wiring boards, rigid and flexible circuitry with either additive or subtractive processes; techniques for metal deposition, metal deposition and recovery processes; hybrid circuits design and fabrication, thick and thin film circuits; printed wiring workshop panel discussion; and hybrid circuit workshop panel discussion.

Please address any inquiries to: Richard C. Baker, Bell Laboratories, Room 1A258, Murray Hill, N.J. 07974.

Certificates, Pins, and Keys

The following items are available to Active Members:

Membership Certificates	$ 5.00
Gold Membership Pin	$ 7.50
Gold Membership Key	$15.00

Those interested should send their order accompanied by check to The Electrochemical Society, Inc., P.O. Box 2071, Princeton, N.J. 08540

OBITUARY

Hugh L. Logan, 74, retired physicist from the National Bureau of Standards and an internationally known authority on stress corrosion cracking, died June 23, 1975, after an illness in Arlington, Virginia. A native of Colorado, Mr. Logan joined the National Bureau of Standards in 1936 and remained there until his retirement in 1967. He obtained a B.S. in chemistry from Tarkio College, Tarkio, Missouri, and an M.S. in physics at the University of Colorado. He had completed all requirements for the Ph.D. degree in physics at the University of Colorado with the exception of two courses when the opportunity to come to the Bureau arose in 1936. He retired in 1967.

His major work at the National Bureau of Standards was concerned with stress corrosion cracking. During his career, he became one of the outstanding workers in this important field. In 1952, he proposed the film rupture theory of stress corrosion, and over the years this theory has seen increasing acceptance. It is considered one of the major mechanisms for stress corrosion cracking. He is the author of the book "Stress Corrosion of Metals."

This is the only book on the subject by a single author and is used extensively by corrosion engineers and metallurgists. It is the first book in the Corrosion Monograph Series of The Electrochemical Society. He organized, along with Dr. E. H. Phelps of the United States Steel Corporation, a symposium on stress corrosion at the 2nd International Congress on Metallic Corrosion held in New York in 1963. He published over thirty papers and books.

He was a member of the National Association of Corrosion Engineers, The Electrochemical Society, and American Society for Metals, and a fellow of the Washington Academy of Sciences. As recognition for his outstanding achievements, he received the Silver Medal of the Department of Commerce in 1960, and he was the recipient of the Burgess Memorial Award of the Washington Chapter of the American Society of Metals in 1964.

He is survived by his wife, Ethel, a son, Hugh, Jr., and a grandson.

BOOK REVIEWS

"Liquid Phase Epitaxy," edited by G. M. Blom, S. L. Blank, and J. M. Woodall. Published by North-Holland Publishing Co., Amsterdam (1974). 332 pages; $66.75.

This book is a collection of papers on the subject of LPE (liquid phase epitaxy) which had been published in the "Journal of Crystal Growth" (also a North-Holland publication) during 1974.

The enormous interest which has developed in this technology has prompted the publication of this collection of papers. Many papers on the subject have appeared in other journals ("Solid State Electronics," "IEEE Proceedings," "Journal of Applied Physics," etc.), but the papers appearing in the "Journal of Crystal Growth" are certainly most germane to a detailed survey on LPE. Many of the authors have decisively participated in the perfection of this technology which has not only promised but shown great achievements in the field of practical device development and high performance.

H. Nelson, who was one of the first to develop LPE and its applications to GaAs, describes the role of this method in a short introductory paper. The advantages cited—higher deposition rates, wide choice of dopants, and simple equipment—do not seem to fully explain the reason for its preponderance. There is, above all, the fact of a more perfect layer growth due to a melt-back and outgrowth of dislocations not easily achieved in VPE (vapor phase epitaxy).

A number of well-known authors develop the theory and praxis of binary, ternary, and quaternary compound crystal growth in epitaxy.

M. B. Panish, the noted Bell Laboratories metallurgist, who first developed methods to grow the complex DH (double heterostructure) close confinement lasers, contributes a paper on "A Thermodynamic Solution Treatment of the Ga-P, In-P, and Ga-As Systems." The solution interaction parameters from both the liquidus and the vapor pressures of these compounds are analyzed. It is shown that the comparison of parameters on account of the III-rich liquidus of these systems is correct and agrees with available thermodynamic data for liquid As and P, if the interaction parameter α (T) is considered. Available data for these compounds are discussed.

A further paper on phase diagrams deals with the "simple solution model" (Springfellow) where the excess free energy of mixing is expressed by a composition independent interaction parameter Ω. This model seems to allow even calculation of phase diagrams for quaternary compounds. Sol, Clariou, Linh, and Moulin give refined solubility data for P in Ga, As in Ga, and P in In. A number of papers deal with the epitaxial growth process, surface morphology, and constitutional variations. There is no consensus concerning the layered or step growths visible at epitaxial surfaces. While some authors discuss their origin in terms of temperature gradients, constitutional supercooling, and convection depletion (Small, Crossley) then conclude that a temperature gradient vertical to the growth surface is needed and melt thickness limitation is required in diffusion limited growth (Moon), other authors (Hsieh, Bauser) emphasize that growth steps and hillocks disappear when the usual (100) crystal plane has a misorientation $\delta \leq 5$ min of arc. Precisely oriented (100) surfaces of 1 μm thick epitaxial layers of GaAs show little structure, are smooth, and have no terraces. The apparent contradiction is resolved when one considers that: (i) the growth of relatively thin layers (1-10 μm) is less prone to terrace growth; (ii) a precise substrate orientation within min of arc may not be industrially feasible; (iii) sensitivity to the orientation is decreased when the package is subjected to a vertical temperature gradient (paper by Mattes and Route); and (iv) the (100) plane possesses the highest liquid/solid interfacial energy density and is therefore especially sensitive to misorientation.

A number of papers deal with the related problems of lattice parameter control and dislocation generation. The interesting possibility of impurity-stress compensation in GaAlAsP (Rozgonyi, Petroff, and Panish) has important consequences for the extension of the useful life of DH lasers and LED's (light emitting diodes) as was shown recently for InGaAs. Defects in epitaxial multilayers (misfit dislocations) are the sub-

continued over

ADVERTISERS' INDEX

Academic Press 347C
Institute of Gas Technology 347C
Pellon Corporation 331C
Petreco Division, Petrolite Corp. 333C
Princeton Applied Research Corp. 332C
G. D. Searle 346C

Book Reviews continued

ject of a paper on CVD (Matthews and Blakeslee) of GaAs and $GaAs_{0.5}P_{0.5}$, and in the case of (GaAl)As on GaP (LPE) (Astles and Rowland) surface texture was investigated in view of transmission photocathode work. Further structure-oriented contributions to be mentioned here are letters concerning crystal growth terraces and surface reconstruction (Rode), the effect of germanium on the distribution coefficient of Al in the system solid $Al_xGa_{1-x}As$/liquid Ga-Al-As-Ge (Minden), and the work on LPE growth of GaSb (Woelk-Benz).

Of particular interest for the electronics engineer and the solid-state physicist in industry are the contributions concerned with difficult device design and production based on LPE. We have to limit our discussion to the most important points to convey to the reader the gist of this monograph. There are the many methods based on "rotary crucibles" (Thompson and Kirkby), multiple boat growth with graphite slider (Dawson, Lockwood, Kressel), and the dipping method (Davies). There is also a "multislice slider" system which decants the melt and brings the substrate in contact with only a thin melt (Saul, Lorimor). Here, some of the difficulties encountered with thick melts are overcome, and it looks as if the rotating system of Lorimor may solve the industrial production problems. Finally, one should mention the papers on characterization by photoluminescence, a method already used industrially (Hitchens and Holonyak, and Outon, Lorenz, and Woodall).

The monograph is made complete by the reports on the work in microwave devices and garnet films based on LPE.

It seems astonishing that LPE has replaced CVD in many cases where the latter technology has had considerable lead time. The reasons for this are not industrial applicability, which would give preponderance to CVD, but the fact of higher structural perfection achieved which is decisive in layers for microwave applications (Rosztoczy) and bubble domain memories (Roberton, Linares, Glass, Davies, Morgan, Miller, Stacy, Hiskes, Pierce, and Clover). It is well known that it is not only the generation-recombination noise decrease in GaAs-FET's, but also the decreased trapping rate in Gunn devices which lend importance to LPE, while in the case of garnet growth for bubble domain devices, regular impurity distribution, lattice match, and high perfection are more readily achieved than in CVD. Even in the case of growth of crystals for far infrared applications, such as $Pb_{1-y}Sn_yTe$ and $Pb_{1-y}Sn_ySe$, we see a tendency to apply LPE (Kasai and Basset). Finally, the growth of SiC from transition-metal silicide solutions shows the general applicability of LPE (Pellegrini and Feldman).

The book is an excellent compilation of the latest work in this field which promises to become a central technology for research, development, and production of a wide variety of important electronic devices. It is recommended to all specialists working in the field of electronic materials properties and applications.

H. F. Mataré
Los Angeles, California

Book Reviewers Needed

The Electrochemical Society needs competent individuals to review books for the Journal.

Any Society member who wishes to volunteer his services should send his name, address, and field of competence to the attention of the Book Review Editor, Dr. Julius Klerer, c/o The Electrochemical Society, P.O. Box 2071, Princeton, N.J. 08540

"Introduction to Organic Electrochemistry," by M. R. Rifi and Frank H. Covitz (Techniques and Applications in Organic Synthesis Series, edited by R. L. Augustine). Published by Marcel Dekker, Inc., New York (1974). 417 pages; $26.50.

The increasing interest in organic electrochemistry is additionally underscored by the appearance of this recent book. Since 1970, some twelve years after Allen's "Organic Electrode Processes" directed itself uniquely to the general organic research chemist, there has appeared slightly more than a book a year of substantial interest or directed predominantly to the organic chemist. A roll call of these books is pertinent here: C. K. Mann, "Electrochemical Reactions in Nonaqueous Systems," Marcel Dekker, Inc., New York (1970); L. Eberson and H. Schäfer, "Organic Electrochemistry," Springer-Verlag, New York (1971); A. P. Tomilov, S. G. Mairanovski, M. Ya. Fioshin, and V. A. Smirnov, "The Electrochemistry of Organic Compounds, Halsted Press, New York (1972); A. J. Fry, "Synthetic Organic Electrochemistry," Harper & Row, New York (1972); M. M. Baizer, Editor, "Organic Electrochemistry, An Introduction and a Guide," Marcel Dekker, Inc., New York (1973); and N. L. Weinberg, Editor, "Techniques of Electro-organic Synthesis, Parts I and II," John Wiley & Sons, Inc., New York (1974-1975). (This two volume work was not completed at the time of this review.)

There are other books forthcoming in the field, including one or more volumes on organic electrochemistry, in the monumental "Encyclopedia of Electrochemistry of the Elements" series edited by Allen Bard, being published by Marcel Dekker, Inc.

Both Rifi and Covitz have excellent credentials for this undertaking, and each has made fundamental contributions to the field of organic electrochemistry. Their offset-printed book is divided into the following chapter headings: "Introduction," "Basic Principles," "Apparatus and Techniques," "Reduction of Functional Groups," "Oxidation of Functional Groups," "Electroinitiated Polymerization," and "Electrocoating." There are three appendices—"Questions and Answers," "Glossary of Terms Commonly Used in Electrochemistry," and "Charts of Useful Electrode Potentials"—and both author and subject indices. One might say that about 15 per cent of the book is devoted to basic principles, almost 25 per cent to apparatus and techniques, and somewhat less than 50 per cent to chemical transformations.

Any book should be assessed in the light of its intended audience. The word "Introduction" in the title is not necessarily a clarifying one. Beyond designating the text as a "first," it discloses neither the sophistication expected of the reader nor the depth of the knowledge purveyed. Baizer's 1100 page compendium is also designated an "Introduction," but demands and provides information at a much higher level. It would, perhaps, be reasonably accurate to consider the present volume directed to a level of training corresponding to advanced undergraduate or "rusty" organic chemist seeking a very panoramic, bird's-eye view of the material. For such an audience, the devotion of 34 pages to "Questions and Answers" is defensible, and the descriptive, summary nature of the coverage more reasonable. It is not fully adequate for the active organic researcher seeking fundamental material for his first entry into the specialized electro-organic field and should not, therefore, be considered in competition with Fry's book, the most obvious comparison.

There are a few shortcomings that require comment.

While the number of references is not unreasonable, they are poorly up-to-date. In this 1974 copyrighted book, the reviewer found a single reference to 1972 work (a patent to one of its authors), two references to 1971 work (a "Scientific American" article and a paper by one of the authors), and very few citations of 1970 work. Material from the sixties is not as well represented as it should be. For the chapter on electrocoating, only three references are given: one to a 1927 work, one to a book published in England in 1966, and one to an unpublished work by one of the authors. If this book is to be compared with other recent efforts, this is a serious shortcoming. Even Eberson and Schäfer's book, published three years earlier, has more recent coverage.

continued over

Book Reviews continued

One of the most frequent reasons for consulting an introductory type of book in an unfamiliar area is to see whether a particular goal can be accomplished by the unfamiliar technique. To this end, tables of representative examples are invaluable. The present book has unfortunately few of these. In fact, the major chapter on reduction has but one such table, with six entries, for the reduction of nitrobenzene. The most extensive table in this chapter, almost five pages long, gives half-wave potentials of organic halides but does not indicate products. So extended a listing of $E_{1/2}$ is hardly warranted in the present "introductory" book; such a listing, with products, would be valuable in any book and enormously useful to the potentially interested organic chemist. A number of such tables do appear in the chapter on oxidation.

This pattern of uneven coverage is apparent elsewhere in the book in the space allotted to the various functional groups, i.e., 24 pages to carbon-halogen reduction versus ten for the nitro group and only eleven to carbonyl compounds.

This reviewer checked his own area of maximum expertise (electrochemical reduction of the carbonyl group) as a measure of the practical guidance that could be obtained and found the guidance unsatisfactory or misleading. None of the quoted material on the nature of the electrode is less than 20 years old; it should be considered suspect. The statement that acidic conditions favor pinacol formation while basic conditions give mainly alcohols is at best misleading (pinacol products may fragment or rearrange to alcohols), but more frequently inaccurate. It should be added that the above undoubtedly stems from the very admirable intention of the authors to summarize an essentially indigestible mass of literature from which it is doubtful if any brief over-all summary can be made at present. In such cases, as noted above, tables can stand effectively in lieu of oversimplification. More importantly, the material offered does not provide enough guidance to make the very useful possibilities attractive.

The book does have some real strengths, however. It is written in a simple, straightforward, and, occasionally, pleasantly personalized style. The chapter on basic principles is minimally mathematical and highly pragmatic as is the chapter on apparatus and techniques which contains a great deal of practical information. Very useful experimental details are provided for specific reductions or oxidations of representative functional groups following the pertinent subsections. The appendix which offers a glossary of terms is an attractive feature.

For the audiences suggested above, the book can fill a distinct need not presently met by the other books available, that of a truly introductory learning text oriented to the organic chemist. In such a comparative framework, both the Fry and Eberson/Schäfer books might more properly be designated reference sources with the Baizer and Weinberg offerings properly considered overlapping but not competing compendia; the first having a critical orientation and the second a comprehensive one.

It has become customary to deplore book prices, often using a cost-per-page criterion. Excluding consideration of the merits of a quality-per-unit-weight judgment, in this day of offset vs. typeset printing it was a matter of curiosity to this reviewer to consider similarly the approximate number of characters per representational page of several of the books mentioned above. Found were: Eberson/Schäfer = 3400, Fry = 3200, Baizer = 3300, and Rifi/Covitz = 2200, i.e., the first three provide on a "quantity" basis approximately 50% more "information" per page. Obviously, any price-oriented evaluation should consider such data.

Jack H. Stocker
Louisiana State University
New Orleans, Louisiana

OUT-OF-PRINT SOCIETY VOLUMES

The following volumes sponsored or published by The Electrochemical Society, Inc. are now out-of-print. Xerographic copies* or reprints† of these volumes are available.

* **Vapor Plating.** C. F. Powell, I. E. Campbell, and B. W. Gonser, Editors. A 1955 symposium. 158 pages, **$8.40.**

* **The Structure of Electrolytic Solutions.** W. J. Hamer, Editor. A 1957 symposium. 441 pages, **$22.70.**

* **Technology of Columbium (Niobium).** B. W. Gonser and E. M. Sherwood, Editors. A 1958 symposium. 120 pages, **$6.50.**

* **Surface Chemistry of Metals and Semiconductors.** H. C. Gatos, J. W. Faust, Jr., and W. J. La Fleur, Editors. A 1959 symposium. 526 pages, **$27.00.**

* **Electrode Processes,** First Conference. E. Yeager, Editor. A 1959 symposium. 374 pages, **$19.50.**

* **Mechanical Properties of Intermetallic Compounds.** J. H. Westbrook, Editor. A 1959 symposium. 435 pages, **$22.50.**

* **Zirconium and Its Alloys.** J. P. Pemsler, E. C. W. Perryman, and W. W. Smeltzer, Editors. A 1965 symposium. 205 pages, **$15.10.**

† **Measurement Techniques for Thin Films.** B. Schwartz and N. Schwartz, Editors. 1965 and 1966 symposia. 347 pages, **$12.00** (softbound), **$15.00** (hardbound).

† **Electrode Processes,** Second Conference. E. Yeager, H. Hoffman, and E. Eisenmann, Editors. A 1966 symposium. 190 pages, **$5.00.**

* **Electrolytic Rectification and Conduction Mechanisms in Anodic Oxide Films.** P. F. Schmidt and D. M. Smyth, Editors. A 1967 symposium. 230 pages, **$11.80.**

* **Electrets and Related Electrostatic Charge Storage Phenomena.** L. M. Baxt and M. M. Perlman, Editors. A 1967 symposium. 150 pages, **$7.80.**

* **Dielectrophoretic and Electrophoretic Deposition.** E. F. Pickard and H. A. Pohl, Editors. A 1967 symposium. 138 pages, **$6.90.**

* **Electron and Ion Beam Science and Technology,** Third International Conference. R. Bakish, Editor. A 1968 symposium. 725 pages, **$35.80.**

* **Optical Properties of Dielectric Films.** N. Axelrod, Editor. A 1968 symposium. 325 pages, **$14.50.**

* **Thin Film Dielectrics.** F. Vratny, Editor. A 1968 symposium. 680 pages, **$34.20.**

* **Ohmic Contacts to Semiconductors.** B. Schwartz, Editor. A 1968 symposium. 356 pages, **$18.40.**

* **Semiconductor Silicon.** R. R. Haberecht and E. L. Kern, Editors. A 1969 symposium. 750 pages, **$38.90.**

* **Chemical Vapor Deposition,** Second International Conference. J. M. Blocher, Jr. and J. C. Withers, Editors. A 1970 symposium. 872 pages, **$43.55.**

* **High Temperature Oxidation of Metals.** By P. Kofstad. The Corrosion Monograph Series. 340 pages, **$20.00.**

* Order from University Microfilms, Inc., 300 North Zeeb Street, Ann Arbor, Mich. 48103. Enclose payment with order. Specify an Electrochemical Society volume.

† Order from Johnson Reprint Co., 355 Chestnut St., Norwood, N.J. 07648. Specify an Electrochemical Society volume. Prices subject to change without notice.

Book Reviews continued

"The Founders of Electrochemistry," by Samuel Ruben. Published by Dorrance & Company, Philadelphia (1975). 107 pages; $5.95.

Samuel Ruben has been an active inventor in various areas of electrochemistry for more than 50 years. Quite understandably, he became intrigued in studying the lives and motivations of the pioneers in research which led to the modern concepts of electrochemistry. For this little volume he has chosen four outstanding figures who may be called the founders of electrochemistry: Count Rumford, Alessandro Volta, Humphry Davy, and Michael Faraday.

Count Rumford was never an electrochemist, but he was instrumental in founding the Royal Institution of Great Britain and his recognition of young Humphry Davy's ability started many years of study and invention in the fields of electricity and chemistry. Rumford was born Benjamin Thompson, in Massachusetts, in 1753. At an early age he began the study of explosives and armaments; in the early 1770's he was an ardent Tory and found in expedient to flee to England. There he became a successful manufacturer of armaments, became acquainted with the leading scientists, and was elected Fellow of the Royal Society. About 1782, he took a governmental position in Bavaria, where he was able to upgrade the Bavarian army and to introduce many military and civilian reforms. In recognition, he was given the title of Count, and chose the name Rumford to go with it.

During this time Rumford arranged controlled experiments in boring cannon barrels to study the heat production. It became evident that the energy expended by two horses in driving the boring mechanism was responsible for the heat via friction of the cutting tools. It was impossible at the time to derive a quantitative relation between heat and work; this was done some 50 years later.

Rumford returned to England, in 1794, a wealthy man. He presented his studies before the Royal Society, and, in 1798, founded the Royal Institution. He soon acquired Davy as lecturer in chemistry.

In 1791 Luigi Galvani published experiments with frogs' leg muscles; he felt that "animal electricity" could flow through wires. Volta, on the other hand, felt that the two metals used by Galvani (a copper hook and an iron frying pan?) generated a current. On this basis, Volta set up his famous piles and crown of cups, and with the use of various metals was able to construct an electrochemical series. In 1800 Cruikshank made partitioned cells from which current could be drawn to deposit copper, for example. These crude cells made it possible for Davy to carry out many experiments, including the production of metallic sodium and potassium, and later for Faraday to derive the quantitative laws of electrolysis.

Humphry Davy at an early age became apprentice to a surgeon-apothecary, but by 1797 was mainly interested in chemistry. By 1800 he was able to publish experiments on the production and nature of nitrous oxide, and shortly thereafter was offered a position at the Royal Institution. As part of his duties there he made a comprehensive study of tanning and the treatment of hides, and of certain phases of agriculture. In 1815 he devised the famous miner's safety lamp, and in 1824 invented cathodic protection for the copper sheathing on naval vessels (an invention which unfortunately was not useful). In 1813 Davy engaged a young assistant named Michael Faraday.

Faraday was born in 1791, and in 1804 became errand boy and apprentice to a bookbinder. He was able to read some of the books in the shop, and became intrigued by science. In 1810 he attended lectures on scientific subjects, including lectures by Davy. He applied to Davy for a position and eventually was employed as an assistant. In the course of 5 or 6 years he became well known as a lecturer and experimenter.

Faraday carried out an amazing number of experiments in a wide variety of fields. Best known to electrochemists for his simple laws of electrolysis and the introduction of familiar names (electrolysis, electrodes, ions, anode, cathode, anion, cation), he showed that oxygen is paramagnetic, discovered benzene, and made derivatives such as nitrobenzene. He studied the nature of electrical capacity and capacitors. Most importantly, he showed that a moving magnet induces a current in a wire, or that a wire carrying current in a magnetic field can produce mechanical energy.

Dr. Ruben's thesis is that these four men—and many, many others could no doubt be mentioned—were inspired from early youth with a desire for knowledge. Read, read, read, listen to the men of knowledge, get acquainted and talk to them, discuss matters of interest, experiment, keep fullest notes, publish. But listen critically, read critically, be a skeptic, look for flaws, be sure your views will stand up under the fullest investigation of others.

C. V. King
American Gas & Chemical Company, Limited
New York, New York

Electro-analytical CHEMIST

Searle Laboratories, the pharmaceutical division of G. D. Searle and Company, located in a northern suburb of Chicago, has an immediate opening in the Analytical Research Department.

You will need a B.S. or M.S. in chemistry to develop electroanalytical methods for quality control. As there is a heavy emphasis in polarography, 1 year experience in this specialty is required, preferably dealing with analysis of organic compounds. A desirable background would also possess familiarity with other electroanalytical techniques.

We offer an excellent starting salary as well as an attractive benefit package. Please submit your resume, including salary requirements, in confidence to:

Carol L. Bernacchi

SEARLE **G. D. Searle & Co.**

Box 5110. Chicago. Illinois 60680

Equal Opportunity...
A Practice, Not Just A Policy

POSITIONS AVAILABLE

Assistant Professor in the Metallurgy Section—Candidate should be a Ph.D. with teaching and research interests in the broad areas of hydrometallurgy, electrochemistry, and mineral processing. Send resume to: Professor H. W. Pickering, Chairman, Metallurgy Section, 208 Mineral Industries Building, The Pennsylvania State University, University Park, Pa. 16802. The University is an equal opportunity and an affirmative action employer.

Electrochemist—Advance development in engineering group involving design and conducting of investigations related to the basic chemistry and electrochemistry of lead acid type batteries. Requires B.S. chemistry and several years experience in electrochemistry. Exposure to lead acid systems desirable. Modern facility, Milwaukee suburb. Competitive salary. Excellent benefits. Send resume and salary history to **E. R. Boelk, Globe-Union Inc., P. O. Box 591, Milwaukee, Wisconsin 53201.**

POSITIONS WANTED

Please address replies to the box number shown, c/o The Electrochemical Society, Inc., P. O. Box 2071, Princeton, N. J. 08540.

Chemist—Creative, resourceful, versatile. Experience in battery, fuel cell, electromedical, separator technologies, electrochemistry, polymer applications and testing. Good library, oral, written, and listening skills. Seeks interesting problems and stimulating surroundings. Resume and references. Reply Box C-158.

Materials Scientist—Ph.D. (1973) experienced in preparation and characterization of thin films, evaporation, sputtering, electron microscopy, x-ray techniques, vacuum technology, optical, electrical and magnetic properties. Five years industrial experience. Seeks challenging R&D position. Reply Box C-159.

Electrochemist/Materials Scientist — Ph.D. 1972, 7 years industrial research experience including work on fuel cells and metallic corrosion. Some teaching experience. 10 publications. Seeks responsible position to pursue research in energy conversion, materials science, or related fields. Reply Box C-160.

Semiconductor Materials Scientist—Ph.D. extensive experience in the growth of multilayered liquid-phase epitaxial structure of III-V compound semiconductors and fabrication of LED and laser materials. More than 20 publications. Seeking industrial or teaching position. Reply Box C-161.

Manager/Group Leader—Ph.D. (1970) materials science. Richly experienced in the area of inorganic materials preparation and characterization, display materials (including phosphors), modern characterization techniques including sem/probe, ESCA/Auger, x-ray diffraction/fluorescence. 10 years experience includes R&D at top chemical and electrical companies. Seeking full-time position or part-time consulting. Reply Box C-162.

Electrochemist—Ph.D., 10 years experience in electrochemical energy conversion, corrosion, materials research. Seeks creative environment in energy R&D. Reply Box C-163.

ELECTROCHEMIST

Challenging position with a major energy research institute developing numerous advanced energy conversion systems such as fuel cells, electrolyzers and batteries; H_2 technology; and energy storage systems. Candidate should have proven record of accomplishment, preferably in areas of applied electrochemistry, reaction mechanisms, and corrosion in molten salt and alkali systems.

Liberal benefits include free medical, life insurance, and tuition assistance. Please send resume including salary requirements to:

Mrs. A. Pruss
Institute Of Gas Technology
3424 South State Street
Chicago, Illinois 60631

Equal Opportunity Employer

IGT
EDUCATION · RESEARCH

ATTENTION, MEMBERS AND SUBSCRIBERS

Whenever you write to The Electrochemical Society about your membership or subscription, please include your Magazine address label to ensure prompt service.

Mail to the Circulation Department, The Electrochemical Society, Inc., P. O. Box 2071, Princeton, N.J. 08540.

ATTACH LABEL HERE

Change of Address

To change your address, place magazine address label here. Print your NEW address below. If you have any question about your subscription or membership, place your magazine label here and clip this form to your letter.

name ____________

address ____________

city ____________ state ____________ zip code ____________

ANODIC OXIDATION

by SIDNEY D. ROSS, MANUEL FINKELSTEIN, and ERIC RUDD
A Volume in the ORGANIC CHEMISTRY Series

This book is divided into two sections. The first section (Chapters 1-4) presents the underlying theory for the electrochemical oxidation of organic substrates and briefly discusses the experimental methods and required equipment. The second section (Chapters 5-12) assesses the available literature of the anodic oxidation of organic compounds, classifying the compounds according to the functional group being oxidized, e.g., there are chapters on the oxidation of hydrocarbons, acids, amines, alcohols, ethers, etc.

1975, 352 pp., $37.00/ £17.75

SEMICONDUCTORS AND SEMIMETALS

series editors: R. K. WILLARDSON and ALBERT C. BEER
Volume 11/SOLAR CELLS
by HAROLD J. HOVEL

The effects of solar cell thickness and polycrystallinity, fully detailed here, are highly valuable and not significantly found elsewhere. Also included are valuable detailed discussions of Schottky barrier, heterojunction, vertical multijunction, and organic solar cells, and of back surface field devices, drift field effects, and the optical transmission of metal films. There is an addendum which reviews the important work presented at the recent solar cell conferences (mid-1975).

1975, about 250 pp., in preparation

POWER SOURCES 5

Research and Development in Non-Mechanical Electrical Power Sources
(Proceedings of the 9th International Symposium held at Brighton, September 1974. Sponsored by the Joint Services Electrical Power Sources Committee)
edited by D. H. COLLINS

This book is a unique collection of papers aiming to provide the most up-to-date information on research and development, applications engineering, design studies and user-experience of primary and secondary cells, solar cells, thermoelectric generators and related subjects. An important feature is the inclusion of edited discussions of the papers.

1975, 752 pp., $54.50/ £21.00

N.B.: Postage plus 50¢ handling charge on all orders not accompanied by payment.

Prices subject to change without notice.

ACADEMIC PRESS

A Subsidiary of Harcourt Brace Jovanovich, Publishers
111 Fifth Ave., New York, N. Y. 10003
24-28 Oval Road, London NW1 7DX

The Electrochemical Society, Inc.
P.O. Box 2071, Princeton, New Jersey 08540 • 609/924-1902

Instructions to Authors of Papers

Revised July 1, 1972

JOURNAL OF THE ELECTROCHEMICAL SOCIETY is the official journal of the Society and contains three sections totaling some 2500 editorial pages annually: Electrochemical Science and Technology, Solid-State Science and Technology, and Reviews and News.

GENERAL

Manuscripts submitted to the Journal should be sent in **triplicate** (one original and two clear copies, preferably Xeroxed), to the Editorial Office, P.O. Box 2071, Princeton, New Jersey 08540. They must be typewritten, double-spaced, on one side only of white bond 8½ x 11 in. paper, 2½-4 cm (1-1½ in.) margins. Illustrations should also be sent in triplicate, with one original and two copies that are clear enough for easy review.

Titles should be brief and properly descriptive, followed by the author's name, professional connection and complete address, including city, state, and zip code. **Text** should be as brief as is consistent with clarity and should omit introductory or explanatory material which may be regarded as familiar to specialists in the particular field. Papers should be written in concise and **good** English and authors are urged to ensure they have been carefully edited and proofread before they are submitted. Suitable headings and subheadings should be included but sections should not be numbered. For current form and style, papers in recent issues should be consulted. Proprietary and trade names should be generally avoided; if used with discretion, they should be capitalized to protect the owners' rights.

If a paper was presented at a meeting of the Electrochemical Society, it should be mentioned in the covering letter sent with the original manuscript.

Under present Society policy, the review procedure is handled by the various Divisional Editors, with final acceptance or rejection by the Editor. Manuscripts are usually reviewed in several weeks and those returned to the author for revision should be resubmitted promptly to the appropriate Divisional Editor. This generally allows publication in five months or less from date of original receipt.

Authors are encouraged to suggest qualified reviewers for their manuscripts, with the editors reserving the right to final choice. It is helpful if the author tells which ECS division (listed in the front of each issue of the Journal) would be most interested in his paper.

Inquiries concerning submitted manuscripts should be addressed to the Editor, President's Office, Rice University, Houston, Texas 77001.

TYPES OF ARTICLES

Articles of wide diversity of interest are acceptable, but subjects primarily covered in the other specialized journals (e.g., analytical or nuclear chemistry) are not considered appropriate.

Technical Papers are divided into two categories: fundamental and applied. The former describes original research of basic nature and must have scientific depth. The latter may deal with any practical aspect of the fields of interest to the Society, e.g., plant design or operation, production and control methods, economics. Each paper should be introduced by an abstract stating the scope of the paper and summarizing fully its results and contents.

Review Papers furnish a current and critical analysis of the subject with citation only of truly pertinent references, and normally should not exceed 20 manuscript pages. An abstract is required.

Technical Notes are used for reporting brief research, developmental work, process technology, new or improved devices, materials, techniques, processes which do not involve more extensive basic scientific study. No abstract is required.

Brief Communications are used to report information of scientific or technological importance which warrants rapid dissemination, even though not necessarily a completed research. Length should be limited to 1000 words or less, with no more than two illustrations. No abstract is required. Publishing time is normally less than three months.

KEY WORDS

Authors are responsible for supplying a list of from three to five single key words to facilitate information retrieval. No paper will be published without them. Generic terms generally are to be avoided as are terms already contained in the title. Key words acceptable to **Chemical Abstracts** are also generally acceptable in Society publications. List key words at the bottom of the first page of the manuscript.

EQUATIONS

Mathematical equations should be written on a single line if possible, and parentheses, brackets, the solidus (/), negative exponents, etc., may be used freely for this purpose. Authors are urged to consult Chapter VI of the "Style Manual" of the American Institute of Physics (available for $2.50 at the American Institute of Physics, 335 East 45 Street, New York, N. Y. 10017) and to follow the patterns described there.

SYMBOLS

Authors are encouraged to use symbols extensively. These should be defined in a list at the end of the paper, with units given. For example:

$a, b \ldots$ = empirical constants of Brown equation
f_i = fugacity of pure ith component, atm
D_v = volume diffusion coefficient, cm²/sec

ABBREVIATIONS UNITS

The AIP "Style Manual" referred to here gives a suitable list of common **Abbreviations.** Units usually will be abbreviated without periods throughout the text, as sec, min, hr, cm, mm, etc. **Metric Units** should be used throughout, unless English units are clearly more appropriate in the area of discussion.

POTENTIAL SIGNS

Electrode potentials: Authors are urged to state and make use of the polarity of test electrodes with respect to the reference electrode used, **i.e.,** Zn is normally negative, Cu normally positive with respect to the standard hydrogen electrode. The sign for the emf of a cell should conform to the free energy change of the chemical reaction as written or implied, in accordance with the definition $\Delta G = -nFE$. These suggestions agree with the IUPAC conventions adopted in 1953.

REFERENCES

Literature References should be listed on a separate sheet at the end of the paper in the order in which they are cited in the text. Authors' initials must be given, and the style and abbreviations adopted by **Chemical Abstracts** should be used. Any recent issue of Society journals may be consulted. Literature cited should be readily available; consequently personal communications, Department of Defense (DOD), and Office of Technical Services (OTS) citations should be minimized. When references are not readily accessible, **Chemical Abstracts** citation numbers must be supplied.

TABLES

Tables should be typed on separate sheets.

ILLUSTRATIONS

Photographs should be used sparingly, must be glossy prints, and should be mailed with protection against folding. **Micrographs** should have a labeled length unit drawn or posted on the picture. On both, label "top" where any uncertainty might arise. **Captions** for figures (including photographs) must be included on a separate sheet. Figure numbers must **not** appear in the body of the figure; they will be removed if they do. **Numerical Data** should not be duplicated in tables and figures.

Drawings and **Graphs** ordinarily will be reduced to 8.3 cm (3¼ in.) column width, and after such reduction should have lettering no less than 0.15 cm high. Lettering must be of letter-guide quality. India ink on tracing cloth or paper is preferred, but India ink on coordinate paper with blue ruling is acceptable. Line weight 2 is used for borders and zero lines. When several curves are shown, each may be numbered and described in the caption. Lettering shown is approximately ⅛ in. In plotting current or potential as ordinate, increasing negative values should go down.

PUBLICATION CHARGE

To cover part of the cost of publication a page charge of $50.00 per printed page is requested for the publication of technical material. A 10% reduction is allowed if at least one author of an article is an ECS member or an employee of a Patron or Sustaining Member firm. However, acceptance of a manuscript is on the basis of merit and is in no way dependent on such payment. The charge may be waived in individual cases.

Call for Papers
149th Meeting, Washington, D.C.
May 2-7, 1976

Divisions which have scheduled sessions are listed on the overleaf, along with symposium topics.

1. Symposium Papers.

Authors desiring to contribute papers to a symposium listed on the overleaf should check first with the symposium chairman to ascertain appropriateness of the topic.

2. General Session Papers.

Each of the several Society Divisions which will meet in Washington, D.C., can plan a general session. If your paper does not fit readily into a planned symposium, you should specify "General Session."

3. To Submit a Meeting Paper.

Each author who submits a paper for presentation at a Society Meeting must do three things:

A—Submit one original 75-word abstract of paper to be delivered. Use the form printed on the overleaf or a facsimile. **Deadline for receipt of 75-word abstract is December 1, 1975.**

B—Submit original and one copy of an Extended Abstract of the paper. **Deadline for receipt of Extended Abstract is January 1, 1976.** See (5) below for details.

C—Determine whether the meeting paper is to be submitted to the Society Journal for publication. See (6) below for details.

Send all material to The Electrochemical Society, Inc., P.O. Box 2071, Princeton, N.J. 08540.

Unless the 75-word and required Extended Abstracts are received at Society Headquarters by stated deadlines, the papers will not be considered for inclusion in the program.

4. Meeting Paper Acceptance.

Notification of acceptance for meeting presentation, along with scheduled time, will be mailed to authors with general instructions no earlier than two months before the meeting. Those authors who require more prompt notification are requested to submit with their abstracts a self-addressed postal card with full author-title listing on the reverse.

5. Extended Abstract Volume Publication.

All scheduled papers will be published in the EXTENDED ABSTRACTS volume of the meeting. The volume is published by photo-offset directly from typewritten copy submitted by the author. Therefore, special care should be given to the following instructions to insure legibility.

A—Abstracts are to be from 500 to 1000 words in length and should not exceed two pages, single spaced. The abstract should contain to whatever extent practical all significant experimental data to be presented during oral delivery.

B—Abstracts should be typed single spaced on the typing guide forms which are sent to each author after the submission of a short abstract. If it is necessary to use white bond paper, it should be 8½ x 11 inches with 1¼ inch margins on all sides. Submit all copy in black ink. Do not use handwritten corrections.

C—Title of paper should be in capital letters. Author(s) name and affiliation and address should be typed immediately below in capital and lower case letters. Please include zip code in address. It is not necessary to designate paper as "Extended Abstract" or to quote the divisional symposium involved.

D—If figures, tables, or drawings are used, they should follow the body of the text and should not exceed one page. Submit only the important illustrations and avoid use of halftones. Lettering and symbols should be no smaller than ⅛ inch in size. Figure captions should be typed beneath the figure and be no wider than the figure. Table titles should be typed above, and the same width as, the table.

E—Mail original and one copy of the abstract to: The Electrochemical Society, Inc., P.O. Box 2071, Princeton, N.J. 08540, unfolded.

Abstracts exceeding the stipulated length will be returned to author for condensation and retyping.

6. Manuscript Publication in Society Journal.

All meeting papers upon presentation become the property of The Electrochemical Society, Inc. However, presentation incurs no obligation to publish. If publication in Journal is desired, papers should be submitted as promptly as possible in full manuscript form in order to be considered. If publication elsewhere after presentation is desired, written permission from Society Headquarters is required.

Washington, D.C., Meeting Symposia Plans—Spring 1976
May 2-7, 1976

a.) For receipt no later than December 1, 1975, submit a 75-word abstract of the paper to be delivered, on the form overleaf.
b.) For receipt no later than January 1, 1976, submit two copies of an extended abstract, 500-1000 words.
c.) Send all abstracts to The Electrochemical Society, Inc., P.O. Box 2071, Princeton, N.J. 08540. See details on preceding page.

BATTERY AND ELECTRONICS DIVISIONS

Materials for Batteries and Fuel Cells

This symposium is intended, in part, to be a continuation of the "Materials Problems in Batteries and Fuel Cells" symposium conducted at the Toronto Meeting (May 1975). Again, emphasis will be placed on the materials aspects of electrochemical power source components; papers dealing with these general subject areas are solicited. In particular, papers are solicited in the context of the following topics:

1. Battery systems with high energy per unit volume.
2. New button cell materials and technology.
3. Self-discharge processes induced by cell operation.
4. Sealants and sealing technology for portable power sources.
5. High rate charging of portable, ambient temperature batteries.
6. Materials of construction for high temperature power sources.
7. Low weight, portable fuel cells.
8. The low cost fuel cell system.
9. High capacity, electrochemical stand-by power systems.

Several invited papers will be presented, and contributed papers are solicited. Suggestions and inquiries should be directed to the Symposium Co-Chairmen: Raymond J. Jasinski, Texas Instruments Inc., P.O. Box 5936, M/S 147, Dallas, Texas 75222; or John M. Parry, Arthur D. Little, Inc., Acorn Park, Cambridge, Mass. 02140.

CORROSION DIVISION

General Session

The Corrosion Division will schedule a General Session. All aspects of low temperature and high temperature corrosion will be considered. Techniques for the study of corrosion phenomena are of interest. Suggestions and inquiries should be directed to: Roger W. Staehle, Dept. of Metallurgical Engineering, Ohio State University, 116 West 19th Ave., Columbus, Ohio 43210.

CORROSION AND INDUSTRIAL ELECTROLYTIC DIVISIONS

Electrochemistry and Corrosion Processes in Caustic Solutions

Papers are solicited for a symposium session, sponsored by the Corrosion and Industrial Electrolytic Divisions, on Electrochemistry and Corrrosion Processes in Caustic Solutions. Included are topics dealing with:

1. Low temperature and high temperature corrosion studies with or without electrochemical monitoring.
2. Other electrochemical studies, such as reaction rates on various substrates, gas evolution, or other electrolytic breakdown.
3. Caustic solutions, pure fused caustics, or fused caustic mixtures.
4. Batteries.

The purpose of having a symposium covering all aspects of caustic studies is to make all researchers in this general area aware of ongoing research that may not be directly related to their particular realm of endeavor. Therefore, review papers and scientific theoretical papers are welcome as well as papers dealing with engineering studies. A symposium volume of the papers is planned.

Please direct suggestions and inquiries to the Symposium Co-Chairmen: Arun Agrawal, Dept. of Metallurgical Engineering, Ohio State University, 116 West 19th Ave., Columbus, Ohio 43210; or George J. Theus, Babcock & Wilcox Co., Alliance Research Center, 1562 Beeson Rd., Alliance, Ohio 44601; or Anthony Misercola, Hooker Chemical Co., P.O. Box 344, Niagara Falls, N.Y. 14302.

DIELECTRICS AND INSULATION DIVISION

General Session

A General Session is planned at this meeting. Suggestions and inquiries for papers pertaining to dielectrics and insulators should be directed to: B. H. Vromen, IBM Corp., Dept. 265, Bldg. 300-100, Hopewell Junction, N.Y. 12533.

DIELECTRICS AND INSULATION AND ELECTRONICS DIVISIONS

Etching

This symposium is directed toward current advances in electronic materials etching and an exchange of ideas on the theory and practice of etching for pattern definition. Insulators, semiconductors, and metals are included, and gaseous as well as aqueous etching. Contributed papers are solicited on such topics as:

1. Etch rates, kinetics, and reactions mechanisms; autocatalysis, induction periods, and inhibition.
2. Gas-phase etching and etch phenomena, including reactive plasma, ion milling, reactive sputtering, and equipment therefor; etch stops.
3. Aqueous etching including the chemistry and scientific basis of etch formulations, electrochemistry, electrolytic etching, circuit pattern potentials and sensitivity in conductor etching and equipment.
4. Novel etches, alternative etches to meet problems in environmental effects, safety, and chemical shortages.
5. Factors influencing contours and topography of etched patterns, etch step profiles, etch mask adherence, and the associated photoresist technology.
6. Resistant spots, etch residues, and alloy or compound etcning.
7. The influence of film deposition techniques on etching characteristics, including orientation dependence.

Each presentation including discussion will be scheduled for 25 min. Longer times can be arranged if requested at the time the short abstract is submitted. A symposium volume may be published if sufficient interest develops. Suggestions and inquiries should be directed to the Symposium Co-Chairmen: Myron J. Rand, Bell Laboratories, 555 Union Blvd., Allentown, Pa. 18103; or Henry G. Hughes, Motorola, SPD, M/S B136, 5005 East McDowell Rd., Phoenix, Ariz. 85008.

DIELECTRICS AND INSULATION, ELECTRONICS, AND ELECTROTHERMICS AND METALLURGY DIVISIONS

Control and Utilization of Defects in Nonmetallic Solids

This jointly sponsored symposium will focus attention on the control and use of defects (point, line, and/or surface defects) in nonmetallic solids. Papers are solicited which involve ceramics and semiconductors used in all types of applications, such as in solid-state electrolytes, dielectric layers, light emitting diodes, photovoltaic devices, sensors, insulators, electrodes, etc. The emphasis will be on the definition of the number and type of defects and their relation to the end use of the material. Papers on the subject of gettering in semiconductor device technology are also solicited. This will include gettering on or in insulators as well as the semiconductor itself.

Suggestions and inquiries should be directed to the Symposium Co-Chairmen: J. Bruce Wagner, Jr., Northwestern University, Materials Research Center, Evanston, Ill. 60201; Donald M. Smyth, Lehigh University, Materials Research Center, Bethlehem, Pa. 18015; or Edward Nicollian, Bell Laboratories, 600 Mountain Ave., Murray Hill, N. J. 07974.

ELECTRONICS DIVISION

Semiconductors

General Session

A broad range of topics in semiconductor device fabrication and materials characterization will be treated in the Semiconductors General Session. Invited tutorial and review papers will be presented in several of the sessions. Original papers are requested on the following topics:

1. Characterization of processed semiconductor material; profiling and surface characterization techniques, process monitors and nondestructive testing, correlation with device characteristics, and cross-correlation between various techniques.
2. Doping of semiconductors; diffusion, ion implantation, segregation phenomena, crystalline defects, and radiation enhanced diffusion.
3. Device isolation and gettering techniques; yield, reliability, and density implications, leakage defects, and gettering models.
4. Compound and amorphous semiconductors; preparation, characterization, and device modeling.
5. Thin-film device technology; characterization, reliability, dual dielectrics, and processing effects on thin-film integrity.
6. Semiconductor processing technology; homo- and hetero-epitaxy, photolithography, metallization, interconnections, passivation, encapsulation, and large scale integration.

Suggestions and inquiries concerning the general sessions will be welcomed by: W. A. Keenan, IBM Corp., Dept. G34, Bldg. 966-1, P.O. Box A, Essex Junction, Vt. 05452.

Luminescence

Surface Properties of Phosphors and Photoconductors

Invited and contributed papers will address the problem of understanding the surface properties of powder, thin-film and single crystal luminescent and photoconductive materials by both physical and chemical methods.

Of particular interest will be which factors in the processing of these materials effect their surface properties and, consequently, their behavior in the systems in which they are used. These factors may include:

1. Methods of synthesis.
2. Treatments.
3. Coatings.

Papers concerning instrumental methods of characterizing surfaces of powders, thin films, and single crystals are also encouraged. These may include LEED, ESCA, ISS, Auger, SEM, and SIMS.

Suggestions and inquiries should be directed to the Symposium Chairman: Peter M. Plaksin, United States Radium Corp., P.O. Box 409, Hackettstown, N.J. 07840.

General Sessions

General sessions will be held around all topics of luminescence in inorganic solids, of which the following are only illustrative examples: phosphor efficiency, cathodo-luminescence mechanisms, energy transfer, thin-film electroluminescence, low voltage phosphors, luminescence in insulators and semiconductors, radioluminescence, radiation damage in phosphors, and performance of phosphors in CRT's display panels and other devices.

Twenty-five minutes will be allotted for each paper including discussions. Review or survey papers of a didactic nature requiring a longer time will also be considered. Suggestions and inquiries for papers should be directed to: Herbert N. Hersh, Zenith Radio Corp., Research Dept., Chicago, Ill. 60639.

General Materials and Processes

General Session

This session covers the general area of materials and processes which are not sufficiently electronic in nature to be included in the semiconductor general session or symposia. Follow-up papers in areas covered in recent symposia of the Electronics Division are encouraged as well as papers in new emerging areas of materials science and technology. Papers are solicited in areas such as magnetic bubbles, integrated optics, energy generation and storage, material preparation, device processing, and other areas of interest.

Suggestions and inquiries should be directed to: T. S. Plaskett, IBM Corp., Thomas J. Watson Research Center, P.O. Box 218, Yorktown Heights, N.Y. 10598.

ELECTRONICS AND ELECTROTHERMICS AND METALLURGY DIVISIONS

International Symposium on Solar Energy

Contributed papers for this symposium are solicited covering materials aspects of solar energy conversion. Topics pertinent to this symposium include: preparation and properties of monolithic and thin-film solar energy cells based on silicon, CdS-Cu S, GaAs, and other III-V and II-IV semiconductors; photogalvanic cells; selective absorbers for solar thermal applications; long term stability of solar hardware; storage for solar energy conversion systems; materials and energy utilization in solar system fabrication; and corrosion in liquid-cooled collectors and ocean thermal gradient systems.

It is planned that the symposium proceedings will be published and available for distribution at the time of the meeting. Final manuscripts will be required from the author by December 15, 1975.

Suggestions and inquiries should be directed to the Symposium Co-Chairmen: Joan B. Berkowitz, Arthur D. Little, Inc., Acorn Park, Cambridge, Mass. 02140; or I. Arnold Lesk, Motorola Inc., Central Research Laboratories, 6143 East Exeter Blvd., Scottsdale, Ariz. 85251.

Seventh International Conference on Electron and Ion Beam Science and Technology

The Seventh International Conference on Electron and Ion Beam in Science and Technology seeks papers which will permit the scheduling of the following sessions:

1. Physics of electron and ion beams and physics of beam material interactions.
2. New developments in the application of electron and ion beams considering both the field of instrumentation and production equipment.
3. Electron beam welding. It is our intention this year to include a special session on numerical control electron beam welding operations and possibly a round table discussion on the subject.
4. Electron and ion beams in microelectronics. Here we are seeking contributions in the following areas: Electron beams in devices and IC manufacture, electron beams in devices and IC production monitoring and control, sputtering processes, and ion implantation considering both systems and applications.
5. The success of our session on x-ray photolithography and the continuation of activities here make it desirable to again schedule a session on the subject.
6. Electron beams in material processing including production, equipment, and properties of electron beam processes materials.
7. Electron beams in recording, information storage, and retrieval.
8. Electron and ion beams in surface analysis.

Suggestions and inquiries should be directed to the Symposium Chairman: Robert Bakish, Bakish Materials Corp., 171 Sherwood Place, Englewood, N.J. 07631.

INDUSTRIAL ELECTROLYTIC DIVISION

Engineering Analysis and Scale-Up of Electrochemical Systems

The purpose of the symposium is to contribute to the understanding of industrial problems which involve current and potential distribution phenomena within electrochemical cells. Of special interest are those topics which emphasize industrial aspects of high-rate processes such as:

1. Scale-up, optimization, and over-all analysis of electrochemical systems.
2. New concepts in electrosynthesis.
3. Methods for early evaluation of electrochemical synthesis and related process routes.
4. Examples of laboratory to pilot plant to full scale case histories.
5. Current and potential distribution phenomena, especially modeling of electrochemical systems.
6. New developments in theoretical methods of analysis.
7. New design concepts for high-rate cells, including flow-through porous electrodes.
8. Effect of electric fields on liquid-liquid extraction processes.

Suggestions and inquiries should be directed to the Symposium Co-Chairmen: Richard Alkire, Dept. of Chemical Engineering, University of Illinois, Urbana, Ill. 61801; or Robert E. Visco, Western Electric Corp., 4500 South Laburnum Ave., Richmond, Va. 23231.

INDUSTRIAL ELECTROLYTIC AND ORGANIC AND BIOLOGICAL ELECTROCHEMISTRY DIVISIONS

Industrial Electro-Organic Processes

This joint symposium (under the guidance of D. N. Goens of the Industrial Electrolytic Division and M. M. Baizer of the Organic and Biological Electrochemistry Division) aims to bring together the electro-organic chemists and the electrochemical engineers to focus on the unique factors involved in development of organic electrochemical reactions. Examples of topics which may be included are:

1. Novel electrode and cell design.
2. Economic considerations.
3. Pilot plant operations (scale-up studies).
4. Potential industrial reactions.

A number of invited papers will be presented and contributed papers are solicited. Suggestions and inquiries should be directed to the Symposium Chairman: John H. Wagenknecht, Monsanto Co., Corporate Research Dept., 800 North Lindbergh Blvd., St. Louis, Mo. 63141.

ORGANIC AND BIOLOGICAL ELECTROCHEMISTRY DIVISION

Electrochemical Oxidations

This symposium reflects the rapidly growing quantity of research on anodic reactions in recent years. Papers relating to all aspects of electro-organic oxidations may be included, e.g.:

1. New reactions.
2. Effects of electrolytes.
3. Effects of solvents.
4. Effects of electrode material.
5. Stereochemistry.
6. Substituent effects.
7. Mechanistic studies by electroanalytical techniques.

A number of invited papers will be presented and contributed papers are solicited. Suggestions and inquiries should be directed to the Symposium Chairman: John H. Wagenknecht, Monsanto Co., Corporate Research Dept., 800 North Lindbergh Blvd., St. Louis, Mo. 63141.

General Session

In addition to the joint symposium with the Industrial Electrolytic Division on Industrial Electro-Organic Processes and the symposium on Electrochemical Oxidations, the Division's program will include a General Session.

Suggestions and inquiries should be directed to: M. Manuel Baizer, Monsanto Co., 800 North Lindbergh Blvd., St. Louis, Mo. 63141.

PHYSICAL ELECTROCHEMISTRY DIVISION

Spectroscopic Methods in Electrochemical Studies

This international symposium is intended to provide a comparison between the various spectroscopic methods which have recently become available to electrochemists as an aid to characterizing electrode surfaces and the electrode-solution interface. Sessions are planned covering the use of rapid scanning spectrometry, laser scattering from electrodes, photoemission techniques, electrode surface reflection spectroscopy, and the various high energy spectroscopies (ESCA, LEED/Auger, mass spectrometry, Mössbauer) in electrochemical studies. Emphasis will also be placed on the application of these methods to heterogeneous kinetic processes as well as homogeneous follow-up chemical events.

Many invited papers will be presented and contributed papers are solicited. Suggestions and inquiries should be sent to the Symposium Chairman: Nicholas Winograd, Dept. of Chemistry, Purdue University, West Lafayette, Ind. 47907.

General Session

In addition to the symposium on Spectroscopic Methods in Electrochemical Studies, the Division's program will include a General Session. Suggestions and inquiries should be directed to: James D. E. McIntyre, Bell Laboratories, 600 Mountain Ave., Murray Hill, N. J. 07974.

NEW TECHNOLOGY SUBCOMMITTEE, CORROSION, ELECTROTHERMICS AND METALLURGY, AND INDUSTRIAL ELECTROLYTIC DIVISIONS

International Symposium on Molten Salts

This symposium seeks to convene the leading active participants in molten salt research and technology from throughout the world to assess the current status of the field and to provide an outlook for the future. Sessions will contain keynote addresses, invited, and contributed papers.

Molten Salt Community-at-Large.—Thermodynamic and transport properties, physical property measurements, structure of highly concentrated ionic liquids, inorganic and organic reactions in molten salts, electroanalytical chemistry, catalysis, hydrous melts, information sources.

Corrosion Division.—Corrosion of metals, alloys, and nonmetallic solids; determination of corrosion product.

Electrothermics and Metallurgy Division.—Applications of mathematical modeling of metal extraction and purification processes in laboratory and plant scale studies; thermodynamics of alloys from galvanic cells.

Industrial Electrolytic Division.—Electrolytic processes for recovering and purifying metals; kinetics and mass transfer phenomena at phase boundaries and electrodes; preparation handling, transfer, and recovery of molten salts; applications in fume abatement, heat transfer, and crystal growth.

Suggestions and inquiries should be directed to the Symposium Co-Chairmen: (General) J. Paul Pemsler, Kennecott Copper Corp., 128 Spring St., Lexington, Mass. 02173; or (Corrosion) K. Nobe, University of California, School of Engineering and Applied Science, Los Angeles, Calif. 90024; or (Electrothermics and Metallurgy) D. R. Morris, Dept. of Chemical Engineering, University of New Brunswick, Fredericton, N.B., Canada; or (Industrial Electrolytic) N. E. Richards, Reynolds Metal Co., P.O. Box 191, Sheffield, Ala. 35661; or (Molten Salt Community-at-Large) J. Braunstein, Oak Ridge National Laboratory, Chemistry Div., P.O. Box X, Oak Ridge, Tenn. 37830.

NEW TECHNOLOGY SUBCOMMITTEE AND DIELECTRICS AND INSULATION AND ELECTRONICS DIVISIONS

Inorganic Dielectric Materials for Display and Storage Devices

It is intended to cover under this general title a number of sessions dealing with related materials, so that parallel sessions will be avoided. The individual sessions are as follows:

1. Chromic Materials.—Papers are solicited on the preparation and characterization of photochromic, cathodochromic, electrochromic, and chromic energy conversion materials. Papers should be sent to: P. N. Yocom, RCA Laboratories, Princeton, N.J. 08540.

2. Ceramic and Glass Materials for Display Devices.—This symposium will be devoted to the study of nonmetallic inorganic materials employed in electronic display devices and their packaging. Emphasis will be placed on the dielectric properties of such materials. Of particular interest are conventionally formulated glasses and ceramics now widely used in the electronics industry as dielectric and sealing materials. Suggested topics are: electric properties of multilayer ceramic structures, mechanism of conduction in dielectric materials in display devices, dielectric properties as a function of composition of glasses, characterization of dielectric films in display devices, effect of hostile environment on dielectric materials and seals, and surface and interfacial properties of dielectric layers with substrates or metallic conductors.

Keynote papers from invited speakers will be presented and contributed papers are solicited. Suggestions and inquiries should be directed to the appropriate chairman. Those papers primarily concerned with the chemical aspects of dielectric materials should go to: R. G. Frieser, IBM Corp., East Fishkill Facility, Dept. 365, Bldg. 330-145, Hopewell Junction, N.Y. 12533. Papers which have as their main interest the physical aspects of dielectrics should be sent to: L. D. Locker, Airpax Electronics, Corporate Offices, P.O. Box 8488, Fort Lauderdale, Fla. 33310.

3. Dielectrics for Image and Hologram Storage and Display.—Papers are solicited on hologram storage in lithium niobate, SBN, and similar materials; image storage and display using PLZT, Pockel's effect readout devices, and on related effects and devices. It is intended to include papers on the basic physical processes and on materials' properties, as well as papers on specific devices or potential device applications. Inquiries and suggestions should be directed to: Lawrence Young, Dept. of Electrical Engineering, University of British Columbia, Vancouver B.C., Canada. Papers on PLZT materials, their characterization and performance, should be submitted to: C. E. Land, Sandia Laboratories, Div. 5133, Albuquerque, N.M. 87115.

75-Word Abstract Form

(Deadline for receipt—December 1, 1975)

WASHINGTON, D.C., MEETING—MAY 2-7, 1976

Submit to: The Electrochemical Society, Inc.
P.O. Box 2071, Princeton, N.J. 08540

Schedule for .... of ....
Symposium ECS Division

Abstract No. ....
(do not write in this space)

(Title of paper) ....

....

(Authors) (Underline name of author presenting paper) ....

....

(Business Affiliation and Address) ....

....

....
(ZIP Code) (Tel. No.)

(Type abstract in this area—double spaced.)

Do you require any audiovisual equipment?
- ☐ 35 mm (2 x 2 in.) slide projector
- ☐ vugraph
- ☐ other (specify)

Is a full length paper on this work to be submitted for Society Journal publication?
☐ Yes ☐ No

Papers presented before a Society technical meeting become the property of the Society and may not be published elsewhere without written permission of the Society. Papers presented at Society technical meetings must be authored by a member or sponsored by an active member.

....
Insert name of Society member author or sponsor

THE ELECTROCHEMICAL SOCIETY PATRON MEMBERS

Bell Telephone Laboratories, Inc.
Murray Hill, N.J.

Dow Chemical Co.
Inorganic Chemicals Dept., Midland, Mich.

General Electric Co.
Battery Business Section, Gainesville, Fla.
Chemical Laboratory, Knolls Atomic Power Laboratory, Schenectady, N.Y.
Electronic Capacitor & Battery Dept., Irmo, S.C.
Lamp Div., Cleveland, Ohio
Materials & Process Laboratory, Large Steam Turbine-Generator Dept., Schenectady, N.Y.
Research and Development Center, Physical Chemistry Laboratory & Power Systems Laboratory, Signal Processing & Communication Laboratory, Schenectady, N.Y.
Semiconductor Products Dept., Syracuse, N.Y.

The International Nickel Co., Inc.
New York, N.Y.

Olin Corporation
Chemicals Div., Research Dept., New Haven, Conn.

Philips Research Laboratories
Eindhoven, Holland

Union Carbide Corp.
Battery Products Div., Corporate Research Dept., New York, N.Y.

Westinghouse Electric Corp.
Electronic Tube Div., Elmira, N.Y.
Lamp Div., Bloomfield, N.J.
Semiconductor Div., Youngwood, Pa.
Research Laboratories, Pittsburgh, Pa.
K. W. Battery Co., Westinghouse Subsidiary, Skokie, Ill.

THE ELECTROCHEMICAL SOCIETY SUSTAINING MEMBERS

Airco Speer Carbon-Graphite
St. Marys, Pa.

Allied Chemical Corp.
Industrial Chemicals Division
Solvay, N.Y.

Aluminum Co. of America
New Kensington, Pa.

Aluminum Co. of Canada, Ltd.
Montreal, P.Q., Canada

American Gas & Chemicals, Inc.
New York, N.Y.

American Metal Climax, Inc.
New York, N.Y.

American Smelting and Refining Co.
South Plainfield, N.J.

AMP Incorporated
Harrisburg, Pa.

Analog Devices, Inc.
Norwood, Mass.

Applied Materials, Inc.
Santa Clara, Calif.

BASF Wyandotte Corporation
Wyandotte, Mich.

Beckman Instruments, Inc.
Fullerton, Calif.

Bell-Northern Research
Ottawa, Ont., Canada

Bethlehem Steel Corp.
Bethlehem, Pa.

Boeing Co.
Seattle, Wash.

The Borg-Warner Corp.
Roy C. Ingersoll Research Center
Des Plaines, Ill.

Brown, Boveri & Co., Ltd.
Research Center
Baden, Switzerland

Canadian Industries Ltd.
Montreal, P.Q., Canada

Carborundum Co.
Niagara Falls, N.Y.

Cominco Ltd.
Trail, B.C., Canada

Corning Glass Works
Corning, N.Y.

Crawford & Russell Inc.
Stamford, Conn.

Diamond Shamrock Corp.
Painesville, Ohio

E. I. du Pont de Nemours and Co.
Central Research Department
Wilmington, Del.

Eastman Kodak Co.
Rochester, N. Y.

Electrode Corporation
Chardon, Ohio

Eltra Corp.
Prestolite Div., Toledo, Ohio
C&D Batteries, Conshohocken, Pa.

Engelhard Minerals & Chemicals Corp.
Murray Hill, N.J.

ESB Inc.
Philadelphia, Pa. (2 memberships)

Esso Research and Engineering Co.
Engineering Technology Div.
Florham Park, N.J.

SUSTAINING MEMBERS (CONTINUED)

Ever Ready Co. (Holdings) Ltd.
Whetstone, London, England

Exmet Corporation
Bridgeport, Conn.

Fairchild Camera & Instrument Corp.
Research and Development Laboratory
Palo Alto, Calif.

Falconbridge Nickel Mines Ltd.
Thornhill, Ont., Canada

FMC Corp.
Inorganic Chemicals Div.
Buffalo, N.Y.

Foote Mineral Co.
Exton, Pa.

Ford Motor Co.
Dearborn, Mich.

GAF Corporation
Inorganic Chemicals Department
Glens Falls, N.Y.

General Motors Corporation
Delco Electronics Div., Kokomo, Ind.
Delco-Remy Div., Anderson, Ind.
Research Laboratories Div., Warren, Mich.

Globe-Union, Inc.
Milwaukee, Wisc.

GTE Laboratories
Waltham, Mass.

B. F. Goodrich Chemical Co.
Cleveland, Ohio

Gould Inc.
Gould Laboratories, Rolling Meadows, Ill.
Gould Laboratories—Energy Research, St. Paul, Minn.
Gould Laboratories—Materials Research, Cleveland, Ohio

Great Lakes Carbon Corp.
New York, N.Y.

Harshaw Chemical Co.
Cleveland, Ohio (2 memberships)

Hill Cross Co., Inc.
West New York, N.J.

Honeywell, Inc.
Power Sources Center
Horsham, Pa.

Hooker Chemical Corp.
Niagara Falls, N.Y. (2 memberships)

HP Associates
Palo Alto, Calif.

Hughes Research Laboratories
Div. of Hughes Aircraft Co.
Malibu, Calif.

International Business Machines Corp.
New York, N.Y.

Kaiser Aluminum & Chemical Corp.
Pleasanton, Ca.

Kawecki Berylco Industries, Inc.
Boyertown, Pa.

Kennecott Copper Corp.
New York, N.Y.

Kerr-McGee Corporation
Technical Center
Oklahoma City, Okla.

Arthur D. Little, Inc.
Cambridge, Mass.

Mallory Battery Company
Tarrytown, N.Y. (2 memberships)

Marathon Battery Co.
Cold Spring, N.Y.

The Marstolin Group
Hamilton, Bermuda

Matsushita Electric Industrial Co., Ltd.
Osaka, Japan

Metallurgical Research Center of Iran
Tehran, Iran

Microwave Associates, Inc.
Burlington, Mass.

Molybdenum Corporation of America
New York, N.Y.

Monsanto Company
St. Louis, Mo.

Motorola Inc.
Phoenix, Ariz.

M&T Chemicals Inc.
Detroit, Mich.

National Steel Corp.
Weirton, W. Va.

NL Industries, Inc.
New York, N.Y.

OKI Electric Industry Co., Ltd.
Tokyo, Japan

Olin Corporation
Metals Research Laboratories
New Haven, Conn.

Owens-Illinois Glass Co.
Toledo, Ohio

Phelps Dodge Refining Corp.
Maspeth, N.Y.

Philips Laboratories. Inc.
Briarcliff Manor, N.Y.

PPG Industries, Inc.
Chemical Div.
Pittsburgh, Pa.

Princeton Applied Research Corp.
Princeton, N.J.

RCA Corporation
Electronic Components and Devices
Lancaster, Pa.

Republic Foil
National Aluminum
A Unit of
National Steel Corp.
Danbury, Conn.

Reynolds Metals Co.
Reduction Research Div.
Sheffield, Ala.

Rockwell International
El Segundo, Calif.

SAFT America, Inc.
Valdosta, Ga.

Signetics Corp.
Sunnyvale, Ca.

Sobin Chemical Co.
Orrington, Maine

Sprague Electric Co.
North Adams, Mass.

Stackpole Carbon Co.
St. Marys, Pa.

Standard Telecommunication Laboratories Ltd.
Essex, England

Stauffer Chemical Co.
Dobbs Ferry, N.Y.

Teletype Corp.
Skokie, Ill.

Texas Instruments Inc.
Attleboro, Mass.
Dallas, Texas

Tokyo Shibaura Electric Co., Ltd.
Toshiba Research and
Development Center
Kawasaki, Japan

Udylite Corp.
Detroit, Mich. (4 memberships)

United States Steel Corp.
Research Laboratory
Monroeville, Pa.

Varian Associates
Palo Alto, Calif.

Wacker Chemitronic
Burghausen, Germany

Xerox Corporation
Rochester, N.Y.

Yardney Electric Division
Pawcatuck, Conn.

Zenith Radio Corp.
Chicago, Ill.

20.W.9 25 18